M-OSRP ANNUAL REPORT

Qiang Fu, Xinglu Lin, Fang Liu, Chao Ma, Arthur B. Weglein, Jing Wu, Jinlong Yang, and Yanglei Zou

Report 2015, Jun 2015

Corporate Sponsors

Anadarko ..... Yafei Wu
BGP/CNPC ..... Shaohua Zhang, Lei Na
BP ..... Imtíaz Ahmed
Chevron ..... Sam Kaplan
ConocoPhillips ..... Haiyan Zhang
Devon Energy ..... Alex Bridge
Encana ..... David Bonar
Hess ..... Scott Morton
IBM ..... Michael Perrone, Tom McClure
Ion ..... Jacques Leveille
Kuwait Oil Company ..... Adel El-Emam
Pemex ..... Pamela Diaz
Petrobras ..... Paulo M. Carvalho, Neiva Zago
PGS ..... Nizar Chemingui
Repsol ..... Gladys Gonzalez, Francisco Ortigosa
Saudi Aramco ..... Yi Luo, Tim Keho
Statoil ..... Hongbo Zhou, Lasse Amundsen
Total ..... Bertrand Duquet
WesternGeco ..... Clement Kostov

Federal Support

DOE Basic Sciences award DE-FG02-05ER15697 ..... Nick Woodward
NSF-CMG award DMS-0327778 ..... Henry A. Warchall

M-OSRP Personnel

Faculty, Adjunct Faculty, Research Faculty, Postdocs

Lasse Amundsen (Statoil) ..... Adjunct Professor (Physics)
Douglas J. Foster (ConocoPhillips) ..... Adjunct Professor (Physics)
Kristopher A. Innanen (Associate Professor, University of Calgary) .. Adjunct Professor (Physics)
Robert G. Keys (ConocoPhillips) ..... Adjunct Professor (Physics)
Jacques Leveille (Ion) ..... Adjunct Professor (Physics)
Fang Liu ..... Research Assistant Professor (Physics)
Ken H. Matson (Shell) ..... Adjunct Associate Professor (Physics)
James D. Mayhan ..... Post Doctoral Fellow (Physics)
Mark Meier (ExxonMobil) ..... Adjunct Professor (Physics)
Jon Sheiman (Shell) ..... Adjunct Professor (Physics)
Robert H. Stolt (ConocoPhillips) ..... Adjunct Professor (Physics)
T. Hing Tan (Shell) ..... Adjunct Professor (Physics)
Arthur B. Weglein ..... Cullen Professor (Physics)
Daniel Whitmore (PGS) ..... Adjunct Professor (Physics)
Jinlong Yang ..... Post Doctoral Fellow (Physics)

Graduate Students (PhD candidates)

Qiang Fu ..... Physics
Xinglu Lin ..... Physics
Chao Ma ..... Physics
Jing Wu ..... Physics
Yanglei Zou ..... Physics

Recent Alumni

Hichem Ayadi ..... Physics
Andre Ferreira[2] ..... Geosciences
Zhiqiang Guo ..... Geosciences
Wilberth Herrera ..... Physics
Shih-Ying Hsu ..... Physics
Xu Li ..... Physics
Hong Liang ..... Physics
Jose Eduardo Lira[2] ..... Geosciences
Fang Liu ..... Physics
James D. Mayhan ..... Physics
Francisco Miranda ..... Physics
Mozhdeh Niazmand ..... Physics
Adriana Citlali Ramírez ..... Physics
Simon A. Shaw ..... Geosciences
Lin Tang ..... Physics
Zhiqiang Wang ..... Physics
Jinlong Yang ..... Physics
Haiyan Zhang ..... Physics
Jingfeng Zhang ..... Physics

Administrative Support

Jennifer Chin-Davis ..... Associate Director, Physics Department
Andrew Fortney ..... Computer/IT Support
Chris Watts ..... Webmaster/NSM IT
Andrea Arias-Rodriguez ..... NSM IT
Anne Thomas ..... Copy Editor

[2]Petrobras, Brazil

2015 — TABLE OF CONTENTS

INTRODUCTION

PART I

Claerbout III imaging for one way and two way wave migration: a new and more capable migration method for RTM:

Multiples: part 3: Beyond internal multiple attenuation: algorithms for eliminating internal multiples and spurious events, providing essential and necessary added value when there are numerous generators and interfering and proximal primaries and multiples

Amplitude analysis: Direct inverse solutions and a direct comparison with iterative linear inverse (behind current AVO/FWI)

Mission-Oriented Seismic Research Program

2015 Annual Technical Review and Meeting

UH Hilton
4800 Calhoun Road, Houston, Texas, 77004
(On the UH Main Campus, entrance 4 (four), University Drive off Calhoun Road, below ground parking, at the hotel)

The meeting and breakfast will be in the Plaza Room and lunch in Shamrock A.
The dinner on Friday, June 5th at 6:00PM is in Shamrock A.

AGENDA

Thursday, June 4, 2015

7:30 AM Welcome, breakfast/reception

8:00 AM Technical Program begins: Meeting Overview

Green's theorem tutorial Part I: for wave field separation (separation of reference and scattered wave-fields, and for de-ghosting)
*Arthur B. Weglein**

9:00 AM Preprocessing in the PS space for on-shore seismic processing: removing ground roll and ghosts without damaging the reflection data
*Jing Wu**

9:30 AM Preprocessing in displacement space for on-shore seismic processing: removing ground roll and ghosts without damaging the reflection data
*Jing Wu**

9:50 AM Morning break

10:15 AM Green's theorem tutorial Part II: for wave field prediction: imaging conditions, one-way and two-way wave equation migration for a more effective and capable RTM (Claerbout III imaging for migrating in a volume with two way propagating waves)
(Glossary of imaging conditions: in our usage, Claerbout imaging I is the exploding reflector model, Claerbout II imaging , is the space and time coincidence of up and downgoing waves, and Claerbout III refers to predicting a coincident source and receiver experiment at depth at time equals zero.)
These migration methods require a velocity model.
*Arthur B. Weglein**

The Clearbout II imaging principle resides behind all current leading edge RTM methods used in industry. Benefits of the new Claerbout III imaging for two way propagating waves (RTM): (1) provides added-value and advantages for both structural determination and amplitude analysis in migration and (2) provides clarity on the role of primaries and multiples in imaging and migration

11:00 AM Claerbout II imaging condition (current leading edge RTM) and III for two way migration, backscatter artifacts and its removal (for example, Faqi Liu et.al, 2011; Crawley and Whitmore, 2012)
*Qiang Fu**

12:00 PM Lunch

Claerbout III imaging for one way and two way wave migration: a new and more capable migration method for RTM:

1:00 PM Analysis and comparison of Claerbout III imaging condition for one way waves(pre-stack Stolt FK migration) and its asymptotic approximation, that is, Kirchhoff migration
Yanglei Zou, Qiang Fu, Chao Ma, Jing Wu and Arthur B. Weglein*

1:30 PM Analysis and comparison of Claerbout II imaging (current leading edge RTM) for one way propagating waves and Claerbout III imaging for one way propagating waves
*Yanglei Zou**

2:00 PM Afternoon break

2:30 PM Claerbout III imaging for structure and amplitude analysis beneath a reflector
*Qiang Fu**

3:10 PM Claerbout III imaging for two way propagating waves provides a clear and definitive response to the role of primaries and multiples in imaging and inversion: Multiples: signal or noise?
*Arthur B. Weglein**

Only primaries are required for imaging and inversion, but when there is inadequate acquisition of primaries, multiples can be used to provide an approximate image of an unrecorded primary

3:40 PM A clear example of using multiples to enhance seismic imaging -- providing an approximate image of an unrecorded primary
*Chao Ma**

4:10 PM Multiples can be useful (at times) to enhance imaging, by providing an approximate image of an unrecorded primary, but it's always primaries that are migrated or imaged

What's the big picture, bottom line and our seismic imaging and inversion strategy with respect to primaries and multiples----the updated seismic processing chain
*Arthur B. Weglein**

Friday, June 5, 2015

7:30 AM Breakfast/reception/welcome

8:30 AM A tutorial on the inverse scattering series: distinct isolated task subseries for removing free surface and internal multiples
*Arthur B. Weglein**

Multiples: part I: Background/Introduction/Update

9:15 AM Multiple attenuation: recent progress, and a plan to address open, prioritized and pressing issues and challenges
*Arthur B. Weglein**

10:00 AM Morning Break

10:15 AM Reviewing the historic Saudi Aramco onshore ISS internal multiple attenuation examples
*Qiang Fu**

10:40 AM Inverse scattering series internal multiple attenuation in an absorptive dispersive earth, without knowing, needing or estimating elastic or inelastic subsurface properties: update with pre-stack data examples
*Jing Wu**

Multiples: part II: Advances to enhance the effectiveness of free surface multiple elimination and internal multiple attenuation algorithms

11:00 AM The impact of accommodating the source radiation pattern on the inverse scattering series free-surface multiple elimination algorithm on data with interfering or proximal primaries and multiples
*Jinlong Yang**

11:30 AM Lunch

12:30 PM The significance of incorporating a 3-D point source in the inverse scattering series free-surface multiple elimination algorithm for a 1-D subsurface
*Xinglu Lin**

1:00 PM Incorporating a 3-D point source in the inverse scattering series internal multiple attenuation algorithm for a 2-D subsurface
*Xinglu Lin**

1:20 PM Afternoon Break

Multiples: part III: Beyond internal multiple attenuation: algorithms for *eliminating* internal multiples and *spurious events*, providing essential and necessary added value when there are numerous generators and interfering and proximal primaries and multiples

1:35 PM A new Inverse Scattering Series (ISS) internal-multiple-attenuation algorithm that predicts the accurate time and approximate amplitude of the first-order internal multiples and *addresses spurious events*: Analysis and Tests in 2D
*Chao Ma**

2:10 PM An internal-multiple *elimination* algorithm for all first-order internal multiples for a 1D earth
*Yanglei Zou**

2:45 PM Inverse scattering series depth imaging: direct depth imaging without a velocity model, the Marmousi model tests, and *a plan for a documented code delivery this year (2015)*
Fang Liu and Arthur B. Weglein*

Amplitude analysis: Direct inverse solutions and a comparison with iterative linear inverse (the latter resides behind current AVO/FWI)

3:20 PM A direct inverse solution for AVO/FWI parameter estimation objectives
*Arthur B. Weglein**

3:50 PM A first comparison of the inverse scattering series non-linear inversion and the iterative linear inversion for parameter estimation
Jinlong Yang and Arthur B. Weglein*

SUMMARY

4:15 PM Summary of M-OSRP proprietary code delivery to-date and schedule of on-going code development and delivery
*Jim Mayhan**

Primaries and multiples: the effective removal of all multiples remains an open issue and challenge- a strategy, plan, recent progress and steps towards delivering the next and necessary level of effectiveness and capability
*Arthur B. Weglein**

5:15 PM Meeting adjournment
6:00 PM Reception and dinner

Introduction: 2015 M-OSRP Annual Report

Arthur B. Weglein

The industry downturn and M-OSRP

We recognize that with the current downturn in the petroleum industry that budgets and expenditures are examined and scrutinized, and naturally enough that process is also taking place within M-OSRP. Most importantly, it is incumbent upon us, more than ever, to describe what benefit, delivery and value derived, and derives, from your support and sponsorship of M-OSRP. The 2015 Annual Technical Review and the Annual Report are part of how we communicate the value delivered to-date, our delivery this year, and our plans going forward.

The Annual Report is organized to sync with the Annual Technical Review

The 2015 M-OSRP Annual Report documents the technical progress and deliverables this past year, and describes our near term and longer term priorities, plans and deliverables.

A memory stick with this report will be distributed at the Annual Technical Review June 4, 5, 2015 and will be express-mailed to those sponsors, at great distances from Houston, who could not attend.

The way the Annual Report is organized allows those attending the Annual Technical Review to see the Reports, submitted and published papers and SEG Abstracts in the order of the presentations on the Agenda. The Agenda of the Annual Technical Review can be found on pages 1-4 of this Report.

The Annual Technical Review on June 4,5 will be video recorded with synced slides and will be available as a link on the M-OSRP website, two weeks after the meeting.

As part of our Annual Reporting, below please find links to video recordings with synced slides with: (1) a March 9, 2015 M-OSRP executive summary overview and (2) two key-note invited presentations at international SEG workshops/conferences this past year that supplement and complement the Report and Technical Review.

Executive summary video: the M-OSRP delivered added value and documented E&P impact, March 9, 2015

http://mosrp.uh.edu/news/mar-9-exec-summary-video

Keynote address, Abu Dhabi, March 31st, 2015 presented at the SEG **FWI**, Workshop, Filling the gaps in **Abu-Dhabi** "A direct inversion method for FWI/AVO objectives"

http://mosrp.uh.edu/news/mar-30-apr-1-fwi-workshop-abu-dhabi

Key-note address, Kuwait Oil Company SEG Workshop, December 3, 2014, "**Multiples: signal or noise?**"

http://mosrp.uh.edu/news/a-b-weglein-nov-2014-m-osrp-executive-summary-and-2-video-for-kuwait-oil-company-seg-workshop-december-1-3-2014

The organization of the Annual Report

The Report has two parts: in the first part there are Green's theorem methods for: (1) wave separation and (2) wave field prediction. This year, the former, **for wave field separation**, provides an advance for on-shore preprocessing for predicting and **separating the reference wave (including ground roll) from reflection data**, without damaging the reflection data.

The Green's theorem for **wave field prediction** provides **a fundamentally new approach and method for RTM**, with superior structural imaging and amplitude analysis capability compared to the current leading-edge methods for RTM employed in industry today. This new method for imaging in a volume with two way propagating waves, **also provides a definitive and unequivocal conclusion to the role of primaries and multiples in migration and inversion.**

The new RTM method, that we are reporting on, fits within current, conventional, mainstream migration thinking, and hence requires a velocity model. For this project, we seek to demonstrate value and generate interest with our sponsors in the promise and relevant added value that it represents. We plan to take this project a few more steps to show its potential with structural complexity, with, for example, rapidly undulating reflectors and pinch-outs.

In the second part of this report, we describe the outstanding open issues and pressing challenges in offshore and on-shore **multiple removal** — and our strategy, progress and plans — and our schedule of delivery of the next generation of required higher effectiveness and capability.

We also describe progress on the **inverse scattering series direct depth imaging** without a velocity model and the plan to add a well-documented code to our sponsor's seismic imaging toolbox this year (2015).

The direct inversion for parameter estimation from the inverse scattering series is reviewed, and a first clear and useful comparison with iterative linear inversion (that resides behind AVO and FWI) is described and analyzed. There are many significant and substantive differences between the direct solution for changes in earth mechanical properties provided from the inverse scattering series and iterative linear methods. Please see the video in the link above shown at the SEG Abu Dhabi Workshop. In this specific study in this report we examine, analyze and compare these approaches under the simplest possible situation, a plane wave normally incident on an acoustic medium, with one reflector and where only the velocity changes. That allows us to isolate one difference in these approaches, and where there is agreement on the data requirements. It is a pure and perfect test of the algorithms when that's the only issue. The inverse scattering subseries for parameter estimation always converges, whereas the iterative linear inverse does not, and when they both converge the ISS converges much faster. Under more realistic and important circumstances the differences are much more serious and substantive, but there is never a chance the iterative linear updating and the direct inverse derived from the inverse scattering series are equivalent.

In the general area of amplitude analysis, we plan to work together with Doug Foster to determine the exploration, appraisal and development circumstances where a more accurate parameter estimation provides relevant added-value, for example, for drill, no-drill decisions in frontier exploration, and optimizing development drilling.

Our project on 4D applications will be a central part of our plans going forward.

Multiples: the stand-alone capability delivered by M-OSRP has become the industry standard and widely recognized and indicated choice under the most daunting and challenging circumstances

M-OSRP's delivery of the distinct inverse scattering series free surface multiple eliminator and the internal multiple attenuator has provided stand-alone industry wide capability that's documented in the March 9th, 2015 executive summary video with a selection of published papers from CGG, Western Geco/Schlumberger, and PGS, among service companies, and a plethora of oil companies with 2D and 3D field data examples. The one characteristic that separates the multiple attenuation methods that only M-OSRP pioneers, develops and delivers from all others, is that it is direct and doesn't require subsurface information. What once made many uncomfortable and was considered irrational, controversial and difficult to believe has now become fully mainstream and conventional.

Multiples: the challenge today, provide the next generation of significantly higher capability in removing multiples without damaging proximal or interfering primaries

There are many offshore and on-shore areas and plays where the nature of the problem with multiples is fundamentally beyond our industry's current collective capability to effectively address.

The main near term focus for M-OSRP will be to deliver the next level of multiple removal capability, internal multiple elimination, for circumstances where primaries and multiples are proximal and interfering, without damaging primaries. That next generation of capability will be designed specifically for the most complex and daunting off-shore and on-shore plays. That goal will be reached, and that capability will be delivered, directly and without needing or requiring any subsurface information.

M-OSRP is uniquely qualified, by its history and experience, to deliver that next level of effectiveness — and thereby to open E&P opportunities and plays that are currently precluded as off-limits or unreasonable high risks in the most difficult and forbidding off-shore and on-shore arenas.

We are grateful for your encouragement and support, and we will continue to work hard and effectively to earn and deserve your confidence and trust. M-OSRP has been, and remains, a good investment for research, delivering new high impact seismic capability, and educating, mentoring and training students.

We look forward to seeing you at our technical review June 4, 5 at the UH Hilton.

Best regards,

Art

Arthur B. Weglein

May 27, 2015

Preprocessing in the PS space in preparation for onshore seismic processing: removing ground roll and ghosts without damaging the reflection data

Jing Wu & Arthur B. Weglein

Abstract

Prerequisites to processing, such as the removal of the reference wave and the ghosts, are important preparation for seismic processing of onshore data. This paper derives an elastic Green's theorem-based wave-separation algorithm for data in the PS space. Application of the algorithm presented in this paper can effectively remove both the reference waves (including the direct wave and the surface wave) and the ghosts. The method is tested on a layered elastic-earth model. The results indicate that it is effective for reducing the ground roll and ghosts without harming the upgoing reflection, in preparation for onshore processing.

1 Introduction

Onshore seismic exploration and processing seek to use reflection data (the scattered wavefield) to detect the subsurface information. The measured total wavefield consists of the reflection data and the reference wavefield, which contains the surface wave/ground roll; hence, it is necessary to separate the reference wave and the scattered wave. Typically, filtering methods are employed to remove the reference wave, particularly the ground roll, but that occurs at the expense of damaging the reflection data when ground roll is interfering with the scattered wavefield. As a flexible and useful tool, Green's theorem provides methods that can separate the reference wave from the reflection data without damaging the reflection data. Application of these methods represents unique advantages for offshore plays (e.g., Weglein et al., 2002; Zhang, 2007; Mayhan et al., 2011; Mayhan and Weglein, 2013; Tang et al., 2013; Yang et al., 2013).

For onshore plays, a key problem is the complex and laterally varying near surface. Our study starts with a simpler example by assuming that the space just below the free surface is homogeneous and known but the earth below the measurement surface is unknown and heterogeneous. Wu and Weglein (2014) derive the elastic Green's theorem reference and scattered wave separation algorithm for data in the PS space, and they successfully test the algorithm on an initial model without subsurface reflectors. In this paper, for a more realistic situation, we also add one reflector in the tested model so that the measured data contain both the reference wave and the scattered wave.

In addition, for buried sources and receivers, the reflection data contain not just upgoing waves but also ghosts, whose existence can cause notches in the spectrum. Thus, after the reflection data have been obtained, removal of the ghosts from the reflection data is another prerequisite. In this study, we will assume that the source is located slightly above the air/earth surface (could be infinitely close, or on the air/earth surface) and the receivers are slightly beneath the air/earth surface. Therefore, there are receiver ghosts but no source ghosts in our study. Green's theorem can also be applied for deghosting, by taking a whole-space homogeneous elastic medium as the reference medium. A numerical test is shown for examining the accuracy of the deghosting algorithm.

2 Background of 2D elastic wave theory

We derive the wave-separation method for onshore application, starting with the elastic formulation. For convenience, the basis is changed from $\mathbf{u} = \begin{pmatrix} u_x \\ u_z \end{pmatrix}$ to $\mathbf{\Phi} = \begin{pmatrix} \phi^P \\ \phi^S \end{pmatrix}$. $\mathbf{u}$ represents the displacement, consisting of x and z components; $\mathbf{\Phi}$ has P-wave and S-wave components.

In the PS space, the basic wave equations (Weglein and Stolt, 1995; Zhang, 2006) are

$$\hat{\mathbf{L}}\mathbf{\Phi} = \mathbf{F}, \tag{1}$$

$$\hat{\mathbf{L}}\hat{\mathbf{G}} = \delta, \tag{2}$$

$$\hat{\mathbf{L}}_0\mathbf{\Phi}_0 = \mathbf{F}, \tag{3}$$

$$\hat{\mathbf{L}}_0\hat{\mathbf{G}}_0 = \delta, \tag{4}$$

where $\hat{\mathbf{L}}$ and $\hat{\mathbf{L}}_0$ are the differential operators that describe the wave propagation in the actual medium and the reference medium, respectively; $\mathbf{F}$ is the source term; $\hat{\mathbf{G}}$ and $\hat{\mathbf{G}}_0$ are the corresponding Green's function operators for the actual and reference media.

For a homogeneous medium,

$$\hat{\mathbf{L}}_0 = \begin{pmatrix} \bigtriangledown^2 + \frac{\omega^2}{\alpha_0^2} & \\ & \bigtriangledown^2 + \frac{\omega^2}{\beta_0^2} \end{pmatrix} = \begin{pmatrix} \hat{L}_0^P & \\ & \hat{L}_0^S \end{pmatrix}, \tag{5}$$

where α_0 and β_0 are P-wave velocity and S-wave velocity, respectively; and

$$\hat{\mathbf{G}}_0 = \begin{pmatrix} \hat{G}_0^P & 0 \\ 0 & \hat{G}_0^S \end{pmatrix}. \tag{6}$$

Eqn.12 and Eqn.A-8 are diagonal. However, in an actual inhomogeneous medium, $\hat{\mathbf{G}}$ is no longer a diagonal matrix, but has a form

$$\hat{\mathbf{G}} = \begin{pmatrix} \hat{G}^{PP} & \hat{G}^{PS} \\ \hat{G}^{SP} & \hat{G}^{SS} \end{pmatrix}. \tag{7}$$

For the superscripts, the right one represents the wave type of source side, whereas the left one represents the wave type of receiver side.

3 Green's theorem wave-separation algorithm in the PS space

3.1 Description of the model for wave separation

Transforming the elastic wave equations from displacement space to PS space, we have

$$\hat{\mathbf{L}}\mathbf{\Phi} = \mathbf{F},$$

$$\hat{\mathbf{L}}_0\hat{\mathbf{G}}_0 = \delta,$$

$$\hat{\mathbf{L}} = \hat{\mathbf{L}}_0 - \hat{\mathbf{V}}. \tag{8}$$

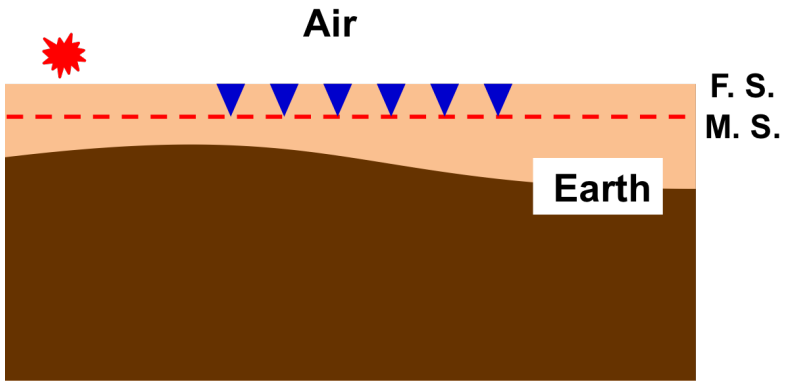

Figure 1: A generic model describing the onshore experiment. In this and subsequent figures, the blue triangles represent the receivers.

The basic forms of these equations are the same as those for the acoustic case. On the basis of the successful applications of the Green's theorem wave-separation to the acoustic case (e.g., Zhang, 2007; Mayhan et al., 2011), it is feasible to apply the Green's theorem wave-separation algorithm to the elastic world in a similar way.

As is seen in Figure 1, the model here consists of a half-space of air and a half-space of elastic earth. Receivers are buried in the earth, and the source is located slightly above the free surface (F.S.). The measurement surface (M.S.) can be infinitely close to the free surface, as in the case of the on-surface acquisition, or several meters below the free surface, as in the case of the buried-receiver acquisition. However, the receivers are coupled with the elastic medium in both situations.

3.2 Reference-wave and scattered-wave spearation in PS Space

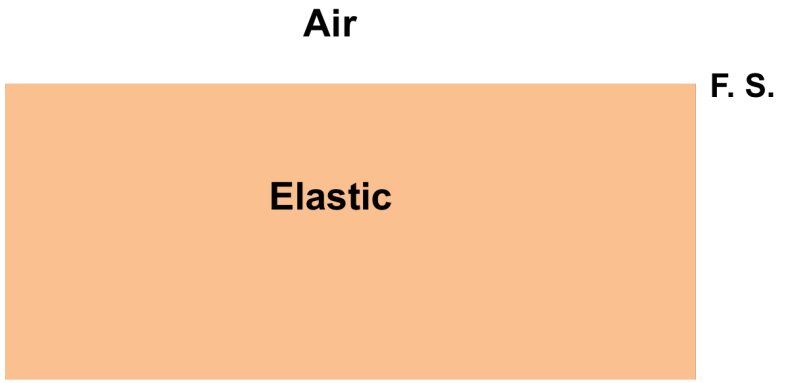

Figure 2: Reference medium for separation of the reference wave and the scattered wave.

The reference wave is the wave in the reference medium. In exploration seismology, it is useful for us to choose the reference medium to agree with the actual earth at and above the measurement surface. If we assume that the actual earth has known and homogeneous near-surface properties, the simplest reference medium can be chosen to be two discontinuous half-spaces, with homogeneous air over homogeneous elastic earth (see Figure 2). Two sources act on the reference medium (see

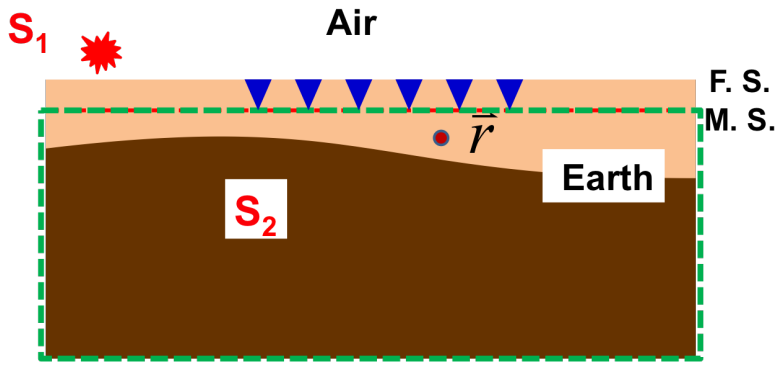

Figure 3: Reference wave separated out from the total wavefield with the surface integral along the closed surface marked by the dashed line, and the evulation point **r** is below the measurement surface.

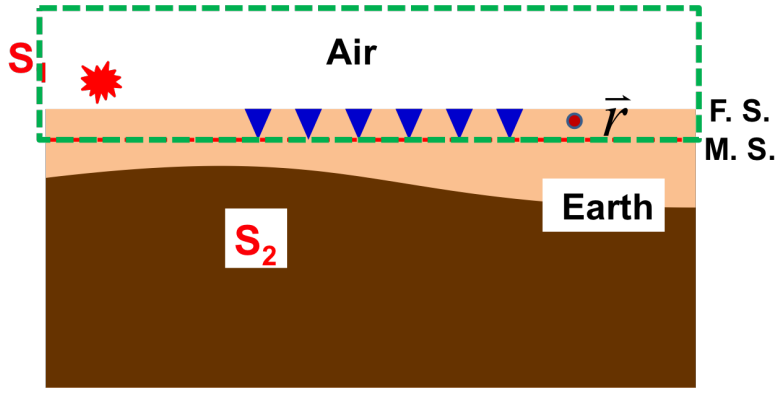

Figure 4: Scattered wave separated out from the total wavefield with the surface integral along the closed surface marked by the dashed line, and the evulation point **r** is ablove the measurement surface.

Figure 3): the active source (S_1), generating the reference wave, and the earth's heterogeneity, or passive source (S_2), generating the scattered wave.

Wu and Weglein (2014) have shown that, with the application of Green's theorem, a semi-infinite surface integral with the measurement surface as its upper boundary will separate out the reference wavefield $\mathbf{\Phi}_0$ from the total wavefield $\mathbf{\Phi}$, if the evaluation point $\mathbf{r}$ is inside the volume and below the measurement surface (see Figure 3). On the other hand, the surface integral with the measurement surface as its lower bounded will separate out the scattered wave $\mathbf{\Phi}_s$ from $\mathbf{\Phi}$, for $\mathbf{r}$ above the measurement surface (see Figure 4).

The Green's theorem-based formula for separating reference waves and scattered waves in the space-frequency (x, ω) domain is

$$\begin{aligned}&\oint \left(\mathbf{\Phi}(\mathbf{r}^{'}, \mathbf{r}_s, \omega) \cdot \nabla^{'} \hat{\mathbf{G}}_0(\mathbf{r}^{'}, \mathbf{r}, \omega) - \nabla^{'} \mathbf{\Phi}(\mathbf{r}^{'}, \mathbf{r}_s, \omega) \cdot \hat{\mathbf{G}}_0(\mathbf{r}^{'}, \mathbf{r}, \omega)\right) \cdot \hat{n} dS' \\ =&\begin{cases} \mathbf{\Phi}_0(\mathbf{r}, \mathbf{r}_s, \omega) & \mathbf{r} \text{ is below the M.S.,} \\ \mathbf{\Phi}_s(\mathbf{r}, \mathbf{r}_s, \omega) & \mathbf{r} \text{ is above the M.S.,} \end{cases}\end{aligned} \tag{9}$$

$\mathbf{\Phi}_0(\mathbf{r}, \mathbf{r}_s) = \begin{pmatrix} \Phi_0^P(\mathbf{r}, \mathbf{r}_s) \\ \Phi_0^S(\mathbf{r}, \mathbf{r}_s) \end{pmatrix}$,$\mathbf{\Phi}_s(\mathbf{r}, \mathbf{r}_s) = \begin{pmatrix} \Phi_s^P(\mathbf{r}, \mathbf{r}_s) \\ \Phi_s^S(\mathbf{r}, \mathbf{r}_s) \end{pmatrix}$, $\mathbf{\Phi}(\mathbf{r}, \mathbf{r}_s) = \begin{pmatrix} \Phi^P(\mathbf{r}, \mathbf{r}_s) \\ \Phi^S(\mathbf{r}, \mathbf{r}_s) \end{pmatrix}$, and Green's function $\hat{\mathbf{G}}_0(\mathbf{r}^{'}, \mathbf{r}, \omega)$ for the reference medium is

$$\begin{aligned}&\hat{\mathbf{G}}_0(\mathbf{r}^{'}, \mathbf{r}, \omega) \\ =&\begin{pmatrix} \hat{G}_0^P(\mathbf{r}^{'}, \mathbf{r}, \omega) + \hat{G}_0^{PP}(\mathbf{r}^{'}, \mathbf{r}, \omega) & \hat{G}_0^{PS}(\mathbf{r}^{'}, \mathbf{r}, \omega) \\ \hat{G}_0^{SP}(\mathbf{r}^{'}, \mathbf{r}, \omega) & \hat{G}_0^S(\mathbf{r}^{'}, \mathbf{r}, \omega) + \hat{G}_0^{SS}(\mathbf{r}^{'}, \mathbf{r}, \omega) \end{pmatrix} \\ =&\frac{1}{2\pi} \int e^{ik_x(x'-x)} dk_x \left[\begin{pmatrix} \frac{e^{i\nu_2|z'-z|}}{2i\nu_2} & 0 \\ 0 & \frac{e^{i\eta_2|z'-z|}}{2i\eta_2} \end{pmatrix} + \begin{pmatrix} \acute{P}\grave{P}\frac{e^{i\nu_2 z}e^{i\nu_2 z'}}{2i\nu_2} & \acute{S}\grave{P}\frac{e^{i\eta_2 z}e^{i\nu_2 z'}}{2i\eta_2} \\ \acute{P}\grave{S}\frac{e^{i\nu_2 z}e^{i\eta_2 z'}}{2i\nu_2} & \acute{S}\grave{S}\frac{e^{i\eta_2 z}e^{i\eta_2 z'}}{2i\eta_2} \end{pmatrix} \right],\end{aligned} \tag{10}$$

where $\acute{P}\grave{P}$, $\acute{P}\grave{S}$, $\acute{S}\grave{P}$, $\acute{S}\grave{S}$ represent the reflection coefficients along the air/elastic-earth boundary, the subscript 2 represents the elastic half-space, and

$$\nu_2 = \begin{cases} \sqrt{k_{\alpha_2}^2 - k_x^2} & \text{if } k_x < k_{\alpha_2} \\ i\sqrt{k_x^2 - k_{\alpha_2}^2} & \text{if } k_x > k_{\alpha_2} \end{cases} \quad k_{\alpha_2} = \frac{\omega}{\alpha_2} \quad ,$$

$$\eta_2 = \begin{cases} \sqrt{k_{\beta_2}^2 - k_x^2} & \text{if } k_x < k_{\beta_2} \\ i\sqrt{k_x^2 - k_{\beta_2}^2} & \text{if } k_x > k_{\beta_2} \end{cases} \quad k_{\beta_2} = \frac{\omega}{\beta_2} \quad .$$

where α_2 and β_2 represent P-wave and S-wave velocities, respectively, in the elastic medium.

Since both $\mathbf{\Phi}$ and $\hat{\mathbf{G}}_0$ in the integral are tensors, the symbol $\cdot$ represents a tensor product. (The derivation of the Green's function in PS space and Green's theorem reference and scattered wave separation algorithm in PS space are shown in **?**.)

If the measurement surface is horizontal, the outward normal vector $\hat{n} = (0, \mp 1)$, where -1 corresponds to the situation shown in Figure 3, and +1 corresponds to the situation in Figure 4. Then Equation 1 can be rewritten as

$$\begin{aligned}&\int \left(\mathbf{\Phi}(\mathbf{r}^{'},\mathbf{r}_s,\omega)\cdot\partial_{z'}\hat{\mathbf{G}}_0(\mathbf{r}^{'},\mathbf{r},\omega)-\partial_{z'}\mathbf{\Phi}(\mathbf{r}^{'},\mathbf{r}_s,\omega)\cdot\hat{\mathbf{G}}_0(\mathbf{r}^{'},\mathbf{r},\omega)\right)dx'\\ =&\begin{cases}-\mathbf{\Phi}_0(\mathbf{r},\mathbf{r}_s,\omega) & \mathbf{r}\text{ is below the M.S.},\\ \mathbf{\Phi}_s(\mathbf{r},\mathbf{r}_s,\omega) & \mathbf{r}\text{ is above the M.S.}.\end{cases}\end{aligned} \tag{11}$$

Using the reciprocity of the Green's function and Fourier transforming over x in Equation 1 with $\int e^{-ik_x x}dx$, the formula in the wavenumber-frequency (k_x,ω) domain will be

$$\begin{aligned}&\left[\tilde{\mathbf{\Phi}}(k_x,z,\mathbf{r}_s,\omega)\cdot\partial_{z'}\tilde{\hat{\mathbf{G}}}_0^T(k_x,z,z',\omega)-\partial_{z'}\tilde{\mathbf{\Phi}}(k_x,z,\mathbf{r}_s,\omega)\cdot\tilde{\hat{\mathbf{G}}}_0^T(k_x,z,z',\omega)\right]|_{z'=\epsilon_g}\\ =&\begin{cases}-\tilde{\mathbf{\Phi}}_0(k_x,z,\mathbf{r}_s,\omega) & z\geq\epsilon_g^+,\\ \tilde{\mathbf{\Phi}}_s(k_x,z,\mathbf{r}_s,\omega) & z\leq\epsilon_g^-.\end{cases}\end{aligned} \tag{12}$$

Tildes represent the terms in the k_x domain, $\tilde{\hat{\mathbf{G}}}_0^T$ is the transpose of $\tilde{\hat{\mathbf{G}}}_0$, and ϵ_g is the receiver's depth. z' is evaluated at ϵ_g.

We should emphasize that by applying the algorithm in the (k_x,ω) domain, we can arrange to locate the output point $\mathbf{r}$ on the measurement surface to separate the actual measured data into the reference wave and the scattered wave. We can obtain the reference wave of the measured data by choosing $\mathbf{r}$ on the measurement surface to be part of the volume below the measurement surface, or, we can obtain the scattered wave of the measured data by choosing $\mathbf{r}$ on the measurement surface to be part of the volume above the measurement surface.

3.3 Deghosting the Scattered Wave in PS Space

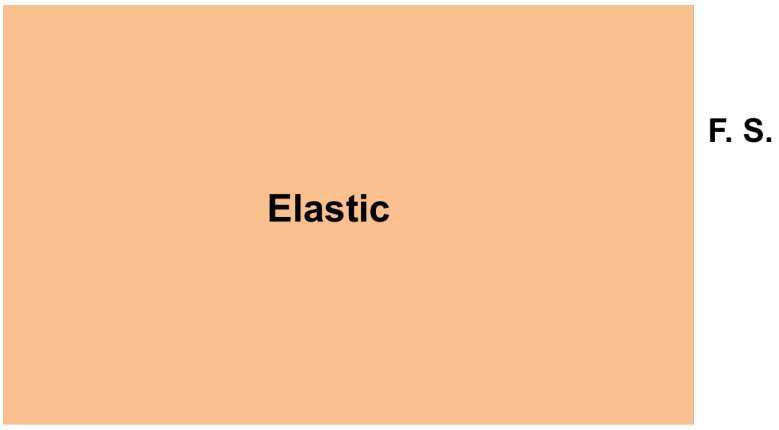

Figure 5: Reference medium used for deghosting the scattered wave

Green's theorem can be further applied to deghost the reflection data. For this exercise, the properties along the measurement surface are assumed to be homogeneous and known. The reference medium is a whole-space of homogeneous elastic earth(see Figure 5), whose properties are consistent with those of the actual earth along the measurement surface. Similarly to the case for the theory that is used for separation of the reference wave and scattered wave, here a semi-infinite

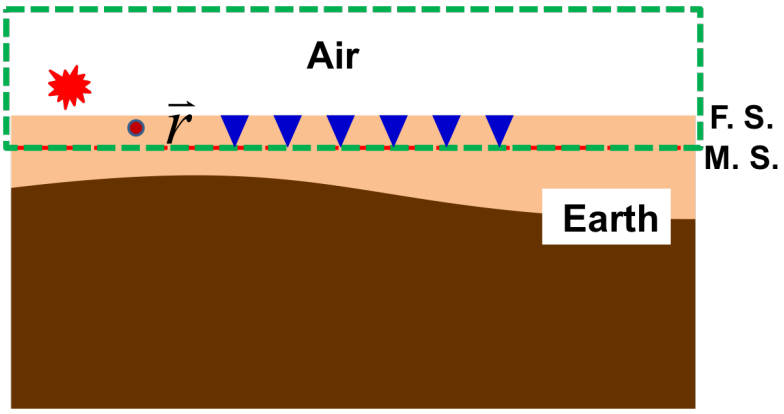

Figure 6: Upgoing wave separated out from the reflection data by using the surface integral along the closed surface marked by the dashed line, and the evulation point **r** is above the measurement surface.

surface integral whose lower boundary is the measurement surface will separate out the upgoing wave $\mathbf{\Phi}_{up}$ from the scattered wave $\mathbf{\Phi}_s$, for **r** inside the volume (see Figure 6).

The elastic Green's theorem deghosting formula in the space-frequency (x, ω) domain is

$$\mathbf{\Phi}_{up}(\mathbf{r}, \mathbf{r}_s, \omega) = \oint \Big(\mathbf{\Phi}_s(\mathbf{r}', \mathbf{r}_s, \omega) \cdot \nabla' \hat{\mathbf{G}}_0(\mathbf{r}', \mathbf{r}, \omega) - \nabla' \mathbf{\Phi}_s(\mathbf{r}', \mathbf{r}_s, \omega) \cdot \hat{\mathbf{G}}_0(\mathbf{r}', \mathbf{r}, \omega) \Big) \cdot \hat{n} dS', \quad (13)$$

where $\mathbf{\Phi}_{up}(\mathbf{r}, \mathbf{r}_s) = \begin{pmatrix} \Phi^P_{up}(\mathbf{r}, \mathbf{r}_s) \\ \Phi^S_{up}(\mathbf{r}, \mathbf{r}_s) \end{pmatrix}$ is the separated upgoing wave, and $\hat{\mathbf{G}}_0(\mathbf{r}', \mathbf{r}, \omega)$ of the reference medium is

$$\hat{\mathbf{G}}_0(\mathbf{r}', \mathbf{r}, \omega) = \begin{pmatrix} \hat{G}^P_0(\mathbf{r}', \mathbf{r}, \omega) & 0 \\ 0 & \hat{G}^S_0(\mathbf{r}', \mathbf{r}, \omega) \end{pmatrix} = \frac{1}{2\pi} \int e^{ik_x(x'-x)} dk_x \begin{pmatrix} \frac{e^{i\nu_2|z'-z|}}{2i\nu_2} & 0 \\ 0 & \frac{e^{i\eta_2|z'-z|}}{2i\eta_2} \end{pmatrix}. \quad (14)$$

Similarly, we can Fourier transform Equation 5 to the (k_x, ω) domain if the measurement surface is horizontal and flat.

4 Numerical Evaluation

Layer Number	P-Velocity (m/s)	S-Velocity (m/s)	Density (kg/m^3)
1	340	0	3
2	2000	1200	1500
3	4000	3000	1800

Table 1: Parameters of the air/elastic-earth model.

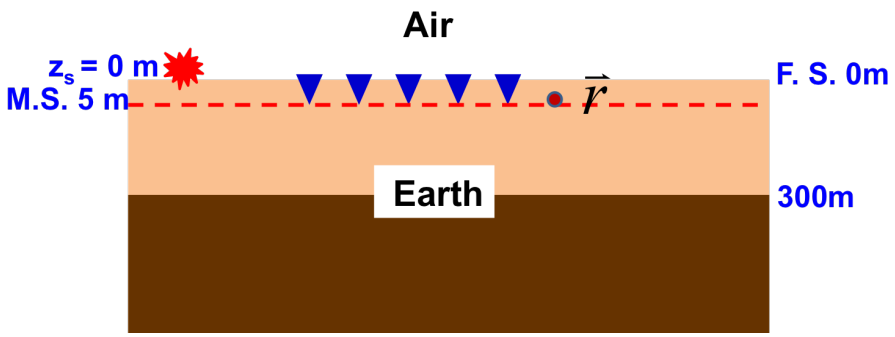

Figure 7: The air/elastic-model for the numerical tests.

4.1 Evaluation of the reference-wave and scattered-wave separation results

The methods that we develop in this paper for separating the reference wave and the scattered wave, and for deghosting, we can test on an air/elastic-earth model. As is shown in Figure 7, the model consists of a half-space of air and a half-space of two-layered elastic earth, the parameters of which are listed in Table 1. A P source is applied on the free surface. The receivers are 5m below the free surface and record both P- and S-waves. The output point **r** is on the measurement surface and the formula in the (k_x, ω) domain is applied.

The data for the total wavefields in the PS space (Figure 8a for Φ^P and Figure 8d for Φ^S) are created with the convolution of the wavelet and the analytic forms of Green's function, and consist of the reflection data and the reference wave, which includes the ground roll. They will be substituted into Equation 4 for separation of the reference wave and the scattered wave. Since the output **r** is on the measurement surface, we can obtain the reference wave (Figure 8b for Φ_0^P and Figure 8e for Φ_0^S) of measured data by choosing **r** to be part of volume below, and we can also obtain the scattered wave (Figure 8c for Φ_s^P and Figure 8f for Φ_s^S) of the measured data by choosing **r** to be part of the volume above the measurement surface. All the images are at the same scale. Comparing the separated reference waves from the Green's theorem wave-separation algorithm with those of the input data, all of the amplitudes and phases match well. The same close match applies for the scattered waves.

4.2 Evaluation of the deghosting results

The scattered wavefield (Figure 9a for Φ_s^P and Figure 9d for Φ_s^S) can be further separated into upgoing and downgoing waves. We apply the deghosting algorithm to separate the upgoing wave (Figure 9b for separated Φ_{up}^P and Figure 9e for separated Φ_{up}^S), by choosing the output point **r** on the measurement surface to be part of the volume above. To evaluate the result, we analytically create data that have just upgoing waves by using the given model (Figure 9c for synthetic Φ_{up}^P and Figure 9f for synthetic Φ_{up}^S). Comparing Figure 9b with Figure 9c for the P components, and comparing Figure 9e with Figure 9f for the S components, we see that the upgoing waves are effectively extracted.

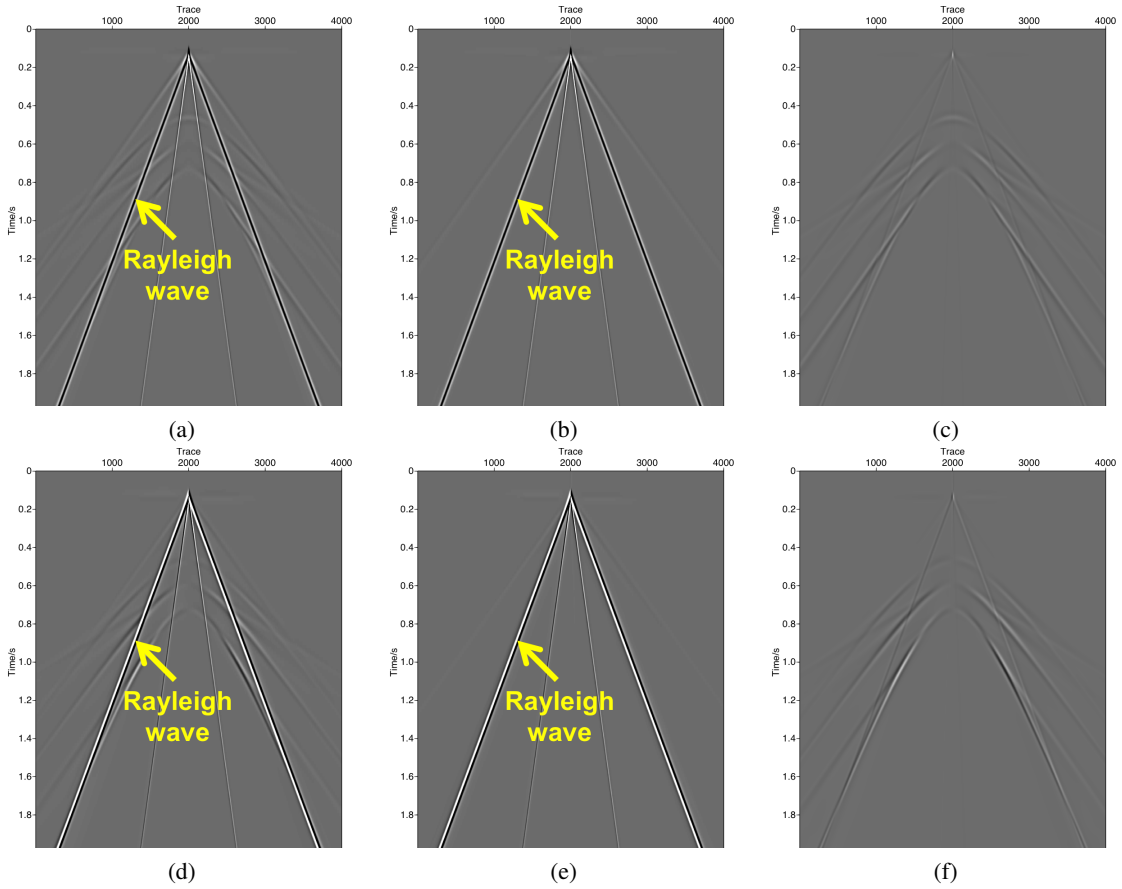

Figure 8: Results from separating the reference and scattered wave. (a) The total P wave; (b) the separated P component of the reference wave, by choosing **r** to be part of volume below; (c) the separated P component of the scattered wave, by choosing **r** to be part of the volume above; (d) the total S wave; (e) the separated S component of the reference wave; and (f) the separated S component of the scattered wave.

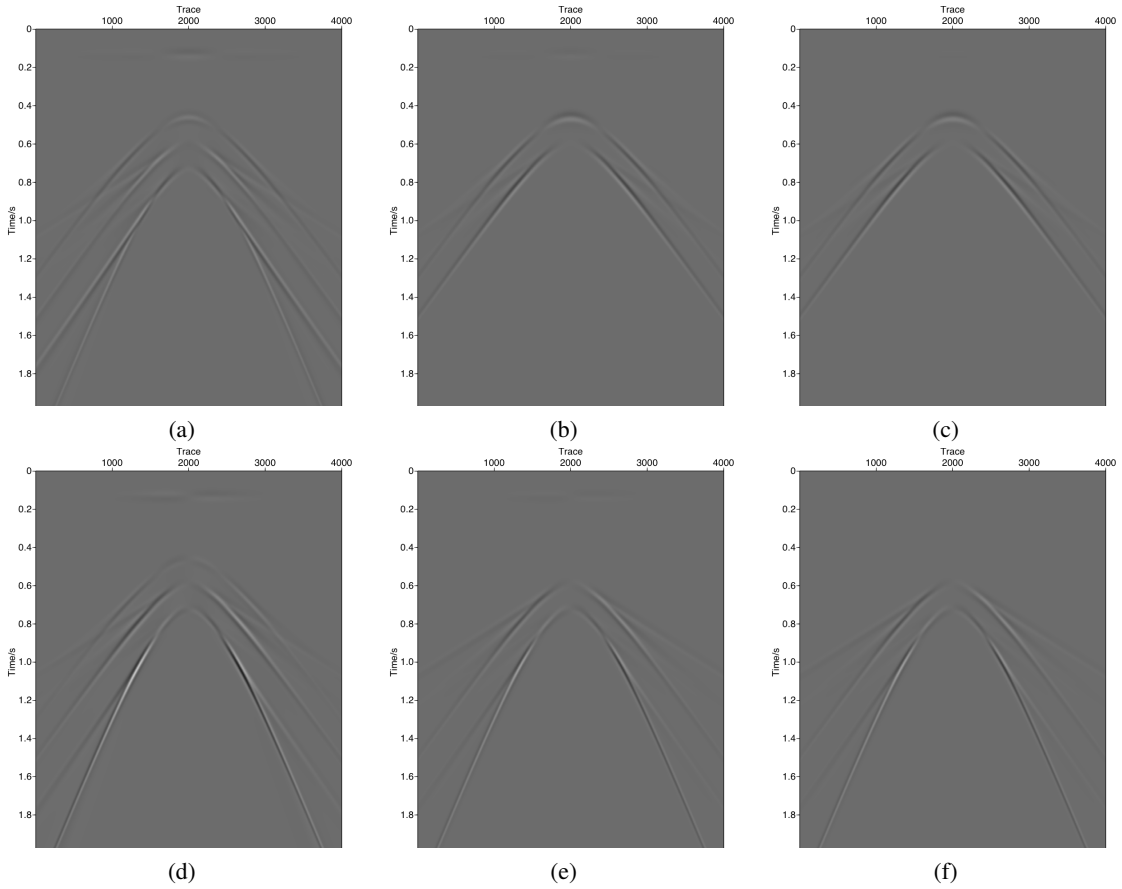

Figure 9: Deghosting results. (a) The P component of the input scattered wave; (b) the separated P component of the upgoing wave, by choosing $\mathbf{r}$ to be part of the volume above; (c) the synthetic P component of upgoing wave, obtained with convlution of the wavelet and the analytic form of Green's function; (d) the S component of the input scattered wave; (e) the separated S component of the upgoing wave; and (f) the synthetic S component of the upgoing wave.

5 Conclusions

We apply the elastic Green's theorem method to separate the reference wave and the scattered wave and to remove the ghosts from the reflection data. For onshore experiments, this method has the potential to remove the ground roll, which is part of the reference wave and is a major and serious issue, and also to remove the ghosts from the reflection data, all without damaging the reflection data. To make the method more readily applicable in practice, our research plan is to reduce the data requirements and to pursue an alternative approach that does not require near-surface information.

6 Acknowledgements

We are grateful to all M-OSRP sponsors for their encouragement and support in this research.

References

Mayhan, J. D., P. Terenghi, A. B. Weglein, and N. Chemingui. "Green's theorem derived methods for preprocessing seismic data when the pressure P and its normal derivative are measured." *81st Annual International Meeting, SEG, Expanded Abstracts* (2011): 2722–2726.

Mayhan, J. D. and A. B. Weglein. "First application of Green's theorem-derived source and receiver deghosting on deep-water Gulf of Mexico synthetic (SEAM) and field data." *Geophysics* 78 (2013): WA77–WA89.

Tang, L., J. D. Mayhan, J. Yang, and A. B. Weglein. "Using Green's theorem to satisfy data requirements of multiple removal methods: The impact of acquisition design." *83rd Annual International Meeting, SEG, Expanded Abstracts* (2013): 4392–4396.

Weglein, A. B., S. .A. Shaw, K. H. Matson, J. L. Sheiman, R. H. Solt, T. H. Tan, A. Osen, G. P. Correa, K. A. Innanen, Z. Guo, and J. Zhang. "New approaches to deghosting towed-streamer and ocean-bottom pressure measurements." *72th Annual International Meeting, SEG, Expanded Abstracts* (2002): 1016–1019.

Weglein, A. B. and R. H. Stolt. "I. The wave physics of downward continuation, wavelet estimation and volume and surface scattering. II. Approaches to linear and nonlinear migration inversion." *Mathematical Frontiers in Reflection Seismology: SEG/SIAM publication* (1995).

Wu, J. and A. B. Weglein. "Elastic Green's theorem preprocessing for on-shore internal multiple attenuation: theory and initial synthetic data tests." *84th Annual International Meeting, SEG, Expanded Abstracts* (2014): 4299–4304.

Yang, J., J. D. Mayhan, L. Tang, and A. B. Weglein. "Accommodating the source (and receiver) array in free-surface multiple elimination algorithm: Impact on interfering or proximal primaries and multiples." *83rd Annual International Meeting, SEG, Expanded Abstracts* (2013): 4184–4189.

Zhang, H. *Direct non-linear acoustic and elastic inversion: Towards fundamentally new comprehensive and realistic target identification*. PhD thesis, University of Houston, 2006.

Zhang, J. *Wave theory based data preparation for inverse scattering multiple removal, depth imaging and parameter estimation: analysis and numerical tests of Green's theorem deghosting theory*. PhD thesis, University of Houston, 2007.

Preprocessing in the PS space for on-shore seismic processing: removing ground roll and ghosts without damaging the reflection data

Jing Wu and Arthur B. Weglein, M-OSRP, University of Houston

SUMMARY

Prerequisites (e.g., the removal of the reference wave and the ghosts) are important for on-shore seismic processing. This paper derives an elastic Green's theorem wave separation algorithm for data in the PS space. Applying the algorithm presented in this paper, both the reference waves (including the direct wave and the surface wave) and the ghosts can be effectively removed. The method is tested on a layered elastic earth model. The results indicate its effectiveness for reducing the ground roll and ghosts, and without harming the up-going reflection, in preparation for on-shore processing.

INTRODUCTION

On-shore seismic exploration and processing seeks to use reflection data (the scattered wavefield) to detect the subsurface information. The measured total wavefield consists of the reflection data and the reference wavefield that contains the surface wave/ground roll; hence, it is necessary to separate the reference wave and the scattered wave. Filtering methods are typically employed to remove the reference wave, particularly the ground roll, but at the expense of damaging reflection data when ground roll is interfering with the scattered wavefield. As a flexible and useful tool, Green's theorem provides methods that can separate the reference wave from the reflection data without damaging the reflection. The application of these methods represents the unique advantages for off-shore plays (e.g., Weglein et al., 2002; Zhang, 2007; Mayhan et al., 2011; Mayhan and Weglein, 2013; Tang et al., 2013; Yang et al., 2013).

For on-shore plays, one of the key problems is the complex and laterally varying near surface. Our study starts with a simpler example, by assuming the space just below the free surface is homogeneous and known, but the earth below the measurement surface is unknown and heterogenous. Wu and Weglein (2014) derive the elastic Green's theorem reference and scattered wave separation algorithm for data in the PS space, and successfully test the algorithm on an initial model without subsurface reflectors. In this paper, for more realistic situation, we add one reflector in the tested model so that the measured data contain both the reference wave and the scattered wave.

In addition, for buried sources and receivers, not only up-going waves are in the reflection data but also ghosts, whose existence can cause notches in the spectrum. Thus, after obtaining the reflection data, removing the ghosts from the reflection data is another prerequisite. In this study, we will assume the source is located slightly above the air/earth surface (could be infinitely close, or on the air/earth surface), and the receivers are slightly beneath the air/earth surface. Therefore, there are receiver ghosts but no source ghosts in our study. Green's theorem can also be applied for deghosting, by taking a whole space homogeneous elastic medium as reference. A numerical test is shown to examine the accuracy of the deghosting algorithm.

GREEN'S THEOREM WAVE SEPARATION THEORY IN THE PS SPACE

Background of 2D elastic wave theory

We are deriving the wave separation method for on-shore application and starting with the elastic formulation. For convenience, the basis is changed from $\mathbf{u} = \begin{pmatrix} u_x \\ u_z \end{pmatrix}$ to $\Phi = \begin{pmatrix} \phi^P \\ \phi^S \end{pmatrix}$. $\mathbf{u}$ represents the displacement, consisting of x and z components; whereas Φ has P-wave and S-wave components.

In the PS space, the basic wave equations (Weglein and Stolt, 1995; Zhang, 2006) are

$$\begin{aligned} \hat{\mathbf{L}}\Phi &= \mathbf{F} \\ \hat{\mathbf{L}}\hat{\mathbf{G}} &= \delta, \\ \hat{\mathbf{L}}_0\Phi_0 &= \mathbf{F}, \\ \hat{\mathbf{L}}_0\hat{\mathbf{G}}_0 &= \delta, \end{aligned} \tag{1}$$

where $\hat{\mathbf{L}}$ and $\hat{\mathbf{L}}_0$ are the differential operators describing the properties of the actual medium and the reference medium, respectively. $\mathbf{F}$ is the source term. $\hat{\mathbf{G}}$ and $\hat{\mathbf{G}}_0$ are the Green's function operators for the actual and reference media, respectively.

The basic forms of these equations are the same as those for the acoustic case. On the basis of the successful applications of Green's theorem wave separation to the acoustic case (e.g., Zhang, 2007; Mayhan et al., 2011), it is feasible to apply the Green's theorem wave separation algorithm to the elastic world in a similar way.

Description of the model for wave separation

As seen in Figure 1, the model here consists of a half space of air and a half space of elastic earth. Receivers are buried in the earth, and the source is located slightly above the free surface (F.S.). The measurement surface (M.S.) can be infinitely close to the free surface, like the on-surface acquisition, or several meters below the free surface, like the buried-receiver acquisition; however, the receivers are coupled with the elastic medium in both situations.

Reference and scattered wave separation

The reference wave is the wave in the reference medium. It's useful for the purpose of exploration seismology to choose the reference medium to agree with the actual earth at and above the measurement surface. If we assume the actual earth

has known and homogeneous near surface properties, the simplest reference medium can be chosen as discontinuous two half-spaces, homogeneous air over homogeneous elastic earth (see Figure 2). There are two sources acting on the reference medium (see Figure 3). One is the active source (S_1), generating the reference wave; the other is the earth heterogeneity, or passive source (S_2), generating the scattered wave.

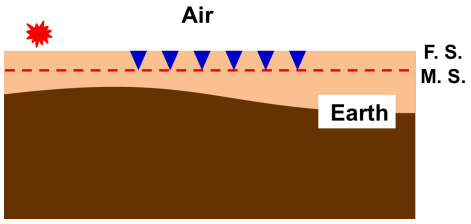

Figure 1: A generic model describing the land experiment

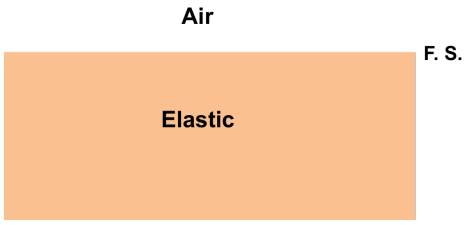

Figure 2: Reference medium for reference and scattered wave separation

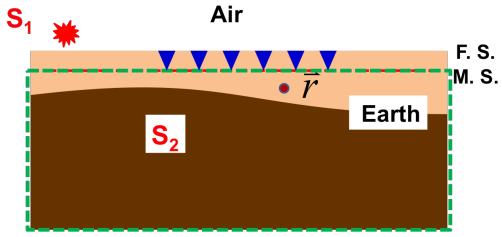

Figure 3: Reference wave separated from the total wavefield with surface integral along the dash line, for **r** below the M.S.

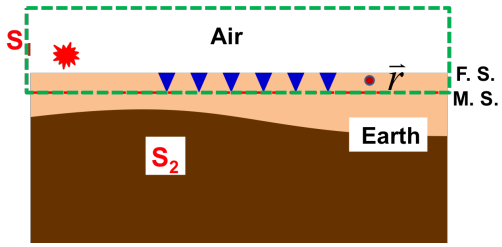

Figure 4: Scattered wave separated from the total wavefield with surface integral along the dash line, for **r** above the M.S.

Wu and Weglein (2014) have shown that, by applying Green's theorem, a semi-infinite surface integral upper bounded by the measurement surface will separate the reference wavefield Φ_0 from the total wavefield Φ, for the evaluation point **r** inside the volume and below the measurement surface (see Figure 3); whereas, the surface integral lower bounded by the measurement surface will separate the scattered wave Φ_s from Φ, for **r** above the measurement surface (see Figure 4).

The Green's theorem based formula for reference and scattered wave separation in the space-frequency (x,ω) domain is

$$\oint \left(\Phi(\mathbf{r}',\mathbf{r}_s,\omega)\cdot\nabla'\hat{\mathbf{G}}_0(\mathbf{r}',\mathbf{r},\omega)-\nabla'\Phi(\mathbf{r}',\mathbf{r}_s,\omega)\cdot\hat{\mathbf{G}}_0(\mathbf{r}',\mathbf{r},\omega)\right)\cdot\hat{n}dS'$$
$$=\begin{cases}\Phi_0(\mathbf{r},\mathbf{r}_s,\omega) & \mathbf{r}\text{ is below the M.S.},\\ \Phi_s(\mathbf{r},\mathbf{r}_s,\omega) & \mathbf{r}\text{ is above the M.S.},\end{cases} \tag{2}$$

where the symbol $'\cdot'$ represents a tensor product.

$\Phi_0(\mathbf{r},\mathbf{r}_s)=\begin{pmatrix}\Phi_0^P(\mathbf{r},\mathbf{r}_s)\\ \Phi_0^S(\mathbf{r},\mathbf{r}_s)\end{pmatrix}$, $\Phi_s(\mathbf{r},\mathbf{r}_s)=\begin{pmatrix}\Phi_s^P(\mathbf{r},\mathbf{r}_s)\\ \Phi_s^S(\mathbf{r},\mathbf{r}_s)\end{pmatrix}$, $\Phi(\mathbf{r},\mathbf{r}_s)=\begin{pmatrix}\Phi^P(\mathbf{r},\mathbf{r}_s)\\ \Phi^S(\mathbf{r},\mathbf{r}_s)\end{pmatrix}$, and Green's function $\hat{\mathbf{G}}_0(\mathbf{r}',\mathbf{r},\omega)$ for the reference medium is

$$\hat{\mathbf{G}}_0(\mathbf{r}',\mathbf{r},\omega)$$
$$=\begin{pmatrix}\hat{G}_0^P(\mathbf{r}',\mathbf{r},\omega)+\hat{G}_0^{PP}(\mathbf{r}',\mathbf{r},\omega) & \hat{G}_0^{PS}(\mathbf{r}',\mathbf{r},\omega)\\ \hat{G}_0^{SP}(\mathbf{r}',\mathbf{r},\omega) & \hat{G}_0^S(\mathbf{r}',\mathbf{r},\omega)+\hat{G}_0^{SS}(\mathbf{r}',\mathbf{r},\omega)\end{pmatrix}$$
$$=\frac{1}{2\pi}\int e^{ik_x(x'-x)}dk_x\begin{pmatrix}\frac{e^{i\nu_2|z'-z|}}{2i\nu_2}+\acute{P}\grave{P}\frac{e^{i\nu_2 z}e^{i\nu_2 z'}}{2i\nu_2} & \acute{S}\grave{P}\frac{e^{i\eta_2 z}e^{i\nu_2 z'}}{2i\eta_2}\\ \acute{P}\grave{S}\frac{e^{i\nu_2 z}e^{i\eta_2 z'}}{2i\nu_2} & \frac{e^{i\eta_2|z'-z|}}{2i\eta_2}+\acute{S}\grave{S}\frac{e^{i\eta_2 z}e^{i\eta_2 z'}}{2i\eta_2}\end{pmatrix}, \tag{3}$$

where $\acute{P}\grave{P}$, $\acute{P}\grave{S}$, $\acute{S}\grave{P}$, $\acute{S}\grave{S}$ represent the reflection coefficients along the air-elastic boundary, the subscript '2' represents the elastic half-space, and

$$\nu_2=\begin{cases}\sqrt{k_{\alpha_2}^2-k_x^2} & \text{if } k_x<k_{\alpha_2}\\ i\sqrt{k_x^2-k_{\alpha_2}^2} & \text{if } k_x>k_{\alpha_2}\end{cases}\qquad k_{\alpha_2}=\frac{\omega}{\alpha_2}\ ,$$

$$\eta_2=\begin{cases}\sqrt{k_{\beta_2}^2-k_x^2} & \text{if } k_x<k_{\beta_2}\\ i\sqrt{k_x^2-k_{\beta_2}^2} & \text{if } k_x>k_{\beta_2}\end{cases}\qquad k_{\beta_2}=\frac{\omega}{\beta_2}\ .$$

α_2 and β_2 represent P and S velocities in the elastic medium.

If the measurement surface is horizontal, the outward normal vector $\hat{n}=(0,\mp 1)$, where -1 is corresponding to the situation as shown in Figure 3, and 1 is for Figure 4.

Using reciprocity of the Green's function and Fourier transforming over x in Equation 2 with $\int e^{-ik_x x}dx$, the formula in the wavenumber-frequency (k_x,ω) domain will be

$$\left[\tilde{\Phi}(k_x,z,\mathbf{r}_s)\cdot\partial_{z'}\tilde{\hat{\mathbf{G}}}_0^T(k_x,z,z')-\partial_{z'}\tilde{\Phi}(k_x,z,\mathbf{r}_s)\cdot\tilde{\hat{\mathbf{G}}}_0^T(k_x,z,z')\right]|_{z'=\varepsilon_g}$$
$$=\begin{cases}-\tilde{\Phi}_0(k_x,z,\mathbf{r}_s) & z\geq\varepsilon_g^+,\\ \tilde{\Phi}_s(k_x,z,\mathbf{r}_s) & z\leq\varepsilon_g^-.\end{cases} \tag{4}$$

Tildes represent the terms in k_x domain, $\tilde{\hat{\mathbf{G}}}_0^T$ is the transpose of $\tilde{\hat{\mathbf{G}}}_0$, and ε_g is the receiver's depth. z' is evaluated at ε_g.

It is deserving emphasis that applying the algorithm in the (k_x,ω) domain, we can arrange to locate the output point **r** on the measurement surface to separate the actual measured data into the reference wave and the scattered wave. We can obtain the reference wave of measured data by choosing **r** on the measurement surface to be part of the volume below; otherwise, we can obtain the scattered wave of measurement by

choosing **r** on the measurement surface to be part of the volume above.

Deghosting the reflection data

Green's theorem can be further applied for deghosting the reflection data. For this time, the property along the measurement surface is assumed to be homogeneous and known. The reference medium is a whole space of homogeneous elastic (see Figure 5), whose properties are consistent with the actual earth along the measurement surface. Similar to the theory of reference and scattered wave separation, a semi-infinite surface integral lower bounded by the measurement surface will separate the up-going wave Φ_{up} from the scattered wave Φ_s, for **r** inside the volume (see Figure 6).

The elastic Green's theorem deghosting formula in space-frequency (x,ω) domain is

$$\begin{aligned}&\Phi_{up}(\mathbf{r},\mathbf{r}_s,\omega)\\ &=\oint\left(\Phi_s(\mathbf{r}',\mathbf{r}_s,\omega)\cdot\nabla'\hat{\mathbf{G}}_0(\mathbf{r}',\mathbf{r},\omega)-\nabla'\Phi_s(\mathbf{r}',\mathbf{r}_s,\omega)\cdot\hat{\mathbf{G}}_0(\mathbf{r}',\mathbf{r},\omega)\right)\cdot\hat{n}dS',\end{aligned} \tag{5}$$

where $\Phi_{up}(\mathbf{r},\mathbf{r}_s)=\begin{pmatrix}\Phi^P_{up}(\mathbf{r},\mathbf{r}_s)\\ \Phi^S_{up}(\mathbf{r},\mathbf{r}_s)\end{pmatrix}$ is the separated up wave, and $\hat{\mathbf{G}}_0(\mathbf{r}',\mathbf{r},\omega)$ of the reference medium is

$$\begin{aligned}\hat{\mathbf{G}}_0(\mathbf{r}',\mathbf{r},\omega)&=\begin{pmatrix}\hat{G}^P_0(\mathbf{r}',\mathbf{r},\omega) & 0\\ 0 & \hat{G}^S_0(\mathbf{r}',\mathbf{r},\omega)\end{pmatrix}\\ &=\frac{1}{2\pi}\int e^{ik_x(x'-x)}dk_x\begin{pmatrix}\frac{e^{i\nu_2|z'-z|}}{2i\nu_2} & 0\\ 0 & \frac{e^{i\eta_2|z'-z|}}{2i\eta_2}\end{pmatrix}.\end{aligned} \tag{6}$$

Similarly, we can Fourier transform Equation 5 to (k_x,ω) domain if the measurement surface is horizontal and flat.

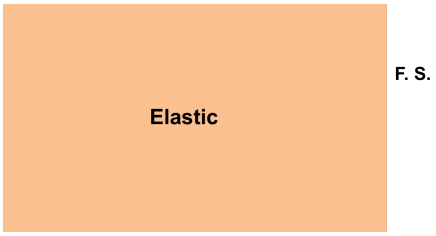

Figure 5: Reference medium for deghosting

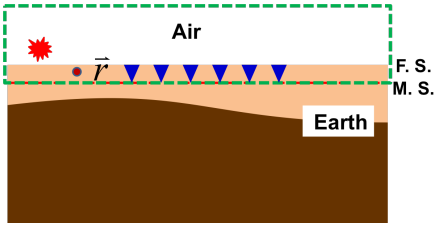

Figure 6: Up wave separated from the reflection data with surface integral along the dash line, for **r** above the M.S.

NUMERICAL EVALUATION

The reference and scattered wave separation and deghosting methods that are developed in the paper are tested on an air/elastic-earth model. As shown in Figure 7, the model consists of a half-space of air and a half-space of two layered elastic earth, and the parameters are listed in Table 1. A P source is applied on the free surface. The receivers are 5m below the free surface and they record both P and S waves. The output point **r** is on the measurement surface and the formula in (k_x,ω) domain is applied.

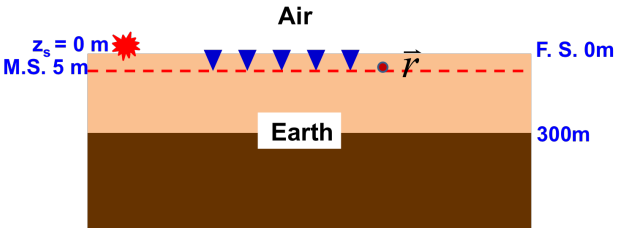

Figure 7: The air/elastic model for the numerical tests

Layer Number	P Velocity (m/s)	S Velocity (m/s)	Density (kg/m^3)
1	340	0	3
2	2000	1200	1500
3	4000	3000	1800

Table 1: The air/elastic model parameters

Reference and scattered wave separation

The data of total wavefields in the PS space (Figure 8(a) for Φ^P and Figure 8(d) for Φ^S) are created with the analytic forms, consisting of the reflection data and the reference wave that includes the ground roll. They will be substituted into Equation 4 for reference and scattered wave separation. Since the output **r** is on the measurement surface, we can obtain the reference wave (Figure 8(b) for Φ^P_0 and Figure 8(e) for Φ^S_0) of measured data by choosing **r** to be part of volume below, and we can also obtain the scattered wave (Figure 8(c) for Φ^P_s and Figure 8(f) for Φ^S_s) of measured data by choosing **r** to be part of volume above. All the figures are in the same scales. Comparing the separated reference waves from Green's theorem wave separation algorithm with those of the input data, both their amplitudes and phases match well. The conclusion retains for the scattered waves.

Deghosting

The scattered wavefield (Figure 9(a) for Φ^P_s and Figure 9(d) for Φ^S_s) can be further separated into up-going and down-going waves. We apply the deghosting algorithm to separate the up wave (Figure 9(b) for separated Φ^P_{up} and Figure 9(e) for separated Φ^S_{up}), for the output point **r** on the measurement surface to be part of volume above. To evaluate the result, we analytically create the data with only up wave using the given model (Figure 9(c) for synthetic Φ^P_{up} and Figure 9(f) for synthetic Φ^S_{up}). Comparing Figure 9(b) with Figure 9(c) for P

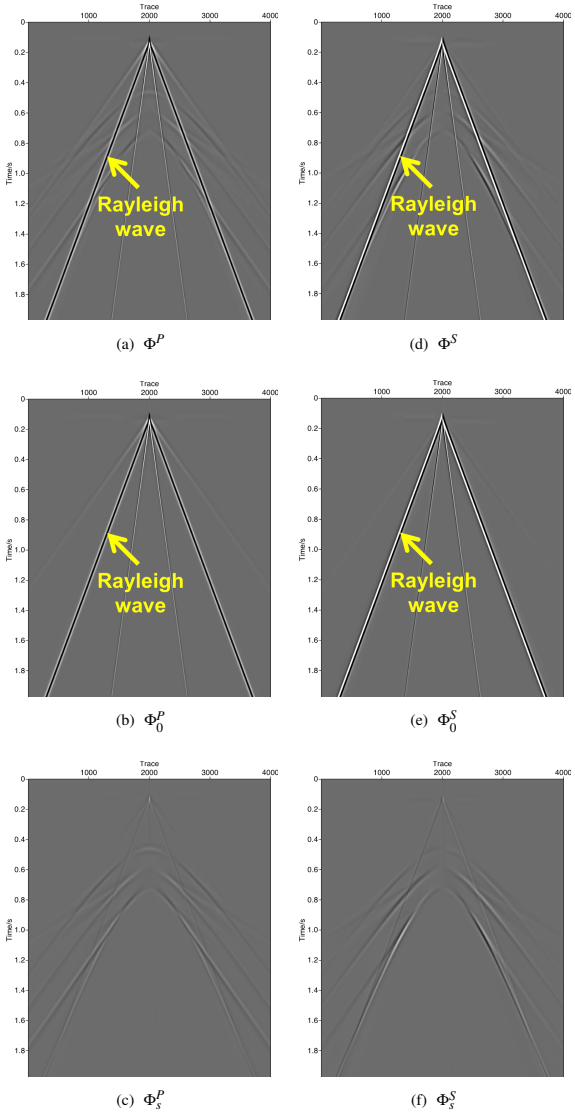

(a) Φ^P (d) Φ^S

(b) Φ_0^P (e) Φ_0^S

(c) Φ_s^P (f) Φ_s^S

Figure 8: Reference and scattered wave separation results. (a) is the total P wave; (b) is the separated P component of reference wave, by choosing **r** to be part of volume below; (c) is the separated P component of scattered wave, by choosing **r** to be part of volume above; (d) is the total S wave; (e) is the separated S component of reference wave; (f) is the separated S component of scattered wave.

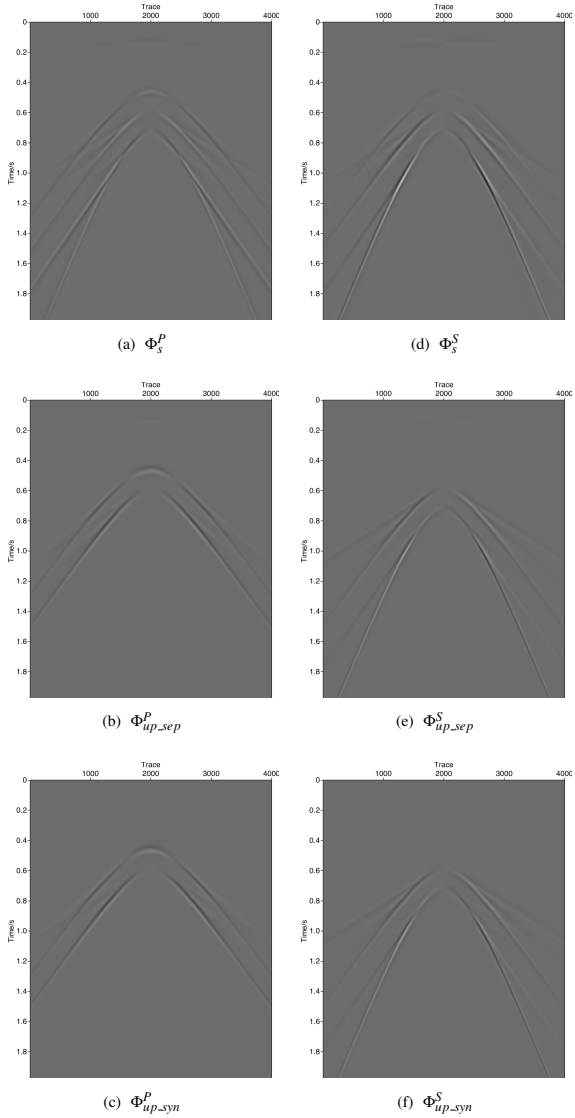

(a) Φ_s^P (d) Φ_s^S

(b) $\Phi_{up\_sep}^P$ (e) $\Phi_{up\_sep}^S$

(c) $\Phi_{up\_syn}^P$ (f) $\Phi_{up\_syn}^S$

Figure 9: Deghosting results. (a) is P component of the input scattered wave; (b) is the separated P component of up-going wave, by choosing **r** to be part of volume above; (c) is the synthetic P component of up-going wave, with analytic form; (d) is S component of the input scattered wave; (e) is the separated S component of up-going wave; (f) is the synthetic S component of up-going wave.

components, and comparing Figure 9(e) with Figure 9(f) for S components, the up-going waves are effectively extracted.

CONCLUSION

We apply the elastic Green's theorem method to separate the reference and scattered wave and remove the ghosts of the reflection data. It has the potential to remove the ground roll, which is a major and serious issue and part of the reference wave, and to remove the ghosts, for on-shore experiments without damaging the reflection data. To make the method more readily applicable in practice, our research plan is in reducing the data requirements and pursuing an alternative approach without the need for near surface information.

ACKNOWLEDGEMENTS

We are grateful to all M-OSRP sponsors for encouragement and support in this research.

REFERENCES

Mayhan, J. D., P. Terenghi, A. B. Weglein, and N. Chemingui, 2011, Green's theorem derived methods for preprocessing seismic data when the pressure P and its normal derivative are measured: SEG Technical Program Expanded Abstracts, Soc. Expl. Geophys., 2722–2726.

Mayhan, J. D., and A. B. Weglein, 2013, First application of Green's theorem-derived source and receiver deghosting on deep-water Gulf of Mexico synthetic (SEAM) and field data: Geophysics, **78**, WA77–WA89.

Tang, L., J. D. Mayhan, J. Yang, and A. B. Weglein, 2013, Using Green's theorem to satisfy data requirements of multiple removal methods: The impact of acquisition design: SEG Technical Program Expanded Abstracts, Soc. Expl. Geophys., 4392–4395.

Weglein, A. B., S. A. Shaw, K. H. Matson, J. L. Sheiman, R. H. Solt, T. H. Tan, A. Osen, G. P. Correa, K. A. Innanen, Z. Guo, and J. Zhang, 2002, New approaches to deghosting towed-streamer and ocean-bottom pressure measurements: 72nd Annual International Meeting, SEG, Expanded Abstracts, 1016–1019.

Weglein, A. B., and R. H. Stolt, 1995, I. the wave physics of downward continuation, wavelet estimation and volume and surface scattering. II. approaches to linear and nonlinear migration inversion: Mathematical Frontiers in Reflection Seismology: SEG/SIAM publication.

Wu, J., and A. B. Weglein, 2014, Elastic green's theorem preprocessing for on-shore internal multiple attenuation: theory and initial synthetic data tests: SEG Technical Program Expanded Abstracts, Soc. Expl. Geophys., 4299–4304.

Yang, J., J. D. Mayhan, L. Tang, and A. B. Weglein, 2013, Accommodating the source (and receiver) array in free-surface multiple elimination algorithm: Impact on interfering or proximal primaries and multiples: SEG Technical Program Expanded Abstracts, Soc. Expl. Geophys., 4184–4189.

Zhang, H., 2006, Direct non-linear acoustic and elastic inversion: Towards fundamentally new comprehensive and realistic target identification: PhD thesis, University of Houston.

Zhang, J., 2007, Wave theory based data preparation for inverse scattering multiple removal, depth imaging and parameter estimation: analysis and numerical tests of Green's theorem deghosting theory: PhD thesis, University of Houston.

Preprocessing in displacement space in preparation for onshore seismic processing: removing ground roll and ghosts without damaging the reflection data

Jing Wu & Arthur B. Weglein

Abstract

This paper derives an elastic Green's theorem-based wave-separation method for onshore data in displacement space. A single application of the algorithm presented in this paper effectively removes both the surface wave and the ghosts. The method is tested on a layered elastic-earth model. The results indicate that it is effective for reducing the ground roll and ghosts at the same time onshore without harming the upgoing reflections, in preparation for onshore processing.

1 Introduction

Onshore seismic exploration and processing seek to use reflection data (the scattered wavefield) to make inferences about the subsurface. The measured total wavefield consists of the reflection data and the reference wave, which contains the direct wave and the surface wave/ground roll; hence, one prerequisite in preprocessing is to separate the reference wave and the scattered wave. Typically, filtering methods are employed to remove the reference wave, particularly the ground roll. However, that can be at the expense of damaging the reflection data when the ground roll is interfering with the scattered wavefield.

In addition, for buried sources and receivers, not just upgoing waves are in the reflection data – there are also ghosts, whose existence can cause notches in the spectrum. Thus, removal of the ghosts from the reflection data is another prerequisite. In this study, we will assume that the source is located slightly above the air/earth surface (it could be infinitely close, or actually on, the air/earth surface), and that the receivers are slightly beneath the air/earth surface. Therefore, there are receiver ghosts but no source ghosts in our study.

As a flexible and useful tool, Green's theorem provides a method to satisfy both prerequisites – removal of the reference wave without damaging the reflection data, and removal of the ghosts from the reflection data without destroying the upgoing reflected data. The distinct advantages of applying the method based on Green's theorem in offshore plays have already been demonstrated by Weglein et al. (2002); Zhang (2007); Mayhan et al. (2011); Mayhan and Weglein (2013); Tang et al. (2013); Yang et al. (2013).

Basically, wave separation by using Green's theorem employs a model of the world that consists of the **reference medium** and the **sources**. The choice of reference medium is arbitrary, and that choice will determine what the sources have to be in order to arrange for the reference medium and the sources together to correspond to the actual medium and to the experiment (Weglein et al., 2003). For onshore plays, the Green's theorem wave-separation method is applicable for data either in displacement space (Pao and Varatharajulu, 1976; Weglein and Secrest, 1990) or in the PS space (Wu and Weglein, 2014). In this paper, for data in displacement space, we choose a homogeneous elastic whole space as the reference medium. In such a case, both the ground roll and the receiver

ghosts can be removed in one step by applying the elastic Green's theorem wave-separation algorithm. Note: As is presented in a companion paper (Wu and Weglein, 2015), for data in the PS space, the reference medium is first chosen to be composed of two homogeneous half-spaces – an air/acoustic half-space over an elastic half-space – and the Green's theorem method then can extinguish the reference wave (including the ground roll) without harming the reflection data. In that case, after the reflection data have been obtained, the Green's theorem provides a reflection-data-deghosting algorithm with the choice of a whole-space homogeneous elastic-earth reference medium(Wu and Weglein, 2015).

2 Description of the generic onshore model: reference medium + sources

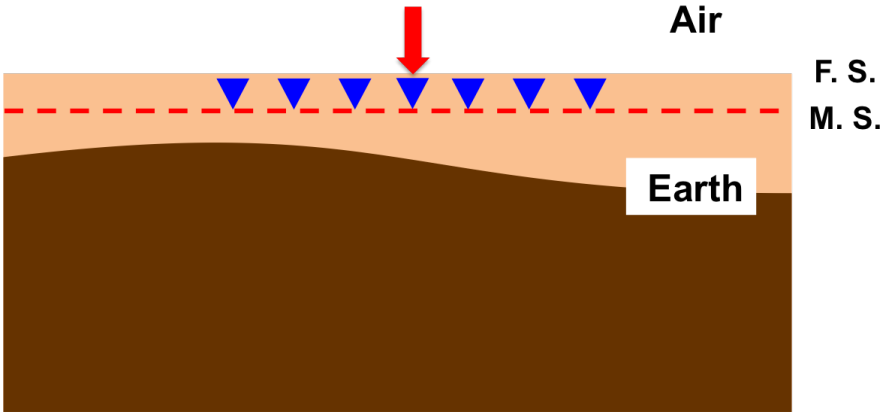

Figure 1: A generic model describing the onshore experiment. In this and subsequent figures, the blue triangles represent the receivers

As is shown in Figure 1, the generic onshore model consists of an air half-space and an elastic-earth half-space. Receivers are buried in the earth, and the active source in the form of a vertical force is applied on the free surface (F.S.). Therefore, ghosts exist at the receiver side only. The measurement surface (M.S.) can be infinitely close to the free surface, as in the case of on-surface acquisition, or several meters below the free surface, as in buried-receiver acquisition. However, the receivers are coupled with the elastic medium in both situations.

In this paper, we will assume that the portion of earth along the measurement surface is homogeneous and known. Within that assumption, we choose the reference medium to be a homogeneous elastic whole space, as shown in Figure 2, whose properties agree with those of the actual earth along the measurement surface.

There are three sources acting on the homogeneous reference medium that is described in Figure 2. As is shown in Figure 3, one is the active source (the vertical force S_1) and the other two are passive sources (the perturbations S_2 and S_3) on two sides of the measurement surface, respectively. S_1 and S_2 produce the ground roll and the downgoing waves (including direct wave and the receiver ghost). S_3 generates upgoing waves from the earth. All three of these sources contribute to providing the actual total wavefield, and the upgoing waves due to S_3 are expected to be separated out from the waves caused by both S_1 and S_2.

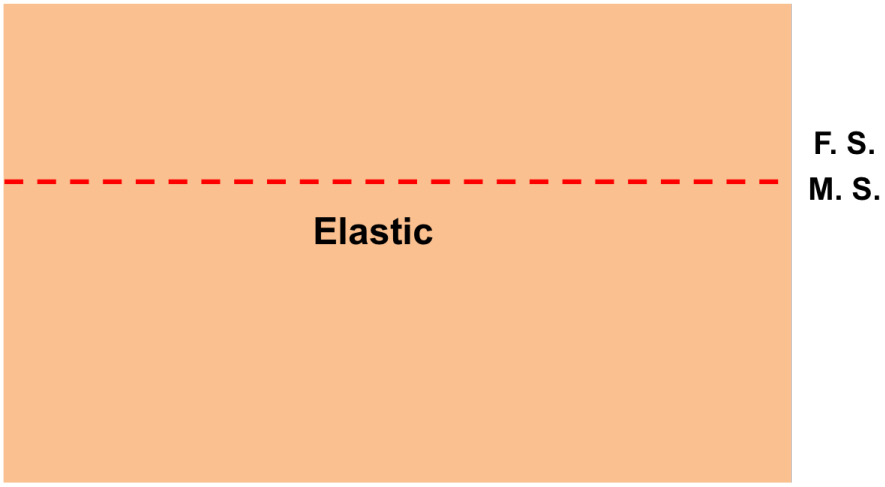

Figure 2: A homogeneous elastic-whole-space reference medium.

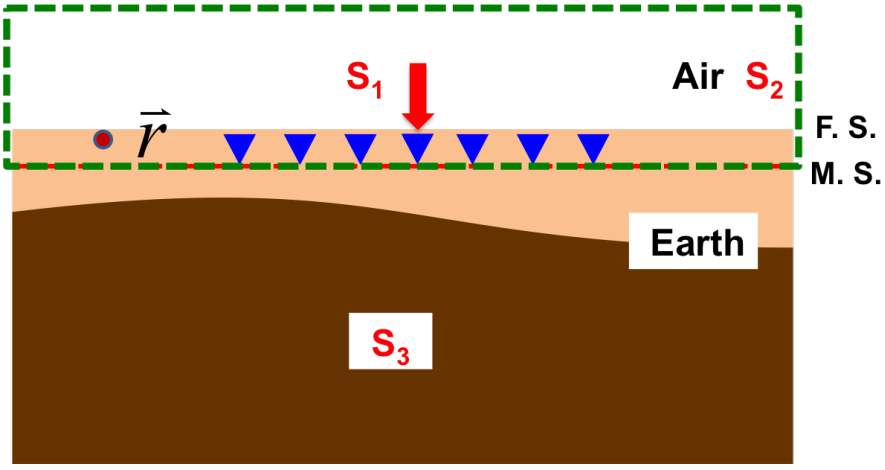

Figure 3: Three sources are acting on the reference medium that is depicted in Figure 2, and the surface integral along the measurement surface will remove the contributions from S_1 and S_2, which are inside the enclosed surface.

3 Elastic Green's theorem wave separation theory

3.1 Background of 2D elastic wave theory

The wave equation for a 2D elastic isotropic medium is

$$\nabla \cdot \boldsymbol{\tau}(\mathbf{r},\omega) + \rho\omega^2 \mathbf{u}(\mathbf{r},\omega) = \mathbf{f}(\mathbf{r},\omega), \tag{1}$$

where

$$\boldsymbol{\tau} = \lambda \nabla \cdot \mathbf{u}\,\mathbf{I} + \mu\left(\nabla \mathbf{u} + \mathbf{u}\nabla\right). \tag{2}$$

$\mathbf{u} = \begin{pmatrix} u_x \\ u_z \end{pmatrix}$ is the displacement, the 2^{nd}-order tensor $\boldsymbol{\tau} = \begin{pmatrix} \tau_{xx} & \tau_{xz} \\ \tau_{zx} & \tau_{zz} \end{pmatrix}$ is the stress, $\mathbf{f} = \begin{pmatrix} f_x \\ f_z \end{pmatrix}$ is the source, λ and μ are Lam$\acute{e}$'s parameters, and ρ is the density.

The impulse response of the reference medium can be written as

$$\nabla \cdot \boldsymbol{\Sigma}_0(\mathbf{r},\omega) + \rho_0\omega^2 \mathbf{G}_0(\mathbf{r},\omega) = \delta(\mathbf{r})\,\mathbf{I}, \tag{3}$$

where

$$\Sigma_{0ijk} = \lambda_0 \partial_m G_{0mk}\delta_{ij} + \mu_0(\partial_i G_{0jk} + \partial_j G_{0ik}), \qquad i,j,k = x,z. \tag{4}$$

The 2^{nd}-order tensor $\mathbf{G}_0 = \begin{pmatrix} G_{0xx} & G_{0xz} \\ G_{0zx} & G_{0zz} \end{pmatrix}$ is the Green's displacement tensor, the 3^{rd}-order tensor $\boldsymbol{\Sigma}_0$ is the Green's stress tensor, and the source term consists of a diagonal matrix.

3.2 Elastic Green's theorem wave-separation algorithm in the (x,ω) domain

As can be seen in Figure 3, by applying Green's theorem, we apply the integral which is along the closed semi-infinite surface whose lower boundary is the measurement surface, and in so doing we separate out the portion of the wavefield that is inside the enclosed volume but that is due to S_3, located outside the volume.

Starting from Equation 1 and Equation 3, and using Green's theorem, we can obtain the wave-separation algorithm (see Appendix A for the detailed derivation); that is, we can extract the upgoing waves generated by the source S_3.

In the (x,ω) domain, the formula is

$$\mathbf{u}^{up}(\mathbf{r},\omega) = -\int_{m.s.} [(\hat{n}' \cdot \boldsymbol{\tau}(\mathbf{r}',\omega)) \cdot \mathbf{G}_0(\mathbf{r}',\mathbf{r},\omega) - \mathbf{u}(\mathbf{r}',\omega) \cdot (\hat{n}' \cdot \boldsymbol{\Sigma}_0(\mathbf{r}',\mathbf{r},\omega))] d\mathbf{r}', \tag{5}$$

where $\hat{n}'$ is the normal outside vector along the surface.

On the measurement surface, $\mathbf{r}' = (x', z' = \epsilon_g)$,

$$\boldsymbol{\tau}(x', z' = \epsilon_g, \omega) = \lambda_0 \nabla' \cdot \mathbf{u}(x', z' = \epsilon_g, \omega)\,\mathbf{I} + \mu_0(\nabla' \mathbf{u}(x', z' = \epsilon_g, \omega) + \mathbf{u}(x', z' = \epsilon_g, \omega)\nabla'), \tag{6}$$

where ϵ_g is the receiver's depth. Since in this paper we have assumed that the properties along the measurement surface are homogeneous, λ_0 and μ_0 are constants along the measurement surface. The choice of the reference medium depends on these invariant parameters.

By applying Equation 5 in the (x, ω) domain, we can remove the reference wave (particularly the ground roll) and the ghosts simultaneously. There is no assumption about the shape of the measurement surface – it can be either flat or rugose.

3.3 Elastic Green's theorem wave-separation algorithm in the (k_x, ω) domain

If the measurement surface is horizontal and flat, then $\hat{n}' = (0, 1)$. Equation 5 can be Fourier transformed into the (k_x, ω) domain.

Equation 5 is expanded to be

$$\begin{aligned}
&u_x^{up}(\mathbf{r}, \omega) \\
=&-\int_{m.s.} [\tau_{zx}(\mathbf{r}', \omega) G_{0xx}(\mathbf{r}', \mathbf{r}, \omega) + \tau_{zz}(\mathbf{r}', \omega) G_{0zx}(\mathbf{r}', \mathbf{r}, \omega) \\
&- u_x(\mathbf{r}', \omega) \Sigma_{0zxx}(\mathbf{r}', \mathbf{r}, \omega) - u_z(\mathbf{r}', \omega) \Sigma_{0zzx}(\mathbf{r}', \mathbf{r}, \omega)] dx', \\
&u_z^{up}(\mathbf{r}, \omega) \\
=&-\int_{m.s.} [\tau_{zx}(\mathbf{r}', \omega) G_{0xz}(\mathbf{r}', \mathbf{r}, \omega) + \tau_{zz}(\mathbf{r}', \omega) G_{0zz}(\mathbf{r}', \mathbf{r}, \omega) \\
&- u_x(\mathbf{r}', \omega) \Sigma_{0zxz}(\mathbf{r}', \mathbf{r}, \omega) - u_z(\mathbf{r}', \omega) \Sigma_{0zzz}(\mathbf{r}', \mathbf{r}, \omega)] dx'.
\end{aligned} \tag{7}$$

With reciprocity,

$$\begin{aligned}
G_{0ij}(\mathbf{r}', \mathbf{r}, \omega) &= G_{0ji}(\mathbf{r}, \mathbf{r}', \omega), \\
\Sigma_{0ijk}(\mathbf{r}', \mathbf{r}, \omega) &= \lambda_0 \partial_{i'} G_{0ki}(\mathbf{r}, \mathbf{r}', \omega) \delta_{ij} + \mu_0 (\partial_{i'} G_{0kj}(\mathbf{r}, \mathbf{r}', \omega) + \partial_{j'} G_{0ki}(\mathbf{r}, \mathbf{r}', \omega)), \\
&\quad i, j, k = x, z.
\end{aligned} \tag{8}$$

By applying a Fourier transform over x in Equation 7 with $\int e^{-ik_x x} dx$, we will have

$$\begin{aligned}
&\tilde{u}_x^{up}(k_x, z, \omega) \\
=&-[\tilde{\tau}_{zx}(k_x, z', \omega) \tilde{G}_{0xx}(k_x, z, z', \omega) + \tilde{\tau}_{zz}(k_x, z', \omega) \tilde{G}_{0xz}(k_x, z, z', \omega) \\
&- \tilde{u}_x(k_x, z', \omega) \tilde{\Sigma}_{0zxx}(k_x, z', z, \omega) - \tilde{u}_z(k_x, z', \omega) \tilde{\Sigma}_{0zzx}(k_x, z', z, \omega)]|_{z'=\epsilon_g}, \\
&\tilde{u}_z^{up}(k_x, z, \omega) \\
=&-[\tilde{\tau}_{zx}(k_x, z', \omega) \tilde{G}_{0zx}(k_x, z, z', \omega) + \tilde{\tau}_{zz}(k_x, z', \omega) \tilde{G}_{0zz}(k_x, z, z', \omega) \\
&- \tilde{u}_x(k_x, z', \omega) \tilde{\Sigma}_{0zxz}(k_x, z', z, \omega) - \tilde{u}_z(k_x, z', \omega) \tilde{\Sigma}_{0zzz}(k_x, z', z, \omega)]|_{z'=\epsilon_g},
\end{aligned} \tag{9}$$

where tildes represent the terms in the k_x domain, and z' is evaluated at the receiver's depth ϵ_g. Specifically,

$$\begin{aligned}
\tilde{\Sigma}_{0zxx}(k_x, z', z, \omega) &= \mu_0 [\partial_{z'} \tilde{G}_{0xx}(k_x, z, z', \omega) - ik_x \tilde{G}_{0xz}(k_x, z, z', \omega)], \\
\tilde{\Sigma}_{0zzx}(k_x, z', z, \omega) &= \gamma_0 \partial_{z'} \tilde{G}_{0xz}(k_x, z, z', \omega) - \lambda_0 (ik_x) \tilde{G}_{0xx}(k_x, z, z', \omega), \\
\tilde{\Sigma}_{0zxz}(k_x, z', z, \omega) &= \mu_0 [\partial_{z'} \tilde{G}_{0zx}(k_x, z, z', \omega) - ik_x \tilde{G}_{0zz}(k_x, z', z, \omega)], \\
\tilde{\Sigma}_{0zzz}(k_x, z', z, \omega) &= \gamma_0 \partial_{z'} \tilde{G}_{0zz}(k_x, z, z', \omega) - \lambda_0 (ik_x) \tilde{G}_{0zx}(k_x, z, z', \omega),
\end{aligned} \tag{10}$$

where γ_0 is the bulk modulus, and $\gamma_0 = \lambda_0 + 2\mu_0$.

For a reference medium that is a homogeneous elastic whole space, both the Green's displacement tensor and its stress tensor can be expressed analytically (see Appendix B for $\mathbf{G}_0$).

We should emphasize that by applying the algorithm in the (k_x, ω) domain, we can locate the output point **r** on the measurement surface and can arrange for it to become part of the volume above that surface. Then, we are able to extract the upgoing wavefield that is a portion of the actual, measured data.

4 Numerical Evaluation

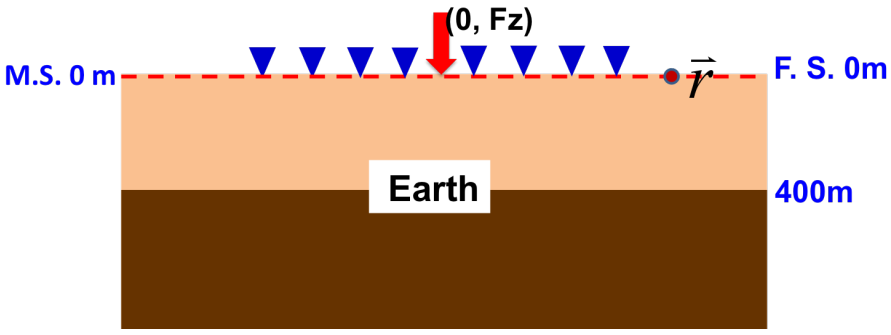

Figure 4: A two-layer elastic earth model for our numerical test.

We can test the (k_x, ω) domain wave-separation algorithm on a two-layer elastic earth model, as is seen in Figure 3. A vertical force $(0, F_z)$ is applied on the free surface, and receivers are in the earth, at a depth of 0m. For simplicity, the space above the free surface is set to be a vacuum. The properties of the earth are listed in Table 1. The output point **r** is arranged to be on the measurement surface and is treated as part of the volume above that surface.

Layer Number	P-Velocity (m/s)	S-Velocity (m/s)	Density (kg/m^3)
1	1800	1200	1500
2	4000	2500	1800

Table 1: The parameters of the earth model in Figure 3

The trace interval is 2m, the maximum offset is 3000m, the time sampling interval is 4ms, and the total time sampling length is 2.5s. The data of displacement **u** with both x and z components are generated by using analytic forms. As can be seen in Figure 5a and Figure 5b, the data reveal a strong Rayleigh wave and a relatively weak scattered wave. In addition, the ghosts are interfering with the upgoing waves. Note that all these images are at the same scale.

By putting the multicomponent data into the wave-separation formula of Equation 9, we can separate the upgoing waves with x and z components. To evaluate the accuracy of the results, we analytically create the data consisting of only the up waves, with the model of Figure 3. These data will serve as criteria for examining the calculation results. The x component of separated upgoing waves from the Green's theorem wave-separation algorithm (Figure 6a) is compared with the x component of upgoing waves created with the analytic form of Green's function (Figure 6b), and

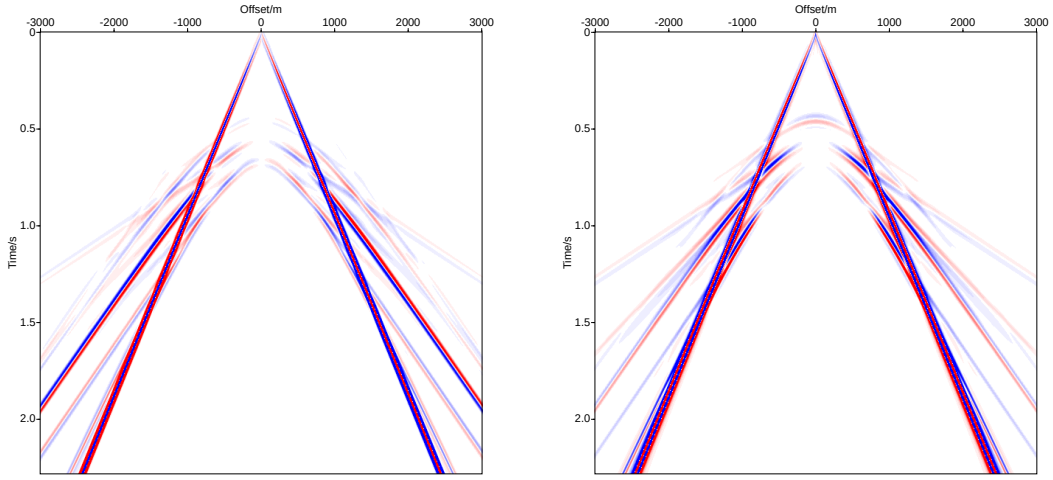

(a) (b)

Figure 5: The data for the total wavefields in displacement space, by using the earth model as Figure 3. (a) The x-component total wave u_x, and (b) the z-component total wave u_z.

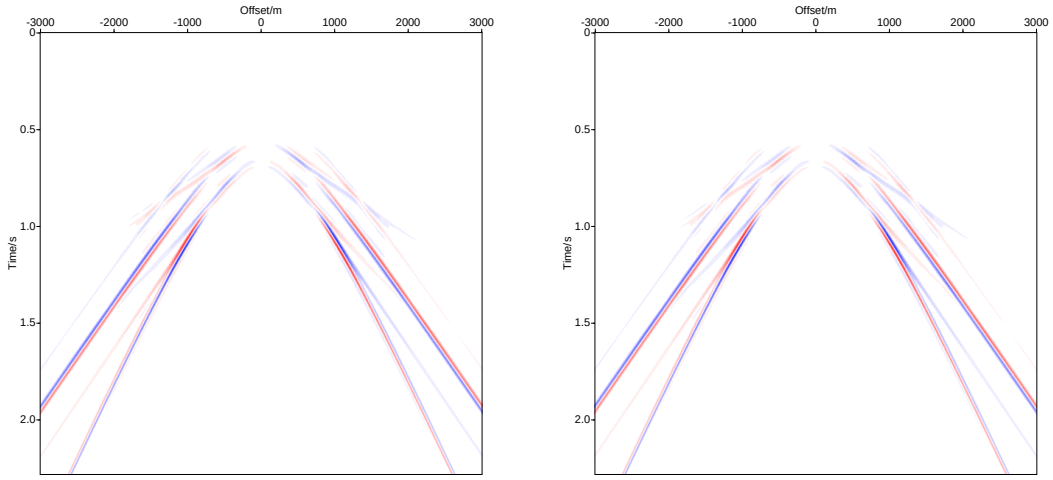

(a) (b)

Figure 6: X-component wave-separation results. (a) The x-component separated upgoing wave; (b) the x-component upgoing wave created with the analytic form of Green's function.

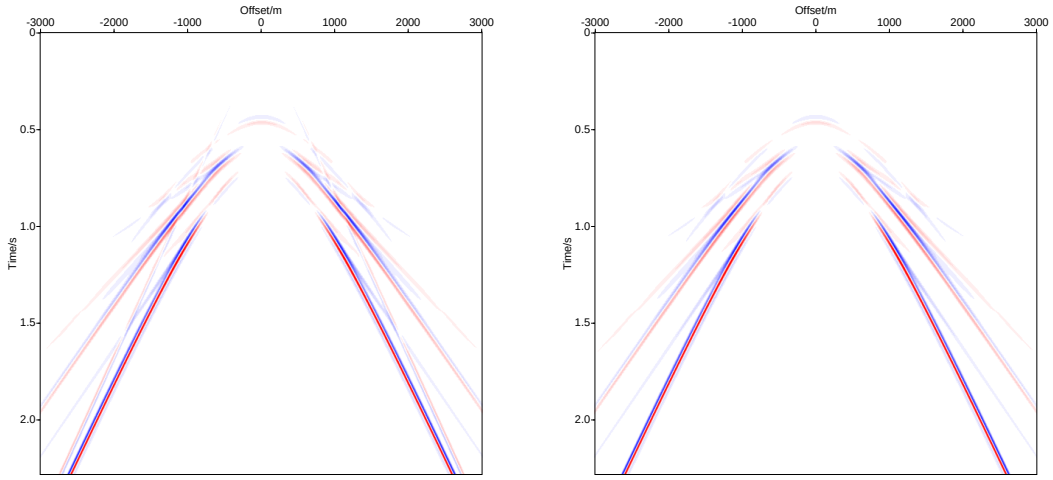

(a) (b)

Figure 7: Z-component wave-separation results. (a) The z-component separated upgoing wave; (b) the z-component upgoing wave created with the analytic form of Green's function.

the comparison shows that both sets of amplitudes and phases match very well. The conclusion is the same for the comparison of z components (see Figure 7a and Figure 7b). As the results in Figure 6a and Figure 7a show, both the Rayleigh waves and ghosts are extinguished, and the upgoing reflection data are not harmed.

5 Selection of the reference medium

As we described in the introduction, we have two strategies with which we can remove the reference waves (including the direct wave and the surface wave) and the ghosts. One approach is arranging to remove the direct wave, surface wave and the ghosts at the same time by choosing a homogeneous elastic whole space as the reference medium. The other strategy is to first remove the reference waves by choosing a two-half-space reference medium that is a half-space of homogeneous air over a half-space of homogeneous elastic earth, and then to deghost with the reference medium being a whole space of homogeneous elastic earth. Conceptually, either approach is applicable; however, based on our present study, the Green's function is complicated for a discontinuous medium, especially in a situation in which both the source and receiver points of Green's function are close to the air-elastic boundary/free surface. Practically, the wave-separation formula with such a complicated Green's function may produce an unstable result. We are working to address this issue. For that reason, if our objective is only obtaining the upgoing reflection data, we can select the first strategy, which uses a Green's function that has a simpler analytic form. That strategy provides a stable and useful approach for onshore preprocessing of onshore data.

6 Conclusion

From the theoretical derivation and numerical test that we use in this paper, the elastic Green's theorem-based wave-separation method in displacement space has the ability to remove both the ground roll and the ghosts from onshore data. In addition, by choosing a homogeneous elastic whole space as the reference medium, we can remove these two waves simultaneously. The algorithm that we develop in this paper has two requirements: (1) both the displacement and the traction (or the derivative of displacement) must occur along the measurement surface, and (2) the properties along the measurement surface must be homogeneous and known .

We are interest in reducing the demands of onshore data collection and the requirement of knowing near-surface properties, and those goals motivate the next steps in our research: (1) by altering the Green's function in the algorithm with a Dirichlet boundary condition, we hope to reduce the requirement of traction; and (2) by pursuing an alternative approach for these wave-separation objectives we seek to remove the requirement of knowing the properties along the measurement surface.

7 Acknowledgements

We are grateful to all M-OSRP sponsors for encouragement and support in this research.

Appendix

8 Derivation of the Elastic Green's theorem wave separation algorithm in the displacement space

Following Pao and Varatharajulu (1976), and with some modification, we go through the derivation of elastic Green's theorem wave separation method in (x, ω) domain.

We choose $\mathbf{u}(\mathbf{r}', \omega)$ to represent the displacement at $\mathbf{r}'$ in the actual medium (with $\rho(\mathbf{r}')$, $\lambda(\mathbf{r}')$, and $\mu(\mathbf{r}')$), and choose $\mathbf{G}_0(\mathbf{r}', \mathbf{r}, \omega)$ to represent the Green's displacement at $\mathbf{r}'$ by source at $\mathbf{r}$ in the reference medium (with $\rho_0(\mathbf{r}')$, $\lambda_0(\mathbf{r}')$, and $\mu_0(\mathbf{r}')$).

$\mathbf{G}_0(\mathbf{r}', \mathbf{r}, \omega)$ satisfies

$$\nabla' \cdot \mathbf{\Sigma}_0(\mathbf{r}', \mathbf{r}, \omega) + \rho_0(\mathbf{r}')\omega^2 \mathbf{G}_0(\mathbf{r}', \mathbf{r}, \omega) = \delta(\mathbf{r}' - \mathbf{r})\,\mathbf{I}, \tag{A-1}$$

where,

$$\Sigma_{0ijk}(\mathbf{r}', \mathbf{r}, \omega) = \lambda_0(\mathbf{r}')\partial_{m'} G_{0mk}(\mathbf{r}', \mathbf{r}, \omega)\delta_{ij} + \mu_0(\mathbf{r}')(\partial_{i'} G_{0jk}(\mathbf{r}', \mathbf{r}, \omega) + \partial_{j'} G_{0ik}(\mathbf{r}', \mathbf{r}, \omega)). \quad i, j, k = x, z \tag{A-2}$$

$\mathbf{u}(\mathbf{r}', \omega)$ satisfies

$$\nabla' \cdot \boldsymbol{\tau}(\mathbf{r}', \omega) + \rho(\mathbf{r}')\omega^2 \mathbf{u}(\mathbf{r}', \omega) = \mathbf{f}(\mathbf{r}', \omega), \tag{A-3}$$

where,

$$\boldsymbol{\tau}(\mathbf{r}', \omega) = \lambda(\mathbf{r}')\nabla' \cdot \mathbf{u}(\mathbf{r}', \omega)\,\mathbf{I} + \mu(\mathbf{r}')\left(\nabla' \mathbf{u}(\mathbf{r}', \omega) + \mathbf{u}(\mathbf{r}', \omega)\nabla'\right). \tag{A-4}$$

To make the parameters of left side of Equation 7 be consistent with that of Equation 5, we rewrite Equation 7 as

$$\begin{aligned} &\nabla' \cdot \boldsymbol{\tau_1}(\mathbf{r}', \omega) + \rho_0(\mathbf{r}')\omega^2 \mathbf{u}(\mathbf{r}', \omega) = \mathbf{f}(\mathbf{r}', \omega) - (\rho(\mathbf{r}') - \rho_0(\mathbf{r}'))\omega^2 \mathbf{u}(\mathbf{r}', \omega) \\ &- \nabla' \cdot [(\lambda(\mathbf{r}') - \lambda_0(\mathbf{r}'))\nabla' \cdot \mathbf{u}(\mathbf{r}', \omega)\,\mathbf{I} + (\mu(\mathbf{r}') - \mu_0(\mathbf{r}'))(\nabla' \mathbf{u}(\mathbf{r}', \omega) + \mathbf{u}(\mathbf{r}', \omega)\nabla')], \end{aligned} \tag{A-5}$$

and

$$\boldsymbol{\tau_1}(\mathbf{r}', \omega) = \lambda_0(\mathbf{r}')\nabla' \cdot \mathbf{u}(\mathbf{r}', \omega)\,\mathbf{I} + \mu_0(\mathbf{r}')(\nabla' \mathbf{u}(\mathbf{r}', \omega) + \mathbf{u}(\mathbf{r}', \omega)\nabla'). \tag{A-6}$$

Now we rename $\boldsymbol{\tau_1}$ as $\boldsymbol{\tau}$, rename $\mathbf{f} - (\rho - \rho_0)\omega^2 \mathbf{u} - \nabla' \cdot [(\lambda - \lambda_0)\nabla' \cdot \mathbf{u}\,\mathbf{I} + (\mu - \mu_0)(\nabla' \mathbf{u} + \mathbf{u}\nabla')]$ as $\mathbf{f}$, and then $\mathbf{f}$ becomes a generalized source, including both the active source and the passive source by earth perturbation. Equation 10 and Equation 11 change to be

$$\nabla' \cdot \boldsymbol{\tau}(\mathbf{r}', \omega) + \rho_0(\mathbf{r}')\omega^2 \mathbf{u}(\mathbf{r}', \omega) = \mathbf{f}(\mathbf{r}', \omega), \tag{A-7}$$

and

$$\boldsymbol{\tau}(\mathbf{r}', \omega) = \lambda_0(\mathbf{r}')\nabla' \cdot \mathbf{u}(\mathbf{r}', \omega)\,\mathbf{I} + \mu_0(\mathbf{r}')(\nabla' \mathbf{u}(\mathbf{r}', \omega) + \mathbf{u}(\mathbf{r}', \omega)\nabla'). \tag{A-8}$$

Multiplying Equation 12 with $\mathbf{G}_0(\mathbf{r}', \mathbf{r}, \omega)$, multiplying Equation 5 with $\mathbf{u}(\mathbf{r}', \omega)$, and then a subtraction between them will produce

$$\nabla' \cdot \boldsymbol{\tau}(\mathbf{r}', \omega) \cdot \mathbf{G}_0(\mathbf{r}', \mathbf{r}, \omega) - \mathbf{u}(\mathbf{r}', \omega) \cdot \nabla' \cdot \mathbf{\Sigma}_0(\mathbf{r}', \mathbf{r}, \omega) = \mathbf{f}(\mathbf{r}', \omega) \cdot \mathbf{G}_0(\mathbf{r}', \mathbf{r}, \omega) - \mathbf{u}(\mathbf{r}', \omega)\delta(\mathbf{r}' - \mathbf{r}). \tag{A-9}$$

Using the relationships that

$$\begin{aligned} \nabla' \cdot (\boldsymbol{\tau} \cdot \mathbf{G}_0) &= (\nabla' \cdot \boldsymbol{\tau}) \cdot \mathbf{G}_0 + \boldsymbol{\tau} \colon \nabla' \mathbf{G}_0, \\ \nabla' \cdot (\mathbf{u} \cdot \mathbf{\Sigma}_0) &= (\nabla' \cdot \mathbf{u}) \cdot \mathbf{\Sigma}_0 + \mathbf{u} \colon \nabla' \mathbf{\Sigma}_0, \end{aligned} \tag{A-10}$$

and

$$\boldsymbol{\tau}\colon \nabla' \mathbf{G}_0 - \mathbf{u}\colon \nabla' \boldsymbol{\Sigma}_0 = 0, \tag{A-11}$$

we have

$$\nabla' \cdot (\boldsymbol{\tau}(\mathbf{r}', \omega) \cdot \mathbf{G}_0(\mathbf{r}', \mathbf{r}, \omega) - \mathbf{u}(\mathbf{r}', \omega) \cdot \boldsymbol{\Sigma}_0(\mathbf{r}', \mathbf{r}, \omega)) = \mathbf{f}(\mathbf{r}', \omega) \cdot \mathbf{G}_0(\mathbf{r}', \mathbf{r}, \omega) - \mathbf{u}(\mathbf{r}', \omega) \delta(\mathbf{r}' - \mathbf{r}). \tag{A-12}$$

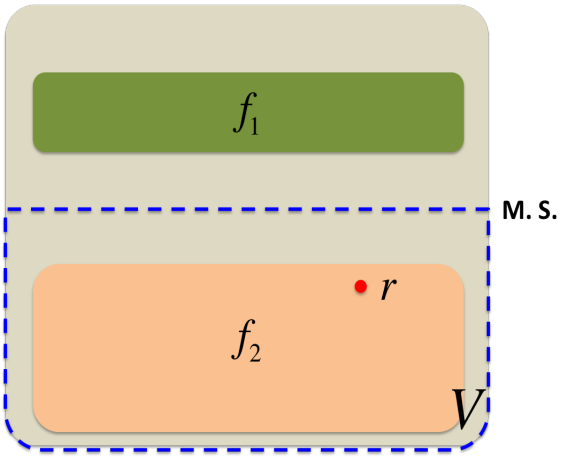

Figure A-1: A schemetic plot indicating that surface integral along the dash line will extract the contribution from $\mathbf{f}_1$ to $\mathbf{r}$

Considering Figure A-1, there are two sources acting on the reference medium, $\mathbf{f}_1$ and $\mathbf{f}_2$, and $\mathbf{f} = (\mathbf{f}_1 + \mathbf{f}_2)$.

From Lippmann–Schwinger equation, the wavefield at $\mathbf{r}$ can be expressed as

$$\begin{aligned} \mathbf{u}(\mathbf{r}, \omega) &= \int_{\infty} \mathbf{f}(\mathbf{r}', \omega) \cdot \mathbf{G}_0(\mathbf{r}', \mathbf{r}, \omega) d\mathbf{r}' \\ &= \int_{\infty - V} \mathbf{f}_1(\mathbf{r}', \omega) \cdot \mathbf{G}_0(\mathbf{r}', \mathbf{r}, \omega) d\mathbf{r}' + \int_{V} \mathbf{f}_2(\mathbf{r}', \omega) \cdot \mathbf{G}_0(\mathbf{r}', \mathbf{r}, \omega) d\mathbf{r}', \end{aligned} \tag{A-13}$$

for a causal Green's Function of the reference medium, and $\mathbf{r}$ is inside V.

On the other hand, if we put a close surface marked with dashed blue line, and integrate over the volume V on both side of Equation 16, the application of Green's Second Identity will result in

$$\begin{aligned} &\int_V \nabla' \cdot [\boldsymbol{\tau}(\mathbf{r}', \omega) \cdot \mathbf{G}_0(\mathbf{r}', \mathbf{r}, \omega) - \mathbf{u}(\mathbf{r}', \omega) \cdot \boldsymbol{\Sigma}_0(\mathbf{r}', \mathbf{r}, \omega)] d\mathbf{r}' \\ &= \int_{m.s.} [(\hat{n}' \cdot \boldsymbol{\tau}(\mathbf{r}', \omega)) \cdot \mathbf{G}_0(\mathbf{r}', \mathbf{r}, \omega) - \mathbf{u}(\mathbf{r}', \omega) \cdot (\hat{n}' \cdot \boldsymbol{\Sigma}_0(\mathbf{r}', \mathbf{r}, \omega))] d\mathbf{r}' \\ &= \int_V \mathbf{f}_2(\mathbf{r}', \omega) \cdot \mathbf{G}_0(\mathbf{r}', \mathbf{r}, \omega) d\mathbf{r}' - \mathbf{u}(\mathbf{r}, \omega), \end{aligned} \tag{A-14}$$

where, $\hat{n}'$ is the outside normal direction along the measurement surface (M.S.). Then,

$$\begin{aligned} \mathbf{u}(\mathbf{r}, \omega) = &\int_V \mathbf{f}_2(\mathbf{r}', \omega) \cdot \mathbf{G}_0(\mathbf{r}', \mathbf{r}, \omega) d\mathbf{r}' \\ &- \int_{m.s.} [(\hat{n}' \cdot \boldsymbol{\tau}(\mathbf{r}', \omega)) \cdot \mathbf{G}_0(\mathbf{r}', \mathbf{r}, \omega) - \mathbf{u}(\mathbf{r}', \omega) \cdot (\hat{n}' \cdot \boldsymbol{\Sigma}_0(\mathbf{r}', \mathbf{r}, \omega))] d\mathbf{r}'. \end{aligned} \tag{A-15}$$

Comparing Equation 17 with Equation 19, and choosing the Green's Function $\mathbf{G}_0$ in Equation 19 to be causal, it's evident that the surface integral is corresponding to the contribution from the source $\mathbf{f}_1$ that is outside the volume; i.e.,

$$\begin{aligned} &-\int_{m.s.}[(\hat{n'}\cdot\boldsymbol{\tau}(\mathbf{r}',\omega))\cdot\mathbf{G}_0(\mathbf{r}',\mathbf{r},\omega)-\mathbf{u}(\mathbf{r}',\omega)\cdot(\hat{n'}\cdot\boldsymbol{\Sigma}_0(\mathbf{r}',\mathbf{r},\omega))]d\mathbf{r}' \\ &=\int_{\infty-V}\mathbf{f}_1(\mathbf{r}',\omega)\cdot\mathbf{G}_0(\mathbf{r}',\mathbf{r},\omega)d\mathbf{r}'. \end{aligned} \tag{A-16}$$

The important physical meaning existing in this equation is the basis of wave separation method in the paper.

9 Derivation of the Analytic Form of the Green's Function

For a whole-space homogeneous medium, we can express the impulse response in both displacement and PS spaces (Weglein and Stolt, 1995; Zhang, 2006) with

$$\begin{aligned} \mathbf{L}_0\mathbf{G}_0&=\delta, \\ \hat{\mathbf{L}}_0\hat{\mathbf{G}}_0&=\delta, \end{aligned} \tag{A-17}$$

where $\mathbf{L}_0$ is the differential operator in displacement space representing the property of the medium, and $\hat{\mathbf{L}}_0$ is the differential operator in PS space. The Green's function operators $\mathbf{G}_0$ and $\hat{\mathbf{G}}_0$ have the relationship of

$$\mathbf{G}_0=\boldsymbol{\Gamma}_0^{-1}\boldsymbol{\Pi}^{-1}\hat{\mathbf{G}}_0\boldsymbol{\Pi}, \tag{A-18}$$

where $\boldsymbol{\Pi}=\begin{pmatrix}\partial_x & \partial_z\\ -\partial_z & \partial_x\end{pmatrix}$, $\boldsymbol{\Gamma}_0=\begin{pmatrix}\gamma_0 & \\ & \mu_0\end{pmatrix}$, and $\hat{\mathbf{G}}_0=\begin{pmatrix}\hat{G}_0^P & \\ & \hat{G}_0^S\end{pmatrix}$. In PS space, the Green's function only has the direct wave components, direct P wave and direct S wave.

In $(\mathbf{r},\omega)$ domain, $\hat{\mathbf{G}}_0(\mathbf{r}',\mathbf{r},\omega)$ can be expressed as

$$\begin{aligned} \hat{\mathbf{G}}_0(\mathbf{r}',\mathbf{r},\omega)&=\begin{pmatrix}\hat{G}_0^P(\mathbf{r}',\mathbf{r},\omega) & 0\\ 0 & \hat{G}_0^S(\mathbf{r}',\mathbf{r},\omega)\end{pmatrix} \\ &=\frac{1}{2\pi}\int e^{ik_x(x'-x)}dk_x\begin{pmatrix}\frac{e^{i\nu_0|z'-z|}}{2i\nu_0} & 0\\ 0 & \frac{e^{i\eta_0|z'-z|}}{2i\eta_0}\end{pmatrix}, \end{aligned} \tag{A-19}$$

where

$$\nu_0=\begin{cases}\sqrt{k_{\alpha_0}^2-k_x^2} & if\ \ k_x<k_{\alpha_0}\\ i\sqrt{k_x^2-k_{\alpha_0}^2} & if\ \ k_x>k_{\alpha_0}\end{cases}\qquad k_{\alpha_0}=\tfrac{\omega}{\alpha_0}\ \ ,$$

$$\eta_0=\begin{cases}\sqrt{k_{\beta_0}^2-k_x^2} & if\ \ k_x<k_{\beta_0}\\ i\sqrt{k_x^2-k_{\beta_0}^2} & if\ \ k_x>k_{\beta_0}\end{cases}\qquad k_{\beta_0}=\tfrac{\omega}{\beta_0}\ \ ,$$

and α_0 and β_0 are the P-wave velocity and the S-wave velocity of the whole space homogeneous elastic medium, respectively.

With the relationship Equation A-18 and the analytic form of $\hat{\mathbf{G}}_0(\mathbf{r}^{'},\mathbf{r},\omega)$ in Equation A-19, the analytic form of $\mathbf{G}_0(\mathbf{r}^{'},\mathbf{r},\omega)$ can be derived,

$$
\begin{aligned}
&\mathbf{G}_0(\mathbf{r}^{'},\mathbf{r},\omega)\\
=&-\frac{1}{\rho_0\omega^2}\mathbf{\Pi}^T\hat{\mathbf{G}}_0(\mathbf{r}^{'},\mathbf{r},\omega)\mathbf{\Pi}\delta\mathbf{I}\\
=&-\frac{1}{\rho_0\omega^2}\int\begin{pmatrix}\partial_{x'} & -\partial_{z'}\\ \partial_{z'} & \partial_{x'}\end{pmatrix}\begin{pmatrix}\hat{G}_0^P(\mathbf{r}^{'},\mathbf{r},\omega) & 0\\ 0 & \hat{G}_0^S(\mathbf{r}^{'},\mathbf{r},\omega)\end{pmatrix}\begin{pmatrix}\partial_{x''} & \partial_{z''}\\ -\partial_{z''} & \partial_{x''}\end{pmatrix}\begin{pmatrix}\delta(\mathbf{r}''-\mathbf{r}) & 0\\ 0 & \delta(\mathbf{r}''-\mathbf{r})\end{pmatrix}d\mathbf{r}''\\
=&\frac{1}{\rho_0\omega^2}\begin{pmatrix}\partial_{x'} & -\partial_{z'}\\ \partial_{z'} & \partial_{x'}\end{pmatrix}\begin{pmatrix}\hat{G}_0^P(\mathbf{r}^{'},\mathbf{r},\omega) & 0\\ 0 & \hat{G}_0^S(\mathbf{r}^{'},\mathbf{r},\omega)\end{pmatrix}\begin{pmatrix}\partial_{x} & \partial_{z}\\ -\partial_{z} & \partial_{x}\end{pmatrix}\\
=&\frac{1}{\rho_0\omega^2}\frac{1}{2\pi}\int\begin{pmatrix}\partial_{x'} & -\partial_{z'}\\ \partial_{z'} & \partial_{x'}\end{pmatrix}\begin{pmatrix}\partial_{x} & \partial_{z}\\ -\partial_{z} & \partial_{x}\end{pmatrix}\begin{pmatrix}\frac{e^{i\nu_0|z'-z|}}{2i\nu_0} & 0\\ 0 & \frac{e^{i\eta_0|z'-z|}}{2i\eta_0}\end{pmatrix}e^{ik_x(x'-x)}dk_x\\
=&\frac{1}{2\pi}\int\begin{pmatrix}\tilde{G}_{xx}(k_x,z',z,\omega) & \tilde{G}_{xz}(k_x,z',z,\omega)\\ \tilde{G}_{zx}(k_x,z',z,\omega) & \tilde{G}_{zz}(k_x,z',z,\omega)\end{pmatrix}e^{ik_x(x'-x)}dk_x,
\end{aligned}
\tag{A-20}
$$

where

$$
\begin{aligned}
\tilde{G}_{xx}(k_x,z',z,\omega)&=\frac{1}{\rho_0\omega^2}\left(k_x^2\frac{e^{i\nu_0|z'-z|}}{2i\nu_0}+\eta_0^2\frac{e^{i\eta_0|z'-z|}}{2i\eta_0}\right),\\
\tilde{G}_{xz}(k_x,z',z,\omega)&=\frac{1}{\rho_0\omega^2}\left(k_x\nu_0 sgn(z'-z)\frac{e^{i\nu_0|z'-z|}}{2i\nu_0}-k_x\eta_0 sgn(z'-z)\frac{e^{i\eta_0|z'-z|}}{2i\eta_0}\right),\\
\tilde{G}_{zx}(k_x,z',z,\omega)&=\frac{1}{\rho_0\omega^2}\left(k_x\nu_0 sgn(z'-z)\frac{e^{i\nu_0|z'-z|}}{2i\nu_0}-k_x\eta_0 sgn(z'-z)\frac{e^{i\eta_0|z'-z|}}{2i\eta_0}\right),\\
\tilde{G}_{zz}(k_x,z',z,\omega)&=\frac{1}{\rho_0\omega^2}\left(\nu_0^2\frac{e^{i\nu_0|z'-z|}}{2i\nu_0}+k_x^2\frac{e^{i\eta_0|z'-z|}}{2i\eta_0}\right).
\end{aligned}
\tag{A-21}
$$

After deriving the analytic form of Green's function in displacement space, we can further obtain the analytic expression for the stress of Green's function via Equation 10.

References

Mayhan, J. D., P. Terenghi, A. B. Weglein, and N. Chemingui. "Green's theorem derived methods for preprocessing seismic data when the pressure P and its normal derivative are measured." *81st Annual International Meeting, SEG, Expanded Abstracts* (2011): 2722–2726.

Mayhan, J. D. and A. B. Weglein. "First application of Green's theorem-derived source and receiver deghosting on deep-water Gulf of Mexico synthetic (SEAM) and field data." *Geophysics* 78 (2013): WA77–WA89.

Pao, Y. H. and V. Varatharajulu. "Huygens principle, radiation conditions, and integral formulas for the scattering of elastic waves." *J. Acoust. Soc. Am.* 59 (1976): 1361–1371.

Tang, L., J. D. Mayhan, J. Yang, and A. B. Weglein. "Using Green's theorem to satisfy data requirements of multiple removal methods: The impact of acquisition design." *83rd Annual International Meeting, SEG, Expanded Abstracts* (2013): 4392–4396.

Weglein, A. B., F. V. Araújo, P. M. Carvalho, R. H. Stolt, K. H. Matson, R. T. Coates, D. Corrigan, D. J. Foster, S. A. Shaw, and H. Zhang. "Inverse Scattering Series and Seismic Exploration." *Inverse Problems* (2003): R27–R83.

Weglein, A. B. and B. G. Secrest. "Wavelet estimation for a multidimensional acoustic earth model." *Geophysics* 55 (1990): 902–913.

Weglein, A. B., S. .A. Shaw, K. H. Matson, J. L. Sheiman, R. H. Solt, T. H. Tan, A. Osen, G. P. Correa, K. A. Innanen, Z. Guo, and J. Zhang. "New approaches to deghosting towed-streamer and ocean-bottom pressure measurements." *72th Annual International Meeting, SEG, Expanded Abstracts* (2002): 1016–1019.

Weglein, A. B. and R. H. Stolt. "I. The wave physics of downward continuation, wavelet estimation and volume and surface scattering. II. Approaches to linear and nonlinear migration inversion." *Mathematical Frontiers in Reflection Seismology: SEG/SIAM publication* (1995).

Wu, J. and A. B. Weglein. "Elastic Green's theorem preprocessing for on-shore internal multiple attenuation: theory and initial synthetic data tests." *84th Annual International Meeting, SEG, Expanded Abstracts* (2014): 4299–4304.

Wu, J. and A. B. Weglein. "Preprocessing in PS space for on-shore seismic processing: removing ground roll and ghosts without damaging the reflection data." *85th Annual International Meeting, SEG, Expanded Abstracts, submitted* (2015).

Yang, J., J. D. Mayhan, L. Tang, and A. B. Weglein. "Accommodating the source (and receiver) array in free-surface multiple elimination algorithm: Impact on interfering or proximal primaries and multiples." *83rd Annual International Meeting, SEG, Expanded Abstracts* (2013): 4184–4189.

Zhang, H. *Direct non-linear acoustic and elastic inversion: Towards fundamentally new comprehensive and realistic target identification*. PhD thesis, University of Houston, 2006.

Zhang, J. *Wave theory based data preparation for inverse scattering multiple removal, depth imaging and parameter estimation: analysis and numerical tests of Green's theorem deghosting theory*. PhD thesis, University of Houston, 2007.

Preprocessing in displacement space for on-shore seismic processing: removing ground roll and ghosts without damaging the reflection data

Jing Wu and Arthur B. Weglein, M-OSRP, University of Houston

SUMMARY

This paper derives an elastic Green's theorem wave separation method for on-shore data in displacement space. Applying the algorithm presented in this paper only once, both the reference waves (including the direct wave and the surface wave) and the ghosts can be effectively removed. The method is tested on a layered elastic earth model. The results indicate its effectiveness for reducing the ground roll and ghosts at the same time, and without harming the up-going reflections, in preparation for on-shore processing.

INTRODUCTION

On-shore seismic exploration and processing seeks to use reflection data (the scattered wavefield) to make inferences about the subsurface. The measured total wavefield consists of the reflection data and the reference wave that contains the direct wave and the surface wave/ground roll; hence, one prerequisite is to separate the reference wave and scattered wave. Filtering methods are typically employed to remove the reference wave, particularly the ground roll. That can be at the expense of damaging reflection data when ground roll is interfering with the scattered wavefield.

In addition, for buried sources and receivers, not only up-going waves are in the reflection data but also ghosts, whose existence can cause notches in the spectrum. Thus, removing the ghosts from the reflection data is another prerequisite. In this study, we will assume the source is located slightly above the air/earth surface (could be infinitely close, or on the air/earth surface), and the receivers are slightly beneath the air/earth surface. Therefore, there are receiver ghosts but no source ghosts in our study.

As a flexible and useful tool, Green's theorem provides a method to satisfy both prerequisites; i.e., removing the reference wave without damaging the reflection data and removing the ghosts from the reflection data without destroying the up-going reflected data. The distinct advantages of applying the method based on Green's theorem in off-shore plays have been demonstrated by Weglein et al. (2002); Zhang (2007); Mayhan et al. (2011); Mayhan and Weglein (2013); Tang et al. (2013); Yang et al. (2013).

Basically, wave separation from Green's theorem has a model of the world that consists of the **reference medium** and the **sources**. The choice of reference medium is arbitrary, and the choice of reference will determine what the sources have to be to arrange for the reference medium and sources together to correspond to the actual medium and experiment (Weglein et al., 2003). For on-shore plays, Green's theorem wave separation method is applicable for data either in displacement space (Pao and Varatharajulu, 1976; Weglein and Secrest, 1990) or in the PS space (Wu and Weglein, 2014). In this paper, for data in displacement space, we choose a homogeneous elastic whole space as the reference, then both the reference wave and receiver ghosts can be removed in one step while applying the elastic Green's theorem wave separation algorithm. In a companion paper (Wu and Weglein, 2015b), and for data in the PS space, the reference medium is chosen to be composed of two homogenous half-spaces, an air/acoustic half-space over an elastic half-space, then Green's theorem method can extinguish the reference wave (including the ground roll) without harming the reflection data. After obtaining the reflection data, Green's theorem provides a reflection data deghosting algorithm with a choice of a whole-space homogenous elastic reference (Wu and Weglein, 2015b).

DESCRIPTION OF THE MODEL: REFERENCE MEDIUM + SOURCES

As shown in Figure 1, the model consists of an air half-space and an elastic-earth half-space. Receivers are buried in the earth, and the active source in the form of a vertical force is applied on the free surface (F.S.). Therefore, ghosts exist at the receiver side only. The measurement surface (M.S.) can be infinitely close to the free surface, like on-surface acquisition, or several meters below the free surface, like buried-receiver acquisition; however, the receivers are coupled with the elastic medium in both situations.

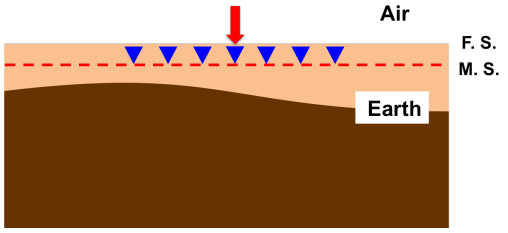

Figure 1: A generic model describing the land experiment

In this paper, we will assume that the portion of earth along the measurement surface is homogeneous and known. Within this assumption, we choose the reference medium to be a homogenous elastic whole space, as shown in Figure 2, whose property agrees with the actual earth along the measurement surface.

There are three sources acting on the homogeneous reference medium that is described in Figure 2. As shown in Figure 3, one is the active source (or the vertical force S_1) and the other two are passive sources (or the perturbations S_2 and S_3) on two sides of the measurement surface, respectively. S_1 produces the direct waves. S_2 produces the ground roll; it also produces

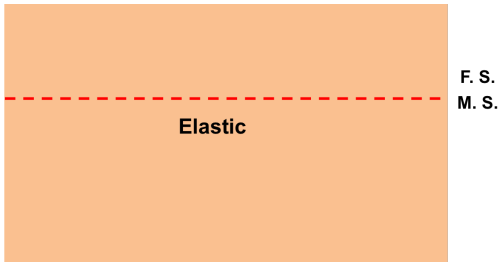

Figure 2: A homogeneous elastic whole-space reference medium

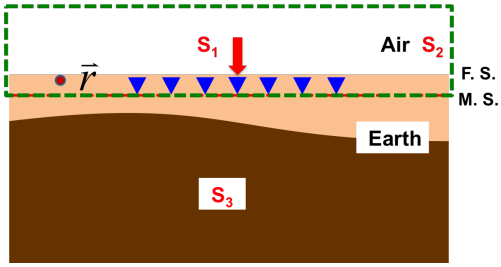

Figure 3: Three sources are acting on the reference medium that is depicted in Figure 2, and surface integral along the measurement surface will move out the contribution from S_1 and S_2 inside the enclosed the surface.

the ghosts by transferring the up-going waves that are propagating from the earth, to the down-going ones. S_3 generates up-going waves from the earth. All of these three sources contribute to providing the actual total wavefield, and the up waves due to S_3 are expected to be separated from the waves caused by both S_1 and S_2.

ELASTIC GREEN'S THEOREM WAVE SEPARATION THEORY

Background of 2D elastic wave theory

The wave equation for a 2D elastic isotropic medium is

$$\nabla\cdot\tau(\mathbf{r},\omega)+\rho\omega^2\mathbf{u}(\mathbf{r},\omega)=\mathbf{f}(\mathbf{r},\omega), \tag{1}$$

where:

$$\tau=\lambda\nabla\cdot\mathbf{u}\,\mathbf{I}+\mu\left(\nabla\mathbf{u}+\mathbf{u}\nabla\right). \tag{2}$$

$\mathbf{u}=\begin{pmatrix}u_x\\u_z\end{pmatrix}$ is the displacement, the 2^{nd} order tensor $\tau=\begin{pmatrix}\tau_{xx}&\tau_{xz}\\\tau_{zx}&\tau_{zz}\end{pmatrix}$ is the stress, $\mathbf{f}=\begin{pmatrix}f_x\\f_z\end{pmatrix}$ is the source, λ and μ are Lamé's parameters, and ρ is the density.

The impulse response of the reference medium can be written as

$$\nabla\cdot\Sigma_0(\mathbf{r},\omega)+\rho_0\omega^2\mathbf{G}_0(\mathbf{r},\omega)=\delta(\mathbf{r})\,\mathbf{I}, \tag{3}$$

where:

$$\Sigma_{0ijk}=\lambda_0\partial_m G_{0mk}\delta_{ij}+\mu_0(\partial_i G_{0jk}+\partial_j G_{0ik}),\qquad i,j,k=x,z. \tag{4}$$

The 2^{nd} order tensor $\mathbf{G}_0=\begin{pmatrix}G_{0xx}&G_{0xz}\\G_{0zx}&G_{0zz}\end{pmatrix}$ is the Green's displacement tensor, the 3^{rd} order tensor Σ_0 is the Green's stress tensor, and the source term consists of a diagonal matrix.

Elastic Green's theorem wave separation algorithm in (x,ω) domain

As seen in Figure 3, applying Green's theorem, the integral, that is along the closed semi-infinite surface lower bounded by the measurement surface, will separate the portion of the wavefield that is inside the enclosed volume due to S_3 that is outside the volume.

Starting from Equation 1 and Equation 3, and using the Green's theorem, we can obtain the wave separation algorithm (see Wu and Weglein (2015a) for the detailed derivation); i.e., we can extract the up-going waves generated by the source S_3.

In (x,ω) domain, the formula is

$$\begin{aligned}&\mathbf{u}^{up}(\mathbf{r},\omega)\\&=-\int_{m.s.}[(\hat{n}'\cdot\tau(\mathbf{r}',\omega))\cdot\mathbf{G}_0(\mathbf{r}',\mathbf{r},\omega)-\mathbf{u}(\mathbf{r}',\omega)\cdot(\hat{n}'\cdot\Sigma_0(\mathbf{r}',\mathbf{r},\omega))]d\mathbf{r}',\end{aligned} \tag{5}$$

where $\hat{n}'$ is the normal outside vector along the surface.

On the measurement surface, $\mathbf{r}'=(x',z'=\varepsilon_g)$,

$$\begin{aligned}\tau(x',z'=\varepsilon_g,\omega)=&\lambda_0\nabla'\cdot\mathbf{u}(x',z'=\varepsilon_g,\omega)\,\mathbf{I}\\&+\mu_0(\nabla'\mathbf{u}(x',z'=\varepsilon_g,\omega)+\mathbf{u}(x',z'=\varepsilon_g,\omega)\nabla'),\end{aligned} \tag{6}$$

where ε_g is the receiver's depth. Since the properties along the measurement surface have been assumed to be homogeneous in the paper, λ_0 and μ_0 are constants along the measurement surface. The choice of the reference medium depends on these invariant parameters.

Applying Equation 5 in the (x,ω) domain, we can remove the reference wave (particularly the ground roll) and the ghosts simultaneously. There is no assumption about the shape of the measurement surface; i.e., it can be either flat or rugose.

Elastic Green's theorem wave separation algorithm in (k_x,ω) Domain

If the measurement surface is horizontal and flat, then $\hat{n}'=(0,1)$. Equation 5 can be Fourier transformed to (k_x,ω) domain.

Equation 5 is expanded to be

$$\begin{aligned}&u_x^{up}(\mathbf{r},\omega)\\&=-\int_{m.s.}[\tau_{zx}(\mathbf{r}',\omega)G_{0xx}(\mathbf{r}',\mathbf{r},\omega)+\tau_{zz}(\mathbf{r}',\omega)G_{0zx}(\mathbf{r}',\mathbf{r},\omega)\\&\quad-u_x(\mathbf{r}',\omega)\Sigma_{0zxx}(\mathbf{r}',\mathbf{r},\omega)-u_z(\mathbf{r}',\omega)\Sigma_{0zzx}(\mathbf{r}',\mathbf{r},\omega)]dx',\\&u_z^{up}(\mathbf{r},\omega)\\&=-\int_{m.s.}[\tau_{zx}(\mathbf{r}',\omega)G_{0xz}(\mathbf{r}',\mathbf{r},\omega)+\tau_{zz}(\mathbf{r}',\omega)G_{0zz}(\mathbf{r}',\mathbf{r},\omega)\\&\quad-u_x(\mathbf{r}',\omega)\Sigma_{0zxz}(\mathbf{r}',\mathbf{r},\omega)-u_z(\mathbf{r}',\omega)\Sigma_{0zzz}(\mathbf{r}',\mathbf{r},\omega)]dx'.\end{aligned} \tag{7}$$

With reciprocity,

$$G_{0ij}(\mathbf{r}',\mathbf{r},\omega) = G_{0ji}(\mathbf{r},\mathbf{r}',\omega), i,j,k = x,z. \tag{8}$$

Applying Fourier transform over x in Equation 7 with $\int e^{-ik_x x}dx$, it will become

$$\begin{aligned}
&\tilde{u}_x^{up}(k_x,z,\omega)\\
&= -[\tilde{\tau}_{zx}(k_x,z',\omega)\tilde{G}_{0xx}(k_x,z,z',\omega) + \tilde{\tau}_{zz}(k_x,z',\omega)\tilde{G}_{0xz}(k_x,z,z',\omega)\\
&- \tilde{u}_x(k_x,z',\omega)\tilde{\Sigma}_{0zxx}(k_x,z',z,\omega) - \tilde{u}_z(k_x,z',\omega)\tilde{\Sigma}_{0zzx}(k_x,z',z,\omega)]|_{z'=\varepsilon_g},\\
&\tilde{u}_z^{up}(k_x,z,\omega)\\
&= -[\tilde{\tau}_{zx}(k_x,z',\omega)\tilde{G}_{0zx}(k_x,z,z',\omega) + \tilde{\tau}_{zz}(k_x,z',\omega)\tilde{G}_{0zz}(k_x,z,z',\omega)\\
&- \tilde{u}_x(k_x,z',\omega)\tilde{\Sigma}_{0zxz}(k_x,z',z,\omega) - \tilde{u}_z(k_x,z',\omega)\tilde{\Sigma}_{0zzz}(k_x,z',z,\omega)]|_{z'=\varepsilon_g},
\end{aligned} \tag{9}$$

where tildes represent the terms in k_x domain, and z' is evaluated at the receiver's depth ε_g. Specifically,

$$\begin{aligned}
&\tilde{\Sigma}_{0zxx}(k_x,z',z,\omega)\\
=&\mu_0[\partial_{z'}\tilde{G}_{0xx}(k_x,z,z',\omega) - ik_x\tilde{G}_{0xz}(k_x,z,z',\omega)],\\
&\tilde{\Sigma}_{0zzx}(k_x,z',z,\omega)\\
=&\gamma_0\partial_{z'}\tilde{G}_{0xz}(k_x,z,z',\omega) - \lambda_0(ik_x)\tilde{G}_{0xx}(k_x,z,z',\omega),\\
&\tilde{\Sigma}_{0zxz}(k_x,z',z,\omega)\\
=&\mu_0[\partial_{z'}\tilde{G}_{0zx}(k_x,z,z',\omega) - ik_x\tilde{G}_{0zz}(k_x,z',z,\omega)],\\
&\tilde{\Sigma}_{0zzz}(k_x,z',z,\omega)\\
=&\gamma_0\partial_{z'}\tilde{G}_{0zz}(k_x,z,z',\omega) - \lambda_0(ik_x)\tilde{G}_{0zx}(k_x,z,z',\omega),
\end{aligned} \tag{10}$$

where γ_0 is the bulk modulus, and $\gamma_0 = \lambda_0 + 2\mu_0$.

For a reference medium as homogenous elastic whole space, both the Green's displacement tensor and its stress tensor can be expressed analytically (see appendix A for $\mathbf{G}_0$).

It is deserving emphasis that applying the algorithm in (k_x,ω) domain, we can locate the output point $\mathbf{r}$ on the measurement surface to be part of the volume above, to extract the the up-going wavefield that is portion of the actually measured data.

NUMERICAL EVALUATION

We test the (k_x,ω) domain wave separation algorithm on a two layered elastic earth model, as seen in Figure 4. A vertical force $(0,F_z)$ is applied on the free surface, and receivers are buried at depth 30m. For simplicity, the space above the free surface is set to be vacuum. The properties of the earth are listed in Table 1. The output point $\mathbf{r}$ is arranged to be on the measurement surface and treated as part of the volume above.

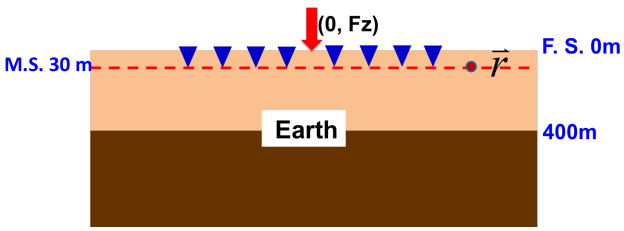

Figure 4: A two layered elastic earth model for numeric test

Layer's Number	P Velocity (m/s)	S Velocity (m/s)	Density (kg/m^3)
1	1800	1200	1500
2	4000	2500	1800

Table 1: The parameters of the earth model in Figure 4

The trace interval is 2m, the maximum offset is 3000m, the time sampling interval is 4ms, and the total time sampling length is 3s. Then the data of displacement $\mathbf{u}$ with both x and z components are generated using analytic forms. As shown in Figure 5(a) and Figure 5(d), the data have strong Rayleigh wave and relatively weak scattered wave. Besides, the ghosts are interfering with the up-going waves. All the figures are in the same scales.

Putting the multicomponent data into the wave separation formula of Equation 9, the up-going waves can be separated, with x and z components. To evaluate the accuracy of the results, we analytically create the data consisting of only the up waves, with the given model of Figure 4. These data will play as criteria to examine the calculation results. The x component of separated up waves from Green's theorem separation algorithm (Figure 5(b)) is compared with the x component created up waves with analytic form (Figure 5(c)), and the comparison shows that both their amplitudes and phases match very well. The conclusion is the same for the comparison of z components (see Figure 5(e) and Figure 5(f)). As the results shown in Figure 5, both the Rayleigh waves and ghosts are extinguished, and there is no harm to the up-going reflection data.

DISCUSSION OF SELECTING THE REFERENCE MEDIUM

As described in the introduction, we have two strategies to remove the reference waves (including the direct wave and the surface wave) and the ghosts. One is removing both of them at the same time by choosing a homogenous elastic whole space as the reference medium. The other is first removing the reference waves by choosing a two-half-space reference medium that is a half-space of homogenous air over a half-space of homogenous elastic earth, then deghosting with the reference medium to be a whole space of homogeneous elastic. Conceptually, it's applicable either way; however, based on our present study, the Green's function in displacement space is complicated for a discontinuous medium, especially for the situation that both the source and receiver points of Green's function are close to the air-elastic boundary/free surface. Practically, the wave separation formula with such a complicated Green's function may produce an unstable result. That's the reason why we select the first strategy that uses a Green's function with a simpler analytic form. That strategy provides a stable and useful approach for on-shore preprocessing in displacement space.

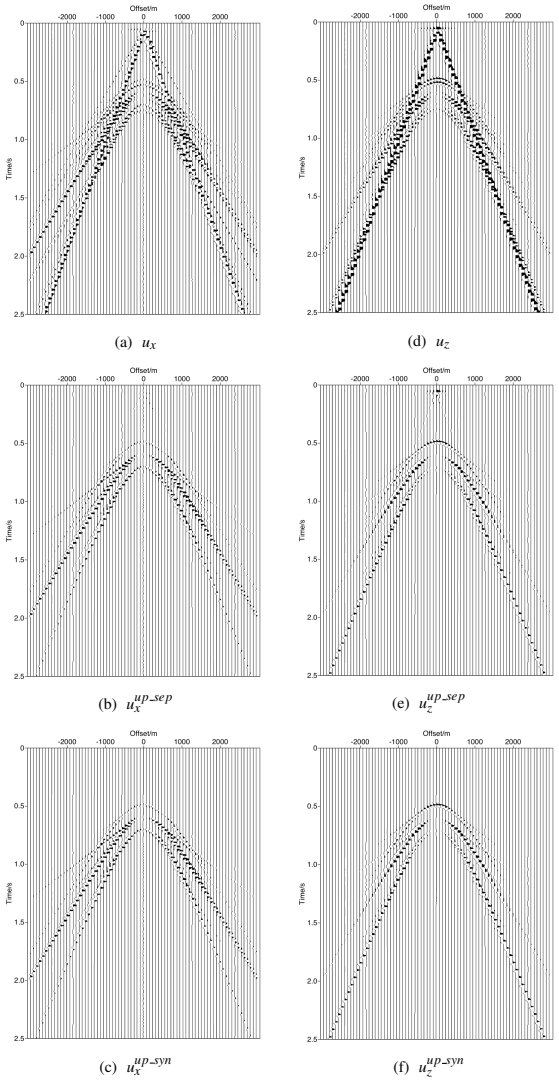

(a) u_x (d) u_z

(b) $u_x^{up\_sep}$ (e) $u_z^{up\_sep}$

(c) $u_x^{up\_syn}$ (f) $u_z^{up\_syn}$

Figure 5: Wave separation results. (a) is x component total wave; (b) is the x component separated up wave; (c) is the x component created up wave with analytic form; (d) is z component total wave; (e) is the z component separated up wave; (f) is the z component created up wave with analytic form.

.

CONCLUSION

From the theoretic derivation and numeric test in this paper, the elastic Green's theorem based wave separation method in displacement space has the potential to remove both the ground roll and the ghosts from on-shore data. In addition, by choosing a homogenous elastic whole space as reference, we can remove these two waves simultaneously. The algorithm that we develop in this paper has two requirements: (1) both the displacement and the traction (or the derivative of displacement) along the measurement surface; and (2) the homogeneous and known properties along the measurement surface. Our interest in reducing the demanding on-shore data collection and requiring near surface properties motivates the next steps in our research: (1) altering the Green's function with a Dirichlet boundary condition to reduce the requirement of traction; (2) pursuing an alternative approach for these wave separation objectives without the requirement of known properties along the measurement surface.

ACKNOWLEDGEMENTS

We are grateful to all M-OSRP sponsors for encouragement and support in this research.

APPENDIX A: ANALYTIC FORM OF THE GREEN'S FUNCTION

For a whole space homogeneous elastic medium, the Green's function in displacement space can be expressed analytically as

$$\begin{aligned}&\mathbf{G}_0(\mathbf{r}',\mathbf{r},\omega)\\ =&\frac{1}{2\pi}\int\begin{pmatrix}\tilde{G}_{xx}(k_x,z',z,\omega) & \tilde{G}_{xz}(k_x,z',z,\omega)\\ \tilde{G}_{zx}(k_x,z',z,\omega) & \tilde{G}_{zz}(k_x,z',z,\omega)\end{pmatrix}e^{ik_x(x'-x)}dk_x,\end{aligned} \tag{A-1}$$

where

$$\begin{aligned}&\tilde{G}_{xx}(k_x,z',z,\omega)\\ =&\frac{1}{\rho_0\omega^2}\left(k_x^2\frac{e^{i\nu_0|z'-z|}}{2i\nu_0}+\eta_0^2\frac{e^{i\eta_0|z'-z|}}{2i\eta_0}\right),\\ &\tilde{G}_{xz}(k_x,z',z,\omega)\\ =&\frac{1}{\rho_0\omega^2}\left(k_x\nu_0 sgn(z'-z)\frac{e^{i\nu_0|z'-z|}}{2i\nu_0}-k_x\eta_0 sgn(z'-z)\frac{e^{i\eta_0|z'-z|}}{2i\eta_0}\right),\\ &\tilde{G}_{zx}(k_x,z',z,\omega)\\ =&\frac{1}{\rho_0\omega^2}\left(k_x\nu_0 sgn(z'-z)\frac{e^{i\nu_0|z'-z|}}{2i\nu_0}-k_x\eta_0 sgn(z'-z)\frac{e^{i\eta_0|z'-z|}}{2i\eta_0}\right),\\ &\tilde{G}_{zz}(k_x,z',z,\omega)\\ =&\frac{1}{\rho_0\omega^2}\left(\nu_0^2\frac{e^{i\nu_0|z'-z|}}{2i\nu_0}+k_x^2\frac{e^{i\eta_0|z'-z|}}{2i\eta_0}\right),\end{aligned} \tag{A-2}$$

and

$$\nu_0=\begin{cases}\sqrt{k_{\alpha_0}^2-k_x^2} & \text{if } k_x<k_{\alpha_0}\\ i\sqrt{k_x^2-k_{\alpha_0}^2} & \text{if } k_x>k_{\alpha_0}\end{cases}\qquad k_{\alpha_0}=\frac{\omega}{\alpha_0}\ ,$$

$$\eta_0=\begin{cases}\sqrt{k_{\beta_0}^2-k_x^2} & \text{if } k_x<k_{\beta_0}\\ i\sqrt{k_x^2-k_{\beta_0}^2} & \text{if } k_x>k_{\beta_0}\end{cases}\qquad k_{\beta_0}=\frac{\omega}{\beta_0}\ .$$

α_0 and β_0 are P wave velocity and S wave velocity in the medium, respectively.

REFERENCES

Mayhan, J. D., P. Terenghi, A. B. Weglein, and N. Chemingui, 2011, Green's theorem derived methods for preprocessing seismic data when the pressure P and its normal derivative are measured: SEG Technical Program Expanded Abstracts, Soc. Expl. Geophys., 2722–2726.

Mayhan, J. D., and A. B. Weglein, 2013, First application of Green's theorem-derived source and receiver deghosting on deep-water Gulf of Mexico synthetic (SEAM) and field data: Geophysics, **78**, WA77–WA89.

Pao, Y. H., and V. Varatharajulu, 1976, Huygens principle, radiation conditions, and integral formulas for the scattering of elastic waves: J. Acoust. Soc. Am., **59**, 1361–1371.

Tang, L., J. D. Mayhan, J. Yang, and A. B. Weglein, 2013, Using Green's theorem to satisfy data requirements of multiple removal methods: The impact of acquisition design: SEG Technical Program Expanded Abstracts, Soc. Expl. Geophys., 4392–4395.

Weglein, A. B., F. V. Araújo, P. M. Carvalho, R. H. Stolt, K. H. Matson, R. T. Coates, D. Corrigan, D. J. Foster, S. A. Shaw, and H. Zhang, 2003, Inverse scattering series and seismic exploration: Inverse Problems, R27–R83.

Weglein, A. B., and B. G. Secrest, 1990, Wavelet estimation for a multidimensional acoustic earth model: Geophysics, **55**, 902–913.

Weglein, A. B., S. A. Shaw, K. H. Matson, J. L. Sheiman, R. H. Solt, T. H. Tan, A. Osen, G. P. Correa, K. A. Innanen, Z. Guo, and J. Zhang, 2002, New approaches to deghosting towed-streamer and ocean-bottom pressure measurements: 72nd Annual International Meeting, SEG, Expanded Abstracts, 1016–1019.

Wu, J., and A. B. Weglein, 2014, Elastic green's theorem preprocessing for on-shore internal multiple attenuation: theory and initial synthetic data tests: SEG Technical Program Expanded Abstracts, Soc. Expl. Geophys., 4299–4304.

———, 2015a, Elastic Green's theorem preprocessing method in displacement space for on-shore seismic processing: Presented at the Mission-Oriented Seismic Research Program (M-OSRP) Annual Report, University of Houston.

———, 2015b, Preprocessing in PS space for on-shore seismic processing: removing ground roll and ghosts without damaging the reflection data: SEG Technical Program Expanded Abstracts, Soc. Expl. Geophys., submitted.

Yang, J., J. D. Mayhan, L. Tang, and A. B. Weglein, 2013, Accommodating the source (and receiver) array in free-surface multiple elimination algorithm: Impact on interfering or proximal primaries and multiples: SEG Technical Program Expanded Abstracts, Soc. Expl. Geophys., 4184–4189.

Zhang, J., 2007, Wave theory based data preparation for inverse scattering multiple removal, depth imaging and parameter estimation: analysis and numerical tests of Green's theorem deghosting theory: PhD thesis, University of Houston.

(Short note) Back scattering artifacts in Reverse Time Migration (RTM)

Qiang Fu and Arthur B. Weglein

1 Introduction

Recently, reverse time migration (RTM) has been widely used in seismic exploration, especially in an area with complex geology, because it shows advantages over other imaging methods in handling complicated structures. Usually it is considered that reverse time migration utilizes the second of three imaging conditions proposed by Claerbout, Lowenthal and their colleagues in the 1970s and 1980's (Claerbout, 1971; Riley and Claerbout, 1976; Lowenthal et al., 1985), which we refer to as Claerbout Imaging Condition II. In fact the imaging condition used in RTM implementation is not exactly the Claerbout Imaging Condition II. The difference between the proposed form of Claerbout imaging condition II and the actual implementation in RTM will cause strong high amplitude and low wavenumber artifacts (which are well known in the exploration geophysics community as RTM back scattering artifacts). In this short note we will show how RTM back scattering artifacts are generated and what methods are usually used to address this issue.

2 Claerbout Imaging Condition II, imaging condition used in RTM implementation and RTM back scattering artifacts

Methods that use the wave equation to perform seismic migration have two ingredients: (1) a wave propagation component and (2) an imaging principle or concept. Claerbout (Claerbout, 1971; Riley and Claerbout, 1976) was the initial and key wave-equation-migration imaging-concept pioneer and algorithm developer; together with Stolt (Stolt, 1978) and Lowenthal (Lowenthal et al., 1985) and their colleagues, they introduced imaging conditions for locating reflectors at depth from surface-recorded data. The three Claerbout imaging conditions that were introduced are:
I. the exploding-reflector model
II. time and space coincidence of up and down-going waves
III. predicting a source and receiver experiment at a coincident-source-and-receiver subsurface point, and asking for time equals zero.

Usually it is considered that reverse time migration utilizes the Claerbout Imaging Condition II. The reason for this thinking is that the imaging condition in RTM is the time and space coincidence of source wave-field and receiver wave-field which looks similar to Claerbout Imaging Condition II (which is time and space coincidence of up and down-going waves). However, the actual source and receiver wave-fields may not contain only unidirectional (up-going or down-going) waves. If the velocity model in RTM contains sharp velocity contrasts (e.g., at the top or bottom boundary of a salt body), there will be reflection energy (back scattering) in both source and receiver wave-fields. Then both the source and receiver wave-fields are not unidirectional. The non-unidirectional parts in both wave-fields will cause high amplitude and low wavenumber (continuous) RTM back scattering artifacts.

Using a smooth velocity (and density) migration model may relieve this issue. However, the smooth model will cause inaccuracy in imaging reflectors beneath the smoothed area. Furthermore, for strong contrasts in the model (e.g., at the boundary of a salt body), smoothing the model is usually not enough to fully avoid RTM back scattering artifacts.

Because Claerbout Imaging Condition III uses predicted experiments with source and receiver locations at the imaging point and never requires coincidence of two different wave-fields, there are no similar artifacts in imaging using Claerbout Imaging Condition III.

3 Usual methods to remove RTM back scattering artifacts

Now that we know the cause of the back scattering artifacts, let's look at how to remove them. There are two categories for the methods attempting to remove RTM back scattering artifacts:
1. restore unidirectional property of source and receiver wave-fields (which is required in Claerbout imaging condition II)
2. directly remove the RTM back scattering artifacts in the image by utilizing their low wavenumber characteristic.

For the first category, the method works by first decomposing the source and receiver wave-fields to their one-way propagation components, followed by applying a correlation-based imaging condition to the appropriate combinations of the decomposed wave-fields (Liu et al., 2011; Whitmore and Crawley, 2012; Yoon and Marfurt, 2006).

For the second category, the method uses image processing techniques to remove the low wavenumber components of the image (Zhang and Sun, 2009).

4 A toy example to show RTM back scattering artifacts

Here we use a toy example to show RTM back scattering artifacts generated by the imaging condition used in RTM. We use a two-layer 1.5D medium (consisted of a whole space homogeneous velocity model and two-half-space density model and conventional RTM implementation in this toy example.

Figure 1 shows the velocity and density models used in this example. The left panel is a whole space homogeneous velocity model (the velocity is 2000m/s) and the right panel is two-half spaces density model (with density equals 2 and 1 for lower and upper half-space respectively). Figure 2 shows the acquisition geometry used in this example. The shot point is in the middle of the survey line (at depth=0m) and the maximum offset is about 12000m with offset increment of 20m, so there are about 1200 receivers in the survey line. The thick rectangle in the center of the figure indicates the imaging area. Figure 3 shows the synthetic data used in this example. Left panel is the whole data, and right panel is the data after removing the direct arrival. Both are shot gathers.

For simplicity, we first show the images using one trace (offset=3800m) to get the image. Figure 4 shows the RTM image achieved from one trace. We can see strong back scattering artifacts (in the rabbit ears shape). Figure 5 shows the image by the wave-field separation method propose by Liu et al. (2011). The back scattering artifacts are removed except in the vicinity of the source and receiver locations. We will see that the residual artifacts in the vicinity of the source and receiver locations can be removed by summing images from difference traces.

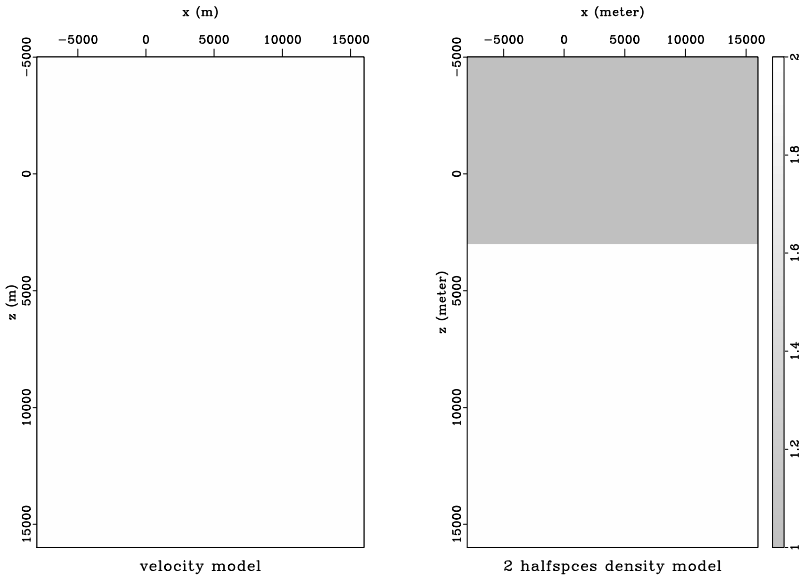

Figure 1: The velocity and density models used in this example. The left panel is a whole space homogeneous velocity model (the velocity is 2000m/s) and the right panel is two-half spaces density model (with density equals 2 and 1 for lower and upper half-space respectively).

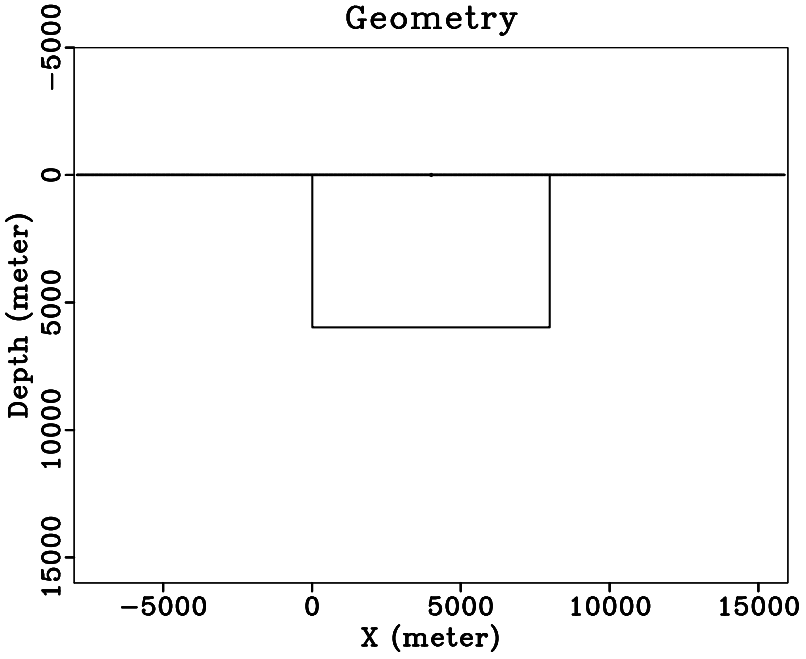

Figure 2: The acquisition geometry used in this example. The shot point is in the middle of the survey line (at depth=0m) and the maximum offset is about 12000m with offset increment of 20m, so there are about 1200 receivers in the survey line. The thick rectangle in the center of the figure shows the imaging area.

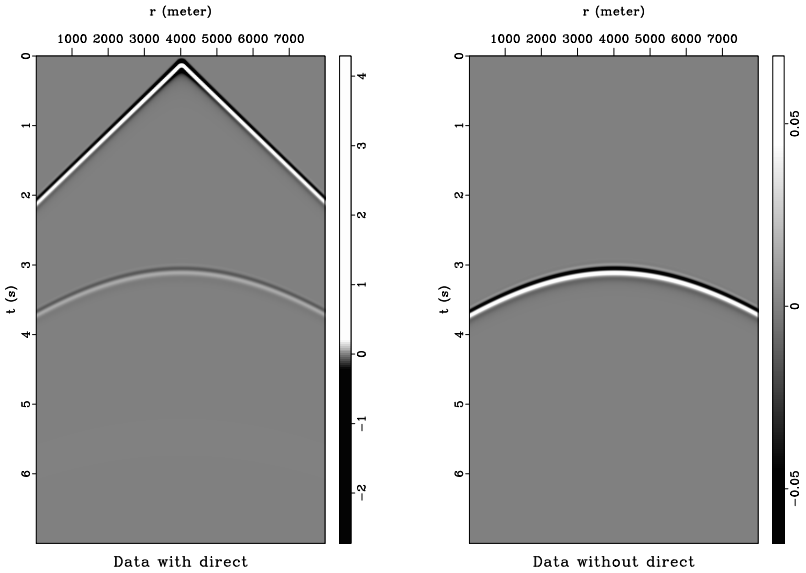

Figure 3: The synthetic data used in this example. Left panel is the whole data, and right panel is the data after removing the direct arrival. Both are shot gathers.

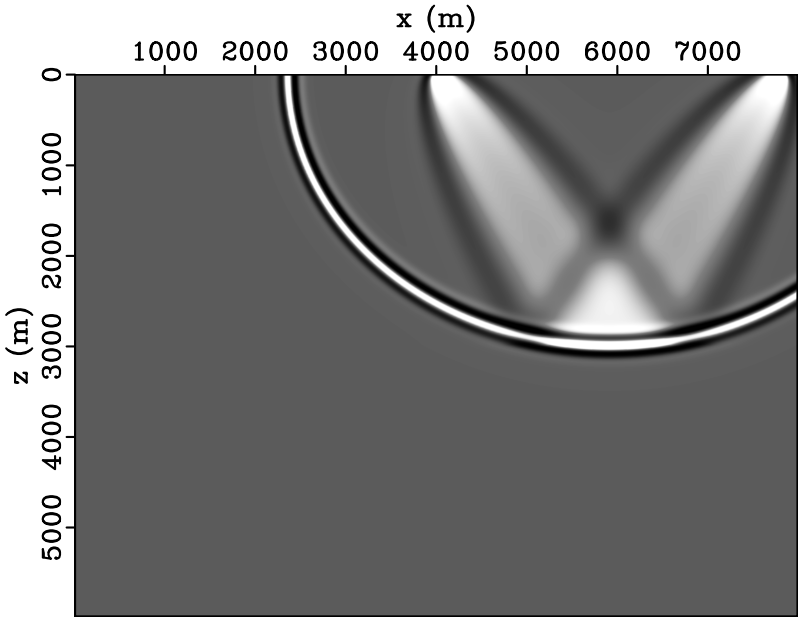

Figure 4: The RTM image achieved from one trace. We can see strong back scattering artifacts (in the rabbit ears shape).

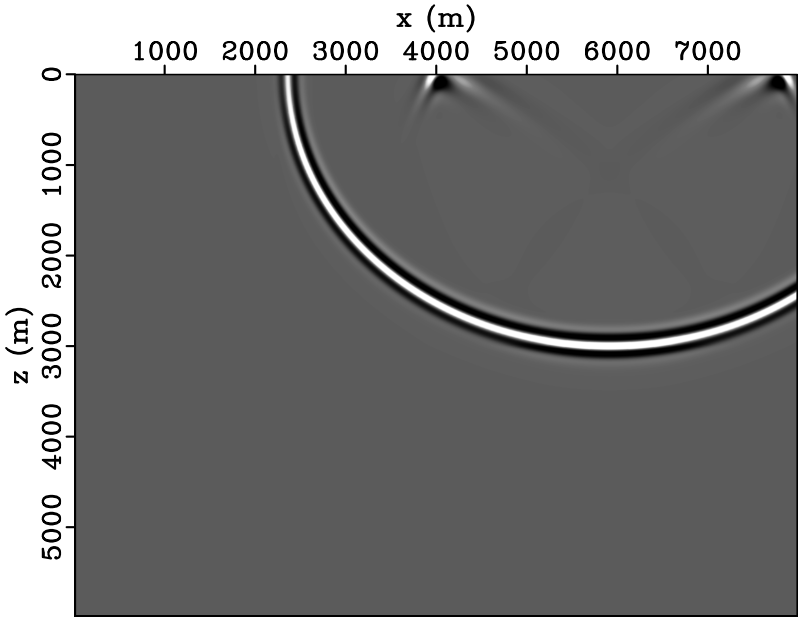

Figure 5: The image by wave-field separation method propose by Liu et al. (2011). The back scattering artifacts are removed except in the vicinity of the source and receiver locations.

Next we show the images using the whole shot gather.

Figures 6 and 7 show the raw RTM image and the image after field separation method respectively. The back scattering artifacts are removed except in the vicinity of the source location. The residual artifacts in the vicinity of the receiver locations in Figure 5 are removed by the cancellation effects in summing all traces within a shot gather. In a similar way, if we add all images from all shot gathers to get the image from the whole survey line, the residual artifact in the vicinity of the shot location in Figure 7 is also removed.

5 Summary

In this short note we have shown a toy example to demostrat the imaging condition used in RTM implementations is not exactly the Claerbout Imaging Condition II. The missing requirement of unidirectional (only up-going or only down-going) waves in Claerbout Imaging Condition II causes RTM back scattering artifacts. There are two categories of methods to remove the RTM back scattering artifacts: 1. restore unidirectional property of source and receiver wave-fields; 2. directly remove the RTM back scattering artifacts in the image by utilizing their low wavenumber characteristic. And Claerbout imaging condition III will not suffer the similar artifact issue.

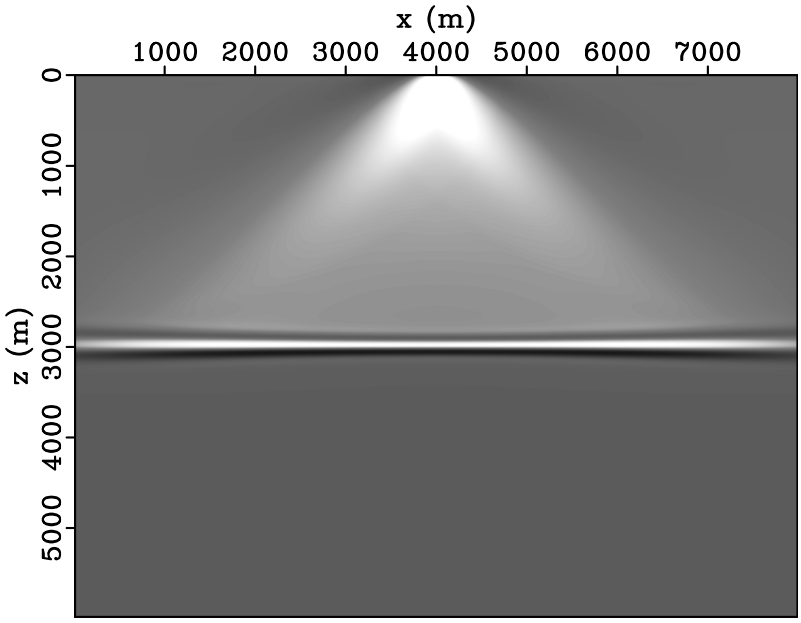

Figure 6: The RTM image achieved from a whole shot gather

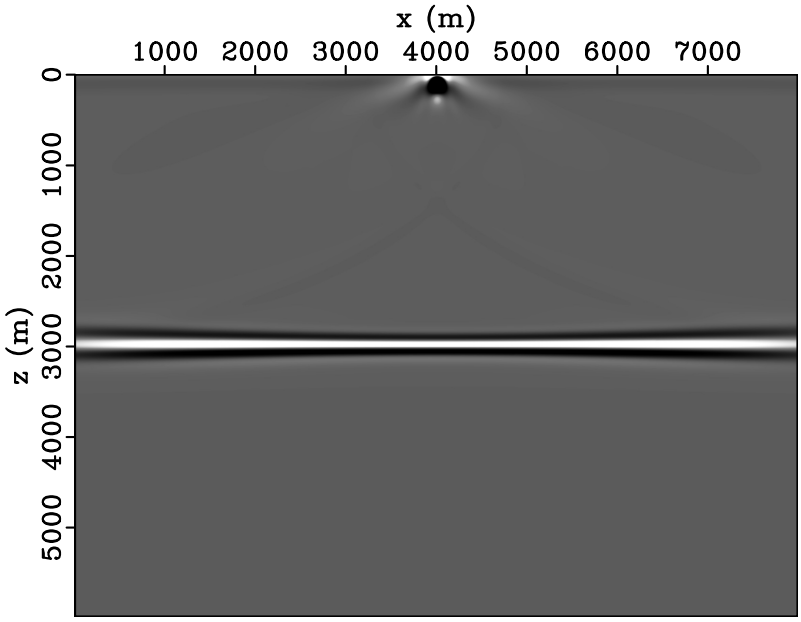

Figure 7: The image by the wave-field separation method proposed by Liu et al. (2011). The back scattering artifacts are removed except in the vicinity of the source location.

References

Claerbout, Jon F. "Toward a unified theory of reflector mapping." *Geophysics* 36 (June 1971): 467–481.

Liu, Faqi, Guanquan Zhang, Scott A. Morton, and Jacques P. Leveille. "An effective imaging condition for reverse-time migration using wavefield decomposition." *Geophysics* (2011): S29–S39.

Lowenthal, D., L. Lu, R. Roberson, and J. W. C. Sherwood. "The wave equation applied to migration." *Geophysical Prospecting* 24 (1985): 380–399.

Riley, D. C. and J. F. Claerbout. "2D multiple reflections." *Geophysics* 41 (1976): 592–620.

Stolt, R. H. "Migration by Fourier transform." *Geophysics* 43 (1978): 23–48.

Whitmore, N. D. and Sean Crawley. "Applications of RTM inverse scattering imaging conditions." *SEG Expanded Abstracts* (2012).

Yoon, K. and K. J. Marfurt. "Reverse-time migration using the pointing vector." *Exploration Geophysics* (2006): 102–107.

Zhang, Yu and J. Sun. "Practical issues in reverse-time migration: True amplitude gathers, noise removal and harmonic-source encoding." *First Break* (2009): 19–25.

Comparison of the amplitude properties of two important imaging conditions: 1 the space-time coincidence of up and down waves, and 2 the predicted coincident source and receiver experiment at depth at time zero

Yanglei Zou, Qiang Fu, Chao Ma, Jing Wu, Arthur B. Weglein

Abstract

In the 1970's Claerbout, Lowenthal and their colleagues (Claerbout, 1971; Riley and Claerbout, 1976; Lowenthal et al., 1985) introduced three imaging conditions. We refer to these as Claerbout Imaging Condition I, II and III, respectively. For a normal incident plane wave on a single horizontal reflector these imaging conditions are equivalent. For a shot record recorded above a single horizontal reflector or more complicated situations they are no longer equivalent. Claerbout III is superior to Claerbout I and II in that it provides the most quantitative and interpretable image amplitude. Stolt and his colleagues (Clayton and Stolt, 1981; Stolt and Weglein, 1985; Stolt and Benson, 1986) originally formulated Claerbout III for one-way waves. Weglein, Fang and their colleagues (Weglein et al., 2011a,b; Liu, 2013) extended Claerbout III for two way propagating waves. Claerbout III and Claerbout II have the same principle for both one-way and two-way waves. Therefore, to better understand the benefits/added value that this new Claerbout III two-way algorithm will bring to seismic exploration, we first examine the differences between Claerbout III and Claerbout II for one-way waves. In this paper, the first direct and detailed comparison of Claerbout III and Claerbout II is carried out for the simplest circumstance where they will produce a different result. The differences are significant and substantive, with implications far beyond the simple example that allows for transparent analysis and analytic evaluation and conclusions.

1 Introduction

Methods that use the wave equation to perform seismic migration have two ingredients: (1) a wave propagation component and (2) an imaging principle or concept. Claerbout (Claerbout, 1971; Riley and Claerbout, 1976) was the initial and key wave-equation-migration imaging-concept pioneer and algorithm developer, together with Stolt (Stolt (1978)) and Lowenthal (Lowenthal et al. (1985)) and their colleagues, they introduced imaging conditions for locating reflectors at depth from surface-recorded data. The three key imaging conditions that were introduced are:

I. the exploding-reflector model
II. time and space coincidence of up and downgoing waves
III. predicting a source and receiver experiment at a coincident-source-and-receiver subsurface point, and asking for time equals zero (the definition of wave-equation migration)

For a normal-incident spike plane wave on a horizontal reflector, these three imaging concepts are totally equivalent. However, a key point to make clear is that for a non-zero-offset surface seismic-data experiment, with either a one-dimensional or a multi-dimensional subsurface, they are no longer equivalent. Wave-equation migration is defined as using the Claerbout Imaging Condition III, predicting a source and receiver experiment at depth at time equals zero. Stolt and his colleagues

(Clayton and Stolt, 1981; Stolt and Weglein, 1985; Stolt and Benson, 1986; Stolt and Weglein, 2012; Weglein and Stolt, 1999) extended and formulated the experiment-at-depth concept to allow a separated source and receiver experiment at time equals zero for one way propagating waves. Weglein, Fang and their colleagues (Weglein et al., 2011a,b; Liu, 2013) extended Claerbout III for two way propagating waves.

Claerbout III and Claerbout II have the same principle for both one-way and two-way waves. In order to understand the benefits that the two way wave propagation form of Claerbout III will bring to seismic exploration, we first examine the differences between Claerbout III and other imaging conditions for one way wave. In this paper, we first compare the imaging results of Clearbout III - Stolt migration and its asymptotic form - Kirchhoff migration. Stolt migration is Claerbout III for one-way waves. Kirchhoff migration is its natural approximation. Kirchhoff migration shares some kind of behavior with RTM (Claerbout II), including producing candidate and depending on the coherent summing over candidate. Then we compare the imaging results of Clearbout III - Stolt migration and Clearbout II - RTM. These comparisons and results show that Claerbout III is superior to Claerbout I and II in that it provides the most quantitative and interpretable image amplitude. Claerbout Imaging Condition III predicts a physical experiment with both source and receiver at depth, allowing it to provide the imaging definitiveness and physical interpretation that other imaging conditions cannot match. Claerbout III is also extendable/generalizable to provide an angle dependent reflection coefficient. For the purpose of determining quantitative information on the physical meaning of the image, the clear choice is Claerbout Imaging Condition III.

2 Stolt migration (Clearbout Imaging Condition III for one way wave) and Kirchhoff migration (a asymptotic form of Stolt migration)

In this section we give a review of the 2D pre-stack Stolt migration and following Stolt and Weglein (2012) derive an approximate asymptotic 2D Kirchhoff migration algorithm. The 3D expressions are straight forward extensions.

2.1 2D Stolt migration

First, we can denote the wave field as $P(x_g, z_g, x_s, z_s, t)$ for an experiment where a source locates at (x_s, z_s) and an observation point/receiver locates at (x_g, z_g).

Given a 2D data $D(x_g, x_s, t)$[1] with source location $(x_s, z_s = 0)$, receiver location $(x_g, z_g = 0)$, and time t, we have

$$P(x_g, 0, x_s, 0, t) = D(x_g, x_s, t). \tag{1}$$

One can perform a Fourier transform over all coordinates:

$$\begin{aligned} P(k_{gx}, 0, k_{sx}, 0, \omega) =& D(k_{gx}, k_{sx}, \omega) \\ =& \int dx_g \int dx_s \int dt D(x_g, x_s, t) e^{i(k_{sx}x_s - k_{gx}x_g + \omega t)} \end{aligned} \tag{2}$$

[1] In this paper, if sources and receivers are at $z = 0$, we use D to denote the data , otherwise we use P to denote the data/wave field.

One can predict the data of an experiment where the source depth is z and receiver depth is 0,

$$P(k_{gx}, 0, k_{sx}, z, \omega) = D(k_{gx}, k_{sx}, \omega)e^{-ik_{sz}z}, \tag{3}$$

where the vertical wavenumber component k_{sz} is defined as

$$k_{sz} = \frac{\omega}{c}\sqrt{1 - \frac{{k_{sx}}^2 c^2}{\omega^2}}. \tag{4}$$

Similarly, one can predict the data of an experiment where the source depth is z and receiver depth is z,

$$\begin{aligned} P(k_{gx}, z, k_{sx}, z, \omega) &= P(k_{gx}, 0, k_{sx}, z, \omega)e^{ik_{gz}z} \\ &= D(k_{gx}, k_{sx}, \omega)e^{i(k_{gz}-k_{sz})z}, \end{aligned} \tag{5}$$

where the vertical wavenumber component k_{gz} is

$$k_{gz} = -\frac{\omega}{c}\sqrt{1 - \frac{{k_{gx}}^2 c^2}{\omega^2}}. \tag{6}$$

If we make two inverse Fourier transform of k_{gx} and k_{xs} to the same x, we can predict the data of an experiment where a source and a receiver are both at location (x, z),

$$\begin{aligned} P(x, z, x, z, \omega) &= \frac{1}{(2\pi)^2}\int dk_{sx}e^{-ik_{sx}x}\int dk_{gx}e^{ik_{gx}x}P(k_{gx}, z, k_{sx}, z, \omega) \\ &= \frac{1}{(2\pi)^2}\int dk_{sx}e^{-i(k_{sz}z+k_{sx}x)}\int dk_{gx}e^{i(k_{gz}z+k_{gx}x)}D(k_{gx}, k_{sx}, \omega) \end{aligned} \tag{7}$$

Next, letting the time of the wave field to be zero, one can get the 2D Stolt migration image,

$$\begin{aligned} M^{Stolt}(x, z) &= \frac{1}{2\pi}\int d\omega e^{-i\omega t}P(x, z, x, z, \omega)|_{t=0} \\ &= \frac{1}{(2\pi)^3}\int d\omega\int dk_{sx}e^{-i(k_{sz}z+k_{sx}x)}\int dk_{gx}e^{i(k_{gz}z+k_{gx}x)}D(k_{gx}, k_{sx}, \omega) \end{aligned} \tag{8}$$

where $M^{Stolt}(x, z)$ is the image function [2].

2.2 2D Kirchhoff migration

Following Stolt and Weglein (2012), one can derive the Kirchhoff migration from Stolt migration.

First, rewriting the 2D Stolt migration algorithm ,i.e., equation 48 with the data in space-time domain, one can obtain

$$\begin{aligned} M^{Stolt}(x, z) =& \frac{1}{(2\pi)^3}\int\int\int d\omega dx_g dx_s\int dk_{sx}e^{-i(k_{sz}z+k_{sx}(x-x_s))}\int dk_{gx}e^{i(k_{gz}z+k_{gx}(x-x_g))} \\ &\int dte^{i\omega t}D(x_g, x_s, t) \end{aligned} \tag{9}$$

[2] In Stolt and Weglein (2012), the image function $M^{Stolt}(x, z)$ has a half-integral filter. In this section we do not include the half-integral filter.

An asymptotic approximation can be made with the stationary phase approximation,

$$\int dk_{sx} e^{-i(k_{sz}z+k_{sx}(x-x_s))} \simeq e^{-i\omega r_s/c}\sqrt{\frac{2\pi i\omega z^2}{cr_s^3}} \tag{10}$$

$$\int dk_{gx} e^{i(k_{gz}z+k_{gx}(x-x_g))} \simeq e^{-i\omega r_g/c}\sqrt{\frac{2\pi i\omega z^2}{cr_g^3}} \tag{11}$$

$$r_s = \sqrt{z^2+(x-x_s)^2} \tag{12}$$

$$r_g = \sqrt{z^2+(x-x_g)^2} \tag{13}$$

$$r = r_s + r_g \tag{14}$$

One can obtain the approximate asymptotic 2D Kirchhoff migration,

$$\begin{aligned}
M^{Kirchhoff}(x,z) &= \frac{z^2}{(2\pi)^2 c}\int dx_g \int dx_s \int dt \frac{D(x_g,x_s,t)}{(r_s r_g)^{3/2}} \int d\omega i\omega e^{i\omega(t-r/c)} \\
&= \frac{z^2}{(2\pi)^2 c}\int dx_g \int dx_s \int d\omega i\omega e^{-i\omega r/c}\frac{D(x_g,x_s,\omega)}{(r_s r_g)^{3/2}} \\
&= \frac{z^2}{(2\pi)^2 c}\int dx_g \int dx_s \int d\omega i\omega \int dt e^{-i\omega t}\delta(t-r/c)\frac{D(x_g,x_s,\omega)}{(r_s r_g)^{3/2}} \\
&= \frac{z^2}{(2\pi)^2 c}\int dx_g \int dx_s \int dt\delta(t-r/c) \int d\omega i\omega e^{-i\omega t}\frac{D(x_g,x_s,\omega)}{(r_s r_g)^{3/2}} \\
&= -\frac{z^2}{2\pi c}\int dx_g \int dx_s \int dt\delta(t-r/c)\frac{\frac{d}{dt}D(x_g,x_s,t)}{(r_s r_g)^{3/2}} \\
&= -\frac{z^2}{2\pi c}\int dx_g \int dx_s \frac{\frac{d}{dt}D(x_g,x_s,t)|_{t=r/c}}{(r_s r_g)^{3/2}}
\end{aligned} \tag{15}$$

In the last 4 steps use the following Fourier transform convention,

$$D(x_g,x_s,\omega) = \int dt D(x_g,x_s,t)e^{i\omega t} \tag{16}$$

$$D(x_g,x_s,t) = \frac{1}{2\pi}\int d\omega D(x_g,x_s,\omega)e^{-i\omega t} \tag{17}$$

and

$$\int d\omega\ i\omega D(x_g,x_s,\omega)e^{-i\omega t} = -2\pi\frac{d}{dt}D(x_g,x_s,t). \tag{18}$$

Equation 15 is the 2D Kirchhoff migration formula. It is a weighted summation of the data along a trajectory of travel-times corresponding to ray-paths from the source to image point and then to receiver.

3 Analysis and numerical tests for the differences of Stolt migration and Kirchhoff migration due to the stationary phase approximation

As we have discussed in the previous section, the differences of Stolt migration and Kirchhoff migration are due to two stationary phase approximations, i.e., equation 10 and 11. In this section, we analyze and test the effect due to receiver side stationary phase approximation, while the source side effect is similar.

3.1 Receiver side stationary phase approximation

Following section 2, given a 2D data $P(x_g, z_g, x_s, z_s, \omega)$ with (x_s, z_s) the sources location, (x_g, z_g) the receivers location and ω the frequency, we can predict the wave field $P(x, z, x_s, z_s, \omega)$ at (x, z) by Stolt migration algorithm,

$$P^{Stolt}(x, z, x_s, z_s, \omega) = \frac{1}{2\pi} \int dx_g \int dk_{gx} e^{i(k_{gz}(z-z_g)+k_{gx}(x-x_g))} P(x_g, z_g, x_s, z_s, \omega) \qquad (19)$$

Apply the stationary phase approximation

$$\int dk_{gx} e^{i(k_{gz}(z-z_g)+k_{gx}(x-x_g))} \simeq e^{-i\omega r_g/c} \sqrt{\frac{2\pi i\omega(z-z_g)^2}{cr_g^3}},$$

of the receiver side, we have

$$P^{Asymptotic}(x, z, x_s, z_s, \omega) = \frac{1}{2\pi} \int dx_g e^{-i\omega r_g/c} \sqrt{\frac{2\pi i\omega(z-z_g)^2}{cr_g^3}} P(x_g, z_g, x_s, z_s, \omega) \qquad (20)$$

$P^{Asymptotic}(x, z, x_s, z_s, \omega)$ is the predicted wave field at (x, z) generated by a source at (x_s, z_s) using the Kirchhoff-like asymptotic algorithm.

3.2 Numerical tests

In this test, we use the Cagniard-de Hoop method (Appendix A) to generate the synthetic data for an acoustic one reflector model shown in figure 1. The Reflector depth z_d is $2,000m$; source location is $(x_s = 0m, z_s = 0m)$; receiver depth is $z_g = 400m$; receiver interval dx is 4m; time sampling interval dt is 0.001s ($T_{max} = 5s$). Velocities are $2,000m/s$ and $1,000m/s$ in the first and second medium, respectively. The generated synthetic data is shown in figure 3.

Given the data $P(x_g, z_g, x_s, z_s, \omega)$ with source location $(x_s = 0m, z_s = 0m)$ and receiver depth $z_g = 400m$, we compare the predicted wave field $P^{Stolt}(x, z, x_s, z_s, \omega)$ and $P^{Asymptotic}(x, z, x_s, z_s, \omega)$ with the exact wave field P^{CdH} at depth z=600m (at 0m offset and 2,000m offset). In all these following figures, the black line is the exact data generated by using the Cagniard-de Hoop method at depth $z = 600m$, the red line is the asymptotic prediction result $P^{Asymptotic}$, and the blue line is the wave-equation prediction result P^{Stolt}, respectively.

The Stolt migration algorithm prediction of the receivers at depth takes a highly nonlinear dependence of the phase in equation 19 (from k_{gz}) and the Kirchhoff-like asymptotic approximation

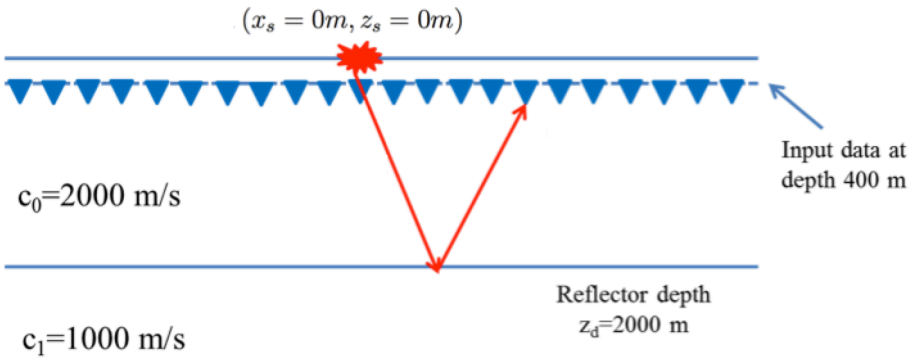

Figure 1: Model to generate CdH synthetic test data as input

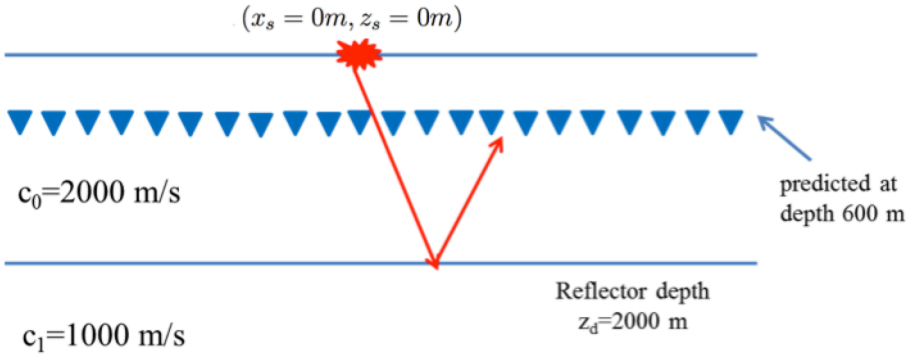

Figure 2: Predicted wavefield at depth 600 m

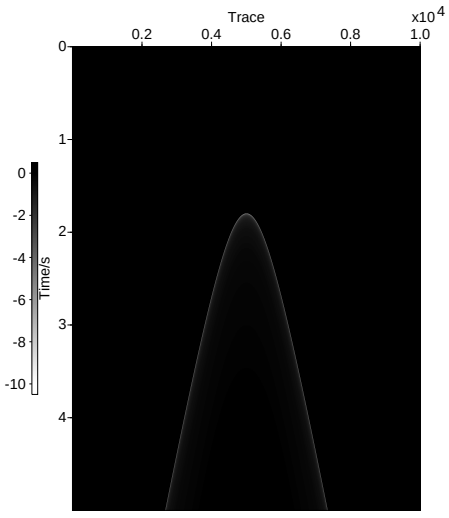

Figure 3: CdH synthetic test data generated from the one reflector model in figure 1

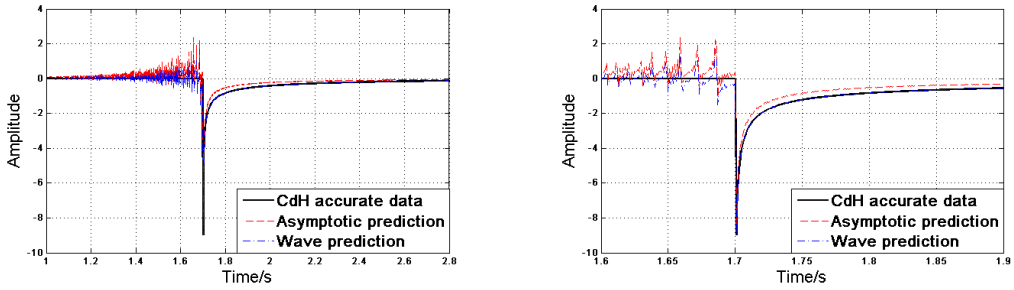

(a) (b)

Figure 4: Left: Space-time domain comparison at x=0m, z=600m, 1.0s to 2.8s. Right: Zoom-in of Left figure from 1.6s to 1.9s.

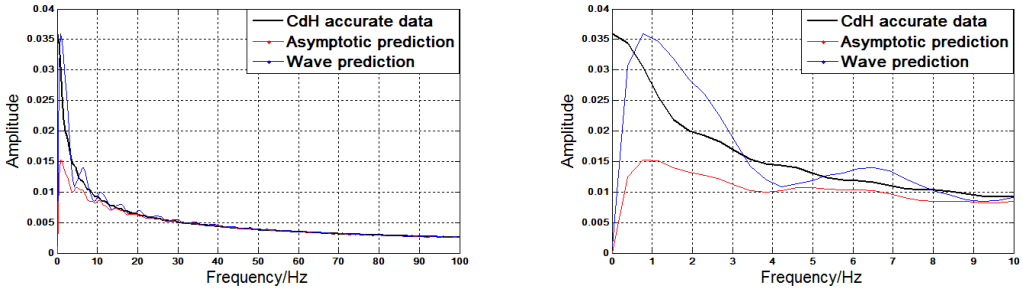

(a) (b)

Figure 5: Left: Space-frequency domain comparison at x=0m, z=600m, 0Hz-100Hz. Right: Zoom-in of left figure from 0Hz to10Hz.

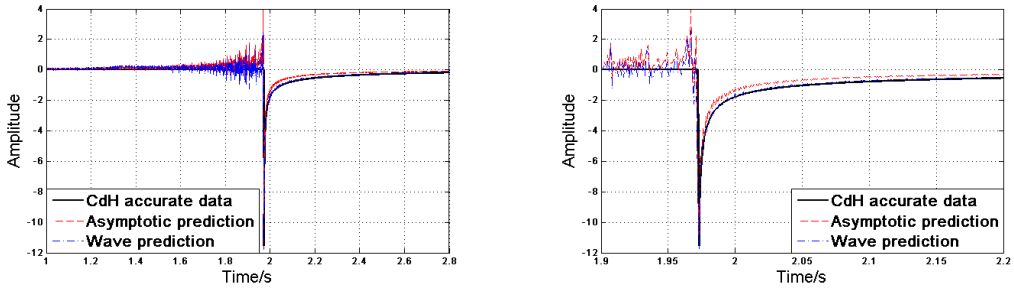

(a) (b)

Figure 6: Left: Space-time comparison at x=2,000m, z=600m, 1.0s to 2.8s. Right: Zoom-in of left figure from 1.9s to 2.2s.

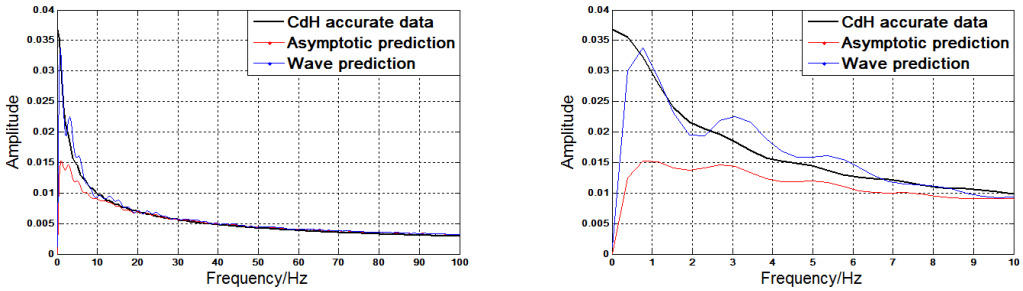

(a) (b)

Figure 7: Left: Space-frequency domain comparison at x=2,000m, z=600m, 0Hz-100Hz. Right: Zoom-in of left figure from 0Hz to 10Hz.

replace it with a liner dependence on the phase in equation 20. The resultant difference in spectrum at the low end has a dramatic impact on subsequent imaging steps, and makes the Kirchhoff-like asymptotic migration method not an approximated source and receiver coincident at time equals zero.

4 Obtaining the angle dependent reflection coefficient from Stolt migration and Kirchhoff migration

4.1 Obtaining the angle dependent reflection coefficient from Stolt migration

Wave-equation migration, i.e., migration algorithms such as Stolt migration utilizing Claerbout Imaging Condition III, can be extended to predict non-zero offset data at depth and provide imaging result with subsurface angle information. In order to obtain the subsurface angle information, we first change the integral variables in the wave equation migration formula from k_{sx}, k_{gx}, ω to k_x, k_h, k_z, where

$$\begin{aligned} k_z &\equiv k_{gz} - k_{sz} \\ &= -\frac{\omega}{c}\left(\sqrt{1-\frac{{k_{gx}}^2 c^2}{\omega^2}} + \sqrt{1-\frac{{k_{sx}}^2 c^2}{\omega^2}}\right) \end{aligned} \tag{21}$$

$$k_x \equiv k_{gx} - k_{sx} \tag{22}$$

$$k_h \equiv k_{gx} + k_{sx} \tag{23}$$

the Jacobian for a change of variables is

$$|\mathrm{Det}\left[\frac{\partial(k_x, k_h, k_z)}{\partial(k_{sx}, k_{gx}, \omega)}\right]| = \frac{2\omega k_z}{c^2 k_{sx} k_{gx}}, \tag{24}$$

and the Stolt migration formula equation 48 can be rewritten as

$$M^{Stolt}(x,z) = \frac{c^2}{2(2\pi)^3}\int dk_z \int dk_x \int dk_h D(k_{gx}, k_{sx}, \omega)\frac{k_{sz}k_{gz}}{\omega k_z} e^{ik_z z} e^{ik_x x}. \tag{25}$$

In equation 25, since two of the integrals are inverse Fourier transform, we can obtain the image result in k_x, k_z domain

$$M^{Stolt}(k_x,k_z) = \frac{c^2}{4\pi^2}\int dk_h D(k_{gx}, k_{sx}, \omega)\frac{k_{sz}k_{gz}}{\omega k_z}. \tag{26}$$

Now the formula only contains an integral of k_h, which is the Fourier conjugate of subsurface offset x_h. We obtain the migration imaging result with subsurface offset information,

$$M^{Stolt}(k_x,k_z,k_h) = \frac{c^2}{4\pi^2}\frac{k_{sz}k_{gz}}{\omega k_z} D(k_{gx}, k_{sx}, \omega). \tag{27}$$

From equation 27, we can easily get angle dependent reflection coefficient as well as other angle dependent information.

4.2 Obtaining the angle dependent reflection coefficient from kirchhoff migration

4.2.1 Obtaining the angle dependent reflection coefficient by interpreting the Kirchhoff migration result as a fictitious experiment

In equation 15, $M^{Kirchhoff}(x,z)$ is Kirchhoff migration image. Although it is a function of x and z, $M^{Kirchhoff}(x,z)$ is not directly related to the reflection coefficient at image point (x,z). It has limited value (if any) in being interpreted as a reflection coefficient, let alone as the angle dependence of a reflection coefficient. A coincident source and receiver experiment, directly above a reflector at small positive time, is related to the reflection coefficient of that local reflection point. If the migration concept does not correspond to that experiment at depth, one could be able to correctly locate structure but cannot obtain the exact local reflection coefficient. If you nevertheless decide to interpret $M^{Kirchhoff}(x,z)$ in equation 15 as though it was the output of an imagined or fictitious zero offset experiment at $t=0$, then taking that leap we would write

$$M^{Kirchhoff}(x,z) = M^{Kirchhoff}(x,z,x_h=0). \tag{28}$$

Furthermore, and in addition for the interpretation of the right hand member of equation 28 we will assume by causality that for $x_h \neq 0$ at $t=0$ the measurement would be zero, that is

$$M^{Kirchhoff}(x,z,x_h) = 0 \quad \text{for} \quad x_h \neq 0. \tag{29}$$

By assuming this interpretation to Kirchhoff migration, we bent over backwards to allow a way to compare $M^{Stolt}(x,z,x_h)$ with $M^{Kirchhoff}(x,z,x_h)$ in terms of amplitude information from the actual and fictitious experiment output by Stolt migration and Kirchhoff migration, respectively.

4.2.2 Obtaining the angle dependent reflection coefficient by an alternative ray-theory-based algorithm

According to equation 15

$$M^{Kirchhoff}(x,z) = -\frac{z^2}{2\pi c}\int dx_g \int dx_s \frac{\frac{d}{dt}D(x_g,x_s,t)|_{t=r/c}}{(r_s r_g)^{3/2}},$$

Kirchhoff migration is a weighted summation of the derivative of data with respect to time over all sources and receiver positions, along a travel-time trajectory(shown in figure 8) from the source to the image point and then to the receiver.

As pointed out in Stolt and Weglein (2012), the formula 15 does not imply that the summation must be over all sources and receivers. One can pluck out a subset of the complete data set, corresponding to a line or curve on the surface, and consider that as a partial migration, that related to what that portion of the data contributes to the migration result (given by 15).

Here we are going to show a ray-theory-based algorithm to choose a specific subset of the complete data set, corresponding to a constant incident/dip angle. In Kirchhoff migration, for every image point, we can calculate an incident angle and a dip angle for each source and receiver, as shown in figure 9.

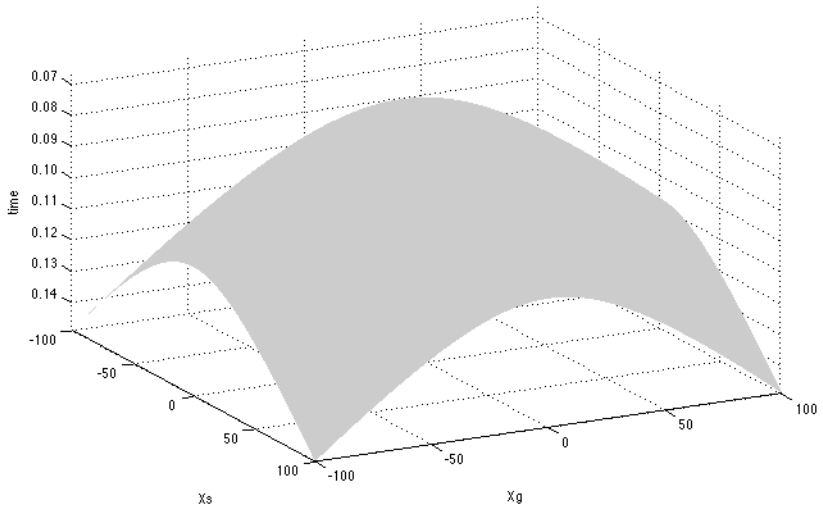

Figure 8: an example of trajectory function $t(x_s, x_g) = r/c$

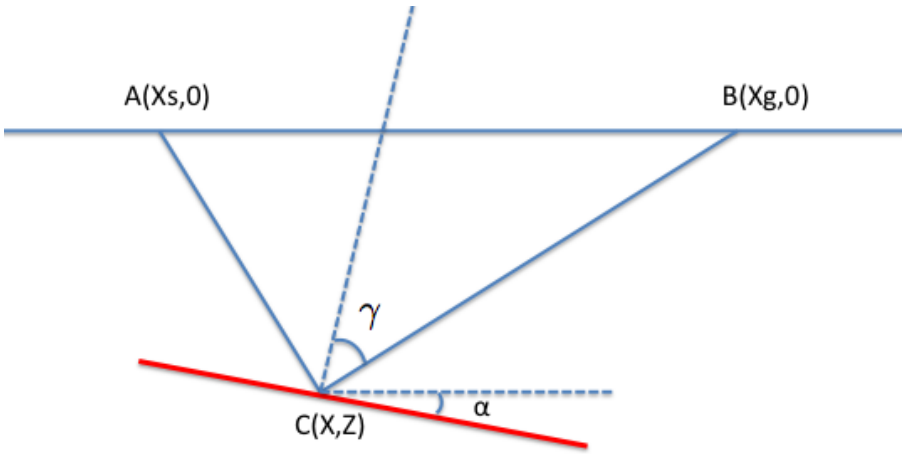

Figure 9: For every image point $C(x, z)$ we can calculate an incident angle γ and a dip angle α for each source $A(x_s, 0)$ and receiver $B(x_g, 0)$.

First we can calculate two new variables ξ and η;

$$\xi = tan\gamma = \frac{-(x_s - x)\sqrt{(x - x_g)^2 + z^2} + (x_g - x)\sqrt{(x - x_s)^2 + z^2}}{z(\sqrt{(x - x_g)^2 + z^2} + \sqrt{(x - x_s)^2 + z^2})} = \frac{-(x_s - x)r_g + (x_g - x)r_s}{zr} \tag{30}$$

$$\eta = tan\alpha = \frac{(x_s - x)\sqrt{(x - x_g)^2 + z^2} + (x_g - x)\sqrt{(x - x_s)^2 + z^2}}{z(\sqrt{(x - x_g)^2 + z^2} + \sqrt{(x - x_s)^2 + z^2})} = \frac{(x_s - x)r_g + (x_g - x)r_s}{zr}, \tag{31}$$

where γ is the incident angle and α is the dip angle. The angle convention is defined as follows:

$$\begin{aligned} when\ x_g \geq x_s \quad & \gamma \in [0, \frac{\pi}{2}) \\ when\ x_g < x_s \quad & \gamma \in (-\frac{\pi}{2}, 0) \\ when\ (x_g - x) \geq (x - x_s) \quad & \alpha \in [0, \frac{\pi}{2}) \\ when\ (x_g - x) < (x - x_s) \quad & \alpha \in (-\frac{\pi}{2}, 0) \end{aligned}$$

Now we can rearrange the 2D Kirchhoff migration from integrals of source and receiver locations to integrals of ξ and η:

$$\begin{aligned} M^{Kirchhoff}(x, z) &= -\frac{z^2}{2\pi c} \int dx_g \int dx_s \frac{\frac{d}{dt} D(x_g, x_s, t)|_{t=r/c}}{(r_s r_g)^{3/2}} \\ &= -\frac{z^2}{2\pi c} \int d\xi \int d\eta |\frac{\partial(x_s, x_g)}{\partial(\xi, \eta)}| \frac{\frac{d}{dt} D(x_g, x_s, t)|_{t=r/c}}{(r_s r_g)^{3/2}} \end{aligned} \tag{32}$$

Then we have

$$\begin{aligned} M^{Kirchhoff}(x, z, \xi, \eta) &= -\frac{z^2}{2\pi c} |\frac{\partial(x_s, x_g)}{\partial(\xi, \eta)}| \frac{\frac{d}{dt} D(x_g, x_s, t)|_{t=r/c}}{(r_s r_g)^{3/2}} \\ &= \frac{z^2 r^2}{4\pi c (r_s r_g)^{3/2}} \frac{d}{dt} D(x_g, x_s, t)|_{t=r/c}, \end{aligned} \tag{33}$$

where the Jacobian $|\frac{\partial(x_s, x_g)}{\partial(\xi, \eta)}|$ can be calculated as follows:

$$\frac{\partial \xi}{\partial x_s} = \frac{(x - x_g)(x - x_s)r_g - z^2 r_g - r_s r_g^2}{z r_s r^2} \tag{34}$$

$$\frac{\partial \xi}{\partial x_g} = \frac{-(x - x_g)(x - x_s)r_s + z^2 r_s + r_s^2 r_g}{z r_g r^2} \tag{35}$$

$$\frac{\partial \eta}{\partial x_s} = \frac{(x - x_g)(x - x_s)r_g + z^2 r_g + r_s r_g^2}{z r_s r^2} \tag{36}$$

$$\frac{\partial \eta}{\partial x_g} = \frac{(x - x_g)(x - x_s)r_s + z^2 r_s + r_s^2 r_g}{z r_g r^2} \tag{37}$$

$$|\frac{\partial(\xi, \eta)}{\partial(x_s, x_g)}| = -\frac{2}{(r_s + r_g)^2} = -\frac{2}{r^2} \tag{38}$$

$$|\frac{\partial(x_s, x_g)}{\partial(\xi, \eta)}| = (|\frac{\partial(\xi, \eta)}{\partial(x_s, x_g)}|)^{-1} = -\frac{r^2}{2} \tag{39}$$

The $M^{Kirchhoff}(x, z, \xi, \eta)$ in equation 33 is an algorithm that can provide ray-theory-based angle dependent information from Kirchhoff migration. As shown in figure 9, where each red line corresponds to one ξ and each blue line corresponds to one η. If we do not know the dip angle, we can sum along all η (each blue line) to obtain the function $M^{Kirchhoff}(x, z, \xi)$ for each imaging point, and retrieve angle information from this equation. If we know the actual dip angle α_0 and $\eta = tan\alpha_0$, we can simply select a part of the image $M^{Kirchhoff}(x, z, \xi, \eta = tan\alpha_0)$ and retrieve angle information from it.

Please understand that while we have provided ray-theory-based angle dependent information for each incident/dip angle subset of the data, that information is now provided over a set of candidate image points. That is in contrast with the uncollapsed Stolt pre-stack migration. Stolt migration(equation 48) provides a definite image point and angle dependent information at the image point.

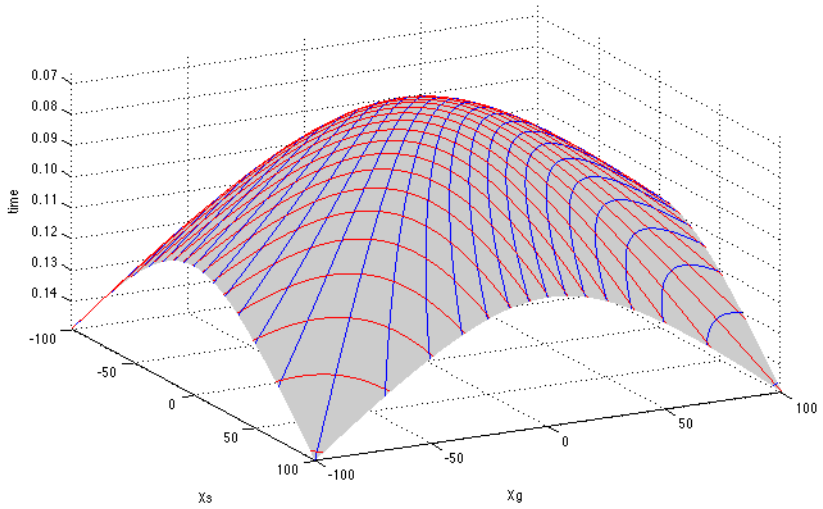

Figure 10: an example of trajectory function $t(x_s, x_g) = r/c$, where each red lines corresponds to one incident angle and each blue line correspnds to one dip angle

4.3 A numerical test and comparison for obtaining the angle dependent reflection coefficient from Stolt migration and kirchhoff migration

In the following section, we will demonstrate the differences of the predicted angel dependent reflection coefficient between wave-equation migration (Stolt migration) and its asymptotic approximation (Kirchhoff migration) in the simplest possible case with offset data.

Figure 11 shows the migration procedure for wave-equation migration and its asymptotic form.

	wave-equation migration	asymptotic migration
imaging condition	Claerbout Imaging Condition III	approximation of Claerbout III
migration method	Stolt migration	Kirchhoff migration
test data generation	Reflectivity method	Cagniard-de Hoop method
imaging result	$M^{Stolt}(x,z)$	$M^{Kirchhoff}(x,z)$
imaging result with subsurface offset information	$M^{Stolt}(x,z,x_h)$	N/A Alternative ways: 1. $M^{Kirchhoff}(x,z,x_h)$ 2. $M^{Kirchhoff}(x,z,\xi)$

40

Figure 11: Test content

4.3.1 Test: model

The simplest scenario for such a test would be a two-layer acoustic model, in which each layer is homogeneous. Figure 3 shows the model we used to generate the data.

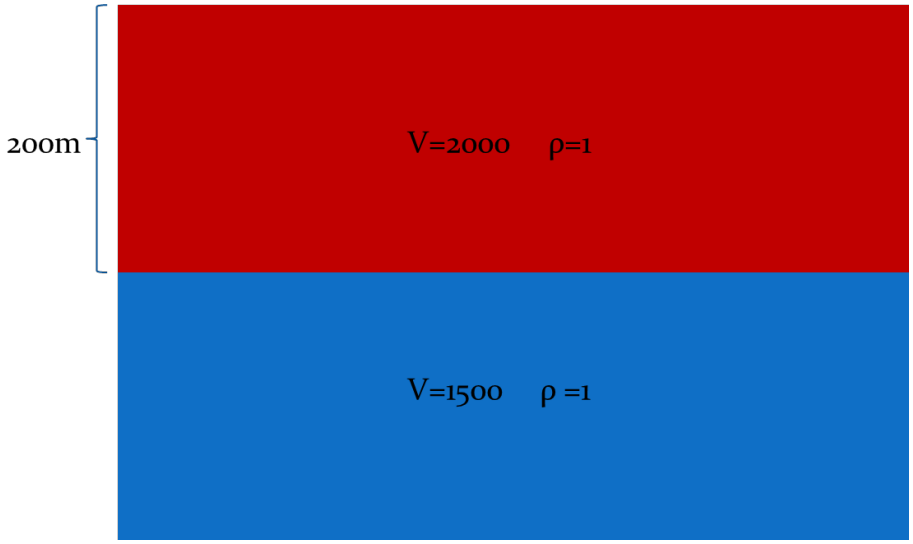

Figure 12: Model. In the model the velocity in the first layer is greater than the velocity of the second layer, the reflection data does not have a post-critical component.

We test the amplitudes of both wave-equation migration (Stolt migration) and its asymptotic approximation (Kirchhoff migration) to see how the amplitudes of their images relate to the angle dependent reflection coefficient. We use analytic data for both Stolt migration (reflectivity method, see appendix B) and Kirchhoff migration (Cagniard-de Hoop method, see appendix A). Using analytic data will avoid the effect of any numerical inaccuracy in the data generating procedure and all differences will be attributable to the processing methods being compared.

4.3.2 Test: Stolt migration and Kirchhoff migration results

We compare the Stolt migration result $M^{Stolt}(x, z, x_h)$ and the Kirchhoff migration result $M^{Kirchhoff}(x, z, x_h)$ in different domains. As in this test, the earth is 1D, the x variable is trivial. Given a fixed x, figure 13 shows $M^{Stolt}(x, z, x_h)$ and $M^{Kirchhoff}(x, z, x_h)$; figure 14 shows the absolute value of $M^{Stolt}(x, z, k_h)$ and $M^{Kirchhoff}(x, z, k_h)$; figure 15 shows the absolute value of $M^{Stolt}(x, k_z, k_h)$ and $M^{Kirchhoff}(x, k_z, k_h)$. We can see they are quite different.

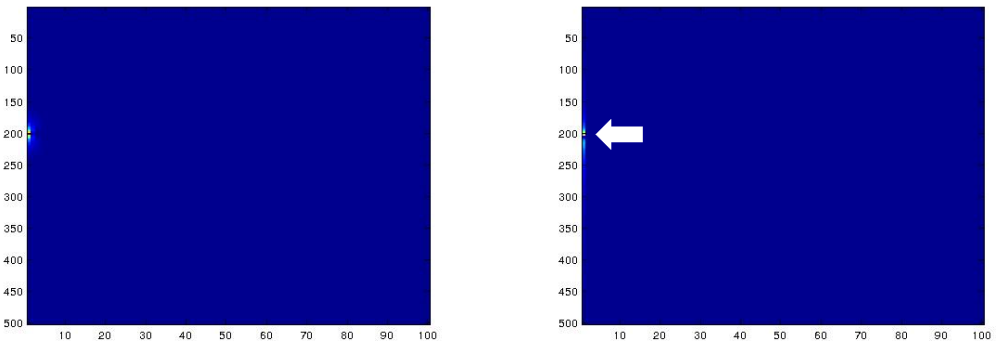

(a) (b)

Figure 13: Left: wave-equation migration image in $z - x_h$ domain; Right: asymptotic migration image in $z - x_h$ domain.

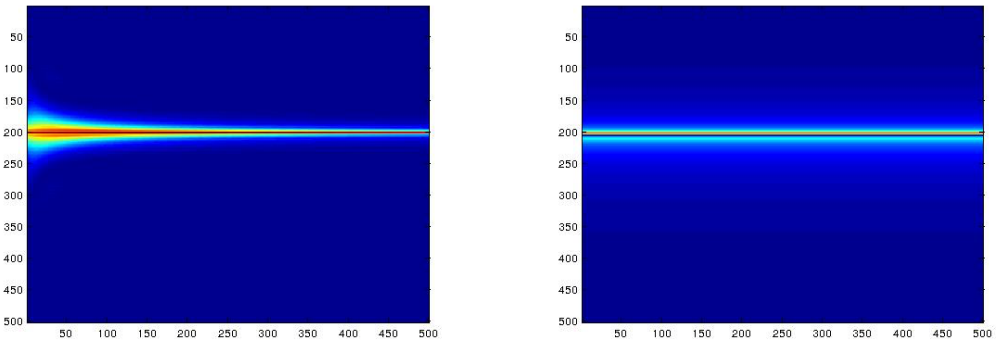

(a) (b)

Figure 14: Left: wave-equation migration image in $z - k_h$ domain; Right: asymptotic migration image in $z - k_h$ domain.

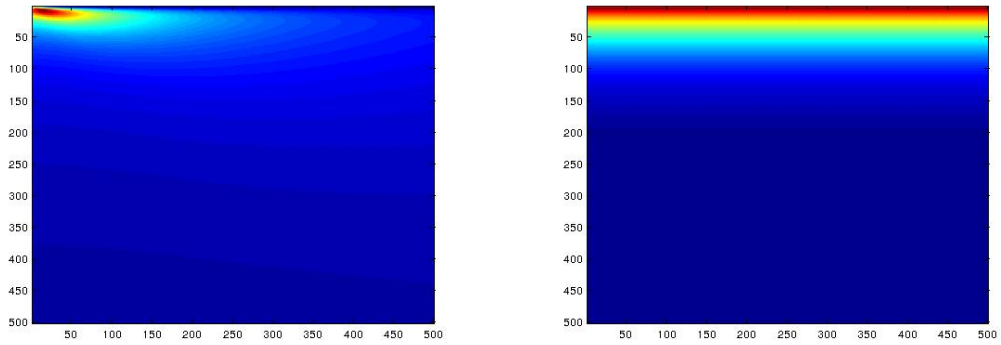

(a) (b)

Figure 15: Left: wave-equation migration image in $k_z - k_h$ domain; Right: asymptotic migration image in $k_z - k_h$ domain.

4.3.3 Test: obtaining the angle dependent reflection coefficient by interpreting the Kirchhoff migration result as a fictitious experiment

We use

$$r(k_{sx}, k_{sz}) = \frac{\rho_2 k_{sz} - \rho_1 k_{sz2}}{\rho_2 k_{sz} + \rho_1 k_{sz2}}. \tag{40}$$

to calculate the exact angle dependent reflection coefficient of the reflector (Left figure in figure 16). k_{sz} and k_{sx} are incident vertical and horizontal wave numbers in the first layer, respectively, k_{sz2} is the vertical wavenumber in the second layer, which can be calculated by

$$k_{sz2} = \sqrt{\frac{c_1^2}{c_2^2}(k_{sz}^2 + k_{sx}^2) - k_{sx}^2} \tag{41}$$

We can retrieve the angle dependent reflection coefficients from Stolt migration using equation 27)

$$M^{Stolt}(k_x, k_z, k_h) = \frac{c^2}{4\pi^2}\frac{k_{gz}k_{sz}}{\omega k_z} D(k_{gx}, k_{sx}, \omega)$$

As for one horizontal reflector in this test, the data can be calculated by reflectivity method as discussed in appendix B,

$$\begin{aligned} D(k_{gx}, k_{sx}, \omega) =& \int_{-\infty}^{+\infty} dx_g e^{-ik_{gx}x_g} \frac{r(k_{sx}, k_{sz}) e^{ik_{sx}x_g} e^{2ik_{sz}z_r}}{4\pi i k_{sz}} \\ =& \delta(k_{gx} - k_{sx}) \frac{r(k_{sx}, k_{sz}) e^{2ik_{sz}z_r}}{4\pi i k_{sz}}. \end{aligned} \tag{42}$$

Combining equation 27 and equation 42, we have

$$\begin{aligned} M^{Stolt}(k_x, k_z, k_h) &= \delta(k_{gx} - k_{sx}) \frac{c^2}{4\pi^2}\frac{k_{gz}k_{sz}}{\omega k_z} \frac{r(k_{sx}, k_{sz}) e^{2ik_{sz}z_r}}{4\pi i k_{sz}} \\ &= \delta(k_x) \frac{c^2 e^{-ik_z z_r}}{32\pi^3 \omega} r(k_{sx}, k_{sz}) \end{aligned} \tag{43}$$

Thus we can obtain the angle dependent plane wave reflection coefficient from Stolt migration by

$$r(k_{sx}, k_{sz}) = \int dk_x \frac{32\pi^3\omega}{c^2 e^{-ik_z z_r}} M^{Stolt}(k_x, k_z, k_h) \tag{44}$$

For Kirchhoff migration, as discussed in section 4.2.1, we can interpreted the imaging process as a fictitious experiment at depth. Then we can also use the same algorithm as as shown above in equation 44,

$$r(k_{sx}, k_{sz}) = \int dk_x \frac{32\pi^3\omega}{c^2 e^{-ik_z z_r}} M^{Kirchhoff}(k_x, k_z, k_h) \tag{45}$$

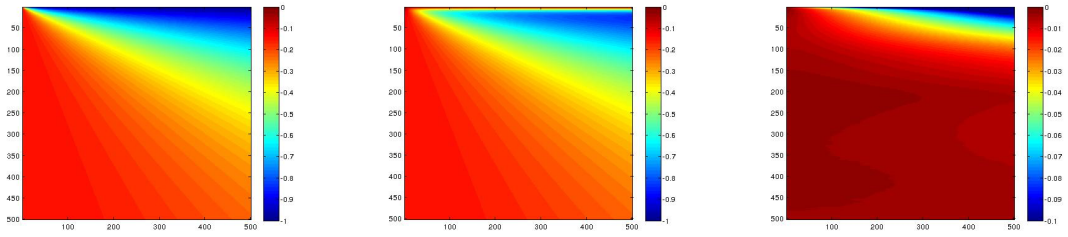

(a) (b) (c)

Figure 16: Left: The angle dependent reflection coefficient by analytic calculation; Middle: The angle dependent reflection coefficient inverted from wave-equation migration imaging; Right: The angle dependent reflection coefficient inverted from asymptotic migration imaging.

to obtain the reflection coefficient.

By comparing left and middle figures of 16, we find the inverted angle dependent reflection coefficient from wave-equation migration image is almost identical as the theoretical value except for the small vertical wavenumber part. The differences are due to the numerical stabilizing scheme for the division by small vertical wavenumber. Besides these differences, the result is perfect. However, the inverted angle dependent reflection coefficient from asymptotic migration image (right figure in16) is not even close to the theoretical value.

4.3.4 Test: obtaining the angle dependent reflection coefficient by an alternative ray-theory-based algorithm

An alternative ray-theory-based algorithm to obtain the angle dependent reflection coefficient from Kirchhoff migration is using the algorithm discussed in section 4.2.2.

In this test we know the actual dip angle α (which is 0), we can chose $\eta = tan\alpha$ such that

$$M^{Kirchhoff}(x, z, \xi, \eta = tan\alpha) = \frac{z^2 r^2}{4\pi c (r_s r_g)^{3/2}} \frac{d}{dt} D(x_g, x_s, t)|_{t=r/c}. \tag{46}$$

(Note that both sides of the equation only depend on ξ.)

Compare this equation with the synthetic data generated by Cagniard-de Hoop method (Appendix A)

$$D(x_g, x_s, t) = \frac{1}{2\pi} \mathrm{Re}(\widehat{pp}) \frac{H(t - r/c_0)}{\sqrt{t - r^2/{c_0}^2}},$$

we can obtain a ray-theory-based angle dependent reflection coefficient by

$$\begin{aligned} r^{asymptotic}(\xi) =& (\frac{d}{dt} \mathrm{Re}(\widehat{pp}) \frac{H(t - r/c_0)}{\sqrt{t - r^2/{c_0}^2}})|_{t=r/c} \\ =& \frac{8\pi^2 c (r_s r_g)^{3/2}}{z^2 r^2} M^{Kirchhoff}(x, z, \xi, \eta = tan\alpha) \end{aligned} \tag{47}$$

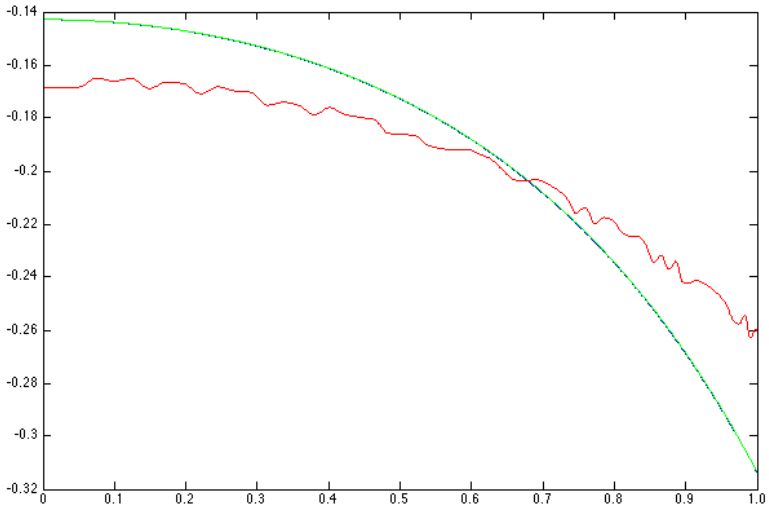

Figure 17: Predicted angle dependent reflection coefficient. Blue line: Actual reflection coefficient; Green line: prediction from stolt migration; Red line: prediction from this ray-theory-based algorithm.

Figure 17 shows the predicted angle dependent reflection coefficient from wave equation migration (green) and this ray-theory-based algorithm (red).

In figure 17 we find that the inverted angle dependent reflection coefficient from wave-equation migration image (green line) is almost identical as the theoretical value (blue line). However, the inverted angle dependent reflection coefficient from this ray-theory-based algorithm (red line) is very different from the theoretical value (blue line), while the trend is similar [3].

[3]Note that due to numerical issue, the inverted angle dependent reflection coefficient from this asymptotic algorithm has been normalized.

5 Single source and receiver image for Kirchhoff migration and RTM

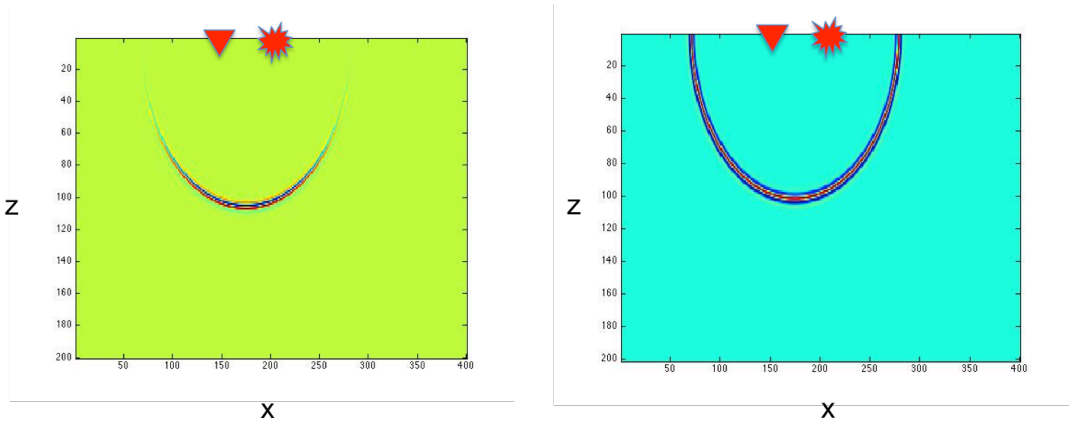

(a) (b)

Figure 18: Left: single source and receiver image for Kirchhoff migration. Right: single source and receiver image for RTM.

In this section, we compare the single source and receiver image of Kirchhoff migration and RTM, as shown in Figure 18. The left figure is the single source and receiver image of Kirchhoff migration and the right figure is the single source and receiver image of RTM. The images are ellipses in both cases and this is an indication that Kirchhoff migration and RTM are related.

6 A 1D pre-stack example examining the amplitude differences between Stolt migration and RTM

As discussed in the previous section, the Stolt migration is given by,

$$M^{Stolt}(x,z) = \frac{1}{(2\pi)^3}\int d\omega \int dk_{sx} e^{-i(k_{sz}z+k_{sx}x)} \int dk_{gx} e^{i(k_{gz}z+k_{gx}x)} D(k_{gx},k_{sx},\omega) \tag{48}$$

where $M^{Stolt}(x,z)$ is the image function.

RTM (Reverse Time Migration) utilizes Claerbout Imaging Condition II for imaging primaries. In RTM, the source wavefield is forward propagated to the subsurface and the receiver wavefield is backward propagated to the subsurface; the imaging result is obtained by cross-correlation, i.e., the space and time coincidence of up and down waves. The Claerbout Imaging Condition II RTM formula (Baysal et al., 1983; Whitmore, 1983; McMechan, 1983) is

$$I(\vec{r}) = \sum_{x_s}\sum_{\omega} S^*(\vec{r},x_s,\omega)R(\vec{r},x_s,\omega) \tag{49}$$

where R is the back-propagated reflection data, S is the forward-propagated source wavefield, S^* is the complex conjugate of S. The zero-lag cross-correlation is indicated by the sum over angular frequency, ω, and the sum over sources adds candidate-image travel-time trajectories.

7 Example

In this section, we will show the images generated by Reverse Time Migration (Claerbout Imaging Condition II) and Stolt migration (Claerbout Imaging Condition III) for a single horizontal reflector.

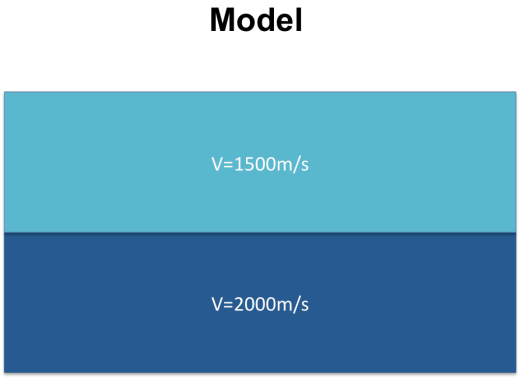

Figure 19: model

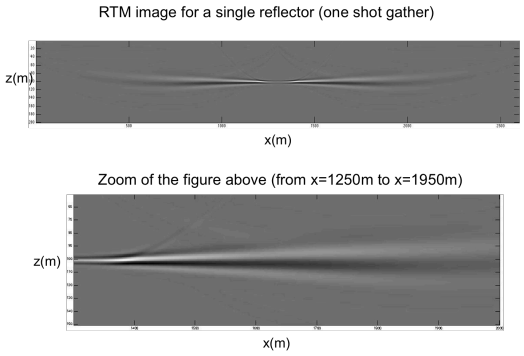

Figure 20: image result (one shot gather) following Claerbout Imaging Conidtion II. The figure below is a zoom of the upper figure. The Claerbout II image shows an inconsistent amplitude and shape of the image along the single reflector.

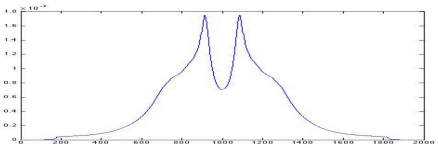

Figure 21: Maximum amplitude of Figure 20 over x

Figure 19 shows the one-reflector model we used for this test. Figure 20 shows the image generated by Reverse Time Migration with a single shot gather (one source) and figure 21 shows the maximum amplitude of the image over x ; we observe that there is a blur on the image as well as some artifacts generated by the limited aperture[4]. In practice, a sum over all sources is taken

[4]In this test, we used a very large aperture to minimize the aperture artifacts. However, we can still observe this kind of artifacts on the image.

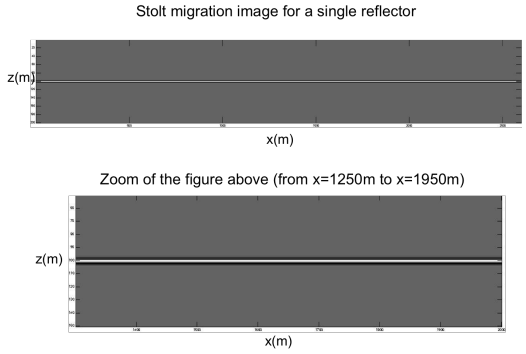

Figure 22: image result following Claerbout Imaging Condition III. The figure below is a zoom of the upper figure. The Claerbout III image in this figure shows an amplitude and shape consistent image. The exact same data was used in the simplest 1D earth prestack Claerbout II and Claerbout III tests and comparisons, indicating their intrinsic and substantive differences even in the simplest circumstances. As pointed out in Weglein (2015) the differences are much more serious when the target is complicated and imaging through and beneath a rapidly changing velocity.

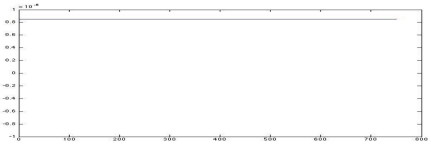

Figure 23: Maximum amplitude of Figure 22 over x

with the assumption that the blur and artifacts will go away. However, summing over all sources does not have a clear physical meaning and it is not guaranteed that all the blur and artifacts will go away. Figure 22 shows the image generated by Stolt migration with exactly the same data and figure 23 shows the maximum amplitude of the image over x. We can observe that the image is flat and with few artifacts. The sum over sources in Stolt migration brings the source down to a point in the subsurface, while the sum over sources in RTM (equation 49) seeks to mitigate intrinsic artifacts in Claerbout II imaging. More importantly, every step in Stolt migration has a clear physical meaning. We can readily obtain interpretable amplitude information, such as angle dependent reflection coefficient, from Stolt migration.

8 Conclusion

In this paper we first compared a Claerbout III wave equation migration - Stolt migration and its asymptotic form - Kirchhoff migration. We first studied and tested the effects caused by the stationary phase approximation which has dramatic impact on subsequent imaging steps, and makes the asymptotic migration method not an approximated source and receiver coincident at time equals zero. Then we compared the amplitudes of Stolt migration and Kirchhoff migration for the simplest possible overburden, with both perfect data in the domain each requires, and attempt to retrieve the angle dependent reflection coefficient from both migration methods. For Stolt migration, the retrieved angle dependent reflection coefficient is almost identical as the theoretical value. For Kirchhoff migration, we have two different ways to retrieve the angle dependent reflection coefficient: 1, interpreting the Kirchhoff migration result as a fictitious experiment. 2, using an alternative ray-theory-based algorithm. And in both cases the predicted angle dependent reflection coefficient is not as good as the wave equation migration prediction.This result shows that the Claerbout III wave equation migration - Stolt migration and its asymptotic form - Kirchhoff migration are quite different. Stolt migration can provide a clear physics meaning with predicting a source and receiver experiment at depth and one can readily obtain the correct angle dependent reflection coefficient. Kirchhoff migration loses the definitive ”yes” or ”no” to a point being imaged and the ability to provide a correct angle dependent reflection coefficient. And then we compare the single source and receiver image of Kirchhoff migration and RTM, the images indicate that these two migration methods are related.

Next we discussed the second test, a comparison between the Claerbout Imaging Conidtion III - utilized in Stolt migration, and Claerbout Imaging Conidtion II- utilized in Reverse Time Migration, in the simplest 1D earth, with exactly the same prestack data. This result shows that the Claerbout Imaging Conidtion III and Claerbout Imaging Conidtion II are intrinsically and substantively different even in the simplest circumstances. The Claerbout II image (one shot gather) shows an inconsistent amplitude and shape of the image along the single reflector. The Claerbout III image shows an amplitude and shape consistent image. As pointed out in Weglein (2015) the differences are much more serious when the target is complicated and imaging through and beneath a rapidly changing velocity. Claerbout III can provide a clear physics meaning with predicting a source and receiver experiment at depth, collapsed and un-collapsed images with meaningful amplitude and definitiveness that the Kirchhoff like migrations and Claerbout II cannot provide. Claerbout III capability and advantages also include amplitude analysis and imaging and imaging-inversion at specular and non-specular reflectors.

The discussions and conclusions for Claerbout II and III for one way wave in this paper are indications for the benefits that the two way wave propagation form of Claerbout III will bring to seismic exploration. And in evaluating the role of multiples in imaging in Weglein (2015) the two way-wave propagation form of Claerbout III was called upon to provide a definition response to the question ”multiples: signal or noise?”. (see also (Weglein et al., 2011a,b; Liu, 2013))

9 Acknowledgements

We are grateful to all M-OSRP sponsors for their encouragement and support in this research. We would like to thank all our coworkers for their help toward finishing this paper and also for their valuable discussions in this research program.

Appendix

10 Synthetic data generation by Cagniard-de Hoop method

For one reflector model, the analytic data can be calculated by Cagniard-de Hoop method in space-time domain (as utilized inZhang and Weglein (2006)). In an acoustic medium, for a source at (x_s, z_s), and a receiver at (x_g, z_g), the pre-critical reflection data is

$$P(x_s, x_g, z_s, z_g, t) = \frac{1}{2\pi}\mathrm{Re}(\widehat{pp})\frac{H(t - r/c_0)}{\sqrt{t - r^2/{c_0}^2}}, \tag{A-1}$$

with

$$r = \sqrt{(x_s - x_g)^2 + (z_s + z_g - 2z_r)^2}, \tag{A-2}$$

where z_r is the depth of the reflector, c_0 is the velocity in the first layer and t is the recorded time.

11 Synthetic data generation by reflectivity method

For 1D earth, the analytic data can be calculated by the reflectivity method in the frequency-wave number domain, e.g., in Ewing et al. (1957). For one reflector in an acoustic medium, assuming the a source and a receiver are located at $(x_s, 0)$ and $(x_g, 0)$ respectively, the data can be calculated as

$$\begin{aligned} D(k_{sx}, k_{gx}, \omega) =& \int_{-\infty}^{+\infty} dx_g e^{-ik_{gx}x_g}\frac{r(k_{sx}, k_{sz})e^{ik_{sx}x_g}e^{2ik_{sz}z_r}}{4\pi i q_s} \\ =& \delta(k_{sx} - k_{gx})\frac{r(k_{sx}, k_{sz})e^{2ik_{sz}z_r}}{4\pi i k_{sz}}. \end{aligned} \tag{A-3}$$

where k_{sx} and k_{gx} are the Fourier transform of x_s and x_g respectively, k_{gx} is defined in the same way in Section 2, ω is the temporal frequency and z_r is the depth of the reflector.

References

Baysal, Edip, Dan D. Kosloff, and John W. C. Sherwood. "Reverse time migration." *Geophysics* 48 (1983): 1514–1524.

Claerbout, Jon F. "Toward a unified theory of reflector mapping." *Geophysics* 36 (June 1971): 467–481.

Clayton, R. W. and R. H. Stolt. "A Born-WKBJ inversion method for acoustic reflection data." *Geophysics* 46 (1981): 1559–1567.

Ewing, W. M., W. S. Jardetzky, and F. Press. *Elastic waves in layered media*. McGraw-Hill Book Co., 1957.

Liu, Fang. The first wave theory RTM, examples with a layered medium, predicting the source and receiver at depth and then imaging, providing the correct location and reflection amplitude at every depth location, and where the data includes primaries and all internal multiples. Presentation given at the 2013 M-OSRP Annual Meeting, available online at mosrp.uh.edu, May 2013.

Lowenthal, D., L. Lu, R. Roberson, and J. W. C. Sherwood. "The wave equation applied to migration." *Geophysical Prospecting* 24 (1985): 380–399.

McMechan, G. A. "Migration by extrapolation of time dependent boundary values." *Geophysical Prospecting* 31 (1983): 413–420.

Riley, D. C. and J. F. Claerbout. "2D multiple reflections." *Geophysics* 41 (1976): 592–620.

Stolt, R. H. "Migration by Fourier transform." *Geophysics* 43 (1978): 23–48.

Stolt, R. H. and A. B. Weglein. "Migration and inversion of seismic data." *Geophysics* 50 (1985): 2458–2472.

Stolt, Robert H. and Alvin K. Benson. *Seismic migration: theory and practice*. London—Amsterdam: Geophysical Press, 1986.

Stolt, Robert H. and Arthur B. Weglein. *Seismic Imaging and Inversion: Application of Linear Inverse Theory*. Cambridge University Press, February 2012.

Weglein, A. B. and R. H. Stolt. "Migration-Inversion Revisited." *The Leading Edge* Aug (1999): 950.

Weglein, A. B., R. H. Stolt, and J. D. Mayhan. "Reverse-time migration and Green's theorem: Part I — The evolution of concepts, and setting the stage for the new RTM method." *Journal of Seismic Exploration* 20 (February 2011): 73–90.

Weglein, A. B., R. H. Stolt, and J. D. Mayhan. "Reverse time migration and Green's theorem: Part II — A new and consistent theory that progresses and corrects current RTM concepts and methods." *Journal of Seismic Exploration* 20 (May 2011): 135–159.

Weglein, Arthur B. "Multiples, single or noise?." *Geophysics, Submitted* (2015).

Whitmore, D. N. "Iterative depth imaging by back time propagation." *53rd Annual International Meeting, SEG, Expanded Abstracts*. 1983, 382–385.

Zhang, Jingfeng and Arthur B. Weglein. "A note on data modelling using the Cagniard-de Hoop method." *M-OSRP 2005-2006 Annual Report*. 2006, 126–138.

A 1D pre-stack example examining the differences in two important imaging conditions: the space-time coincidence of up and down waves and the predicted coincident source and receiver experiment at depth at time zero.

Yanglei Zou, Arthur B. Weglein, M-OSRP/Physics Dept./University of Houston

SUMMARY

In the 1970's Claerbout, Lowenthal and their colleagues (Claerbout, 1971; Riley and Claerbout, 1976; Lowenthal et al., 1985) introduced three imaging conditions : (1) the exploding reflector model for zero offset data (2) the space and time coincidence of up and down going waves and (3) predicting a coincide source and receiver experiment at depth at time equals zero. We refer to these as Claerbout Imaging Condition I, II and III, respectively. For a normal incident plane wave on a single horizontal reflector they are equivalent. For a shot record recorded above a single horizontal reflector or more complicated situations they are no longer equivalent. Claerbout III is superior to Claerbout I and II in that it provides the most quantitative and interpretable image amplitude. Claerbout III is also extendable/generalizable to provide an angle dependent reflection coefficient. Stolt and his colleagues (Clayton and Stolt, 1981; Stolt and Weglein, 1985; Stolt and Benson, 1986) originally formulated Claerbout III for one-way waves. For imaging two way propagating waves, Whitmore and his colleagues (Whitmore (1983)) launched from Claerbout II. Weglein, Fang and their colleagues (Weglein et al., 2011a,b; Liu, 2013) extended Claerbout III for two way propagating waves. In this paper, the first direct and detailed comparison of Claerbout II and III is carried out for the simplest circumstance where they will produce a different result. The differences are significant and substantive, with implications far beyond the simple example that allows for transparent analysis and analytic evaluation and conclusions.

INTRODUCTION

Methods that use the wave equation to perform seismic migration have two ingredients: (1) a wave propagation component and (2) an imaging principle or concept. Claerbout (Claerbout, 1971; Riley and Claerbout, 1976) was the initial and key wave-equation migration imaging-concept pioneer and algorithm developer, together with Stolt (Stolt (1978)) and Lowenthal (Lowenthal et al. (1985)) and their colleagues, they introduced imaging conditions for locating reflectors at depth from surface-recorded data. The three key imaging conditions that were introduced are:

I. the exploding-reflector model
II. time and space coincidence of up and downgoing waves
III. predicting a source and receiver experiment at a coincident-source-and-receiver subsurface point, and asking for time equals zero (the definition of wave-equation migration)

For a normal-incident spike plane wave on a horizontal reflector, these three imaging concepts are totally equivalent. However, a key point to make clear for this paper, is that for a non-zero-offset surface seismic-data experiment, with either a one-dimensional or a multi-dimensional subsurface, they are no longer equivalent. Wave-equation migration is defined as using the Claerbout Imaging Condition III, predicting a source and receiver experiment at depth at time equals zero. Stolt and his colleagues (Clayton and Stolt, 1981; Stolt and Weglein, 1985; Stolt and Benson, 1986; Stolt and Weglein, 2012; Weglein and Stolt, 1999) extended and formulated the experiment-at-depth concept to allow a separated source and receiver experiment at time equals zero for one way propagating waves. Weglein, Fang and their colleagues (Weglein et al., 2011a,b; Liu, 2013) extended Claerbout III for two way propagating waves. Claerbout III is superior to Claerbout I and II in that it provides the most quantitative and interpretable image amplitude. Claerbout III is also extendable/generalizable to provide an angle dependent reflection coefficient. For the purpose of determining quantitative information on the physical meaning of the image, the clear choice is Claerbout Imaging Condition III.

In this paper, we will compare the imaging results obtained by Claerbout Imaging Condition II and III. The Claerbout Imaging Condition III predicts a physical experiment with both source and receiver at depth, allowing it to provide the imaging definitiveness and physical interpretation that Claerbout Imaging Condition II cannot match.

STOLT MIGRATION

Stolt migration represents Claerbout Imaging Condition III for one-way propagating waves. Following Stolt and Weglein (2012), given a 2D data $D(x_g, x_s, t)$ with source location $(x_s, z_s = 0)$, receiver location $(x_g, z_g = 0)$, and time t, we can perform a Fourier transform over all coordinates:

$$D(k_{gx}, k_{sx}, \omega) = \int dx_g \int dx_s \int dt D(x_g, x_s, t) e^{i(k_{sx}x_s - k_{gx}x_g + \omega t)}. \tag{1}$$

where k_{gx}, k_{sx} and ω are Fourier conjugates of x_g x_s and t, respectively.

Then we can predict the data from an experiment where the sources and receivers are all at depth z,

$$P(k_{gx}, z, k_{sx}, z, \omega) = D(k_{gx}, k_{sx}, \omega) e^{i(k_{gz} - k_{sz})z}, \tag{2}$$

where the vertical wavenumber component k_{gz} and k_{sz} are de-

fined as

$$k_{gz} = -\frac{\omega}{c}\sqrt{1-\frac{{k_{gx}}^2 c^2}{\omega^2}}$$
$$k_{sz} = \frac{\omega}{c}\sqrt{1-\frac{{k_{sx}}^2 c^2}{\omega^2}}. \quad (3)$$

If we make two inverse Fourier transform of k_{gx} and k_{xs} to the same x, we can predict the data of an experiment where a source and a receiver are both at location (x,z),

$$\begin{aligned} P(x,z,x,z,\omega) &= \frac{1}{(2\pi)^2}\int dk_{sx} e^{-ik_{sx}x}\int dk_{gx} e^{ik_{gx}x} P(k_{gx},z,k_{sx},z,\omega) \\ &= \frac{1}{(2\pi)^2}\int dk_{sx} e^{-i(k_{sz}z+k_{sx}x)} \\ &\quad \times \int dk_{gx} e^{i(k_{gz}z+k_{gx}x)} D(k_{gx},k_{sx},\omega) \end{aligned} \quad (4)$$

Next, predict the coincident source and receiver at time equals zero, we obtain the 2D Stolt migration result,

$$\begin{aligned} M^{Stolt}(x,z) &= \frac{1}{2\pi}\int d\omega e^{-i\omega t} P(x,z,x,z,\omega)|_{t=0} \\ &= \frac{1}{(2\pi)^3}\int d\omega \int dk_{sx} e^{-i(k_{sz}z+k_{sx}x)} \\ &\quad \times \int dk_{gx} e^{i(k_{gz}z+k_{gx}x)} D(k_{gx},k_{sx},\omega) \end{aligned} \quad (5)$$

where $M^{Stolt}(x,z)$ is the image function *.

REVERSE TIME MIGRATION

RTM (Reverse Time Migration) is a kind of migration adopting Claerbout Imaging Condition II for primaries in a medium where waves are two way propagating. In RTM, the source wavefield is forward propagated to the subsurface and the receiver wavefield is backward propagated to the subsurface; the imaging result is obtained by cross-correlation, i.e., the space and time coincidence of up and down waves. The Claerbout Imaging Condition II RTM formula (Baysal et al., 1983; Whitmore, 1983; McMechan, 1983) is

$$I(\vec{r}) = \sum_{x_s}\sum_{\omega} S^*(\vec{r},x_s,\omega) R(\vec{r},x_s,\omega) \quad (6)$$

where R is the back-propagated reflection data, S is the forward-propagated source wavefield, S^* is the complex conjugate of S. The zero-lag cross-correlation is indicated by the sum over angular frequency, ω, and the sum over sources adds candidate-image travel-time trajectories.

*In Stolt and Weglein (2012), the image function $M^{Stolt}(x,z)$ has a half-integral filter. In this section we do not include the half-integral filter.

EXAMPLE

In this section, we will show the images generated by Reverse Time Migration (Claerbout Imaging Condition II) and Stolt migration (Claerbout Imaging Condition III) for a single horizontal reflector.

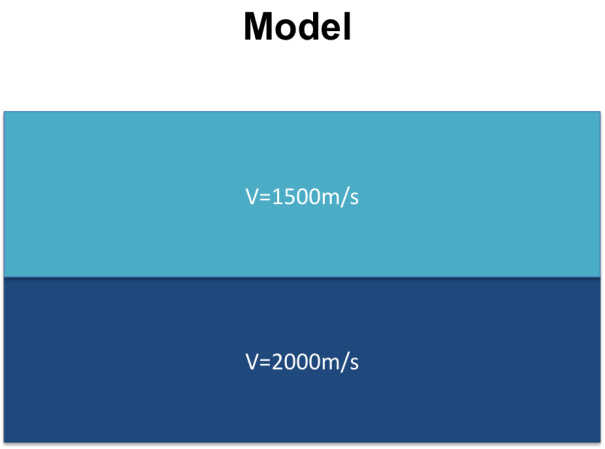

Figure 1: model

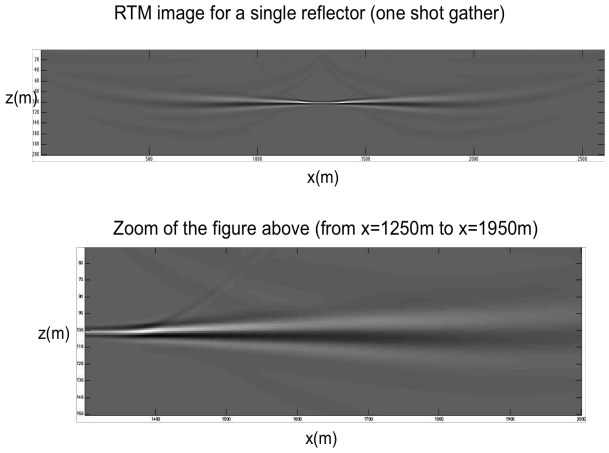

Figure 2: image result (one shot gather) following Claerbout Imaging Conidtion II. The figure below is a zoom of the upper figure. The Claerbout II image shows an inconsistent amplitude and shape of the image along the single reflector.

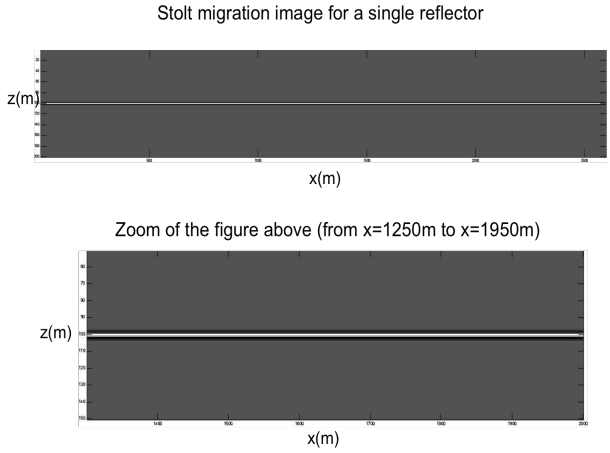

Figure 3: image result following Claerbout Imaging Condition III. The figure below is a zoom of the upper figure. The Claerbout III image in this figure shows an amplitude and shape consistent image. The exact same data was used in the simplest 1D earth prestack Claerbout II and Claerbout III tests and comparisons, indicating their intrinsic and substantive differences even in the simplest circumstances. As pointed out in Weglein (2015) the differences are much more serious when the target is complicated and imaging through and beneath a rapidly changing velocity.

Figure 1 shows the one-reflector model we used for this test. Figure 2 shows the image generated by Reverse Time Migration with a single shot gather (one source); we observe that there is a blur on the image as well as some artifacts generated by the limited aperture[†]. In practice, a sum over all sources is taken with the assumption that the blur and artifacts will go away. However, summing over all sources does not have a clear physical meaning and it is not guaranteed that all the blur and artifacts will go away. Figure 3 shows the image generated by Stolt migration with exactly the same data. We can observe that the image is flat and with few artifacts. The sum over sources in Stolt migration brings the source down to a point in the subsurface, while the sum over sources in RTM (equation 6) seeks to mitigate intrinsic artifacts in Claerbout II imaging. More importantly, every step in Stolt migration has a clear physical meaning. We can readily obtain interpretable amplitude information, such as angle dependent reflection coefficient, from Stolt migration (see Zou (2015) for more detail).

CONCLUSION

In this paper we compared the Claerbout Imaging Conidtion III - Stolt migration, and Claerbout Imaging Conidtion II- utilized in Reverse Time Migration, in the simplest 1D earth, with exactly the same prestack data. This result shows that the Claerbout Imaging Conidtion III (wave equation migration) - Stolt migration, and Claerbout Imaging Conidtion II- Reverse Time Migration, are intrinsically and substantively different even in the simplest circumstances. The Claerbout II image (one shot gather) shows an inconsistent amplitude and shape of the image along the single reflector. The Claerbout III image shows an amplitude and shape consistent image. As pointed out in Weglein (2015) the differences are much more serious when the target is complicated and imaging through and beneath a rapidly changing velocity. Claerbout Imaging Condition III (the wave equation migration) can provide a clear physics meaning with predicting a source and receiver experiment at depth. Thus we can readily obtain interpretable amplitude information, such as angle dependent reflection coefficient, from Claerbout imaging conidtion III. And in evaluating the role of multiples in imaging in Weglein (2015) a two way-wave propagation form of Claerbout III was called upon to provide a definition response to the question ”multiples: signal or noise?”. (see also (Weglein et al., 2011a,b; Liu, 2013))

ACKNOWLEDGMENTS

We are grateful to all M-OSRP sponsors for their encouragement and support in this research. We would like to thank all our coworkers for their help in reviewing this paper and their valuable discussions.

[†]In this test, we used a very large aperture to minimize the aperture artifacts. However, we can still observe this kind of artifacts on the image.

REFERENCES

Baysal, E., D. D. Kosloff, and J. W. C. Sherwood, 1983, Reverse time migration: Geophysics, **48**, 1514–1524.

Claerbout, J. F., 1971, Toward a unified theory of reflector mapping: Geophysics, **36**, 467–481.

Clayton, R. W., and R. H. Stolt, 1981, A Born-WKBJ inversion method for acoustic reflection data: Geophysics, **46**, 1559–1567.

Liu, F., 2013, The first wave theory rtm, examples with a layered medium, predicting the source and receiver at depth and then imaging, providing the correct location and reflection amplitude at every depth location, and where the data includes primaries and all internal multiples. Presentation given at the 2013 M-OSRP Annual Meeting, available online at mosrp.uh.edu.

Lowenthal, D., L. Lu, R. Roberson, and J. W. C. Sherwood, 1985, The wave equation applied to migration: Geophysical Prospecting, **24**, 380–399.

McMechan, G. A., 1983, Migration by extrapolation of time dependent boundary values: Geophysical Prospecting, **31**, 413–420.

Riley, D. C., and J. F. Claerbout, 1976, 2D multiple reflections: Geophysics, **41**, 592–620.

Stolt, R. H., 1978, Migration by Fourier transform: Geophysics, **43**, 23–48.

Stolt, R. H., and A. K. Benson, 1986, Seismic migration: theory and practice: Geophysical Press.

Stolt, R. H., and A. B. Weglein, 1985, Migration and inversion of seismic data: Geophysics, **50**, 2458–2472.

———, 2012, Seismic imaging and inversion: Application of linear inverse theory: Cambridge University Press.

Weglein, A. B., 2015, Multiples, single or noise?: Geophysics, Submitted.

Weglein, A. B., and R. H. Stolt, 1999, Migration-inversion revisited: The Leading Edge, **Aug**, 950.

Weglein, A. B., R. H. Stolt, and J. D. Mayhan, 2011a, Reverse-time migration and Green's theorem: Part I — The evolution of concepts, and setting the stage for the new RTM method: Journal of Seismic Exploration, **20**, 73–90.

———, 2011b, Reverse time migration and Green's theorem: Part II — A new and consistent theory that progresses and corrects current RTM concepts and methods: Journal of Seismic Exploration, **20**, 135–159.

Whitmore, D. N., 1983, Iterative depth imaging by back time propagation: 53rd Annual International Meeting, SEG, Expanded Abstracts, 382–385.

Zou, Y. Q. Fu, C. M. J. W. A. W., 2015, Comparison of the amplitude properties of the one-way wave equation migration (stolt migration) and its approximate asymptotic form (kirchhoff migration): implications for the differences between two-way wave equation migration (claerbout imaging condition iii) and conventional rtm (claerbout imaging condition ii): M-OSRP 2015 Annual Report.

(Short Note) Claerbout imaging condition III in 1.5D medium for two-way propagating wave by using the special Green's function doubly vanishing at the lower boundary

Qiang Fu, Arthur B. Weglein and Fang Liu

1 Introduction

In the 1970s and 1980s Claerbout, Lowenthal and their colleagues (Claerbout, 1971; Riley and Claerbout, 1976; Lowenthal et al., 1985) introduced three imaging conditions. We refer to these as Claerbout Imaging Condition I, II and III, respectively.

The three key imaging conditions that were introduced are:
I. the exploding-reflector model
II. time and space coincidence of up and down-going waves
III. predicting a source and receiver experiment at a coincident-source-and-receiver subsurface point, and asking for time equals zero.

For a normal incident plane wave on a single horizontal reflector these imaging conditions are equivalent. For a more complicated situation Claerbout III is superior to Claerbout I and II in that it provides the most quantitative and interpretable image amplitude. Stolt and his colleagues (Clayton and Stolt, 1981; Stolt and Weglein, 1985; Stolt and Benson, 1986) originally formulated Claerbout III for one-way waves. Weglein, Liu (Weglein et al., 2011a,b; Liu, 2013) and their colleagues in M-OSRP extended Claerbout III for two way propagating waves. Fu et al. (2014) compared the Claerbout III and Claerbout II for one-way waves. In this short note, we will present the first imaging result of Claerbout imaging condition III in 1.5D medium for two-way propagating waves.

2 Theory

Weglein and Liu (Weglein et al., 2011a,b; Liu, 2013) have provided the derivations for the Claerbout imaging condition III in a 1D medium for two-way propagating waves by using the special doubly vanishing Green's function G_0^{DN}; here we extend the algorithm to 1.5D. For simplicity, in this short note, we use a simple two half-space homogeneous model for all calculations.

The Claerbout Imaging condition III predicts a experiment with source and receiver at the imaging depth and asks for distance between source and receiver (subsurface offset) of the experiment and the travel time of the experiment at 0 (from a limit approach). We have different choices for predicting an experiment with source and receiver both at depth. Here we use the Green's theorem wave prediction method (Weglein et al., 2011a,b; Liu, 2013).

Figure 1: The 1.5D two half-space homogeneous velocity model I used in the example.

2.1 Green's theorem wave prediction in 1.5D with G_0^{DN}

The general form of Green's theorem wave prediction is

$$\left.\begin{array}{ll} p(\vec{r}) & (\vec{r} \text{ in } v) \\ 0 & (\vec{r} \text{ out } v) \end{array}\right\} = \int\limits_v \rho(\vec{r'}) G(\vec{r}, \vec{r'}) d\vec{r'} + \oint\limits_s (p(\vec{r'}) \nabla' G(\vec{r}, \vec{r'}) - G(\vec{r}, \vec{r'}) \nabla' p(\vec{r'})) \cdot \hat{n} ds \quad (1)$$

where $p(\vec{r})$ is wave-field at location $\vec{r}$, $G(\vec{r}, \vec{r'})$ is any valid Green's function with source point at $\vec{r'}$ and field point at $\vec{r}$, s is a closed surface around the volume v, and $\rho(\vec{r'})$ is the source located at $\vec{r'}$.

Equation 1, if we predict wave-field inside a volume, we need the measurements on the entire closed surface of the volume, which in our 1.5D case would be the top and bottom surfaces for our volume (there is no velocity change along the horizontal direction, so we can arrange the volume to go to infinity along the horizontal direction, so for limited time the evaluation on the "side walls" would be not be contributing in the calculation). If we use the special Green's function G_0^{DN} with both its value and derivative vanishing on the bottom surface, the integral in equation 1 would vanish at the bottom surface and the only part that needs to be evaluated is the top surface of the volume.

If we assume there is no source within the volume v, equation 1 becomes

$$\left.\begin{array}{ll} p(\vec{r}) & (\vec{r} \text{ in } v) \\ 0 & (\vec{r} \text{ out } v) \end{array}\right\} = \int_{\textbf{top surface}} (p(\vec{r'}) \nabla' G_0^{DN}(\vec{r}, \vec{r'}) - G_0^{DN}(\vec{r}, \vec{r'}) \nabla' p(\vec{r'})) \cdot \hat{n} ds. \quad (2)$$

3 Analytic calculation for Claerbout III image beneath single reflector

In this section we will use the Green's theorem wave prediction in 1.5D with G_0^{DN} to calculate an analytic solution for Claerbout III image beneath the reflector. We will start with data on the mea-

surement surface ($D(x_g, z_g, x_s, z_s, t)$) and will use the Green's theorem wave prediction (equation 2) twice to bring the receiver and source down to the image depth ($D(x_g, z_i, x_s, z_i, t)$) and then ask for subsurface offset and time equal to zero to get the image ($I(x_i, z_i) = D(x_i, z_i, x_i, z_i, 0)$). Because our calculation is in 1.5D medium, we can exploit the benefit of 1.5D medium to simplify our calculation by doing the Green's theorem wave prediction in frequency domain. So before we do the calculation, we simplify the Green's theorem wave prediction (equation 2) in frequency domain first. We start with the normal 2D acoustic wave equation,

$$\left(\nabla^2 + \frac{\omega^2}{c^2(\vec{r})}\right) p(\vec{r}, \omega) = \rho(\vec{r}, \omega). \tag{3}$$

For the 2D acoustic wave equation, we can separate the x and z directions as

$$\left(\frac{\partial^2}{\partial z^2} + \frac{\partial^2}{\partial x^2} + \frac{\omega^2}{c^2(z,x)}\right) p(x, z, \omega) = \rho(x, z, \omega). \tag{4}$$

1.5D means we have a 2D line source but the medium itself changes only along the z direction, not in the x direction. Now let's start with the 2D acoustic wave equation to get a 1.5D acoustic wave equation in frequency domain by using the constraint that the medium changes only along the z direction.

Because there is no velocity varying along the x direction, we can easily perform a Fourier Transform along the x direction to get

$$\left(\frac{\partial^2}{\partial z^2} - k_x^2 + \frac{\omega^2}{c^2(z)}\right) p(z, k_x, \omega) = \rho(z, k_x, \omega). \tag{5}$$

Then we can define

$$k_z^2 \equiv \frac{\omega^2}{c^2(z)} - k_x^2. \tag{6}$$

The 1.5D wave equation in frequency domain would be

$$\left(\frac{\partial^2}{\partial z^2} + k_z^2\right) p(z, k_x, \omega) = \rho(z, k_x, \omega). \tag{7}$$

k_x is a free variable so each k_x component for equation 7 is independent. Thus a single k_x component in equation 7 looks very similar to 1D wave equation in frequency domain (if we ignore the evanescent part),

$$\left(\frac{\partial^2}{\partial z^2} + k^2\right) p(z, \omega) = \rho(z, \omega). \tag{8}$$

The Green's theorem wave prediction (equation 2) will also become a simpler form similar to its 1D version

$$\begin{aligned} \left.\begin{array}{ll} p(z, k_x, \omega) & (z \in [z_{\text{top}}, z_{\text{bottom}}]) \\ 0 & (z \notin [z_{\text{top}}, z_{\text{bottom}}]) \end{array}\right\} &= \left[p(z', k_x, \omega)\frac{\partial G(z, z', k_x, \omega)}{\partial z'} - G(z, z', k_x, \omega)\frac{\partial p(z', k_x, \omega)}{\partial z'}\right]\Bigg|_{z'=top}^{bottom} \\ &= \left[G_0^{DN}(z, z', k_x, \omega)\frac{\partial p(z', k_x, \omega)}{\partial z'} - p(z', k_x, \omega)\frac{\partial G_0^{DN}(z, z', k_x, \omega)}{\partial z'}\right]\Bigg|_{z'=top} \end{aligned} \tag{9}$$

For simplicity, we omit the independent variables k_x and ω in all following equations. The Green's theorem wave prediction in frequency domain for 1.5D medium (equation 9) becomes

$$\left.\begin{array}{ll} p(z) & (z \in [z_{\text{top}}, z_{\text{bottom}}]) \\ 0 & (z \notin [z_{\text{top}}, z_{\text{bottom}}]) \end{array}\right\} = \left[G_0^{DN}(z,z')\frac{\partial p(z')}{\partial z'} - p(z')\frac{\partial G_0^{DN}(z,z')}{\partial z'}\right]\Bigg|_{z'=top} \tag{10}$$

Now let's start our first Green's theorem wave prediction to bring receiver depth for surface measurement data ($D(z_g, z_s)$) from z_g down to image depth z_i

$$\widetilde{D}(z_i,z_s) = D(z_g,z_s)\frac{\partial G(z_i,z_g)}{\partial z_g} - G(z_i,z_g)\frac{\partial D(z_g,z_s)}{\partial z_g}\Bigg|_{z_g=top}^{bottom} \tag{11}$$

$$= G_0^{DN}(z_i,z_g)\frac{\partial D(z_g,z_s)}{\partial z_g} - D(z_g,z_s)\frac{\partial G_0^{DN}(z_i,z_g)}{\partial z_g}\Bigg|_{z_g=top} \tag{12}$$

The special Green's function G_0^{DN} for 1.5D medium in frequency with only one reflector (at depth a) is

$$G_0^{DN}(z,z') = \left\{\begin{array}{ll} \frac{e^{ik_1|z'-z|}-e^{ik_1(z'-z)}}{2ik_1} & z<a \\ \left\{\begin{array}{ll} \frac{[Re^{ik_2(z-a)}-e^{ik_2(a-z)}]e^{ik_1(z'-a)}+[e^{ik_2(z-a)}-Re^{ik_2(a-z)}]e^{ik_1(a-z')}}{2ik_2(1+R)} & z'<a \\ \frac{e^{ik_2|z'-z|}-e^{ik_2(z'-z)}}{2ik_2} & z'>a \end{array}\right\} & z>a \end{array}\right. \tag{13}$$

where z is the source point for the Green's function, z' is the field point for the Green's function. k_1 is the k_z defined by equation 6 in the upper half-space and k_2 is k_z in the lower half-space. R is the angle dependent reflection coefficient corresponding to the plain wave.

Its derivative with respect to z' is

$$\frac{\partial G_0^{DN}(z,z')}{\partial z'} = \left\{\begin{array}{ll} \frac{\text{sign}(z'-z)e^{ik_1|z'-z|}-e^{ik_1(z'-z)}}{2} & z<a \\ \left\{\begin{array}{ll} ik_1\frac{[Re^{ik_2(z-a)}-e^{ik_2(a-z)}]e^{ik_1(z'-a)}-[e^{ik_2(z-a)}-Re^{ik_2(a-z)}]e^{ik_1(a-z')}}{2ik_2(1+R)} & z'<a \\ \frac{\text{sign}(z'-z)e^{ik_2|z'-z|}-e^{ik_2(z'-z)}}{2} & z'>a \end{array}\right\} & z>a \end{array}\right. \tag{14}$$

It is obvious that the forms of Green's function are different when the field point of the Green's function is above and below the reflector. This is why we can get different polarities for the image above and below the reflector (depth equals a) consistent with the fact that the reflection coefficients from above and below the reflector have different polarities. In this section we only show the calculation for beneath the reflector $z_{img} > a$, because Claerbout image condition II can not give us the image for a reflector from beneath. For the image from above, the calculation is similar.

The data we use in our calculation is analytic data in the frequency domain. There are two events in the data, the direct event (we call D_d) and the reflection event (we call D_r). The data with source and receiver on the measurement surface is

$$D(z_g,z_s) = D_d(z_g,z_s) + D_r(z_g,z_s) = \frac{e^{ik_1(z_g-z_s)}}{2ik_1} + \frac{Re^{ik_1(2a-z_g-z_s)}}{2ik_1} \tag{15}$$

where z_g and z_s are the depth for receiver and source respectively.

The derivative of the data with respect z_g on the measurement surface is

$$\frac{\partial D(z_g,z_s)}{\partial z_g}=\frac{\partial D_d(z_g,z_s)}{\partial z_g}+\frac{\partial D_r(z_g,z_s)}{\partial z_g}=\frac{e^{ik_1(z_g-z_s)}}{2}+\frac{-Re^{ik_1(2a-z_g-z_s)}}{2} \tag{16}$$

Now we substitute equations 15 and 16 into equation 10 to calculate a virtual data with receiver down to the image depth. We perform the Green's theorem wave prediction for the two events (D_d and D_r) in the data separately and then add them together. We put a tilde on $\widetilde{D_d}(z_i,z_s)$ to remind us that the new predicted data $\widetilde{D_d}(z_i,z_s)$ with receiver at depth is from Green's theorem wave prediction rather than actual measurements.

$$\begin{aligned}\widetilde{D_d}(z_i,z_s)=&G_0^{DN}(z_i,z_g)\frac{\partial D_d(z_g,z_s)}{\partial z_g}-D_d(z_g,z_s)\frac{\partial G_0^{DN}(z_i,z_g)}{\partial z_g}\\ =&\frac{[Re^{ik_2(z_i-a)}-e^{ik_2(a-z_i)}]e^{ik_1(z_g-a)}+[e^{ik_2(z_i-a)}-Re^{ik_2(a-z_i)}]e^{ik_1(a-z_g)}}{2ik_2(1+R)}\frac{e^{ik_1(z_g-z_s)}}{2}\\ &-\frac{e^{ik_1(z_g-z_s)}}{2ik_1}ik_1\frac{[Re^{ik_2(z_i-a)}-e^{ik_2(a-z_i)}]e^{ik_1(z_g-a)}-[e^{ik_2(z_i-a)}-Re^{ik_2(a-z_i)}]e^{ik_1(a-z_g)}}{2ik_2(1+R)}\\ =&\frac{[e^{ik_2(z_i-a)}-Re^{ik_2(a-z_i)}]e^{ik_1(a-z_s)}}{2ik_2(1+R)}\end{aligned} \tag{17}$$

$$\begin{aligned}\widetilde{D_r}(z_i,z_s)=&G_0^{DN}(z_i,z_g)\frac{\partial D_r(z_g,z_s)}{\partial z_g}-D_r(z_g,z_s)\frac{\partial G_0^{DN}(z_i,z_g)}{\partial z_g}\\ =&-\frac{[Re^{ik_2(z_i-a)}-e^{ik_2(a-z_i)}]e^{ik_1(z_g-a)}+[e^{ik_2(z_i-a)}-Re^{ik_2(a-z_i)}]e^{ik_1(a-z_g)}}{2ik_2(1+R)}\frac{Re^{ik_1(2a-z_g-z_s)}}{2}\\ &-\frac{Re^{ik_1(2a-z_g-z_s)}}{2ik_1}ik_1\frac{[Re^{ik_2(z_i-a)}-e^{ik_2(a-z_i)}]e^{ik_1(z_g-a)}-[e^{ik_2(z_i-a)}-Re^{ik_2(a-z_i)}]e^{ik_1(a-z_g)}}{2ik_2(1+R)}\\ =&-R\left[\frac{[Re^{ik_2(z_i-a)}-e^{ik_2(a-z_i)}]e^{ik_1(a-z_s)}}{2ik_2(1+R)}\right]\end{aligned} \tag{18}$$

$$\begin{aligned}\widetilde{D}(z_i,z_s)=&\widetilde{D_d}(z_i,z_s)+\widetilde{D_r}(z_i,z_s)\\ =&-R\frac{[Re^{ik_2(z_i-a)}-e^{ik_2(a-z_i)}]e^{ik_1(a-z_s)}}{2ik_2(1+R)}+\frac{[e^{ik_2(z_i-a)}-Re^{ik_2(a-z_i)}]e^{ik_1(a-z_s)}}{2ik_2(1+R)}\\ =&\frac{(1-R)e^{ik_2(z_i-a)}e^{ik_1(a-z_s)}}{2ik_2}=\frac{(1+R)e^{ik_2(z_i-a)}e^{ik_1(a-z_s)}}{2ik_1}\end{aligned} \tag{19}$$

where the variable R represents the angle dependent reflection coefficient $R=\frac{k_1-k_2}{k_1+k_2}$ and $1+R$ is the transmission coefficient. Next we bring the source down to the image depth (by exploiting reciprocity). We perform the Green's theorem wave prediction again to bring the source down. Again we add another tilde to remind us the new data $\widetilde{\widetilde{D}}(z_i,z_i)$ with both source and receiver at

depth is from two Green's theorem wave predictions.

$$\begin{aligned}\frac{\partial \widetilde{D}(z_i,z_s)}{\partial z_s} =& \frac{\partial \widetilde{D_d}(z_i,z_s)}{\partial z_s} + \frac{\partial \widetilde{D_r}(z_i,z_s)}{\partial z_s} \\ =& \frac{-(1+R)e^{ik_2(z_i-a)}e^{ik_1(a-z_s)}}{2}\end{aligned} \tag{20}$$

$$\begin{aligned}\widetilde{\widetilde{D}}(z_i,z_i) =& G_0^{DN}(z_i,z_s)\frac{\partial \widetilde{D}(z_i,z_s)}{\partial z_s} - \widetilde{D}(z_i,z_s)\frac{\partial G_0^{DN}(z_i,z_s)}{\partial z_s} \\ =& [\frac{[Re^{ik_2(z_i-a)} - e^{ik_2(a-z_i)}]e^{ik_1(z_s-a)} + [e^{ik_2(z_i-a)} - Re^{ik_2(a-z_i)}]e^{ik_1(a-z_s)}}{2ik_2(1+R)}] \\ & \frac{-(1+R)e^{ik_2(z_i-a)}e^{ik_1(a-z_s)}}{2} \\ & - \frac{(1+R)e^{ik_2(z_i-a)}e^{ik_1(a-z_s)}}{2ik_1} \\ & ik_1[\frac{[Re^{ik_2(z_i-a)} - e^{ik_2(a-z_i)}]e^{ik_1(z_s-a)} - [e^{ik_2(z_i-a)} - Re^{ik_2(a-z_i)}]e^{ik_1(a-z_s)}}{2ik_2(1+R)}] \\ =& \frac{1-Re^{2ik_2(z_i-a)}}{2ik_2}\end{aligned} \tag{21}$$

It is easy to know that in the predicted experiment with both source and receiver at the image depth, $\widetilde{\widetilde{D}}(z_i,z_i) = \frac{1-Re^{2ik_2(z_i-a)}}{2ik_2}$ also contains two events: direct event and reflection event. Only the reflection event is related to our imaging goal, therefore we remove the direct event and keep only the reflection event.

$$\widetilde{\widetilde{D'}}(z_i,z_i) = \frac{-Re^{2ik_2(z_i-a)}}{2ik_2} \tag{22}$$

Finally we want to see what will be the image for the reflector by the calculation we did above. We set the image depth at depth of the reflector $z_i = a$, and transform the result in equation 22 back into space-time domain. And then we ask for time and offset at zero to get the image for the reflector from beneath,

$$I(z_i = a) = -R \tag{23}$$

which is the correct reflection coefficient from beneath the reflector.

4 Numerical results

In previous section we did the analytic calculations for Claerbout III imaging in 1.5D two-half space model. In this section we perform the same calculation numerically. We use reflectivity method to generate the synthetic data and then numerically calculate the Green's theorem wave prediction (equation 10) twice to bring source and receiver depth for surface measurement data ($D(z_g,z_s)$) from z_s and z_g down to image depth z_i. For the final predicted experiment $\widetilde{\widetilde{D}}(z_i,z_i)$ we remove the direct event as we did in analytic calculation.

Figure 2 shows the synthetic data $D(z_g, z_s)$ generated by reflectivity method in the frequency domain with source and receiver at measurement surface. We can see the direct event, the reflection event and two truncation artifacts caused by truncating the evanescent part in frequency domain.

Figure 3 shows the result of the first Green's theorem wave prediction $\widetilde{D}(z_i, z_s)$ with source at measurement surface and receiver at the reflector depth $z_i = a = 1500m$. The truncation artifacts caused by truncating the evanescent part in frequency domain appear as well.

Figure 4 shows the result of the second Green's theorem wave prediction $\widetilde{\widetilde{D}}(z_i, z_i)$ with both source and receiver at reflector depth $z_i = a = 1500m$. We remove the direct event by subtracting an analytic direct event generated by reflectivity method.

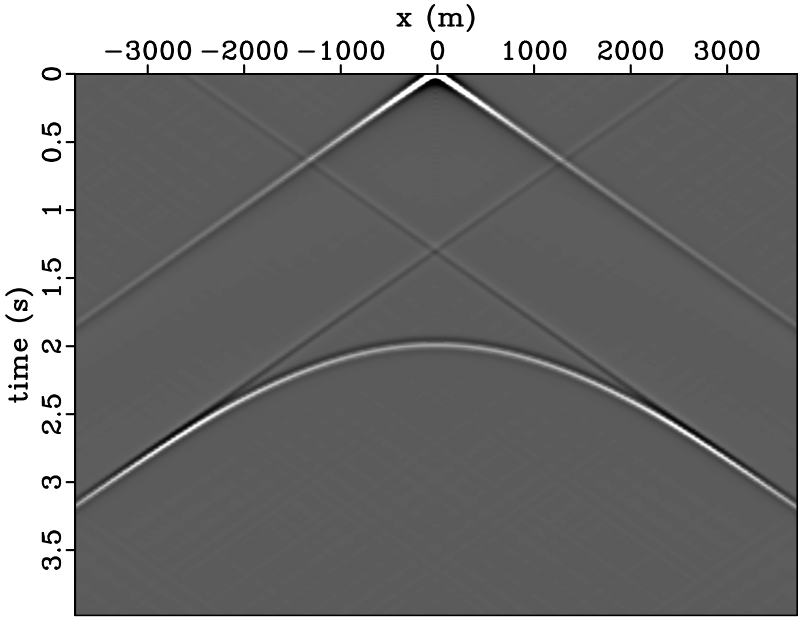

Figure 2: Synthetic data $D(z_g, z_s)$ generated by reflectivity method in the frequency domain with source and receiver at measurement surface. We can see the direct event, the reflection event and two truncation artifacts caused by truncating the evanescent part in frequency domain.

Figure 5 shows the results of the second Green's theorem wave prediction with the sources and receivers are set at or below the reflector $z_i \geq a$. We attempt to remove the direct event by subtracting an analytic direct event generated by reflectivity method but some residual is still left for the difference between numerical direct event and analytic direct event.

To better understand the residual direct event caused by the difference between numerical direct event and analytic direct event, Figure 6 shows a wiggle comparison for one trace in the predicted experiment $\widetilde{\widetilde{D}}(z_i, z_i)$: Figure 6a shows the numerical result (direct event and reflection event); Figure 6b shows the analytic direct event; Figure 6c shows the subtraction result; and Figure 6d shows the overlay comparison. From Figure 6d the overlay comparison we can see the consistency between numerical direct event and analytic direct event is not bad. However, due to the direct event being much stronger than the reflection event, the difference between numerical direct event and analytic direct event is still not very small comparing with the reflection event.

Figure 7 shows the final image from Claerbout imaging condition III, which is set the imaging

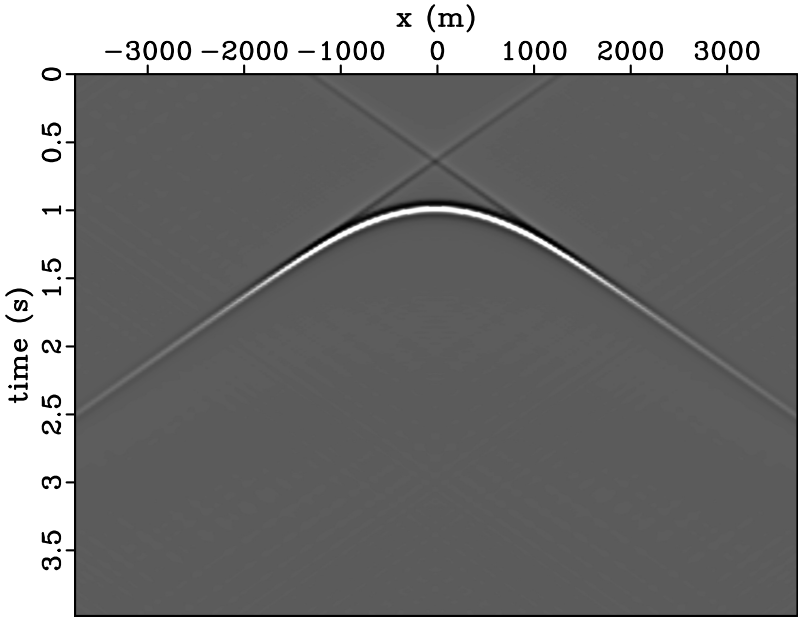

Figure 3: The result of the first Green's theorem wave prediction $\widetilde{D}(z_i, z_s)$ with source at measurement surface and receiver at reflector depth $z_i = a = 1500m$. The truncation artifacts caused by truncating the evanescent part in frequency domain appear as well.

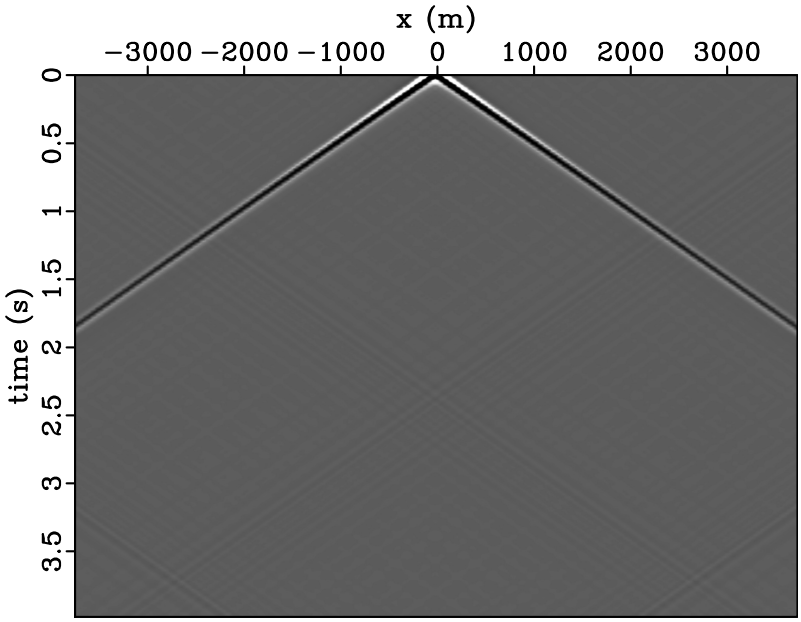

Figure 4: The result of the second Green's theorem wave prediction $\widetilde{\widetilde{D}}(z_i, z_i)$ with both source and receiver at reflector depth $z_i = a = 1500m$. We removed the direct event by subtracting an analytic direct event generated by reflectivity method.

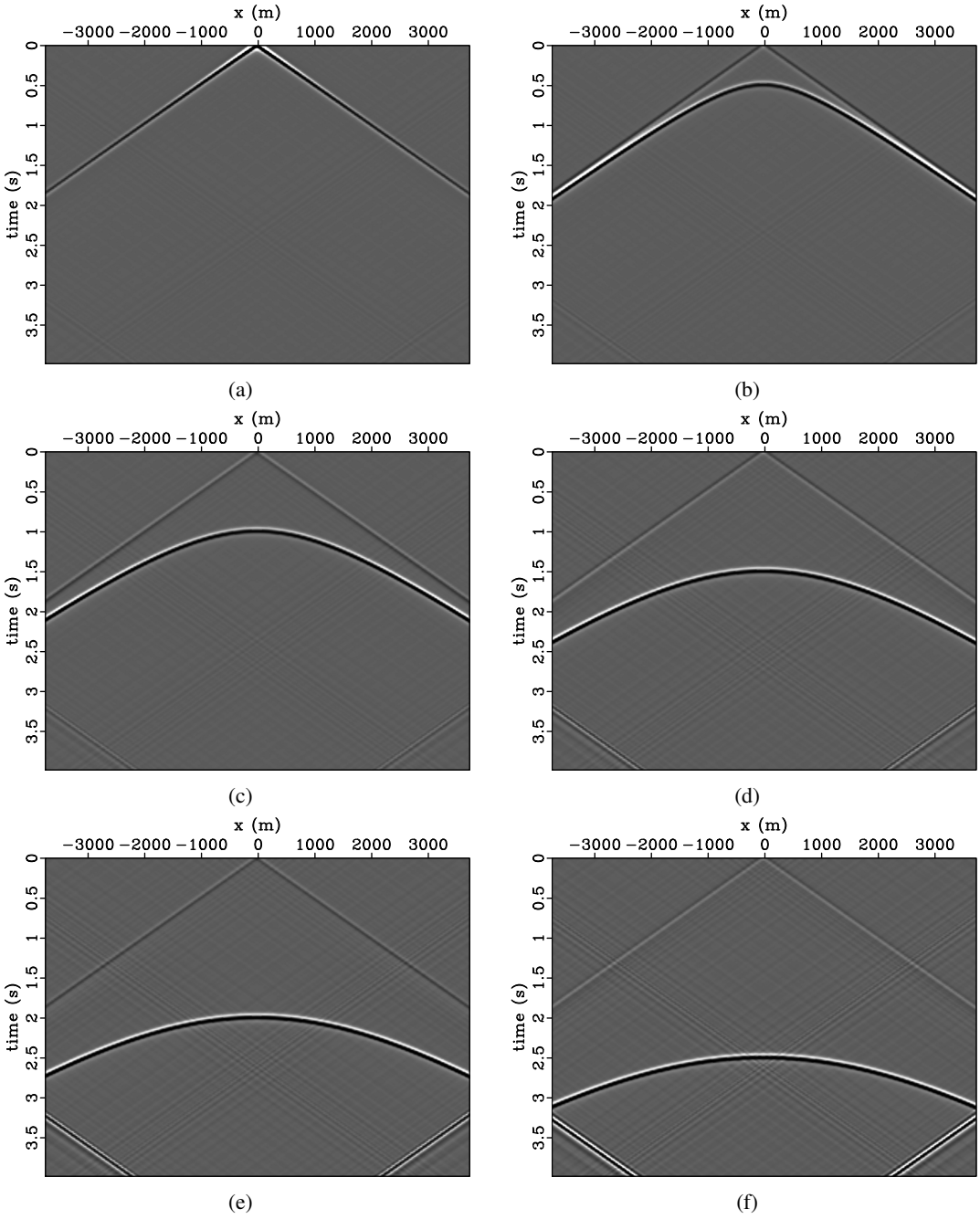

Figure 5: The results of the second Green's theorem wave prediction with the sources and receivers are set at or below the reflector $z_i \geq a$. We attempt to remove the direct event by subtracting an analytic direct event generated by reflectivity method but some residual is still left for the difference between numerical direct event and analytic direct event. The panels are for source and receiver at depth (a) 1500m (right on the reflector); (b) 2000m; (c) 2500m; (d) 3000m (e) 3500m (f) 4000m.

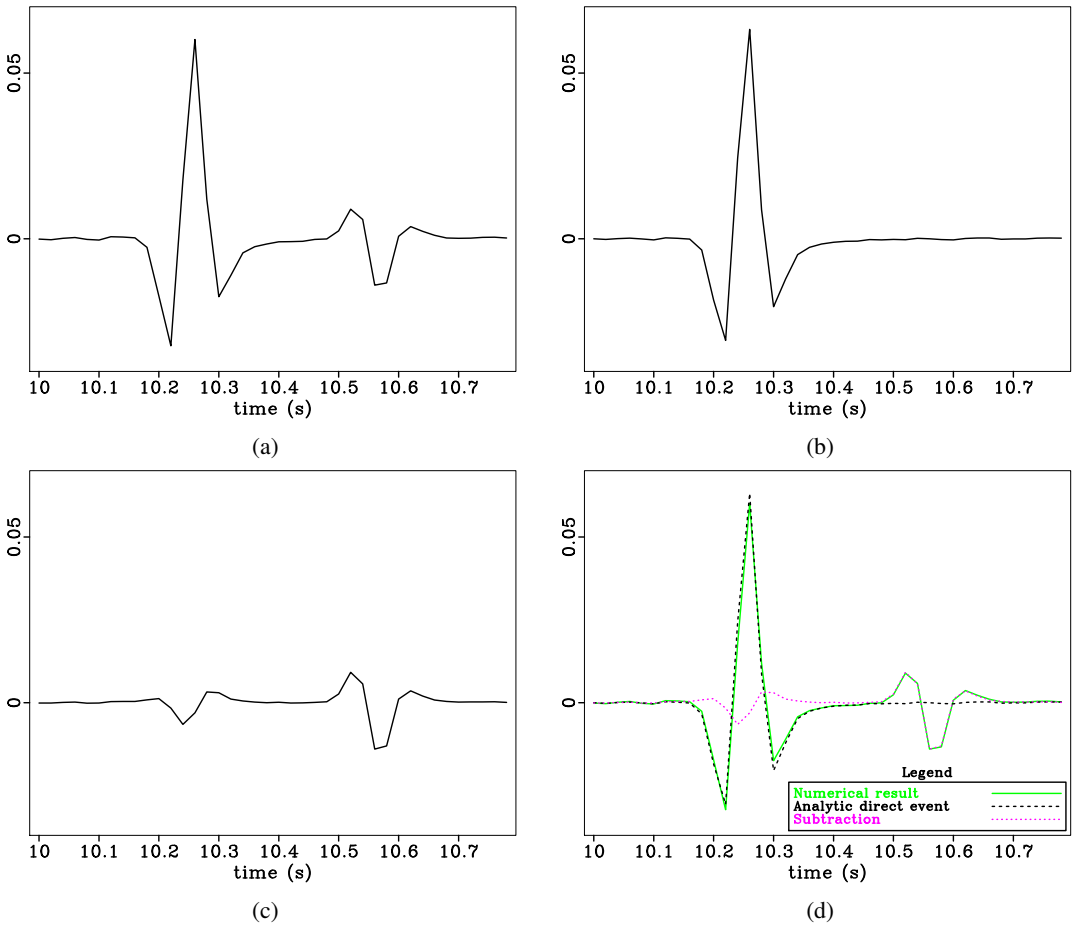

Figure 6: The residual direct event caused by the difference between numerical direct event and analytic direct event. (a) The numerical result (direct event and reflection event); (b) the analytic direct event; (c) the subtraction result; (d) overlay comparison.

depth for the second Green's theorem wave prediction $\widetilde{\widetilde{D}}(z_i, z_i)$ at every depth and then ask time and offset at 0. Please note the image below the reflector (1500m) the polarity is negative which is consistent with the reflection coefficient from beneath the reflector.

Figure 7: The final image from Claerbout imaging condition III, which is set the imaging depth for the second Green's theorem wave prediction $\widetilde{\widetilde{D}}(z_i, z_i)$ at every depth and then ask time and offset at 0.

5 Summary

In this short notes, we present the first Claerbout III image from beneath the reflector with for 1.5D medium one reflector from both analytic and numerical approaches. And the result from above and beneath the reflector are consistent with the reflection coefficients from above and beneath the reflector respectively. There are no back scattering artifacts (like in RTM) for Claerbout imaging condition III for a sharp discontinuous medium.

References

Claerbout, Jon F. "Toward a unified theory of reflector mapping." *Geophysics* 36 (June 1971): 467–481.

Clayton, R. W. and R. H. Stolt. "A Born-WKBJ inversion method for acoustic reflection data." *Geophysics* 46 (1981): 1559–1567.

Fu, Qiang, Yanglei Zou, Aurther B. Weglein, and Robert H. Stolt. "Asymptotic (Kirchhoff) migration and Wave Equation Migration for one-way waves: comparison of the migrated images amplitude as a function of angle: implications for asymptotic and WEM RTM." *M-OSRP 2014 Annual Report.* (2014).

Liu, Fang. The first wave theory RTM, examples with a layered medium, predicting the source and receiver at depth and then imaging, providing the correct location and reflection amplitude at every depth location, and where the data includes primaries and all internal multiples. Presentation given at the 2013 M-OSRP Annual Meeting, available online at mosrp.uh.edu, May 2013.

Lowenthal, D., L. Lu, R. Roberson, and J. W. C. Sherwood. "The wave equation applied to migration." *Geophysical Prospecting* 24 (1985): 380–399.

Riley, D. C. and J. F. Claerbout. "2D multiple reflections." *Geophysics* 41 (1976): 592–620.

Stolt, R. H. and A. B. Weglein. "Migration and inversion of seismic data." *Geophysics* 50 (1985): 2458–2472.

Stolt, Robert H. and Alvin K. Benson. *Seismic migration: theory and practice*. London—Amsterdam: Geophysical Press, 1986.

Weglein, A. B., R. H. Stolt, and J. D. Mayhan. "Reverse-time migration and Green's theorem: Part I — The evolution of concepts, and setting the stage for the new RTM method." *Journal of Seismic Exploration* 20 (February 2011): 73–90.

Weglein, A. B., R. H. Stolt, and J. D. Mayhan. "Reverse time migration and Green's theorem: Part II — A new and consistent theory that progresses and corrects current RTM concepts and methods." *Journal of Seismic Exploration* 20 (May 2011): 135–159.

Multiples can be useful (at times) to enhance imaging, by providing an approximate image of an unrecorded primary, but its always primaries that are migrated or imaged

Arthur B. Weglein, M-OSRP, Physics Department, University of Houston

SUMMARY

Primaries are seismic reflection events with one reflection in their history, whereas multiples are events that have experienced more than one reflection. Migration was originally, and remains today, basically and unequivocally about taking a primary event on a recorded seismic trace in time, and to locate where in space that reflection event was generated by a reflector; that concept assumes the event in time has only one reflection in its history. Since, by definition, only primaries have experienced one reflector in their history, migration relates to and only has meaning for primaries. Migration has no meaning for multiples. We will see in this paper that not only did the original definition of migration only have meaning for primaries, but, in addition, when using the most complete physically interpretable and quantitative imaging condition for wave equation migration that only primaries contribute to the image at any reflector, in depth, and both free surface and internal multiples do not. However, we also show that multiples can be useful (at times) by providing an approximate image of an unrecorded primary.

INTRODUCTION

In this paper, we briefly review methods for migrating data where waves are: (1) one way propagating and (2) two way propagating. Methods that use wave theory to migrate data have two ingredients, a wave propagation component and an imaging condition. There were three landmark imaging conditions introduced by Claerbout (1971); Loewenthal et al. (1985) and Stolt (1978) and their colleagues in the 1970's. Those three imaging conditions are: (1) the exploding reflector model, for zero offset data, (2) the space and time coincidence of up and down-going waves, and (3) predicting a coincident source and receiver experiment at depth and asking for time equals zero. We will refer to these three imaging conditions as Claerbout imaging I, II, and III, respectively. The third imaging condition predicts an actual seismic experiment at depth, and that predicted experiment consists of all the events that experiment would record, if you had a source and receiver at that subsurface location. That experiment would have its own recorded events, the primaries and multiples for that predicted experiment. All of the recorded primaries and multiples contribute to the events in the predicted coincident source and receiver experiment at depth. But only the recorded primaries contribute to the coincident source and receiver experiment at time equals zero. Hence, only recorded primaries contribute to seismic imaging.

SUMMARY OF WAVE EQUATION MIGRATION FOR ONE WAY AND TWO WAY PROPAGATING WAVES

For one-way wave propagation, the experiment at depth is

$$D(\text{at depth}) = \int_{S_s} \frac{\partial G_0^{-D}}{\partial z_s} \int_{S_g} \frac{\partial G_0^{-D}}{\partial z_g} D\, dS_g\, dS_s, \tag{1}$$

where D in the integrand is equal to the data on the measurement surface. G_0^{-D} is the anticausal Green's function with Dirichlet boundary condition on the measurement surface, s = shot, and g = receiver. For two-way wave propagation, the experiment at depth is:

$$D(\text{at depth}) = \int_{S_s} \left[\frac{\partial G_0^{DN}}{\partial z_s} \int_{S_g} \left\{ \frac{\partial G_0^{DN}}{\partial z_g} D + \frac{\partial D}{\partial z_g} G_0^{DN} \right\} dS_g + G_0^{DN} \frac{\partial}{\partial z_s} \int_{S_g} \left\{ \frac{\partial G_0^{DN}}{\partial z_g} D + \frac{\partial D}{\partial z_g} G_0^{DN} \right\} dS_g \right] dS_s, \tag{2}$$

where D in the integrand is equal to the data on the measurement surface. G_0^{DN} is the Green's function for the model of the finite volume that vanishes along with its normal derivative on the lower surface and the walls (Weglein et al., 2011a,b).

Liu and Weglein (2014) and Weglein (2015) take the next step towards our goal and objective. The role of recorded primaries and multiples in contributing first to the predicted source and receiver experiment at depth, and then to the (Claerbout Imaging III) coincident source and receiver experiment at time equals zero provides a definitive response to whether or not multiples contribute to seismic imaging.

We summarize the conclusion of those references (Liu and Weglein (2014) and Weglein (2015))

1. All recorded events, primaries, internal multiples and free surface multiples contribute to the predicted coincident source and receiver experiment at depth
2. Only the recorded primaries contribute to the image, that is once the time equal zero imaging condition is called on, only recorded primaries contribute to the image at any depth.
3. The location of each reflector is determined, along with the reflection coefficient for the experiment both from above and from below each reflector (Figure 1). The latter is not achievable using Claerbout Imaging II.

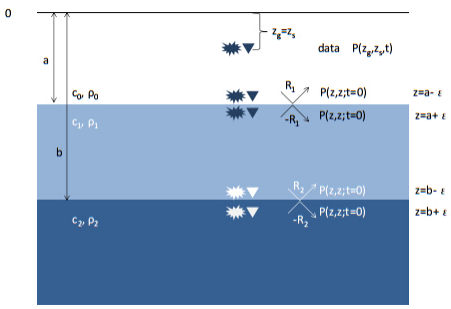

Figure 1: Green's theorem predicts the wavefield at an arbitrary depth z between the shallower depth a and deeper depth b. The experiment illustrated here corresponds to a plane wave normal incident on a layered medium with two reflectors. The measurement coordinates are z_g and z_s , the coincident source and receiver depths. $a-\varepsilon$, $a+\varepsilon$, $b-\varepsilon$, $b+\varepsilon$ are the depth of the predicted source and receiver experiment at depths above and below the first reflector at $z=a$ and the second reflector at $z=b$.

If you remove the multiples in the recorded data, the coincident source and receiver experiment at depth would change, but once the imaging condition is applied, the image's location at the correct depth and its amplitude, the reflection coefficient, will not be affected. If, in these examples, your data consisted of only multiples, you will have no image at any depth. These conclusions are all shown in full detail in the above cited references (Liu and Weglein, 2014; Weglein, 2015).

Hence, for the purposes of imaging and inversion (and employing the most capable and quantitative imaging condition Claerbout imaging III), primaries are the events that contribute to imaging and inversion and multiples are not.

CLAERBOUT II AND CLAERBOUT III IMAGING RESULTS

In Claerbout imaging II, the time and space coincidence of up and down waves is formulated as

$$I(\vec{x}) = \sum_{\vec{x}_s} \sum_{\omega} D^*(\vec{x},\vec{x}_s,\omega) U(\vec{x},\vec{x}_s,\omega), \tag{3}$$

where D is the downgoing wave and U is the upgoing wave, respectively, and $*$ represents the complex conjugate.

The sum over receivers for a given shot record realizes the Claerbout II imaging concept. The sum over sources is "introduced" in an ad hoc manner to mitigate the inconsistent amplitude and phase of images, that can be clearly seen from imaging results with exact data and imaging a single horizontal reflector (please see the example in Ma and Zou (2015); Zou and Weglein (2015)). A comparison with a Claerbout imaging III result for the same reflector and the same data, produces an accurate and consistent reflection coefficient at every point on the reflector, for a single shot record.

For Claerbout III, the sum over receivers predicts the receiver experiment at depth for a source on the measurement surface, and then the sum over sources then precisely predicts the experiment with the source at depth, as well. The integrations over receivers and over sources bring the source and receiver experiment to depth. There is nothing ad hoc or designed to fix something amiss (as though the data had random noise, to be mitigated by stacking). The noise is algorithmic, within Claerbout imaging II and is present with exact, analytic noise free data in the first integral over receivers in Claerbout imaging II. That is the reason we state that Claerbout III is on the firmest physics foundation, with an interpretable, quantitative and consistent meaning to the image. We adopt Claerbout III for the analysis of the role of primaries and multiples in imaging (in Liu and Weglein (2014) and Weglein (2015)).

For our immediate purpose of examining how multiples can be used to provide an approximate image of an unrecorded primary, we look at Claerbout II with a few examples since the "migrating of multiples" activity is inspired and motivated by that algorithm with different up and down going waves chosen for different uses/objectives/purposes.

IMAGING PRIMARIES WITH CLAERBOUT IMAGING CONDITION II

1D normal incident analytic example

In this section, we use a 1D normal incident analytic example to illustrate the idea of imaging a primary with Claerbout imaging condition II. Assume a down-going spike data that starts at $z=\varepsilon_s$ at $t=t_0=0$. The down-going wavefield from the source side that is being forward propagated to depth z is $D=e^{i\omega[\frac{z-\varepsilon_s}{c_0}]}$ whereas the up-going wavefield from the receiver side that is being back propagated to depth z is $U=R_1 e^{i\omega[\frac{d-\varepsilon_s}{c_0}+\frac{d-z}{c_0}]}$, where R_1 and d are the reflection coefficient and the depth of the reflector, respectively (see Figure 2).

Applying the Claerbout imaging condition II we have

$$\begin{aligned} I_p &= \int (e^{-i\omega[\frac{z-\varepsilon_s}{c_0}]}) \times (R_1 e^{i\omega[\frac{d-\varepsilon_s}{c_0}+\frac{d-z}{c_0}]}) d\omega \\ &= \int R_1 e^{-i\omega[\frac{2d-2z}{c_0}]} d\omega = \pi c_0 R_1 \delta(z-d) \end{aligned} \tag{4}$$

We obtain the correct image location at depth d with an amplitude of $\pi c_0 R_1$.

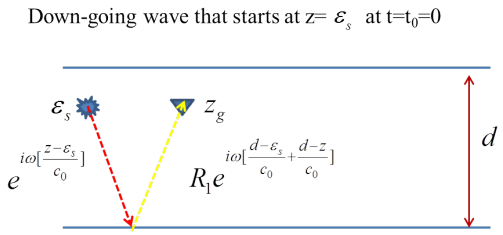

Figure 2: Migrating a primary with Claerbout II to find an image.

USING A MULTIPLE TO APPROXIMATELY IMAGE AN UNRECORDED PRIMARY

1D normal incident analytic example

In this section, we apply Claerbout imaging condition II to a

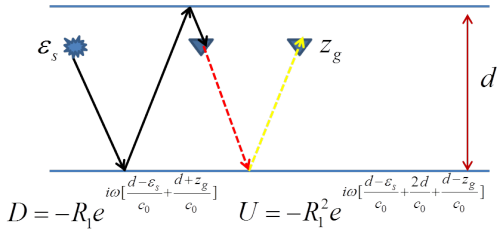

Figure 3: Use of a multiple to find an approximate image of an unrecorded primary.

seismic data set that contains a first-order free-surface multiple. Similarly, assuming a down-going spike data starts at $z = \varepsilon_s$ at $t = t_0 = 0$ (see Figure 3). A first-order free-surface multiple is recorded at z_g. The down-going wavefield from a "virtual source" (represented by the dashed red line in Figure 3) that is being forward propagated to depth z is $D = -R_1 e^{i\omega[\frac{d-\varepsilon_s}{c_0}+\frac{d+z}{c_0}]}$, whereas the up-going wavefield from the receiver side (represented by the yellow dashed line in Figure 4) that is being back propagated to depth z is $U = -R_1^2 e^{i\omega[\frac{d-\varepsilon_s}{c_0}+\frac{2d}{c_0}+\frac{d-z}{c_0}]}$, where we have assumed the downward reflection coefficient at the free-surface to be -1 in deriving the up and down wavefield (see Figure 3). Applying the Claerbout imaging condition II, we have

$$I_M = \int (-R_1 e^{-i\omega[\frac{d-\varepsilon_s}{c_0}+\frac{d+z}{c_0}]}) \times (-R_1^2 e^{i\omega[\frac{d-\varepsilon_s}{c_0}+\frac{2d}{c_0}+\frac{d-z}{c_0}]}) d\omega$$
$$= \int R_1^3 e^{-i\omega[\frac{2d-2z}{c_0}]} = \pi c_0 R_1^3 \delta(z-d) \qquad (5)$$

We obtain the correct image location at depth d, with a different amplitude of $\pi c_0 R_1^3$, Hence, this use of a multiple can produce an approximate image of an unrecorded primary.

The methods that seek to use multiples today as "signal" are really seeking to approximate images due to primaries that have not been recorded, due to limitations in acquisition. They are not really using the multiple itself as an event to be followed into the subsurface for imaging purposes. Figure 4 illustrates the idea.

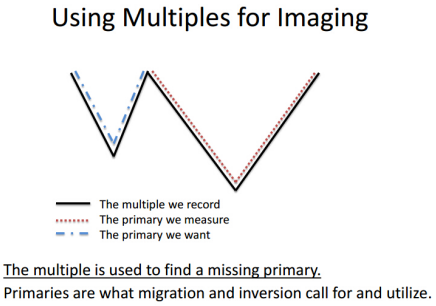

Figure 4: Using multiples for imaging.

In a Recent Advances and the Road Ahead presentation, "Multiples: signal or noise?", Weglein (2014a) (please see Weglein (2014b)) showed field data examples, from PGS, where there was clear added-value demonstrated for the enhanced image from using multiples.

However, there is another issue: in order to predict a free surface or internal multiple, the primary sub-events that constitute the multiple must be in the data. If a primary is not recorded, the multiple that contains that unrecorded primary will not be predicted as a multiple. That issue and basic contradiction within the method is recognized by those who practice this method, and instead of predicting the multiple, they use all the events in the recorded data, primaries and multiples, and while the multiples can be useful for predicting approximate images of missing primaries, the primaries in the data will cause artifacts. There are other artifacts that also come along with this method (from the inability to isolate primaries from multiples with unrecorded primaries) that have been noted in the literature (see Figure 5).

Values has been demonstrated for using multiples to enhance imaging (e.g., Berkhout and Verschuur (1994); Guitton (2002); Shan (2003); Muijs et al. (2007); Whitmore et al. (2010); Lu et al. (2011); Liu et al. (2011), Valenciano et al. (2014) and Weglein (2014a)).

Since the procedure is itself ad hoc, depending on an (Claerbout II) imaging condition for primaries which starts off as somewhat ad hoc (summing over sources), it cannot be easily or naturally improved because there is no starting point or framework without the artifacts that utilizes multiples for an

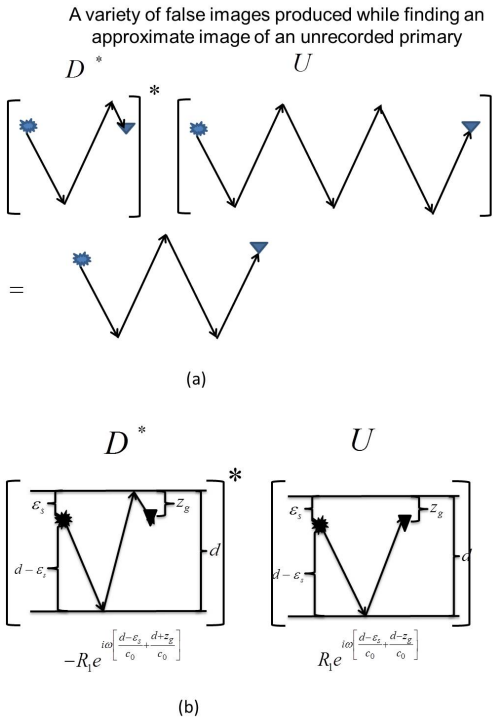

Figure 5: Examples of different types of false images generated by the use of multiples to predict the approximate image of an unrecorded primary. Figure 5a will produce an artifact due to an image of a multiple and figure 5b will produce an artifact at $z = 0$ (the origin) that is beyond false image due to output mages of multiples.

enhanced image. One response to the artifacts is to collect the required primaries.

CONCLUSIONS

Hence, primaries are signal and multiples can be useful, at times, for predicting the image of missing primaries. But it's primaries that are signal, that we use for structure and inversion.

Primaries are signal for all methods that seek to locate and identify targets.

Given an accurate discontinuous velocity and density model, and data with primaries and multiples, then Liu and Weglein (2014) and Weglein (2015) demonstrated that only primaries contributed to the images at every depth. If you predicted the source and receiver experiment at depth with a smooth velocity, it is possible to correctly locate (but not invert) each recorded primary event but with a smooth velocity model every free surface and internal multiple will then produce a false image/artifact/event. If you removed the multiples first you can correctly locate structure from recorded primaries using a smooth velocity model. The methods that are using multiples to enhance imaging require a velocity model. All velocity analysis methods require multiples to have been effectively removed. Hence, an effective multiple removal step is a prerequisite for the methods that utilize multiples.

We emphasize that the inability, in practice, to provide an accurate discontinuous velocity model is why multiples need to be removed before imaging. That reality has been the case, is the case, and will remain true for the foreseeable future. Multiples need to be removed before velocity analysis and they need to be removed before imaging. Many things are useful for creating primaries: money, the seismic boat, the air-guns, the observer, the cable, computers, etc., but we don't call all useful things signal.

One serious problem and real danger is not in the procedure itself, but the serious misuse of the term "migration" as in referring to multiples being migrated. What's the problem with the label? We all know that primaries are migrated, and if multiples are now migrated as well, they must be on equal footing with primaries, and since they are now rehabilitated as good seismic citizens, we should no more seek to remove multiples than we seek to remove primaries. That is part of the danger of the misuse of the term migration in this process of trying to have a more complete and approximate set of primaries.

The danger in this mislabeling and overselling in this case is two-fold, one is a discounting of the actual substantive value represented by the method, and avoiding disappointment and an inevitable back-lash, and the second is it can advertently or inadvertently distract from serious matters of substance (e.g., internal multiple **elimination** for offshore and onshore applications).

All methods that provide a more complete set of primaries are to be supported and encouraged. Those methods include: (1) advances, in and more complete, acquisition, (2) interpolation and extrapolation methods, and (3) using multiples to predict missing primaries. However, a recorded primary is still the best and most accurate way to provide a primary, and the primary is the seismic signal. On balance, the value that multiples can provide to improve imaging can often outweigh issues resulting from artifacts.

ACKNOWLEDGMENTS

I would like to thank the sponsors of M-OSRP for their encouragement and support. Many thanks to Chao Ma, Yanglei Zou, Jim Mayhan, Jinlong Yang, Xinglu Lin, Jing Wu, Qiang Fu and Fang Liu for their assistance in the writing and editing of this paper.

REFERENCES

Berkhout, A. J., and D. J. Verschuur, 1994, Multiple technology: Part 2, migration of multiple reflections: SEG Technical Program Expanded Abstracts, 1497–1500.

Claerbout, J. F., 1971, Toward a unified theory of reflector mapping: Geophysics, **36**, 467–481.

Guitton, A., 2002, Shot-profile migration of multiple reflections: SEG Technical Program Expanded Abstracts, 1296–1299.

Liu, F., and A. B. Weglein, 2014, The first wave equation migration RTM with data consisting of primaries and internal multiples: theory and 1D examples: Journal of Seismic Exploration, **23**, 357–366.

Liu, Y., X. Chang, D. Jin, R. He, H. Sun, and Y. Zheng, 2011, Reverse time migration of multiples for subsalt imaging: Geophysics, 209–216.

Loewenthal, D., L. Lu, R. Roberson, and J. W. C. Sherwood, 1985, The wave equation applied to migration: Geophysical Prospecting, **24**, 380–399.

Lu, S., N. Whitemore, A. Valenciano, and N. Chemingui, 2011, Imaging of primaries and multiples with 3d seam synthetic: SEG Technical Program Expanded Abstracts, 3217–3221.

Ma, C., and Y. Zou, 2015, A clear example of using multiples to enhance and improve imaging; a comparison of two imaging conditions that are relevant to this analysis: Submitted to The Leading Edge.

Muijs, R., J. O. A. Robertsson, and K. Holliger, 2007, Prestack depth migration of primary and surface-related multiple reflections: Part i imaging: Geophysics, S59–S69.

Shan, G., 2003, Source-receiver migration of multiple reflections: SEG Technical Program Expanded Abstracts, 1008–1011.

Stolt, R. H., 1978, Migration by Fourier transform: Geophysics, **43**, 23–48.

Valenciano, A. A., S. Crawley, E. Klochikhina, N. Chemingui, S. Lu, and D. Whitemore, 2014, Imaging complex structures with separated up- and down-going wavefields: SEG Technical Program Expanded Abstracts, 3941–3945.

Weglein, A. B., 2014a, Multiples: Signal or noise? Invited presentation given at the SEG Convention special session on Recent advances and the road ahead, Denver, Colorado.

———, 2014b, Multiples: Signal or noise?: `https://vts.inxpo.com/scripts/Server.nxp?LASCmd=L:0&AI=1&ShowKey=21637&LoginType=0&InitialDisplay=1&ClientBrowser=0&DisplayItem=NULL&LangLocaleID=0&RandomValue=1415030021699`. ([Online; accessed 2014-10]).

———, 2015, Multiples: signal or noise?: Geophysics. (Submitted).

Weglein, A. B., R. H. Stolt, and J. D. Mayhan, 2011a, Reverse-time migration and Green's theorem: Part I — The evolution of concepts, and setting the stage for the new RTM method: Journal of Seismic Exploration, **20**, 73–90.

———, 2011b, Reverse time migration and Green's theorem: Part II — A new and consistent theory that progresses and corrects current RTM concepts and methods: Journal of Seismic Exploration, **20**, 135–159.

Whitmore, N. D., A. Valenciano, W. Sllner, and S. Lu, 2010, Imaging of primaries and multiples using adual-sensor towed streamer: SEG Technical Program Expanded Abstracts, 3187–3192.

Zou, Y., and A. Weglein, 2015, A 1d pre-stack example examining the differences in two important imaging conditions: the space-time coincidence of up and down waves and the predicted coincident source and receiver experiment at depth at time zero: submitted to SEG Technical Program Expanded Abstracts.

Implementing the Claerbout III imaging condition in a laterally varying medium

Fang Liu &Arthur B. Weglein & and Qiang Fu

Abstract

In the Claerbout III imaging conditions Weglein (2014), the physical measurement of an actual source-receiver pair at depth is predicted and the image is obtained by setting time $t = 0$. This is different from the popular idea of space and time coincidence of up and down waves (Claerbout II) imaging condition in current RTM methods. The Claerbout III imaging condition was implemented (for up going waves in a homogeneous medium) in the classic FK migration article by Stolt (1978). The availability of an actual experiment closer to the target offers valuable insights to study the angle dependent reflection coefficients beyond the standard structural map offered by a typical migrated section (Clayton and Stolt, 1981; Weglein and Stolt, 1999,?).

Weglein et al. (2011a,b); Liu and Weglein (2013, 2014) went one step further and predicted source and receiver experiment imaging condition (Imaging condition III) for two-way waves in arbitrary layered medium without lateral variation. The key idea to predict two way waves in the layered medium is the construction of G_0^{DN}: the Green's function with vanishing Dirichlet and Neumann boundary conditions at the prediction depth.

However, an even much greater challenge is to extend Claerbout condition III for two way waves in medium with lateral variation. The objective of this article is to solve this issue.

1 Introduction

In Weglein (2014), three imaging conditions propoese by Claerbout are summarized as follows:

1. the exploding reflector model;
2. the space and time coincidence of up and down waves;
3. the predicted coincident source and receiver experiment at depth, at time equals zero.

Because of its clarity and definitiveness naturally associated with an actual experiment at depth much closer the the target, the third imaging condition has been extended for detailed angle-dependent amplitude analysis at the target and for specular and non-specular reflection (Clayton and Stolt, 1981; Stolt and Weglein, 1985; Stolt and Benson, 1986; Weglein and Stolt, 1999; Stolt and Weglein, 2012).

The third imaging condition predicts an actual seismic experiment (in other words, the total wave field that satisfies the wave equation) at depth, and that predicted experiment consists of all the events that experiment would record, just as if a source and receiver were at that subsurface location.

Recently, several papers by Weglein and his colleagues (Weglein et al., 2011a,b; Liu and Weglein, 2013) provided the next step in the evolution of migration based on the Claerbout predicted source and receiver experiment imaging condition (imaging condition III), extending the prediction

of the source and receiver experiment in a volume containing two way propagating waves. The Claerbout III imaging condition is powerful. For example, for numerical example of Liu and Weglein (2013), inside the second layer, events exist with arrival time independent of the location of the source-rfeceiver pair (a counter-intuitive result). We initially thought there must errors in the calculationr, but after careful counting of the ray paths (which exist in the 1D normal incidence case), such events actually exist!

The experiment is predicted at depth by:

1. Using Green's theorem in equation (4) with the Green's function G_0^{DN} that vanishes (along with its normal derivatives) pn the lower portion of the closed surface to predict an experiment with receivers at depth (the source is still on top of the closed surface);

2. Experiment with source at depth and receiver on top is constructed by exchanging the source and receiver locations using the reciprocity principle;

3. An experiment with receivers at depth is predicted by a second application of Green's theorem with G_0^{DN}. Now both sources and receivers are at depth.

The significance of researches seeling imaging methods to achieve amplitude with more physical meaning is due to the fact that, all current RTM methods use the second of Claerbout's imaging conditions (rather than Claerbout's imaging condition III, a source and receiver experiment at depth).

The progresses documented in this article are:

- It provides a stable and accurate scheme to compute the Green's function with vanishing Dirichlet and Neumann boundary conditions (G_0^{DN}) for a medium with lateral variation.

- It is the first implementation of the Claerbout III imaging condition for two-way waves for a laterally-varying medium.

- It proposes a stable computational framework in the frequency-wavenumber domain to predict wavefield at depth using the measurements on top without modification to the wave equation or approximation to the dispersion relation.

- The predicted experiment at depth with Claerbout III imaging condition has more physical meaning than Claerbout II imaging condition and offers more useful amplitude information for AVO analysis.

- It offers an explicit solution for the Helmholtz equation using both Dirichlet and Neumann boundary conditions from only one side, rather than an implicit scheme using either Dirichlet or Neumann condition everywhere on the boundary around the unknown region.

The following notations are worth mentioning at the beginning: G_0^+ and G_0^- are used to denote causal and anti-causal Green's functions, respectively. G_0^{DN} is used to denote the Green's function with vanishing Dirichlet and Neumann boundary conditions at the deeper boundary. The wavenumber k is the Fourier conjugate of the lateral variable x, and the angular frequency ω is the Fourier conjugate of time t.

The forward and inverse Fourier transforms between the lateral variable x and wavenumber k are defined as follows:

$$\begin{aligned} \widetilde{f}(k) &= \int_{-\infty}^{\infty} f(x) e^{-ikx} dx, \\ f(x) &= \frac{1}{2\pi} \int_{-\infty}^{\infty} \widetilde{f}(k) e^{ikx} dk. \end{aligned} \tag{1}$$

The Fourier transform pair between time t and frequency ω is chosen as:

$$\begin{aligned} \widetilde{f}(\omega) &= \int_{-\infty}^{\infty} f(t) e^{i\omega t} dt, \\ f(t) &= \frac{1}{2\pi} \int_{-\infty}^{\infty} \widetilde{f}(\omega) e^{-i\omega t} d\omega. \end{aligned} \tag{2}$$

In this article, if the symbol f is used to denote a function, then $\widetilde{f}$ is utilized to denote its corresponding conjugate function (after applying a Fourier transform).

2 Green's theorem for wavefield prediction

In a two dimensional (x', z') coordinate system, the Green's theorem formalism for wavefield prediction pioneered by Weglein et al. (2011a,b) can be summarized as follows: ignoring the dependency of the wavefield P on the fixed ω, the wavefield satisfies the following Helmholtz equation,

$$\left(\frac{\partial^2}{\partial x'^2} + \frac{\partial^2}{\partial z'^2} + \frac{\omega^2}{c^2(x', z')} \right) P(x', z') = 0. \tag{3}$$

As shown in Figure 1, the Green's theorem (see equation (36) of Weglein et al. (2011a) for detail) used to predict the wavefield at another location (x, z) is:

$$P(x, z) = \oint_{S'} ds' \left(P(x', z') \frac{\partial G_0(x, z, x', z')}{\partial \vec{n}} - G_0(x, z, x', z') \frac{\partial P(x', z')}{\partial \vec{n}} \right), \tag{4}$$

where $\vec{n}$ is the unit vector in the direction of the outward pointing normal to the surface S'.

In the procedure developed in this article, the objective is to predict wavefield at depth using the measurement on top, $z' = \mathbf{A}$. We choose $z' = \mathbf{A}$ for the upper boundary of the volume V and let the volume extend to infinity in both directions to get rid of the side boundary; the lower boundary is $z' = \mathbf{B}$, where $\mathbf{B} \geq z$, as shown in Figure 2.

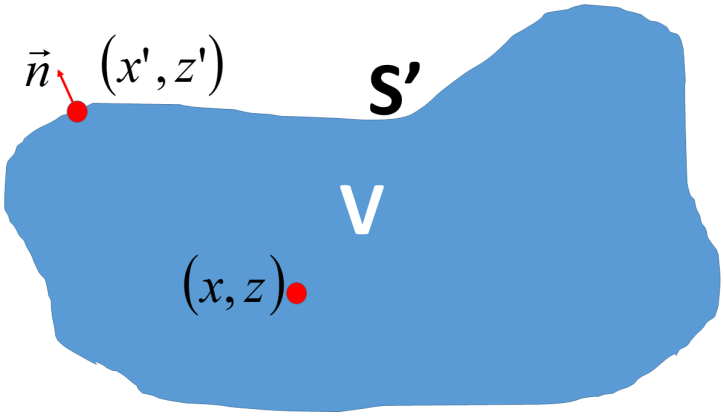

Figure 1: The general schematic view of the volume V and surface S' in this article, where S' is the closed boundary around the volume V. The prediction point (x, z) is within the volume V.

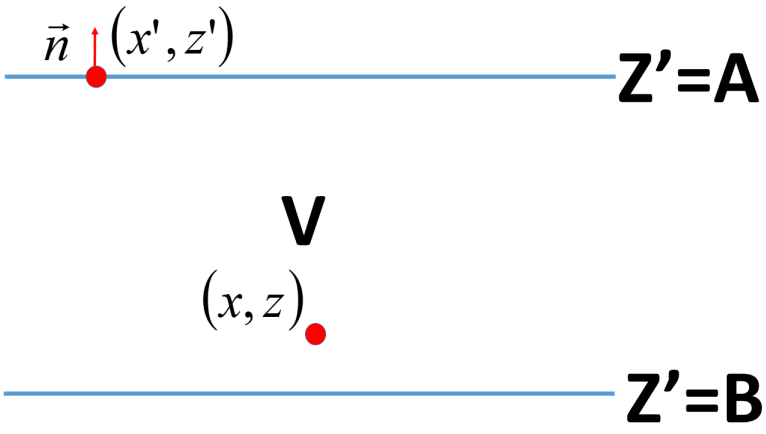

Figure 2: The specifically volume V and its corresponding boundary S' in this article. The volume V is chosen to be the zone (infinite in the x direction) between the upper surface $z' = \mathbf{A}$ and the lower surface $z' = \mathbf{B}$.

3 G_0^{DN}

To predict the wavefield P at (x, z), the values of P on the entire boundary S' are required. The challenge is that the value of P is available only at the measurement surface $z' = \mathbf{A}$, as shown in Figure 2. Weglein et al. (2011a) propose the idea of G_0^{DN}, i.e., the Green's function with vansishing Dirichlet and Neumann boundary conditions on the lower boundary $z' = \mathbf{B}$.

The first G_0^{DN} identified for the medium is a whole space homogeneous velocity c_0, i.e., equation (43) of Weglein et al. (2011a), is

$$G_0^{DN}(k, z, z') = \frac{1}{2iq}\left(e^{iq|z'-z|} - e^{-iq(z-z')}\right), \tag{5}$$

where $q = \sqrt{\frac{\omega^2}{c_0^2} - k^2}$.

4 Properties of G_0^{DN} for models without lateral variation

For a medium with lateral variation, a simple Fourier transform from x to k will simplify the multi-dimensional wave propagation problem into the 1D form listed in Weglein et al. (2011a,b); Liu and Weglein (2013). For example, for the following wave equation with a layered medium:

$$\left(\frac{\partial^2}{\partial x'^2} + \frac{\partial^2}{\partial z'^2} + \frac{\omega^2}{c^2(z')}\right) P(x', z') = 0,$$

a straightforward application of $\int_{-\infty}^{\infty} dx' e^{-ikx'}$ will give:

$$\left(\frac{d^2}{dz'^2} + \left[\frac{\omega^2}{c^2(z')} - k^2\right]\right) \widetilde{P}(k, z') = 0.$$

If we define $q \equiv \sqrt{\frac{\omega^2}{c^2(z')} - k^2}$, we have a 1D wave equation discussed in Weglein et al. (2011a,b); Liu and Weglein (2013, 2014):

$$\left(\frac{d^2}{dz'^2} + q^2\right) \widetilde{P}(k, z') = 0.$$

Note that in our convention, the sign of $q = \sqrt{\frac{\omega^2}{c^2(z')} - k^2}$ is chosen to follow that of ω if $\frac{\omega^2}{c^2(z')} - k^2 \geq 0$, otherwise, q will be an imaginary number; we chose its imaginary part to be positive. This choice implies that the causal solution for the homogeneous medium $G_0^+ = \frac{e^{iq|z_s - z|}}{2iq}$ exponentially decays for large value of k.

According to Liu and Weglein (2013), the properties of G_0^{DN} for models without lateral variation can be summarized as follows:

- The vanishing property: $G_0^{DN}(z, z') \equiv 0$ if $z' > z$. We need $G_0^{DN}(z, z')$ and $\frac{\partial G_0^{DN}(z,z')}{\partial z'}$ vanishes at $z' = \mathbf{B}$; and since the region between z and z' is source-free, the vanishing

Dirichlet and Neumann boundary conditions will uniquely determine the wavefield between z and z'. Since a wavefield with all zeros everywhere is evidently a solution with correct boundary conditions, it is indeed the unique solution to the wave equation in this region. And consequently the wavefield between z and z' must vanish.

- The independence of $G_0^{DN}(z, z')$ from any heterogeneity outside the interval (z', z). This is very different from G_0^+. Since wave goes everywhere, a receiver in a fixed location will record the impact of the velocity field everywhere in space. In other words, G_0^+ depends on heterogeneities everywhere. Since $G_0^{DN}(z, z')$ depends only on the velocity field in the interval (z', z), to predict the wavefield at depth z, we only need to know the velocity between z and z', i.e., the same conclusion as for the finite volume model for seismic migration.

- If the medium has no lateral variation, G_0^{DN} is found to be of finite length in the time domain for a fixed (z', z) pair, while the corresponding G_0^+ can be infinite in length if internal multiples are present.

- $G_0^{DN}(z, z')$ is neither causal nor anti-causal. It can be construted as the sum of G_0^+ (the causal solution) and a solution to the source-free wave equation.

- Reciprocity violated. As an example: $G_0^{DN}(z, z') \equiv 0$ if $z' > z$, but $G_0^{DN}(z, z') \neq 0$ if $z' < z$.

- Exponential growth for large values of k. For example, in the simplest case with homogeneous velocity c_0 everywhere: $G_0^{DN} = \frac{e^{iq|z'-z|} - e^{iq(z'-z)}}{2iq}$, where $q^2 = \frac{\omega^2}{c_0^2} - k^2$. For $z' < z$, $|z' - z|$ equals to $z - z'$, having the opposite sign as $(z' - z)$. Consequently no matter what sign convention we choose, two terms in the numerator of the aforementioned G_0^{DN} formula will have one term with exponetial growth, and anther with exponetial decay. Since G_0^{DN} has exponential growth in the k-domain, its exact x-domain expression cannot be expressed as an ordinary function. To be more specific: its x-domain expression for anywhere $z' < z$ cannot be easily expressed as a discretely sampled series since the condition of sampling theorem[1] is violated.

- It can be constructed as the sum of G_0^+ (the causal Green's function) and a solution to the corresponding source-free wave equation, or homogeneous solution.

5 The properties of $G_0^{DN}(x, z, x', z')$ with lateral variation

By definition G_0^{DN} satisfies the following boundary condition at $z' = \mathbf{B}$:

$$G_0^{DN}(x, z, x', \mathbf{B}) \equiv \frac{\partial G_0^{DN}(x, z, x', \mathbf{B})}{\partial z'} \equiv 0. \tag{6}$$

Note that if we substitute the solution $G_0^{DN}(x, z, x', z') = 0$ (for $z' > z$) into the left hand side of equation (11), we obtain zero. In other words, $G_0^{DN}(x, z, x', z') = 0$ is indeed a solution of equation (11) for $z' > z$. In addition, it satisfies the desired vanishing Dirichlet and Neumann boundary conditions specified in equation (6). Hence it is indeed the unique solution for $G_0^{DN}(x, z, x', z') = 0$ for $z' > z$.

[1] For a sampling scheme in the x direction with sampling rate Δx, there should not be much information beyond the Nyquist wavenumber $\frac{\pi}{\Delta x}$.

Therefore G_0^{DN} with lateral variation satisfies the same vanishing property as G_0^{DN} in the much simpler case where lateral variation is absent.

If we define ϵ an arbitrary small positive number, we know that $G_0^{DN}(x, z, x', z' = z + \epsilon) = 0$. It is more difficult to imagine the value of $G_0^{DN}(x, z, x', z')$ when $z' = z - \epsilon$.

In this paragraph we assume $z' < z$. According to the finite volume model for seismic migration, to predict the wavefield at z using the wavefield at depth z' as input, only the velocity field between z' and z is needed. Since the aforementioned prediction can be carried out by $G_0^{DN}(x, z, x', z')$, $G_0^{DN}(x, z, x', z')$ is independent of the heterogeneities outside the interval (z', z).

Using the independence of $G_0^{DN}(x, z, x', z')$ from heterogeneity outside the interval (z', z), we can obtain the boundary value of $G_0^{DN}(x, z, x', z')$ when $z' \to z - \epsilon$: G_0^{DN} will be the same if the velocity outside the interval $(z - \epsilon, z)$ is replaced by $c(x, z)$, i.e., the local velocity at the source location.

Let us consider the new "replaced medium" as $\epsilon \to 0$:

- The causal solution G^+ for this medium will approach G_0^+ for a homogeneous medium with velocity $c(x', z') \equiv c(x, z)$. This can be easily proven by the forward scattering series using $c(x', z') \equiv c(x, z)$ as the reference medium. In this case, since the size of the interval:

$$(z', z) \qquad = \qquad (z - \epsilon, z)$$

  can be arbitrarily small, and the perturbation $\alpha = \frac{c^2(x,z)}{c^(x',z')} - 1$ is finite in magnitude, the support of the perturbation α approaches zero. And in the forward scattering series[2] to construct the Green's function for the heterogeneous medium:

$$G = G_0 + G_0\omega^2\alpha G_0 + G_0\omega^2\alpha G_0\omega^2\alpha G_0 + \cdots \tag{7}$$

  except for the first term, every other term in the right-hand side of the equation above vanishes since the inclusion of a zero-support perturbation α will reduce an integration over this α to zero. We have $G = G_0$.

- In the procedure to construct G^{DN} as the sum of G^+ and a homogeneous solution to cancel G^+ for $z' > z$, the aforementioned homogeneous solution will approach the homogeneous solution to cancel G_0^+. Consequently G^{DN} should approach G_0^{DN}.

Since in the situation $z' < z$, the G_0^{DN} expression for a homogeneous velocity c_0 is:

$$\begin{aligned} G_0^{DN}(k, z, z') &= \frac{e^{iq(z-z')} - e^{iq(z'-z)}}{q} = \sin(q(z - z'))/q, \\ \frac{\partial G_0^{DN}(k, z, z')}{\partial z'} &= -\cos(q(z - z')). \end{aligned} \tag{8}$$

[2] A detailed description of the forward scattering series can be found in Weglein et al. (2003).

In the special case $z' = z$, equation (8) can be used to serve as the initiation point for further calculating G_0^{DN} through a laterally varying medium: since the region $z' < z$ is again source free. In the special case of $z' = z$, we have:

$$\begin{aligned} &G_0^{DN}(k, z, z' = z) = 0, \\ &\left.\frac{\partial G_0^{DN}(k, z')}{\partial z'}\right|_{z'=z} = -1. \end{aligned} \tag{9}$$

With the boundary values in equation (9), we can start the procedure documented in the next section to calculate G_0^{DN} for smaller and smaller z' values of through a laterally varying medium.

6 Theory

Let us consider the wave progataion problem in a source-free region:

$$\left(\frac{\partial^2}{\partial x'^2} + \frac{\partial^2}{\partial z'^2} - \frac{1}{c^2(x', z')}\frac{\partial^2}{\partial t'^2}\right) P(x', z', t') = 0. \tag{10}$$

Since the velocity field $c(x', z')$ is not a function of time, the wave equation above can be simplified by Fourier transforming into the frequency ω-domain[3].

$$\left(\frac{\partial^2}{\partial x'^2} + \frac{\partial^2}{\partial z'^2} + \frac{\omega^2}{c^2(x', z')}\right) P(x', z') = 0. \tag{11}$$

Note that equation (11) is satisfied for any fixed ω (we purposely omitted the depencence of P on the fixed ω in our notation); the complicated temporal variation is crystalized into a single ω, a significant reduction in complexity.

7 Numerical wavefield prediction in a laterally varying and source-free medium

For the wave propagation problem listed in equation (11), our objective is to predict the wavefield at deeper depth using the measurements from shallower depth. In most publications solving the boundary value problem for a Helmholtz equation, the wavefield (or its normal derivative) at every location on the boundary around the unknown region is known, and a set of coupled finite-difference equations, each in the form of equation (12), are formulated for all of the unknown grids. The scheme is implicit since each finite-difference equation cannot be solved immediately. Consequently the inversion of a huge[4] sparse matrix is necessary. The advantage of this approach is that stability and accuracy is normally better than for an explicit scheme.

---

[3] In the notation of this article, the Fourier transform from time to frequency is defined as: $\int_{-\infty}^{\infty} e^{i\omega t} dt$.

[4] For example, if the dimension for the region of unknown grids is 200 in the x-direction, and 100 in the z-direction, the rank of the matrix we need to invert is $200 \times 100 = 20,000$.

Without the luxury of boundary values being available everywhere around the unknown region, the first author of this article had tried solve it in an explicit scheme. First we express the partial derivatives in second-order finite difference form,

$$\begin{aligned}&\frac{P((n+1)\Delta x, m\Delta z) + P((n-1)\Delta x, m\Delta z) - 2P(n\Delta x, m\Delta z)}{(\Delta x)^2} + \\ &\frac{P(n\Delta x, (m+1)\Delta z) + P(n\Delta x, (m-1)\Delta z) - 2P(n\Delta x, m\Delta z)}{(\Delta z)^2} + \\ &\frac{\omega^2}{c^2(n\Delta x, m\Delta z)} P(n\Delta x, m\Delta z) = 0.\end{aligned} \tag{12}$$

We know the wavefield at shallower depth, i.e., all grid values at depth $z = (m-1)\Delta z$ and $z = m\Delta z$; numerically it is very straightforward to solve the grids at $z = (m+1)\Delta z$ as follows:

$$\begin{aligned}P(n\Delta x, (m+1)\Delta z) = &\left[2\left(1 + \frac{(\Delta z)^2}{(\Delta x)^2}\right) + \frac{\omega^2(\Delta z)^2}{c^2(n\Delta x, m\Delta z)}\right] P(n\Delta x, m\Delta z) \\ - P(n\Delta x, (m-1)\Delta z) &- \frac{P((n+1)\Delta x, m\Delta z) + P((n-1)\Delta x, m\Delta z)}{(\Delta x)^2/(\Delta z)^2}\end{aligned} \tag{13}$$

The scheme in equation (13) is fast and explicit since

- Knowing the grid values at depth $z = (m-1)\Delta z$ and $z = m\Delta z$, all the unknown grid values at depth $z = (m+1)\Delta z$ can be straightforwardly solved using equation (13).
- With all grid values at depth $z = (m+1)\Delta z$ being solved, equation (13) can again be utilized to solve the unknown grids at depth $z = (m+2)\Delta z$ since grid values at depth $z = m\Delta z$ are known.
- In a similar fashion, the grid values at depth $z = (m+3)\Delta z$, $z = (m+4)\Delta z$, $\cdots$ can be found. Then we have an explicit scheme to obtain the unknown grid at an arbitrary depth.

The issue for this scheme is stability; the wavefield is hardly expressible as IEEE floating point numbers after just a couple of iterations. The situation is severe since the aforementioned stability issue is present even for a velocity field without any lateral variations and an input boundary wave with smooth lateral variations. Considering the fact that in our sitiation, the boundary values of G_0^{DN} change too quickly to allow any lateral sampling rate Δx to satisfy Nyquist$-$Shannon sampling theorem, the challenge to solve it is obvious.

Predicting the experiment at depth from the measurement surface had been achieved in FK migration (Stolt, 1978) assuming a one-way wave propagation. The formulism is constructed in the wavenumber (k) domain, and the evanescent part is explicitly excluded due to noise. The success in FK migration suggests that the solution may be easier to construct in the wavenumber (k) domain.

Therefore we consider the solution of the problem in the wavenumber (k) domain. First we assume Δz (the step size in the z-direction) in each step is so small that at each fixed x location, the vertical velocity variation is neglegible. In other words, we consider equation (11) in a very thin

vertical zone such that the vertical velocity variation can be ignored, and the velocity field can be expressed as[5]:

$$\frac{1}{c^2(x',z')} = \frac{1}{2\pi}\int_{-\infty}^{\infty} \widetilde{A}(k)e^{ikx'}dk = \sum_n a_n e^{ix'n\Delta k}. \tag{14}$$

This can be easily achieved though a Fourier transform over x'. And equation (11) can be expressed as:

$$\left(\frac{\partial^2}{\partial x'^2} + \frac{\partial^2}{\partial z'^2} + \omega^2 \sum_n a_n e^{ix'n\Delta k}\right) P(x',z') = 0. \tag{15}$$

Applying a Fourier transform $\int_{-\infty}^{\infty} e^{ikx'}dx'$ to equation (15), we have:

$$\frac{\partial^2 \widetilde{P}(k,z')}{\partial z'^2} + \left(\omega^2 a_0 - k^2\right)\widetilde{P}(k,z') = -\omega^2 \sum_{n\neq 0} a_n \widetilde{P}(k-n\Delta k, z'), \tag{16}$$

where $\widetilde{P}(k,z') = \int_{-\infty}^{\infty} e^{ikx'}P(x',z')dx'$ is the wavefield in the k-domain. Approximating the partial derivatives in a second-order central finite-difference scheme, we have:

$$\frac{\widetilde{P}(k,z'+\Delta z) + \widetilde{P}(k,z'-\Delta z) - 2\widetilde{P}(k,z)}{(\Delta z)^2} + \left(\omega^2 a_0 - k^2\right)\widetilde{P}(k,z') = -\omega^2 \sum_{n\neq 0} a_n \widetilde{P}(k-n\Delta k, z'). \tag{17}$$

According to equation (17), the wavefield at $z' + \Delta z$ is explicitly expressible by the wavefield at shallower depths as follows:

$$\begin{aligned}\widetilde{P}(k,z'+\Delta z) = &-\widetilde{P}(k,z'-\Delta z) + \left[2 + (k\Delta z)^2 - \omega^2(\Delta z)^2 a_0\right]\widetilde{P}(k,z') \\ &- \omega^2(\Delta z)^2 \sum_{n\neq 0} a_n \widetilde{P}(k-n\Delta k, z').\end{aligned} \tag{18}$$

Note that equation (18) is essentially a 1D Helmholtz equation, with an additional extraneous "source term" expressed in the last term. We managed to achieve a stable iterative solution for the wavefield at depth $z' + \Delta z$, $z' + 2\Delta z$, $z' + 3\Delta z$, $\cdots$, to arbitrary depth, for the non-evanescent situations (i.e., $\frac{\omega^2}{c^2} - k^2 \geq 0$).

Use the following backward difference schemes:

[5]This may sound like a very strange point of view about the velocity, since in the real world it is hard to find geology like this. It is a more realistic situation the smaller Δz is. The logic here is nothing but the essence of digitation. With a consecutive series of vertically invariant thin layers, any complicated geology can be sufficiently expressed since the size of Δz is purely artificial and completely within our control.

$$\begin{aligned}\frac{\partial \widetilde{P}(k,z'+\Delta z)}{\partial z'} &\approx \frac{\widetilde{P}(k,z'+\Delta z)-\widetilde{P}(k,z)}{\Delta z},\\ \frac{\partial \widetilde{P}(k,z')}{\partial z'} &= \frac{\widetilde{P}(k,z')-\widetilde{P}(k,z-\Delta z)}{\Delta z}.\end{aligned} \tag{19}$$

If there is no lateral variation, all the coefficients $a_n \equiv 0$ for $n \neq 0$. The last term in equation (18) vanishes, and we have:

$$\begin{pmatrix} \widetilde{P}(k,z'+\Delta z) \\ \partial \widetilde{P}(k,z'+\Delta z)/\partial z' \end{pmatrix} = \begin{pmatrix} 1-(q\Delta z)^2 & \Delta z \\ -q^2\Delta z & 1 \end{pmatrix} \begin{pmatrix} \widetilde{P}(k,z') \\ \partial \widetilde{P}(k,z')/\partial z' \end{pmatrix}. \tag{20}$$

The scheme in equation (20) has obvious issues:

- The variation of the wave prediction as a function of the Δz variable is not consistent; according to the left-hand-side, the partial derivative of the first equation in the scheme above should be equal to the second equation. This is obviously violated if we check the right-hand-side.
- It will have accuracy and convergence issues if Δz, q, or their product $q\Delta z$ is too large since these coefficients are used in multiplcations to produce the wavefield in the next step.

However, the crude scheme in equation (20) can be made self-consistent, 100% accurate and un-conditionally stable by shrinking the size of Δz. Let us consider sub-dividing the Δz interval m times, and repeatedly apply equation (20) m times on the aforementioned sub-inverval, each with thickness $\frac{\Delta z}{m}$.

The aforementioned repeated application of equation (20) m times is equivalent to multiplying the matrix $[\Psi]^m$ in equation (20) where the matrix Ψ is defined as:

$$\Psi = \begin{pmatrix} 1-(q\Delta z/m)^2 & , & \Delta z/m \\ -q^2\Delta z/m & , & 1 \end{pmatrix}. \tag{21}$$

We can diagonalize the matrix $[\Psi]$ to compute $[\Psi]^m$ for large values of m.

$$\Psi = \begin{pmatrix} 1-(q\Delta z/m)^2 & , & \Delta z/m \\ -q^2\Delta z/m & , & 1 \end{pmatrix} = Q \begin{pmatrix} \lambda_1 & 0 \\ 0 & \lambda 2 \end{pmatrix} Q^{-1}, \tag{22}$$

where $\lambda_1 = 1 - \frac{q^2(\Delta z)^2}{2m^2} - \frac{q\Delta z}{2m}\sqrt{\frac{q^2(\Delta z)^2}{m^2}-4}$, $\lambda_2 = 1 - \frac{q^2(\Delta z)^2}{2m^2} + \frac{q\Delta z}{2m}\sqrt{\frac{q^2(\Delta z)^2}{m^2}-4}$, and the matrix Q and its inverse are:

$$\begin{aligned} Q &= \begin{pmatrix} \frac{q\Delta z}{m} + \sqrt{\frac{q^2(\Delta z)^2}{m^2}-4} & , & \frac{q\Delta z}{m} - \sqrt{\frac{q^2(\Delta z)^2}{m^2}-4} \\ 2q & , & 2q \end{pmatrix}, \\ Q^{-1} &= \frac{1}{4q\sqrt{\frac{q^2(\Delta z)^2}{m^2}-4}} \begin{pmatrix} 2q & , & -\frac{q\Delta z}{m} + \sqrt{\frac{q^2(\Delta z)^2}{m^2}-4} \\ -2q & , & \frac{q\Delta z}{m} + \sqrt{\frac{q^2(\Delta z)^2}{m^2}-4} \end{pmatrix}. \end{aligned} \tag{23}$$

The power $[\Psi]^m$ can be computed as follows:

$$[\Psi]^m = \left[Q \begin{pmatrix} \lambda_1 & 0 \\ 0 & \lambda 2 \end{pmatrix} Q^{-1} \right]^m = Q \begin{pmatrix} \lambda_1^m & 0 \\ 0 & \lambda_2^m \end{pmatrix} Q^{-1}. \tag{24}$$

Now we consider the limiting case for $m \to \infty$:

$$\begin{aligned}
\lim_{m\to\infty} Q &= \lim_{m\to\infty} \begin{pmatrix} \frac{q\Delta z}{m} + \sqrt{\frac{q^2(\Delta z)^2}{m^2} - 4} & , & \frac{q\Delta z}{m} - \sqrt{\frac{q^2(\Delta z)^2}{m^2} - 4} \\ 2q & , & 2q \end{pmatrix} = \begin{pmatrix} 2i & , & -2i \\ 2q & , & 2q \end{pmatrix} \\
\lim_{m\to\infty} Q^{-1} &= \lim_{m\to\infty} \frac{1}{4q\sqrt{\frac{q^2(\Delta z)^2}{m^2} - 4}} \begin{pmatrix} 2q & , & -\frac{q\Delta z}{m} + \sqrt{\frac{q^2(\Delta z)^2}{m^2} - 4} \\ -2q & , & \frac{q\Delta z}{m} + \sqrt{\frac{q^2(\Delta z)^2}{m^2} - 4} \end{pmatrix} = \frac{1}{8iq} \begin{pmatrix} 2q & , & 2i \\ -2q & , & 2i \end{pmatrix}
\end{aligned} \tag{25}$$

$$\begin{aligned}
\lim_{m\to\infty} \lambda_1^m &= \lim_{m\to\infty} \left(1 - i\frac{q\Delta z}{m} \sqrt{1 - q^2(\Delta z)^2/(4m^2)} - \frac{q^2(\Delta z)^2}{2m^2} \right)^m \\
&= \exp\left[\lim_{m\to\infty} m \times \left(-i\frac{q\Delta z}{m} \sqrt{1 - q^2(\Delta z)^2/(4m^2)} - \frac{q^2(\Delta z)^2}{2m^2} \right) \right] = e^{-iq\Delta z} \\
\lim_{m\to\infty} \lambda_2^m &= \lim_{m\to\infty} \left(1 + i\frac{q\Delta z}{m} \sqrt{1 - q^2(\Delta z)^2/(4m^2)} - \frac{q^2(\Delta z)^2}{2m^2} \right)^m \\
&= \exp\left[\lim_{m\to\infty} m \times \left(i\frac{q\Delta z}{m} \sqrt{1 - q^2(\Delta z)^2/(4m^2)} - \frac{q^2(\Delta z)^2}{2m^2} \right) \right] = e^{iq\Delta z}
\end{aligned} \tag{26}$$

Combining equations (20)−(26)we have a iterative scheme as follows:

$$\begin{aligned}
\begin{pmatrix} \widetilde{P}(k, z' + \Delta z) \\ \partial\widetilde{P}(k, z' + \Delta z)/\partial z' \end{pmatrix} &= \begin{pmatrix} 2i & , & -2i \\ 2q & , & 2q \end{pmatrix} \begin{pmatrix} e^{-iq\Delta z} & 0 \\ 0 & e^{iq\Delta z} \end{pmatrix} \frac{1}{8iq} \begin{pmatrix} 2q & , & 2i \\ -2q & , & 2i \end{pmatrix} \begin{pmatrix} \widetilde{P}(k, z') \\ \partial\widetilde{P}(k, z')/\partial z' \end{pmatrix} \\
&= \begin{pmatrix} \cos(q\Delta z) & , & \frac{\sin(q\Delta z)}{q} \\ -q\sin(q\Delta z) & , & \cos(q\Delta z) \end{pmatrix} \begin{pmatrix} \widetilde{P}(k, z') \\ \partial\widetilde{P}(k, z')/\partial z' \end{pmatrix}
\end{aligned} \tag{27}$$

The scheme in equation (27) is more accurate than the original scheme since the Δz interval is sub-divided into an infinite number of sub-intervals. Comparing with the original scheme in equation (20), there are many advantages:

- The variation of the wave prediction as a function of the variable Δz is consistent; according to the left-hand-side, the partial derivative of the first equation in the scheme above should be equal to the second equation. This is indeed the case if we check the right-hand-side.
- For a medium without lateral variation (i.e, no cross communication between different k-spectrums), this scheme is one hundred percent accurate for arbitrary Δz. As a quality check,

in a medium with homogeneous velocity c_0, G_0^{DN} from equation (43) of Weglein et al. (2011a) is,

$$G_0^{DN}(k,z,z') = \frac{1}{2iq}\left(e^{iq|z'-z|} - e^{-iq(z-z')}\right).$$

For $z' < z$, it can be expressed as:

$$\begin{aligned} P(k,z') &= \frac{\sin(q(z-z'))}{q}, \\ \frac{\partial P(k,z')}{\partial z'} &= -\cos(q(z-z')). \end{aligned}$$

The wavefield and its normal derivative at another depth $z' + \Delta z$ are:

$$\begin{aligned} \widetilde{P}(k,z'+\Delta z) &= \frac{\sin(q(z-z'-\Delta z))}{q}, \\ \frac{\partial \widetilde{P}(k,z'+\Delta z)}{\partial z'} &= -\cos(q(z-z'-\Delta z)), \end{aligned}$$

respectively. A straightfowd substitution can verify that equation (27) can obtain the wavefield and its normal derivative at another depth $z' + \Delta z$ stably and accurately for arbitrary step size Δz.

The accurate scheme in equation (27) is only for a medium without lateral variation. The modification of the original crude scheme in equation (20) to derive equation (27), although valid for a medium without lateral variation, should shed light on the intuitive leap required for an improved version for the crude scheme in equation (18).

The modifications to the iterative scheme for a medium without lateral variation to derive a scheme for a medium with lateral variation are as follows:

- The matrix element at the first row and first colume is changed from $1-(q\Delta z)^2$ to $\cos(q\Delta z)$. Both schemes become closer and closer to each other as $\Delta z \to 0$. In other words, the original crude scheme is accurate for sufficiently small Δz.
- The matrix element at the first row and second colume is changed from Δz to $\sin(q\Delta z)/q$. The modification agrees with the original crude scheme for very small Δz.
- The matrix element at the second row and first colume is changed from $-q^2\Delta z$ to $-q\sin(q\Delta z)$. The crude coefficient $-q^2\Delta z$, which implies a linear increase for the output in terms of Δz, is modified to let the output have a sinusoidal dependence on the step size Δz, a modification to let the output better satisfy the Helmholtz equation.
- The matrix element at the second row and second colume is changed from 1 to $\cos(q\Delta z)$. The crude coefficient 1, which implies independence of the output in terms of Δz, a phenomena obviously unreasonable for big Δz, is again modified to let the output have a sinusoidal dependence on the step size Δz, a modification to let the output better satisfy the Helmholtz equation.

The ideas behind the aforementioned modifications can be used to improve our scheme with lateral variation as shown in equation (18). Since the other coefficients have been dealt with, the only remaining coefficient is the last one, namely $\omega^2(\Delta z)^2$. This coefficient implies a quadratic increase for the output in terms of Δz, obvious unreasonable for a wavefield satisfying the Helmholtz equation in a large Δz situation. We modify it to $\frac{\cos(q\Delta z)-1}{q^2}(q^2+k^2)$, which agrees with the original coefficient when Δz is sufficiently small, and results in an output better fitting the Helmholtz equation. With this modification, the wavefield prediction formula equation (18) becomes:

$$\widetilde{P}(k,z'+\Delta z)=\cos(q\Delta z)\widetilde{P}(k,z')+\frac{\sin(q\Delta z)}{q}\frac{\partial\widetilde{P}(k,z')}{\partial z'}+\frac{\cos(q\Delta z)-1}{q^2}\omega^2\sum_{n\neq 0}a_n\widetilde{P}(k-n\Delta k,z'). \tag{28}$$

Its second-order partial derivative over the depth variation Δz is:

$$\frac{\partial^2\widetilde{P}(k,z'+\Delta z)}{\partial(\Delta z)^2}=-q^2\cos(q\Delta z)\widetilde{P}(k,z')-q\sin(q\Delta z)\frac{\partial\widetilde{P}(k,z')}{\partial z'}-\cos(q\Delta z)\omega^2\sum_{n\neq 0}a_n\widetilde{P}(k-n\Delta k,z'). \tag{29}$$

According to the result from equations (28) and (29), we have

$$\frac{\partial^2\widetilde{P}(k,z'+\Delta z)}{\partial(\Delta z)^2}+q^2\widetilde{P}(k,z'+\Delta z)=-\omega^2\sum_{n\neq 0}a_n\widetilde{P}(k-\Delta k,z'). \tag{30}$$

The right-hand-side of the equation above is not perfect, but is nevertheless very close to $-\omega^2\sum_{n\neq 0}a_n\widetilde{P}(k-\Delta k,z'+\Delta z)$ under that condition that Δz is small, i.e., the desired result that is 100% consistent with the original Helmholtz equation with lateral variation. Note that as Δz is getting smaller, each $\widetilde{P}(k-\Delta k,z')$ becomes a better approximation for $\widetilde{P}(k-\Delta k,z'+\Delta z)$, and consistency with the original Helmholtz equation improves.

Taking the partial derivative of the predicted wavefield $\widetilde{P}(k,z'+\Delta z)$ in equation (28) over the depth variation Δz, we have the normal derivative values necessary for the next step iteration:

$$\frac{\partial\widetilde{P}(k,z'+\Delta z)}{\partial z'}=-q\sin(q\Delta z)\widetilde{P}(k,z')+\cos(q\Delta z)\frac{\partial\widetilde{P}(k,z')}{\partial z'}-\frac{\sin(q\Delta z)}{q}\omega^2\sum_{n\neq 0}a_n\widetilde{P}(k-n\Delta k,z'). \tag{31}$$

We can combine equations (28) and (31) to have a scheme to predict wavefield and its normal derivative to another depth $(z'+\Delta z)$ using the wavefield P and its normal derivative at depth z.

$$\widetilde{P}(k,z'+\Delta z)=\cos(q\Delta z)\widetilde{P}(k,z')+\frac{\sin(q\Delta z)}{q}\frac{\partial\widetilde{P}(k,z')}{\partial z'}+\frac{\cos(q\Delta z)-1}{q^2}\omega^2\sum_{n\neq 0}a_n\widetilde{P}(k-n\Delta k,z'),$$
$$\frac{\partial\widetilde{P}(k,z'+\Delta z)}{\partial z'}=-q\sin(q\Delta z)\widetilde{P}(k,z')+\cos(q\Delta z)\frac{\partial\widetilde{P}(k,z')}{\partial z'}-\frac{\sin(q\Delta z)}{q}\omega^2\sum_{n\neq 0}a_n\widetilde{P}(k-n\Delta k,z'). \tag{32}$$

With the value of the wavefield $\widetilde{P}$ and its normal derivative at depth $z'+\Delta z$, we can apply equation (32) again to compute the wavefield at depth $z'+2\Delta z$. This iteration be repeated until we reach the desired depth level z.

Note that with lateral variation, to predict the wavefield $\widetilde{P}(k,z'+\Delta z)$, the spectrum at other k values is also needed, in other words, the k-spectrum is convolved together. To predict $\widetilde{P}(k,z'+\Delta z)$ with sufficient accuracy, we need a range of spectrum centered at k. In seismic data, the evanescent part of a spectrum is famous for noise. To actually predict data using equation (32), the exclusion of the evanescent spectrum is tricky since its influence on the prediction result for non-evanescent spectrum is ways there, yet the most popular choice of completely excluding their contribution will shut down a large amount of connection between the input data and output prediction.

If equation (32) is used to construct $G_0^{\mathcal{DN}}$ from the boundary at $z'=z$, the input for the scheme is completely noise free. The numerical procedure of iteratively applying equation (32), although it will produce numerically demanding numbers (as it should in the evanescent part of $\widetilde{P}(k)$), it can be made accurate if:

- the step size Δz is sufficiently small;
- the range of the k spectrum is sufficiently wide.

After obtaining the value of $G_0^{\mathcal{DN}}$ and its normal derivatives with sufficient accuracy, we can then choose a reasonable range of spectrum for $G_0^{\mathcal{DN}}$ to predict a source-receiver experiment at depth.

If the input data for equation (32) have the following conjugate symmetry:

$$\widetilde{P}(-k,z')=\left[\widetilde{P}(k,z')\right]^*,$$
$$\frac{\partial\widetilde{P}(-k,z')}{\partial z'}=\left[\frac{\partial\widetilde{P}(k,z')}{\partial z'}\right]^* \tag{33}$$

(where * indicated complex conjugation), then its output result also satisfies the same symmetry, due to the following factors: when the argumen of $\widetilde{P}$ is changed from k to $-k$ in equation (32), we have:

1. the following coefficients are kept unchanged: q, $\cos(q\Delta z)$, $\frac{\sin(q\Delta z)}{q}$, $q\sin(q\Delta z)$, and $\frac{\cos(q\Delta z)-1}{q^2}$;

2. the following quantities become the conjugate of the originals: $\widetilde{P}(-k,z') = \left[\widetilde{P}(k,z')\right]^*$ and $\frac{\partial \widetilde{P}(-k,z')}{\partial z'} = \left[\frac{\partial \widetilde{P}(k,z')}{\partial z'}\right]^*$;

3. the common sum for both equations in the last becomes the conjugate of the original:

$$\begin{aligned}\sum_{n\neq 0} a_n \widetilde{P}(-k-n\Delta k,z') &= \sum_{n\neq 0} a_n \left[\widetilde{P}(k+n\Delta k,z')\right]^* = \sum_{n\neq 0} [a_{-n}]^* \left[\widetilde{P}(k+n\Delta k,z')\right]^* \\ &= \sum_{n\neq 0} \left[a_{-n}\widetilde{P}(k+n\Delta k,z')\right]^* = \left[\sum_{n\neq 0} a_{-n}\widetilde{P}(k+n\Delta k,z')\right]^* \\ &= \left[\sum_{n\neq 0} a_n \widetilde{P}(k-n\Delta k,z')\right]^*\end{aligned}$$

The symmetry relation above is very important in numerical implementation since it can reduce the calculation by half. We obtained very stable G_0^{DN} (for non-evanescent k) result in the wavenumber domain. The encouraging fact is that, the smaller the iteration step Δz, the more smooth G_0^{DN}. This means that:

1. G_0^{DN} is a well defined smooth function in the non-evanescent region. And the non-evanescent ks are the only part of the spectrum we should apply on data due to noise.

2. The evanescent part of G_0^{DN} is also used for the input boundary conditions, it will not cause instability issue for the calculation of the non-evanescent part of G_0^{DN}.

The issue for this approach is the computational cost. For the model we tested, it is very costly to reach a converging solution. Another approach, aiming at higher-order of accuracy rather than smaller Δz size, is proposed as below. In this approach, the lateral variation of the velocity field is expressed as a continuous Fourier transform, rather than a discrete Fourier sum to single out the current wavefield $\widetilde{P}(k,z')$ which is essential for the completeness of a discretized 1D Helmholtz equation. The content of this new approach can also be formulated in terms discrete Fourier sum, but it is much shorter and cleaner in a continuous form. First we again consider solving the problem in a region sufficiently thin that the vertical variation can be ignored,

$$\left(\frac{\partial^2}{\partial x'^2} + \frac{\partial^2}{\partial z'^2} + \frac{\omega^2}{c^2(x')}\right) P(x',z') = 0. \tag{34}$$

It can be transformed into the wavenumber k domain with the following Fourier transform[6]: $\int_{-\infty}^{\infty} e^{-ikx'} dx'$,

[6]The Fourier transform for the product of $\frac{1}{c^2(x)}$ and $P(x',z')$ is a convolution in the k domain. In our case: $\frac{1}{c^2(x')} = \frac{1}{2\pi}\int_{-\infty}^{\infty} \widetilde{A}(k)e^{ikx'}dk$, and $P(x',z') = \frac{1}{2\pi}\int_{-\infty}^{\infty} \widetilde{P}(k,z')e^{ikx'}dk$. We have $\int_{-\infty}^{\infty} \frac{P(x',z')}{c^2(x')}e^{ikx'} = \frac{1}{2\pi}\int_{-\infty}^{\infty} \widetilde{A}(\lambda)\widetilde{P}(k-\lambda,z')$.

$$\left(\frac{\partial^2}{\partial z'^2} - k^2\right)\widetilde{P}(k,z') = -\frac{\omega^2}{2\pi}\int_{-\infty}^{\infty}\widetilde{A}(\lambda)\widetilde{P}(k-\lambda,z')d\lambda. \tag{35}$$

$$\frac{\partial^2}{\partial z'^2}\widetilde{P}(k,z') = \int_{-\infty}^{\infty}\left(k^2\delta(\lambda) - \frac{\omega^2\widetilde{A}(\lambda)}{2\pi}\right)\widetilde{P}(k-\lambda,z')d\lambda. \tag{36}$$

If we define: $\widetilde{B}(k,\lambda) \equiv \omega^2\widetilde{A}(\lambda) - 2\pi k^2\delta(\lambda)$, we have,

$$\frac{\partial^2}{\partial z'^2}\widetilde{P}(k,z') = -\frac{1}{2\pi}\int_{-\infty}^{\infty}\widetilde{B}(k,\lambda)\widetilde{P}(k-\lambda,z')d\lambda. \tag{37}$$

Taking the $\partial^2/\partial z'^2$ operation on the equation above, we can calculate the fourth-order derivative:

$$\begin{aligned}\frac{\partial^4}{\partial z'^4}\widetilde{P}(k,z') &= -\frac{1}{2\pi}\int_{-\infty}^{\infty}\widetilde{B}(k,\lambda)\frac{\partial^2\widetilde{P}(k-\lambda,z')}{\partial z'^2}d\lambda \\ &= -\frac{1}{2\pi}\int_{-\infty}^{\infty}\widetilde{B}(k,\lambda)\left(-\frac{1}{2\pi}\int_{-\infty}^{\infty}\widetilde{B}(k-\lambda,\mu)\widetilde{P}(k-\lambda-\mu,z')d\mu\right)d\lambda \\ &= \frac{1}{2\pi}\int_{-\infty}^{\infty}\widetilde{P}(k-\lambda,z')\widetilde{B}^{(2)}(k,\lambda),\end{aligned} \tag{38}$$

where $\widetilde{B}^{(2)}(k,\lambda) = \frac{1}{2\pi}\int_{-\infty}^{\infty}\widetilde{B}(k,\mu)\widetilde{B}(k-\mu,\lambda-\mu)d\mu$. Taking the $\partial^2/\partial z'^2$ operation on the equation above, we can calculate the sixth-order derivative:

$$\begin{aligned}\frac{\partial^6}{\partial z'^6}\widetilde{P}(k,z') &= \frac{1}{2\pi}\int_{-\infty}^{\infty}\widetilde{B}^2(k,\lambda)\frac{\partial^2\widetilde{P}(k-\lambda,z')}{\partial z'^2}d\lambda \\ &= \frac{1}{2\pi}\int_{-\infty}^{\infty}\widetilde{B}^2(k,\lambda)\left(-\frac{1}{2\pi}\int_{-\infty}^{\infty}\widetilde{B}(k-\lambda,\mu)\widetilde{P}(k-\lambda-\mu,z')d\mu\right)d\lambda \\ &= -\frac{1}{2\pi}\int_{-\infty}^{\infty}\widetilde{P}(k-\lambda)\widetilde{B}^{(3)}(k,\lambda),\end{aligned} \tag{39}$$

where $\widetilde{B}^{(3)}(k,\lambda) = \frac{1}{2\pi}\int_{-\infty}^{\infty}\widetilde{B}^{(2)}(k,\mu)\widetilde{B}(k-\mu,\lambda-\mu)d\mu$. We have obtained all even order derivatives of $\widetilde{P}(k,z')$ with respect to z'. Note that these partial derivatives are computed from the

wavefield $\widetilde{P}$ on the same boundary location z', in other words, conviently available from the known boundary conditions. To reconstruct the precise value of $\widetilde{P}(k, z' + \Delta z)$, we still need the odd order derivatives, that can be provided by $\widetilde{P}_z(k, z')$ which in our notation means:

$$\widetilde{P}_z(k, z') \equiv \frac{\partial \widetilde{P}(k, z')}{\partial z'}. \tag{40}$$

The first-order variation is provided by the normal derivative on the boundry z':

$$\frac{\partial \widetilde{P}(k, z')}{\partial z'} = \widetilde{P}_z(k, z'). \tag{41}$$

And all other odd-order derivatives can be computed from the normal derivative $\widetilde{P}_z(k, z')$ at the boundary as well,

$$\begin{aligned}
\frac{\partial^{2m+1}}{\partial z'^{2m+1}} \widetilde{P}(k, z') &= \frac{\partial}{\partial z'} \frac{\partial^{2m}}{\partial z'^{2m}} \widetilde{P}(k, z') \\
&= \frac{\partial}{\partial z'} \left(\frac{(-1)^m}{2\pi} \int_{-\infty}^{\infty} \widetilde{B}^{(2m)}(k, \lambda) \widetilde{P}(k - \lambda, z') d\lambda \right) \\
&= \frac{(-1)^m}{2\pi} \left(\int_{-\infty}^{\infty} \widetilde{B}^{(2m)}(k, \lambda) \widetilde{P}_z(k - \lambda, z') d\lambda \right).
\end{aligned} \tag{42}$$

With derivatives of every order available, we can calculate $\widetilde{P}(k, z' + \Delta z)$ using a Taylor expansion,

$$\begin{aligned}
\widetilde{P}(k, z' + \Delta z) &= \widetilde{P}(k, z') + \sum_{m=1}^{\infty} \frac{\partial^m \widetilde{P}(k, z')}{\partial z'^m} \frac{(\Delta z)^m}{m!} \\
&= \widetilde{P}(k, z') + \widetilde{P}_z(k, z') \Delta z \\
&\quad + \sum_{m=1}^{\infty} \frac{(-1)^m}{2\pi} \frac{(\Delta z)^{2m}}{(2m)!} \int_{-\infty}^{\infty} \widetilde{B}^{(m)}(k, \lambda) \widetilde{P}(k - \lambda, z') d\lambda \\
&\quad + \sum_{m=1}^{\infty} \frac{(-1)^m}{2\pi} \frac{(\Delta z)^{2m+1}}{(2m+1)!} \int_{-\infty}^{\infty} \widetilde{B}^{(m)}(k, \lambda) \widetilde{P}_z(k - \lambda, z') d\lambda,
\end{aligned} \tag{43}$$

where $\widetilde{B}^{(1)}$ is used to denote $\widetilde{B}^{(1)}(k, \lambda) \equiv \widetilde{B}(k, \lambda)$.

With equation (43) and the benefit from smaller step size Δz, we can predict the wavefield at another depth $z' + \Delta z$ with high precision through an interval with thickness Δz with no vertical variation of medium properties. Since the prediction is an activity under our control we can choose

the size of Δz to match the actual geology. The normal derivative of $\widetilde{P}$ should also be predicted in order to provide a sufficient boundary condition for the next step prediction[7]:

$$\begin{aligned}\widetilde{P}_z(k,z'+\Delta z) &= \widetilde{P}_z(k,z') \\ &+ \sum_{m=1}^{\infty} \frac{(-1)^m}{2\pi} \frac{(\Delta z)^{2m-1}}{(2m-1)!} \int_{-\infty}^{\infty} \widetilde{B}^{(m)}(k,\lambda)\widetilde{P}(k-\lambda,z')d\lambda \\ &+ \sum_{m=1}^{\infty} \frac{(-1)^m}{2\pi} \frac{(\Delta z)^{2m}}{(2m)!} \int_{-\infty}^{\infty} \widetilde{B}^{(m)}(k,\lambda)\widetilde{P}_z(k-\lambda,z')d\lambda,\end{aligned} \tag{44}$$

8 Numerical example

The experiment in this article is designed for an easy verification of the effectiveness of wavefield prediction in a laterally varying medium. The geological model, shown in Figure 5, is symmetrical in the z-direction in terms of a fifty-meter-thick laterally heterogeneous region at depth $475m$. The sources are located at $0m$ depth, with receiver line at $2.5m$. Our plan is to predict an experiment at depth that is exactly symmetrical with the original experiment. And our input data can be used to check the quality of our work and the effectiveness of the procedure.

Fourth order finite difference scheme published in Alford et al. (1974) is used to generate the data. The source signature is the first derivative of a Gaussian function. The detail of the experiment is shown in Figure 3.

Inside the $50(m)$ layer with lateral variation, there is no vertical variation. The lateral velocity variation in this layer is:

$$\frac{1}{c^2(x)} = \left(\frac{1}{1500}\right)^2 - \frac{1}{9250}\frac{1}{2\sqrt{\pi 10^4}} e^{-x^2/(4\times 10^4)}.$$

Consequently, the lateral variation of $\frac{1}{c^2(x)}$ can be approximately expressed in the wavenumber (k) domain as a smooth Gaussian distribution:

$$\int_{-\infty}^{\infty} dx \frac{e^{ikx}}{c^2(x)} = \frac{2\pi\delta(k)}{1500^2} - \frac{1}{9250} e^{-10^4 k^2}.$$

A typical shot gather is shown in Figure 4.

9 Conclusions

We have proposed a stable and accurate scheme to compute the Green's function with vanishing Dirichlet and Neumann boundary conditions (G_0^{DN}) for a medium with lateral variation. After the

[7] It can be achieved by taking the $\frac{\partial}{\partial(\Delta z)}$ operation on equation (43).

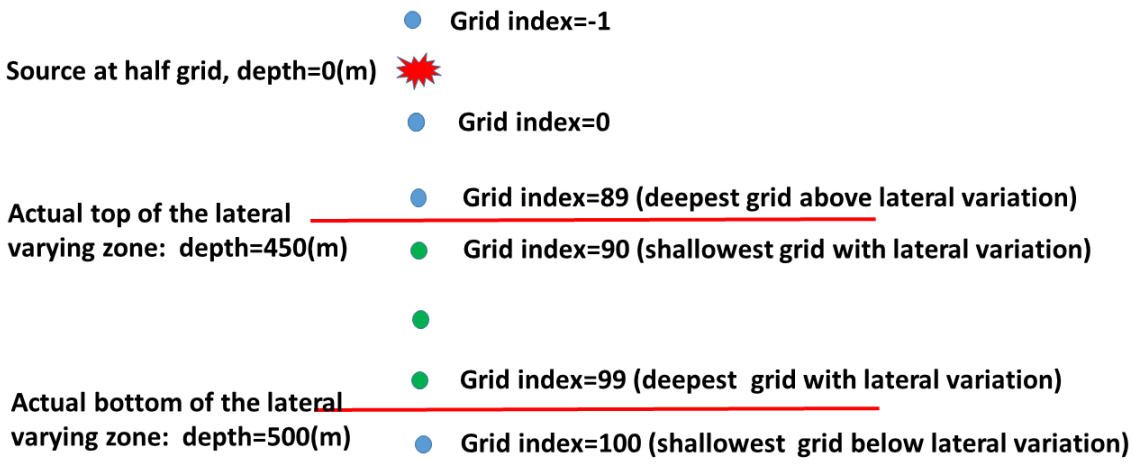

Figure 3: Grid configuration

computation of G_0^{DN}, we implemented the first the Claerbout III imaging condition for two-way waves for a laterally-varying medium. This article proposes a stable computational framework in the frequency-wavenumber domain to predict wavefield at depth using the measurements on top without modification to the wave equation or approximation to the dispersion relation. The explicit solution in this article for the Helmholtz equation using both Dirichlet and Neumann boundary conditions from only one side, is very different from the most popular implicit schemes using either Dirichlet or Neumann condition everywhere on the boundary around the unknown region.

10 Acknowledgement

Jim Mayhan offered tremendous help on proof reading the manuscript. The authors would like to thank all M-OSRP members and sponsors. This work has been partially funded by NSFCMG award DMS-0327778 and DOE Basic Energy Sciences Award DE-FG02-05ER15697.

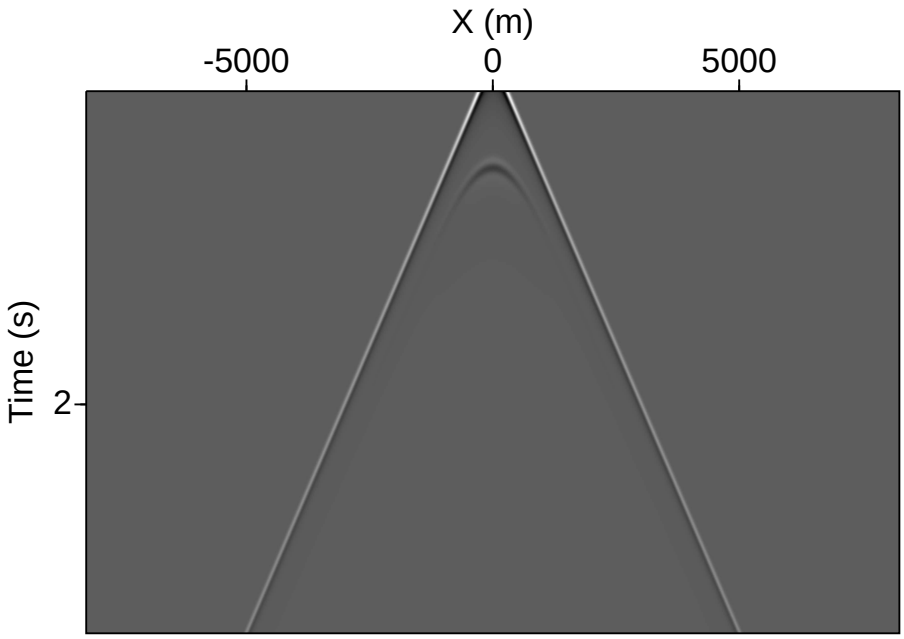

Figure 4: The shot gather with $x_s = 0(m)$.

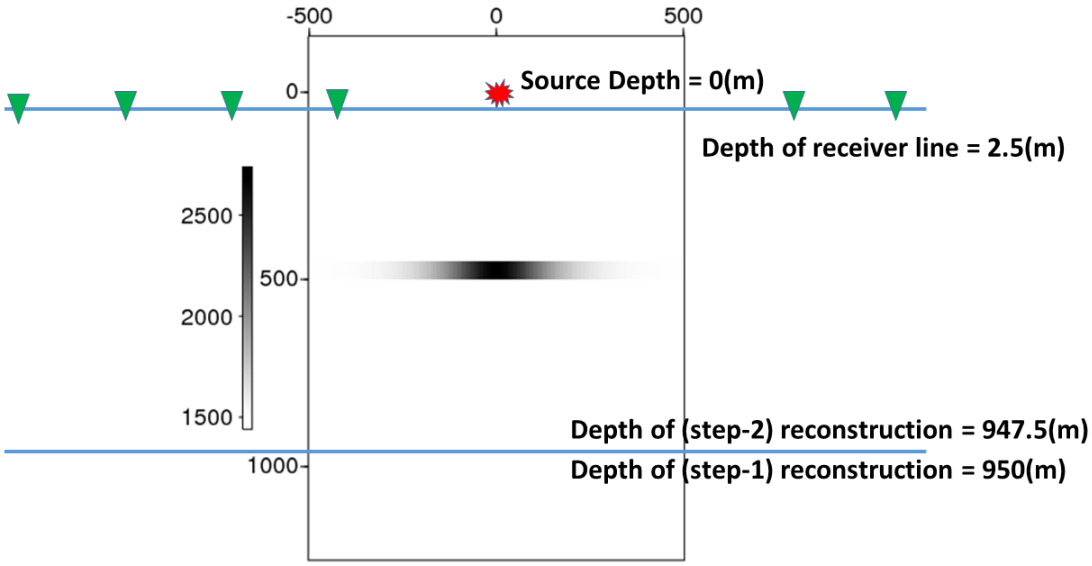

Figure 5: The geological model.

References

Alford, R. M., K. R. Kelly, and D. M. Boore. "Accuracy of finite-difference modeling of the acoustic wave equation." *Geophysics* 39 (1974): 834–842.

Clayton, R. W. and R. H. Stolt. "A Born-WKBJ inversion method for acoustic reflection data." *Geophysics* 46 (1981): 1559–1567.

Liu, F. and A. B. Weglein. "The first *wave theory* RTM, examples with a layered medium, predicting the source and receiver at depth and then imaging, providing the correct location and reflection amplitude at every depth location, and where the data includes primaries and all internal multiples." *2012 M-OSRP Annual Report* (2013): 284–335.

Liu, F. and A. B. Weglein. "The first wave equation migration RTM with data consisting of primaries and internal multiples: theory and 1D examples." *Journal of Seismic Exploration* 23 (2014): 357–366.

Stolt, R. H. "MIGRATION BY FOURIER TRANSFORM." *Geophysics* 43 (1978): 23–48.

Stolt, R. H. and A. B. Weglein. "Migration and inversion of seismic data." *Geophysics* 50 (1985): 2458–2472.

Stolt, R. H. and A. B. Weglein. *Seismic imaging and inversion: Application of linear inverse theory*. Cambridge University Press, 2012.

Stolt, Robert H. and Alvin K. Benson. *Seismic migration: theory and practice*. Geophysical Press, 1986.

Weglein, A. B., F. V. Araújo, P. M. Carvalho, R. H. Stolt, K. H. Matson, R. T. Coates, D. Corrigan, D. J. Foster, S. A. Shaw, and H. Zhang. "Inverse scattering series and seismic exploration." *Inverse Problems* 19 (2003): R27–R83.

Weglein, A. B. and R. H. Stolt. "Migrationinversion revisited (1999)." *The Leading Edge* 18 (1999): 950–975.

Weglein, A. B., R. H. Stolt, and J. D. Mayhan. "Reverse-time migration and Green's theorem: Part I — The evolution of concepts, and setting the stage for the new RTM method." *Journal of Seismic Exploration* 20 (February 2011): 73–90.

Weglein, A. B., R. H. Stolt, and J. D. Mayhan. "Reverse time migration and Green's theorem: Part II — A new and consistent theory that progresses and corrects current RTM concepts and methods." *Journal of Seismic Exploration* 20 (May 2011): 135–159.

Weglein, Arthur B. "Multiples: signal or noise?." *84th Annual International Meeting, SEG, Expanded Abstracts*. Society of Exploration Geophysicists, 2014, **4393–4399**.

A clear example of using multiples to enhance and improve imaging

Chao Ma & Arthur B. Weglein

Abstract

In this report, we use a 1D prestack example to examine the use of multiples to obtain an approximate image of an unrecorded primary. Following those who have pioneered, developed and applied this concept (see e.g., Berkhout and Verschuur (1994); Guitton (2002); Shan (2003); Muijs et al. (2007) and Whitmore et al. (2010)), we adopt the imaging condition of space-and-time coincidence of upgoing and downgoing waves (Claerbout, 1971) (referred to as Claerbout's imaging condition II in Weglein (2015)). The result shows that the approximate image of an unrecorded primary can be used to augment and enhance subsurface imaging when there is inadequate or insufficient recording of primaries.

1 Introduction

Imaging and migration concept began with an intent in taking an event or a time section and determining the spatial location of the reflector (and the reflection point) that generated that event. For example, Claerbout (1971) introduces the reflector mapping principle: "*reflectors exist at points in the ground where the first arrival of the downgoing wave is time coincident with an upgoing wave*". The reflector mapping principle for a single shot can be expressed by

$$Map(x,z) = U(x,z,t_d)/D(x,z,t_d), \tag{1}$$

where x and z are horizontal and vertical coordinates, respectively; t_d is the time of the first arrival on the downgoing wave $d(x,z,t)$. Figure 1[1] illustrates the basic principle of reflector mapping. There will be overlap in time of the downgoing (D) and upgoing waves (U) at a point which is at or near a reflector (e.g., point P_2 in Figure 1). That time overlap can be used in the construction of a map of reflection positions. Another map formular which derived from equation 1 is

$$Map(x,z) = \int U(x,z,\omega)D^*(x,z,\omega)d\omega. \tag{2}$$

As discussed in Claerbout (1971), because the practical schemes will have no knowledge of the interface, there will be an erroeous[2] upgoing wave U_3 at P_3 (indicated by dots before the arrival of the downgoing wave) and that error has no bad effect (no overlap in time) on the reflector mapping formulas which utilize time coincidence of upgoing and downgoing waves. However, there could be an overlap in time at P_3 between the downgoing and upgoing waves if a multiple, which arrives latter than a primary, is present in the upgoing wave. Therefore, multiple removal (e.g., Carvalho et al. (1991), Verschuur et al. (1992), Araujo et al. (1994); and Weglein et al. (1997)) is required before imaging.

However, whereas imaging requires only primaries, circumstances exist in which the extent, sampling and acquisition of primaries is incomplete and less than adequate to achieve imaging

[1] Adapted from Claerbout (1971).

[2] In principle, there is no upgoing wave U below the reflector at the point P_3.

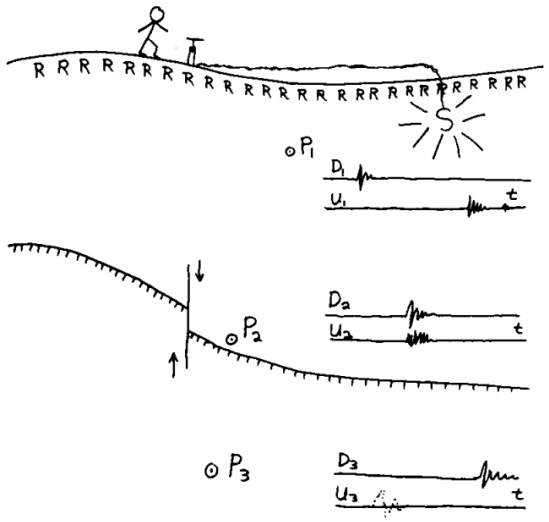

Figure 1: Illustration of the basic principle of reflector mapping. Figure adapted from Claerbout (1971).

objectives. Researchers (e.g., Berkhout and Verschuur (1994); Guitton (2002); Shan (2003); Muijs et al. (2007); Whitmore et al. (2010); Lu et al. (2011) and Valenciano et al. (2014)) seeking methods that use multiples to extract an approximate image of an unrecorded primary were influenced and inspired by the Claerbout imaging condition II (designated for imaging primaries) to consider the space-and-time coincidence of other events for different useful purposes. The example in Figure 2 illustrates one way that such a method has been realized.

For the purpose of using a multiple to find an approximate image of an unrecorded primary, we consider the field U (in equation 2) as the source-and-receiver deghosted first-order multiple (represented by the black-red-yellow line in Figure 2), and the field D as the source-deghosted, but the receiver ghost of the primary (represented by the black line in Figure 2) that is a subevent of a recorded multiple. That interpretation of equation 2, with that input D and U, will produce an appropriate image of the unrecorded subevent of the multiple (see Weglein (2015) for more details).

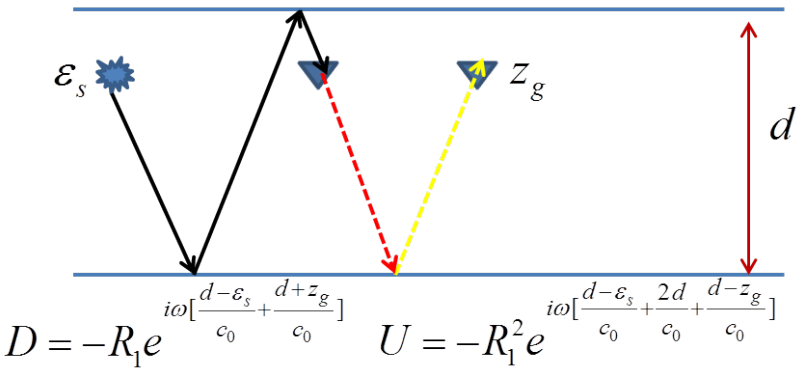

Figure 2: Imaging of an unrecorded primary that extracted from a recorded multiple. Figure adapted from Weglein (2015).

Methods that seek to use a multiple to produce an approximate image of an unrecorded primary also require a velocity model for wavefield propagation. That in turn requires a step in which multiples are first removed. Therefore, the recent interest in (and approaches for) using a multiple to provide an approximate primary depend on an effective removal of multiples before the method starts.

Within that understanding, we use a 1D prestack example to examine the imaging result of an unrecorded primary that we can extracted from multiples following Claerbout's imaging condition II. Within that understanding, we use a 1D prestack example to examine the imaging result of an unrecorded primary that we can extracted from multiples.

2 Prestack image enhancement by imaging an unrecorded primary extracted from a multiple

In this section, we first provide a 1D prestack numerical example, based on a one horizontal reflector model, to examine the result of approximately imaging an unrecorded primary extracted from a recorded multiple. The image results are obtained by the following equation[3]:

$$Map(x,z) = \int U(x,z,t)D(x,z,t)dt. \tag{3}$$

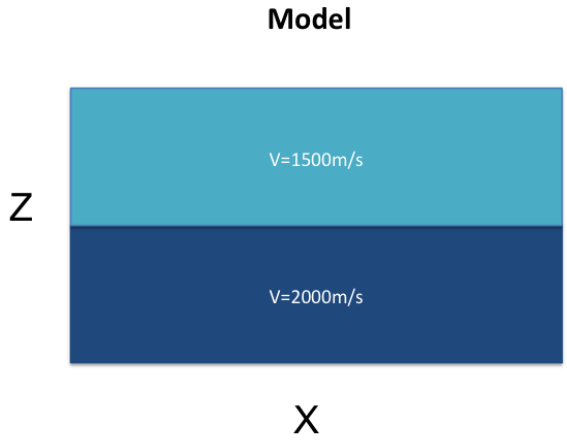

Figure 3: A test model for a case of a single horizontal reflector.

The test data are generated from a model that contains one horizontal reflector (Figure 3). In imaging the recorded primary (Figure 4a), the downgoing wavefield that is being forward propagated is the source wavefield, and the upgoing wavefield that is being backward propagated is the

[3]This is the Equation 5 in Claerbout (1971), we provide a derivation of this equation from equation 2 in the Appendix.

primary. In imaging the unrecorded primary (Figure 4b), the downgoing wavefield that is being forward propagated is the receiver-side ghost of the primary, and the upgoing wavefield that is being backward propagated is the source-receiver-side-deghosted first-order free-surface multiple.

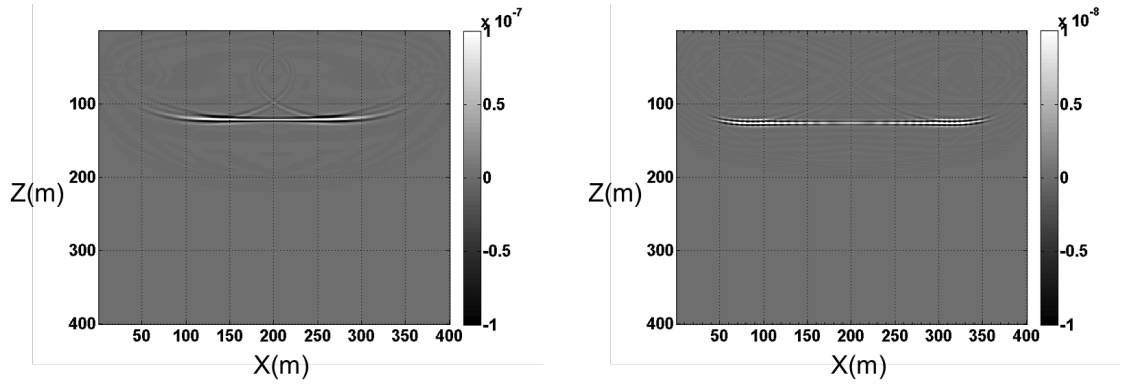

(a) (b)

Figure 4: 4a:result from imaging a primary following Claerbout's imaging condition II, 4b: result from imaging an extracted primary from a first-order free-surface multiple following Claerbout's imaging condition II.

Comparing the result in Figure 4a with the result in Figure 4b, we note that the reflector is correctly imaged in both results. However, the image from the unrecorded primary (extracted from a multiple) shows broader illumination (with smaller image amplitude) compared with the image from the recorded primary (see Weglein (2015) for analysis in amplitude difference).

It is important to point out that in obtaining the result of Figure 4b in this synthetic example, we purposefully chose the receiver-side ghost of the primary and the source-receiver-side-deghosted first-order free-surface multiple as the down-going (D) and up-going (U) wavefields, respectively. Methods that seek to obtain an approximate image of an unrecorded primary require an effective up-down wavefield separation, which can be achieved by modern seismic acquisition techniques (e.g., GeoStreamer or over/under cable). Notice that, among different combinations between the downgoing and upgoing events, cross-talk artifacts can happen (e.g., Liu et al. (2011), Lu et al. (2011)).

Next, we will use a two-reflector model to examine the use of multiple to provide an approximate image of a deeper reflector. Figure 5 shows the two-reflector model. To use multiple to obtain the approximate image of the second-reflector (see Figure 7b), the downgoing wavefield is receiver-side ghost of the first primary (represented by the blue line in Figure 5) and the upgoing wavefield is source-and-receiver-side deghosted first-order free-surface multiple with the two upward reflections at the first and second reflector (represented by the blue line and the green line in Figure 5). The velocity model we use is a discontinous velocity shown in Figure 6. For the purpose of comparison, we provide the imaging result from migrating the primary corresponding to the deeper reflector in Figure 7a.

The reason is the prediction of an events as a multiple depends on having the subevents of the multiple recorded. Since the problem being addressed by definition has unrecorded primaries, multiples with unrecorded primary subevents cannot be identified as a multiple. To address that issue in practice the entire data set is input where on one side primaries belong and on the other side multiples are called for.

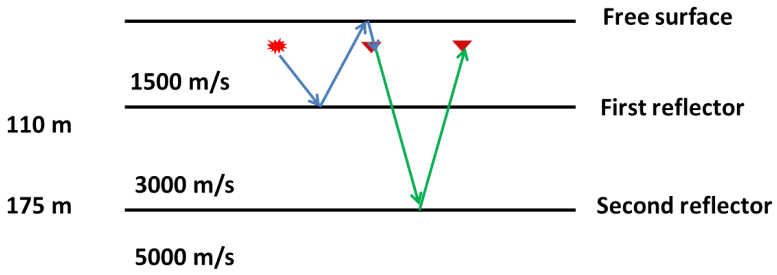

Figure 5: A test model for the case of two horizontal reflector and a free-surface. The first and the second reflector are at depth 110 m and 175 m, repsectively. The blue line represents the downgoing wavefield and the blue line and the green line represents the upgoing wavefield.

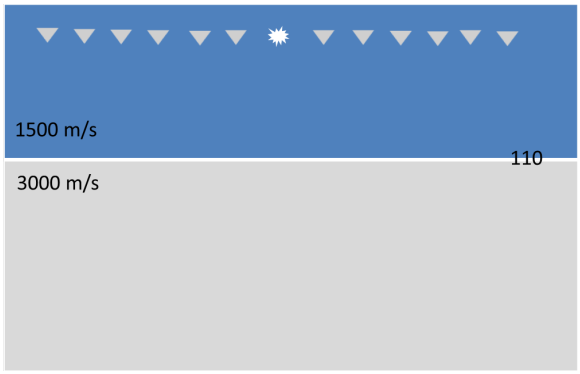

Figure 6: A discontinuous velocity model used to propagate the wavefield. There is one reflector at 110 m, the velocities are 1500 m/s and 3000 m/s above and below the reflector, respectively.

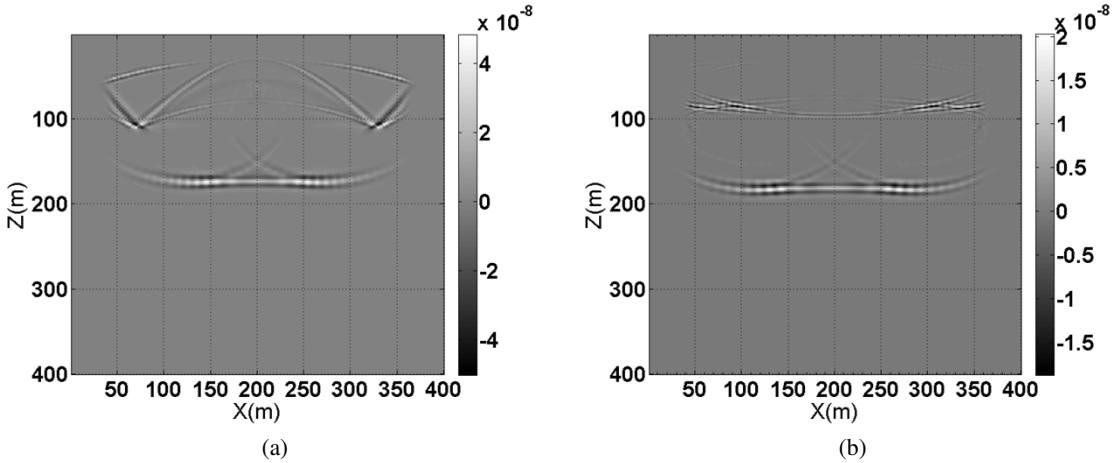

Figure 7: Figure on the left is Figure 7a and Figure on the right is Figure 7b. Notice antifacts in both cases due to the discontinuous velocity and limited model.

There are circumstances where the benefit derived from the enhanced imaging greatly outweighs the deficit of false event prediction (e.g., Valenciano et al. (2014) and Weglein (2014)).

3 Conclusions

In this paper, we provide a very clear example of how multiples can (at times) be used to provide an approximate image of an unrecorded primary. That approximate image, taken together with the images from recorded primaries, can enhance and provide added-value from imaging recorded primaries and approximate unrecorded primaries. However, there are artifacts (e.g., unwanted cross-talk) in the real applications that use multiples to improve subsurface imaging. Therefore, this procedure needs to be judiciously implemented in real-world applications. Whitmore et al. (2010); Lu et al. (2011); Valenciano et al. (2014) and Weglein (2014) showed several convincing field-data examples that illustrated considerable added value from using multiples to enhance imaging.

The Claerbout's imaging condition II allowed/encouraged the consideration of the space-and-time-coincidence idea for different upgoing and downgoing wavefields (in addition to the uses that the original imaging concept was intended) in an interpretation to provide added value for using multiples to approximate the image of an unrecorded primary. There are numerous examples that show significant benefit for imaging from this procedure, and where that benefit outweighs any issues caused by artifacts.

4 Acknowledgement

We are grateful to all M-OSRP sponsors for their encouragement and support of this study. We'd like to thank Fang Liu, Jim Mayhan and Xinglu Lin for helpful reviews.

5 Appendix

We provide a derivation of equation 3 from equation 2.

Consider

$$U(x,z,\omega) = \int U(x,z,t)e^{i\omega t}dt, \tag{4}$$

and

$$D^*(x,z,\omega) = \int D(x,z,u)e^{-i\omega u}du. \tag{5}$$

Substitude equations 4 and 5 into equation 2,

$$Map(x,z) = \int\int\int U(x,z,t)D(x,z,u)e^{i\omega(t-u)}dtdud\omega, \tag{6}$$

Set $t-u=\tau$,

$$\begin{aligned} Map(x,z) &= \int\int\int U(x,z,t)D(x,z,t-\tau)e^{i\omega\tau}dtd\tau d\omega \\ &= \int\int U(x,z,t)D(x,z,t-\tau)dtd\tau \int e^{i\omega\tau}d\omega \\ &= \int\int U(x,z,t)D(x,z,t-\tau)dtd\tau\delta(\tau) \\ &= \int U(x,z,t)D(x,z,t)dt \end{aligned} \tag{7}$$

References

Araujo, F. V., A. B. Weglein, P. M. Carvalho, and R. H. Stolt. "Inverse scattering series for multiple attenuation: An example with surface and internal multiples." *SEG Technical Program Expanded Abstracts* (1994): 1039–1041.

Berkhout, A. J. and D. J. Verschuur. "Multiple technology: Part 2, Migration of multiple reflections." *SEG Technical Program Expanded Abstracts* (1994): 1497–1500.

Carvalho, P. M., A. B. Weglein, and R. H. Stolt. "Examples of a nonlinear inversion method based on the T-matrix of scattering theory: Application to multiple suppression." *61st Ann. Internat. Mtg: Soc. of Expl. Geophys., Expanded Abstracts*. . Soc. Expl. Geophys., 1991. 1319–1322.

Claerbout, J. F. "Toward a unified theory of reflector mapping." *Geophysics* 36 (1971): 467–481.

Guitton, A. "Shot-profile migration of multiple reflections." *SEG Technical Program Expanded Abstracts* (2002): 1296–1299.

Liu, Y., X. Chang, D. Jin, R. He, H. Sun, and Y. Zheng. "Reverse time migration of multiples for subsalt imaging." *Geophysics* (2011): 209–216.

Lu, S., N.D. Whitemore, A.A. Valenciano, and N. Chemingui. "Imaging of Primaries and Multiples with 3D SEAM Synthetic." *SEG Technical Program Expanded Abstracts* (2011): 3217–3221.

Muijs, R., J. O. A. Robertsson, and K. Holliger. "Prestack depth migration of primary and surface-related multiple reflections: Part I Imaging." *Geophysics* (2007): S59–S69.

Shan, G. "Source-receiver migration of multiple reflections." *SEG Technical Program Expanded Abstracts* (2003): 1008–1011.

Valenciano, A. A., S. Crawley, E. Klochikhina, N. Chemingui, S. Lu, and D.N. Whitemore. "Imaging complex structures with separated Up- and Down-going wavefields." *SEG Technical Program Expanded Abstracts* (2014): 3941–3945.

Verschuur, D. J., A. J. Berkhout, and C. P. A. Wapenaar. "Adaptive surface-related multiple elimination." *Geophysics* 57 (1992): 1166–1177.

Weglein, A. B. "Multiples, single or noise?." *Submitted to Geophysics* (2015).

Weglein, A. B., F. A. Gasparotto, P. M. Carvalho, and R. H. Stolt. "An Inverse-Scattering Series Method for Attenuating Multiples in Seismic Reflection Data." *Geophysics* 62 (November-December 1997): 1975–1989.

Weglein, A.B. "Multiples: Signal or noise?." *SEG Technical Program Expanded Abstracts* (2014): 4393–4399.

Whitmore, N. D., A. Valenciano, W. Sllner, and S. Lu. "Imaging of primaries and multiples using adual-sensor towed streamer." *SEG Technical Program Expanded Abstracts* (2010): 3187–3192.

A clear example of using multiples to enhance and improve imaging

*Chao Ma * and Arthur B. Weglein, M-OSRP/Physics Dept./University of Houston*

SUMMARY

In this paper, we use a 1D prestack example to examine the use of multiples to obtain an approximate image of an unrecorded primary. We employ the imaging condition of space-and-time coincidence of upgoing and downgoing waves Claerbout (1971) (referred to as Claerbout's imaging condition II in Weglein (2015)). The result shows that the approximate image of an unrecorded primary (extracted from a recorded multiple) can be used to augment and enhance subsurface imaging when there is inadequate or insufficient recording of primaries.

INTRODUCTION

In Claerbout's imaging condition II (i.e., space-and-time coincidence of upgoing and downgoing waves), the source wavefield is forward propagated to the subsurface and the receiver wavefield is backward propagated to the subsurface. The imaging result is obtained by deconvolution via equation 1 (or cross-correlation, via equation 2) imaging condition (e.g., Claerbout (1971), Whitmore et al. (2010)):

$$I(\vec{x}) = \sum_{\vec{x}_s}\sum_{\omega} \frac{U(\vec{x},\vec{x}_s,\omega)}{D(\vec{x},\vec{x}_s,\omega)}, \tag{1}$$

$$I(\vec{x}) = \sum_{\vec{x}_s}\sum_{\omega} D^*(\vec{x},\vec{x}_s,\omega)U(\vec{x},\vec{x}_s,\omega). \tag{2}$$

In equation 1 (and equation 2), $D(\vec{x},\vec{x}_s,\omega)$ and $U(\vec{x},\vec{x}_s,\omega)$ represent downgoing and upgoing wavefields, respectively, and $*$ in equation 2 represents the complex conjugate.

Claerbout's imaging condition II assumes that the data consist of primaries. Hence, multiples need to be removed prior to imaging (see e.g., Carvalho et al. (1991), Verschuur et al. (1992), Araujo et al. (1994); and Weglein et al. (1997)). Claerbout's imaging condition II also requires a velocity model for wavefield propagation, and velocity-analysis methods assume that multiples have been removed.

However, whereas imaging requires only primaries, circumstances exist in which the extent, sampling and acquisition of primaries is incomplete and less than adequate to achieve imaging objectives. Researchers (e.g., Berkhout and Verschuur (1994); Guitton (2002); Shan (2003); Muijs et al. (2007); Whitmore et al. (2010); Lu et al. (2011) and Valenciano et al. (2014)) seeking methods that use multiples to extract an approximate image of an unrecorded primary were influenced and inspired by the Claerbout imaging condition II (designged for imaging primaries) to consider the space-and-time coincidence of other events for different useful purposes. The example in Figure 1 illustrates one way that such an extension has been realized.

For the purpose of using a multiple to find an approximate image of an unrecorded primary, we consider the field U (in equation 1 or 2) as the source-and-receiver deghosted first-order multiple, and the field D as the source-deghosted, but the receiver ghost of the primary that is a subevent of a recorded multiple. That interpretation of equations 1 and 2, with that input D and U, will produce an appropriate image of the unrecorded subevent of the multiple (see Weglein (2015) for more details).

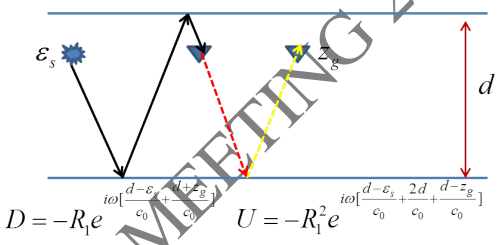

Figure 1: Imaging of an unrecorded primary that extracted from a recorded multiple. Figure adapted from Weglein (2015).

Methods that seek to use a multiple to produce an approximate image of an unrecorded primary also require a velocity model for wavefield propagation. That in turn requires a step in which multiples are first removed. Therefore, the recent interest in (and approaches for) using a multiple to provide an approximate primary depend on an effective removal of multiples before the method starts.

Within that understanding, we use a 1D prestack example to examine the imaging result of an unrecorded primary that we can extracted from multiples following Claerbout's imaging condition II (i.e., equation 2). We compare that result with the image results obtained from the recorded primaries, following that same Claerbout's imaging condition.

PRESTACK IMAGE ENHANCEMENT BY IMAGING AN UNRECORDED PRIMARY EXTRACTED FROM A MULTIPLE

In this section, we provide a 1D prestack numerical example to examine the result of approximately imaging an unrecorded primary extracted from a recorded multiple. Multiples can be useful for extracting an unrecorded primary's image and thereby for enhancing the subsurface image.

The test data are generated from a model that contains one horizontal reflector (Figure 2). In imaging the recorded primary (Figure 3a), the downgoing wavefield that is being forward propagated is the source wavefield, and the upgoing wavefield that is being backward propagated is the primary. In imaging the unrecorded primary (Figure 3b), the downgoing

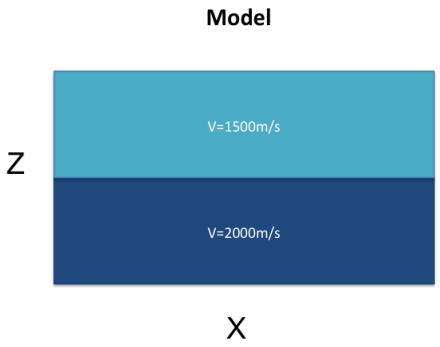

Figure 2: A test model for a case of a single horizontal reflector.

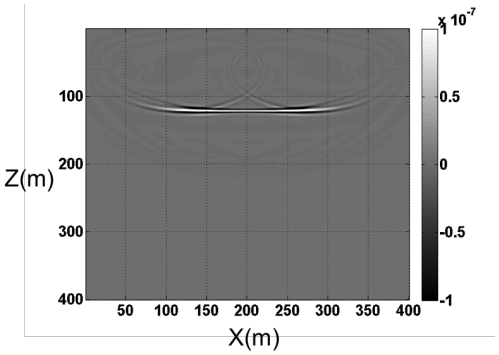

Figure 3a: Result from imaging a primary following Claerbout's imaging condition II.

wavefield that is being forward propagated is the receiver-side ghost of the primary, and the upgoing wavefield that is being backward propagated is the source-receiver-side-deghosted first-order free-surface multiple.

Comparing the result in Figure 3a with the result in Figure 3b, we note that the reflector is correctly imaged in both results. However, the image from the unrecorded primary (extracted from a multiple) shows broader illumination (with smaller image amplitude) compared with the image from the recorded primary (see Weglein (2015) for analysis in amplitude difference).

It is important to point out that in obtaining the result of Figure 3b in this synthetic example, we purposefully chose the receiver-side ghost of the primary and the source-receiver-side-deghosted first-order free-surface multiple as the down-going (D) and up-going (U) wavefields, respectively. Methods that seek to obtain an approximate image of an unrecorded primary require an effective up-down wavefield separation, which can be achieved by modern seismic acquisition techniques (e.g., GeoStreamer or over/under cable). Notice that, among different combinations

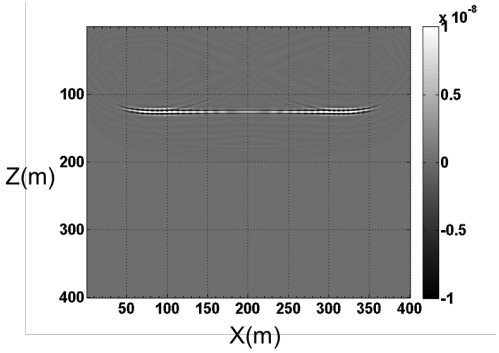

Figure 3b: Result from imaging an extracted primary from a first-order free-surface multiple following Claerbout's imaging condition II.

between the downgoing and upgoing events, cross-talk artifacts can happen (e.g., Liu et al. (2011), Lu et al. (2011)).

The reason is the prediction of an events as a multiple depends on having the subevents of the multiple recorded. Since the problem being addressed by definition has unrecorded primaries, multiples with unrecorded primary subevents cannot be identified as a multiple. To address that issue in practice the entire data set is input where on one side primaries belong and on the other side multiples are called for.

There are circumstances where the benefit derived from the enhanced imaging greatly overweights the deficit of false event prediction (e.g., Valenciano et al. (2014) and Weglein (2014)).

CONCLUSIONS

Following Claerbout's imaging condition II, multiples can be used to extract the image of unrecorded primaries and thereby to complement the subsurface imaging results in the case in which the recording of primaries is inadequate. However, there are artifacts (e.g., unwanted cross-talk) in the real applications that use multiples to improve subsurface imaging. Therefore, this procedure needs to be judiciously implemented in real-world applications. Whitmore et al. (2010); Lu et al. (2011); Valenciano et al. (2014) and Weglein (2014) showed several convincing field-data examples that illustrated considerable added value from using multiples to enhance imaging. The Claerbout's imaging condition II allowed/encouraged the consideration of the space-and-time-coincidence idea for different upgoing and downgoing wavefields (in addition to the uses that the original imaging concept was intended) in an interpretation to provide added value for using multiples to approximate the image of an unrecorded primary. There are numerous examples that show significant benefit for imaging from this procedure, and where that benefit outweighs any issues caused by artifacts.

ACKNOWLEDGMENTS

We are grateful to all M-OSRP sponsors for their encouragement and support of this study. We'd like to thank Fang Liu, Jim Mayhan and Xinglu Lin for helpful reviews.

REFERENCES

Araujo, F. V., A. B. Weglein, P. M. Carvalho, and R. H. Stolt, 1994, Inverse scattering series for multiple attenuation: An example with surface and internal multiples: SEG Technical Program Expanded Abstracts, 1039–1041.

Berkhout, A. J., and D. J. Verschuur, 1994, Multiple technology: Part 2, migration of multiple reflections: SEG Technical Program Expanded Abstracts, 1497–1500.

Carvalho, P. M., A. B. Weglein, and R. H. Stolt, 1991, Examples of a nonlinear inversion method based on the T-matrix of scattering theory: Application to multiple suppression, *in* 61st Ann. Internat. Mtg: Soc. of Expl. Geophys., Expanded Abstracts: Soc. Expl. Geophys., 1319–1322.

Claerbout, J. F., 1971, Toward a unified theory of reflector mapping: Geophysics, **36**, 467–481.

Guitton, A., 2002, Shot-profile migration of multiple reflections: SEG Technical Program Expanded Abstracts, 1296–1299.

Liu, Y., X. Chang, D. Jin, R. He, H. Sun, and Y. Zheng, 2011, Reverse time migration of multiples for subsalt imaging: Geophysics, 209–216.

Lu, S., N. Whitemore, A. Valenciano, and N. Chemingui, 2011, Imaging of primaries and multiples with 3d seam synthetic: SEG Technical Program Expanded Abstracts, 3217–3221.

Muijs, R., J. O. A. Robertsson, and K. Holliger, 2007, Prestack depth migration of primary and surface-related multiple reflections: Part i imaging: Geophysics, S59–S69.

Shan, G., 2003, Source-receiver migration of multiple reflections: SEG Technical Program Expanded Abstracts, 1008–1011.

Valenciano, A. A., S. Crawley, E. Klochikhina, N. Chemingui, S. Lu, and D. Whitemore, 2014, Imaging complex structures with separated up- and down-going wavefields: SEG Technical Program Expanded Abstracts, 3941–3945.

Verschuur, D. J., A. J. Berkhout, and C. P. A. Wapenaar, 1992, Adaptive surface-related multiple elimination: Geophysics, **57**, 1166–1177.

Weglein, A., 2014, Multiples: Signal or noise?: SEG Technical Program Expanded Abstracts, 4393–4399.

Weglein, A. B., 2015, Multiples, single or noise?: Submitted to Geophysics.

Weglein, A. B., F. A. Gasparotto, P. M. Carvalho, and R. H. Stolt, 1997, An inverse-scattering series method for attenuating multiples in seismic reflection data: Geophysics, **62**, 1975–1989.

Whitmore, N. D., A. Valenciano, W. Sllner, and S. Lu, 2010, Imaging of primaries and multiples using adual-sensor towed streamer: SEG Technical Program Expanded Abstracts, 3187–3192.

A clear example of using multiples to enhance and improve imaging: a comparison of two imaging conditions that are relevant to this analysis

Chao Ma[1] and Yanglei Zou[1]

[1]*M-OSRP/Department of Physics/University of Houston*

Abstract

In this paper, we use a 1D pre-stack example to examine the use of multiples to obtain an approximate image of an unrecorded primary by using the space-and-time coincidence of upgoing and downgoing waves (Claerbout, 1971) (referred to as Claerbout's imaging condition II in Weglein, 2015). The result shows that the image of an unrecorded primary (extracted from a recorded multiple) can be used to augment and enhance subsurface imaging from recorded primaries, when there is inadequate or insufficient acquisition of primaries. In addition, we carefully examine and analyze imaging results from two different and classic imaging conditions: (1) the predicted coincident-source-and-receiver experiment at depth, at time equals zero (referred to as Claerbout's imaging condition III in Weglein, 2015), and (2) Claerbout's imaging condition II. The result of that comparison represents the advantages of Claerbout's imaging condition III over Claerbout's imaging condition II in terms of image definitiveness and amplitude analysis. However, an adaptation that is motivated and inspired by Claerbout's imaging condition II can be used to improve imaging results, by providing an approximate image

of an unrecorded primary subevent of a recorded multiple. We provide a clear example of that method and the added value for imaging that it can represent.

Introduction

In Claerbout's imaging condition II (Claerbout, 1971), the source wavefield is forward propagated to the subsurface and the receiver wavefield is backward propagated to the subsurface. The imaging result is obtained by deconvolution via equation 1 (or cross-correlation, via equation (2)) in accord with the imaging condition (i.e., with the space-and-time coincidence of upgoing and downgoing waves):

$$I(\vec{x}) = \sum_{\vec{x}_s} \sum_{\omega} \frac{U(\vec{x}, \vec{x}_s; \omega)}{D(\vec{x}, \vec{x}_s; \omega)} \tag{1}$$

$$I(\vec{x}) = \sum_{\vec{x}_s} \sum_{\omega} D^*(\vec{x}, \vec{x}_s; \omega) U(\vec{x}, \vec{x}_s; \omega). \tag{2}$$

In equation 1 and equation 2, $D(\vec{x}, \vec{x}_s; \omega)$ and $U(\vec{x}, \vec{x}_s; \omega)$ represent down-going and up-going wavefields, respectively, and $*$ represents the complex conjugate.

Claerbout's imaging condition II assumes that the data consist of primaries. Hence, multiples need to be removed prior to imaging. However, whereas imaging requires only primaries, circumstances exist in which the extant, sampling and acquisition of primaries is incomplete and less than adequate to achieve imaging objectives. Researchers (see e.g., Muijs et al, 2007; Whitmore et al., 2010) seeking methods to use multiples to extract an approximate image of an unrecorded primary, were influenced and inspired by the Claerbout imaging condition II (designed for imaging primaries) to consider the space-and-time coincidence for other useful purposes. The example below illustrates one way that such an extension has been realized.

For the purpose of using a multiple to find an approximate image of an unrecorded primary, we consider the field *U* (in equation 1 or 2) as the source-and-receiver deghosted first-order multiple and the field *D* as the source-deghosted, but the receiver ghost of the primary that is a recorded subevent of the multiple. That interpretation of equations 1 and 2, with that input *D* and *U*, will produce an appropriate image of the unrecorded subevent of the multiple (see Weglein (2015) for more details).

Methods that seek to use a multiple to produce an approximate image of an unrecorded primary require a velocity model. That in turn requires a step in which multiples are first removed. Therefore, the recent interest in (and approaches for) using a multiple to provide an approximate image of an unrecorded primary depend on an effective removal of multiples before the method starts. Within that understanding, in this paper, we use a 1D pre-stack example to examine the image result of an unrecorded primary using Claerbout's imaging condition II (i.e., equation 1). We compare that result with the images obtained from the recorded primaries using that same Claerbout imaging condition II.

Furthermore, we will compare the results of imaging primaries obtained by two different imaging conditions (i.e., Claerbout's imaging condition II and Claerbout's imaging condition III). Claerbout's imaging condition III was first introduced by Claerbout (1971) for predicting the coincident-source-and-receiver experiment at depth, at time equals zero. Claerbout's imaging condition III predicts a physical experiment with both source and receiver at depth, and thereby allows it to provide the imaging definitiveness that Claerbout's imaging condition II cannot provide. On the other hand, the idea behind Claerbout's imaging condition II has inspired and influenced researchers to use multiples to provide an approximate image of an unrecorded

142

primary. That is an advantage of Claerbout's imaging condition II over Claerbout's imaging condition III.

Prestack image enhancement by imaging an unrecorded primary

In this section, we provide a 1D prestack numerical example that allows us to examine of how multiples can be used to provide an approximate image of an unrecorded primary, thereby enhance the subsurface image.

The test data are generated from a model that contains one horizontal reflector (see Figure 1). In imaging the recorded primary (Figure 2), the down-going wavefield that is being forward propagated is the source wavefield, and the up-going wavefield that is being backward propagated is the primary. In imaging the unrecorded primary (Figure 3), the down-going wavefield that is being forward propagated is the receiver-side ghost of the primary, and the up-going wavefield that is being backward propagated is the source-receiver-side-deghosted first-order free-surface multiple. Comparing the result in Figure 2 with the result in Figure 3, we note that the reflector is correctly imaged in both results. However, the image from the unrecorded primary shows broader illumination compared with the image from the recorded primaries only.

It is important to point out that in obtaining the result of Figure 3 in this synthetic example, we purposefully chose the **receiver-side ghost of the primary** and the **source-receiver-side-deghosted first-order free-surface multiple** as the down-going (D) and up-going (U) wavefields, respectively. Methods that seek to obtain an approximate image of an unrecorded primary require an effective up-down wavefield separation, which can be achieved by modern seismic acquisition techniques (e.g., GeoStreamer or over/under cable). Notice that, among

different combinations between the downgoing and upgoing events, cross-talk artifacts can happen.

A 1D prestack example and the differences between Claerbout's Imaging Conditions II and III

Claerbout's Imaging Condition III (i.e., the predicted coincident-source-and-receiver experiment at depth, at time equals zero) is the definition of wave-equation migration. Claerbout's Imaging Condition II is not equivalent to Claerbout's Imaging Condition III in any situation beyond 1D normal incidence or zero-offset data.

In this section, we will show the images generated by Reverse Time Migration (Claerbout's Imaging Condition II) and Stolt migration, as given in equation 3 (Claerbout's Imaging Condition III for a one-way wave) for a single horizontal reflector

$$I^{Stolt}(x,z) = \frac{1}{(2\pi)^3}\int d\omega \int dk_{sx}\, e^{-i(k_{sz}z + k_{sx}(x-x_s))} \int dk_{gx}\, e^{i(k_{gz}z + k_{gx}(x-x_g))} \iiint dx_g dx_s dt\, e^{i\omega t} D(x_g, x_s; t) \tag{3}$$

Figure 1 shows the one-reflector model that we used for this test. Figure 4 is the image generated by Reverse Time Migration with a single shot gathers (one source); we observe that there is a blur on the image and there are artifacts generated by the limited aperture. In practice, a sum over all sources is taken with the assumption that the blur and artifacts will go away. However, summing over all sources does not have a clear physical meaning, there is no guarantee that all of the blur and artifacts will disappear. The point we want to make here is that summing over all sources does not have a clear physical meaning and it is no guaranteed that all of the blur and artifacts will disappear.

Figure 5 is the image generated by Stolt migration. We can see that the image is flat and has few artifacts. Notice that the exact same data were used in this comparisons of Claerbout II and Claerbout III, indicating their intrinsic and substantive differences even in the simplest circumstances. As pointed out in Weglein (2015) the differences are much more serious when the target is complicated and imaging through and beneath a region with rapidly changing velocity. More importantly, every step in Stolt migration has a clear physical meaning. Thus we can readily obtain interpretable amplitude information, such as angle-dependent reflection coefficient, from Stolt migration.

Conclusion

In this paper, we provide a very clear example of how multiples can (at times) be used to provide an approximate image of an unrecorded primary, that, taken together with the images from recorded primaries, can enhance and provide added-value from imaging recorded primaries and approximate unrecorded primaries. However, there are artifacts (e.g., unwanted cross-talk) in the real-world applications that use multiples to improve subsurface imaging. Therefore, this procedure needs to be judiciously implemented in real applications to provide added values. For example, Whitmore et al. (2010) and Valenciano et al. (2014) showed several convincing examples with considerable added value from this method to enhance imaging. Comparison of the imaging results of primaries following two different imaging conditions (Claerbout's imaging condition II and III) demonstrates the superiority of Claerbout's imaging condition III over Claerbout's imaging condition II in terms of the definitiveness and consistency of the image. The Claerbout's imaging condition II allowed/encouraged the consideration of the space-and-time-coincidence idea for different upgoing and downgoing wavefields (in addition to the uses for which the original imaging concept was intended). Such an extension could provide added

value for using multiples to approximate the image of an unrecorded primary. The latter advantage is not available in the more definitive Claerbout imaging condition III.

Acknowledgement

We are grateful to all M-OSRP sponsors for their encouragement and support of this study. We would like to thank Arthur B. Weglein for many useful discussions. We would also like to thank Fang Liu, Jim Mayhan and Xinglu Lin for helpful reviews.

146

References

Claerbout, J. F. , 1971, Toward a unified theory of reflector mapping: Geophysics, 36, 467–481.

Muijs, R., J. O. A. Robertsson, and K. Holliger, 2007, Prestack depth migration of primary and surface-related multiple reflections: Part I — Imaging: Geophysics, 72, no. 2, S59 –S69.

Valenciano, A. A., S. Crawley, E. Klochikhina, N. Chemingui, S. Lu and D.N. Whitemore, 2014, Imaging complex structures with separated Up- and Down-going wavefields: SEG Technical Program Expanded Abstracts, 3941–3945.

Weglein, A. B., 2015, Multiples, single or noise?: Submitted to Geophysics.

Whitmore, N. D., A. Valenciano, W. Söllner, and S. Lu, 2010, Imaging of primaries and multiples using adual-sensor towed streamer: SEG Technical Program Expanded Abstracts, 3187–3192.

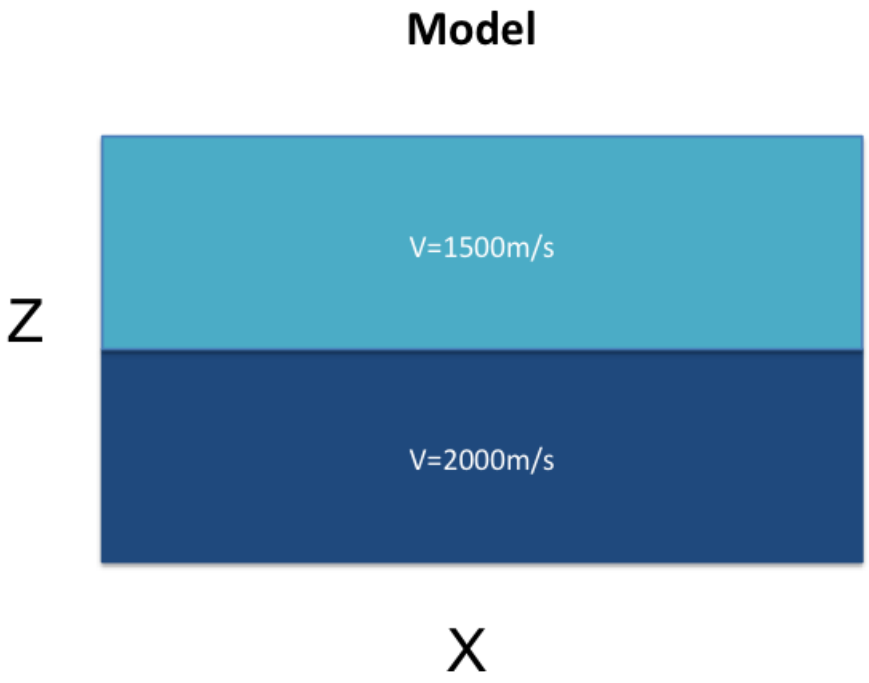

Figure 1, A one horizontal reflector test model.

148

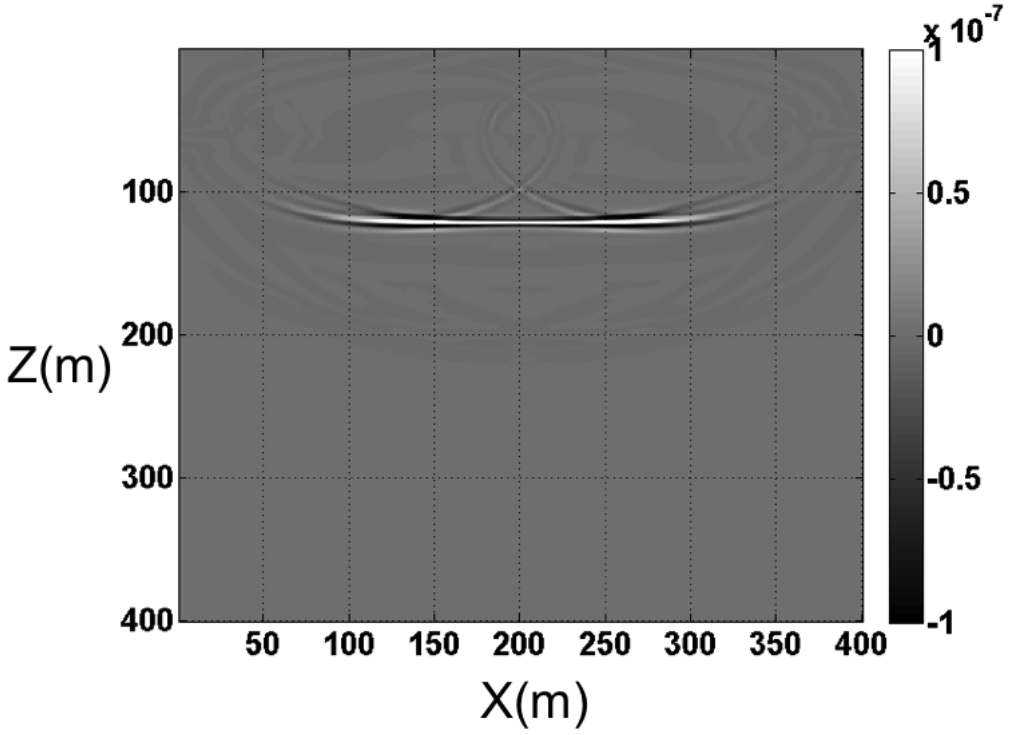

Figure 2, Imaging result by imaging a primary following Claerbout imaging condition II.

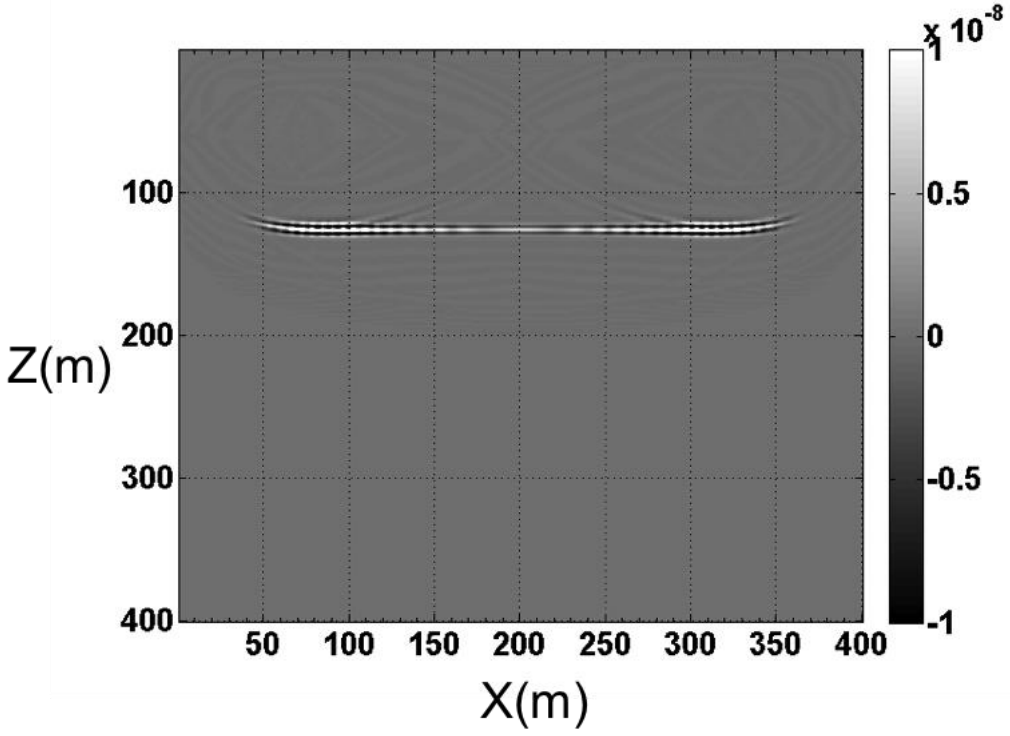

Figure 3, Imaging result by imaging an extracted primary from a first-order free-surface multiple following Claerbout imaging condition II

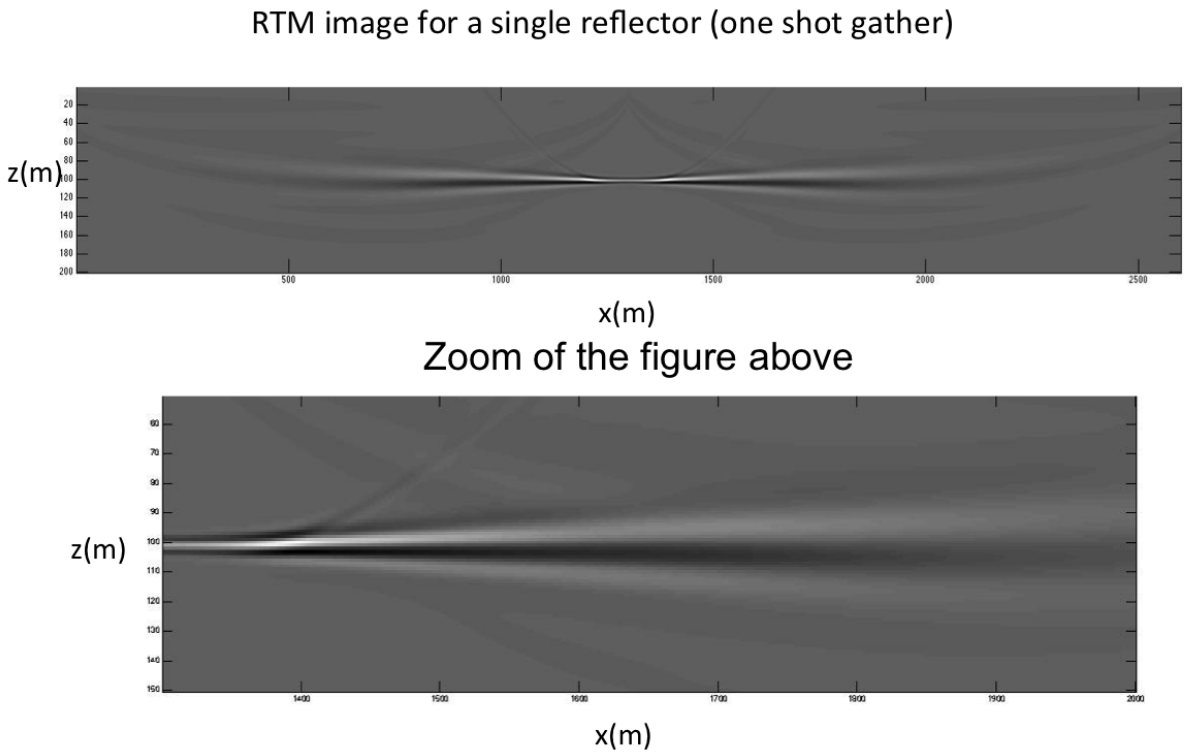

Figur 4, image result (one shot gather) following Claerbout imaging conidtion II. The figure below is zoom of the figure above. The Claerbout II image shows an inconsistent amplitude and shape of the image along the single reflector.

150

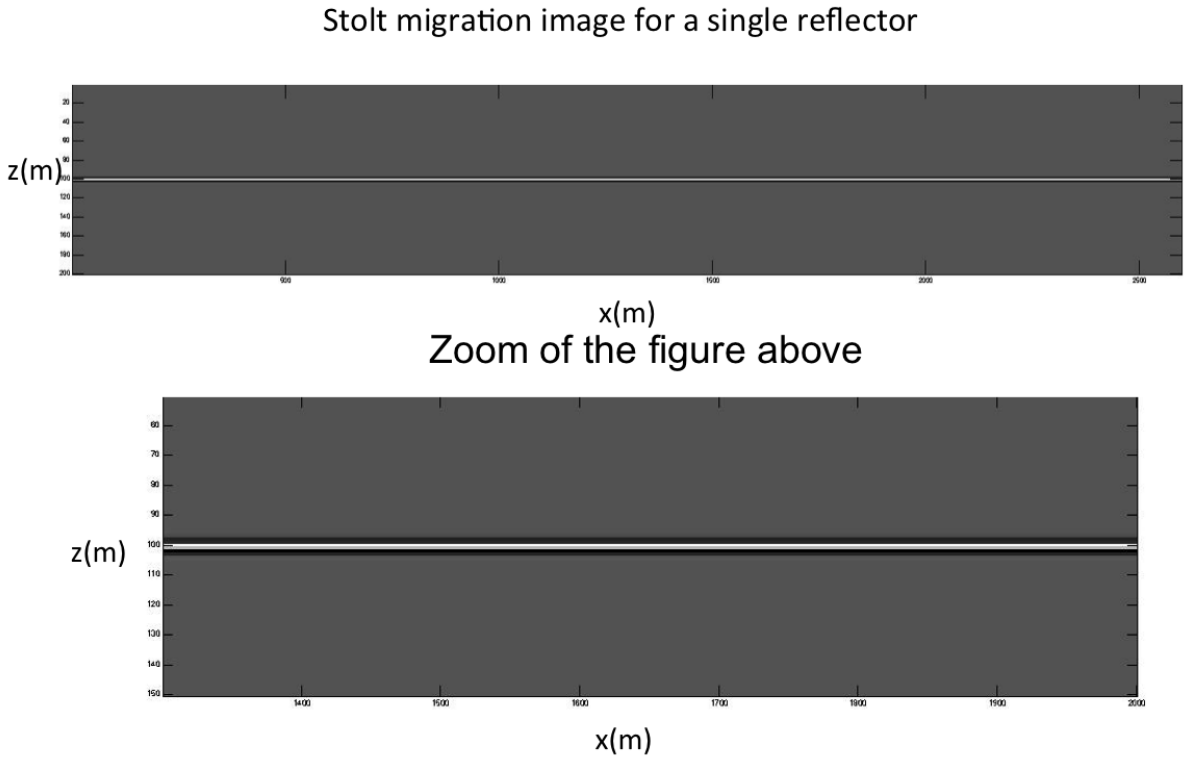

Figure 5, image result following Claerbout imaging conidtion III. The figure below is zoom of the figure above. The Claerbout III image in this figure shows an amplitude and shape consistent image. The exact same data was used in the simplest 1D earth prestack Claerbout II and Claerbout III tests and comparisons, indicating their intrinsic and substantive differences even in the simplest circumstances. As pointed out in Weglein (2015) the differences are much more serious when the target is complicated and imaging through and beneath a rapidly changing velocity.

Multiple removal: open issues, pressing challenges and recent progress towards providing the next and higher level of required capability

Arthur B. Weglein, M-OSRP, Physics Department, University of Houston

SUMMARY

This paper provides: (1) a brief overview of the current status of multiple attenuation in the petroleum industry; (2) recent progress for marine and on-shore plays; (3) open issues and pressing challenges and (4) a plan to address those high priority challenges and recent progress towards that goal.

INTRODUCTION

The demand for new and improved capability in removing multiples is driven by the portfolio of the petroleum industry and by current and anticipated future exploration trends. For example, the industry moved to deep water roughly 30 years ago. With that move, highly effective multiple-removal methods that were being applied industry-wide suddenly bumped up against their statistical assumptions, when applied to deep water plays, and failed.

Since then, the overall industry trend to explore in progressively more complex and remote areas, with ill-defined and difficult-to-estimate subsurface properties motivates the search for capabilities that will not require subsurface information. Methods for multiple removal that require various forms of subsurface information include, *e.g.*, stacking, F-K and Radon filters, and Feedback demultiple methods.

The inverse scattering series provides the opportunity to achieve all processing objectives directly and without subsurface information. The current inverse-scattering-series (ISS) internal-multiple-attenuation algorithm has a unique capability to predict the exact phase (time) and approximate amplitude of all internal multiples, at once, automatically, and without subsurface information. These properties separate the ISS internal-multiple-attenuation algorithm from all other methods, and make it the high-water mark of current internal-multiple effectiveness. That is, those ISS properties and strengths are what all other current demultiple methods (*e.g.*, Feedback loop methods, modeling and subtracting multiples, and filter methods) do not possess (*e.g.*, Hung et al. (2014); Kelamis et al. (2013a); Luo et al. (2011); Ferreira (2011)).

Carvalho (1992), Carvalho and Weglein (1994), Araújo (1994), Araújo et al. (1994), Weglein et al. (1997), and Weglein et al. (2003) developed ISS free-surface-multiple elimination algorithms and internal-multiple attenuation algorithms. Field-data applications demonstrated their effectiveness. Several marine and onshore data examples are noted below.

However, at every period in the history of E&P, the arrival of new capability to address the latest set of challenges has encouraged industry to explore in yet more difficult circumstances — situations never previously imagined, let alone considered, and beyond current capability to accommodate. That will once again demand a new and fundamentally higher level of capability and effectiveness. In this article, we describe how that's the state of affairs for multiple attenuation today.

The petroleum industry's current worldwide portfolio of both conventional and unconventional onshore plays, and of increasingly complex offshore plays — with new and unforeseen challenges — has returned and rejuvenated an interest in multiple removal (and a demand for substantially increased effectiveness). We will see why multiple removal interest (and research) has come back to center stage for the petroleum-industry.

MARINE

Early marine field-data examples of the promise and delivery of ISS free-surface-multiple and internal-multiple algorithms can be found in the above-cited papers, SEG Abstracts, theses, and, *e.g.*, in Matson et al. (1999) and the Mississippi Canyon data tests in Weglein et al. (2003) pages R69 and R70.

For example, those algorithms were employed on data from offshore Brazil, and the results were reported in Ferreira (2011) (see Figure 1). One of the conclusions in those field-data tests at Petrobras was that "no other method was able to show similar effectiveness in attenuating the internal multiples generated by the salt layers."

ONSHORE

Fu et al. (2010), Terenghi et al. (2011), and Luo et al. (2011) describe the motivation, evaluation, and comparison of different approaches to the removal of internal multiples on complex synthetic and onshore data. Fu et al. (2010) concluded that "Their (ISS internal multiple algorithm) performance was demonstrated with complex synthetic and challenging land field data sets with encouraging results, where other internal multiple suppression methods were unable to demonstrate similar effectiveness."

Goodway (2013), Goodway and Mackidd (2013), and Griffiths et al. (2013) were among those that came to the same conclusion. A paper by Kelamis et al. (2013b) presented at the Inter-

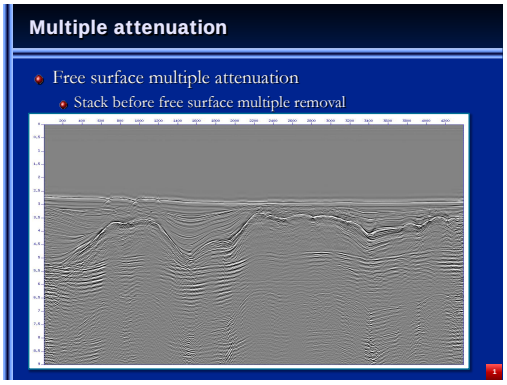

Figure 1a: Before free-surface-multiple removal.

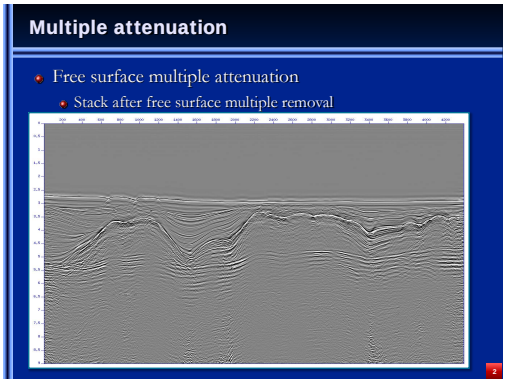

Figure 1b: After free-surface-multiple removal.

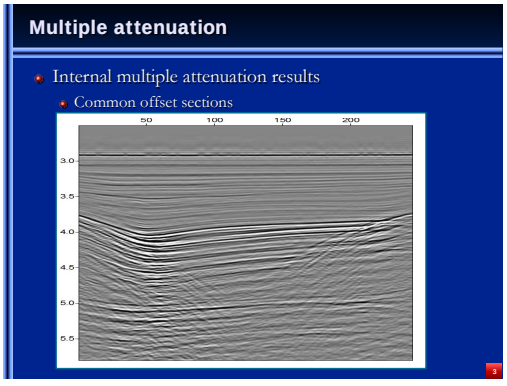

Figure 1c: Common offset sections before internal-multiple attenuation.

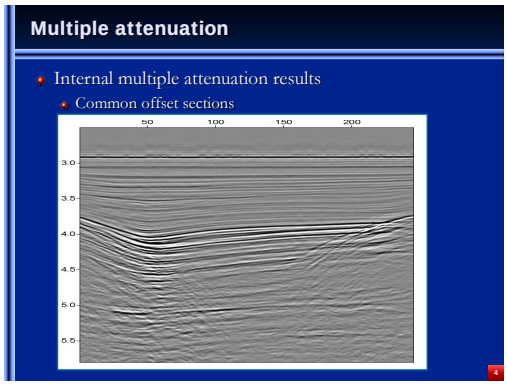

Figure 1d: Common offset sections after internal-multiple attenuation.

national Petroleum Technology Conference in Beijing, China was entitled "Strategies of Land Internal Multiple Elimination based on Inverse Scattering Series."

THE GOOD NEWS

At the 2013 post-convention SEG Internal Multiple Workshop (Thursday, September 26, 2013) it was encouraging to see nine of the eleven presentations describe and exemplify the industry-wide impact and stand-alone capability (for complex offshore and onshore plays) of the inverse-scattering-series (ISS) internal-multiple-attenuator. ISS internal-multiple attenuation has become fully mainstream within the petroleum industry.

THE OUTSTANDING OPEN ISSUES AND THE HIGH PRIORITY CHALLENGES WE FACE

With all this "good news", what could be the problem? Industry's portfolio/trend and focus today (and for the foreseeable future) makes it clear that a large and significant gap exists between the current challenge for the removal of free-surface multiples and internal multiples and the collective capabilities of the world-wide seismic exploration community (including, of course, M-OSRP). The specific issues are that: (1) the multiple generators and the subsurface properties are ill-defined and increasingly complex and (2) too often the multiple is proximal to or interfering with the primaries. The latter serious and significant issue can occur in many marine circumstances (*e.g.*, in the North Sea, Duquet et al. (2013)) and frequently occurs with onshore plays. That type of challenge of removing multiples proximal to, and/or overlapping with, primaries (without damaging primaries) is well beyond the collective capability of the petroleum industry, service companies and academic research groups and consortia to effectively address. It is not an

issue that new and more complete data collection and acquisition will, by itself, be able to address. We simply don't have the theory and fundamental concepts in place today that are needed for algorithm development, implementation and application. That's the reason we are unable to address that challenge faced today in the world-wide petroleum industry. To adequately address the current industry challenge (proximal and interfering multiples and primaries), we will need to be able to predict exactly the phase and amplitude of all internal multiples and surgically remove (eliminate) the multiples at all offsets, directly, and without subsurface information, and without damaging primaries. No one is able to provide that newer and necessary capability today for marine applications, let alone for the frequently more challenging onshore plays.

There is a need for new basic concepts and fundamental theory development that must begin with a frank and forthright recognition of the problem, its economic moment and significance, and the current technical gap. New concepts, theory and algorithms will need to be produced, and then will be followed by addressing the practical application, implementation and compute issues.

A PROPOSED PLAN

At the 2013 SEG International Conference (Recent Advances and the Road Ahead Session), we proposed and described a three-pronged strategy (please see the links below) that M-OSRP will pursue as a direct response to that challenge. It will have the potential to provide the necessary step-change increase in capability, and thereby to respond effectively to this current and pressing problem. Multiple removal has returned from being viewed as a relatively mature subject and project that helped M-OSRP "pay the rent" and is back to occupying center stage as a major fundamental research project.

The three-pronged strategy to respond to the current open issues and pressing challenges in removing multiples is as follows:
(1) Develop the ISS prerequisites for predicting the reference wave field (wavelet and radiation pattern) and producing deghosted data (in particular, for on-shore and ocean bottom acquisition) that are direct, and do not require subsurface information;
(2) Develop internal-multiple-**elimination** algorithms from the inverse scattering series;
(3) Develop a replacement for the energy-minimization criteria for adaptive subtraction, that derives from, and always aligns with and serves, the inverse-scattering-series free-surface and internal-multiple algorithms.
This three-pronged strategy represents a consistent and aligned processing chain, with one single objective: providing a direct and practical solution to the removal of all multiples, without requiring any subsurface information, and without damaging primaries.

The plan is first to progress and deliver items (2) and (3) for marine applications (since item (1) is relatively mature for marine application), and simultaneously to progress item (1) for onshore plays. Then, we will return to onshore exploration with the full suite of (1), (2) and (3) ingredients in place. Our plan is to progress in stages, with offshore delivery coming before onshore delivery.

RECENT PROGRESS ON A THREE-PRONGED PLAN TO ADDRESS CURRENT OPEN ISSUES AND CHALLENGES

In discussing the second of the three prongs, that is, the upgrade of the ISS internal multiple attenuator, we need to begin with a review of its strengths and limitations. The first order ISS internal multiple attenuator always attenuates all internal multiples of first order from all reflectors at once, directly and without subsurface information, automatically and without interpretive intervention. That's a tremendous strength, and is a constant and holds independent of the circumstances and complexity of the geology and the play. The primaries in the reflection data that enters the algorithm provides that delivery, without our requiring the primaries to be identified or in any way separated. The other events in the reflection data, that is, the internal multiples, when they enter the first order ISS internal multiple algorithm will alter and prep the higher order internal multiples and thereby assist and cooperate with higher order ISS internal multiple attenuation terms, to attenuate higher order internal multiples. That's a benefit and definite asset, and it's always in action and completely automatic. However, there is a downside, a limitation. There are cases when internal multiples that enter the first order attenuator can predict spurious or false events. That is a well-understood shortcoming of the leading order term, when taken in isolation, but is not an issue for the entire ISS internal multiple capability. It is anticipated by the ISS and higher order ISS internal multiple terms exist to precisely remove that issue of spurious event prediction, and taken together with the first order term, no longer experiences spurious event prediction. Chao Ma and Hong Liang provided those higher order terms and tests with complex multiple generators show the effectiveness of their spurious removal higher order ISS internal multiple attenuation algorithms (Liang et al., 2013; Ma and Weglein, 2013, 2014a,b, 2015a,b). In a similar way, there are higher order ISS internal multiple terms that provide the elimination of internal multiples when taken together with the leading order attenuator term. Yanglei Zou has produced a general elimination algorithm for first order internal multiples in a 1D acoustic or elastic earth. Please see Zou and Weglein (2013), Zou and Weglein (2014a), and Zou and Weglein (2014b, 2015a,b).

The first tests that evaluated the ability of the ISS attenuator

to perform in inelastic media showed it maintained its effectiveness in a medium where waves are attenuated and experiencing Q absorption, without any need or interest in knowing the absorptive mechanism (Wu and Weglein, 2014b). Our strategy includes eliminating internal multiples in an inelastic medium without knowing the absorptive/dispersive properties of the subsurface.

There are times, for example, in pre-salt plays in the North Sea, the deep water Gulf of Mexico, offshore Brazil and the Red Sea where the strategy and algorithms to eliminate internal multiples in an absorptive inelastic medium will be called for and necessary. There are other circumstances, for example, in certain on-shore and off-shore plays where elastic internal multiple elimination will be sufficient.

Progress to report within our plan and strategy to provide a next generation of multiple removal capability includes: Jing Wu et al. (Wu and Weglein, 2014a, 2015c,d,a,b) has contributed to extending off-shore Green's theorem preprocessing for wavelet estimation and deghosting to the on-shore elastic wave-field separation, in preparation for on-shore ISS internal multiple attenuation/elimination. Mayhan et al. (Mayhan et al., 2012; Mayhan and Weglein, 2013) has demonstrated the ability of Green's theorem marine preprocessing to be effective with SEAM data and marine field data. That paper reviewed and summarized the impact of that preprocessing on subsequent multiple removal (Zhang, 2007; Wang et al., 2012; Yang et al., 2013; Tang et al., 2013) that motives the on-shore extension. Jinlong Yang extended the ISS free surface and internal multiple algorithms to accommodate a source signature and radiation pattern (Yang et al., 2013). Shih-Ying Hsu (Hsu et al., 2011) described the relative insensitivity of the ISS internal multiple attenuator to the near surface reference velocity. Lin Tang (Tang and Weglein, 2014) presented a method to use an invariance of Green's theorem preprocessing to back out the reference medium properties. Xinglu Lin (Lin and Weglein, 2015a,b) demontrates the importance of including a 3D source in internal multiple algorithm (independent of the dimension of the subsurface). Qiang Fu has contributed the first published results on applying the ISS internal multiple attenuator to field data from Saudi Aramco and Encana (Fu et al., 2010; Fu and Weglein, 2014). Fang Liu (Liu and Weglein, 2013; Liu et al., 2011) has pioneered: (1) new wave equation migration methods for RTM and (2) ISS direct depth imaging without a velocity model, with viability demonstrated on the Kristin North Sea field data. The latter advances in depth imaging depend on an effective removal of multiples to be able to deliver their promise and impact.

CONCLUSIONS

Today, the ISS internal-multiple attenuator combined with an energy-minimization adaptive subtraction is the most capable method for removing internal multiples. However, the current ISS attenuator-plus-adaptive-subtraction method will fail under the pressing and prioritized challenge of removing internal multiples that are proximal to and/or interfering with primaries. In this note, we describe a three-pronged strategy for providing an effective response to this pressing and prioritized challenge while retaining and adding to the strengths of the current ISS internal-multiple attenuator. We have documented recent progress within that strategy to deliver the next generation of required multiple removal. To achieve that goal without requiring subsurface information requires Green's theorem wave separation methods for preprocessing, and mining the Inverse Scattering Series for increased effectiveness and predictive capability.

ACKNOWLEDGMENTS

We thank the M-OSRP sponsors for their constant encouragement and strong support. We thank Dr. Jim D. Mayhan for his assistance in preparing this Abstract.

REFERENCES

Araújo, F. V., 1994, Linear and non-linear methods derived from scattering theory: backscattering tomography and internal-multiple attenuation.: PhD thesis, Universidade Federal da Bahía, Brazil. (In Portuguese).

Araújo, F. V., A. B. Weglein, P. M. Carvalho, and R. H. Stolt, 1994, Inverse scattering series for multiple attenuation: An example with surface and internal multiples: 64th Annual International Meeting, SEG, Expanded Abstracts, 1039–1041.

Carvalho, P. M., 1992, Free-surface multiple reflection elimination method based on nonlinear inversion of seismic data: PhD thesis, Universidade Federal da Bahia. (In Portuguese).

Carvalho, P. M., and A. B. Weglein, 1994, Wavelet estimation for surface multiple attenuation using a simulated annealing algorithm: 64th Annual International Meeting, SEG, Expanded Abstracts, 1481–1484.

Duquet, B., A. Chavanne, J. P. Poupion, M. Rowlands, B. Santos-Luis, and J. Ugolini, 2013, Seimic processing and imaging in Central North Sea area - recents advances and remaining challenges: Presented at the 75th EAGE Conference Exhibition, Extended Abstracts.

Ferreira, A., 2011, Internal multiple removal in offshore Brazil seismic data using the Inverse Scattering Series: Master's thesis, University of Houston.

Fu, Q., Y. Luo, P. G. Kelamis, S. Huo, G. Sindi, S.-Y. Hsu, and A. B. Weglein, 2010, The inverse scattering series approach towards the elimination of land internal multiples: 80th Annual International Meeting, SEG, Expanded Abstracts, 3456–3461.

Fu, Q., and A. B. Weglein, 2014, Inverse scattering series internal multiple attenuation on encana data: 84th Annual International Meeting, SEG, Expanded Abstracts. (Submitted).

Goodway, W., 2013, Preliminary results of synthetic and land internal multiple removal by inverse scattering. Presentation given at the Post SEG Convention Workshop on Internal Multiples.

Goodway, W., and D. Mackidd, 2013, Multiples…the elephant in the room. Presentation given at the Post SEG Convention Workshop on Internal Multiples, Houston, Texas.

Griffiths, M., A. Pica, and B. Hung, 2013, Internal multiple removal solutions for multiple environments. Presentation given at the Post SEG Convention Workshop on Internal Multiples, Houston, Texas.

Hsu, S.-Y., P. Terenghi, and A. B. Weglein, 2011, The properties of the inverse scattering series internal multiple attenuation algorithm: Analysis and evaluation on synthetic data with lateral variations, choosing reference velocity and examining its sensitivity to near surface properties: M-OSRP 2010-2011 Annual Report, 16–28.

Hung, B., M. Wang, K. Yang, and X. Wu, 2014, Enhanced internal multiple attenuation in shallow water environment: SEG Expanded Abstract, 4147–4151.

Kelamis, P. G., Y. Luo, and A. Weglein, 2013a, Strategies of land internal multiple elimination based on inverse scattering series: Presented at the 6th International Petroleum Technology Conference.

Kelamis, P. G., Y. Luo, and A. B. Weglein, 2013b, Strategies of land internal multiple elimination based on inverse scattering series: Technical Session 21: Recent Development in Seismic Imaging/Processing, International Petroleum Technology Conference, Beijing, China, 26-28 March 2013, 1–4.

Liang, H., C. Ma, and A. B. Weglein, 2013, General theory for accommodating primaries and multiples in internal multiple algorithm: Analysis and numerical tests: 83rd Annual International Meeting, SEG, Expanded Abstracts, 4178–4183.

Lin, X., and A. Weglein, 2015a, The significance of incorporating a 3-d point source in the inverse scattering series internal multiple attenuator for a 1-d subsurface: M-OSRP Annual Report.

———, 2015b, The significance of incorporating a 3-d point source in the inverse scattering series internal multiple attenuator for a 1-d subsurface: To be submitted to SEG Expanded Abstract.

Liu, F., X. Li, and A. B. Weglein, 2011, Addressing innate data limitations in ISS imaging algorithms: distinct data regularization methods to address different types of data limitations, to facilitate and allow specific ISS imaging steps and goals: 2010 M-OSRP Annual Report, 50–81.

Liu, F., and A. B. Weglein, 2013, The first *wave theory* RTM, examples with a layered medium, predicting the source and receiver at depth and then imaging, providing the correct location and reflection amplitude at every depth location, and where the data includes primaries and all internal multiples: 2012 M-OSRP Annual Report, 284–335.

Luo, Y., P. G.Kelamis, Q. Fu, S. Huo, G. Sindi, S.-Y. Hsu, and A. Weglein, 2011, Elimination of land internal multiples based on the inverse scattering series: The Leading Edge, **30**, 884–889.

Ma, C., and A. Weglein, 2015a, A new inverse scattering series (iss) internal-multiple-attenuation algorithm that predicts the accurate time and approximate amplitude of the first-order internal multiples and reduces spurious events: Analysis and tests in 2d: To be submitted to SEG Expanded Abstract.

———, 2015b, A new inverse scattering series (iss) internal-multiple-attenuation algorithm that predicts the accurate time and approximate amplitude of the first-order internal multiples and reduces spurious events: Analysis and tests in 2d: M-OSRP Annual Report.

Ma, C., and A. B. Weglein, 2013, One dimensional analysis of the effects of including multiples as part of input into the ISS multiple removal algorithm: comparison between free-surface and internal: M-OSRP 2012-2013 Annual Report,

134–156.

———, 2014a, Including higher-order Inverse Scattering Series terms to address a serious shortcoming/problem of the internal-multiple attenuator: Exemplifying the problem and its resolution: 84th Annual International Meeting, SEG, Expanded Abstracts, 4124–4129.

———, 2014b, Inverse scattering series (ISS) leading-order internal-multiple-attenuation algorithm and higher-order modification to accommodate primaries and internal multiples as input: 1-D normal incident test on interfering events, and extension to multi-D: Presented at the M-OSRP 2013-2014 Annual Report.

Matson, K., D. Corrigan, A. Weglein, C.-Y. Young, and P. Carvalho, 1999, Inverse scattering internal multiple attenuation: Results from complex synthetic and field data examples: 69th Annual International Meeting, SEG, Expanded Abstracts, 1060–1063.

Mayhan, J. D., and A. B. Weglein, 2013, First application of Green's theorem-derived source and receiver deghosting on deep-water Gulf of Mexico synthetic (SEAM) and field data: Geophysics, **78**, WA77–WA89.

Mayhan, J. D., A. B. Weglein, and P. Terenghi, 2012, First application of Green's theorem derived source and receiver deghosting on deep water Gulf of Mexico synthetic (SEAM) and field data: 82nd Annual International Meeting, SEG, Expanded Abstracts, 1–5.

Tang, L., J. D. Mayhan, J. Yang, and A. B. Weglein, 2013, Using Green's theorem to satisfy data requirements of multiple removal methods: The impact of acquisition design: 83rd Annual International Meeting, SEG, Expanded Abstracts, 4392–4396.

Tang, L., and A. B. Weglein, 2014, Predicting reference-medium properties from invariances in greens theorem reference-wave prediction: towards an on-shore near surface medium and reference wave prediction: 29–42.

Terenghi, P., S.-Y. Hsu, A. B. Weglein, and X. Li, 2011, Exemplifying the specific properties of the inverse scattering series internal-multiple attenuation method that reside behind its capability for complex onshore and marine multiples: The Leading Edge, **30**, 876–882.

Wang, Z., A. B. Weglein, J. D. Mayhan, P. Terenghi, and C. Rivera, 2012, Green's theorem derived deghosting: fundamental analysis, numerical test results, and impact on ISS free-surface multiple elimination: 82nd Annual International Meeting, SEG, Expanded Abstracts, 1–5.

Weglein, A. B., F. V. Araújo, P. M. Carvalho, R. H. Stolt, K. H. Matson, R. T. Coates, D. Corrigan, D. J. Foster, S. A. Shaw, and H. Zhang, 2003, Inverse scattering series and seismic exploration: Inverse Problems, **19**, R27–R83.

Weglein, A. B., F. A. Gasparotto, P. M. Carvalho, and R. H. Stolt, 1997, An inverse-scattering series method for attenuating multiples in seismic reflection data: Geophysics, **62**, 1975–1989.

Wu, J., and A. Weglein, 2015a, Elastic green's theorem preprocessing for on-shore application in displacement space: To be submitted to SEG Expanded Abstract.

———, 2015b, Elastic green's theorem preprocessing for on-shore application in displacement space: M-OSRP Annual Report.

———, 2015c, Elastic green's theorem preprocessing for on-shore application in ps space: To be submitted to SEG Expanded Abstract.

———, 2015d, Elastic green's theorem preprocessing for on-shore application in ps space: M-OSRP Annual Report.

Wu, J., and A. B. Weglein, 2014a, Elastic Green's theorem preprocessing for on-shore internal multiple attenuation: Theory and initial synthetic data tests: 84th Annual International Meeting, SEG, Expanded Abstracts, 4299–4304.

———, 2014b, The first test and evaluation of the inverse scattering series internal multiple attenuation algorithm for an attenuating medium: 84th Annual International Meeting, SEG, Expanded Abstracts, 4130–4134.

Yang, J., J. D. Mayhan, L. Tang, and A. B. Weglein, 2013, Accommodating the source (and receiver) array in free-surface multiple elimination algorithm: Impact on interfering or proximal primaries and multiples: 83rd Annual International Meeting, SEG, Expanded Abstracts, 4184–4189.

Zhang, J., 2007, Wave theory based data preparation for inverse scattering multiple removal, depth imaging and parameter estimation: analysis and numerical tests of Green's theorem deghosting theory: PhD thesis, University of Houston.

Zou, Y., and A. Weglein, 2015a, An internal-multiple elimination algorithm for all first-order internal multiples for a 1d earth: M-OSRP Annual Report.

———, 2015b, An internal-multiple elimination algorithm for all first-order internal multiples for a 1d earth: To be submitted to SEG Expanded Abstract.

Zou, Y., and A. B. Weglein, 2013, A new method to eliminate first order internal multiples for a normal incidence plane wave on a 1D earth: 83rd Annual International Meeting, SEG, Expanded Abstracts, 4136–4140.

———, 2014a, The internal-multiple elimination algorithm for all first-order internal multiples generated from all reflectors for a 1d earth: algorithm, discussion and numerical tests: M-OSRP 2013-2014 Annual Report, 112–137.

———, 2014b, An internal-multiple *elimination* algorithm for all reflectors for 1D earth Part I: Strengths and limitations: Journal of Seismic Exploration, **23**, 393–404.

Multiples: signal or noise?

Arthur B. Weglein

M-OSRP/Physics Dept./University of Houston

March 17, 2015

Abstract

In this paper, we examine the topic of whether multiples are signal or noise. A seismic event is considered 'signal' if it intrinsically useful for the purposes of petroleum exploration. Since migration and migration-inversion are the methods used to extract subsurface information from seismic reflection data (events), we review the different wave propagation and imaging condition reside ingredients that behind our migration methods. That examination identifies a migration algorithm for locating and delineating targets in a finite volume with two way propagating waves and with the most advanced and physically meaningful and amplitude interpretable of the various imaging condition.

That migration algorithm allows an unequivocal response to the question at whether multiples are signal or noise. It is obvious that only primaries contribute to imaging. For an accurate discontinuous velocity multiples don't contribute to imaging, and for a continuous velocity, they will cause false images. However, we also show that when you have unrecorded primaries that multiples can be useful and

can provide an approximate image corresponding to the migration of the missing primary. To perform the latter process requires a velocity model, and all velocity analysis methods (e.g., tomography, CIG flatness, and FWI) assume that multiples have been removed.

Migration and migration velocity analysis require primaries, and only primaries are migrated. Multiples can be useful to provide the approximate image due to an unrecorded primary, but multiples need to be removed for velocity analysis and as events they are never migrated, that is they are not moved from their location in time to where they belong as a structure map in space.

Introduction

To begin, "signal" within the context of exploration seismology, and for the purpose of this paper, refers to the **events** in seismic recorded data used for extracting subsurface information. Migration and migration-inversion are the methods used to determine subsurface information from recorded seismic data. Methods that employ the wave equation for migration have two ingredients: (1) a wave propagation concept and (2) an imaging condition. Claerbout (1971) pioneered and developed three imaging conditions for seismic migration. He combined these imaging conditions with one-way wave propagation concepts to determine structure at depth. Claerbout's three landmark imaging conditions are: (1) the exploding reflector model, (2) the space and time coincidence of up and down waves, and (3) the predicted coincident source and receiver experiment at depth, at time equals zero. The third imaging condition stands alone for clarity and definitive-

ness and in its potential to be extended (by Stolt and his colleagues) for detailed angle dependent amplitude analysis at the target and for specular and non-specular reflection. The third imaging condition predicts an actual seismic experiment at depth, and that predicted experiment consists of all the events that experiment would record, if you had a source and receiver at that subsurface location. That experiment would have its own recorded events, the primaries and multiples for that predicted experiment. Stolt and his colleagues (Clayton and Stolt, 1981; Stolt and Weglein, 1985; Stolt and Benson, 1986; Weglein and Stolt, 1999; Stolt and Weglein, 2012) then provided the extension, for one way waves, of the Claerbout source and receiver experiment imaging condition (Imaging condition III) to allow for non coincident source and receiver at time equals zero, to realize both structural and inversion objectives. Due to causality, the offset dependence, at time equals zero, is highly localized about zero offset. The character of that singular function, sharply peaked in offset, is smooth in the Fourier conjugate space of offset wave-number, where the extraction of angle dependent plane wave reflection information naturally occurs. The latter extension and generalization produced migration-inversion (Stolt and Weglein, 1985), or first determining where anything changed (migration) followed by what specifically changed (inversion) at the image location. Recently, several papers by Weglein and his colleagues (Weglein et al., 2011a,b; Liu and Weglein, 2014) provided the next step in the evolution of migration based on the Claerbout predicted source and receiver experiment imaging condition (Imaging condition III), extending the prediction of the source and receiver experiment in a volume within which there are two way propagating waves. The latter

method of imaging based on Imaging condition III for a medium with two way propagating waves, plays a central role in the analysis of this paper. The predicted experiment, in the volume is realized by calling upon Green's theorem and a Green's function that along with its normal derivative vanishes on the lower portion of the closed surface.

All current RTM methods, for two way waves, are extensions and/or variants of the second of Claerbout's imaging conditions, and do not correspond to Claerbout's imaging condition III, a source and receiver experiment at depth.

Migration of two-way propagating waves

One doesn't have to look very far to find an example of the need for a predicted experiment at depth at points in a volume where there is two way wave propagation. Imaging from above or below a single horizontal reflector requires that two way wave propagation and Claerbout's predicted experiment imaging condition. Predicting a source and receiver experiment to locate and to determine the reflection coefficient from above, and, separately, from below, a single reflector requires predicting a source and receiver experiment inside a volume with two way propagating waves, two way wave migration, since the reflection data is upgoing (to a source and receiver experiment located) above the reflector and is downgoing (to that experiment when the source and receiver are located) below the reflector. Of course, the addition of, for example, multiples and/or diving waves also represent examples of two way wave propagation in the region where you want to

predict the seismic experiment at depth.

As we mentioned, migration methods that employ the wave equation have two ingredients: (1) a wave propagation or prediction model and (2) an imaging condition.

For the purposes of this discussion, we are going to adopt the Claerbout predicted coincident source and receiver experiment at time equals zero imaging condition for its peerless clarity, generality and quantitative information value. In the next section, we describe the evolution of the prediction of the source and receiver experiment component of Claerbout imaging condition III.

To predict the source and receiver experiment at depth

The classic well established mathematical physics foundation for predicting a wavefield inside a volume from (measured) values on the surface surrounding the volume was provided by Green (1828) as variants of what we now call Green's theorem. In the next several sections, we describe the evolution and application of Green's theorem for predicting the source and receiver experiment at depth, since that is an essential step in tracing the realization and application of Claerbout's imaging condition III. In that evolution, we will begin with: (1) the original infinite hemisphere volume model, then (2) the reasoning, need for, and description of the finite volume model for one way waves, and finally, (3) the need for and description of the finite volume model prediction of the source and receiver experiment for two way waves.

The material presented below on the evolution of the predicted source and receiver experiment has been published previously in the cited references. We cite and follow those references, but include that in this paper, for: (1) ease of the references, and (2) to make this paper self contained, and (3) because it plays such a critical role in Claerbout imaging III, which in turn is essential to understand the new message that this paper is communicating.

The infinite hemispherical migration model

The earliest wave equation migration pioneers considered the subsurface volume where the source and receiver experiment would be predicted as an infinite hemispherical half space with known mechanical properties, whose upper plane surface corresponded to the measurement surface, as in, *e.g.*, Schneider (1978) and Stolt (1978). See Figure 1.

Those two papers each made a tremendous conceptual and practical contribution to seismic imaging and exploration seismology. However, there are several problems with the infinite hemispherical migration model. That model assumes: (1) that all subsurface properties beneath the measurement surface (MS) are known, and (2) that an anticausal Green's function (*e.g.*, Schneider (1978)), with a Dirichlet boundary condition on the measurement surface, would allow measurements (MS) of the wavefield, P, on the upper plane surface of the hemisphere to determine the value of P within the hemispherical volume, V. The first assumption leads to the contradiction that we have not allowed for anything that is unknown to be determined

in our model, since everything within the closed and infinite hemisphere is assumed to be known. Within the infinite hemispherical model there is nothing and/or nowhere below the measurement surface where an unknown scattering point or reflection surface can serve to produce reflection data whose generating reflectors are initially unknown and being sought by the migration process.

The second assumption, in early infinite hemispherical wave equation migration, assumes that Green's theorem with wavefield measurements on the upper plane surface and using an anticausal Green's function satisfying a Dirichlet boundary condition can determine the wavefield within V. That conclusion assumes that the contribution from the lower hemispherical surface of S vanishes as the radius of the hemisphere goes to infinity. That is not the case, as we explicitly demonstrate below. To examine the various large radius hemispherical surface contributions to Green's theorem wave prediction in a volume, it is instructive to review the relationship between Green's theorem and the Lippmann-Schwinger scattering equation.

Green's theorem review

We begin with a space and time domain Green's theorem. Consider two wavefields P and G_0 that satisfy

$$(\nabla^2 - \frac{1}{c^2}\partial_t^2)P(\mathbf{r},t) \quad = \quad \rho(\mathbf{r},t) \tag{1}$$

and

$$(\nabla^2 - \frac{1}{c^2}\partial_t^2)G_0(\mathbf{r}, t, \mathbf{r}', t') \quad = \quad \delta(\mathbf{r} - \mathbf{r}')\delta(t - t'), \tag{2}$$

where we assume 3D wave propagation and the wavefield velocity c is a constant. ρ is a general source, *i.e.*, it represents both active sources (air guns, dynamite, vibrator trucks) and passive sources (heterogeneities in the earth). The causal solution to equation 1 can be written as

$$P(\mathbf{r}, t) = \int_{-\infty}^{t^+} dt' \int_{\infty} d\mathbf{r}' \rho(\mathbf{r}', t') G_0^+(\mathbf{r}, t, \mathbf{r}', t'), \tag{3}$$

where G_0^+ is the causal whole space solution to equation 2 and $t^+ = t + \epsilon$ where ϵ is a small positive quantity. The integral from t^+ to ∞ is zero due to the causality of G_0^+ (please see Morse and Feshbach, 1981, page 836). Equation 3 represents the linear superposition of causal solutions G_0^+ with weights $\rho(\mathbf{r}', t')$ summing to produce the physical causal wavefield solution to equation 1. Equation 3 is called the scattering equation and represents an all space and all time causal solution for $P(\mathbf{r}, t)$. It explicitly includes all sources and produces the field at all points of space and time. No additional boundary or initial conditions are required in equation 3.

Now consider the integral

$$\begin{aligned} &\int_0^{t^+} dt' \int_V d\mathbf{r}' (P\nabla'^2 G_0 - G_0 \nabla'^2 P) \\ &= \int_0^{t^+} dt' \int_V d\mathbf{r}' \nabla' \cdot (P\nabla' G_0 - G_0 \nabla' P), \end{aligned} \tag{4}$$

and we rewrite equation 4 using Green's theorem

$$\begin{aligned}&\int_0^{t^+} dt' \int_V d\mathbf{r}' \nabla' \cdot (P\nabla' G_0 - G_0 \nabla' P) \\ &= \int_0^{t^+} dt' \int_S dS' \hat{n} \cdot (P\nabla' G_0 - G_0 \nabla' P). \end{aligned} \tag{5}$$

This is essentially an identity, within the assumptions on functions and surfaces, needed to derive Green's theorem. Now choose $P = P(\mathbf{r}', t')$ and $G_0 = G_0(\mathbf{r}, t, \mathbf{r}', t')$ from equations 1 and 2. Then replace $\nabla'^2 P$ and $\nabla'^2 G_0$ from the differential equations 1 and 2.

$$\nabla'^2 G_0 = \frac{1}{c^2}\partial_t'^2 G_0 + \delta(\mathbf{r} - \mathbf{r}')\delta(t - t') \tag{6}$$

$$\nabla'^2 P = \frac{1}{c^2}\partial_t'^2 P + \rho(\mathbf{r}', t'), \tag{7}$$

and assume that the output variables $(\mathbf{r}, t)$ are in the intervals of integration: $\mathbf{r}$ in V, $t > 0$. The left hand side of equation 4 becomes:

$$\begin{aligned}&\int_0^{t^+} dt' \int_V d\mathbf{r}' \frac{1}{c^2}(P\partial_{t'}^2 G_0 - G_0 \partial_{t'}^2 P) + P(\mathbf{r}, t) \\ &- \int_0^{t^+} dt' \int_V d\mathbf{r}' \rho(\mathbf{r}', t') G_0(\mathbf{r}, t, \mathbf{r}', t'). \end{aligned} \tag{8}$$

The expression inside the first set of parentheses is a perfect derivative

$\partial_{t'}(P\partial_{t'}G_0 - G_0\partial_{t'}P)$ integrated over t'. The result is (for $\mathbf{r}$ in V and $t > 0$)

$$\begin{aligned} P(\mathbf{r},t) = &\int_V d\mathbf{r}' \int_0^{t^+} dt' \rho(\mathbf{r}',t') G_0(\mathbf{r},t,\mathbf{r}',t') \\ &- \frac{1}{c^2}\Big|_{t'=0}^{t^+} \int_V d\mathbf{r}' [P\partial_{t'}G_0 - G_0\partial_{t'}P] \\ &+ \int_0^{t^+} dt' \int_S dS' \hat{n} \cdot (P\nabla' G_0 - G_0 \nabla' P). \end{aligned} \tag{9}$$

We assumed differential equations 6 and 7 in deriving equation 9 and G_0 can be any solution of equation 6 in the space and time integrals in equation 4, causal, anticausal, or neither. Each term on the right hand side of equation 9 will differ with different choices of G_0, but the sum of the three terms will always be the same, $P(\mathbf{r},t)$.

If we now choose G_0 to be causal ($= G_0^+$) in equation 9, then in the second term on the right hand side the upper limit gives zero because G_0^+ and $\partial_{t'}G_0^+$ are zero at $t' = t^+$. The causality of G_0^+ and $\partial_{t'}G_0^+$ causes only the lower limit $t' = 0$ to contribute in

$$-\frac{1}{c^2}\Big|_{t'=0}^{t^+} \int_V d\mathbf{r}' [P\partial_{t'}G_0^+ - G_0^+\partial_{t'}P]. \tag{10}$$

If we let the space and time limits in equation 9 both become unbounded, *i.e.*, $V \to \infty$ and the t' interval becomes $[-\infty, t^+]$, and choose $G_0 = G_0^+$, the whole space causal Green's function, then by comparing equations 3 and 9 we see that for $\mathbf{r}$ in V and $t > 0$ that

$$\int_{-\infty}^{t^+} dt' \int_S dS' \hat{n} \cdot (P \nabla' G_0^+ - G_0^+ \nabla' P)$$
$$- \frac{1}{c^2} \Big|_{-\infty}^{t^+} \int_\infty d\mathbf{r}' [P \partial_{t'} G_0^+ - G_0^+ \partial_{t'} P] = 0. \quad (11)$$

$V = \infty$ means a volume that spans all space, and $\infty - V$ means all points in ∞ that are outside the volume V.

The solution for $P(\mathbf{r}, t)$ in equation 3 expresses the fact that if all of the factors that both create the wavefield (active sources) and that subsequently influence the wavefield (passive sources, *e.g.*, heterogeneities in the medium) are explicitly included in the solution as in equation 9, then the causal solution is provided explicitly and linearly in terms of those sources, as a weighted sum of causal solutions, and no surface, boundary or initial conditions are necessary or required.

If all sources for all space and all time are explicitly included as in equation 3, then there is no need for boundary or initial conditions to produce the physical/causal solution derived from a linear superposition of elementary causal solutions.

In the $(\mathbf{r}, \omega)$ domain equations 1 and 2 become

$$(\nabla^2 + k^2) P(\mathbf{r}, \omega) = \rho(\mathbf{r}, \omega) \quad (12)$$
$$(\nabla^2 + k^2) G_0(\mathbf{r}, \mathbf{r}', \omega) = \delta(\mathbf{r} - \mathbf{r}'), \quad (13)$$

where $\int_{-\infty}^{\infty} P(\mathbf{r}, t) e^{i\omega t} dt = P(\mathbf{r}, \omega)$ and $\int_{-\infty}^{\infty} G_0(\mathbf{r}, \mathbf{r}', t) e^{i\omega t} dt = G_0(\mathbf{r}, \mathbf{r}', \omega)$, t' is chosen to be zero in equation 2. The causal all space and temporal

frequency solution analogous to equation 3 is

$$P(\mathbf{r},\omega) = \int_{\infty} d\mathbf{r}' \rho(\mathbf{r}',\omega) G_0^+(\mathbf{r},\mathbf{r}',\omega), \tag{14}$$

and Green's second identity is

$$\int_V d\mathbf{r}' (P\nabla'^2 G_0 - G_0 \nabla'^2 P) = \oint_S dS'\, \hat{n} \cdot (P\nabla' G_0 - G_0 \nabla' P). \tag{15}$$

Substituting $\nabla^2 G_0 = -k^2 G_0 + \delta$ and $\nabla^2 P = -k^2 P + \rho$ in Green's theorem, we find

$$\left.\begin{array}{l} P(\vec{r},\omega) \\ \vec{r}\, in\, V \\ \\ 0 \\ \vec{r}\, out\, V \end{array}\right\} = \int_V d\mathbf{r}' P(\mathbf{r}',\omega)\delta(\mathbf{r}-\mathbf{r}')$$

$$= \int_V \rho(\vec{r}',\omega) G_0(\vec{r},\vec{r}',\omega)\, d\vec{r}' + \oint_S (P\nabla' G_0 - G_0 \nabla' P)\cdot \hat{n}\, dS. \tag{16}$$

There are no initial conditions (temporal boundary conditions), since in $\mathbf{r},\omega$ we have already explicitly included <u>all</u> time in Fourier transforming from t to ω. The contributions from sources for all times are explicitly included in the $(\vec{r},\omega)$ formulation of Green's Theorem, equation 16. In $\mathbf{r},\omega$ the only issue is whether sources are inside or outside V. The Lippmann-Schwinger equation (14) provides the causal physical solution for P for all $\mathbf{r}$ due to the sources in all space. Equation 14 is the $\mathbf{r},\omega$ version of equation 3 and must choose $G_0 = G_0^+$ (causal) to have P as the physical solution built

from the superposition (and linearity of weighted elementary causal solution, $G_0^+(\vec{r},\vec{r}',\omega)$). In contrast, equation 16 (as in equation 9) will produce the physical solution, P, with any solution for G_0 that satisfies equation 13.

Equation 14 can be written as:

$$\int_V \rho G_0^+ + \int_{\infty - V} \rho G_0^+. \tag{17}$$

For $\mathbf{r}$ in V, the second term on the right hand side of equation 16 (with choosing $G_0 = G_0^+$ in equation 16) equals the second term in equation 17, *i.e.*,

$$\int_{\infty - V} d\mathbf{r}' \rho G_0^+ = \oint_S dS' \hat{n} \cdot (P \nabla' G_0^+ - G_0^+ \nabla' P). \tag{18}$$

Thus, the first term in equation 17 gives contribution to P, for $\mathbf{r}$ in V due to sources in V, and the second term in equation 17 gives contribution to P, for $\mathbf{r}$ in V due to sources not in V. With $G_0 = G_0^+$

$$\oint_S dS' \hat{n} \cdot (P \nabla' G_0^+ - G_0^+ \nabla' P), \tag{19}$$

provides the contribution to the field, P, inside V due to sources outside the volume V.

What about the large $|\mathbf{r}|$ contribution of the surface integral to the field inside the volume? We use Green's theorem to predict that the contribution to the physical/causal solution P in V from the surface integral in Green's

theorem, in general, and also

$$\oint_S \{P\frac{\partial G_0^+}{\partial n} - G_0^+\frac{\partial P}{\partial n}\}dS, \tag{20}$$

vanishes as $|\mathbf{r}| \to \infty$ and in contrast the contribution to P in V from

$$\oint_S \{P\frac{\partial G_0^-}{\partial n} - G_0^-\frac{\partial P}{\partial n}\}dS, \tag{21}$$

does not vanish as $|\mathbf{r}| \to \infty$.

We begin with equation 16

$$\left.\begin{matrix} P(\vec{r},\omega) \\ \vec{r}\,in\,V \\ \\ 0 \\ \vec{r}\,out\,V \end{matrix}\right\} = \int_V d\mathbf{r}'\rho(\mathbf{r}',\omega)G_0^{\pm}(\mathbf{r},\mathbf{r}',\omega) + \oint_S dS'\{P\frac{\partial G_0^{\pm}}{\partial n} - G_0^{\pm}\frac{\partial P}{\partial n}\} \tag{22}$$

with G_0 either causal G_0^+ or anticausal G_0^-. Taking the limit $|\mathbf{r}| \to \infty$, then for $G_0 = G_0^+$ in 22, the contribution from the second term on the right hand side of equation 22 to P in V must go to zero, following a comparison with

$$P(\mathbf{r},\omega) = \int_\infty d\mathbf{r}'\rho(\mathbf{r}',\omega)G_0^+(\mathbf{r},\mathbf{r}',\omega), \tag{23}$$

(the Lippmann-Schwinger equation). However, with $G_0 = G_0^-$, and as $|\mathbf{r}| \to$

∞,

$$\oint_{S\to\infty} dS'\{P\frac{\partial G_0^-}{\partial n} - G_0^-\frac{\partial P}{\partial n}\} + \int_{V\to\infty} d\mathbf{r}'\rho(\mathbf{r}',\omega)G_0^-(\mathbf{r},\mathbf{r}',\omega)$$
$$= \int_{V\to\infty} d\mathbf{r}'\rho(\mathbf{r}',\omega)G_0^+(\mathbf{r},\mathbf{r}',\omega) + 0, \tag{24}$$

so

$$\oint_{S\to\infty} \{P\frac{\partial G_0^-}{\partial n} - G_0^-\frac{\partial P}{\partial n}\}dS$$
$$= \int_{\infty} [G_0^+(\mathbf{r},\mathbf{r}',\omega) - G_0^-(\mathbf{r},\mathbf{r}',\omega)]\rho(\mathbf{r}',\omega)d\mathbf{r}' \neq 0 \tag{25}$$

for all $\vec{r}$. Hence, the large distance surface contribution to the physical field, P, within V with the surface values of the physical field P and $\partial P/\partial n$ and an anticausal Green's function G_0^- will not vanish as $|\mathbf{r}| \to \infty$. As we mentioned earlier, this will be chosen to be one of the two problems with the infinite hemisphere model of seismic migration.

Although

$$P(\mathbf{r},\omega) = \int_{\infty} d\mathbf{r}'\rho(\mathbf{r}',\omega)G_0^-(\mathbf{r},\mathbf{r}',\omega), \tag{26}$$

would be a solution to equations 12 for all $\mathbf{r}$, it would not be the causal/physical solution to equations 12. And hence, in summary the contribution to the causal/physical solution for $P(\mathbf{r},\omega)$ for $\mathbf{r}$ in V from

$$\int_S dS' \left(P\frac{dG_0^+}{dn} - G_0^+\frac{dP}{dn}\right), \tag{27}$$

goes to zero as $|R| \rightarrow \infty$ where P and dP/dn corresponds to physical/causal boundary values of P and dP/dn, respectively. Physical measurements of P and dP/dn on S are always causal/physical values. The integral

$$\int_S dS' \left(P \frac{dG_0^-}{dn} - G_0^- \frac{dP}{dn} \right), \tag{28}$$

does not go to zero for anti-causal, G_0^-, and causal/physical P and dP/dn. The latter fact bumps up against a key assumption in the infinite hemisphere models of migration. That combined with the fact the infinite hemisphere model assumes the entire subsurface, down to "infinite" depth is known, suggests the need for a different model. That model is the finite volume model (see, e.g., Weglein et al., 2011a,b).

Finite volume model for migration

The finite model for migration assumes that we know or can adequately estimate earth medium properties (e.g., velocity) down to the reflector we seek to image. The finite volume model assumes that beneath the sought after reflector the medium properties are, and will remain, unknown. The "finite volume model" corresponds to the volume within which we assume the earth properties are known and within which we predict the wavefield from surface measurements. We have addressed the two issues of the infinite hemisphere model, *i.e.*, (1) the assumption we know the subsurface to all depths and (2) the contribution from the lower surface of the closed surface (as $|\mathbf{r}| \rightarrow \infty$) to the surface integral with an anticausal Green's function has

no contribution to the field being predicted in the volume.

The finite volume model removes both of the problematic assumptions behind the infinite hemisphere model. However, we are now dealing with a finite volume V, and with a surface S, consisting of upper surface S_U, lower surface S_L and walls, S_W (Figure 2). We only have measurements on S_U. In the following sections on: (1) Green's theorem for one-way propagation; and (2) Green's theorem for two-way propagation we show how the choice of Green's function allows the finite volume migration model to be realized. The construction of the Green's function that can accommodate two-way propagation in V, from contributions only on S_U, is a new contribution (Weglein et al., 2011a,b) that allows Claerbout Imaging III to be realized in a volume with two-way propagating waves. That places RTM on a firm wave theoretical Green's theorem basis, for the first time, with algorithmic consequence and with a clear mathematical physics understanding of the amplitude of the RTM image. The new Green's function is neither causal, anticausal, nor a combination of causal and/or anticausal Green's functions. In the important paper by Amundsen (1994), a finite volume model for wavefield prediction is developed which requires knowing (*i.e.*, predicting through solving an integral equation) for the wavefield at the lower surface. In parts I and II we show that for one and two-way propagation, respectively, that with a proper and distinct choice of Green's function, in each case, that absolutely no wavefield measurement information on the lower surface is required or needs to be estimated/predicted. Below, we review how to choose the Green's functions that allow for two-way propagation (for RTM application) without the need for measurements on the lower boundary of

the closed surface in Green's theorem.

Finite volume model for migration (Claerbout Imaging Condition III): Green's theorem for predicting the source and receiver experiment for one way waves

Consider a 1D upgoing plane wavefield $P = Re^{-ikz}$ propagating upward through the 1D homogeneous volume without sources between $z = a$ and $z = b$ (Figure 3). The wave P inside V can be predicted from

$$P(z,\omega) \;=\; \Big|_{z'=a}^{b} \{P(z',\omega)\; \frac{dG_0}{dz'}(z,z',\omega) - G_0(z,z',\omega)\frac{dP}{dz'}(z',\omega)\} \qquad (29)$$

with a Green's function, G_0, that satisfies

$$\left(\frac{d^2}{dz'^2} + k^2\right)\; G_0(z,z',\omega) \;=\; \delta(z-z') \qquad (30)$$

for z and z' in V. To be more precise in our language, we want to predict what a receiver at depth would record in terms of what a surface receiver records. We can easily show that for an upgoing wave, $P = Re^{-ikz}$, that if one chooses $G_0 \;=\; G_0^+$ (causal, $e^{ik|z-z'|}/(2ik)$), the lower surface (i.e. $z' = b$) constructs P in V and the contribution from the upper surface vanishes. On the other hand, if we choose $G_0 = G_0^-$ (anticausal solution $e^{-ik|z-z'|}/(-2ik)$), then the upper surface $z = a$ constructs $P = Re^{-ikz}$ in V and there is no contribution from the lower surface $z' = b$. The

effective sources $(P(b), P'(b))$ on the lower surface $z' = b$ with a causal Green's function, G_0^+, will produce a wave moving away from the source at $z = b$, hence upward in the region between $a < z < b$. At the upper surface $z' = a$, the anticausal G_0^- will produce waves moving towards the source at $z = a$ and hence moving upward for $a < z < b$. Also, using the anticausal Green's function, G_0^-, takes the wavefield (and its derivative) at $z = a$, and predict where it was previously at earlier time. For an upwave at $z = a$, that prediction of where it was previously is between $z = a$ and $z = b$.

Since in exploration seismology the reflection data is typically upgoing, once it is generated at the reflector, and we only have measurements at the upper surface $z' = a$, we choose an anticausal Green's function G_0^- in one-way wave prediction in the finite volume model. If ,in addition, we want to remove the need for dP/dz' at $z' = a$ we can impose a Dirichlet boundary condition on G_0^-, to vanish at $z' = a$. The latter Green's function is labeled G_0^{-D},

$$G_0^{-D} \;=\; -\frac{e^{-ik|z-z'|}}{2ik} - \left(-\frac{e^{-ik|z_I-z'|}}{2ik}\right), \tag{31}$$

where z_I is the image of z through $z' = a$. It is easy to see that $z_I = 2a - z$ and that

$$P(z) \;=\; -\frac{dG_0^{-D}}{dz'}(z, z', \omega)\Big|_{z'=a} P(a) \;=\; e^{-ik(z-a)} P(a), \tag{32}$$

in agreement with a simple Stolt FK phase shift for predicting an upward

propagating wave in a volume, that is between $a < z < b$ in terms of the wavefield at $z = a$. Please note that $P(z,\omega) = -dG_0^{-D}/dz'(z,z',\omega)|_{z'=a}P(a,\omega)$ back propagates $P(z' = a,\omega)$, not G_0^{-D}. The latter thinking that G_0^{-D} back propagates (or G_0^{+D} forward propagates) data is a fundamental mistake/flaw in many seismic back propagation migration and inversion theories (and in feedback multiple attenuation methods), that harkens back to the historically earlier and qualitative Huygens principle concepts that preceded Green's theorem and (as is clear in this example) can lead to amplitude issues and errors.

The Green's theorem 3D generalization that predicts an experiment with both sources and receivers at depth for a one way propagating wavefield in the volume is as follows:

$$\begin{aligned} & \int \frac{dG_0^{-D}}{dz_s}(x'_s, y'_s, z'_s, x_s, y_s, z_s; \omega) \\ & \times \left[\int \frac{dG_0^{-D}}{dz_g}(x'_g, y'_g, z'_g, x_g, y_g, z_g; \omega) D(x'_g, y'_g, z'_g, x'_s, y'_s, z'_s; \omega) dx'_g dy'_g \right] dx'_s dy'_s \\ = \; & M(x_s, y_s, z_s, x_g, y_g, z_g; \omega) \\ = \; & M(x_m, y_m, z_m, x_h, y_h, z_h; \omega), \end{aligned} \tag{33}$$

where $x_g + x_s = x_m$, $y_g + y_s = y_m$, $z_g + z_s = z_m$, $x_g - x_s = x_h$, $y_g - y_s = y_h$, and $z_g - z_s = z_h$. In the space and time domain, equation 33 corresponds to "uncollapsed migration", $M(x_m, y_m, z_m, x_h, y_h, z_h = 0; t = 0)$ that extends and generalizes the original Imaging Condition III, to non-zero offset at time equals zero. The retaining of k_h information (rather than stacking over k_h, for $x_h = 0$, hence, uncollapsed) allows for imaging and subsequent AVO

analysis in a multi-D subsurface (see *e.g.* Clayton and Stolt (1981), Stolt and Weglein (1985), Weglein and Stolt (1999)).

For one way propagating wavefields in the finite volume, choosing an anticausal Green's function allows only wavefield measurements on the upper surface to be sufficient to predict the wavefield in the volume. For two way propagating wavefields in a finite volume an anticausal Green's function will not allow for measurements on the upper surface to be sufficient to predict the wavefield in the volume. The Green's function for two-way propagation that will eliminate the need for data at the lower surface of the closed Green's theorem surface is found by finding a general solution to the Green's function for the medium in the finite volume model and imposing both Dirichlet and Neumann boundary conditions at the lower surface.

Predicting the source-receiver experiment at depth where the velocity configuration is $c(x, y, z)$

For a receiver predicted at a point (x, y, z) for determining $P(x, y, z, x_s, y_s, z_s, \omega)$, call on the Green's function, G_0, that satisfies

$$\left\{ \nabla'^2 + \frac{\omega^2}{c^2(x', y', z')} \right\} G_0(x', y', z', x, y, z, \omega)$$
$$= \delta(x - x')\delta(y - y')\delta(z - z') \tag{34}$$

for a source at (x, y, z). P is the physical/causal solution satisfying

$$\left\{ \nabla'^{\,2} + \frac{\omega^2}{c^2(x', y', z')} \right\} P(x', y', z', x_s, y_s, z_s, \omega)$$
$$= A(\omega)\delta(x' - x_s)\delta(y' - y_s)\delta(z' - z_s). \tag{35}$$

As a first step, we want to predict P for a point (x, y, z) in the volume V, for the actual/original source at (x_s, y_s, z_s). For (x, y, z) in V, arrange for G_0 and $\nabla' G_0 \cdot \hat{n}'$ to be zero for (x', y', z') on the lower surface S_L and the walls S_W of the finite volume. The solution for G_0 in V and on S can be found by a numerical modeling algorithm where the "source" is at (x, y, z) and the field, G_0, and $\nabla G_0 \cdot \hat{n}$ at (x', y', z') are both imposed to be zero on S_L and S_W. Once that model is run for a source at (x, y, z) for $G_0(x', y', z', x, y, z, \omega)$ [for every eventual predicted receiver point, (x, y, z), for P] where G_0 satisfies Dirichlet and Neumann conditions for (x', y', z') on S_L and S_W we output $G_0(x', y', z', x, y, z, \omega)$ for (x', y', z') on S_U (the measurement surface).

With that G_0, use Green's theorem to predict the receiver experiment at depth (with the original/actual source at (x_s, y_s, z_s))

$$P(x, y, z, x_s, y_s, z_s, \omega)$$
$$= \int_{S_g} \left\{ \frac{\partial G_0^{DN}}{\partial z'}(x, y, z, x', y', z', \omega) P(x', y', z', x_s, y_s, z_s, \omega) \right.$$
$$\left. - \frac{\partial P}{\partial z'}(x', y', z', x_s, y_s, z_s, \omega) G_0^{DN}(x, y, z, x', y', z', \omega) \right\} dx' dy', \tag{36}$$

where z' = fixed depth of the cable and (x_s, y_s, z_s) = fixed location of the source. S_g is the upper (measurement) surface containing receivers for a

fixed shot on the measurement surface. This predicts the receiver at (x, y, z), a point below the measurement surface in the volume V (for a source on the upper (measurement) surface) in terms of measurements on the upper surface, S_u.

Now predict the experiment corresponding to both the receiver and the source at depth, by invoking reciprocity and performing a Green's theorem surface integral over sources

$$\begin{aligned} & P(x_g, y_g, z, x, y, z, \omega) \\ = & \int_{S_s} \left\{ \frac{\partial G_0^{DN}}{\partial z_s}(x, y, z, x_s, y_s, z_s, \omega) P(x_g, y_g, z, x_s, y_s, z_s, \omega) \right. \\ & \left. - \frac{\partial P}{\partial z_s}(x_g, y_g, z, x_s, y_s, z_s, \omega) G_0^{DN}(x, y, z, x_s, y_s, z_s, \omega) \right\} dx_s dy_s. \end{aligned} \tag{37}$$

S_s is the upper (measurement) surface consisting of shots for a predicted receiver point at depth. The original/actual receiver locations on the upper surface are labeled (x', y', z') and the coordinates of the predicted receiver at depth is now relabeled (x_g, y_g, z) in equation 37, whereas it was (x, y, z) in equation 36. $P(x_g, y_g, z, x, y, z, \omega)$ is the field corresponding to a predicted receiver at (x_g, y_g, z) and the source to (x, y, z) and change to midpoint offset $P(x_m, x_h, y_m, y_h, z_m, z_h = 0, \omega)$ and

$$\begin{aligned} \int_{S_s} \int \int dx_s \, dy_s \, d\omega & \left\{ \frac{\partial G_0^{DN}}{\partial z_s}(x, y, z, x_s, y_s, z_s, \omega) P(x_g, y_g, z, x_s, y_s, z_s, \omega) \right. \\ & \left. - \frac{\partial P}{\partial z_s}(x_g, y_g, z, x_s, y_s, z_s, \omega) G_0^{DN}(x, y, z, x_s, y_s, z_s, \omega) \right\}, \end{aligned} \tag{38}$$

and Fourier transform over x_m, x_h, y_m, y_h to find $\widetilde{P}(k_{x_m}, k_{x_h}, k_{y_m}, k_{y_h}, k_{z_m}, z_h =$

$0, t = 0$). Equation 38 corresponds to Claerbout imaging condition III migration for a general $v(x, y, z)$ velocity configuration, within a volume that allows two way wave propagation in terms of data only on the upper surface.

Summary of wave equation migration for one way and two way propagating waves

Green's theorem based migration and migration-inversion require velocity information for location and velocity, density, absorption... for amplitude analyses at depth. When we say the medium is "known," the meaning of known depends on the goal: migration or migration-inversion. Backpropagation and imaging each evolved and then extended/generalized and merged into migration-inversion (Figure 4).

For one-way wave propagation the double downward continued data, D is

$$D(\text{at depth}) = \int_{S_s} \frac{\partial G_0^{-D}}{\partial z_s} \int_{S_g} \frac{\partial G_0^{-D}}{\partial z_g} D \, dS_g \, dS_s, \tag{39}$$

where D in the integrand = D(on measurement surface), $\partial G_0^{-D}/\partial z_s$ = anticausal Green's function with Dirichlet boundary condition on the measurement surface, s = shot, and g = receiver. For two-way wave double

downward continuation:

$$D(\text{at depth}) = \int_{S_s} \left[\frac{\partial G_0^{DN}}{\partial z_s} \int_{S_g} \left\{ \frac{\partial G_0^{DN}}{\partial z_g} D + \frac{\partial D}{\partial z_g} G_0^{DN} \right\} dS_g \right.$$
$$\left. + G_0^{DN} \frac{\partial}{\partial z_s} \int_{S_g} \left\{ \frac{\partial G_0^{DN}}{\partial z_g} D + \frac{\partial D}{\partial z_g} G_0^{DN} \right\} dS_g \right] dS_s, \quad (40)$$

where D in the integrands = D(on measurement surface). G_0^{DN} is *neither* causal nor anticausal. G_0^{DN} is not an *anti*causal Green's function; it is not the inverse or adjoint of any physical propagating Green's function. It is the Green's function needed for WEM RTM, that is RTM based on Claerbout Imaging Condition III. G_0^{DN} is the Green's function for the model of the finite volume that vanishes along with its normal derivative on the lower surface and the walls. If we want to use the anticausal Green's function of the two-way propagation with Dirichlet boundary conditions at the measurement surface then we can do that, but we will need measurements at depth and on the vertical walls. To have the Green's function for two-way propagation that doesn't need data at depth and on the vertical sides/walls, that requires a non-physical Green's function that vanishes along with its derivative on the lower surface and walls. Green's functions called upon in Green's theorem applications for migration are auxiliary functions and are specific point source wavefield solutions that satisfy the medium properties in the finite volume, and whose other properties are chosen for the convenience of the application. The commitment within Green's theorem applications is for the physical wavefield, $P(x, y, z, x_s, y_s, z_s)$, to relate to the physical reality and to have physical properties and boundary conditions.

In the next section, we take another step closer to our goal and objective. Having established a Claerbout imaging III methodology (please see equations 38 and 40) for a medium (a finite volume) with two way propagating waves, we are in a position to predict source and receiver experiments at depth and then a Claerbout III imaging result for data consisting of primaries and multiples. For the 1D layered medium, and a normal incident wave that we are examining, the data (consisting of primaries and internal multiples) and the predicted source and receiver experiment at depth results and the migration algorithm's results are analytic, transparent and the conclusions unambiguous. The role of recorded primaries and multiples in contributing first to the predicted source and receiver experiment at depth, and then to the (Claerbout Imaging III) coincident source and receiver experiment at time equals zero provides a definitive response to whether or not multiples contribute to seismic imaging. Understanding the physics behind the mathematics for the case of primaries and internal multiples, allows for an immediate set of similar conclusions to be drawn for the role of free surface multiples in migration. In the section below, we provide the explicit Green's theorem source and receiver at depth prediction and then Claerbout III imaging for a general layered medium where the velocity and density vary and where the data consists of primaries and internal multiples.

Green's theorem wavefield prediction in a 1D layered medium with velocity and density variation

First, let us assume the wave propagation problem in a (one dimensional) volume V bounded by a shallower depth a and deeper depth b to be governed by the differential equation:

$$\left\{ \frac{\partial}{\partial z'} \frac{1}{\rho(z')} \frac{\partial}{\partial z'} + \frac{\omega^2}{\rho(z')c^2(z')} \right\} D(z', \omega) = 0, \tag{41}$$

where $a \leq z' \leq b$ is the depth, and $\rho(z')$ and $c(z')$ are the density and velocity fields, respectively. In exploration seismology, we let the shallower depth a be the measurement surface where the seismic acquisition takes place (please see equation 29). The volume V is the finite volume defined in the "finite volume model" for migration, the details of which can be found in Weglein et al. (2011a). We measure D at the measurement surface $z' = a$, and the objective is to predict D anywhere between the shallower surface and another surface with greater depth, $z' = b$. This can be achieved via the solution of the wave-propagation equation in the same medium by an idealized impulsive source or Green's function:

$$\left\{ \frac{\partial}{\partial z'} \frac{1}{\rho(z')} \frac{\partial}{\partial z'} + \frac{\omega^2}{\rho(z')c^2(z')} \right\} G_0(z, z', \omega) = \delta(z - z'), \tag{42}$$

where z is the location of the source, and $a < z' < b$ and z increases in a downward direction. Abbreviating $G_0(z, z', \omega)$ as G_0, the solution for D in the interval $a < z < b$ is given by Green's theorem (the generalization of

equation 29 for the case of variable velocity and density):

$$D(z,\omega) = \frac{1}{\rho(z')}\left\{D(z',\omega)\frac{\partial G_0}{\partial z'} - G_0\frac{\partial D(z',\omega)}{\partial z'}\right\}\Bigg|_{z'=a}^{z'=b}, \tag{43}$$

where a and b are the shallower and deeper boundaries, respectively, of the volume to which the Green's theorem is applied. It is identical to equation (43) of Weglein et al. (2011a), except for the additional density contribution to the Green's theorem. Interested readers may find the derivation of equation (43) in section 2 of Liu and Weglein (2014).

Note that in equation (43), the field values on the closed surface of the volume V are necessary for predicting the field value inside V. The surface of V contains two parts: the shallower portion $z' = a$ and the deeper portion $z' = b$. In seismic exploration, the data at $z' = b$ is not available. For example, one of the significant artifacts of the current RTM procedures is caused by this phenomenon: there are events necessary for accurate wavefield prediction that reach $z' = b$ but never return to $z' = a$, as is demonstrated in Figure 5. The solution, based on Green's theorem without any approximation, was first published in Weglein et al. (2011a) and Weglein et al. (2011b). The basic idea is summarized below.

Since the wave equation is a second-order differential equation, its general solution has a great deal of freedom/flexibility. In other words, for a wave equation with a specific medium property, there are an infinite number of solutions. This freedom in choosing the Green's function has been taken advantage of in many seismic-imaging procedures. For example, the most popular choice in wavefield prediction is the physical solution G_0^+. In

downward continuing a one way propagating upgoing wavefield to a point in the subsurface, the anti-causal solution G_0^- is often used in equation 43 (as we have shown in the earlier sections, i.e., equations 31 and 32).

Weglein et al. (2011a,b) show that (with the G_0^- choice), the contribution from $z' = B$ will be zero under one way wave assumptions, and only measurements are required at $z' = A$. For two way propagating waves, G_0^- will not make the contribution for $z' = B$ vanish. However, if both G_0 and $\partial G_0/\partial z'$ vanish at the deeper boundary $z' = b$, where measurements are not available, then only the data at the shallower surface (i.e., the actual measurement surface) is needed in the calculation. We use G_0^{DN} to denote the Green's function with vanishing Dirichlet and Neumann boundary conditions at the deeper boundary.

Predicting the source and receiver at depth in a 1D layered medium

The original Green's theorem in equation (43) is derived to predict the wavefield (i.e., receivers) in the subsurface. It can also be used to predict the sources in the subsurface by taking advantage of reciprocity: the recording is the same after the source and receiver locations are exchanged.

Assuming we have data on the measurement surface: $D(z_g, z_s)$ (the ω dependency is ignored), we can use $G_0^{DN}(z, z_g)$ to predict it from the receiver

depth z_g to the target depth z:

$$D\left(z,z_s\right)=\frac{1}{\rho(z_g)}\left\{\frac{\partial D\left(z_g,z_s\right)}{\partial z_g}G_0^{DN}\left(z,z_g\right)-D\left(z_g,z_s\right)\frac{\partial G_0^{DN}\left(z,z_g\right)}{\partial z_g}\right\}. \tag{44}$$

Taking the $\frac{\partial}{\partial z_s}$ operation on equation (44), we have a similar procedure to predict $\partial D(z_g,z_s)/\partial z_s$ to the subsurface:

$$\frac{\partial D\left(z,z_s\right)}{\partial z_s}=\frac{1}{\rho(z_g)}\left\{\frac{\partial^2 D\left(z_g,z_s\right)}{\partial z_g\partial z_s}G_0^{DN}\left(z,z_g\right)-\frac{\partial D\left(z_g,z_s\right)}{\partial z_s}\frac{\partial G_0^{DN}\left(z,z_g\right)}{\partial z_g}\right\}. \tag{45}$$

Equations 44 and 45 are the 1D versions of equations 36 and 37.

With equations (44) and (45), we predict the data D and its partial derivative over z_s to the subsurface location z. According to reciprocity, $D\left(z,z_s\right)=E\left(z_s,z\right)$, where $E\left(z_s,z\right)$ is resulted from exchanging the source and receiver locations in the experiment to generate D at the subsurface. The predicted data $E\left(z_s,z\right)$ can be considered as the recording of receiver at z_s for a source located at z.

For this predicted experiment, the source is located at depth z, according to the Green's theorem, we can downward continue the recording at z_s to any depth shallower than or equal to z.

In seismic migration, we predict $E\left(z_s,z\right)$ at the same subsurface depth z

Depth Range	Velocity	Density
$(-\infty, a_1)$	c_0	ρ_0
(a_1, a_2)	c_1	ρ_1
(a_2, ∞)	c_2	ρ_2

Table 1: The properties of an acoustic medium with two reflectors, at depth a_1 and a_2.

with $G_0^{DN}(z, z_s)$ to have an experiment with coincident source and receiver:

$$\begin{aligned} E(z,z) &= \frac{1}{\rho(z_s)} \left\{ \frac{\partial E(z_s,z)}{\partial z_s} G_0^{DN}(z,z_s) - E(z_s,z) \frac{\partial G_0^{DN}(z,z_s)}{\partial z_s} \right\}, \\ &= \frac{1}{\rho(z_s)} \left\{ \frac{\partial D(z,z_s)}{\partial z_s} G_0^{DN}(z,z_s) - D(z,z_s) \frac{\partial G_0^{DN}(z,z_s)}{\partial z_s} \right\}. \end{aligned} \quad (46)$$

Equation 46 is the 1D version of equation 38.

If $z_s < z_g$ and we assume the data is deghosted, the $\frac{\partial}{\partial z_s}$ operation on $D(z_g, z_s)$ is equivalent to multiplying $-ik$, in this case, equation (46) can be further simplified:

$$E(z,z) = -\frac{1}{\rho(z_s) D(z,z_s)} \left\{ \frac{\partial G_0^{DN}(z,z_s)}{\partial z_s} + ikG_0^{DN}(z,z_s) \right\}. \quad (47)$$

Analytic examples (for a 1D layered medium)

As an example, for a 2-reflector model (with an ideal impulsive source located at z_s, the depth of receiver is $z_g > z_s$, the geological model is listed in Table 1), the data and its various derivatives can be expressed as:

$$
\begin{aligned}
D(z_g, z_s) &= \frac{\rho_0 x^{-1}}{2ik}\left\{y + \alpha y^{-1}\right\}, \\
\frac{\partial D(z_g, z_s)}{\partial z_g} &= \frac{\rho_0}{2} x^{-1}\left\{y - \alpha y^{-1}\right\}, \\
\frac{\partial D(z_g, z_s)}{\partial z_s} &= -\frac{\rho_0}{2} x^{-1}\left\{y + \alpha y^{-1}\right\}, \\
\frac{\partial^2 D(z_g, z_s)}{\partial z_g \partial z_s} &= \frac{\rho_0 k}{2i} x^{-1}\left\{y - \alpha y^{-1}\right\},
\end{aligned}
\tag{48}
$$

where $x = e^{ikz_s}$, $y = e^{ikz_g}$, $\sigma = e^{ikz}$, $\alpha = e^{ik(2a_1)}\left(R_1 + (1 - R_1^2)\beta\right)$, and $\beta = \sum_{n=0}^{\infty}(-1)^n R_1^n R_2^{n+1} e^{ik_1(2n+2)[a_2 - a_1]}$. And $R_1 = \frac{c_1\rho_1 - c_0\rho_0}{c_1\rho_1 + c_0\rho_0}$, and $R_2 = \frac{c_2\rho_2 - c_1\rho_1}{c_2\rho_2 + c_1\rho_1}$ are the reflection coefficients from geological boundaries.

The predicted experiment above the first reflector for Claerbout Imaging Condition III

For $z < a_1$, the boundary values of the Green's function are:

$$
\begin{aligned}
G_0^{DN}(z, z_g) &= \rho_0 \tfrac{e^{ik(z - z_g)} - e^{ik(z_g - z)}}{2ik} = \rho_0 \tfrac{\sigma y^{-1} - \sigma^{-1} y}{2ik}, \\
G_0^{DN}(z, z_s) &= \rho_0 \tfrac{\sigma x^{-1} - \sigma^{-1} x}{2ik}, \\
\tfrac{\partial G_0^{DN}(z, z_g)}{\partial z_g} &= \rho_0 \tfrac{\sigma y^{-1} + \sigma^{-1} y}{-2}, \\
\tfrac{\partial G_0^{DN}(z, z_s)}{\partial z_s} &= \rho_0 \tfrac{\sigma x^{-1} + \sigma^{-1} x}{-2}.
\end{aligned}
\tag{49}
$$

After substituting equation (48) into equation (47), we have:

$$
E(z, z) = \frac{1 + e^{ik(2a_1 - 2z)}\left(R_1 + (1 - R_1^2)\beta\right)}{2ik/\rho_0}. \tag{50}
$$

The result above can be Fourier transformed into the time domain to

have:

$$\begin{aligned}\frac{E(z,z,t)}{-\rho_0 c_0/2} =& H(t) + R_1 H\left(t - t_1\right) + (1 - R_1^2) \\ & \times \sum_{n=0}^{\infty} (-1)^n R_1^n R_2^{n+1} H\left(t - t_1 - (2n+2)t_2\right), \end{aligned} \tag{51}$$

where $t_1 = \frac{2a_1 - 2z}{c_0}$ and $t_2 = \frac{(a_2 - a_1)}{c_1}$. Balancing out the $-\frac{\rho_0 c_0}{2}$ factor*, the data after removing the direct wave is denoted as $\hat{D}(z,t) = \frac{-2}{\rho_0 c_0} E(z,z,t) - H(t)$:

$$\begin{aligned}\hat{D}(z,t) =& R_1 H\left(t - t_1\right) \\ & + (1 - R_1^2) \sum_{n=0}^{\infty} (-1)^n R_1^n R_2^{n+1} H\left(t - t_1 - (2n+2)t_2\right). \end{aligned} \tag{52}$$

We take the imaging condition as first letting $z \to a_1$ through values smaller that a_1, and then (subsequently) taking the limit as $t \to 0^+$, that is, approaching zero from positive values, we find:

$$\lim_{t \to 0^+} \left(\lim_{z \to a_1^-} \hat{D}(z,t) \right) = R_1, \tag{53}$$

where

$$\begin{aligned} a_1^- &= a_1 - \epsilon_1 \qquad && \epsilon_1 > 0, \\ 0^+ &= 0 + \epsilon_2 \qquad && \epsilon_2 > 0, \end{aligned} \tag{54}$$

and we obtained the image of the first reflector at the actual depth a_1 with the correct reflection coefficient as amplitude.

*This factor is present in the incident wave, i.e., causal Green's function for a homogeneous medium with density ρ_0 and velocity c_0.

Predicting the source and receiver experiment between the first and second reflectors

For $a_1 < z < a_2$, we have:

$$\begin{aligned} G_0^{DN}(z, z_g) &= [(R_1\lambda - \lambda^{-1})\mu + (\lambda - R_1\lambda^{-1})\mu^{-1}]/[2ik_1(1+R_1)/\rho_1], \\ \frac{\partial G_0^{DN}(z, z_g)}{\partial z_g} &= [(R_1\lambda - \lambda^{-1})\mu - (\lambda - R_1\lambda^{-1})\mu^{-1}]/[2k_1(1+R_1)/(k\rho_1)], \end{aligned} \tag{55}$$

where $\lambda = e^{ik_1(z-a_1)}$, $\mu = e^{ik(z_g-a_1)}$, $k_1 = \frac{\omega}{c_1}$. Substituting equation (55) into equation (48), and transforming the aforementioned result into the time domain, we have:

$$\begin{aligned} E(z,z,t)/(-\rho_1 c_1/2) = H(t) &+ 2\sum_{n=1}^{\infty}(-1)^n R_1^n R_2^n H\{t - [2n(a_2-a_1)/c_1]\} \\ &+ \sum_{n=0}^{\infty}(-1)^{n+1} R_1^{n+1} R_2^n H\{t - [2z + 2na_2 - 2(n+1)a_1]/c_1\} \\ &+ \sum_{n=0}^{\infty}(-1)^n R_1^n R_2^{n+1} H\{t - [2(n+1)a_2 - 2na_1 - 2z]/c_1\}. \end{aligned} \tag{56}$$

Balancing out the $-\rho_1 c_1/2$ factor, the data after removing the direct wave is denoted as $\hat{D}(z,t) = \frac{-2}{\rho_1 c_1} E(z,z,t) - H(t)$:

$$\begin{aligned} \hat{D}(z,t) =& 2\sum_{n=1}^{\infty}(-1)^n R_1^n R_2^n H\{t - [2n(a_2-a_1)/c_1]\} \\ &+ \sum_{n=0}^{\infty}(-1)^{n+1} R_1^{n+1} R_2^n H\{t - [2z + 2na_2 - 2(n+1)a_1]/c_1\} \\ &+ \sum_{n=0}^{\infty}(-1)^n R_1^n R_2^{n+1} H\{t - [2(n+1)a_2 - 2na_1 - 2z]/c_1\}, \end{aligned} \tag{57}$$

and after taking the $t = 0^+$ imaging condition, we have:

$$\hat{D}(z,t) = \begin{cases} -R_1 & \texttt{if } (z = a_1 + \epsilon_1) \\ 0 & \texttt{if } (a_1 < z < a_2) \\ R_2 & \texttt{if } (z = a_2 - \epsilon_2) \end{cases}, \tag{58}$$

where $\epsilon_1, \epsilon_2 \to 0$ and then $t \to 0^+$. Note that in the previous section, i.e., to image above the first reflector at a_1, we obtain the amplitude R_1 when z approach a_1 from above. In this section we image below the first reflector at a_1, the amplitude of the image is $-R_1$ when z approaches a_1 from below, as it should.

Predicting the source and receiver experiment below the second reflector

For $z > a_1$, the boundary value of the Green's function is:

$$G_0^{DN}(z, z_g) = \frac{1}{2ik_2(1+R_1)(1+R_2)/\rho_2} \tag{59}$$
$$\times \{[\nu^{-1}(R_2\lambda - \lambda^{-1}) + R_1\nu(\lambda - R_2\lambda^{-1})]\mu + [R_1\nu^{-1}(R_2\lambda - \lambda^{-1}) + \nu(\lambda - R_2\lambda^{-1})]\mu^{-1}\},$$

where $\lambda = e^{ik_2(z-a_2)}$, $\mu = e^{ik(z_g - a_1)}$, and $\nu = e^{ik_1(a_2-a_1)}$, $k_2 = \omega/c_2$.

The result of the predicted experiment can be expressed as:

$$\begin{aligned} E(z,z) =& (\rho_2/2ik_2)[1 - R_2 e^{ik_2(2z-2a_2)} + (1-R_2^2)e^{ik_2(2z-2a_2)} \\ & \times \sum_{n=0}^{\infty} (-1)^{n+1} R_1^{n+1} R_2^n e^{ik_1(2n+2)(a_2-a_1)}]. \end{aligned} \tag{60}$$

The time domain counterpart of the equation above is:

$$E(z,z,t) = -(\rho_2 c_2/2)\{H(t) - R_2 H[t-(2z-2a_2)/c_2] + (1-R_2^2)H[t-(2z-2a_2)/c_2-(2n+2)(a_2-a_1)/c_1]. \quad (61)$$

Balancing out the $-\rho_2 c_2/2$ factor, the data after removing the direct wave is denoted as $\hat{D}(z,t) = (-2/\rho_2 c_2)E(z,z,t) - H(t)$:

$$\hat{D}(z,t) = - R_2 H[t-(2z-2a_2)/c_2] + (1-R_2^2)H[t-(2z-2a_2)/c_2-(2n+2)(a_2-a_1)/c_1], \quad (62)$$

and after taking the $t = 0^+$ imaging condition, we have:

$$\hat{D}(z,t) = \begin{cases} -R_2 & \texttt{if } (z = a_2 + \epsilon) \\ 0 & \texttt{if } (a_2 < z) \end{cases}, \quad (63)$$

where $\epsilon \to 0^+$. Note that in the previous section, i.e., to image between the first and second reflectors, we obtain the amplitude R_2 when z approach a_2 from above. In this section we image below the second reflector at a_2, the amplitude of the image is $-R_2$ when z approaches a_2 from below, as it should. Please see Figure 6.

This analysis allows us to see how the recorded events contribute to the image for source and receiver experiments above and below each reflector.

Multiples: do they contribute to the image?

How do the recorded events (primaries and free surface and internal multiples) contribute to: (1) the predicted source and receiver experiment at depth and (2) the image at depth that locates and identifies the reflector (the reflection coefficient)?. In this section, we examine, follow and report (for the latter two way-wave wave migration examples) how the individual events (primaries, free surface multiples and internal multiples) each contribute to: (1) the predicted coincident source and receiver experiment at each depth, and then (2) the time equals zero imaging condition evaluation of that experiment.

The example we present provides for the first time an analysis that starts with and follows how surface recorded data (with primaries and free surface and internal multiples) influences and contributes to the subsequent coincident source and receiver experiment at depth and then imaging at each depth level, and specifically: (1) how each individual recorded event in the surface data is involved and contributes to the new individual "events" of the predicted source and receiver experiment at each different depth, and then (2) what happens to the recorded surface event's individual contribution for the predicted experiment at each depth and then how the surface recorded events contribute when applying the time equals zero imaging condition. Please see three cases we examine in the three videos (http://mosrp.uh.edu/events/event-news/multiples-signal-noise-a-clear-example-with-a-definitive-conclusion) and corresponding slide snapshots. In the three examples a unit amplitude plane wave is normal incident on a one-D earth. The first case (please see Figures 7-9) is the example of a single reflector and a single primary, with no free surface or internal multiples. That single

primary is the sole contributor to the events in the experiment above and below that single reflector. When the time equals zero condition is applied, the recorded primary is the only recorded event contributing to the experiment at depth and to the image, both below and above the reflector. For the case of primaries and internal multiples, the detailed mathmatical analysis based on the new two way (Claerbout Imaging III) migration behind these figures is found in equation 49 - 63, in the previous section.

The second case has a single primary and a free surface multiple (please see Figures 10-12). The predicted experiment above the reflector has two surface event contributions, from the primary and the free surface multiple. When the time equals zero imaging condition is applied then only the recorded primary contributes to the image. Below the reflector the predicted experiment has two events, a primary that has a downward reflection at the reflector, and a primary from the source to the free surface and then down to the predicted receiver. The original free surface multiple in the recorded data became a primary in the predicted experiment below the reflector. Hence, the primary and free surface multiple in the recorded data became two primaries for the experiment below the reflector. However, once the time equals zero imaging condition is applied to the predicted experiment, only the recorded primary contributes to the image and the recorded multiple does not.

In the third case (please see Figures 13-17), we consider a subsurface with two reflectors and two recorded primaries and one internal multiple. As you focus on the history that each individual event in the recorded data follows and then contributes to, first in the experiment at depth and then

to the image at each depth, you reach the following conclusion. Recorded primaries and free surface multiples and internal multiples all contribute to events for the predicted experiment at depth. Sometimes multiples in the recorded data even become primaries in the predicted experiment at depth. However, only the recorded primaries contribute to the image at every depth. If you removed the multiples in the recorded data, the coincident source and receiver experiment at depth would change, but once the $t = 0$ imaging condition is applied, the image's location at the correct depth or its amplitude, the reflection coefficient, will not be affected. If, in these examples, your data consisted of only multiples, you would have no image at any depth.

Hence, for the purposes of imaging and inversion, primaries are signal and multiples are not. Multiples are not evil, or bad or irresponsible, but as events they are simply not needed for locating and identifying targets.

The methods that seek to use multiples today as "signal" are really seeking to approximate images due to primaries that have not been recorded, due to limitations in acquisition, and to address the subsequent limited illumination that missing primaries can cause. They are not really using the multiple itself as an event to be followed into the subsurface for imaging purposes. The figure (18) illustrates the idea.

Assume a multiple is recorded, and a long offset primary that is a subevent is also recorded. The idea is to extract and predict the image due to an unrecorded primary, smaller offset, from the recorded multiple and the recorded longer offset primary. All the various incarnations that are using multiples as "signal" are actually, and entirely after removing a recorded

longer offset primary to have the output as a shorter offset unrecorded primary. It's the missing image of unrecorded primaries that the method is seeking to produce and to utilize.

The recipe of taking the multiples back in time and the primaries forward in time and arranging for Imaging Condition II (not III) produces that output. However, that procedure is not migrating the multiples, in the sense of the multiple as an event.

In a Recent Advances and the Road Ahead presentation, "Multiples: signal or noise?", Weglein (2014) (please see `https://vts.inxpo.com/scripts/Server.nxp?LASCmd=L:0&AI=1&ShowKey=21637&LoginType=0&InitialDisplay=1&ClientBrowser=0&DisplayItem=NULL&LangLocaleID=0&RandomValue=1415030021699`) showed a field data example, from PGS, where there was clear added-value demonstrated from beyond actual primaries, plus the approximate images of primaries predicted from multiples, compared to the image from the original primaries.

There is another issue: in order to predict a free surface or internal multiple, the primary sub-events that constitute the multiple must be in the data, for the multiple prediction method to recognize an event as a multiple. If the short offset primary is not recorded, the multiple that is composed of the short and long offset multiple will not be predicted as a multiple. That issue and basic contradiction within the method is recognized by those who practice this method, and instead of predicting the multiple, they use all the events in the recorded data, primaries and multiples, and the multiples can be useful for predicting approximate images of missing primaries but the primaries in the data will cause artifacts. There are other artifacts that

also come along with this method that have been noted in the literature.

The reality of today's methods for using multiples to predict missing "primaries" are aimed at structural improvement, at best, and are not claiming, seeking or delivering the amplitude and phase fidelity of the predicted primary. Those who go so far as to advocate using fewer sources and/or more widely separated cables because recorded multiples can produce "something like" a missing primary need to understand the deficits and costs including generating artifacts, less effectiveness with deeper primaries and the amplitude fidelity of the predicted primary. Whether the tradeoff makes sense ought to depend on, in part, the depth of the target, the type of play, and whether a structural interpretation or amplitude analysis is planned within a drilling program and decision.

By the way, this entire wave equation migration analysis (Claerbout Imaging Condition III) is ultimately based on the idea from Green (1828) that to predict a wave (an experiment) inside a volume you need to know the properties of the medium in the volume.

There is an alternative view: The inverse scattering series methods communicates that all processing objectives can be achieved directly and without subsurface information. The inverse scattering series treat multiples as a form of coherent noise, and provide distinct subseries to remove free surface and internal multiples before the inverse scattering subseries for imaging and inversion achieve their goals using only primaries Weglein et al. (2003) and Weglein et al. (2012). If the inverse scattering series needed multiples to perform migration and inversion, it would not have provided subseries that remove those multiply reflected events. With a velocity model (wave

equation migration) or without a velocity model (inverse scattering series imaging) only primaries are signal , in the sense that they are the events need to locate and delineate targets. If you want to consider a multiple as a conditional 'signal', that can at times enhance imaging, there is no harm in that. But to say that multiples are being migrated, and/or are the same footing as primaries, is simply not ture and relates more to marketing, than to a realistic view of the role that primaries and multiples play in seismic exploration. A complete set of recorded primaries, processed with a wave theory migration (versus asymptotic or ray migration) would not need or benefit from multiples. Multiples need to be removed before performing a velocity analysis using, e.g., tomography, CIG flatness or FWI. And a velocity model is required by all the methods that seek to use multiples to enhance imaging. Another question: what if the assumed unrecorded primary event in the method is actually recorded. Will the image of the recorded primary and the image of the approximate version of the recorded primary from the multiple damaged the image of the actual primary, that has been assumed to not have been recorded?

Conclusions

Hence, primaries are signal and multiples can be useful, at times, for predicting the image of missing primaries. But it's primaries that are signal, that we use for structure and inversion.

Primaries are signal for all methods that seek to locate and identify targets.

The above three examples assumed you had an accurate **discontinu-**

ous velocity and density model. Given an accurate discontinuous velocity and density model, and data with primaries and multiples, then we have convincingly demonstrated that only primaries contributed to the images at every depth. If you predicted the source and receiver experiment at depth with a **smooth** velocity, it is possible to correctly locate (but not invert) each recorded primary event—but with a smooth velocity model every free surface and internal multiple will then produce a false image/artifact/event. If you removed the multiples first you can correctly locate structure from recorded primaries using a smooth velocity model.

Hence, we conclude that the inability, in practice, to provide an accurate discontinuous velocity model is why multiples need to be removed before imaging. That reality has been the case, is the case, and will remain true for the foreseeable future. Multiples need to be removed before velocity analysis and they need to be removed before imaging.

Many things are useful for creating primaries: money, the seismic boat, the air-guns, the observer, the cable, computers, etc., but we don't call all useful things signal.

Methods to provide a more complete set of primaries are to be supported and encouraged. Those methods include: (1) advances in and more complete acquisition, (2) interpolation and extrapolation methods, and (3) using multiples to predict missing primaries. However, a recorded primary is still the best and most accurate way to provide a primary, and the primary is the seismic signal.

A multiple can be useful, at times, for providing an unrecorded synthesized primary that is a subevent of the multiple. Given a data set consist-

ing of: (1) the recorded primaries, (2) the synthesized primaries, (3) the free surface multiples, and (4) internal multiples, the practical necessity of using a smooth continuous velocity for migration demands that all multiples be removed before migration. In exploration seismology, migration and migration-inversion are methods we employ to locate and identify structure. Claerbout Imaging Condition III is the most definitive and quantitative migration concept and procedure. This paper demonstrated that Claerbout Imaging Condition III clearly communicates that primaries are signal and multiples are noise. The original and intuitive migration idea that takes events in time traces to the location of structure in space, only has meaning for primaries. The most sophisticated and physically well-founded migration theory, beased on Claerbout Imaging Condition III, agrees with that assessment and conclusion.

Acknowledgements

M-OSRP sponsors are thanked for their encouragement and support. The author would like to thank Nizar Chemingui, Dan Whitmore and Alejandro Valenciano (PGS), Robert H. Stolt (ConocoPhillips, retired), Clement Kostov and Richard Coates (Schlumberger), Scott Morton (Hess) and Fred Hoffman (Shell, retired) for constructive and worthwhile discussions that benefited this paper. The author gratefully acknowledges PGS for showing how multiples can be used to predict unrecorded primaries, and Lundin Malaysia and PETRONAS for showrights. I would like to thank Yi Luo and Tim Keho (Saudi Aramco) and David Monk and Bill Goodway (Apache

Corp.) for stimulating and useful discussions that motivated and benefited this paper. The author would also thank Fang Liu, Chao Ma, Jim Mayhan, Jinlong Yang and Yanglei Zou for assistance in preparing this paper.

References

Amundsen, L., 1994, The propagator matrix related to the Kirchhoff-Helmholtz integral in inverse wavefield extrapolation: Geophysics, **59**, 1902–1910.

Claerbout, J. F., 1971, Toward a unified theory of reflector mapping: Geophysics, **36**, 467–481.

Clayton, R. W., and R. H. Stolt, 1981, A Born-WKBJ inversion method for acoustic reflection data: Geophysics, **46**, 1559–1567.

Green, G., 1828, An essay on the application of mathematical analysis to the theories of electricity and magnetism: Privately published. (Available at `http://babel.hathitrust.org/cgi/pt?id=hvd.yl131n;view=1up;seq=9`).

Liu, F., and A. B. Weglein, 2014, The first wave equation migration RTM with data consisting of primaries and internal multiples: theory and 1D examples: Journal of Seismic Exploration, **23**, 357–366.

Morse, P. M., and H. Feshbach, 1981, Methods of theoretical physics: Feshbach Publishing, LLC. (Original publication 1953 by The McGraw-Hill Companies, Inc.).

Schneider, W. A., 1978, Integral formulation for migration in two and three dimensions: Geophysics, **43**, 49–76.

Stolt, R. H., 1978, Migration by Fourier transform: Geophysics, **43**, 23–48.

Stolt, R. H., and A. K. Benson, 1986, Seismic migration: theory and practice: Geophysical Press.

Stolt, R. H., and A. B. Weglein, 1985, Migration and inversion of seismic data: Geophysics, **50**, 2458–2472.

———, 2012, Seismic imaging and inversion: Application of linear inverse theory: Cambridge University Press.

Weglein, A. B., 2014, Multiples: Signal or noise?: 84th Annual International Meeting, SEG, Expanded Abstracts, 4393–4399.

Weglein, A. B., F. V. Araújo, P. M. Carvalho, R. H. Stolt, K. H. Matson, R. T. Coates, D. Corrigan, D. J. Foster, S. A. Shaw, and H. Zhang, 2003, Inverse scattering series and seismic exploration: Inverse Problems, **19**, R27–R83.

Weglein, A. B., F. Liu, X. Li, P. Terenghi, E. Kragh, J. D. Mayhan, Z. Wang, J. Mispel, L. Amundsen, H. Liang, L. Tang, and S.-Y. Hsu, 2012, Inverse scattering series direct depth imaging without the velocity model: first field data examples: Journal of Seismic Exploration, **21**, 1–28.

Weglein, A. B., and R. H. Stolt, 1999, Migration-inversion revisited (1999): The Leading Edge, **18**, 950–952, 975.

Weglein, A. B., R. H. Stolt, and J. D. Mayhan, 2011a, Reverse-time migration and Green's theorem: Part I — The evolution of concepts, and setting the stage for the new RTM method: Journal of Seismic Exploration, **20**, 73–90.

———, 2011b, Reverse time migration and Green's theorem: Part II — A new and consistent theory that progresses and corrects current RTM

concepts and methods: Journal of Seismic Exploration, **20**, 135–159.

Figures

Figure 16:

Figure 17:

Figure 18:

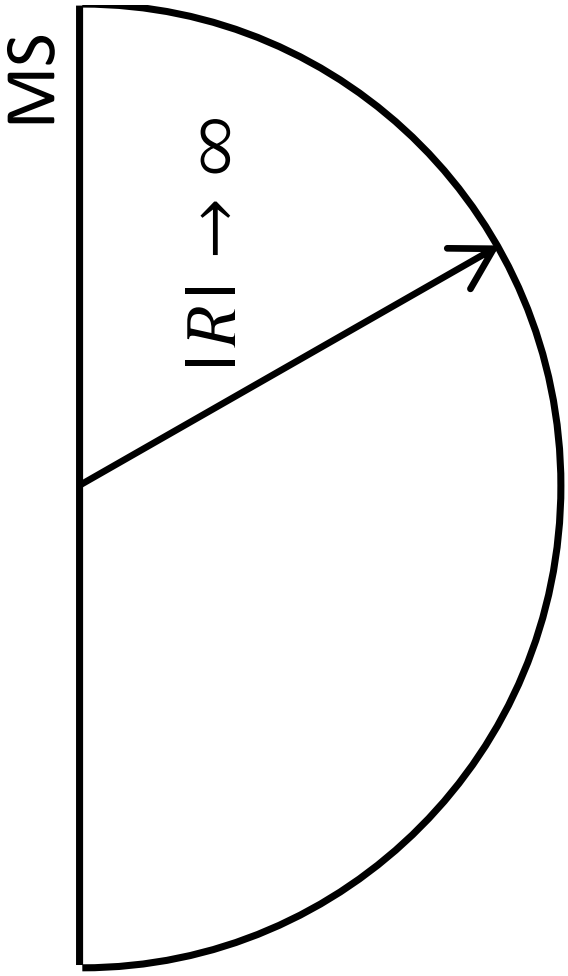

Figure 1: *The infinite hemispherical migration model. The measurement surface is denoted by MS.*

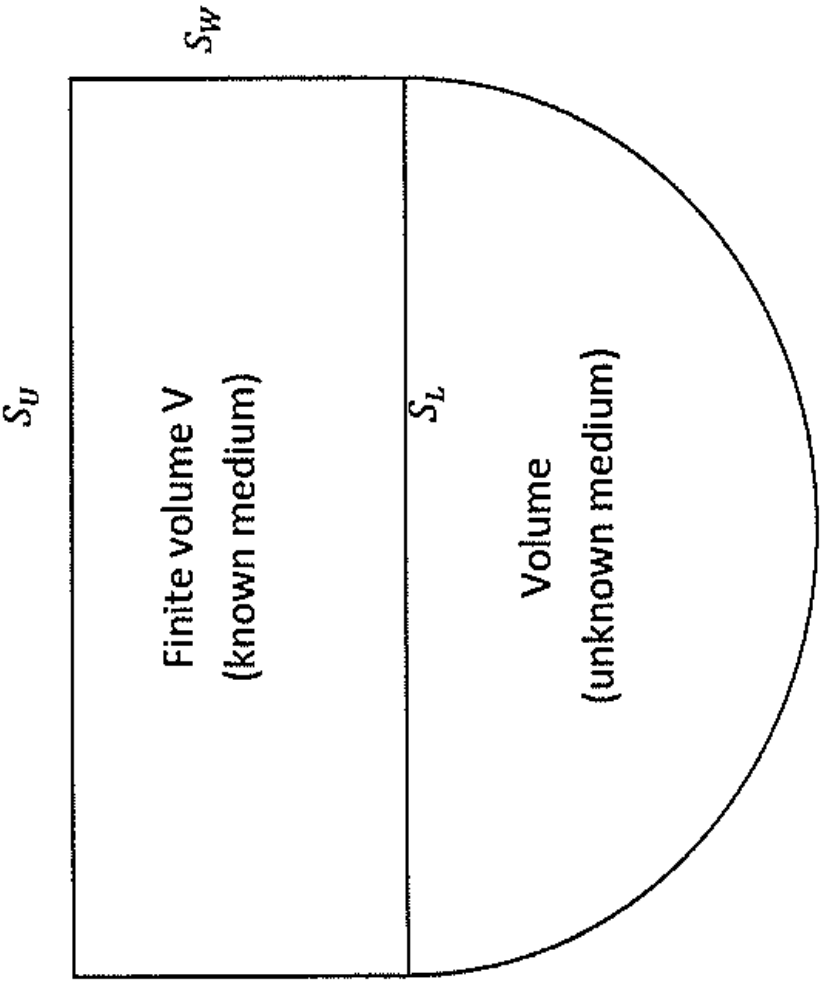

Figure 2: *A finite volume model.*

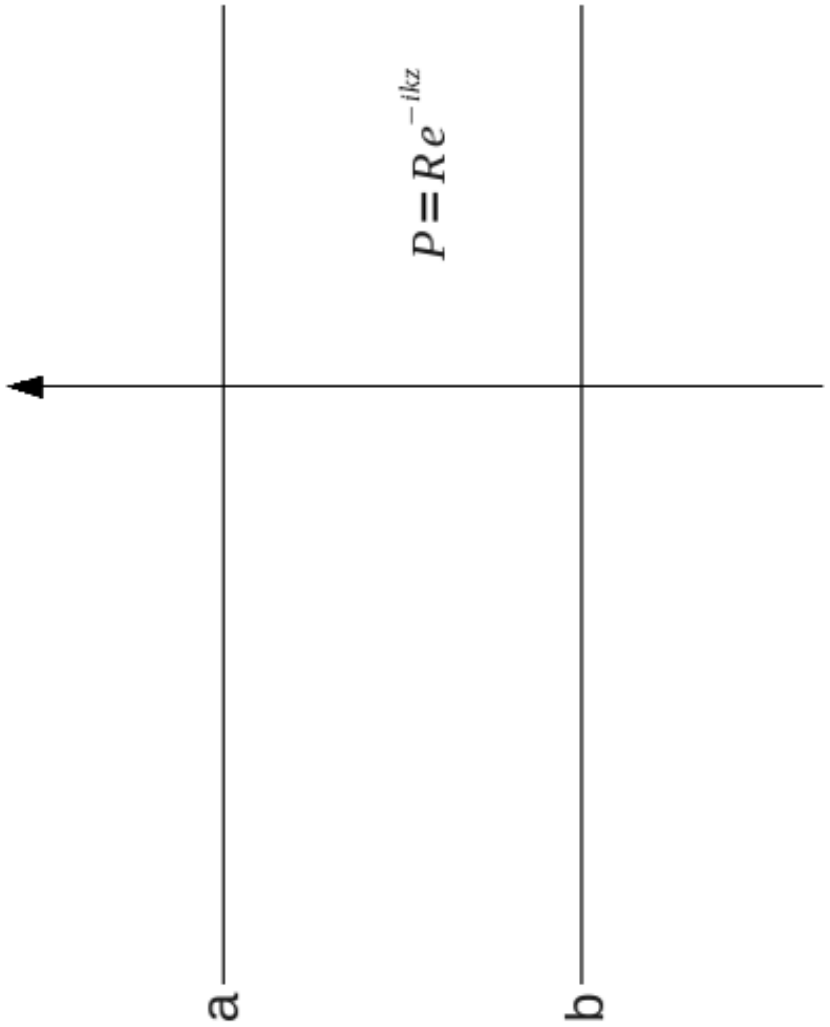

Figure 3: *1D upgoing plane wavefield.*

1. infinite hemisphere with known model

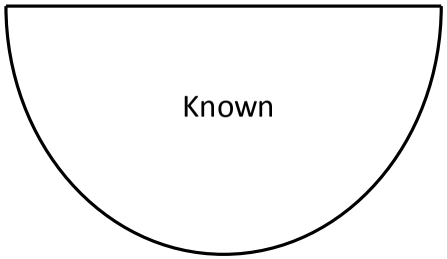

2. finite volume with known model

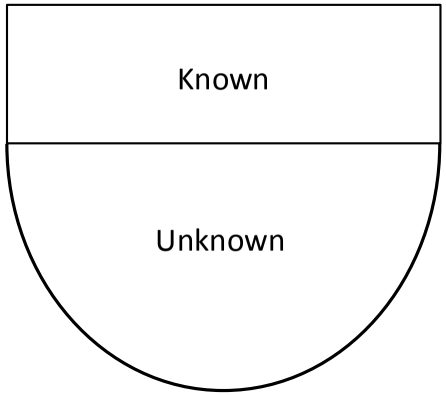

3. finite volume with approximately known model (Stolt, SEP24)

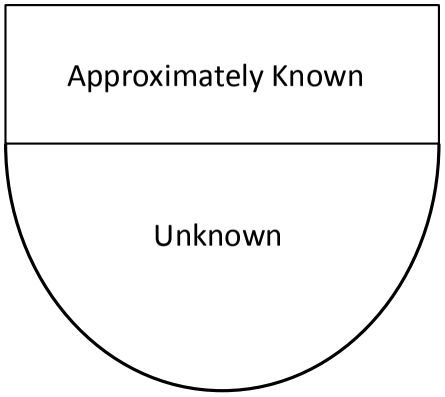

4. infinite hemisphere with unknown model (ISS)

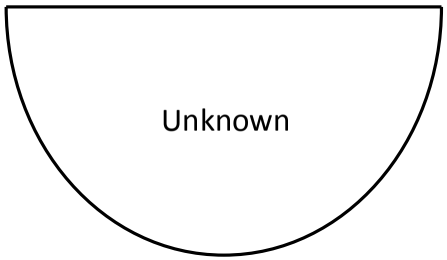

Figure 4: *Backpropagation model evolution.*

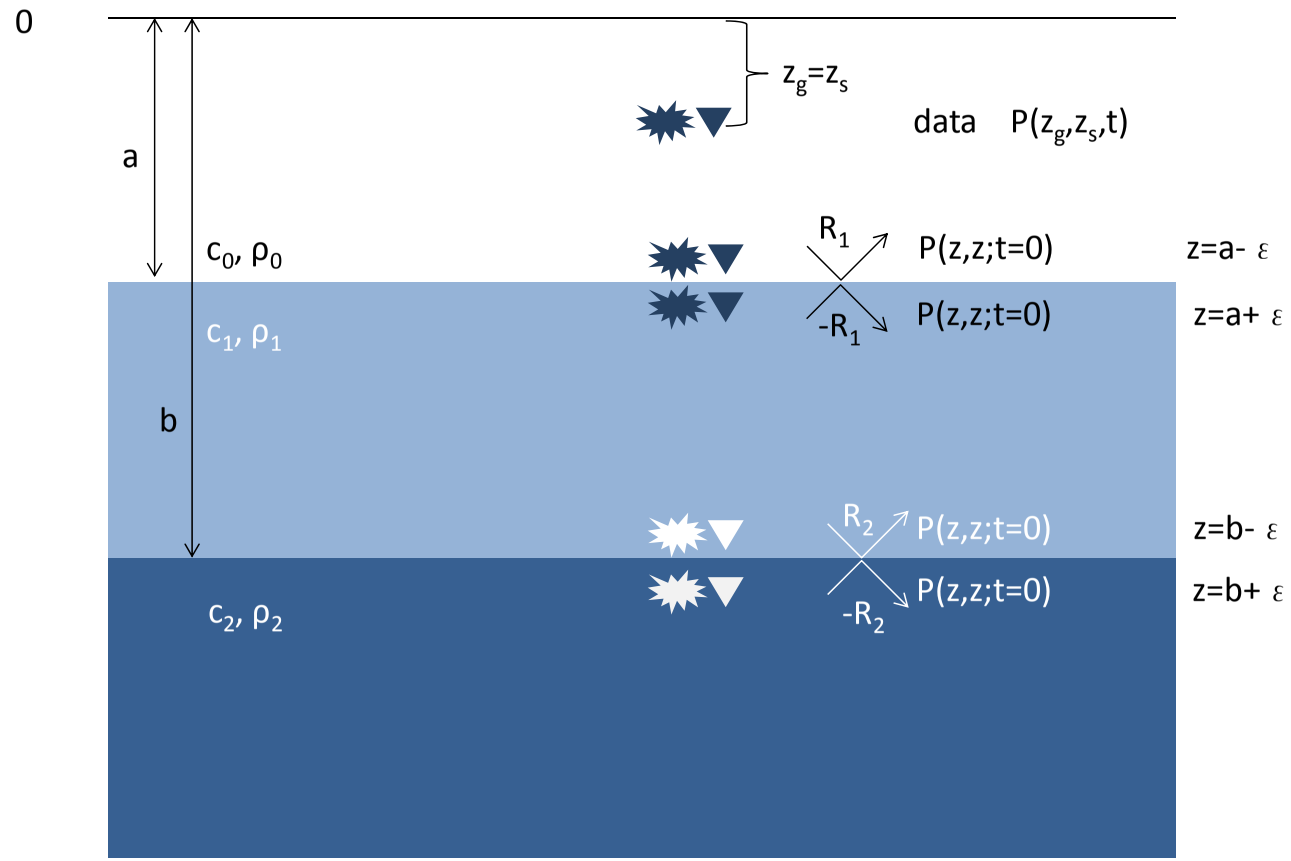

Figure 5: *Green's theorem predicts the wavefield at an arbitrary depth z between the shallower depth a and deeper depth b. The experiment illustrated here corresponds to a plane wave normal incident on a layered medium with two reflectors. The measurement coordinates are z_g and z_s, the coincident source and receiver depths. $a-\varepsilon$, $a+\varepsilon$, $b-\varepsilon$, $b+\varepsilon$ are the depth of the predicted source and receiver experiment at depths above and below the first reflector at $z=a$ and the second reflector at $z=b$.*

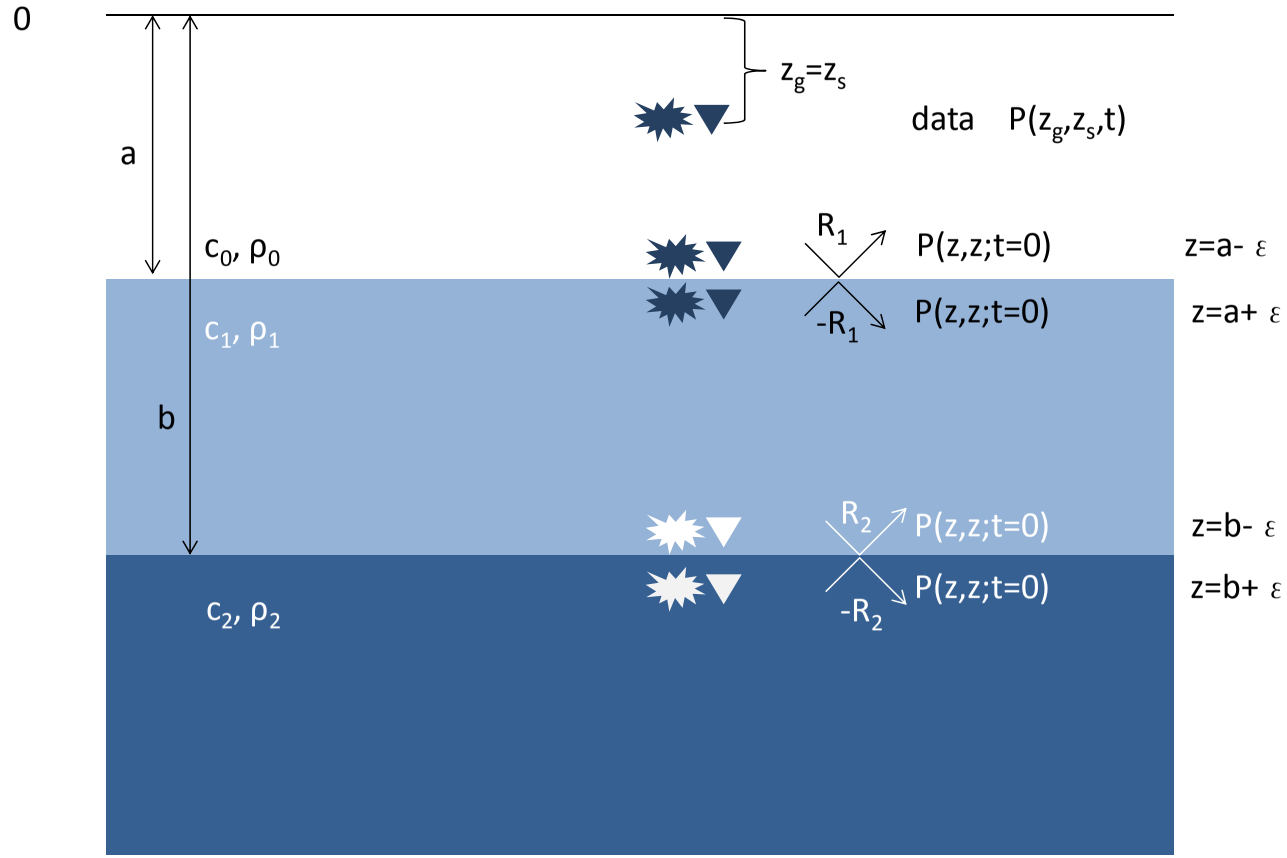

Figure 6: *Imaging with primaries and internal multiples. A double Green's theorem is utilized with the data, and a Green's function that along with its normal derivative vanishes on the lower surface (and on the walls, in multi-D). That is what Claerbout imaging III migration means for waves that are two-way propagating in the medium.*

Case 1: a primary from a single reflector (recorded data)

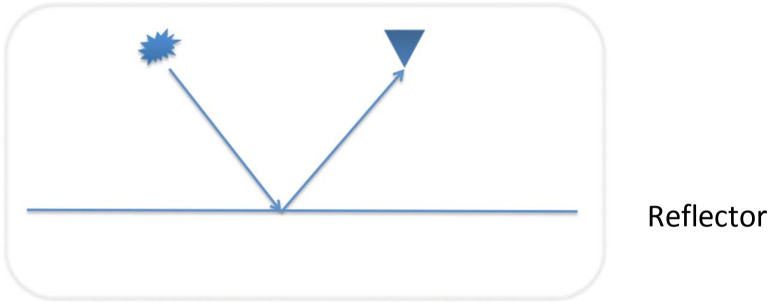

Figure 7:

Case 1: a primary from a single reflector

Above the reflector (predicted experiment at depth)

Coincident source and
receiver at depth for all times

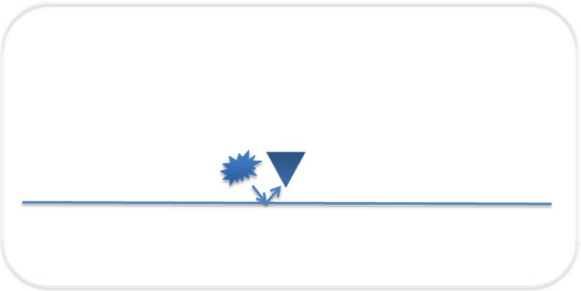

Blue event: primary

Coincident source and
receiver at depth for t = 0

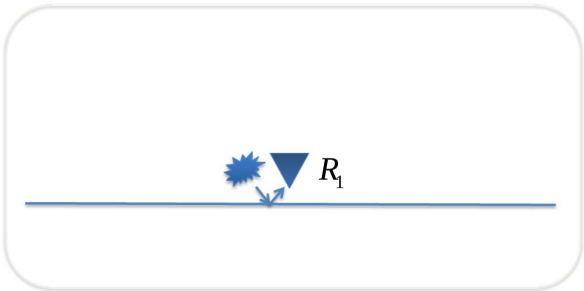

Blue event: primary

Figure 8:

Case 1: a primary from a single reflector

Below the reflector (predicted experiment at depth)

Coincident source and receiver at depth for all times

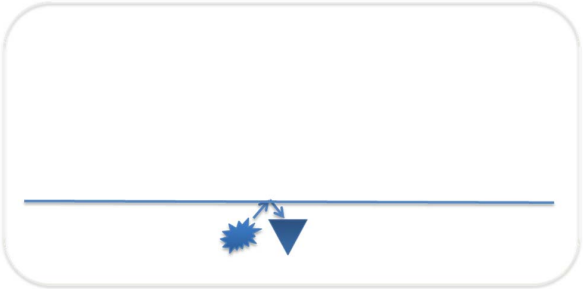

Blue event: primary

Coincident source and receiver at depth for t = 0

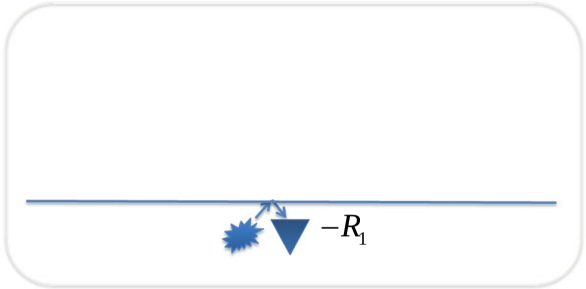

Blue event: primary

Figure 9:

Case 2: a primary and a free-surface multiple (recorded data)

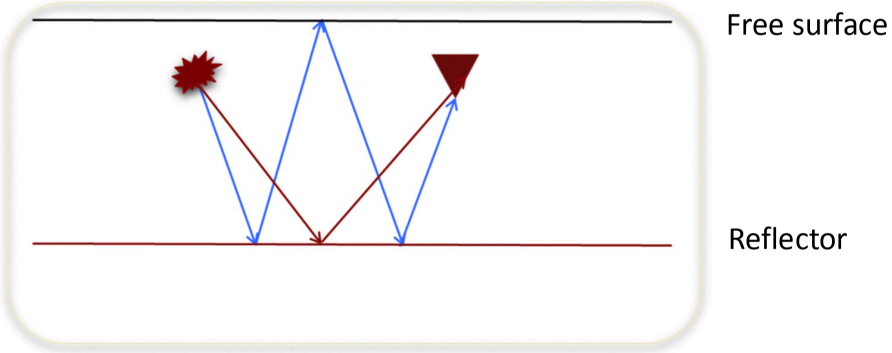

Red event: primary
Blue event: free-surface multiple

Figure 10:

Case 2: a primary and a free-surface multiple

Above the reflector (predicted experiment at depth)

Coincident source and receiver at depth for all times

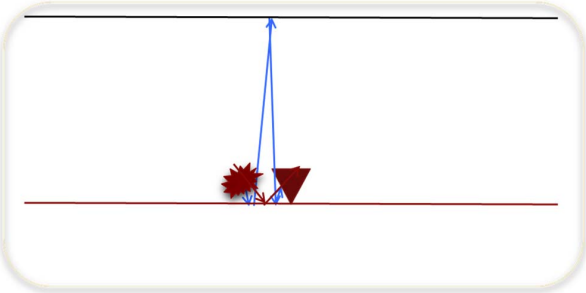

Red event: primary
Blue event: free-surface multiple

Coincident source and receiver at depth for t = 0

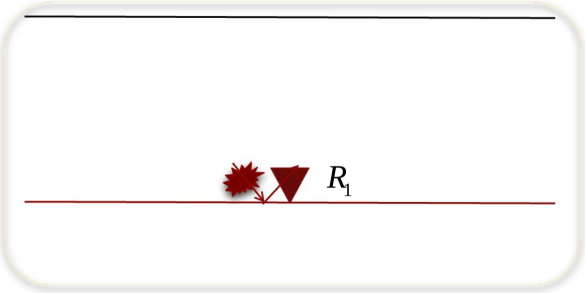

Red event: primary

Figure 11:

Case 2: a primary and a free-surface multiple

Below the reflector (predicted experiment at depth)

Coincident source and receiver at depth for all times

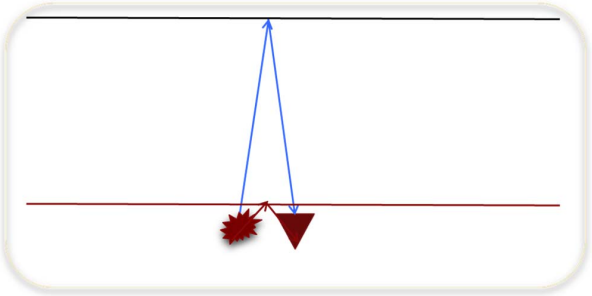

Red event: primary (downward reflection at the reflector)
Blue event: primary (downward reflection at the free surface)

Coincident source and receiver at depth for t = 0

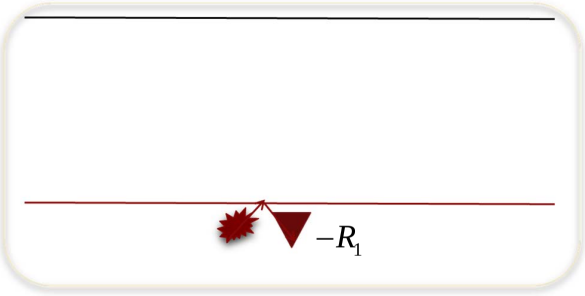

Red event: primary (downward reflection at the reflector)

Figure 12:

Case 3: two primaries and an internal multiple (recorded data)

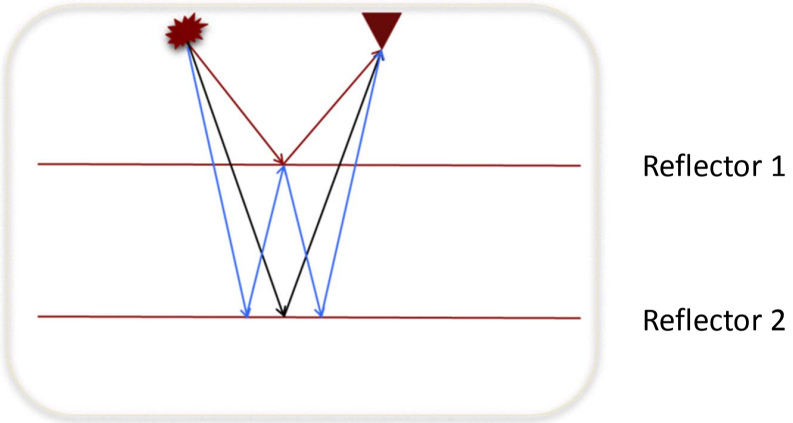

Red event: primary from the first reflector
Black event: primary from the second reflector
Blue event: internal multiple

Figure 13:

Case 3: two primaries and an internal multiple

Above the first reflector (predicted experiment at depth)

Coincident source and
receiver at depth for all times

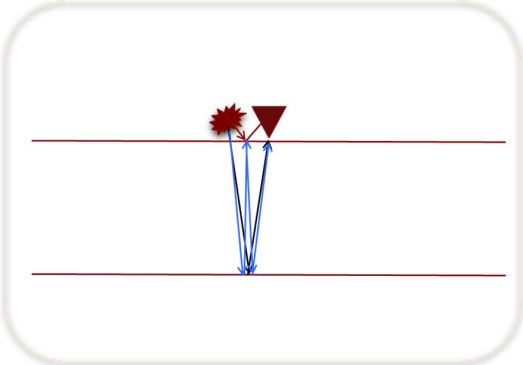

Red event: primary from the first reflector
Black event: primary from the second reflector
Blue event: internal multiple

Coincident source and
receiver at depth for t = 0

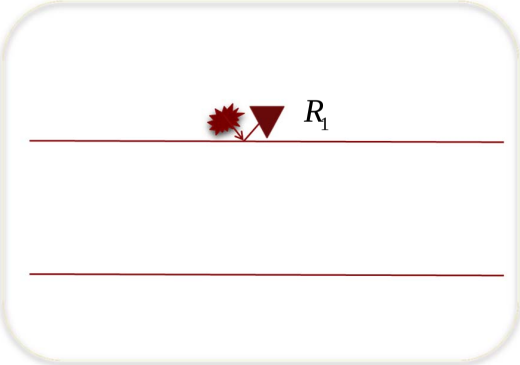

Red event: primary from the first reflector

Figure 14:

Case 3: two primaries and an internal multiple

Below the first reflector (predicted experiment at depth)

Coincident source and receiver at depth for all times

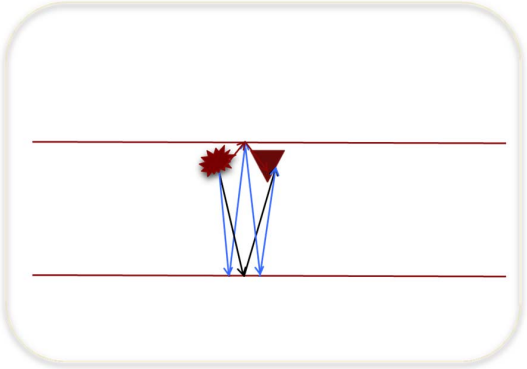

Red event: primary from the first reflector
Black event: primary from the second reflector
Blue event: internal multiple

Coincident source and receiver at depth for t = 0

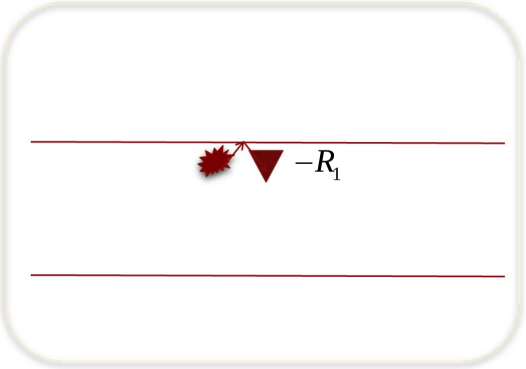

Red event: primary from the first reflector

Figure 15:

Case 3: two primaries and an internal multiple

Above the second reflector (predicted experiment at depth)

Coincident source and receiver at depth for all times

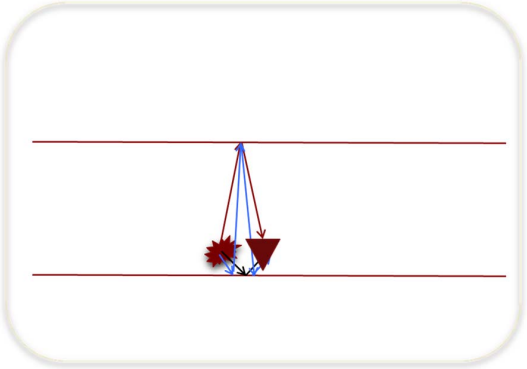

Red event: primary from the first reflector
Black event: primary from the second reflector
Blue event: internal multiple

Coincident source and receiver at depth for t = 0

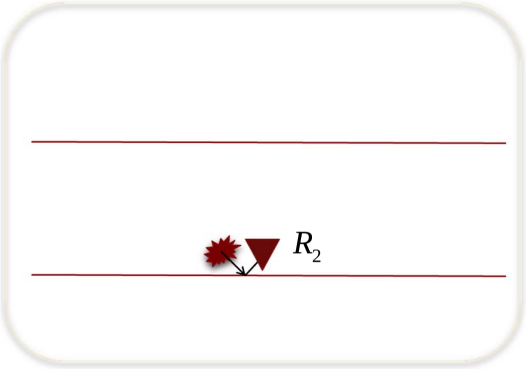

Black event: primary from the second reflector

Figure 16:

Case 3: two primaries and an internal multiple

Below the second reflector (predicted experiment at depth)

Coincident source and receiver at depth for all times

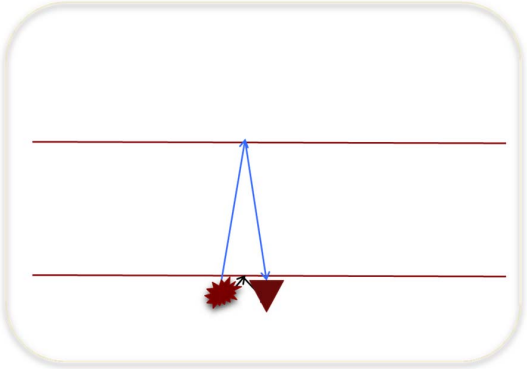

Blue event: primary from the first reflector
Black event: primary from the second reflector

Coincident source and receiver at depth for t = 0

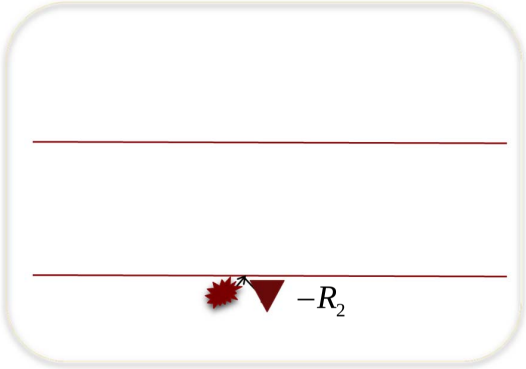

Black event: primary from the second reflector

Figure 17:

Using Multiples for Imaging

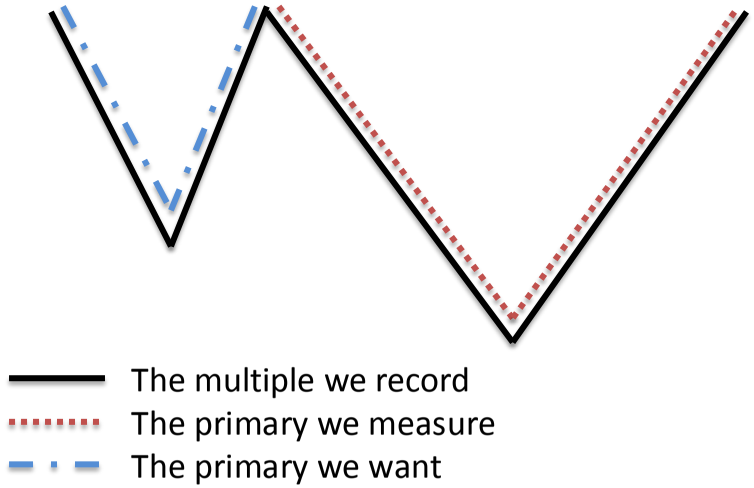

- <u>The multiple is used to find a missing primary.</u>
- Primaries are what migration and inversion call for and utilize.
- For the mathematical details, please see Weglein, A. B., Multiples: Are they signal or noise? TLE, 2015, special issue on "Multiples from attenuation to imaging".

Figure 18:

Multiples can be useful (at times) to enhance imaging by providing an approximate image of an unrecorded primary, but it is only primaries that are migrated for structure and amplitude analysis

Arthur B. Weglein, M-OSRP/Department of Physics/University of Houston

Primaries are seismic-reflection events with one upward reflection in their history, whereas multiples are events that have experienced more than one upward reflection.

Migration was originally, and remains today to be, basically and unequivocally about taking a primary event on a recorded seismic trace in time and locating where in space that reflection event was generated by a reflector. That concept assumes that the event in time has only one reflection in its history. Hence, since by definition only primaries have experienced one reflector in their history, migration relates to and has meaning only for primaries. Migration has no meaning for multiples. We will see in this paper that not only did the original definition of migration have meaning just for primaries, but that, in addition, when we use the most complete physically interpretable and quantitative imaging condition for wave-equation migration (WEM), only primaries contribute to the image at any reflector, in depth, and neither free-surface nor internal multiples contribute. Migration has meaning only for primaries, and primaries are the only seismic events that contribute to depth imaging and inversion at a reflector. Reminding us of that fundamental fact is one key message of this paper.

All wave methods for migration seek to mathematically capture and formulate that basic idea. When that idea is applied appropriately, and as intended, they have

meaning and relate to only primaries. To explain that consistency and to point out where things have become in our view somewhat confused and off track with regard to multiples, we must begin by briefly reviewing the various concepts in wave-theory migration.

In this paper, we briefly review methods for migrating data inside a volume in which waves are (1) one-way propagating, and (2) two-way propagating. Methods that use wave theory to migrate data have two ingredients: a wave-propagation component and an imaging condition. We briefly discuss each of those two components here, beginning with imaging condition.

Three landmark imaging conditions were introduced by Jon Claerbout (1971), Dan Lowenthal (1985), and Bob Stolt (1978) and their colleagues in the 1970s. Those three imaging conditions are (1) the exploding-reflector model, for zero-offset data, (2) the space-and-time coincidence of upgoing and downgoing waves, and (3) the prediction of a coincident-source-and-receiver experiment at depth, at time equals zero. We will refer to these three imaging conditions as Claerbout's imaging conditions I, II, and III, respectively, and occasionally, for brevity, we will simply call them "Claerbout I", "Claerbout II" and "Claerbout III."

The third Claerbout imaging condition predicts an actual seismic experiment at depth, and that predicted experiment consists of all the events that such an experiment would record if we had a source and receiver at the subsurface. To realize structural and inversion objectives, Stolt and his colleagues (Clayton and Stolt, 1981; Stolt and Weglein, 1985; Stolt and Benson, 1986; Weglein and Stolt, 1999; Stolt and Weglein,

2012) have extended, for one-way waves, Claerbout's source-and-receiver-experiment imaging condition (imaging condition III), to allow for a source and receiver that are not coincident at time equals zero.

Recently, Weglein and his colleagues (Weglein et al., 2011a,b; Liu and Weglein, 2014) provided the next step in the evolution of migration that is based on Claerbout's imaging condition of a predicted source-and-receiver experiment (imaging condition III) — they extended the prediction of the source-and-receiver experiment to that of a volume within which there are two-way propagating waves. That method of imaging, based on Claerbout's Imaging condition III for a medium with two-way-propagating waves (required for data with primaries and multiples) and, hence, plays a central role in the analysis in this paper. The predicted experiment in the volume is realized by calling upon Green's theorem and a Green's function that, along with its normal derivative, vanishes on the lower portion of the closed surface.

Summary of wave-equation migration for one-way-propagating and two-way-propagating waves

Backpropagation and imaging each evolved and then were extended and generalized, and ultimately merged, to become migration-inversion (Figure 1).

For one-way wave propagation, the double-downward-continued data, D, are

$$D(\text{at depth}) = \int_{S_s} \frac{\partial G_0^{-D}}{\partial z_s} \int_{S_g} \frac{\partial G_0^{-D}}{\partial z_g} D \, dS_g \, dS_s \qquad (1)$$

where D in the integrand is equal to the data on the measurement surface. $\partial G_0^{-D} / \partial z_s =$ is an anticausal Green's function with a Dirichlet boundary condition on the measurement surface, s is a shot, and g is a receiver. For predicting the source and receiver experiment at depth in a volume with two-way propagating waves, we have (see e.g., Weglen et al 2011a,b)

$$D(\text{at depth}) = \int_{S_s} \left[\frac{\partial G_0^{DN}}{\partial z_s} \int_{S_g} \left\{ \frac{\partial G_0^{DN}}{\partial z_g} D + \frac{\partial D}{\partial z_g} G_0^{DN} \right\} dS_g \right. \\ \left. + G_0^{DN} \frac{\partial}{\partial z_s} \int_{S_g} \left\{ \frac{\partial G_0^{DN}}{\partial z_g} D + \frac{\partial D}{\partial z_g} G_0^{DN} \right\} dS_g \right] dS_s, \qquad (2)$$

where D in the integrand is equal to the data on the measurement surface. G_0^{DN} is neither causal nor anticausal — it is the Green's function needed for wave-equation migration reverse-time migration (WEM RTM); that is, for RTM based on Claerbout's imaging condition III. G_0^{DN} is the Green's function for the model of the finite volume that vanishes along with its normal derivative on the lower surface and the walls. If we want to use the anticausal Green's function of the two-way propagation with Dirichlet boundary conditions at the measurement surface, we can do that, but we will need measurements at depth and on the vertical walls. To provide the experiment at depth without data at the lower boundary and on the vertical sides/walls requires a nonphysical Green's function that vanishes, along with its derivative, on the lower surface and walls.

Fang Liu and A. B. Weglein (2014) and Weglein (2015) have taken us to the next step in our goal and objective. Having established a methodology for Claerbout's imaging condition III (please see equation 2) for a medium (a finite volume) with two-way propagating waves, we are in a position to predict source-and-receiver experiments at depth and then to obtain an imaging result with Claerbout's imaging condition III for data consisting of primaries and multiples. For the 1D layered medium and normal-incident wave that we are examining, the data (consisting of primaries and internal multiples) and the results of the predicted source-and-receiver experiment at depth and of the migration algorithm are all analytic and transparent, and the conclusions are unequivocal and unambiguous. The role of recorded primaries and multiples in contributing first to the predicted source-and-receiver experiment at depth, and then to the coincident-source-and-receiver experiment at time equals zero (the third Claerbout imaging condition), provides a definitive response to the question of whether multiples contribute to seismic imaging.

Liu and Weglein (2014) and Weglein (2015) provide the explicit Green's theorem source-and-receiver-at-depth prediction and then the imaging result of Claerbout's imaging condition III for a general, layered medium in which the velocity and density vary and the data consist of primaries and internal multiples. Those papers arrive at three conclusions:

(1) All recorded events —– primaries, internal multiples, and free-surface multiples —– contribute to the predicted coincident-source-and-receiver experiment at depth.

(2) Only the recorded primaries contribute to the image — that is, once the time-equals-zero imaging condition is called on, only recorded primaries contribute to the image at any depth.

(3) The location of each reflector is determined, along with the reflection coefficients for the experiment both from above and from below each reflector (Figure 2). The reflection coefficients are not obtainable by using Claerbout's imaging condition II (the bases of all current RTM).

If we remove the multiples in the recorded data, the coincident-source-and-receiver experiment at depth will change. However, once the imaging condition is applied, the image's location at the correct depth, and its amplitude, the reflection coefficient, will not be affected. If, in these examples, our data consist only of multiples, we will have no image at any depth. These conclusions are all demonstrated in great detail in Liu and Weglein (2014) and Weglein (2015).

Hence, for the purposes of imaging and inversion (and employing the most capable and quantitative imaging condition), primaries are the events that contribute to imaging and inversion, and are considered to be signal, whereas multiples are not.

Results from Claerbout's imaging conditions II and III

Claerbout's imaging condition II, the time-and-space coincidence of up and down waves, is formulated as

$$I(\vec{x}) = \sum_{\vec{x}_s} \sum_{\omega} D^*(\vec{x}, \vec{x}_s; \omega) U(\vec{x}, \vec{x}_s; \omega) \quad , \qquad (3)$$

where D is the downgoing wave and is U is the upgoing wave, respectively, and * represents the complex conjugate.

The sum over receivers for a given shot record realizes Claerbout's second imaging condition. The sum over sources is "introduced" in an ad hoc manner to mitigate the inconsistent amplitudes and phases of images, which can be clearly seen in imaging results from exact data and the imaging of a single horizontal reflector (please see the example in Chao Ma and Yanglei Zou (2015)). By comparison, the result from Claerbout's third imaging condition, for the same reflector and the same data, produces an accurate and consistent reflection coefficient at every point on the reflector, for a single shot record.

Let us compare Claerbout II imaging (formula 3, above) with the one-way- and two-way-wave versions of Claerbout's imaging condition III, represented in equations 1 and 2.

For Claerbout imaging III, for a volume with two-way propagating waves, given by equation 2, the sum over receivers predicts the receiver experiment at depth for a source on the measurement surface, and the sum over sources then precisely predicts the experiment with the source at depth, as well. The integrations over receivers and over sources predict the source-and-receiver experiment at depth. There is nothing ad hoc or designed to fix something amiss (as though the data had random noise, to be mitigated by stacking). The noise is algorithmic within Claerbout II and is present with

exact, analytic, noise-free data in the earlier integral over receivers, as in formula 3. This is why we say that Claerbout III is on the firmest physics foundation, with an interpretable, quantitative and consistent meaning to the image. And once again, that clarity is why we adopt Claerbout III for analysis of the role of primaries and multiples in imaging (see Liu and Weglein (2014) and Weglein (2015)).

Claerbout's imaging conditions I, II, and III give equivalent imaging results for a normal-incident plane wave on a horizontal reflector. As soon as we consider prestack data for even a single horizontal reflector, however, the significant differences in image interpretability and consistency between the imaging conditions become clear. Furthermore, only Claerbout III can be readily and naturally extended for amplitude analysis at specular, curved surfaces and point diffractors/pinchouts and for imaging both from above, and from beneath, a discontinuous velocity model.

The three Claerbout imaging condition are intended and meaningful only for primaries. However, the language and thinking behind Claerbout imaging II can be the inspiration/motivation for explaining the time and space coincidence of different events, other than primaries, not to migrate them, but for other useful and beneficial purpose.

With a complete set of recorded primaries and a wave theory (not ray, Kirchhoff, Beam or other approximation) migration there is, (in principle), no illumination issue. However, when either a less than complete set of primaries is recorded and/or an asymptotic migration method is employed, then illumination issue can and will arise. We will see that under the latter circumstances, that imaging enhancement can be provided

by using a recorded multiple together with a recorded primary subevent of that multiples to produce an approximate image of an unrecorded primary subevent of the multiple.

In this next section, we illustrate that process and evolution beginning with a brief and elementary review.

Using Claerbout II imaging to migrate a primary, followed by the method it inspired to use a Claerbout II type method to produce an approximate image of an unrecorded primary.

Imaging primaries with Claerbout's imaging condition II

A 1D normal-incident analytic example

In this section, we use a 1D normal-incident analytic example to illustrate the idea of imaging a primary with Claerbout's imaging condition II. Let us assume we have data from a downgoing spike wave that starts at $z = \varepsilon_s$ at $t = t_0 = 0$. The downgoing wavefield from the source side that is being forward propagated to depth z is $D = e^{i\omega[\frac{z-\varepsilon_s}{c_0}]}$, whereas the upgoing wavefield from the receiver side that is being back propagated to depth z is $U = R_1 e^{i\omega[\frac{d-\varepsilon_s}{c_0}+\frac{d-z}{c_0}]}$, where R_1 and d are the reflection coefficient and the depth of the reflector, respectively (see Figure 3). Applying Claerbout's imaging condition II, we have

$$I_P = \int \left(e^{-i\omega\left[\frac{z-\varepsilon_s}{c_0}\right]} \right) \times \left(R_1 e^{i\omega\left[\frac{d-\varepsilon_s}{c_0}+\frac{d-z}{c_0}\right]} \right) d\omega = \int R_1 \, e^{-i\omega\left[\frac{2d-2z}{c_0}\right]} d\omega$$

$$= \pi c_0 R_1 \delta(z-d)$$

232

(4)

We obtain the correct image location at depth d with an amplitude of $\pi c_0 R_1$.

Using a multiple to approximately image an unrecorded primary

1D normal-incident analytic example

Now, we apply Claerbout's imaging condition II to a seismic data set that contains a first-order free-surface multiple. Again, we assume a downgoing spike wave that is at $z = \varepsilon_s$ at $t = t_0 = 0$ (see Figure 4). A first-order free-surface multiple is recorded at z_g. The downgoing wavefield from a "virtual source" (represented by the dashed red line in Figure 4) that is being forward propagated to depth z is $D = -R_1 e^{i\omega[\frac{d-\varepsilon_s}{c_0}+\frac{d+z}{c_0}]}$. The upgoing wavefield from the receiver side (represented by the yellow dashed line in Figure 4) that is being back propagated to depth z is $U = -R_1^2 e^{i\omega[\frac{d-\varepsilon_s}{c_0}+\frac{2d}{c_0}+\frac{d-z}{c_0}]}$. Here, we have assumed the downward reflection coefficient at the free-surface to be -1 in deriving the up and down wavefields (Figure 4). Applying the time and space coincidence of these two wavefields, we have

$$I_M = \int \left(-R_1 e^{-i\omega[\frac{d-\varepsilon_s}{c_0}+\frac{d+z}{c_0}]}\right) \times \left(-R_1^2 e^{i\omega[\frac{d-\varepsilon_s}{c_0}+\frac{2d}{c_0}+\frac{d-z}{c_0}]}\right) d\omega$$

$$= \int R_1^3 \, e^{-i\omega\left[\frac{2d-2z}{c_0}\right]} d\omega = \pi c_0 R_1^3 \delta(z-d) \qquad (5)$$

We obtain the correct image location at depth d, however with a different amplitude of $\pi c_0 R_1^3$, rather than $\pi c_0 R_1$. This procedure can provide an approximate image of a primary subevent if the velocity of the primary subevent can be estimated. This very simple example can be readily extended to the case of the two different primary subevents, where the velocity of the unrecorded primary subevent will allow for its approximate image.

The methods that seek to use multiples today as “signal” are really seeking to approximate images resulting from primaries that were not recorded due to limitations in acquisition, and then to address the subsequent, limited illumination that missing primaries can cause. The methods are not really using the multiple itself as an event to be followed into the subsurface for imaging purposes. Figure 5 illustrates the idea.

Assume that a multiple is recorded, and that a primary that is a subevent is also recorded. The idea is to extract and predict, from the recorded multiple and the recorded primary, the image representing an unrecorded subevent primary. All the various incarnations that use multiples as “signal” actually and entirely are attempting to obtain the approximate image of an unrecorded primary. It is the missing image of unrecorded primaries that the methods seek to produce and to utilize. Such a use of multiples is in itself testament to the fact that a complete set of primaries is sufficient for imaging the subsurface. Using a multiple to achieve an approximate image of an unrecorded primary is an enhanced image due to a more complete set of primaries and is not migration of the multiples.

In an SEG *Recent Advances and the Road Ahead* presentation titled “Multiples: signal or noise?”, Weglein (2014) presented actual field-data examples from PGS in which clear, compelling added value was demonstrated for the image from actual primaries, combined with the approximate images of unrecorded primaries, in comparison with the image from the original primaries. (Please see https://vts.inxpo.com/scripts/Server.nxp?LASCmd=L:0&AI=1&ShowKey=21637&LoginType=0&InitialDisplay=1&ClientBrowser=0&DisplayItem=NULL&LangLocaleID=0&RandomValue=1415030021699) Please also see Whitmore et al. (2010) and Valenciano et al. (2014) for examples of using multiples to enhance image.

Issues

To predict a free-surface multiple or an internal multiple, the primary subevents that constitute the multiple must be in the data in order for the multiple-prediction method to recognize an event as a multiple. If a primary is not recorded, the multiple that contains that unrecorded primary will not be predicted as a multiple. That issue and basic contradiction within the method is recognized by its practitioners. Instead of predicting the multiple, they use all the events in the recorded data — primaries and multiples — and the multiples then can be useful for predicting approximate images of missing primaries. However, the primaries in those data will cause artifacts. Other artifacts also accompany this method, because of the inability to isolate primaries from multiples with unrecorded primaries.

In fact, an enormous number and variety of false events are generated by such a procedure (see e,g., Lu et al., 2011; Liu et al., 2011). Among those false events are

“images of multiples,” as Figure 6 exemplifies. There also are other false images — artifacts that do not correspond to a particular event (e.g., to a multiple).

Today’s methods for using multiples to predict an approximate image of unrecorded primaries are aimed at structural improvement, at best, and do not claim, seek, or deliver the amplitude and phase fidelity of the predicted primary. Whether the tradeoffs make sense ought to depend, in part, on the depth of the target, the type of play, and whether a structural interpretation or amplitude analysis is planned within a drilling program and decision.

We should note here that this entire wave-equation migration analysis (Claerbout’s imaging condition III) is ultimately based on the idea from Green (1828) that to predict a wave (an experiment) inside a volume, we need to know the properties of the medium in that volume.

There is an alternative view: The inverse-scattering-series methods communicate that all processing objectives can be achieved directly and without subsurface information. The inverse scattering series treat multiples as a form of coherent noise and provide distinct subseries that remove free-surface and internal multiples, before the inverse scattering subseries for imaging and inversion achieve their goals by using only primaries (Weglein et al. (2003) and Weglein et al. (2012)). If the inverse scattering series needed multiples to perform migration and inversion, they would not have provided subseries that remove those multiply reflected events. With a velocity model (wave-equation migration) or without a velocity model (inverse scattering series imaging), only primaries are signal, in the sense that they are the events we need in

order to locate and delineate targets. If we want to consider a multiple as a conditional "signal" that at times can enhance imaging, there is no harm in it. To say that multiples are being migrated, however, and/or are on the same footing as primaries, is simply not true. A complete set of recorded primaries, processed with a wave-theory migration (versus asymptotic or ray migration), would neither need nor benefit from multiples. Multiples must be removed before a velocity analysis is performed that uses, for example, tomography, common-image-gather (CIG) flatness, or full-waveform inversion (FWI). Further, a velocity model is required by all the methods that seek to use multiples to enhance imaging. Hence, multiples need to be removed in a separate step prior to this use of multiples for approximate imaging of unrecorded primaries.

Conclusions

Primaries are signal and multiples can be useful, at times, for predicting the approximate images of missing primaries. Hence, primaries are the events used for structural determination and amplitude analysis.

Given an accurate, discontinuous velocity-and-density model, and data with primaries and multiples, Fang Liu and Weglein (2014) and Weglein (2015) demonstrate that only primaries contribute to the images at every depth. If we predict the source-and-receiver experiment at depth with a smooth velocity, it is possible to correctly locate (but not invert) each recorded primary event. With a smooth velocity model, however, every free-surface and internal multiple will produce a false image/artifact/event. If we remove the multiples first, we can correctly locate structure from recorded primaries by using a smooth velocity model.

We conclude, therefore, that the inability, in practice, to provide an accurate, discontinuous velocity model defines why multiples must be removed prior to imaging. That reality has been the case, is the case, and will remain to be true for the foreseeable future. Multiples need to be removed before velocity analysis, and they need to be removed before imaging and inversion.

Methods to provide a more complete set of primaries are to be supported and encouraged. Those methods include: (1) advances in acquisition techniques, and achieving more complete acquisition, (2) interpolation and extrapolation methods, and (3) use of multiples to predict approximate images of missing primaries. However, a recorded primary is still the best and most accurate way to provide a primary, and the primary is the seismic signal.

What if our acquisition of primaries is not adequate? In this paper, we demonstrate that multiples can be useful for improving our imaging, by providing an approximate image of an unrecorded primary that is a subevent of the multiple. However, the multiple is itself not migrated.

Acknowledgments

I would like to thank the sponsors of M-OSRP for their encouragement and support. I also would like to thank Nizar Chemingui and Alejandro Valenciano for the invitation to write this article. Many thanks go as well to Chao Ma, Yanglei Zou, Jim Mayhan, Jinlong Yang, Xinglu Lin, Jing Wu, Qiang Fu, and Fang Liu for their assistance in the writing and editing of this paper.

References

Claerbout, J. F., 1971, Toward a unified theory of reflector mapping: Geophysics, 36, 467-481.

Liu, F., and A. B. Weglein, 2014, The first wave equation migration RTM with data consisting of primaries and internal multiples: theory and 1D examples: Journal of Seismic Exploration, 23, 357-366.

Lu, S., N. D. Whitemore, A. A. Valenciano, and N. Chemingui, 2011, Imaging of primaries and multiples with 3D SEAM synthetic: 81st Annual International Meeting, SEG, Expanded Abstracts, 3217–3221.

Valenciano, A. A., S. Crawley, E. Klochikhina, N. Chemingui, S. Lu and D.N. Whitemore, 2014, Imaging complex structures with separated Up- and Down-going wavefields: SEG Technical Program Expanded Abstracts, 3941–3945.

Weglein, A. B., 2015, Multiples: signal or noise?: Geophysics. (Submitted).

Whitmore, N. D., A. Valenciano, W. Söllner, and S. Lu, 2010, Imaging of primaries and multiples using adual-sensor towed streamer: SEG Technical Program Expanded Abstracts, 3187–3192.

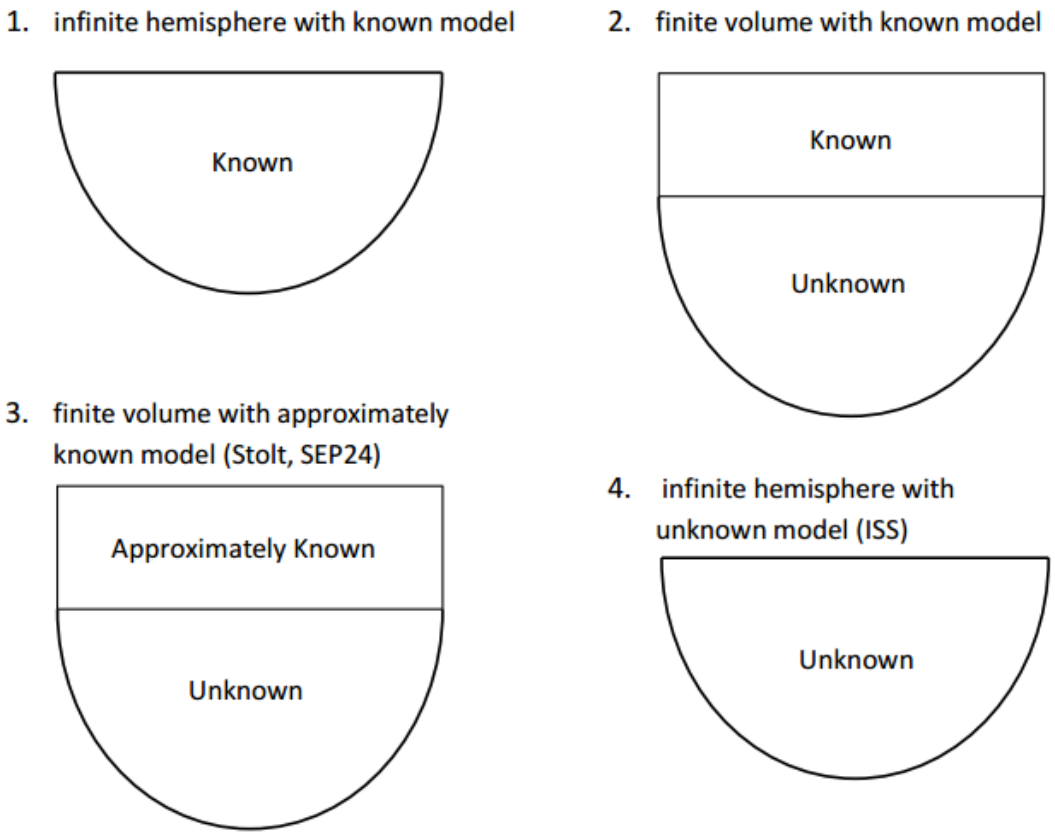

Figure 1: Earth model and subsurface information. The various earth models in the evolution of depth imaging. The first panel, the infinite-hemisphere model, was the first model adopted by migration methods (1978). The second panel, the finite-volume model, in which subsurface information is known only for the area above any given reflector, is the current industry standard. The fourth panel illustrates the basis of depth imaging with the inverse scattering series, wherein the velocity model is unknown and remains so, everywhere; this is the future model of seismic imaging. The fourth model is the model for methods that use the inverse scattering series to eliminate free-surface multiples and attenuate internal multiples.

240

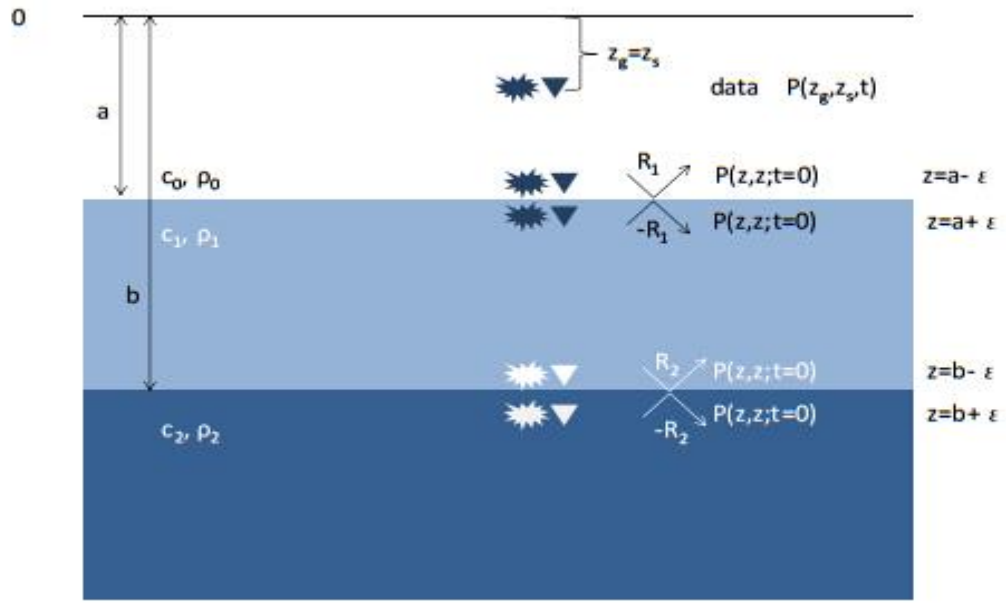

Figure 2: Green's theorem predicts the wavefield at an arbitrary depth z between the shallower depth a and the deeper depth b. The experiment illustrated here corresponds to a plane-wave that is normal incident on a layered medium with two reflectors. The measurement coordinates are z_g and z_s , and the coincident-source-and-receiver depths a- ε, a+ε, b− ε, and b+ε are the depth of the predicted source-and-receiver experiment at depths above and below the first reflector at z=a and the second reflector at z= b.

.

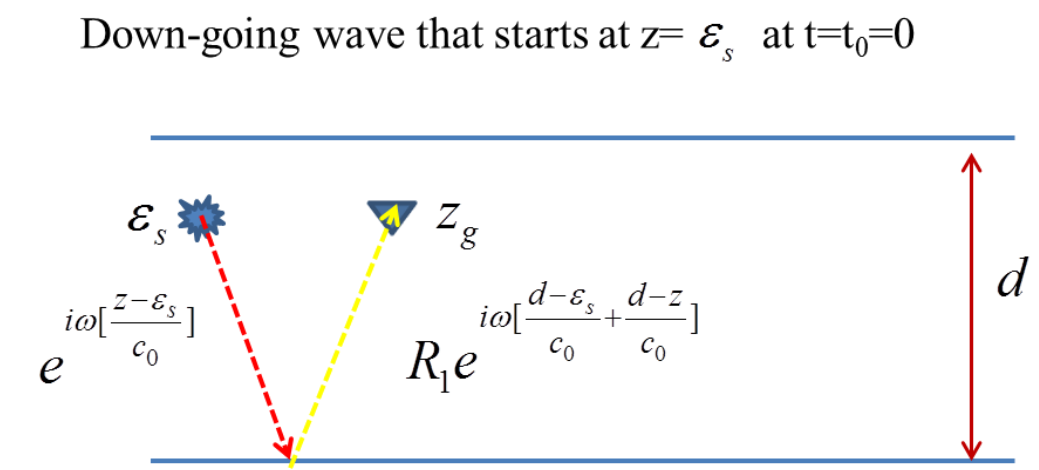

Figure 3: Use of a primary to find an image.

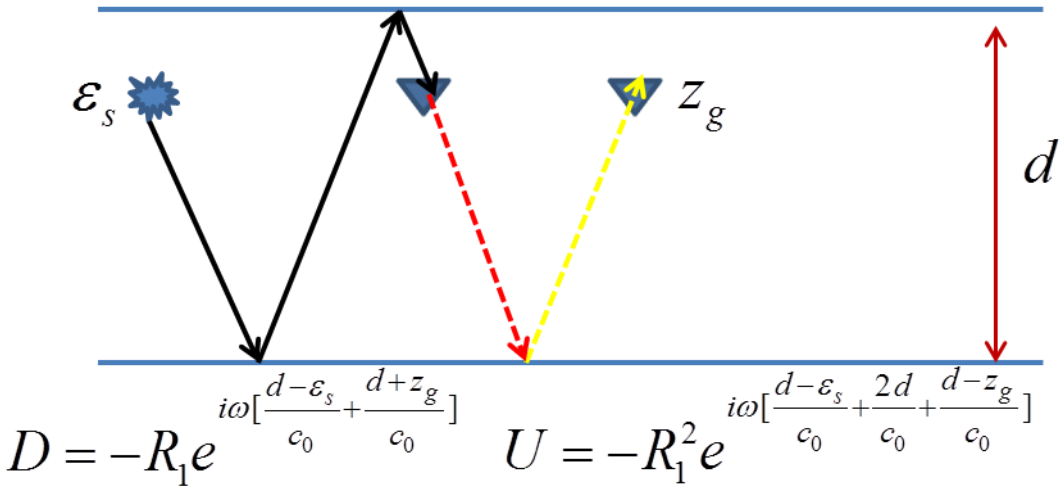

Figure 4: Use of a multiple to find an approximate image of an unrecorded primary.

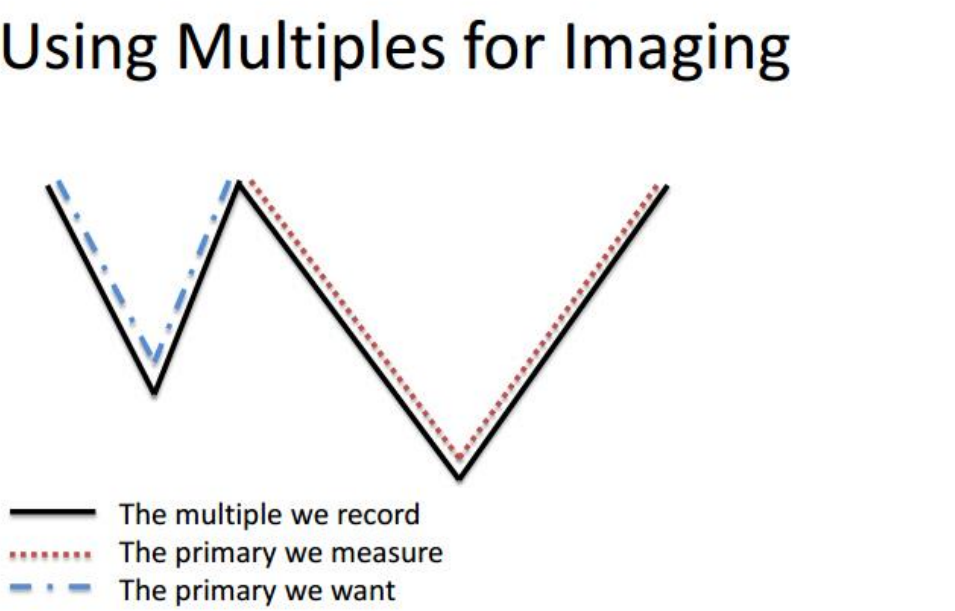

Figure 5: Using multiples for imaging.

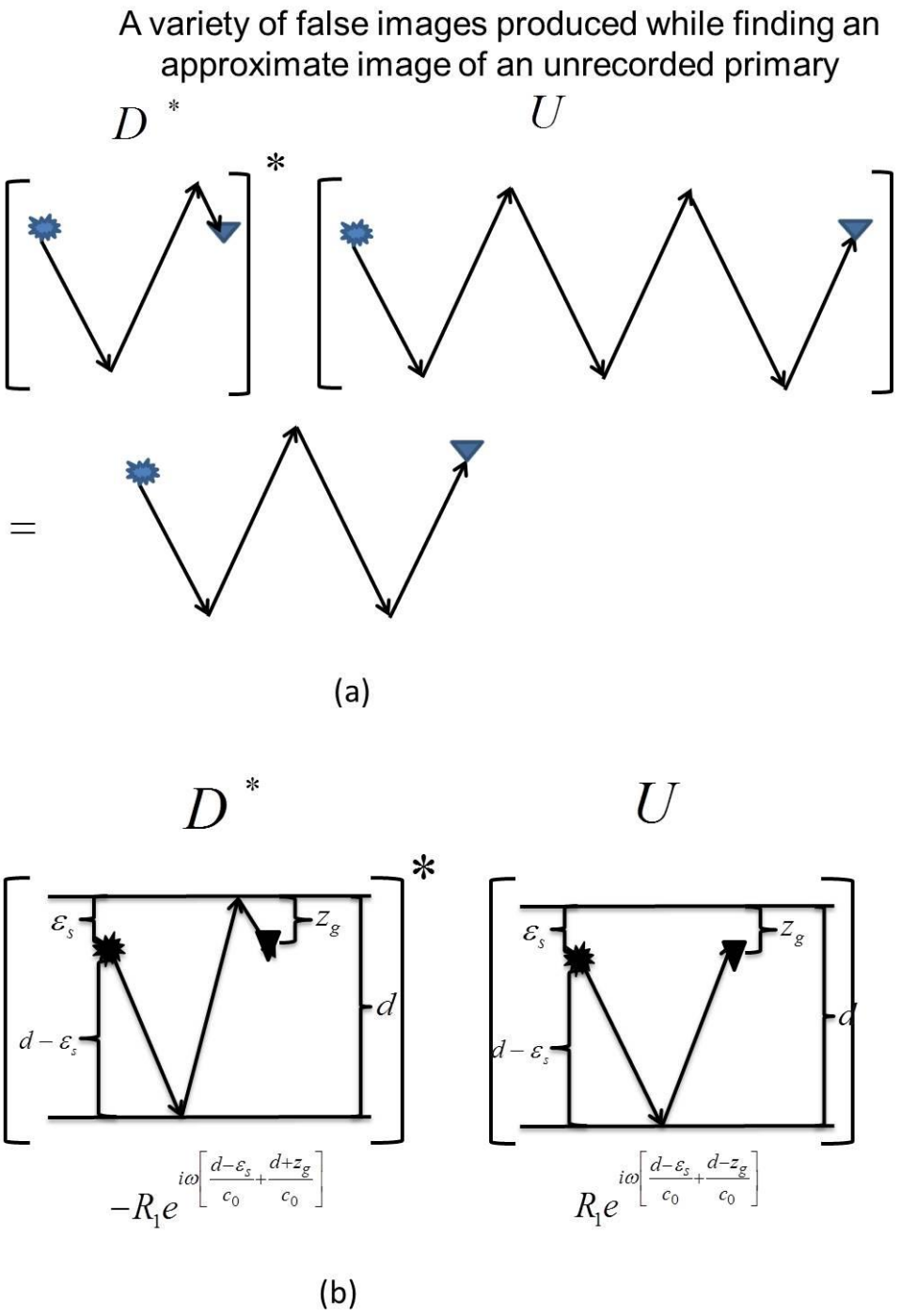

Figure 6: Examples of different types of false images generated by the use of multiples to predict the approximate image of an unrecorded primary. Figure 6a will produce an artifact

due to imaging of a multiple, and figure 6b will produce an artifact at z=0 (the origin) that is beyond the false image that is due to outputting images of multiples.

(Short note) Inverse scattering series internal multiple attenuation in an absorptive dispersive earth, without knowing, needing or estimating elastic or inelastic subsurface properties: update with pre-stack data examples

Jing Wu & Arthur B. Weglein

Abstract

In this paper, the Inverse Scattering Series (ISS) internal multiple attenuation algorithm is analytically and numerically evaluated on pre-stack reflection data from an attenuating medium. The results for an attenuating medium show that the method retains its value to directly predict internal multiples (IM) with the exact phase and an approximate amplitude, without knowing the medium and its absorptive and dispersive properties.

1 Introduction

The inverse scattering series can achieve all processing objectives directly by using distinct isolated task-specific sub-series and without subsurface information (Weglein et al., 2003). The ISS internal multiple attenuator has shown stand-alone capabilities on both marine and on-shore plays (e.g., Ferreira, 2011; Fu et al., 2010). Previous synthetic data tests on this algorithm have involved multidimensional acoustic and elastic media (e.g., Araújo, 1994; Weglein et al., 1997).

For the medium involving absorptive and dispersive properties, the wavefield will be attenuated and broadened while propagating. Using a 1D normal incidence data from an absorptive earth, Wu and Weglein (2014) demonstrate that applying the industry standard ISS internal multiple attenuator will attenuate the multiples. In this paper, we use pre-stack data as the input to evaluate the ISS internal multiple attenuation algorithm, and conclude again that the predicted internal multiple has the correct phase and an approximate amplitude.

2 Wavefiled expression in the absorptive medium

2.1 Green's function

For an absorptive-dispersive medium, Green's function $G_0(\mathbf{r}, \mathbf{r}_s, \omega)$ satisfies wave equation

$$\left(\nabla^2 + \frac{\omega^2}{c^2(\omega)}\right) G_0(\mathbf{r}, \mathbf{r}_s, \omega) = \delta(\mathbf{r} - \mathbf{r}_s), \tag{1}$$

where $\mathbf{r}$ is the receiver point, $\mathbf{r}_s$ is the source point. Assuming a constant Q (or frequency-independent Q) model (e.g. Kolsky, 1956; Kjartansson, 1979), and within a reasonable seismic bandwidth,

$$\frac{1}{c^2(\omega)} = \frac{1}{c_0^2}\left(1 + \frac{F(\omega)}{Q}\right), \tag{2}$$

where

$$F(\omega) = \frac{i}{2} sgn(\omega) - \frac{1}{\pi} log\left(\frac{\omega}{\omega_r}\right). \tag{3}$$

It is constitute of two terms: the first term is related to the energy attenuation, and the second term is related to velocity dispersion. ω_r here is the reference frequency, and it could be chosen as the maximum frequency or the central frequency in the experiment. c_0 is the velocity at the reference frequency.

Q is the quality factor that represents the energy loss for a wave-field propagating in one wave length, and it is defined as

$$Q = \frac{2\pi E}{\Delta E}, \tag{4}$$

where E is the energy of the wave-field, and ΔE is the energy loss in a wavelength of propagation.

Solving Equation 1, we will have

$$G_0(\mathbf{r}, \mathbf{r}_s, \omega) = \frac{1}{(2\pi)^2} \int_{-\infty}^{\infty} \int_{-\infty}^{\infty} \frac{e^{ik_z|z-z_s|}}{2ik_z} e^{ik_x(x-x_s)} e^{ik_y(y-y_s)} dk_x dk_y, \tag{5}$$

where the vertical wavenumber

$$\begin{aligned} k_z &= sgn(\omega)\sqrt{\frac{\omega^2}{c^2(\omega)} - k_x^2 - k_y^2} \\ &= sgn(\omega)\sqrt{\frac{\omega^2}{c_0^2} - k_x^2 - k_y^2 + \frac{\omega^2}{c_0^2}\frac{F(\omega)}{Q}} \\ &= sgn(\omega)\sqrt{q^2 + \frac{\omega^2}{c_0^2}\frac{F(\omega)}{Q}}. \end{aligned} \tag{6}$$

$q = sgn(\omega)\sqrt{\frac{\omega^2}{c_0^2} - k_x^2 - k_y^2}$. In Equation 5, Green's function still can be treated as a sum of weighted plane waves from all the directions. k_z is a complex value caused by the complex $F(\omega)$.

2.2 Wavefield of a one-reflector 1D absorptive model

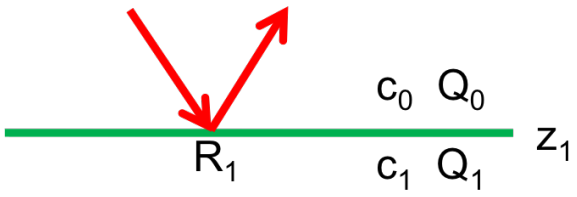

Figure 1: A one-reflector horizontal model.

Given a one-reflector 1D earth model as shown in Figure 1, and the depth of the interface is z_1, we can express the wavefield based on Equation 5. Assuming both the source and receiver are

located at the depth 0 (or $\epsilon_s = \epsilon_g = 0$), a 3D point source can generate the data with cylindrical symmetry that cares the offset only.

$$D(r,\omega) = \frac{1}{2\pi}\int_{-\infty}^{\infty} \frac{R_1(k_r,\omega)e^{i2k_z z_1}}{2ik_z} J_0(k_r r) k_r dk_r, \tag{7}$$

where $r = \sqrt{(x_g - x_s)^2 + (y_g - y_s)^2}$, k_r is the Fourier conjugate of r, and data in wavenumber domain can be transformed back to space domain via Hankel transform.

$$D(k_r,\omega) = \frac{R_1(k_r,\omega)e^{i2k_z z_1}}{2ik_z}. \tag{8}$$

The reflection coefficient for plane wave is

$$R_1(k_r,\omega) = \frac{k_z - k_{z_1}}{k_z + k_{z_1}}, \tag{9}$$

where $k_z = sgn(\omega)\sqrt{\frac{\omega^2}{c_0^2} - k_r^2 + \frac{\omega^2}{c_0^2}\frac{F(\omega)}{Q_0}}$, and $k_{z_1} = sgn(\omega)\sqrt{\frac{\omega^2}{c_1^2} - k_r^2 + \frac{\omega^2}{c_1^2}\frac{F(\omega)}{Q_1}}$.

3 Analytic test of ISS internal multiple attenuation algorithm on pre-stack data

In this section, the pre-stack data $D(r,t)$ from the absorptive-dispersive earth will be used to test the ISS internal multiple attenuator analytically. The algorithm of 3D point source and 1D earth is chosen for the analytic evaluation in this section and the subsequent numerical tests. Besides, we assume that the first layer where the source is located does not involve the absorption and dispersion; i.e., Q_0 in the first layer is infinity or $Q_0 \gg 0$.

For 3D source and 1D earth, the ISS internal multiple attenuation algorithm (Lin and Weglein, Lin and Weglein) is

$$b_3(k_r,2q) = \int_{-\infty}^{\infty} b_1(k_r,z)e^{i2qz}dz \int_{-\infty}^{z-\epsilon} b_1(k_r,z_1)e^{-i2qz_1}dz_1 \int_{z_1+\epsilon}^{\infty} b_1(k_r,z_2)e^{i2qz_2}dz_2, \tag{10}$$

where $q = sgn(\omega)\sqrt{\frac{\omega^2}{c_0^2} - k_r^2}$; and c_0 is the velocity of the first layer, at the reference frequency ω_r.

$b_1(k_r,\omega) = 2iqD(k_r,\omega)$. Since we assume that $Q_0 \gg 0$, the vertical wavenumber in the first layer $k_z = sgn(\omega)\sqrt{q^2 + \frac{\omega^2}{c_0^2}\frac{F(\omega)}{Q_0}} \approx q$, which is approximately a real value. Therefore, multiplying $D(k_r,\omega)$ with $2iq$, the denominator of $D(k_r,\omega)$ as shown in Equation 8 is approximately removed in $b_1(k_r,\omega)$. Applying an uncollapsed migration, then $b_1(k_r,z)$ that is in the pseudo depth domain can be obtained. $b_3(k_r,2q)$ is the predicted internal multiple.

ϵ in the formula is used to ensure that the events satisfy the lower-higher-lower relationship, and its value is chosen on the basis of the length of the wavelet.

As shown in Figure 2, a two-reflector 1D earth model is taken as an example, with zero depths of both the source and the receiver.

Two primaries can be expressed in (k_r,ω) domain with forms

$$\begin{aligned} P^{(1)}(k_r,\omega) &= R_1(k_r,\omega)e^{i2k_z z_1}, \\ P^{(2)}(k_r,\omega) &= T_{01}(k_r,\omega)T_{10}(k_r,\omega)R_2(k_r,\omega)e^{i2k_z z_1}e^{i2k_{z_1}(z_2-z_1)}, \end{aligned} \tag{11}$$

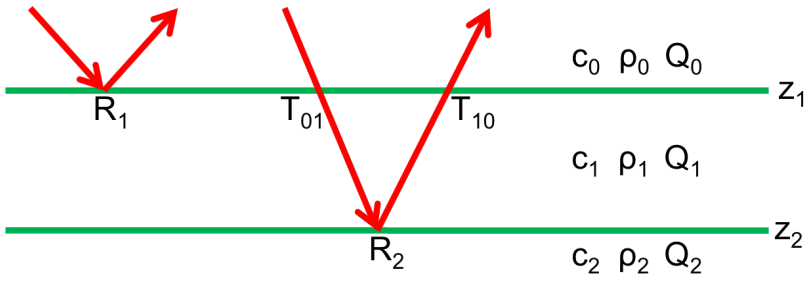

Figure 2: A two-reflector 1D model.

where $k_{z_1} = sgn(\omega)\sqrt{q_1^2 + \frac{\omega^2}{c_1^2}\frac{F(\omega)}{Q_1}}$, and $k_r^2 + q_1^2 = \frac{\omega^2}{c_1^2}$. All the reflection and transmission coefficients are complex values.

$$b_1(k_r, \omega) = P^{(1)}(k_r, \omega) + P^{(2)}(k_r, \omega). \tag{12}$$

Changing the variable from ω to $2q$ ($q = sgn(\omega)\sqrt{\frac{\omega^2}{c_0^2} - k_r^2}$),

$$\begin{aligned} b_1(k_r, 2q) &= P^{(1)}(k_r, 2q) + P^{(2)}(k_r, 2q), \\ P^{(1)}(k_r, 2q) &= R_1(k_r, q)e^{ik_z 2z_1}, \\ P^{(2)}(k_r, 2q) &= T_{01}(k_r, q)T_{10}(k_r, q)R_2(k_r, q)e^{ik_z 2z_1}e^{ik_{z_1} 2(z_2 - z_1)}, \end{aligned} \tag{13}$$

where

$$\begin{aligned} k_z &= sgn(q)\sqrt{(k_r^2 + q^2)(1 + \frac{F(k_r, q)}{Q_0}) - k_r^2}, \\ k_{z_1} &= sgn(q)\sqrt{(k_r^2 + q_1^2(q))(1 + \frac{F(k_r, q_1(q))}{Q_1}) - k_r^2}, \\ F(k_r, q) &= \frac{i}{2}sgn(q) - \frac{1}{\pi}log(\frac{\sqrt{(k_r^2 + q^2)}}{|\omega_r|}), \\ F(k_r, -q) &= F^*(k_r, q). \end{aligned} \tag{14}$$

Similarly the internal multiple of the data can be expressed as

$$IM(k_r, 2q) = -T_{01}(k_r, q)T_{10}(k_r, q)R_1(k_r, q)R_2^2(k_r, q)e^{ik_z 2z_1}e^{ik_{z_1} 4(z_2 - z_1)}. \tag{15}$$

Applying the uncollapse migration (or Fourier transforming b_1 from $2q$ to z),

$$b_1(k_r, z) = P^{(1)}(k_r, z) + P^{(2)}(k_r, z). \tag{16}$$

We substitute b_1 with two primaries into the internal multiple attenuation algorithm as shown in Equation 10. Assuming that the two primaries are isolated and ϵ is chosen reasonably, there is no overlap between the two events among the integrals, then the predicted internal multiple $b_3(k_r, 2q)$ can be obtained finally.

$$\begin{aligned} b_3(k_r, 2q) &= P^{(2)}(k_r, 2q)P^{(1)}(k_r, -2q)P^{(2)}(k_r, 2q) \\ &= (T_{01}(k_r, q)T_{10}(k_r, q))^2 R_1^*(k_r, q)R_2^2(k_r, q)e^{ik_z 2z_1}e^{ik_{z_1} 4(z_2 - z_1)}e^{i(k_z - k_z^*)2z_1} \\ &= (T_{01}(k_r, q)T_{10}(k_r, q))^2 R_1^*(k_r, q)R_2^2(k_r, q)e^{ik_z 2z_1}e^{ik_{z_1} 4(z_2 - z_1)}e^{-\mathrm{IMAG}(k_z)4z_1}, \end{aligned} \tag{17}$$

where IMAG(k_z) is the imaginary part of k_z.

Comparing the analytic forms between the predicted and the actual internal multiples, we find

$$b_3(k_r,2q) = -T_{01}(k_r,q)T_{10}(k_r,q)\frac{R_1^*(k_r,q)}{R_1(k_r,q)}e^{-\text{IMAG}(kz)4z_1}IM(k_r,2q). \tag{18}$$

If we define

$$\begin{aligned} TF &= T_{01}(k_r,q)T_{10}(k_r,q)\frac{R_1^*(k_r,q)}{R_1(k_r,q)}, \\ AF &= e^{-\text{IMAG}(kz)4z_1}, \end{aligned} \tag{19}$$

then

$$b_3(k_r,2q) = -TF{*}AF * IM(k_r,2q). \tag{20}$$

TF is the transmission factor, and AF is the Q absorption factor. For this two-reflector model, TF represents the transmission loss at the first interface; whereas AF represents the transmission loss (energy absorption) in the first layer. Since we assume $Q_0 \gg 0$ in the first layer, AF is actually close to 1. However, if there are more than two reflectors existing in the absorptive media, both TF and AF will have more complicated forms.

If we use $IM^{(j)}$ to represent the multiple that is generated at the j^{th} interface (i.e., the down-reflection happens at the interface of depth z_j), and $j \geq 1$, then

$$\begin{aligned} TF &= \begin{cases} T_{01}T_{10}\frac{R_1^*}{R_1} & j=1 \\ \prod_{i=1}^{i=j}(T_{i-1,i}T_{i,i-1})\frac{R_j^*}{R_j} & j>1 \end{cases} \\ AF &= \begin{cases} e^{-\text{IMAG}(kz)4z_1} \approx 1 & j=1 \\ e^{-\sum_{i=1}^{i=j-1}(\text{IMAG}(kz_i)4(z_{i+1}-z_i))}e^{-\text{IMAG}(kz)4z_1} & j>1 \end{cases} \end{aligned} \tag{21}$$

TF relates to the transmission loss at the interfaces that are above and on the multiple generator; and AF relates to the transmission loss in the layers above the multiple generator. Both TF and AF are smaller than 1, and they will corporate to produce a smaller prediction amplitude.

From the analysis above, even though the data goes through an absorptive medium, as long as the first layer of the earth is not seriously involving the absorptive and dispersive properties, the ISS attenuator can choose a reference medium to be homogeneous acoustic and without absorption/dispersion. Given all that, the prediction has the accurate time and approximate amplitude. Actually, even the first layer is suffering from not slight absorption (e.g., for the model tested in the following numeric section, $Q_0 = 100$), our numeric test still shows satisfying result.

4 Numerical evaluation

In this section, we will use a four-reflector 1D absorptive model to test the ISS internal multiple attenuation algorithm of Equation 10. The parameters of the model are listed in Figure 3.

The data generated by a point source is plotted in Figure 4a (using the software of Schlumberger), and it has four primaries (P1-P4) and a set of internal multiples (IM). Figure 4b shows the

Layer No.	Depth (m)	Velocity (m/s)	Density (kg/m³)	Q
1	400	1500	1000	100
2	850	2000	1200	40
3	1200	2500	1500	80
4	3200	6500	3000	80
5		4000	3500	100

Figure 3: A four-reflector 1D model for numeric test.

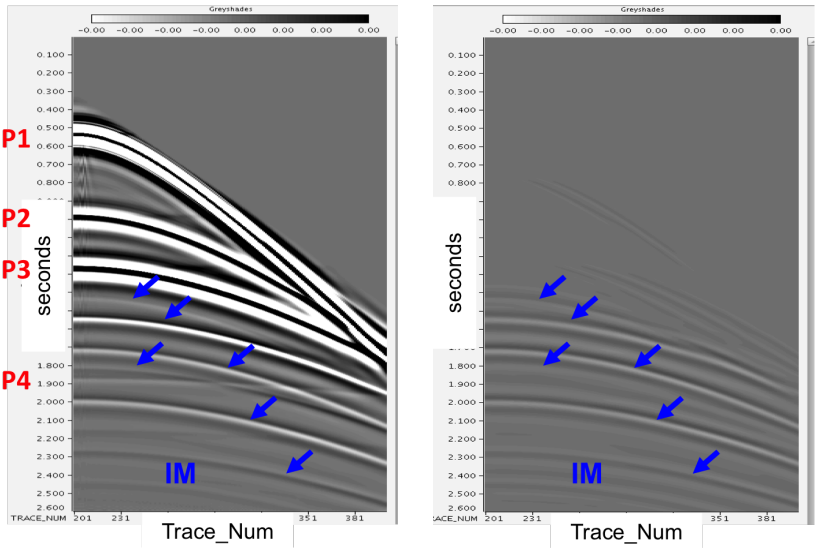

(a) (b)

Figure 4: ISS internal multiple attenuation result. (a) input data with both primaries and internal multiples; (b) predicted internal multiples.

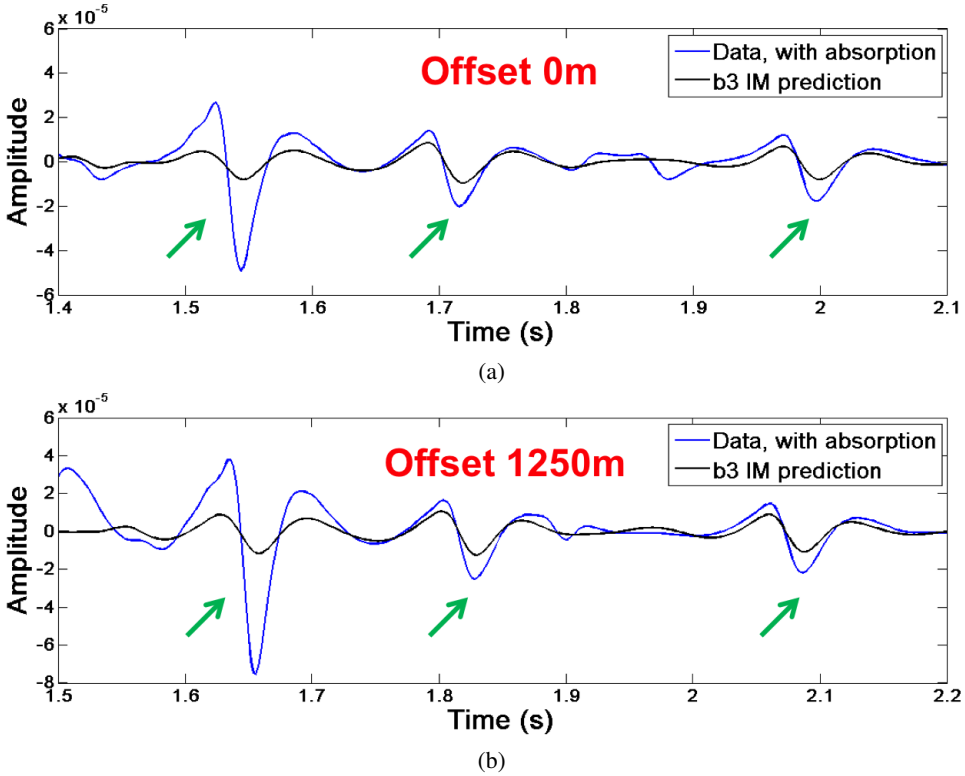

Figure 5: ISS internal multiple attenuation result. (a) trace with offset of 0m; (b) trace with offset of 1250m.

ISS internal multiple prediction result. All the internal multiples are indicated by the arrows. Two traces are selected for detailed comparison in Figure 5a and Figure 5b, where the blue lines represent the input data, suffering absorption, the black lines are corresponding to the prediction results, and the green arrows are pointing to the events of internal multiple. We conclude from the results that the prediction time is accurate, and the amplitude is approximate (smaller than the actual). (This test was performed at WesternGeco/Schlumberger.)

5 Discussion and conclusion

In this paper, the ISS internal multiple attenuation algorithm is tested analytically and numerically using Q-influenced data, with the conclusion that the prediction will have the correct phase and an approximate amplitude.

The discussion in this paper gives us confidence that even for an attenuating medium, the ISS internal multiple attenuator can provide a result that retains the primary and partially removes the internal multiple. This is an important step in a strategy to eliminate internal multiples for both elastic and anelastic media. That will allow application for exploration plays where the geology exhibits significant absorption, e.g., pre-salt plays in the deep water Gulf of Mexico, off-shore Brazil, the Red Sea and the North Sea.

In order to step further for internal multiple elimination in the attenuating medium, there are sets of different approaches and ideas. (1) developing an ISS eliminator in the absorptive media; (2) preprocessing for Q compensation, and then applying the ISS elimination algorithm in the elastic media (Zou and Weglein, 2013). In terms of Q compensation, it can be achieved by method either with Q information or without Q information (e.g., Innanen and Weglein, 2003, 2005; Innanen and Lira, 2008).

6 Acknowledgements

We are grateful to all M-OSRP sponsors for encouragement and support in this research. We thank Clement Kostov, Debra Dishberger and Schlumberger for providing an outstanding internship and mentoring opportunity.

References

Araújo, F. V. *Linear and non-linear methods derived from scattering theory: backscattered tomography and internal multiple attenuation*. PhD thesis, Universidade Federal da Bahia, 1994.

Ferreira, A. Internal multiple removal in offshore Brazil seismic data using the inverse scattering series. Master's thesis, University of Houston, 2011.

Fu, Q., Y. Luo, P. G. Kelamis, S. Huo, G. Sindi, S. Y. Hsu, and A. B.Weglein. "The inverse scattering series approach towards the elimination of land internal multiples." *80th Annual International Meeting, SEG, Expanded Abstracts* (2010): 34563461.

Innanen, K. A. and J.E. Lira. "Direct non-linear Q compensation of primaries in layered media: Theory and synthetic examples.." *Proceedings of the 78th Annual Meeting of the Society of Exploration Geophysicists, Las Vegas, Nevada.* . Soc. Expl. Geophys., 2008.

Innanen, K. A. and A. B. Weglein. "Construction of absorptive/dispersive wave fields with the forward scattering series." *Journal of Seismic Exploration* 12 (2003): 259–282.

Innanen, K. A. and A. B. Weglein. "Towards non-linear construction of a Q-compensation operator directly from reflection seismic data." *Proceedings of the 75th Annual Meeting of the Society of Exploration Geophysicists, Houston, TX.* . Soc. Expl. Geophys., 2005.

Kjartansson, E. *Attenuation of seismic waves in rocks and applications in energy exploration*. PhD thesis, Standford University, 1979.

Kolsky, H. "The propagation of stress pulses in viscoelastic solids." *Philos. Mag.* 1 (1956): 693–710.

Lin, X. and A. B. Weglein. "The significance of incorporating a 3-D point source in the inverse scattering series internal multiple attenuator for a 1-D subsurface." *85th Annual International Meeting, SEG, Expanded Abstracts, submitted*.

Weglein, A. B., F. V. Araújo, P. M. Carvalho, R. H. Stolt, K. H. Matson, R. T. Coates, D. Corrigan, D. J. Foster, S. A. Shaw, and H. Zhang. "Inverse Scattering Series and Seismic Exploration." *Inverse Problems* (2003): R27–R83.

Weglein, A. B., F. A. Gasparotto, P. M. Carvalho, and R. H. Stolt. "An Inverse-Scattering Series Method for Attenuating Multiples in Seismic Reflection Data." *Geophysics* 62 (November-December 1997): 1975–1989.

Wu, J. and A. B. Weglein. "The first test and evaluation of the inverse scattering series internal multiple attenuation algorithm for an attenuating medium." *84th Annual International Meeting, SEG, Expanded Abstracts* (2014): 4130–4134.

Zou, Y. and A. B. Weglein. "A new method to eliminate first order internal multiples for a normal incidence plane wave on a 1D earth." *83rd Annual International Meeting, SEG, Expanded Abstracts* (2013): 4136–4140.

The impact of accommodating the source radiation pattern on the inverse scattering series free-surface multiple elimination algorithm on data with interfering or proximal primaries and multiples

Jinlong Yang and Arthur B. Weglein

Abstract

The inverse scattering series (ISS) free-surface multiple elimination algorithm has certain prerequisites: (1) removal the reference wavefield, (2) estimation and removal of the source wavelet and radiation pattern, and (3) removal of source and receiver ghosts. For the first prerequisite, Weglein and Secrest (1990) describe a method to separate the reference wavefield from the scattered wavefield (reflection data) without requiring subsurface information. In this report, the impacts of prerequisites (2) and (3) on the ISS free-surface multiple elimination algorithm (Carvalho, 1992; Weglein et al., 1997) are discussed and exemplified, and then the algorithm is modified and extended to accommodate for a source radiation pattern. Accommodation for the radiation pattern can provide added value to the algorithm, compared with previous implementations that assumed an isotropic point source for predicting the amplitude and phase of free-surface multiples. It is noteworthy that these three prerequisites listed above can all be satisfied by Green's theorem methods. Green's theorem methods for separating the reference wavefield and the scattered wavefield do not require subsurface information and are consistent with the ISS free-surface multiple elimination algorithm. Our new, extended ISS free-surface multiple elimination algorithm, which accommodates for the source radiation pattern, is tested here on a 1D acoustic model with proximal and interfering primaries and multiples, and the results indicate that when the source has a radiation pattern, the new algorithm can predict free-surface multiples more accurately than methods without that accommodation. This increased effectiveness in prediction is important for removing free-surface multiples without damaging primaries, when the free-surface multiples are proximal to and interfering with primaries (or other multiples). It is important in such cases to increase our predictive effectiveness because other prediction methods, such as surface-related multiple elimination (SRME) algorithm, have difficulties and issues with prediction accuracy, and those issues affect efforts to remove multiples through adaptive subtraction.

1 Introduction

In seismic exploration, preprocessing of the seismic data, including removal of reference waves, estimation of wavelet, and removal of ghosts, is important in order to achieve subsequent processing goals and objectives. The reference wave should be removed because it does not contain subsurface information, and obtaining subsurface information is our interest and objective. To identify subsurface properties from seismic data, we also need to identify and remove the seismic source's effect from the seismic data because both the source and the properties of the earth contribute to the recorded seismic data (e.g., Weglein and Secrest, 1990; Amundsen, 1993; Osen et al., 1998). Source and receiver deghosting will remove the ghost notches and enhance the low-frequency content of the seismic data (e.g., Zhang and Weglein, 2005, 2006; Mayhan et al., 2011, 2012; Mayhan and Weglein, 2013), and those steps are also the prerequisites of all ISS task-specific subseries (Weglein et al., 2003). All three of these preprocessing steps can be achieved by using Green's theorem

methods without requiring subsurface information. Green's theorem methods were pioneered by J. Zhang (Weglein et al., 2002; Zhang and Weglein, 2005, 2006; Zhang, 2007) and developed by J. Mayhan (Mayhan et al., 2011, 2012; Mayhan and Weglein, 2013). Wu and Weglein (2014) extended the Green's theorem method for the reference wave and scattered wave separation from the off-shore acoustic plays to the on-shore elastic plays.

In seismic data preprocessing, multiple removal is a classic and long-standing problem. Various methods have been developed to either attenuate or eliminate free-surface multiples, and each method has different assumptions, advantages, and limitations (see, e.g., Carvalho, 1992; Verschuur et al., 1992; Weglein et al., 1997, 2003; Berkhout and Verschuur, 1999; Dragoset et al., 2008). Among these methods, the ISS free-surface multiple elimination algorithm (Carvalho, 1992; Weglein et al., 1997, 2003) is fully data-driven and does not require any subsurface information, which is a big advantage, especially under conditions of complex geology. The ISS free-surface multiple elimination algorithm (Carvalho, 1992; Weglein et al., 1997, 2003) can, in principle, predict the exact amplitude and phase of the free-surface multiples at all offsets and then can remove them through a simple subtraction. In practice, however, the algorithm may require an adaptive assist. However, SRME algorithm can only provide approximate predictions because it ignores the obliquity factor and retains the source ghosts. Hence, it requires an adaptive step not only in principle but also in practice. Adaptive subtraction (energy minimization, for example) can be a reasonable choice at times; in other situations, however, it can have issues with proximal and interfering events. It is based on the energy minimization criterion, which assumes tha the energy of the data will be minimized after the multiples are removed, but in some cases, after multiple removal, the energy may be increasing rather than decreasing. Therefore, adaptive subtraction can damage primaries or fail to remove the multiples.

For data generated by a general source with a radiation pattern, the ISS free-surface multiple elimination algorithm needs to be modified and extended because it assumes an isotropic point source, where the source has no variation of amplitude or phase with take-off angle. In towed marine acquisition, a source array is commonly used to increase the power of the source, broaden the bandwidth, and cancel the random noise. Such a source array exhibits directivity in the take-off angle (Loveridge et al., 1984), that directivity is an issue for multiple removal and attenuation and for AVO analysis. Thus, in seismic processing, it is essential that we characterize the source array's effect on any seismic processing methods. Therefore, to accommodate a general source with a radiation pattern, we have modified and extended the ISS free-surface multiple elimination algorithm to improve its accuracy in predicting multiples. That accommodation can enhance the fidelity of amplitude and phase prediction of free-surface multiples at all offsets when the source has a radiation pattern. Moreover, it is a necessary preparation for internal multiple removal, because the better we succeed at removing the free-surface multiples, the better we will succeed at achieving the subsequent processing steps, such as internal multiple removal, imaging, and inversion.

2 Theory

The ISS free-surface multiple elimination algorithm in the 2D case starts with the input data $D_1'(k_g, k_s, \omega)$, which are source and receiver deghosted. For an isotropic point source, the algorithm is proposed by (Carvalho, 1992; Weglein et al., 1997, 2003):

$$D_n'(k_g, k_s, \omega) = \frac{1}{i\pi A(\omega)} \int dk D_1'(k_g, k, \omega) q e^{iq(\epsilon_g + \epsilon_s)} D_{n-1}'(k, k_s, \omega), \tag{1}$$

where k_g, k_s and ω represent the Fourier conjugates of receiver, source, and time, respectively. The parameters ϵ_g and ϵ_s are the receivers' and sources' depth below the free surface, respectively. The term q is the obliquity factor $q = sgn(\omega)\sqrt{\omega^2/c_0^2 - k^2}$. c_0 is the reference velocity. $A(\omega)$ is the source signature, which is a function of time or ω in different domains. The free-surface multiples are predicted order-by-order and then added together to give the deghosted and free-surface demultipled data $D'(k_g, k_s, \omega) = \sum_{n=1}^{\infty} D'_n(k_g, k_s, \omega)$.

For data generated by a general source with a radiation pattern, however, the current ISS free-surface multiple elimination algorithm (equation 1) can only predict multiples approximately. To accommodate the source's effect, the ISS free-surface multiple elimination algorithm is modified and extended from an isotropic point source to a general source ρ with a radiation pattern (Yang et al., 2013; Yang, 2014)

$$D'_n(k_g, k_s, \omega) = \frac{1}{i\pi} \int \frac{dk}{\rho(k, q, \omega)} D'_1(k_g, k, \omega) q e^{iq(\epsilon_g + \epsilon_s)} D'_{n-1}(k, k_s, \omega), \tag{2}$$

where $\rho(k, q, \omega)$ is the projection of the source signature in the f-k domain and $k^2 + q^2 = \omega^2/c_0^2$ The projection of the source signature $\rho(k, q, \omega)$ can be achieved from the reference wavefield, which is separated from the total wavefield by using Green's theorem methods (Weglein and Secrest, 1990; Mayhan and Weglein, 2013; Tang et al., 2013).

In this report, we assume that the source array is invariant from one shot to the next. In other words, the geometry or the distribution of the source array is the same for each shot. The direct reference wavefield P_0^d for a 2D case can be expressed as an integral of the direct reference Green's function G_0^d over all air-guns in an array,

$$P_0^d(x, z, x_s, z_s, \omega) = \iint dx' dz' \rho(x', z', \omega) G_0^d(x, z, x' + x_s, z' + z_s, \omega), \tag{3}$$

where (x, z) and (x_s, z_s) are the prediction point and the source point, respectively. Here, (x', z') is the distribution of the source with respect to the source locator (x_s, z_s). Using the bilinear form of Green's function and Fourier transforming over x, we obtain the relationship between ρ and P_0^d as

$$P_0^d(k, z, x_s, z_s, \omega) = \rho(k, q, \omega) \frac{e^{iq|z - z_s|}}{2iq} e^{-ikx_s}. \tag{4}$$

Since $k^2 + q^2 = \omega^2/c_0^2$, q is not a free variable, and hence we can not obtain $\rho(x, z, \omega)$ in the space-frequency domain by taking an inverse Fourier transform on $\rho(k, q, \omega)$. However, the projection of the source signature $\rho(k, q, \omega)$ can always be achieved directly from the direct reference wavefield P_0^d in the f-k domain, where either the variable k or q represents the amplitude variations of the source signature with angles. Ikelle et al. (1997) also proposed a similar quantity, $A(k, \omega)$, the inverse source wavelet, and solved for it indirectly using the energy minimization criterion. We instead apply Green's theorem wave separation methods to find the generalized source signature directly.

By substituting the projection of the source signature $\rho(k, q, \omega)$ into the ISS free-surface multiple removal subseries, we can modify and extend the ISS free-surface multiple elimination algorithm (Yang, 2014). The extended algorithm accommodates a general source with a radiation pattern and can provide added value by improving the fidelity of amplitude and phase predictions of the free-surface multiples at all offsets. The extended ISS free-surface multiple elimination algorithm is fully multidimensional and does not require any subsurface information. Therefore, it is

consistent with Green's theorem methods that provide all the data requirements. The extended free-surface multiple elimination algorithm (equation 2) is also consistent with the previous free-surface multiple elimination algorithm (equation 1) in which the general source (e.g., source array) reduces to an isotropic point source. Finally, this modification easily can be extended to the 3D case.

3 Numerical tests

In this section, the effects of not satisfying the prerequisites of the ISS free-surface multiple elimination algorithm are exemplified, tested, and compared with the effects of satisfying them. For each test, we will show the impact of each prerequisite on the ISS free-surface multiple elimination algorithm separately and then will compare its result with the response when the same prerequisite has been satisfied. We will show the impact of ghosts, of the source wavelet, and of the source radiation pattern on free-surface multiple removal. For exemplifying the impact of ghosts and of the source wavelet on free-surface multiple removal, a point source is applied to generate the data. For exemplifying the impact of the source radiation pattern on free-surface multiple removal, a source array is applied to generate the data.

The tests are organized as follows: First, we test the impact of ghosts and the source wavelet on free-surface multiple removal. Then when both prerequisites – deghosting and source wavelet deconvolution – have been satisfied, the result of free-surface multiple removal is also shown. Second, the impact of the source radiation pattern on free-surface multiple removal is presented. The results of free-surface multiple removal by using the current algorithm (equation 1) are presented and are compared with the results from using the extended algorithm (equation 2), which accommodates for the radiation pattern. Finally, we will show free-surface multiple removal on the data with destructively interfering primaries and multiples.

3.1 The impact of ghosts and source wavelet on free-surface multiple removal

The numerical tests for the impact of ghosts and of the source wavlet on free-surface multiple removal are based on a 1D acoustic model with varying velocity and constant density, as shown in Figure 1. The model has one reflector, at 300m. The depths of the source and receiver are 7m and

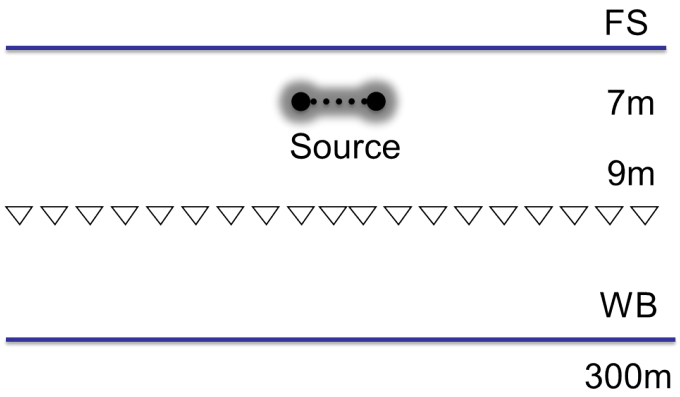

Figure 1: One-dimensional acoustic constant-density medium.

9m, respectively. Synthetic data are generated by using the Cagniard-de Hoop method (de Hoop and van der Hijden, 1983; Aki and Richards, 2002), which can accurately produce any specific event that we are interested in.

For exemplifying the impact of ghosts and of the source wavelet on free-surface multiple removal, a point source is applied to generate the data. We apply the current ISS free-surface multiple elimination algorithm (equation 1) to predict and remove the free-surface multiples from the point-source data. Figure 2 illustrates the impact of ghosts and the source wavelet on free-surface multiple removal. Figure 2a shows the input data with ghosts. Inputting it into the ISS free-surface multiple elimination algorithm gives the free-surface multiple prediction shown in Figure 2b. After subtraction of the prediction from the input data, Figure 2c shows the results of free-surface multiple removal by means of a simple subtraction. From this example, we can see that if the input data are not deghosted, the ISS free-surface multiple elimination algorithm can predict the correct phase but only the approximate amplitude of the free-surface multiples. After ghosts have been removed,

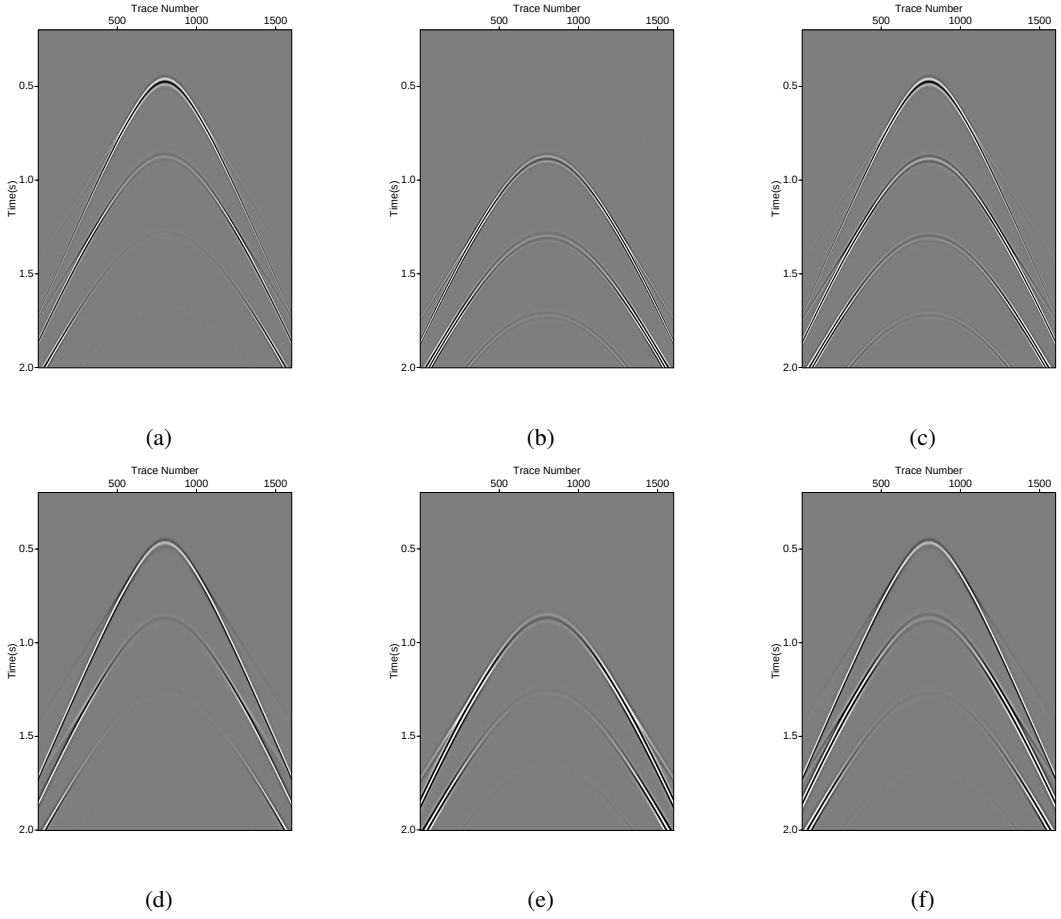

Figure 2: Input data with ghosts (a) and without ghosts (d); Free-surface multiple prediction using the ISS free-surface multiple elimination algorithm with source wavelet deconvolution (b) and without source wavelet deconvolution (e); (c)&(f) Results after free-surface multiple removal through a simple subtraction.

the resulting input data are shown in Figure 2d. Figure 2e shows the predicted free-surface multiples obtained by using the ISS free-surface multiple elimination algorithm without source wavelet

deconvolution. Figure 2f illustrates the results of free-surface multiple removal, again by a simple subtraction. Without incorporating the source wavelet deconvolution, the ISS free-surface multiple elimination algorithm can predict the correct phase but only the approximate amplitude of the free-surface multiples. Therefore, without removing the ghosts and incorporating the source wavelet deconvolution, the ISS free-surface multiple elimination algorithm can only predict approximate free-surface multiples and can not remove them through a simple subtraction.

If all the prerequisites are satisfied – i.e., if the ghosts have been removed and the source wavelet has been deconvolved – we can see in Figure 3 shows the results of following free-surface multiple removal. Figure 3a shows the input data and Figure 3b is the free-surface multiple prediction. After subtracting from the input data through a simple subtraction, Figure 3c shows the result of following free-surface multiple removal. From this example, we can see that if all the prerequisites are satisfied, the free-surface multiples are predicted exactly by using the ISS free-surface multiple elimination algorithm and are removed through a simple subtraction. Most importantly, the primaries are not touched, as is shown in Figure 3c. Therefore, the ISS free-surface multiple elim-

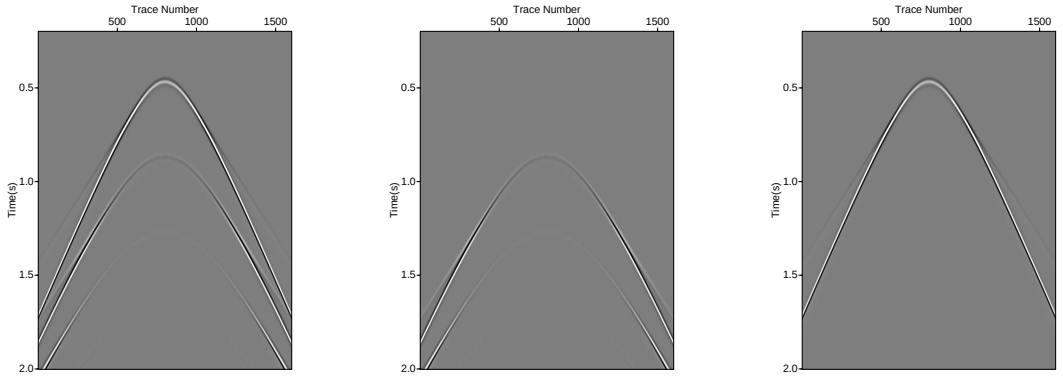

(a) (b) (c)

Figure 3: Free-surface multiple removal with all prerequisites (source wavelet deconvolution and ghost removal) satisfied. (a) Input data; (b) free-surface multiple prediction, and (c) the result after removal of the free-surface multiple.

ination algorithm has the ability to predict accurately the phase and the amplitude of multiples if its prerequisites (incorporation of the source wavelet deconvolution, and deghosting) are satisfied.

3.2 The impact of the source radiation pattern on free-surface multiple removal when there are proximal primaries and multiples

In this test, we move the water bottom from 300m to 90m (Figure 4); hence, the primary now is proximal to and overlapping the free-surface multiples. To evaluate the significance of the source radiation pattern, a source array (Figure 5) with nine air-guns is applied to generate the data. Each air-gun has a different amplitude, which is indicated by the numbers in Figure 5. For simplicity, in the source-array data, only the primary and the first-order free-surface multiple are generated by the Cagniard-de Hoop method. The primary and multiple are overlapping and interfering destructively; hence, only the ISS method may be able to remove the free-surface multiples.

Figure 6a represents the source-array data for this source array, and Figure 6d is its correspond-

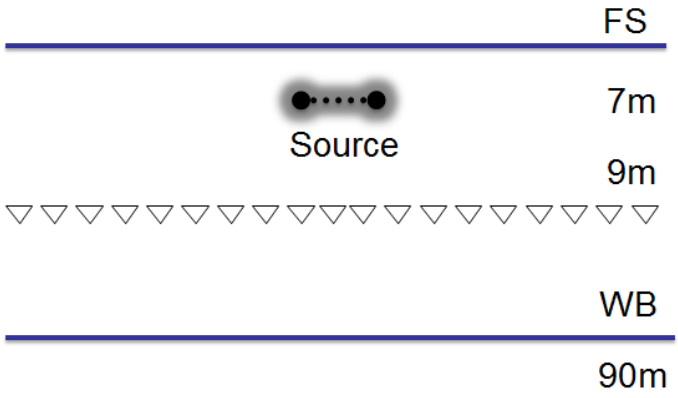

Figure 4: One-dimensional acoustic constant-density medium.

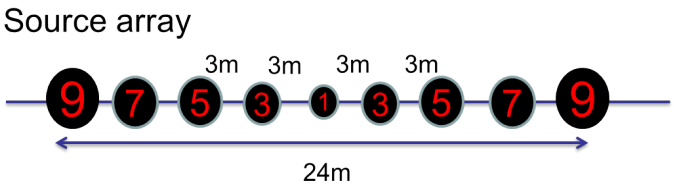

Figure 5: Source array with nine air-guns.

ing wiggle plot for a small window (for times from 1.0s to 1.4s and traces from 1330 to 1420); we can see that the primary and the first-order free-surface multiple overlap when the offset exceeds approximately 1000m. Furthermore, it is clear that they are destructively overlapping. Therefore, the adaptive subtraction method can be invalid or fail for this kind of situation, because the method is based on the energy minimization criterion, which assumes that the energy of the data will be minimized after the multiples are removed. However, in this case, the energy increases after removal of the multiples.

Figures 6b shows the results following free-surface multiple removal by using the current ISS free-surface multiple elimination algorithm (equation 1) and 6c shows the results from using the extended algorithm (equation 2). It can be seen that for the source-array data with a radiation pattern, the current ISS free-surface multiple elimination algorithm can effectively remove free-surface multiples, but some residual multiples remain due to the effect of the source radiation pattern. However, the new, extended ISS free-surface multiple elimination algorithm can remove the free-surface multiples completely through a simple subtraction.

Comparing Figures 6f and 6e, we can see in Figure 6e that the primary is still affected by the residual multiple, whereas in Figure 6f, the primary remains untouched as the original primary. Figure 7 illustrates the details of comparing one trace at $1800m$ offset. After removal of free-surface multiples by using the new algorithm, the primary is the same as the original one in the input data. With the current algorithm, the primary (Figure 6e) is a little weaker than the original primary, and this amplitude error will seriously affect AVO analysis.

For the source-array data, the current ISS free-surface multiple elimination algorithm can predict and remove the free-surface multiples well with some small residues, while the new, extended ISS

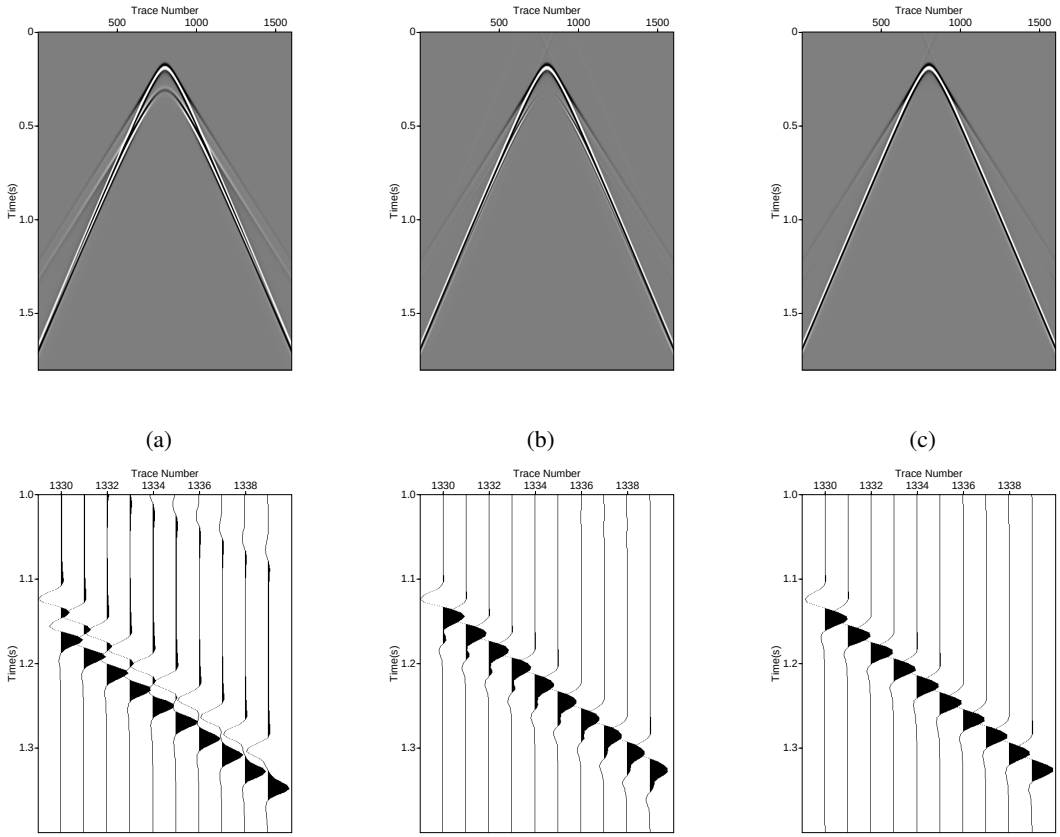

Figure 6: The impact of the source radiation pattern on free-surface multiple removal. (a) The source-array data; (b) the data following free-surface multiple removal using the current ISS free-surface multiple elimination algorithm; note that there are some residual multiples; (c) the data following free-surface multiple removal using the extended ISS free-surface multiple elimination algorithm; note that all the multiples have been completely eliminated. (d), (e), and (f) are their corresponding wiggle plots for the traces from 1330 to 1420 (offset from 1590m to 1860m).

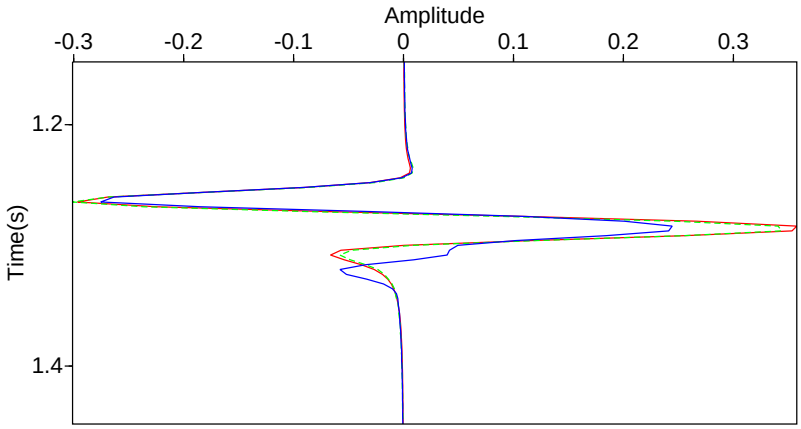

Figure 7: Comparison of one trace at $1800m$ offset. Red line: the original primary in the input data; blue line: the data after multiple removal by using the current free-surface multiple elimination algorithm; dashed green line: the data after multiple removal by using the new, extended free-surface multiple elimination algorithm.

free-surface multiple elimination algorithm can accurately predict and completely eliminate the free-surface multiples without damaging the primaries.

3.3 Free-surface multiple removal on data with destructively interfering primaries and multiples

This test is based on a 1D two-reflector acoustic model with constant velocity and varying density, as shown in Figure 8. The parameters are designed so that the second primary is destructively interfering with the first-order free-surface multiple due to the first reflector. The data are generated by the reflectivity method. Here we do not generate the ghosts, in other words, we do not need to remove ghosts from the data. In practice, we need to remove the ghosts first to prepare for free-surface multiple removal.

First, the point-source data are generated by an isotropic point source to test the current free-surface multiple elimination algorithm. To see the destructive interference, we generate the primaries and free-surface multiples separately. Figure 9 shows the seismic events. P_1 and P_2 are the first two primaries. F_1, F_2 and F_3 are the first-order, second-order, and third-order free-surface multiples. The events in the same color have the same arrival time, hence, they are interfering in the seismic data.

Figure 10 shows one shot gather. Figure 10a represents the two generated primaries and Figure 10b shows the free-surface multiples. Adding them together, we obtain the total point-source data, as shown in Figure 10c. As we can see, the second primary and the first-order free-surface multiple are destructively interfering and are canceling. Therefore, the adaptive subtraction method can be invalid or fail for this kind of situation, because the method is based on the energy minimization criterion, which assumes that the energy of the data will be minimized after the multiples are removed.

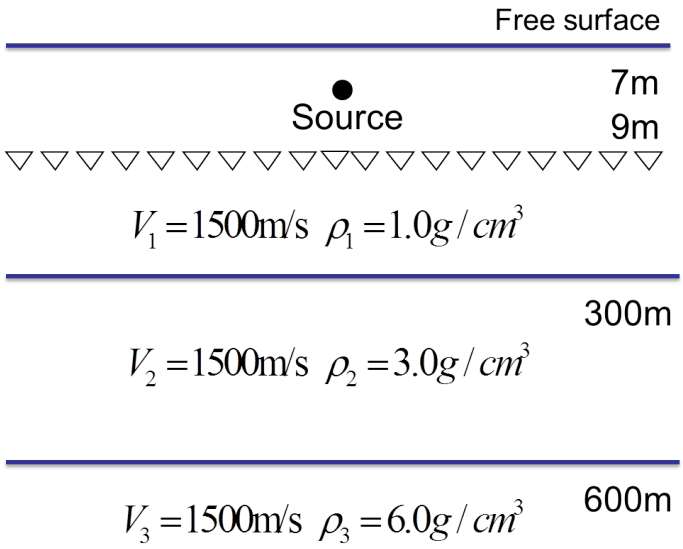

Figure 8: One-dimensional two-reflector acoustic model with constant velocity and varying density.

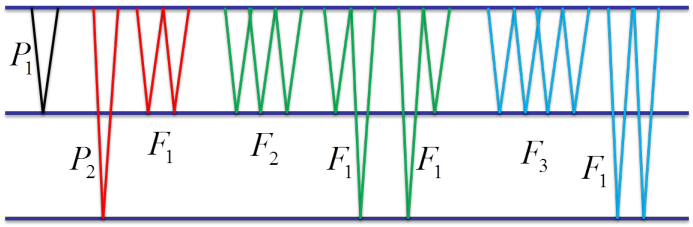

Figure 9: Seismic events. P_1 and P_2 are the first two primaries. F_1, F_2 and F_3 are the first-order, second-order and third-order free-surface multiples. The events with the same color have the same arrival time.

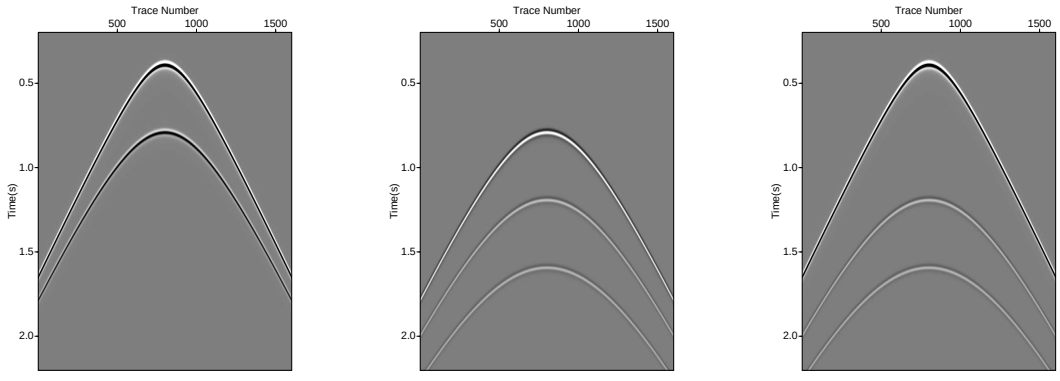

(a) (b) (c)

Figure 10: (a) Primary, (b) free-surface multiple, and (c) point-source data

However, in this case, the energy increases after removal of the first free-surface multiple.

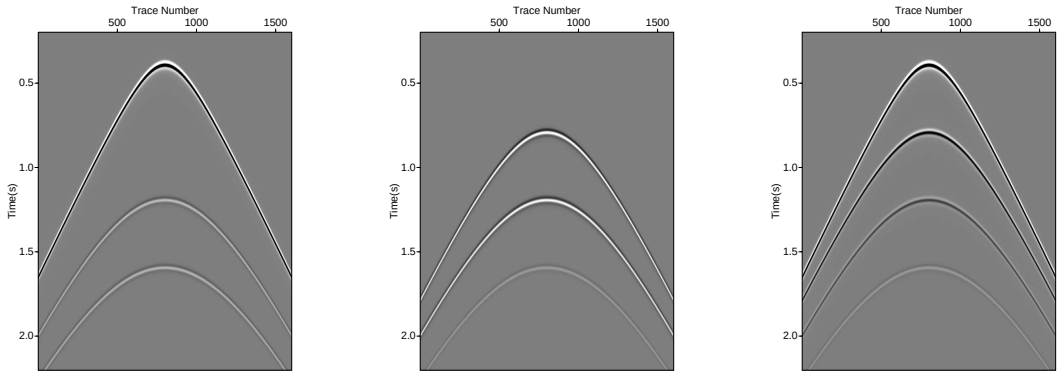

(a) (b) (c)

Figure 11: (a) Point-source data, (b) free-surface multiple prediction, and (c) after free-surface multiple removal

Inputting the point-source data (Figure 11a) into the current free-surface multiple elimination algorithm (equation 1), Figure 11b shows the predicted first-order free-surface multiples. After subtracting the prediction from the total data, Figure 11c presents the multiple removal result. It can be seen that all of the first-order free-surface multiples are removed and all of the higher-order free-surface multiples are altered. The second primary is recovered, since it is interfering only with the first-order free-surface multiple.

To check whether the second primary is fully recovered, we can randomly pick one trace (for example, at $1800m$ offset) from Figures 10a, 11b and 11c. Comparing the original primary (red line) and the multiple removal result (green dash line) in Figure 12, we can see that after free-surface multiple removal, the second primary is fully recovered. In this example, the current free-surface multiple elimination algorithm has the ability to correctly predict both amplitude and time of the free-surface multiples and remove them completely through a simple subtraction without touching the primaries. Most importantly, it recovers the primary that is destructively interfering with a free-surface multiple.

To evaluate the significance of the source radiation pattern for the interfering events example, we apply the same source array as in Figure 5 to generate the data. The primaries and free-surface multiples are generated separately as in the point-source data example. Figure 13a represents the two primaries and Figure 13b is the free-surface multiples. Summing them together, we get the source-array data, as shown in Figure 13c. The second primary is destructively interfering with the first-order free-surface multiple.

We input the source-array data (Figures 14a) into the current and extended free-surface multiple elimination algorithms (equation 2). Figures 15a and 15b are the free-surface multiples, which are predicted by using the current and the extended ISS free-surface multiple elimination algorithms, respectively. Figure 15c is corresponding difference between these two predictions. Figures 14b and 14c are the results following free-surface multiple removal by using the current (equation 1) and extended (equation 2) ISS free-surface multiple elimination algorithms, respectively. It can be seen that both algorithms effectively remove the first-order free-surface multiples and alter the higher-order free-surface multiples. The second primary is also recovered.

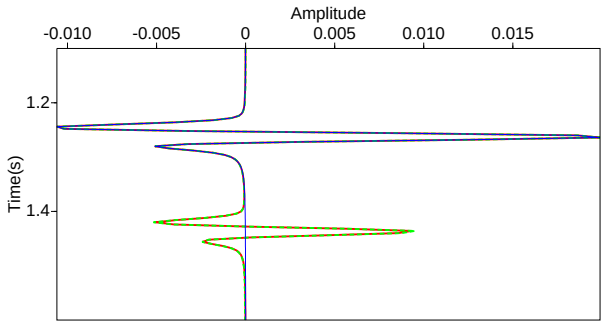

Figure 12: Comparison of one trace at $1800m$ offset. Red line: the two original primaries; blue line: the total data; dashed green line: after multiple removal.

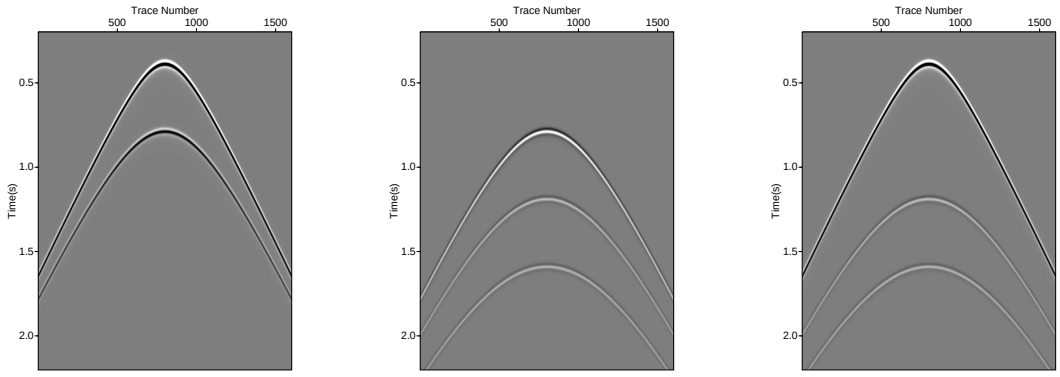

(a) (b) (c)

Figure 13: (a) Primary, (b) free surface multiple, and (c) source-array data

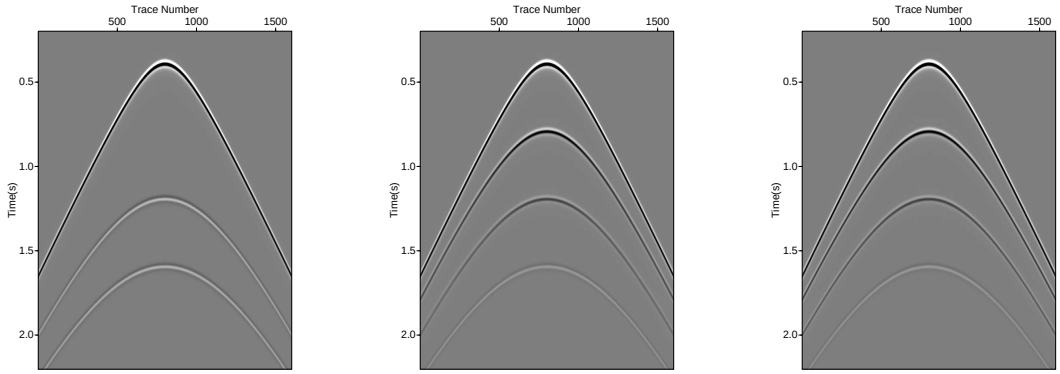

(a) (b) (c)

Figure 14: The impact of the source radiation pattern on free-surface multiple removal. (a) The source-array data; (b) the data following free-surface multiple removal using the current ISS free-surface multiple elimination algorithm; note that there are some residual multiples; (c) the data following free-surface multiple removal using the extended ISS free-surface multiple elimination algorithm; note that all the multiples have been completely eliminated.

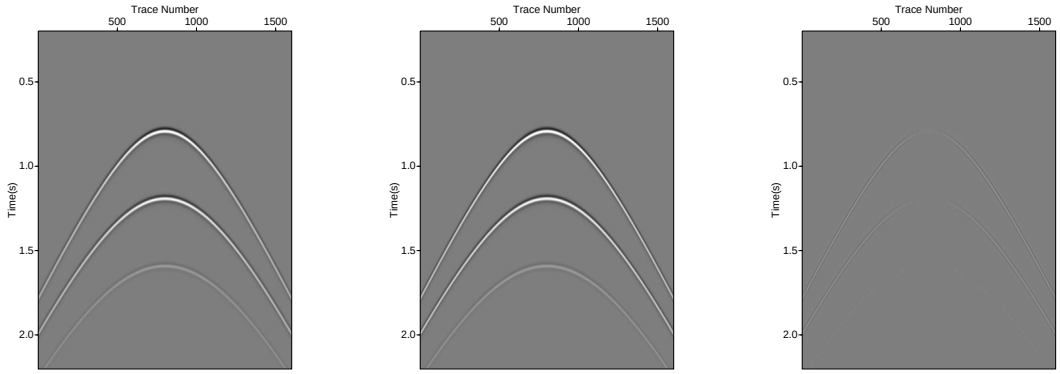

(a) (b) (c)

Figure 15: The free-surface multiples that are predicted by the (a) current and (b) the extended ISS free-surface multiple elimination algorithms. (c) The difference between two predictions.

How do we know the second primary is fully recovered or not? We randomly pick one trace (for instance, at $1800m$ offset) from each figure in Figure 14. Figure 16 illustrates the details of comparing one trace at $1800m$ offset. After removal of free-surface multiples by using the new

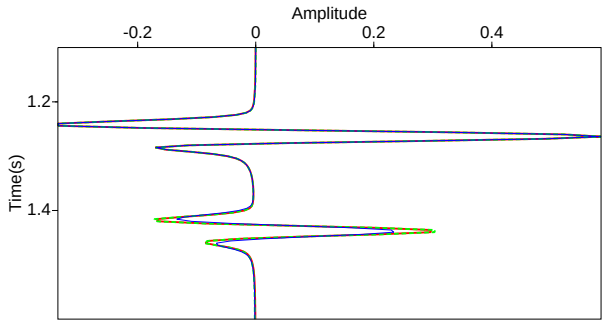

Figure 16: Comparison of one trace at $1800m$ offset. Red line: the two original primaries; blue line: the data after multiple removal by using the current free-surface multiple elimination algorithm; dashed green line: the data after multiple removal using the new, extended free-surface multiple elimination algorithm.

algorithm, the second primary (dashed green line) is recovered as the original primary (red line). With the current algorithm, the second primary (blue line) is weaker than the original primary, and that amplitude error will seriously affect AVO analysis. The numerical tests for the synthetic data with destructively interfering events have demonstrated the effectiveness and ability of the extended ISS free-surface multiple elimination algorithm.

4 Conclusions

We discussed and examined the impact of satisfying versus not satisfying certain prerequisites to the current ISS free-surface multiple elimination algorithm (i.e., removal of ghosts, and estimation and removal of the source wavelet and of the radiation pattern) on the results produced by that algorithm. We then modified and extended the ISS free-surface multiple elimination algorithm to accommodate a general source with a radiation pattern. For that situation, the new, extended algorithm can provide added value, compared with previous methods, by improving the fidelity of amplitude and phase prediction of the free-surface multiples at all offsets. It is multidimensional and does not require any subsurface information. We presented numerical tests showing that if the prerequisites have been satisfied, the new, extended ISS free-surface multiple elimination algorithm can, in principle, predict the free-surface multiples more accurately and then can remove them more effectively. When the free-surface multiples are proximal to or destructively interfering with other events, this accommodation and extension is particularly important, since we can not rely on adaptive subtraction to fix the errors in amplitude and phase of our prediction.

5 Acknowledgments

The first author is grateful to all M-OSRP sponsors for their support of this research. Special thanks go to my advisor, Dr. Arthur B. Weglein, for his teaching and guidance.

References

Aki, K. and P. G. Richards. *Quantitative Seismology*. 2nd edition. University Science Books, 2002.

Amundsen, L. "Estimation of source array signature." *Geophysics* 58 (1993): 1865–1869.

Berkhout, A. J. and D. J. Verschuur. "Removal of internal multiples." *69th Annual International Meeting, SEG, Expanded Abstracts* (1999): 1334–1337.

Carvalho, P. M. *Free-surface multiple reflection elimination method based on nonlinear inversion of seismic data*. PhD thesis, Universidade Federal da Bahia, 1992.

Hoop, A. T.de and J. H. M. T. van der Hijden. "Generation of acoustic waves by an impulsive line source in a fluid/solid configuration with a plane boundary." *Journal of the Acoustical Society of America* 74 (1983): 333–342.

Dragoset, B., I. Moore, M. Yu, and W. Zhao. "Removal of internal multiples." *78th Annual International Meeting, SEG, Expanded Abstracts* (2008): 2426–2430.

Ikelle, L. T., G. Roberts, and A. B. Weglein. "Source signature estimation based on the removal of the first-order multiples." *Geophysics* 62 (1997): 1904–1920.

Loveridge, M. M., G. E. Parkes, L. Hatton, and M. H. Worthington. "Effects of marine source array directivity on seismic data and source signature deconvolution." *First Break* 2 (1984): 16–22.

Mayhan, J., P. Terenghi, A. B. Weglein, and N. Chemingui. "Green's theorem derived methods for preprocessing seismic data when the pressure P and its normal derivative are measured." *81st Annual International Meeting, SEG, Expanded Abstracts* (2011): 2722–2726.

Mayhan, J. D. and A. B. Weglein. "First application of Green's theorem-derived source and receiver deghosting on deep-water Gulf of Mexico synthetic (SEAM) and field data." *Geophysics* 78 (March 2013): WA77–WA89.

Mayhan, J. D., A. B. Weglein, and P. Terenghi. "First application of Green's theorem derived source and receiver deghosting on deep water Gulf of Mexico synthetic (SEAM) and field data." *82nd Annual International Meeting, SEG, Expanded Abstracts* (2012): 1–5.

Osen, Are, Bruce G. Secrest, and Lasse Amundsen. "Wavelet estimation from marine pressure measurements." *Geophysics* 63 (November-December 1998): 2108–2119.

Tang, L., J. D. Mayhan, J. Yang, and A. B. Weglein. "Using Green's theorem to satisfy data requirements of inverse scattering series multiple removal methods." *83rd International Annual Meeting, SEG, Expanded Abstracts* (2013): 4392–4396.

Verschuur, D. J., A. J. Berkhout, and C. P. A. Wapenaar. "Adaptive surface-related multiple elimination." *Geophysics* 57 (1992): 1166–1177.

Weglein, A. B., F. V. Araújo, P. M. Carvalho, R. H. Stolt, K. H. Matson, R. T. Coates, D. Corrigan, D. J. Foster, S. A. Shaw, and H. Zhang. "Inverse scattering series and seismic exploration." *Inverse Problems* 19 (2003): R27–R83.

Weglein, A. B., D. J. Foster, K. H. Matson, S. A. Shaw, P. M. Carvalho, and D. Corrigan. "Predicting the correct spatial location of reflectors without knowing or determining the precise medium and wave velocity: Initial concept, algorithm and analytic and numerical example." *Journal of Seismic Exploration* 10 (2002): 367–382.

Weglein, A. B., F. A. Gasparotto, P. M. Carvalho, and R. H. Stolt. "An inverse-scattering series method for attenuating multiples in seismic reflection data." *Geophysics* 62 (November-December 1997): 1975–1989.

Weglein, A. B. and B. G. Secrest. "Wavelet estimation for a multidimensional acoustic earth model." *Geophysics* 55 (July 1990): 902–913.

Wu, J. and A. B. Weglein. "Elastic Green's theorem preprocessing for on-shore internal multiple attenuation: Theory and initial synthetic data tests." *84th Annual International Meeting, SEG, Expanded Abstracts* (2014): 4299–4304.

Yang, J. *Extending the inverse scattering series free-surface multiple elimination and internal multiple attenuation algorithms by incorporating the source wavelet and radiation pattern: examining and evaluating the benefit and added-value*. PhD thesis, University of Houston, 2014.

Yang, J., J. D. Mayhan, L. Tang, and A. B. Weglein. "Accommodating the source (and receiver) array in free-surface multiple elimination algorithm: Impact on interfering or proximal primaries and multiples." *83rd International Annual Meeting, SEG, Expanded Abstracts* (2013): 4184–4189.

Zhang, J. *Wave theory based data preparation for inverse scattering multiple removal, depth imaging and parameter estimation: analysis and numerical tests of Green's theorem deghosting theory*. PhD thesis, University of Houston, 2007.

Zhang, J. and A. B. Weglein. "Extinction theorem deghosting method using towed streamer pressure data: Analysis of the receiver array effect on deghosting and subsequent free surface multiple removal." *75th International Annual Meeting, SEG, Expanded Abstracts* (2005): 2095–2100.

Zhang, J. and A. B. Weglein. "Application of extinction theorem deghosting method on ocean bottom data." *76th International Annual Meeting, SEG, Expanded Abstracts* (2006): 2674–2678.

The impact of accommodating the source radiation pattern on the inverse scattering series free-surface multiple elimination algorithm

Jinlong Yang and Arthur B. Weglein, M-OSRP, University of Houston*

SUMMARY

The inverse scattering series (ISS) free-surface multiple elimination algorithm has certain prerequisites: (1) removing the reference wavefield, (2) estimation of source wavelet and radiation pattern, and (3) source and receiver deghosting. Weglein and Secrest (1990) describe a method to separate the reference wavefield from the scattered wavefield (reflection data) without subsurface information. In this abstract, the impact of prerequisites (2) and (3) on the ISS free-surface multiple elimination algorithm (Carvalho, 1992; Weglein et al., 1997) is discussed and the algorithm is modified and extended to accommodate the source radiation pattern. That radiation pattern accommodation can provide added value compared to previous methods that assumed an isotropic point source for predicting amplitude and phase of free-surface multiples. All these prerequisites can be provided by Green's theorem methods. Green's theorem methods for wave separation do not require subsurface information. They are consistent with the ISS free-surface multiple elimination algorithm. The extended ISS free-surface multiple elimination algorithm that accommodates the source radiation pattern is tested on a 1D acoustic model, and the results indicate that the new and extended ISS free-surface multiple elimination algorithm can predict more accurate results in comparison with methods without that accommodation when the source has a radiation pattern. This increased effectiveness in prediction is essential for removing free-surface multiples that are proximal or interfering with primaries (or other multiples).

INTRODUCTION

In seismic exploration, preprocessing of seismic data, including the removal of reference waves, wavelet estimation, and removal of ghosts, are very important. The reference wave should be removed because it does not experience reflection from the earth, which is our interest. Both the active source and the properties of the earth contribute to the amplitude and phase of recorded seismic events. To identify subsurface properties from seismic data, we need to identify and remove the source's effect from the seismic data (Weglein and Secrest, 1990). Source and receiver deghosting will remove the ghost notches and enhance the low-frequency content of the seismic data (Mayhan et al., 2011, 2012; Mayhan and Weglein, 2013). These are the prerequisites of the ISS free-surface multiple elimination algorithm (Weglein et al., 2003). All three of these processing steps can be achieved by using Green's theorem methods without requiring subsurface information. Green's theorem methods have been pioneered by J. Zhang (Weglein et al., 2002; Zhang and Weglein, 2005, 2006; Zhang, 2007) and developed by J. Mayhan (Mayhan et al., 2011, 2012; Mayhan and Weglein, 2013). Wu and Weglein (2014) extended Green's theorem reference wave prediction algorithm from the off-shore acoustic to the on-shore elastic wavefield separation.

In addition, multiple removal is a classic long-standing problem. Various methods (e.g., Carvalho, 1992; Verschuur et al., 1992; Weglein et al., 1997, 2003; Berkhout and Verschuur, 1999; Dragoset et al., 2008) have been developed to either attenuate or eliminate free-surface multiples, and each method has different assumptions, advantages, and limitations. Among these methods, the ISS free-surface multiple elimination algorithm (Carvalho, 1992; Weglein et al., 1997, 2003) is fully data-driven and does not need any subsurface information, which is a big advantage, especially under conditions of complex geology. Given its prerequisites, the ISS free-surface multiple elimination algorithm (Carvalho, 1992; Weglein et al., 1997, 2003) can predict the exact amplitude and phase of all free-surface multiples at all offsets and remove them through a simple subtraction without adaptively subtraction using certain criteria (energy minimization, for example). Methods, like SRME, do not provide this ability and they rely on an adaptive subtraction to fill that gap. The adaptive subtraction can be reasonable at times, but at other times, it can have issues with proximal and interfering events, e.g., damaging a primary and failing to remove the multiples.

However, for data generated by a general source with a radiation pattern, the ISS free-surface multiple elimination algorithm assumes an isotropic point source, where the source has no variation of amplitude or phase with take-off angle. In towed marine acquisition, a source array is commonly used to increase the power of the source, broaden the bandwidth, and cancel the random noise. The source array exhibits directivity in take-off angle (Loveridge et al., 1984). That directivity is an issue for multiple removal and attenuation and AVO analysis. In seismic processing, it is essential that we characterize the source array's effect on any seismic processing methods. Therefore, to improve the accuracy of the predicted multiples, the ISS free-surface multiple elimination algorithm is modified and extended by accommodating a general source with a radiation pattern. That accommodation can enhance the fidelity of amplitude and phase prediction of free-surface multiples at all offsets when the source has a radiation pattern.

THEORY

The ISS free-surface multiple elimination algorithm in 2D case starts with the input data $D_1'(k_g,k_s,\omega)$, that is source and receiver deghosted. For an isotropic point source, it is proposed by (Carvalho, 1992; Weglein et al., 1997, 2003):

$$D_n'(k_g,k_s,\omega) = \frac{1}{i\pi A(\omega)} \int dk D_1'(k_g,k,\omega) q e^{iq(\varepsilon_g+\varepsilon_s)} D_{n-1}'(k,k_s,\omega), \quad (1)$$

where k_g, k_s and ω represent the Fourier conjugates of receiver, source, and time, respectively. The parameters ε_g and ε_s are the receivers' and sources' depth below the free surface, respectively. q is the obliquity factor $q = sgn(\omega)\sqrt{\omega^2/c_0^2 - k^2}$, and c_0 is the reference velocity. $A(\omega)$ is the source signature, which is a function of time or ω in different domains. The free-surface multiples are predicted order-by-order and then added together give the deghosted and free-surface demultipled data $D'(k_g,k_s,\omega) = \sum_{n=1}^{\infty} D'_n(k_g,k_s,\omega)$.

For the data generated by a general source with a radiation pattern, the ISS free-surface multiple elimination algorithm can only predict multiples approximately. To accommodate the source's effect, the ISS free-surface multiple elimination algorithm is modified and extended from an isotropic point source to a general source ρ with a radiation pattern (Yang et al., 2013; Yang, 2014)

$$D'_n(k_g,k_s,\omega) = \frac{1}{i\pi}\int \frac{dk}{\rho(k,q,\omega)} D'_1(k_g,k,\omega) q e^{iq(\varepsilon_g+\varepsilon_s)} D'_{n-1}(k,k_s,\omega), \quad (2)$$

where $\rho(k,q,\omega)$ is the projection of source signature in the f-k domain and $k^2+q^2 = \omega^2/c_0^2$ The projection of the source signature $\rho(k,q,\omega)$ can be achieved from the reference wavefield that is separated from the total wavefield by using Green's theorem methods (Weglein and Secrest, 1990; Mayhan and Weglein, 2013; Tang et al., 2013).

In this paper, we assume that the source array is invariant from one shot to the next. In other words, the geometry or the distribution of the source array is the same for each shot. The direct reference wavefield P_0^d for a 2D case can be expressed as an integral of the direct reference Green's function G_0^d over all air-guns in an array,

$$P_0^d(x,z,x_s,z_s,\omega) = \iint dx'dz' \rho(x',z',\omega) G_0^d(x,z,x'+x_s,z'+z_s,\omega), \quad (3)$$

where (x,z) and (x_s,z_s) are the prediction point and source point, respectively. (x',z') is the distribution of the source with respect to the source locator (x_s,z_s). Using the bilinear form of Green's function and Fourier transforming over x, we obtain the relationship between ρ and P_0^d as

$$P_0^d(k,z,x_s,z_s,\omega) = \rho(k,q,\omega)\frac{e^{iq|z-z_s|}}{2iq} e^{-ikx_s}. \quad (4)$$

Since $k^2+q^2 = \omega^2/c_0^2$, q is not a free variable, hence, we can not obtain $\rho(x,z,\omega)$ in space-frequency domain by taking an inverse Fourier transform on $\rho(k,q,\omega)$. However, the projection of the source signature $\rho(k,q,\omega)$ can always be achieved directly from the direct reference wavefield P_0^d in the f-k domain, where the variable k or q represent the amplitude variations of the source signature with angles. Ikelle et al. (1997) also proposed a similar quantity $A(k,\omega)$, the inverse source wavelet, and solved it indirectly using the energy minimization criterion, while we apply Green's theorem wave separation methods to find the generalized source signature directly.

Substituting the projection of the source signature $\rho(k,q,\omega)$ into the inverse scattering free-surface multiple removal subseries, the ISS free-surface multiple elimination algorithm can be modified and extended (Yang, 2014). The extended algorithm accommodates a general source with a radiation pattern and can provide added value for the fidelity of amplitude and phase prediction of the free-surface multiples at all offsets. The extended ISS free-surface multiple elimination algorithm is fully multidimensional and does not require any subsurface information. Therefore, it is consistent with Green's theorem methods that provide all the data requirements. The extended free-surface multiple elimination algorithm (equation 2) is also consistent with the previous free-surface multiple elimination algorithm (equation 1) when the general source (e.g., source array) reduces to an isotropic point source. In addition, this modification can be easily extended into 3D case.

NUMERICAL TESTS

In this section, the effects of satisfying and not satisfying the prerequisites of the ISS free-surface multiple elimination algorithm are exemplified and tested. In each test, we will show the impact of each prerequisite on the ISS free-surface multiple elimination algorithm separately and compare its result with that after accommodating this prerequisite.

We will show the impact of ghosts, source wavelet, and radiation pattern on free-surface multiple removal. The numerical tests are based on a 1D acoustic model with varying velocity and constant density, as shown in Figure 1. The model has

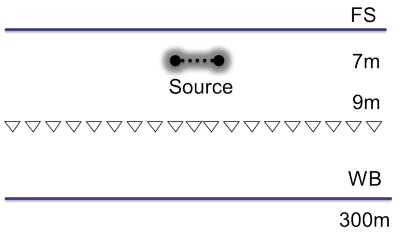

Figure 1: One-dimensional acoustic constant-density medium.

one reflector at 300m. The depths of the source and receiver are 7m and 9m, respectively. The synthetic data are generated by using the Cagniard-de Hoop method (de Hoop and van der Hijden, 1983; Aki and Richards, 2002), which can accurately produce any specific event that we are interested in. For exemplifying the impact of ghosts and source wavelet on the free-surface multiple removal, a point source is applied to generate the data. For exemplifying the impact of source radiation pattern on the free-surface multiple removal, a source array is applied to generate the data.

The tests are organized as follows: First, we test the impact of ghosts and source wavelet on the free-surface multiple removal. If both prerequisites are satisfied, the result of the free-surface multiple removal is also shown. Second, the impact of the source radiation pattern on free-surface multiple removal is presented. The results of the free-surface multiple removal by using the previous algorithm (equation 1) and the extended algorithm (equation 2) are compared.

The impact of ghosts and source wavelet on free-surface multiple removal

For exemplifying the impact of ghosts and source wavelet, a point source is applied to generated the data. We apply the ISS free-surface multiple elimination algorithm (equation 1) to predict and remove the free-surface multiples from the point-source data. Figure 2 shows the impact of ghosts and source wavelet on the free-surface multiple removal. Figure 2a is the input data with ghosts. Inputting it into the ISS free-surface multiple elimination algorithm gives the free-surface multiple prediction as shown in Figure 2b. After subtracting the prediction from the input data, Figure 2c shows the results of after free-surface multiple removal through a simple subtraction. From this example, we can see that if the input data are not deghosted, the ISS free-surface multiple elimination algorithm can only predict the correct phase but approximate amplitude of the free-surface multiples. After removing the ghosts, the

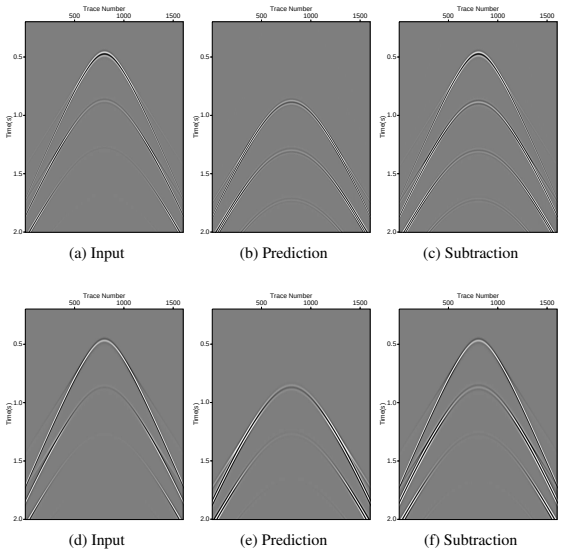

Figure 2: (a)&(d) Input data with and without ghosts; (b)&(e) Free-surface multiple prediction using the ISS free-surface multiple elimination algorithm with and without source wavelet deconvolution; (c)&(f) After free-surface multiple removal through a simple subtraction.

input data is shown in Figure 2d. Figure 2e shows the predicted free-surface multiples using the ISS free-surface multiple elimination algorithm without source wavelet deconvolution. Figure 2f illustrates the results of free-surface multiple removal by a simple subtraction. Without incorporating the source wavelet deconvolution, the ISS free-surface multiple elimination algorithm can only predict the correct phase but approximate amplitude of the free-surface multiples. Therefore, without removing the ghosts and incorporating the source wavelet deconvolution, the ISS free-surface multiple elimination algorithm can only predict approximate free-surface multiples and can not remove through a simple subtraction.

If all the prerequisites are satisfied, i.e., the ghosts have been removed and the source wavelet has been deconvolved, Figure 3 shows the results of after free-surface multiple removal. Figure 3a is the input data and Figure 3b is the free-surface multiple prediction. After subtracting from the input data through a simple subtraction, Figure 3c shows the result of after free-surface multiple removal. From this example, we can see that if all the prerequisites are satisfied, the free-surface multiples are predicted exactly by using the ISS free-surface multiple elimination algorithm and removed through a simple subtraction. Most importantly, all primaries are not touched, as shown in Figure 3c. Therefore, the ISS free-surface multiple elimina-

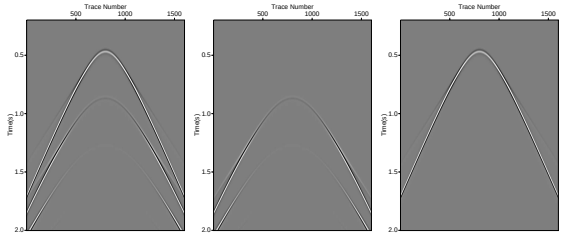

Figure 3: Free surface multiple removal with all prerequisites are satisfied

tion algorithm has the ability to predict accurately the phase and amplitude of multiples if its prerequisites (incorporating the source wavelet deconvolution and deghosting) are satisfied.

The impact of the source radiation pattern on free-surface multiple removal

To evaluate the significance of the source radiation pattern, a source array (Figure 4) with nine air-guns are applied to generated the data. Here, we assume that the source array

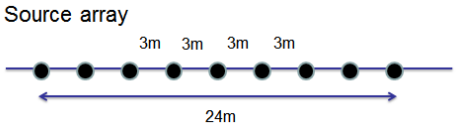

Figure 4: Source array with nine air-guns.

only varies laterally with identical source signatures, but this assumption is not necessary in the ISS free-surface multiple elimination algorithm. In the source-array data, only the primary and free-surface multiples are generated by the Cagniard-de Hoop method.

Figure 5a is the source-array data with nine point sources. Figures 5b and 5c are the results of after the free-surface multiple removal by using the current (equation 1) and extended (equation 2) ISS free-surface multiple elimination algorithms. It can be seen that for the source-array data with radiation pattern, the current ISS free-surface multiple elimination algorithm can effectively remove the free-surface multiples, but there are still some residual multiples due to the effect of the source radiation pattern. While the extended ISS free-surface multiple elimination algorithm can remove the free-surface multiples completely through a simple subtraction.

For details, we pick four traces from the source-array data and compare the results after free-surface multiple removal, by using both the current and extended ISS free-surface multiple elimination algorithms. Here, only the results of after first-order free-surface multiple removal are compared with the in-

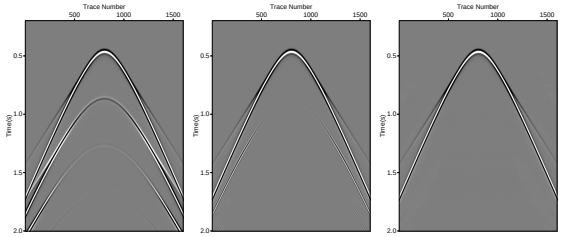

(a) Input (b) current (c) Extended

Figure 5: The impact of source radiation pattern on free-surface multiple removal. (a) the source-array data; (b) following free-surface multiple removal using the current ISS free-surface multiple elimination algorithm, there are some residual multiples; (c) following free-surface multiple removal using the extended ISS free-surface multiple elimination algorithm, all the multiples are completely eliminated.

put data. At zero offset, both the current and extended ISS free-surface multiple elimination algorithms can predict the accurate amplitude and phase of the free-surface multiples and remove them completely through a simple subtraction, as shown in Figure 6a. At large offsets, the current ISS free-surface mul-

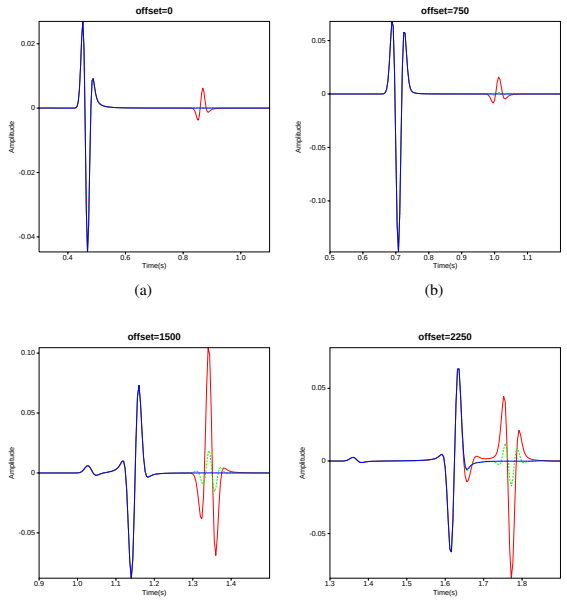

(a) (b) (c) (d)

Figure 6: Comparisons between the input data and the results of after free-surface multiple removal at four different offsets (a) 0m, (b) 750m, (c) 1500m, and (d) 2250m. Red line: The input data; Green dash line: after the free-surface multiple removal by the current ISS free-surface multiple elimination algorithm; Blue line: after the free-surface multiple removal by the extended ISS free-surface multiple elimination algorithm.

tiple elimination algorithm can still predict the correct phase of the free-surface multiples, while the amplitude of the predicted free-surface multiples has some errors. The green dash line in Figures 6b, 6c, and 6d shows the residual free-surface multiples after the free-surface multiple removal using the current ISS free-surface multiple elimination algorithm. With the increasing offset, the residual multiples are larger. The extended ISS free-surface multiple elimination algorithm can predict the accurate amplitude and phase of the free-surface multiples at both zero and large offsets. The blue line in Figure 6 shows the results after the free-surface multiple removal. The multiples are totally removed at any offsets. This is in contrast to SRME that has amplitude and phase errors at all offsets, and relies on adaptive subtraction to fix the errors in prediction.

For the source-array data, the current ISS free-surface multiple elimination algorithm can well predict and remove the free-surface multiples with some small residues, while the extended ISS free-surface multiple elimination algorithm can accurately predict and completely eliminate the free-surface multiples without damaging the primaries.

CONCLUSIONS

We discussed and examined the impact of accommodating prerequisites (ghosts, source wavelet and radiation pattern) on the ISS free-surface multiple elimination algorithm. The ISS free-surface multiple elimination algorithm is modified and extended by accommodating a general source with radiation pattern. The extended algorithm can provide added value compared to previous methods for the fidelity of amplitude and phase prediction of free-surface multiples at all offsets. It is multidimensional and does not require any subsurface information. The numerical tests show that if the prerequisites are provided, the ISS free-surface multiple elimination algorithm can, in principle, have the ability to predict more accurate free-surface multiples and then remove them more effectively. This is particularly important for the case, where free-surface multiples are proximal or interfering with other events and we can not rely on adaptive subtraction to fix the errors in amplitude and phase of the prediction.

ACKNOWLEDGMENTS

We are grateful to the M-OSRP sponsors for their encouragement and support.

REFERENCES

Aki, K., and P. G. Richards, 2002, Quantitative seismology, 2nd ed.: University Science Books.

Berkhout, A. J., and D. J. Verschuur, 1999, Removal of internal multiples: 69th Annual International Meeting, SEG, Expanded Abstracts, 1334–1337.

Carvalho, P. M., 1992, Free-surface multiple reflection elimination method based on nonlinear inversion of seismic data: PhD thesis, Universidade Federal da Bahia.

de Hoop, A. T., and J. H. M. T. van der Hijden, 1983, Generation of acoustic waves by an impulsive line source in a fluid/solid configuration with a plane boundary: Journal of the Acoustical Society of America, **74**, 333–342.

Dragoset, B., I. Moore, M. Yu, and W. Zhao, 2008, Removal of internal multiples: 78th Annual International Meeting, SEG, Expanded Abstracts, 2426–2430.

Ikelle, L. T., G. Roberts, and A. B. Weglein, 1997, Source signature estimation based on the removal of the first-order multiples: Geophysics, **62**, 1904–1920.

Loveridge, M. M., G. E. Parkes, L. Hatton, and M. H. Worthington, 1984, Effects of marine source array directivity on seismic data and source signature deconvolution: First Break, **2**, 16–22.

Mayhan, J., P. Terenghi, A. B. Weglein, and N. Chemingui, 2011, Green's theorem derived methods for preprocessing seismic data when the pressure P and its normal derivative are measured: 81st Annual International Meeting, SEG, Expanded Abstracts, 2722–2726.

Mayhan, J. D., and A. B. Weglein, 2013, First application of Green's theorem-derived source and receiver deghosting on deep-water Gulf of Mexico synthetic (SEAM) and field data: Geophysics, **78**, WA77–WA89.

Mayhan, J. D., A. B. Weglein, and P. Terenghi, 2012, First application of Green's theorem derived source and receiver deghosting on deep water Gulf of Mexico synthetic (SEAM) and field data: 82nd Annual International Meeting, SEG, Expanded Abstracts, 1–5.

Tang, L., J. D. Mayhan, J. Yang, and A. B. Weglein, 2013, Using green's theorem to satisfy data requirements of inverse scattering series multiple removal methods: 83rd International Annual Meeting, SEG, Expanded Abstracts, 4392–4396.

Verschuur, D. J., A. J. Berkhout, and C. P. A. Wapenaar, 1992, Adaptive surface-related multiple elimination: Geophysics, **57**, 1166–1177.

Weglein, A. B., F. V. Araújo, P. M. Carvalho, R. H. Stolt, K. H. Matson, R. T. Coates, D. Corrigan, D. J. Foster, S. A. Shaw, and H. Zhang, 2003, Inverse scattering series and seismic exploration: Inverse Problems, **19**, R27–R83.

Weglein, A. B., D. J. Foster, K. H. Matson, S. A. Shaw, P. M. Carvalho, and D. Corrigan, 2002, Predicting the correct spatial location of reflectors without knowing or determining the precise medium and wave velocity: Initial concept, algorithm and analytic and numerical example: Journal of Seismic Exploration, **10**, 367–382.

Weglein, A. B., F. A. Gasparotto, P. M. Carvalho, and R. H. Stolt, 1997, An inverse-scattering series method for attenuating multiples in seismic reflection data: Geophysics, **62**, 1975–1989.

Weglein, A. B., and B. G. Secrest, 1990, Wavelet estimation for a multidimensional acoustic earth model: Geophysics, **55**, 902–913.

Wu, J., and A. B. Weglein, 2014, Elastic green's theorem preprocessing for on-shore internal multiple attenuation: Theory and initial synthetic data tests: 84th Annual International Meeting, SEG, Expanded Abstracts, 4299–4304.

Yang, J., 2014, Extending the inverse scattering series free-surface multiple elimination and internal multiple attenuation algorithms by incorporating the source wavelet and radiation pattern: examining and evaluating the benefit and added-value: PhD thesis, University of Houston.

Yang, J., J. D. Mayhan, L. Tang, and A. B. Weglein, 2013, Accommodating the source (and receiver) array in free-surface multiple elimination algorithm: Impact on interfering or proximal primaries and multiples: 83rd International Annual Meeting, SEG, Expanded Abstracts, 4184–4189.

Zhang, J., 2007, Wave theory based data preparation for inverse scattering multiple removal, depth imaging and parameter estimation: analysis and numerical tests of green's theorem deghosting theory: PhD thesis, University of Houston.

Zhang, J., and A. B. Weglein, 2005, Extinction theorem deghosting method using towed streamer pressure data: Analysis of the receiver array effect on deghosting and subsequent free surface multiple removal: 75th International Annual Meeting, SEG, Expanded Abstracts, 2095–2100.

———, 2006, Application of extinction theorem deghosting method on ocean bottom data: 76th International Annual Meeting, SEG, Expanded Abstracts, 2674–2678.

Accommodating the source wavelet and radiation pattern in the internal multiple attenuation algorithm: Theory and initial example that demonstrates impact

Jinlong Yang and Arthur B. Weglein, M-OSRP, University of Houston*

SUMMARY

The inverse scattering series (ISS) internal multiple attenuation algorithm (Araújo et al., 1994; Weglein et al., 1997) is modified and extended by accommodating the source wavelet and radiation pattern in order to enhance the fidelity of the amplitude and phase predictions of the internal multiples. The extended ISS internal multiple attenuation algorithm is fully data-driven to predict all first-order internal multiples for all horizons at once, without requiring any subsurface information. For data produced by a point source with a wavelet, the amplitude and shape of the predicted internal multiples are significantly improved by accommodating the source wavelet. For data generated by a general source with a radiation pattern, the new algorithm provides added value for predicting the internal multiples by accommodating the source radiation pattern. Therefore, the new extended ISS internal multiple attenuation algorithm predicts more accurate internal multiples and remove them more effectively when the source has a radiation pattern.

INTRODUCTION

The inverse scattering series allows all seismic processing objectives, such as free surface multiple removal and internal multiple removal to be achieved directly in terms of data, without any estimation of the earth's properties. The ISS internal multiple attenuation algorithm is a fully data-driven and model-type independent algorithm (Weglein et al., 2003). It can predict the correct time and approximate and well-understood amplitude for all first-order internal multiples that generated from all reflectors without any subsurface information.

The ISS internal multiple attenuation algorithm was first proposed by Araújo et al. (1994) and Weglein et al. (1997). Matson et al. (1999) extended the theory for land and OBC applications. Ramírez and Weglein (2005) discussed how to extend the ISS internal multiple attenuation algorithm from attenuation toward elimination of multiples. Herrera and Weglein (2013) developed the 1-D ISS internal multiple elimination algorithm for internal multiple generated by a single shallowest reflector and Zou and Weglein (2013) further derived a general form of the ISS internal multiple elimination algorithm. Liang et al. (2013) and Ma and Weglein (2014) provided higher-order terms in the inverse scattering series to remove spurious events.

The ISS internal multiple attenuation algorithm has certain data requirements: (1) removal of the reference wavefield, (2) an estimation of the source wavelet and radiation pattern, (3) source and receiver deghosting, and (4) removal of the free-surface multiples. The first three requirements can be obtained by Green's theorem methods (Zhang and Weglein, 2005; Mayhan et al., 2012; Tang et al., 2013) and the free-surface multiples can be removed by the ISS free-surface multiple elimination algorithm (Carvalho, 1992; Weglein et al., 2003; Yang et al., 2013). Green's theorem methods and the ISS free-surface multiple elimination algorithm are consistent with the ISS internal multiple attenuation algorithm, since all are multidimensional wave-theoretic processing methods and do not require subsurface information.

The ISS internal multiple attenuation algorithm assumes that the input data are spike wave. In other words, the input data have been deconvolved. If the input data are generated by a source wavelet instead of by a spike wave, the predicted first-order internal multiple has convolved three source wavelets. Hence, the source wavelet has a significant effect on the amplitude and shape of the predicted internal multiple. In this paper, to improve the amplitude and the shape of a predicted internal multiple, the ISS internal multiple attenuation algorithm accommodates a source wavelet.

The new contribution relates to the fact that the ISS internal multiple attenuation algorithm assumes an isotropic point source, i.e., it assumes that the source has no variation of amplitude or phase with take-off angle. A large marine air-gun array will exhibit directivity and produce variations of the source signature (Loveridge et al., 1984). In on-shore exploration, even if there is no source array, the source can have radiation pattern or directivity. That directivity has significant effects on multiple removal or attenuation and AVO analysis. In seismic data processing, it is important that we characterize the source array's effect on any seismic processing methods. Therefore, to further improve the effectiveness of the ISS internal multiple attenuation algorithm, it is extended to accommodate the source radiation pattern. The synthetic data tests show that accommodating the source wavelet and radiation pattern can enhance the fidelity of the amplitude and phase predictions of internal multiples.

THEORY

The ISS internal multiple attenuation algorithm (Araújo, 1994; Weglein et al., 1997, 2003) for first-order internal multiple prediction in a $2D$ earth is given by

$$\begin{aligned} b_3(k_g,k_s,\omega) &= \frac{1}{(2\pi)^2}\int_{-\infty}^{\infty}\int_{-\infty}^{\infty} dk_1 e^{-iq_1(z_g-z_s)} dk_2 e^{iq_2(z_g-z_s)} \\ &\times \int_{-\infty}^{\infty} dz_1 b_1(k_g,k_1,z_1) e^{i(q_g+q_1)z_1} \\ &\times \int_{-\infty}^{z_1-\varepsilon} dz_2 b_1(k_1,k_2,z_2) e^{-i(q_1+q_2)z_2} \\ &\times \int_{z_2+\varepsilon}^{\infty} dz_3 b_1(k_2,k_s,z_3) e^{i(q_2+q_s)z_3}, \end{aligned} \tag{1}$$

where ω, k_s and k_g are temporal frequency and the horizontal wavenumbers for source and receiver coordinates, respec-

tively. q_s and q_g are the corresponding vertical source and receiver wavenumbers, respectively. $q_i = sgn(\omega)\sqrt{\omega^2/c_0^2 - k_i^2}$ for $i = (g,s)$; c_0 is the reference velocity. z_s and z_g are the source and receiver depths; and z_i $(i = 1,2,3)$ represents pseudodepth (vertical depth of the water speed migration). The parameter ε is introduced to insure that the relations $z_1 > z_2$ and $z_3 > z_2$ are satisfied.

From the first-order equation of the inverse scattering series $D = G_0^d V_1 P_0^d$ (Weglein et al., 2003), which can be represented explicitly in 2D case as

$$D(x_g,\varepsilon_g,x_s,\varepsilon_s,\omega) = \int dx_1 \int dz_1 \int dx_2 \int dz_2 \\ G_0^d(x_g,\varepsilon_g,x_1,z_1,\omega) V_1(x_1,z_1,x_2,z_2,\omega) P_0^d(x_2,z_2,x_s,\varepsilon_s,\omega), \quad (2)$$

where the data D have been deghosted and the reference wavefield and free-surface multiples have been removed. G_0^d and P_0^d are the direct reference Green's function and the direct reference wavefield, respectively.

For a unit source, $P_0^d = G_0^d$. We take a Fourier transform over x_s and x_g on both sides of equation 2 and define b_1 as

$$b_1(k_g,k_s,q_g+q_s) \equiv \frac{V_1(k_g,q_g,k_s,q_s,\omega)}{-2iq_g} = -2iq_s D(k_g,k_s,\omega), \quad (3)$$

where b_1 represents effective plane-wave incident data and $D(k_g,k_s,\omega)$ is the Fourier-transformed prestack data. The input b_1 are introduced into equation 1 after an uncollapsed Stolt migration (Weglein et al., 1997) that takes $b_1(k_g,k_s,q_g+q_s)$ into the pseudodepth domain, $b_1(k_g,k_s,z_i)$, by using the reference velocity, c_0. Then, the first-order internal multiples $D_3(k_g,k_s,\omega)$, which are predicted by the ISS internal multiple attenuation algorithm (equation 1), are obtained by

$$D_3(k_g,k_s,\omega) = (-2iq_s)^{-1} b_3(k_g,k_s,q_g+q_s). \quad (4)$$

For an isotropic point source, $P_0^d = A(\omega)G_0^d$. Fourier transforming over x_s and x_g on both sides of equation 2 gives

$$b_1(k_g,k_s,q_g+q_s) = -2iq_s D(k_g,k_s,\omega)/A(\omega), \quad (5)$$

where $A(\omega)$ is the source signature. After b_3 has been predicted by equation 1, the first-order internal multiple is achieved by convolving the source wavelet $A(\omega)$ back

$$D_3(k_g,k_s,\omega) = (-2iq_s)^{-1} A(\omega) b_3(k_g,k_s,q_g+q_s). \quad (6)$$

For a general source with a radiation pattern (e.g., a source array), the direct reference wavefield P_0^d for a 2D case can be expressed as an integral of the direct reference Green's function G_0^d over all air-guns in an array,

$$P_0^d(x,z,x_s,z_s,\omega) \\ = \iint dx'dz' \rho(x',z',\omega) G_0^d(x,z,x'+x_s,z'+z_s,\omega), \quad (7)$$

where (x,z) and (x_s,z_s) are the prediction point and source point, respectively. (x',z') is the distribution of the source with respect to the source locator (x_s,z_s). Using the bilinear form of Green's function and Fourier transforming over x, we obtain the relationship between ρ and P_0^d as

$$P_0^d(k,z,x_s,z_s,\omega) = \rho(k,q,\omega)\frac{e^{iq|z-z_s|}}{2iq} e^{-ikx_s}. \quad (8)$$

On the other hand, the reference wavefield P_0^d can be solved from the measured data by using Green's theorem method (Weglein and Secrest, 1990).

Since $k^2 + q^2 = \omega^2/c_0^2$, q is not a free variable, hence, we can not obtain $\rho(x,z,\omega)$ in space-frequency domain by taking an inverse Fourier transform on $\rho(k,q,\omega)$. However, the projection of the source signature $\rho(k,q,\omega)$ can be achieved directly from the direct reference wavefield P_0^d in the f-k domain, where the variable k or q represent the amplitude variations of the source signature with angles.

Substituting the projection of the source signature ρ into equation 2 and Fourier transforming over x_s and x_g gives

$$b_1(k_g,k_s,q_g+q_s) = -2iq_s D(k_g,k_s,\omega)/\rho(k_g,q_g,\omega). \quad (9)$$

Further details of obtaining ρ can be found in Yang et al. (2013) and Yang (2014). The first-order internal multiple is calculated from b_3,

$$D_3(k_g,k_s,\omega) = (-2iq_s)^{-1}\rho(k_g,q_g,\omega) b_3(k_g,k_s,q_g+q_s). \quad (10)$$

All above derivations are 2D cases, and they can be directly extended to 3D. From the derivations, we can see that the kernel of the ISS internal multiple attenuation algorithm (equation 1) does not change and the source wavelet and radiation pattern are imported by equations 5 and 9. The predicted internal multiples D_3 are also affected by the source wavelet and radiation pattern in equations 6 and 10. If the source wavelet is not incorporated into the ISS internal multiple attenuation algorithm, the amplitudes and shapes of the predicted internal multiples are not comparable with those of the internal multiples in the input data. To improve the effectiveness of the internal multiple prediction, the ISS internal multiple attenuation algorithm should be modified for its input and output by accommodating the source wavelet and radiation pattern. This accommodation can enhance the fidelity of the amplitude and shape of the predictions of internal multiples.

NUMERICAL TESTS

In this section, we will present the numerical tests of the internal multiple prediction for the data generated by a point source and a general source with a radiation pattern. The numerical tests are based on a $1D$ acoustic model with varying velocity and constant density, as shown in Figure 1. The synthetic data that are generated by the finite-difference method. The data have one shot gather with 2001 traces, and each trace has 301 time samples, with $dt = 5ms$. The trace interval is $5m$.

The source wavelet effect on internal multiple prediction

For the data generated by a point source, the internal multiple will be predicted by using the ISS internal multiple attenuation algorithm with and without source wavelet deconvolution. Figure 2 shows the input data and their corresponding predicted internal multiples. They are plotted using the same scale. In the input data, the first two strongest events are the primaries, and the other events are internal multiples. Figures 2(b) and 2(c) show the predicted internal multiples using the

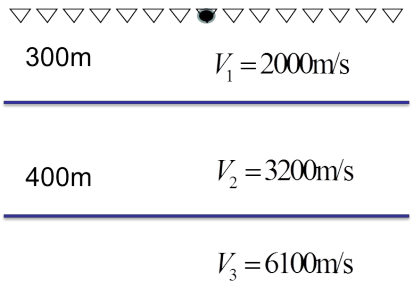

Figure 1: One-dimensional acoustic constant-density medium.

ISS internal multiple attenuation algorithm with and without source wavelet deconvolution. From Figures 2(b) and 2(c), we can see that both algorithms predict the correct traveltimes, but they predict different amplitudes and shapes for the internal multiples. In Figure 2(b), the amplitude of the predicted internal multiple is comparable with the internal multiple in the input data, while the amplitude is totally different from that of the internal multiple in the input data in Figure 2(c).

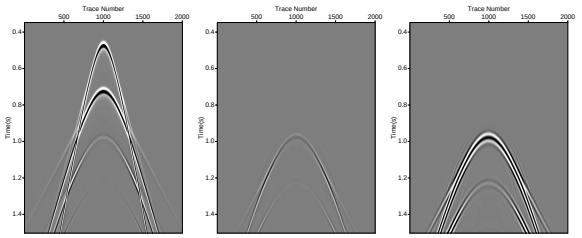

(a) Input (b) With (c) Without

Figure 2: (a) The input data; (b) and (c) The predicted internal multiples.

For details, we pick the middle trace (offset $= 0$) and the far trace (offset $= 1700m$) from each image in Figure 2. The time windows are chosen at $0.85s \sim 1.10s$ for the middle trace and at $1.05s \sim 1.25s$ for the far trace, as shown in Figure 3. For the middle trace, it can be seen that the shape of the internal multiple predicted by the ISS internal multiple attenuation algorithm without source wavelet deconvolution (Figure 3(c)) is totally different from that of the true internal multiple (Figure 3(a)). The predicted and true amplitudes are not comparable, either. This is because the predicted internal multiples convolve three wavelets. However, comparing Figure 3(b) with Figure 3(a), we can see that the amplitude and shape of the internal multiple predicted by the ISS internal multiple attenuation algorithm with source wavelet deconvolution are similar to those of the true internal multiple, as shown in Figure 4(a). It demonstrates that by accommodating the source wavelet deconvolution, the amplitude and shape of the predicted internal multiple are significantly improved for the internal multiple prediction. For the far-offset traces, we obtain the similar results, as shown in Figures 3(e) and 4(b).

From the numerical test, we conclude that by accommodating the source wavelet deconvolution, the ISS internal multiple attenuation algorithm produces more accurate and encouraging results for both zero offset and far offset. The predicted internal multiple has the correct traveltime, and the amplitude and shape are significantly improved.

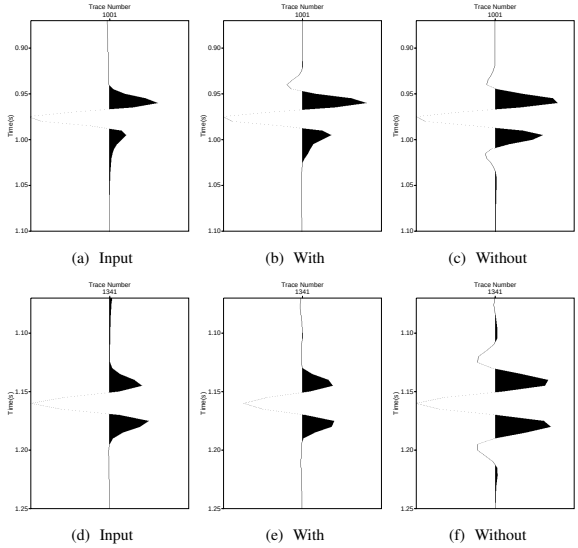

(a) Input (b) With (c) Without

(d) Input (e) With (f) Without

Figure 3: (a), (b), (c) The middle traces, and (d), (e), (f) the far traces.

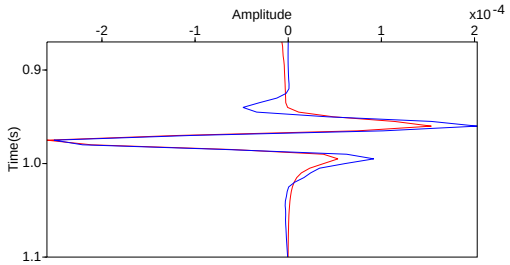

(a) Zero offset

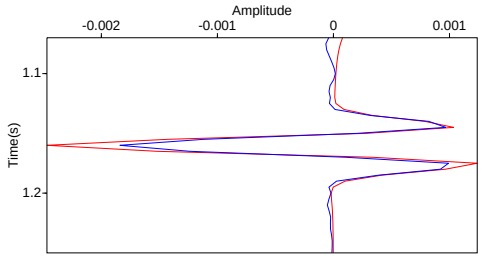

(b) Far offset

Figure 4: The comparison between the internal multiple (red) in the input data and the predicted internal multiple (blue) at (a) zero offset and at (b) far offset ($1700m$).

The radiation pattern effect on internal multiple prediction

For the data generated by a general source with a radiation pattern (e.g., source array), we will predict the internal multiple using the ISS internal multiple attenuation algorithm with and without incorporating the source wavelet and radiation pattern. Here, the synthetic data are generated by a source array using the same model as Figure 1. The source array contains five point sources in one line with $20m$ range. Here, we assume that the source array only varies laterally with identical source signatures, but the assumption is not necessary in the ISS internal multiple attenuation algorithm.

Figure 5(a) shows the input data generated by the source array.

Similar with the data generated by the point source, the first two strongest events are the primaries, and the other events are internal multiples. Figures 5(b) and 5(c) present the internal multiples predicted by using the ISS internal multiple attenuation algorithm with and without incorporating the source wavelet and radiation pattern. From Figures 5(b) and 5(c), we can see that both algorithms can predict the correct traveltime and an acceptable amplitude of the internal multiple.

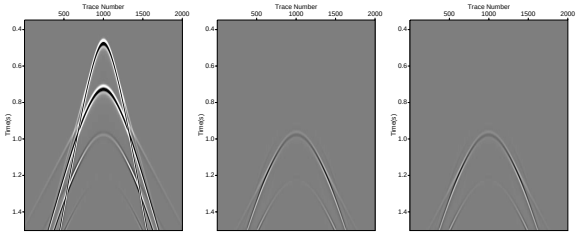

(a) Input (b) With (c) Without

Figure 5: (a) The input data; (b) and (c) the predicted internal multiples.

To compare the internal multiple predictions in detail, the middle trace (offset $= 0$) and the far trace (offset $= 1700m$) are picked from each image in Figure 5. We choose the time windows at $0.85s \sim 1.10s$ for the middle trace and at $1.05s \sim 1.25s$ for the far trace, as shown in Figure 6. Comparing the middle and far traces, we can see that the amplitude and shape of the internal multiple predicted by the ISS internal multiple attenuation algorithm with and without incorporating the radiation pattern are very similar to those for the true internal multiple in the input data. Their comparisons are plotted in Figure 7. At zero offset, there are no visible differences, as shown in Figure 7(a), while at far offset, Figure 7(b) demonstrates that the amplitude of the internal multiple prediction is further improved by accommodating the radiation pattern. Therefore, for the general source data, the modified ISS internal multiple attenuation algorithm that incorporates the source wavelet and radiation pattern can enhance the accuracy and effectiveness of the amplitude prediction of the internal multiple.

CONCLUSIONS

The ISS internal multiple attenuation algorithm is modified and extended by accommodating the source wavelet and radiation pattern. The extended ISS internal multiple attenuation algorithm enhances the fidelity of amplitude and phase predictions of the internal multiple. It retains all the merits of the original algorithm that is fully data-driven and does not require any subsurface information. In synthetic data tests, for point-source data, the predictions of the amplitudes and shapes of internal multiples are significantly improved by incorporating the source wavelet. For data generated by a general source with a radiation pattern, the prediction is further improved by incorporating the source radiation pattern into the ISS internal multiple attenuation algorithm. This contribution plays a part in the plan to deliver a higher level of predictive capability, where primaries and internal multiples are proximal or overlapping and cannot rely on adaptive subtraction to fix errors in the prediction.

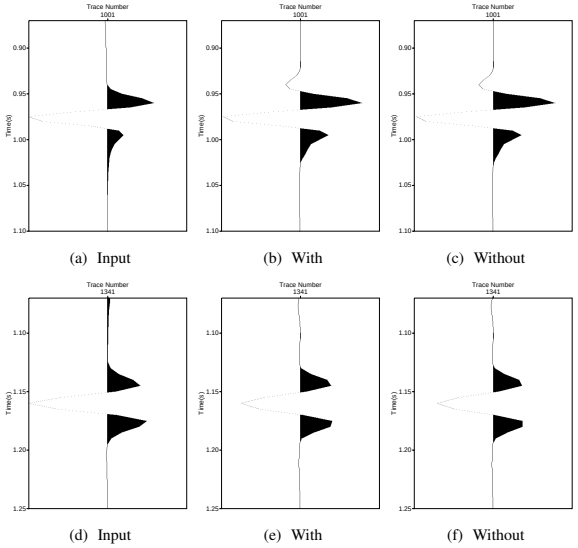

(a) Input (b) With (c) Without

(d) Input (e) With (f) Without

Figure 6: (a), (b), (c) The middle traces, and (d), (e), (f) the far traces.

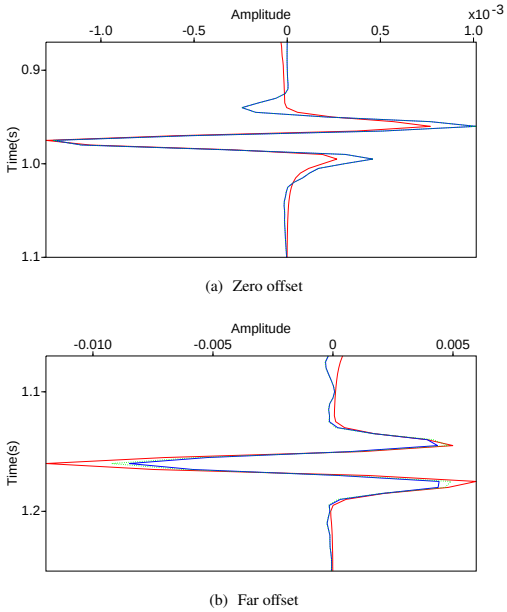

(a) Zero offset

(b) Far offset

Figure 7: The comparison between the true internal multiple (red) in the input data and the internal multiple predicted by the ISS internal multiple attenuationalgorithm with (green dash) and without (blue) incorporating the source wavelet and radiation pattern at (a) zero offset and at (b) far offset ($1700m$).

ACKNOWLEDGMENTS

We are grateful to all M-OSRP sponsors for their encouragement and support of this research.

REFERENCES

Araújo, F. V., 1994, Linear and non-linear methods derived from scattering theory: backscattered tomography and internal multiple attenuation: PhD thesis, Universidade Federal da Bahia.

Araújo, F. V., A. B. Weglein, P. M. Carvalho, and R. H. Stolt, 1994, Inverse scattering series for multiple attenuation: An example with surface and internal multiples: 64th Annual International Meeting, SEG, Expanded Abstracts, 1039–1042.

Carvalho, P. M., 1992, Free-surface multiple reflection elimination method based on nonlinear inversion of seismic data: PhD thesis, Universidade Federal da Bahia.

Herrera, W., and A. B. Weglein, 2013, Eliminating first-order internal multiples with downward reflection at the shallowest interface: Theory and initial examples: 83rd International Annual Meeting, SEG, Expanded Abstracts, 4131–4135.

Liang, H., C. Ma, and A. B. Weglein, 2013, General theory for accommodating primaries and multiples in internal multiple algorithm: Analysis and numerical tests: 83rd International Annual Meeting, SEG, Expanded Abstracts, 4178–4183.

Loveridge, M. M., G. E. Parkes, L. Hatton, and M. H. Worthington, 1984, Effects of marine source array directivity on seismic data and source signature deconvolution: First Break, **2**, 16–22.

Ma, C., and A. B. Weglein, 2014, Including higher-order inverse scattering series terms to address a serious shortcoming/problem of the internal-multiple attenuator: Exemplifying the problem and its resolution: 84th Annual International Meeting, SEG, Expanded Abstracts, 4124–4129.

Matson, K. H., D. C. Corrigan, A. B. Weglein, C. Y. Young, and P. M. Carvalho, 1999, Inverse scattering internal multiple attenuation: results from complex synthetic and field data examples: 69th Annual International Meeting, SEG, Expanded Abstracts, 1060–1063.

Mayhan, J. D., A. B. Weglein, and P. Terenghi, 2012, First application of Green's theorem derived source and receiver deghosting on deep water Gulf of Mexico synthetic (SEAM) and field data: 82nd Annual International Meeting, SEG, Expanded Abstracts, 1–5.

Ramírez, A. C., and A. Weglein, 2005, An inverse scattering internal multiple elimination method: Beyond attenuation, a new algorithm and initial tests: 75th International Annual Meeting, SEG, Expanded Abstracts, 2115–2118.

Tang, L., J. D. Mayhan, J. Yang, and A. B. Weglein, 2013, Using green's theorem to satisfy data requirements of inverse scattering series multiple removal methods: 83rd International Annual Meeting, SEG, Expanded Abstracts, 4392–4396.

Weglein, A. B., F. V. Araújo, P. M. Carvalho, R. H. Stolt, K. H. Matson, R. T. Coates, D. Corrigan, D. J. Foster, S. A. Shaw, and H. Zhang, 2003, Inverse scattering series and seismic exploration: Inverse Problems, R27–R83.

Weglein, A. B., F. A. Gasparotto, P. M. Carvalho, and R. H. Stolt, 1997, An inverse-scattering series method for attenuating multiples in seismic reflection data: Geophysics, **62**, 1975–1989.

Weglein, A. B., and B. G. Secrest, 1990, Wavelet estimation for a multidimensional acoustic earth model: Geophysics, **55**, 902–913.

Yang, J., 2014, Extending the inverse scattering series free-surface multiple elimination and internal multiple attenuation algorithms by incorporating the source wavelet and radiation pattern: examining and evaluating the benefit and added-value: PhD thesis, University of Houston.

Yang, J., J. D. Mayhan, L. Tang, and A. B. Weglein, 2013, Accommodating the source (and receiver) array in free-surface multiple elimination algorithm: impact on interfering or proximal primaries and multiples: 83rd International Annual Meeting, SEG, Expanded Abstracts, 4184–4189.

Zhang, J., and A. B. Weglein, 2005, Extinction theorem deghosting method using towed streamer pressure data: Analysis of the receiver array effect on deghosting and subsequent free surface multiple removal: 2095–2100.

Zou, Y., and A. B. Weglein, 2013, A new method to eliminate first order internal multiples for a normal incidence plane wave on a 1d earth: 83rd International Annual Meeting, SEG, Expanded Abstracts, 4136–4140.

The significance of incorporating a 3-D point source in the inverse scattering series free-surface multiple elimination algorithm for a 1-D subsurface

Xinglu Lin, and Arthur B. Weglein

Abstract

Based on the current 3-D inverse-scattering-series (ISS) free-surface-multiple-elimination (FSME) algorithm (Carvalho, 1992; Weglein et al., 1997, 2003) that was developed for a 3-D point source and 3-D earth, this report derives an ISS FSME algorithm that retains the dimension of the source (i.e., 3D point source) and reduces the subsurface dimension from 3-D to 1-D. Applying this 3D-source-1D-earth algorithm will accurately predict both the phase and the amplitude of the free-surface multiples in seismic data that are generated by a 3-D point source and 1-D earth (e.g., Central North Sea), compared to the frequently applied 1.5-D ISS FSME algorithm that assumes a 2-D line source and 1-D earth.

In this paper, numerical tests are performed on 3-D source synthetic data sets generated from a 1-D subsurface, to examine the significance of incorporating a 3-D source in FSME algorithm and the impacts of FSM residues on the subsequent ISS internal multiple attenuation. The results demonstrate that the 3-D source-1-D earth ISS FSME algorithm can accurately remove the FSM events in 3-D source data. This successful removal of free-surface multiples provides a satisfactory prerequisite for subsequent processing (e.g., internal-multiple attenuation/elimination).

1 Introduction

Multiple removal is a long-standing and challenging task in seismic data processing, which impacts the subsequent imaging and inversion procedures. Many efforts have been made to attenuate or eliminate the free-surface multiples (events that have experienced at least one downward reflection at the air-water surface) in data (e.g., Verschuur et al., 1992; Carvalho, 1992; Weglein et al., 1997, 2003; Weglein and Dragoset, 2008). Among these methods, the inverse scattering series (ISS) free-surface-multiple-elimination (FSME) algorithm provides a multidimensional procedure that eliminates all free-surface multiples (Carvalho, 1992; Weglein et al., 1997, 2003) through a simple subtraction. This approach has its strengths in that it does not require subsurface information, and it can provide the accurate time and amplitude of all free-surface multiples. However, other approaches, such as the SRME method, often adopt adaptive subtraction with certain criteria (e.g., energy minimization) to eliminate the free-surface multiples, because these methods can provide accurate time but approximate amplitude of free-surface multiples. Adaptive subtraction works well at times when the events are isolated, however, it can generate issues when the free-surface multiples and primaries are interfering or destructively overlapping. That is because energy minimization assumes a minimized/decreased energy in data after multiple subtraction, which is invalid when the energy increases after removing destructively overlapping free-surface multiples and at the same time recovering the primaries. In other words, for a complex geology, it is in need of accurate free-surface-multiple predictions for both time and amplitude, where the adaptive subtraction can fail to effectively remove the free-surface multiples and can possibly damage the primaries.

As we mentioned before, the ISS FSME algorithm is a multidimensional procedure that can completely remove the free-surface multiples from data without knowing any subsurface information. If we consider a 3-D point source as the real source dimension, the complete 3-D ISS FSME algorithm, which assumes a 3-D point source and a 3-D subsurface, can successfully predict both accurate time and amplitude of all free-surface multiples with a complete dataset (requires areal coverage of sources and for each source requires the areal coverage of receivers). Even though the 3-D ISS FSME algorithm is a complete and accurate method, there are reasonable circumstances that require less data and less computational cost, for instance, when the earth property only varies in 1-D and the source dimension retains 3-D. For a typical pre-stack shot gather coming from a 1-D subsurface, the 1.5-D ISS FSME algorithm is frequently and naturally applied to predict free-surface multiples (Carvalho, 1992). Since the 1.5-D ISS FSME algorithm is derived from a 2-D line source ISS FSME algorithm for a 1-D subsurface, it can only provide the accurate phase and amplitude of free-surface multiples generated by a 2-D line source, rather than a 3-D point source. When the data come from a 3-D point source and a 1-D subsurface, this 1.5-D algorithm can produce issues and even fail to effectively eliminate the free-surface multiples.

This report will focus on the specific problem of a 3-D source-1-D subsurface ISS FSME algorithm by reducing a complete 3-D ISS FSME algorithm. The reduced algorithm preserves the real 3-D source dimension and demands only one pre-stack shot gather for the 3-D source data coming from a 1-D earth. The numerical tests are performed on 3-D source data sets. The results evaluate the significance of incorporating a 3-D source in a 1-D ISS FSME algorithm by comparing with a frequently used 2-D line source 1-D earth ISS FSME algorithm for 3-D point source data.

2 3-D and 2-D ISS free-surface-multiple elimination algorithm

The preparation of the 3-D FSME algorithm starts from data $D(x_g, y_g, \epsilon_g, x_s, y_s, \epsilon_s; t)$, where (x_g, y_g, ϵ_g) and (x_s, y_s, ϵ_s) are the receiver- and source-location, respectively. In addition, the preprocessing - including reference wave-field removal, deghosting and wavelet estimation - needs to be achieved before the ISS free-surface multiple prediction. The preprocessed data are represented by D'. The 3-D source ISS free-surface multiple elimination algorithm can be written as

$$D'_n(k_{xg}, k_{yg}, k_{xs}, k_{ys}; \omega) = \frac{1}{2i\pi^2\rho_r B(\omega)} \int_{-\infty}^{\infty}\int_{-\infty}^{\infty} dk_x dk_y D'_1(k_{xg}, k_{yg}, k_x, k_y; \omega) \times q D'_{n-1}(k_x, k_y, k_{xs}, k_{ys}; \omega) e^{iq(\epsilon_g+\epsilon_s)}, \quad (1)$$

for $n \geq 2$ and

$$D'(k_{xg}, k_{yg}, k_{xs}, k_{ys}; \omega) = \sum_{n=1}^{\infty} D'_n(k_{xg}, k_{yg}, k_{xs}, k_{ys}; \omega). \quad (2)$$

D' contains only the deghosted primaries and internal multiples. $B(\omega)$ and ρ_r are the source signature and reference medium density, respectively. The vertical wavenumber is defined by $q = \sqrt{(\frac{\omega}{c_0})^2 - k_x^2 - k_y^2}$. The 3-D algorithm in equations (2) and (4) assumes that the acquisition applies 3-D sources and 3-D receivers for a 3-D subsurface.

Similarly, a set of 2-D data $D(x_g, x_s; t)$ can be transformed into wavenumber-frequency domain and deghosted as $D'(k_g, k_s; \omega)$. The 2-D ISS free-surface-multiple-elimination algorithm is,

$$D'_n(k_g, k_s; \omega) = \frac{1}{i\pi\rho_r B(\omega)} \int_{-\infty}^{\infty} dk D'_1(k_g, k; \omega) q D'_{n-1}(k, k_s; \omega) e^{iq(\epsilon_g+\epsilon_s)}, \quad (3)$$

for $n \geq 2$ and

$$D'(k_g, k_s; \omega) = \sum_{n=1}^{\infty} D'_n(k_g, k_s; \omega), \tag{4}$$

where the vertical wave-number is $q = \sqrt{(\frac{\omega}{c_0})^2 - k^2}$. In contrast to the 3-D case, the algorithm in equations (3) and (6) assumes a 2-D subsurface, in which the acquisition corresponds to 2-D line sources and 2-D line receivers.

In the following sections, both the 3-D algorithm and 2-D algorithm are reduced for the data from a 1-D subsurface, where in the 3-D case the source is a 3-D point source and in the 2-D case the source is a 2-D line source. For convenience, the superscript $1DE$ represents the 1-D earth assumption for different sources (For example, 2-D line source 1-D earth: $2D1DE$; 3-D point source 1-D earth: $3D1DE$).

3 The FSME algorithm assuming a 2-D line source and a 1-D subsurface

In developing the algorithm for 1-D earth pre-stack data, it was natural that people started with the 2-D line source ISS FSME algorithm and then reduced it for 1-D subsurface data. The data that occurs in the 2-D earth can be written as $D(x_g, x_s; \omega)$ or $D(x_m, x_h; \omega)$ in the space-frequency domain, where $x_m = x_g + x_s$ and $x_h = x_g - x_s$. The data from a 1-D earth, shown as $D^{2D1DE}(x_h; \omega)$, depends only on the source-receiver offset (x_h) and the frequency (ω). The Fourier transform over the complete 2-D data (D) for a 1-D earth can be shown as,

$$D(k_g, k_s; \omega) = \iint e^{ik_g x_g} e^{-ik_s x_s} D^{2D1DE}(x_h; \omega) dx_g dx_s \tag{5}$$

Rearranging the variables from (k_g, k_s) to (k_h, k_m) can give us,

$$\begin{aligned} D(k_h, k_m; \omega) &= \frac{1}{2} \int e^{ik_h x_h} D^{2D1DE}(x_h; \omega) dx_h \int e^{ik_m x_m} dx_m \\ &= D^{2D1DE}(k_h; \omega)(2\pi)\delta(2k_m), \end{aligned} \tag{6}$$

where $k_h = \frac{k_g + k_s}{2}$ and $k_m = \frac{k_g - k_s}{2}$. The data is independent of x_m and can come out of the x_m integral. Consequently, the Fourier transform integral over x_m can produce a Dirac delta function in k_m. Since the 2-D source ISS FSME algorithm needs data in (k_g, k_s), we can change the variables in equation (6) back to (k_g, k_s) as,

$$D(k_g, k_s; \omega) = D^{2D1DE}(k_g; \omega)(2\pi)\delta(k_g - k_s), \tag{7}$$

where $k_g = k_s = k_m$ defined by the sifting property of the Dirac delta function.

As part of a complete data set, the preprocessed data D' has the same symmetry as D, which is $D'_n(k_g, k_s; \omega) = D'^{2D1DE}_n(k_g; \omega)(2\pi)\delta(k_g - k_s)$. By applying this 1-D earth data D'^{2D1DE}_n to equation (3), the algorithm becomes

$$\begin{aligned} & D'^{2D1DE}_n(k_g; \omega)(2\pi)\delta(k_g - k_s) \\ &= \frac{1}{i\pi\rho_r B(\omega)} \int_{-\infty}^{\infty} dk D'^{2D1DE}_1(k_g; \omega)(2\pi)\delta(k_g - k) \\ &\times q D'^{2D1DE}_{n-1}(k; \omega)(2\pi)\delta(k - k_s) e^{iq(\epsilon_g + \epsilon_s)}. \end{aligned} \tag{8}$$

The lateral integral ($\int dk$) can be evaluated using the Dirac delta functions. Then equation (8) produces the reduced 1.5-D free-surface multiple eliminator as,

$$\begin{aligned} & D_n'^{2D1DE}(k_g;\omega)\delta(k_g-k_s) \\ &= \frac{2}{i\rho_r B(\omega)}\delta(k_g-k_s)D_1'^{2D1DE}(k_g;\omega)qD_{n-1}'^{2D1DE}(k_s;\omega)e^{iq(\epsilon_g+\epsilon_s)}. \end{aligned} \tag{9}$$

Integrating over k_g on both sides will provide the FSME assuming a 2-D line source as

$$D_n'^{2D1DE}(k_h;\omega) = \frac{2}{i\rho_r B(\omega)}D_1'^{2D1DE}(k_h;\omega)qD_{n-1}'^{2D1DE}(k_h;\omega)e^{iq(\epsilon_g+\epsilon_s)}, \tag{10}$$

for $n \geq 2$ and,

$$D'^{2D1DE}(k_h,\omega) = \sum_{n=1}^{\infty} D_n'^{2D1DE}(k_h;\omega), \tag{11}$$

where $k_h = k_g = k_s$ (by evaluating the Dirac delta functions) and $q = sgn(\omega)\sqrt{(\omega/c_0)^2 - k_h^2}$. Free-surface multiple removed data in the space domain can be obtained by an inverse Fourier transform as,

$$D'^{2D1DE}(x_h;\omega) = \frac{1}{2\pi}\int D'^{2D1DE}(k_h;\omega)e^{ik_h x_h}dk_h. \tag{12}$$

The process following equations (8) and then (15) gives us the ISS FSME algorithm assuming a 2-D line source for a 1-D subsurface.

4 The FSME algorithm assuming a 3-D point source and a 1-D subsurface

3-D data generated by a 1-D earth depend only on the source-receiver offset and the frequency and has a spatial circular symmetry in cylindrical coordinates (independent of azimuth angle). This symmetry makes it convenient to study the 1-D earth problem with cylindrical coordinates, which is characterized by a radial length, an azimuth angle and a vertical position. The 3-D vectors (x, y, z) and (k_x, k_y, k_z) in Cartesian coordinates can be transformed to (r_i, θ_i, z_i) and (k_{ri}, ϕ_i, k_{zi}), $i \in \{g, 1, 2, s\}$, in cylindrical coordinates.

The dependence of 3-D data for a 1-D earth can be expressed as $D^{3D1DE}(|\vec{r_g} - \vec{r_s}|, \omega)$ or $D^{3D1DE}(r_h, \omega)$, where $\vec{r_g}$ and $\vec{r_s}$ are the projections of receiver and source locations on to the x-y plane, respectively. r_h is the magnitude of the difference between $\vec{r_g}$ and $\vec{r_s}$. Due to the cylindrical symmetry, the 3-D source-1-D subsurface data can be transformed to the (k_{ri}, ω) domain as (X. Lin, A. Weglein, 2014 M-OSRP Annual Report),

$$D(\vec{k_g}, \vec{k_s}; \omega) = D^{3D1DE}(k_{rh};\omega)(2\pi)^2\frac{\delta(k_{rg}-k_{rs})\delta(\phi_g-\phi_s)}{k_{rg}}, \tag{13}$$

where $k_{rh} = k_{rg}$. The receivers are required along the r-direction in $D^{3D1DE}(r_h, \omega)$, because

$$D_1'^{3D1DE}(k_{rh};\omega) = 2\pi\int_0^{\infty} D'^{3D1DE}(r_h;\omega)J_0(k_{rh}r_h)r_h dr_h. \tag{14}$$

The form of data in the $(k_{ri};\omega)$ domain (equation (13)) contains the Dirac delta functions in cylindrical coordinates, which is equivalent to $\delta(k_{xg} - k_{xs})\delta(k_{yg} - k_{ys})$ in Cartesian coordinates.

Substitute equation (13) into the full 3-D ISS FSME algorithm in equation (2) and change the variables of integration $dk_x dk_y$ to $k_r dk_r d\phi$ to get,

$$\begin{aligned} & D_n'^{3D1DE}(k_{rg};\omega)(2\pi)^2\frac{\delta(k_{rg}-k_{rs})\delta(\phi_g-\phi_s)}{k_{rg}} \\ = & \frac{1}{2i\pi^2\rho_r B(\omega)}\int_{-\infty}^{\infty}\int_{-\infty}^{\infty}k_r dk_r d\phi(2\pi)^2\frac{\delta(k_{rg}-k_r)\delta(\phi_g-\phi)}{k_{rg}}D_1'^{3D1DE}(k_{rg};\omega) \\ & \times q(2\pi)^2\frac{\delta(k_r-k_{rs})\delta(\phi-\phi_s)}{k_r}D_{n-1}'^{3D1DE}(k_r;\omega)e^{iq(\epsilon_g+\epsilon_s)}, \end{aligned} \tag{15}$$

where ϵ_g and ϵ_s are the depth of source and receivers, respectively. The lateral integrals $\iint k_r dk_r d\phi$ can be evaluated due to the Dirac delta functions as above. The equation turns out to be,

$$\begin{aligned} & D_n'^{3D1DE}(k_{rg};\omega)\frac{\delta(k_{rg}-k_{rs})\delta(\phi_g-\phi_s)}{k_{rg}} \\ = & \frac{2}{i\rho_r B(\omega)}\frac{\delta(k_{rg}-k_{rs})\delta(\phi_g-\phi_s)}{k_{rg}}D_1'^{3D1DE}(k_{rg};\omega)qD_{n-1}'^{3D1DE}(k_{rs};\omega)e^{iq(\epsilon_g+\epsilon_s)}. \end{aligned} \tag{16}$$

Integrating over k_{rg} and ϕ_g on both sides gives the 3-D source ISS FSME algorithm for 1-D subsurface as,

$$D_n'^{3D1DE}(k_{rh};\omega) = \frac{2}{i\rho_r B(\omega)}D_1'^{3D1DE}(k_{rh};\omega)qD_{n-1}'^{3D1DE}(k_{rh};\omega)e^{iq(\epsilon_g+\epsilon_s)}, \tag{17}$$

for $n \geq 2$ and

$$D'^{3D1DE}(k_{rh};\omega) = \sum_{n=1}^{\infty}D_n'^{3D1DE}(k_{rh},\omega), \tag{18}$$

where $k_{rh} = k_{rg} = k_{rs}$ and $q = \sqrt{(\frac{\omega}{c_0})^2 - k_{rh}^2}$.

$D_n'^{3D1DE}(k_{rh},\omega)$ (n^{th}-order FS multiple prediction) or $D'^{3D1DE}(k_{rh},\omega)$ (FS multiple removed data) need to be transformed back to the space domain by an inverse Hankel transform (derived from two dimension Fourier transform due to the independence of the azimuth angle), instead of an inverse Fourier transform. The free-surface multiple prediction $D_n'^{3D1DE}(r_h;\omega)$ can be obtained by using,

$$D_n'^{3D1DE}(r_h;\omega) = \frac{1}{2\pi}\int_0^{\infty}D_n'^{3D1DE}(k_{rh};\omega)J_0(k_{rh}r_h)k_{rh}dk_{rh}. \tag{19}$$

Similarly, the FS multiple removed data can be transformed to the space-time domain by,

$$D'^{3D1DE}(r_h;\omega) = \frac{1}{2\pi}\int_0^{\infty}D'^{3D1DE}(k_{rh};\omega)J_0(k_{rh}r_h)k_{rh}dk_{rh}. \tag{20}$$

In an acquisition geometry where sources and receivers are on the same streamer in a 3-D survey, we can take r along any angle in the x-y plane, including $r = x$.

5 Numerical Results

The synthetic 3-D source data are generated based on acoustic layered models using a limited bandwidth. The data sets are generated in the (k_{rh},ω) domain by the reflectivity method. All the datasets

are pre-stack shot records without reference wavefield or ghost, which satisfies the prerequisites of the ISS FSME algorithm. As an initial investigation in Model I, only the leading order FS multiple prediction ($D_2'^{2D1DE}$ or $D_2'^{3D1DE}$) is predicted and removed in all the results. Experiments in Model II applies the 2nd order ISS FS multiple elimination algorithm ($D_3'^{2D1DE}$ or $D_3'^{3D1DE}$) since data contains 2nd-order FS multiple.

5.1 Model I: examine the significance of incorporating a 3-D source in ISS FSME algorithm

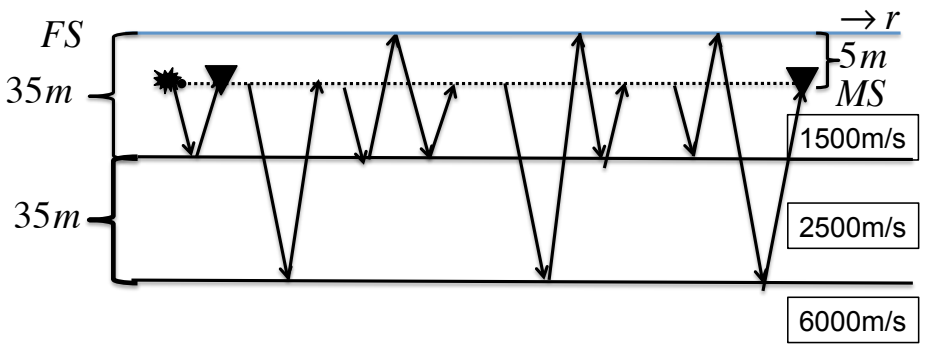

Figure 1: Model I

The first example is tested on the data generated by Model I shown in figure 1. The original 3-D source data is presented in figure 2 (a), which contains two primaries and two free-surface multiples. All the events are isolated in recording time.

Figure 2 presents the FS multiple prediction and removal results assuming a 3-D point source, following equations (18) and (19). Figures 2 (a) and (b) contain the original 3-D source data as input and FS multiple prediction which is the output. The result in figure 2 (b) provides the accurate time and exact amplitude of free-surface multiples. After simply subtracting (b) from (a), the free-surface multiples are completely removed from the input data. The wiggle comparison of trace number 360 in figure 2 (d) illustrates that the multiple events predicted by ISS FSME algorithm assuming a 3-D point source (dashed red line) has the same wavelet shape and amplitude as the free-surface multiples in the data (solid blue line).

In contrast to the 3-D source prediction, the 2-D line source ISS free-surface multiple prediction (figure 3 (b), (d)) can generate a deviated wavelet and a much smaller amplitude than the original free-surface multiple (figure 3 (a)). In this case, subtracting the prediction from the data can produce free-surface multiple residues in the result (figure 3 (c)), which is harmful to subsequent processing (e.g. ISS internal multiple attenuation/elimination).

Generally, the energy minimization criterion will be applied in this situation to make the subtraction effective, which is known as adaptive subtraction. And indeed the adaptive method works well when the events in the data are isolated, as in the synthetic data shown in this section. However, when the primaries and multiple are overlapping, the energy minimization criterion can fail to remove the multiples without harming the primaries.

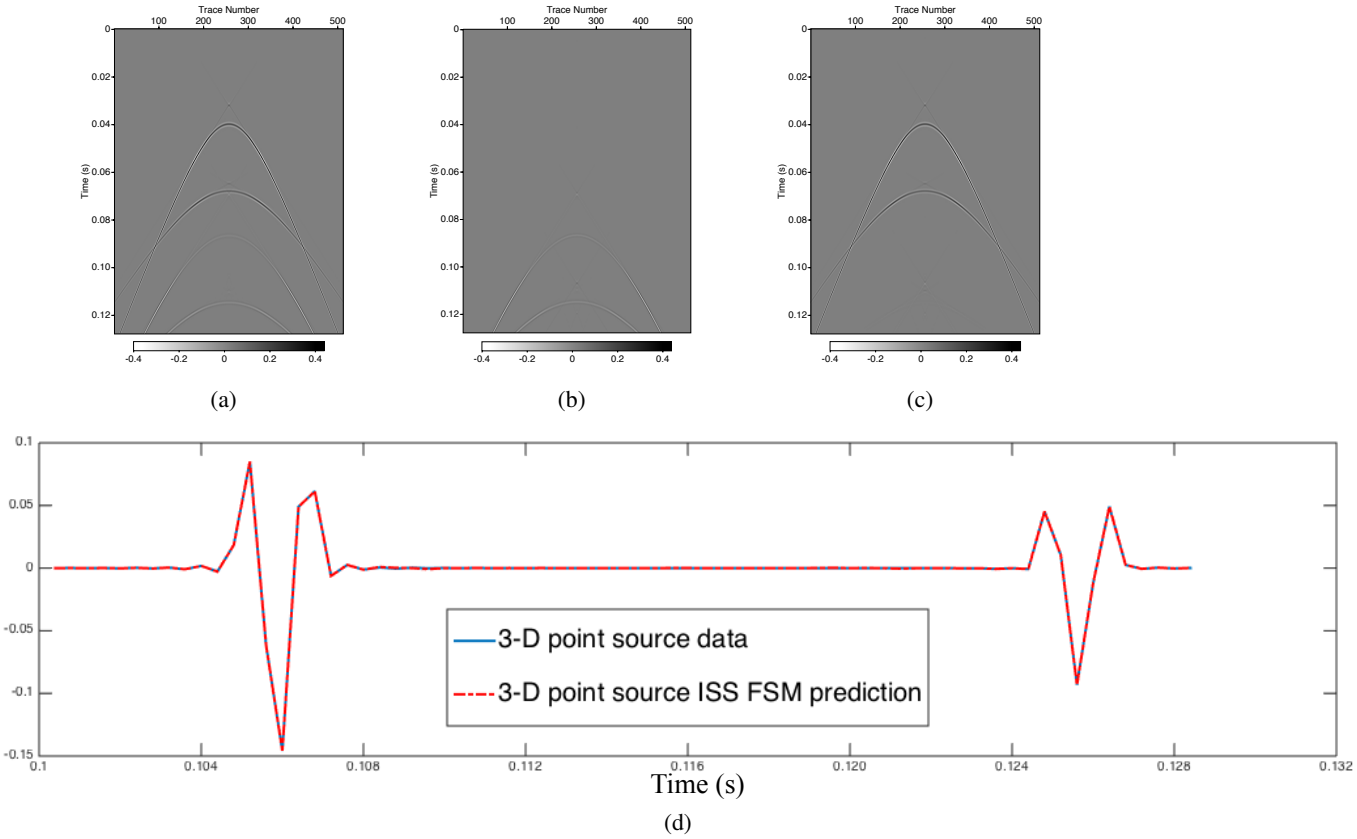

Figure 2: 3-D point source free-surface multiple prediction and removal, (a) 3-D point source data, (b) FS multiple prediction assuming a 3-D point source, (c) FS multiple removal assuming a 3-D point source through simple subtraction, (d) wiggle comparison of trace between the original data (solid blue line) and FS multiple prediction (dashed red line).

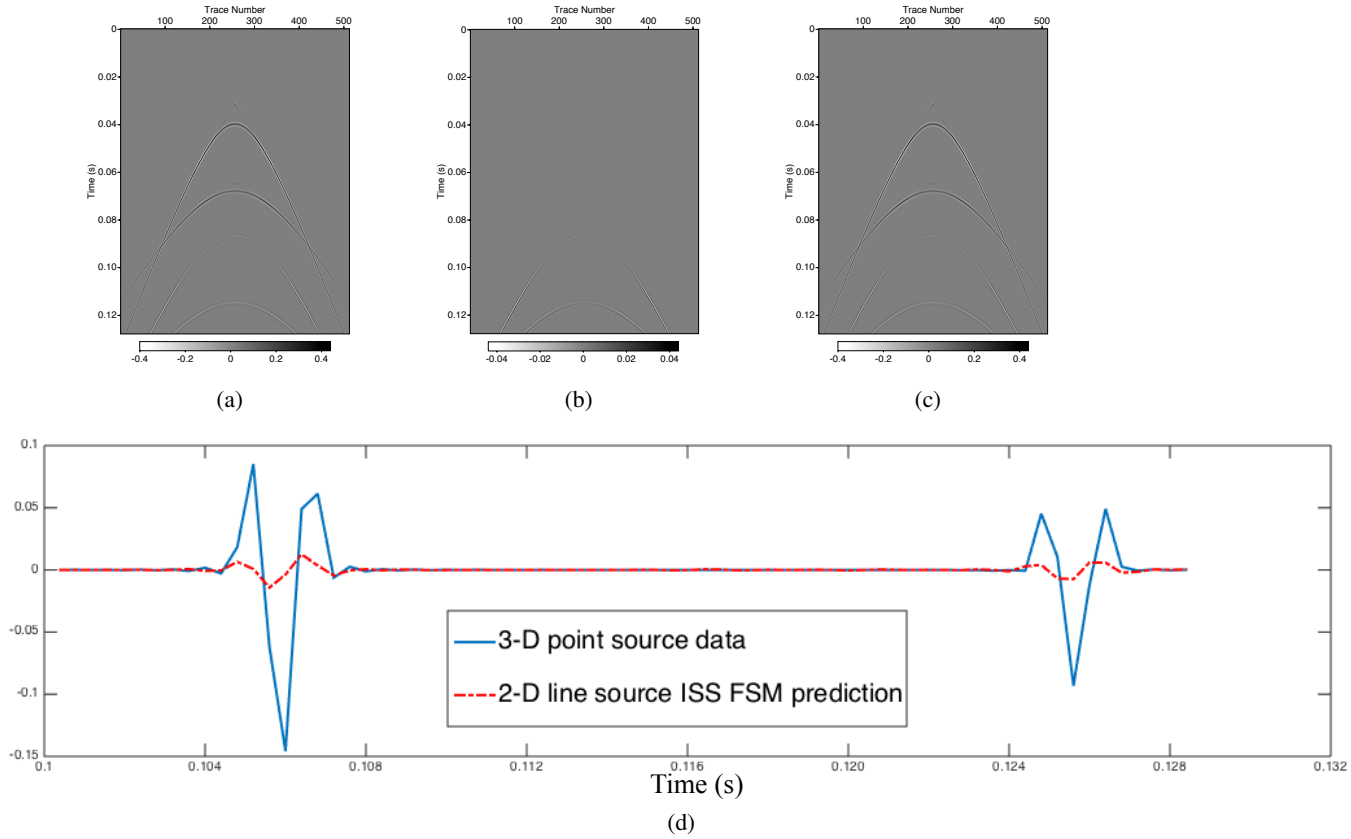

Figure 3: 2-D line source free-surface multiple prediction and removal, (a) 3-D point source data, (b) FS multiple prediction assuming a 2-D line source, (c) FS multiple removal assuming a 2-D line source through simple subtraction, (d) wiggle comparison of trace between the original data (solid blue line) and FS multiple prediction (dashed red line).

5.2 Model II: examine the consequence of mismatching the source dimension in FSM removal on the ISS internal multiple attenuation

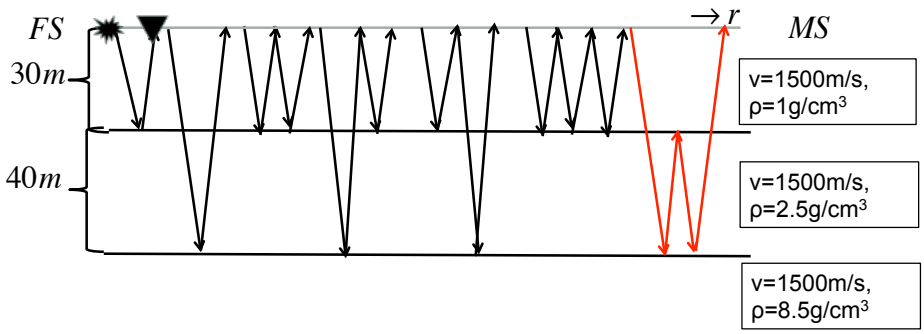

Figure 4: Model II

The second test is performed on the data that is generated by a 3-D point source and density variation model (figure 4) using reflectivity method. The original data in figure 5 (a) contain two primaries, three free-surface multiples and one internal multiple. Since the data contains both first-order and second-order free-surface multiples, the second-order ISS FSME algorithm will be applied to eliminate the free-surface multiples in the original data.

Figure 5 (b) presents the free-surface multiple removed result assuming a 3-D point source, which matches the source dimension in the synthetic data. Incorporating the 3-D source can provide both the accurate time and amplitude for this 3-D point source dataset. Therefore, all the free-surface multiples can be completely removed. The result shown in figure 5 (b) produces the satisfactory prerequisite of subsequent ISS internal multiple attenuation algorithm. Continued ISS internal multiple attenuation prediction has been shown in the right panel of figure 5 (c). The yellow arrow is pointed to the predicted internal multiple event. The internal multiple attenuation prediction works well as an attenuator, which provides accurate time and approximate amplitude of the internal multiple event.

However, applying a frequently used 2-D line source FSME algorithm on a 3-D point source data can make the prediction far from effective. The FS multiple removed result assuming a 2-D line source has been shown in figure 6 (b). Compared to the original data shown in figure 6 (a), the FS multiple residues present in the result after FS multiple removal. If the residues of FS multiples exist in the input of subsequent ISS internal multiple attenuation, several artifacts will occur in the internal multiple prediction. Figure 6 (c) shows the source-dimension-mismatched FSME result in the left panel and the internal multiple prediction using the left panel result as input in the right panel. The artifacts (right panel of figure 6 (c)) can be cataloged as (1) false events (pointed by green arrows), (2) events sitting on the FS multiple residues (pointed by blue arrows), and (3) events sitting on the internal multiple prediction (pointed by yellow arrow).

The causes of different artifacts have been in figure 7, figure 8 and figure 9 with one example. The internal multiple attenuation algorithm selects events, which satisfy the lower-higher-lower relation in vertical time, from input b_1. Summing over the time in two outer b_1 (denoted with a blue font) and then subtracting the time in middle b_1 (denoted with a red font) can produce the phase of the events in prediction. Figure 7 shows the origin of the false events that do not exist in the original data. Generally, false events can occur when the outer b_1s contribute a large time primary and the middle b_1 contributes a earlier free-surface multiple event. Figure 8 presents the second artifact,

which can sit on the free-surface multiple residues. In figure 8, this kind of artifact can make the free-surface multiples residues worse after subtracting the right panel from left panel. Another artifact, sitting on the internal multiple prediction as shown in figure 9, has the possibility to destroy the internal multiple prediction. The artifact event in figure 8 is not supposed to be generated in principle. Nevertheless, if the input data contains FS multiple residues, this event can be generated and it can enlarge the amplitude of the internal multiple prediction. In this case, the attenuation can fail when the amplitude of prediction is over the amplitude of the original internal multiple.

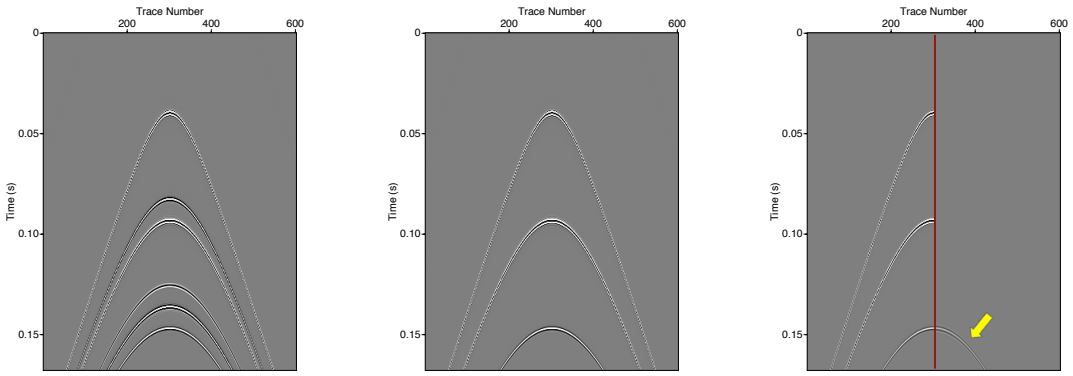

(a) (b) (c)

Figure 5: (a) Original 3-D point source data contain primaries, free-surface multiples and internal multiple (b) ISS free-surface multiple removal result assuming a 3-D point source and (c) comparison between 3-D point source FSME result (shown in (b), left panel) and continued 3-D point source ISS internal multiple attenuation result using the result in (b) as input (right panel). Yellow arrow: internal multiple prediction.

6 Conclusions

In this report, a reduced and modified 3-D source ISS free-surface-multiple-elimination algorithm has been proposed for a 1-D subsurface. The numerical results demonstrate that the modified algorithm can eliminate the free-surface multiple events for one 3-D shot gather. However, using a 2-D line source ISS FSME algorithm can produce a much less effective prediction with small amplitude. When the events are interfering to each other, adaptive methods have difficulties in precisely removing the multiples without harm to primaries, whether one is using local search method (Verschuur et al., 1992) or global search method (Carvalho and Weglein, 1994). Furthermore, the subsequent ISS internal multiple prediction depends on the success of free-surface multiple removal. The results shows that using an input data with free-surface multiple residues can produce artifacts in subsequent ISS internal multiple attenuation algorithm. Therefore, any step/prerequisite that cannot be done will lead to consequence of ineffective subsequent processing. In other words, each prerequisite should be satisfied before the next processing. It is essential to make sure that each step can be done right before the start of subsequent step.

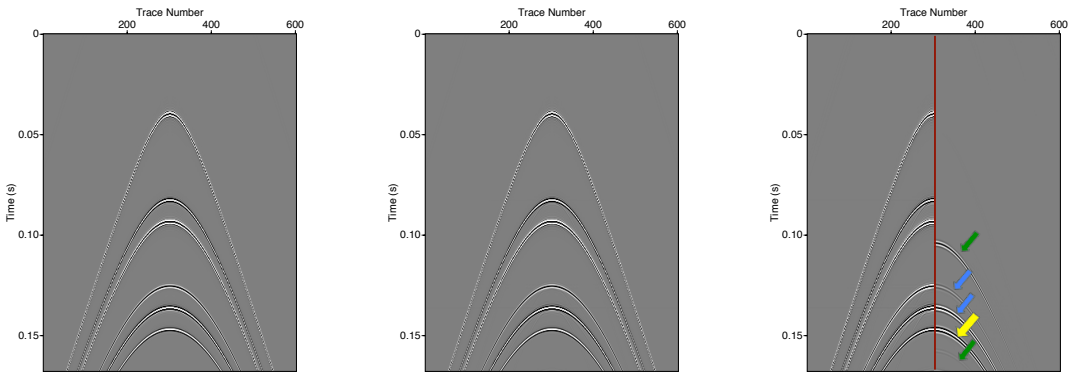

(a) (b) (c)

Figure 6: (a) Original 3-D point source data contain primaries, free-surface multiples and internal multiple (b) ISS free-surface multiple removal result assuming a 2-D line source and (c) comparison between 2-D line source FSME result (shown in (b), left panel) and continued 3-D point source ISS internal multiple attenuation result using the result in (b) as input (right panel). Green arrow: false events; Blue arrow: events sitting on the FSM residues; Yellow arrow: events sitting on the internal multiple prediction.

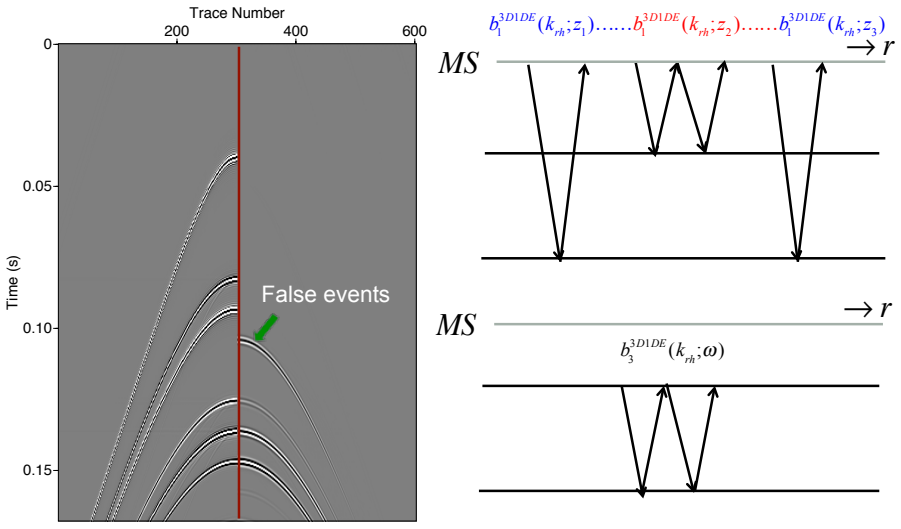

Figure 7: The analysis of the false events generated by ISS internal multiple prediction using the input that contains FS multiple residues.

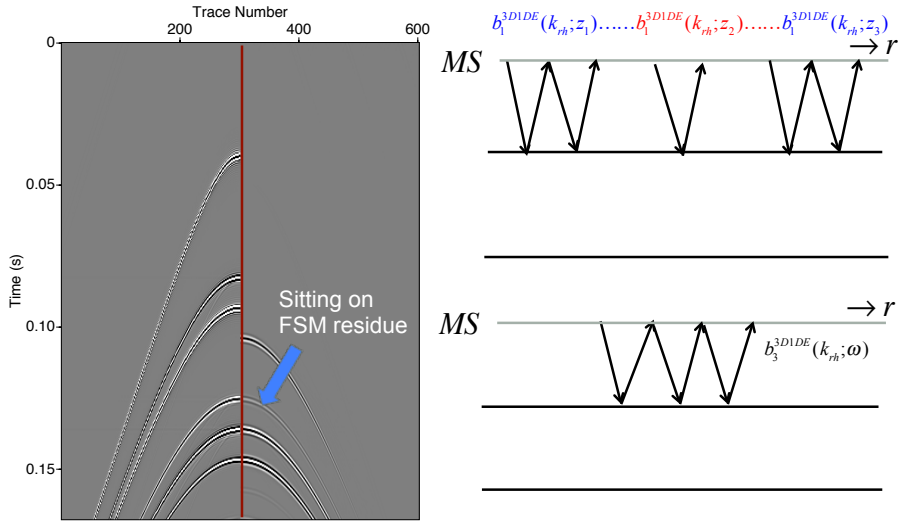

Figure 8: The analysis of the events sitting on the FSM residues generated by ISS internal multiple prediction using the input that contains FS multiple residues.

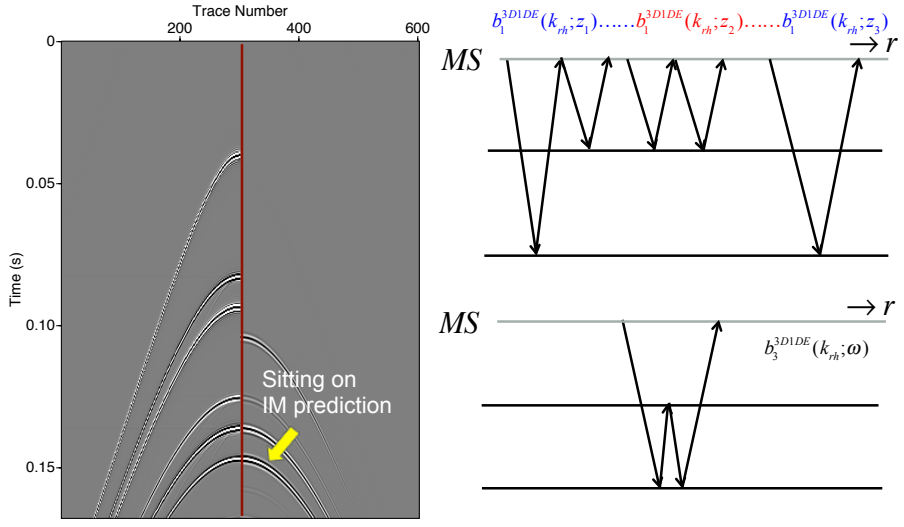

Figure 9: The analysis of the events sitting on the internal multiple prediction generated by ISS internal multiple prediction using the input that contains FS multiple residues.

7 Acknowledgements

We are grateful to all M-OSRP sponsors for their encouragement and support. All members in the M-OSRP group are thanked for their valuable discussions and shared information.

References

Carvalho, P. M. *Free-surface multiple reflection elimination method based on nonlinear inversion of seismic data*. PhD thesis, Universidade Federal da Bahia, 1992.

Carvalho, P. M. and A. B. Weglein. "Wavelet estimation for surface multiple attenuation using a simulated annealing algorithm." *64th Annual International Meeting, SEG, Expanded Abstracts* (1994): 1481–1484.

Verschuur, D. J., A. J. Berkhout, and C. P. Wapenaar. "Adaptive surface-related multiple elimination." *Geophysics* 55 (1992): 1166–1177.

Weglein, A. B., F. V. Araújo, P. M. Carvalho, R. H. Stolt, K. H. Matson, R. T. Coates, D. Corrigan, D. J. Foster, S. A. Shaw, and H. Zhang. "Inverse Scattering Series and Seismic Exploration." *Inverse Problems* (2003): R27–R83.

Weglein, A. B. and W. H. Dragoset. "Multiple Attenuation." *SEG* (2008).

Weglein, A. B., F. A. Gasparotto, P. M. Carvalho, and R. H. Stolt. "An Inverse-Scattering Series Method for Attenuating Multiples in Seismic Reflection Data." *Geophysics* 62 (November-December 1997): 1975–1989.

The significance of incorporating a 3-D point source in the inverse scattering series internal multiple attenuator for a 1-D subsurface

Xinglu Lin and Arthur B. Weglein, M-OSRP/Physics Dept./University of Houston*

SUMMARY

In this paper, the 3-D inverse scattering series (ISS) internal multiple attenuation algorithm (Araújo et al., 1994; Weglein et al., 1997, 2003) is modified for a one-dimensional subsurface to incorporate a 3-D point source in multiple predictions, for improved realism and effectiveness. The new algorithm, which assumes the earth is only varying in the z-direction (1-D subsurface/earth, reasonable in many circumstances in Central North sea (Duquet et al., 2013), on-shore Canada, and the Middle East), represents more than a small increase in effectiveness of predicting the shape and amplitude of multiples, compared to a frequently employed 1.5-D ISS internal multiple attenuator (assuming a 2-D line source and a 1-D earth). The numerical tests are performed on a 3-D source synthetic data set from a 1-D subsurface. The results demonstrate that the new algorithm incorporating a 3-D point source can change the prediction from 'causing harm' to 'providing benefit' in comparison to an internal multiple attenuation algorithm that assumes a 1-D earth and a line source.

INTRODUCTION

The current state of ISS algorithms provides a multidimensional procedure that eliminates all free-surface multiples and attenuates all internal multiples (Carvalho, 1992; Araújo et al., 1994; Weglein et al., 1997, 2003). Yanglei Zou and Chao Ma are pioneering new ISS capability for internal multiple removal (Zou and Weglein, 2014; Liang et al., 2013; Ma and Weglein, 2014). This approach has its unique strengths in that it does not require subsurface information and is even independent of the earth model-type. These multidimensional methods, the ISS internal multiple attenuation algorithm (Araújo et al., 1994; Weglein et al., 1997) can predict the accurate time and approximate amplitude of internal multiple (that are generated by the reflectors below the free-surface). The data requirement of this method depends on how many dimensions are assumed to be spatially variable in the subsurface. For example, the original 2-D ISS internal multiple attenuation algorithm (assuming 2-D line sources and 2-D line receivers) requires a collection of shot records on a line. However, for a 3-D subsurface (assuming 3-D point sources and 3-D point receivers), the algorithm needs the sources everywhere on the measurement plane and each source needs the receivers everywhere on the plane.

The implementations on this method have shown promising results for marine (e.g. Ferreira, 2011; Matson and Weglein, 1996) and on-shore cases (e.g. Fu et al., 2010; Luo et al., 2011; Terenghi et al., 2011). There are circumstances where it is reasonable to assume a 1-D subsurface (e.g. Central North sea (Duquet et al., 2013), on-shore Canada, and the Middle East). Recently, the 1.5-D ISS internal multiple attenuator (the algorithm reduced from a complete 2-D ISS internal multiple attenuation algorithm for a 1-D subsurface) has been successfully applied on Saudi Aramco on-shore data (Luo et al., 2011) and also produced a positive result for the Encana land data (Fu and Weglein, 2014).

In this abstract, we will incorporate a 3-D point source into the 1-D subsurface ISS internal multiple attenuation algorithm to develop a more realistic algorithm and to evaluate the significance of including the 3-D source in the algorithm.

THE 3-D AND 2-D ISS INTERNAL MULTIPLE ATTENUATION ALGORITHM

The ISS internal multiple attenuator was originally proposed by Araújo et al. (1994) and Weglein et al. (1997). The preparation of the 3-D ISS internal multiple prediction starts from data $D(x_g,y_g,\varepsilon_g,x_s,y_s,\varepsilon_s,t)$, where (x_g,y_g,ε_g) and (x_s,y_s,ε_s) are the receiver- and source-location, respectively. For the fixed depth of sources and receivers (omit $\varepsilon_s,\varepsilon_g$), the b_1 term is defined by the data in wavenumber-frequency domain as $b_1(\vec{k}_g,\vec{k}_s,q_g+q_s) = -2iq_s \cdot D(\vec{k}_g,\vec{k}_s,\omega)$, where the vertical wavenumber is $q_i = sgn(\omega)\sqrt{(\omega/c_0)^2 - k_{x_i}^2 - k_{y_i}^2}$, $i \in \{g,s\}$ and $\vec{k}_g = (k_{x_g},k_{y_g})$, $\vec{k}_s = (k_{x_s},k_{y_s})$. The b_1 term can be Fourier transformed to the depth domain as $b_1(\vec{k}_g,\vec{k}_s,z)$, and corresponds to an un-collapsed Stolt migration. The ISS internal multiple attenuation algorithm in 3-D is

$$
\begin{aligned}
& b_3^{3D}(k_{x_g},k_{y_g},k_{x_s},k_{y_s};\omega) \\
&= \frac{1}{(2\pi)^4}\iint dk_{x_1}dk_{x_2}\iint dk_{y_1}dk_{y_2}e^{-iq_1(\varepsilon_g-\varepsilon_s)}e^{iq_2(\varepsilon_g-\varepsilon_s)} \\
&\quad\times\int_{-\infty}^{+\infty} dz_1 b_1(k_{x_g},k_{y_g},k_{x_1},k_{y_1},z_1)e^{i(q_g+q_1)z_1} \\
&\quad\times\int_{-\infty}^{z_1-\varepsilon} dz_2 b_1(k_{x_1},k_{y_1},k_{x_2},k_{y_2},z_2)e^{-i(q_1+q_2)z_2} \\
&\quad\times\int_{z_2+\varepsilon}^{+\infty} dz_3 b_1(k_{x_2},k_{y_2},k_{x_s},k_{y_s},z_2)e^{i(q_2+q_s)z_3}, \qquad (1)
\end{aligned}
$$

where the $q_i = sgn(\omega)\sqrt{(\omega/c_0)^2 - k_{x_i}^2 - k_{y_i}^2}$, $i \in \{g,1,2,s\}$, and $b_3^{3D}(k_{x_g},k_{y_g},k_{x_s},k_{y_s},\omega)$ is a 3-D internal multiple attenuator in wavenumber-frequency domain. The 3-D algorithm in equation (1) assumes that the acquisition applies 3-D sources and 3-D receivers for a 3-D subsurface. Two dimension space and time inverse Fourier transforming $b_3^{3D}(k_{x_g},k_{y_g},k_{x_s},k_{y_s},\omega)/(-2iq_s)$ can produce the 3-D space-time attenuator, which predict the internal multiple accurately in time and approximately in amplitude. In addition, $(b_1+b_3)/(-2iq_s)$ can generate the result after multiple removal when it is returned to the space-time domain.

Similarly, a set of 2-D data $D(x_g,x_s,t)$ can be transformed into wavenumber-frequency domain as $D(k_g,k_s,\omega)$, which defines

the 2-D $b_1(k_g,k_s,q_g+q_s) = -2iq_s \cdot D(k_g,k_s,\omega)$. And then the 2-D ISS internal multiple attenuation algorithm is

$$\begin{aligned} & b_3^{2D}(k_g,k_s;\omega) \\ &= \frac{1}{(2\pi)^2}\iint dk_1 dk_2 e^{-iq_1(\varepsilon_g-\varepsilon_s)} e^{iq_2(\varepsilon_g-\varepsilon_s)} \\ &\times \int_{-\infty}^{+\infty} dz_1 b_1(k_g,k_1,z_1) e^{i(q_g+q_1)z_1} \\ &\times \int_{-\infty}^{z_1-\varepsilon} dz_2 b_1(k_1,k_2,z_2) e^{-i(q_1+q_2)z_2} \\ &\times \int_{z_2+\varepsilon}^{+\infty} dz_3 b_1(k_2,k_s,z_2) e^{i(q_2+q_s)z_3}, \end{aligned} \tag{2}$$

where the vertical wavenumber is $q_i = sgn(\omega)\sqrt{(\omega/c_0)^2 - k_i^2}$, $i \in \{g,1,2,s\}$, $b_1(k_g,k_s,z)$ is an un-collapsed Stolt migration of a 2-D data (transform $b_1(k_g,k_s,q_g+q_s)$ back to depth domain) , and $b_3^{2D}(k_g,k_s,\omega)$ is a 2-D internal multiple attenuator in wavenumber-frequency domain. The 2-D attenuator in space-time domain can be obtained by inverse Fourier transforming $b_3^{2D}(k_g,k_s,\omega)/(-2iq_s)$. In contrast to the 3-D case, algorithm in equation (2) assumes a 2-D subsurface, in which the acquisition corresponds to 2-D line sources and 2-D line receivers.

In the following sections, both the 3-D algorithm and 2-D algorithm are reduced for the data from a 1-D subsurface, where in the 3-D case the source is a 3-D point source and in the 2-D case the source is a line source. For convenience, the superscript $1DE$ represents the 1-D earth assumption for different sources (For example, 2-D line source 1-D earth: $2D1DE$; 3-D point source 1-D earth: $3D1DE$).

THE ISS INTERNAL MULTIPLE ATTENUATOR ASSUMING A 2-D LINE SOURCE FOR A 1-D SUBSURFACE

In developing the algorithm for a 1-D earth pre-stack data, it was natural that people started with the 2-D ISS internal multiple attenuation algorithm and then reduced it for a 1-D subsurface data. The data that occurs in the 2-D earth can be presented as $D(x_g,x_s,\omega)$ or $D(x_m,x_h,\omega)$ in space-frequency domain, where $x_m = x_g + x_s$ and $x_h = x_g - x_s$. The data from a 1-D earth, shown as $D^{2D1DE}(x_h,\omega)$, only depends on the source-receiver offset (x_h) and the frequency (ω). The Fourier transform over the 2-D data for a 1-D earth, which is needed for the algorithm, can be shown as,

$$\begin{aligned} D(k_g,k_s;\omega) &= \iint e^{ik_g x_g} e^{-ik_s x_s} D^{2D1DE}(x_h,\omega) dx_g dx_s \\ &= \frac{1}{2}\int e^{ik_h x_h} D^{2D1DE}(x_h,\omega) dx_h \int e^{ik_m x_m} dx_m \\ &= D^{2D1DE}(k_h,\omega)(2\pi)\cdot\delta(k_g-k_s), \end{aligned} \tag{3}$$

where $k_h = \frac{k_g+k_s}{2}$ and $k_m = \frac{k_g-k_s}{2}$. The data is independent of x_m and can come out of the integral. Consequently, the Fourier transform integral over x_m can produce a Dirac delta function in k_m. b_1 is defined as $b_1(k_g,k_s,q_g+q_s) = -2iq_s \cdot D(k_g,k_s,\omega)$. The un-collapsed Stolt migration b_1 can be expressed by b_1^{2D1DE} as,

$$b_1(k_g,k_s,z) = b_1^{2D1DE}(k_h,z)(2\pi)\cdot\delta(k_g-k_s). \tag{4}$$

By applying this 1-D earth b_1 to the equation (2), the lateral integrals ($\int\int dk_1 dk_2$) can be evaluated by the Dirac delta functions. Then equation (2) produces the reduced 1.5-D internal multiple attenuator as,

$$\begin{aligned} & b_3^{2D1DE}(k_h;\omega) = \\ & \int_{-\infty}^{+\infty} dz_1 b_1^{2D1DE}(k_h,z_1) e^{i2qz_1} \int_{-\infty}^{z_1-\varepsilon} dz_2 b_1^{2D1DE}(k_h,z_2) e^{-i2qz_2} \\ & \times \int_{z_2+\varepsilon}^{+\infty} dz_3 b_1^{2D1DE}(k_h,z_3) e^{i2qz_3}, \end{aligned} \tag{5}$$

where $k_h = k_g = k_s$ (evaluating by the Dirac delta functions) and $q = sgn(\omega)\sqrt{(\omega/c_0)^2 - k_h^2}$. Prediction D_3 in the space domain can be obtained by an inverse Fourier transform as,

$$D_3^{2D1DE}(x_h;\omega) = \frac{1}{2\pi}\int b_3^{2D1DE}(k_h;\omega)/(-2iq_s) e^{ik_h x_h} dk_h. \tag{6}$$

The process following equations (5) and then (6) gives us the ISS internal multiple attenuation algorithm assuming a 2-D line source for a 1-D subsurface.

THE ISS INTERNAL MULTIPLE ATTENUATOR ASSUMING A 3-D POINT SOURCE FOR A 1-D SUBSURFACE

The 3-D data generated by a 1-D earth only depends on the source-receiver offset and the frequency, which has a spatial circular symmetry in cylindrical coordinates (independence of azimuth angle). This symmetry makes it convenient to study the 1-D earth problem with cylindrical coordinates. The 3-D vectors (x,y,z) and (k_x,k_y,k_z) in Cartesian coordinates can be transformed to (r_i,θ_i,z_i) and (k_{ri},ϕ_i,k_{zi}), $i \in \{g,1,2,s\}$, in cylindrical coordinates, which is characterized by a radial length, an azimuth angle and a vertical position. The dependence of a 3-D data for a 1-D earth can be expressed as $D^{3D1DE}(|\vec{r}_g - \vec{r}_s|,\omega)$ or $D^{3D1DE}(r_h,\omega)$, where the $\vec{r}_g$ and $\vec{r}_s$ are the projection of receiver and source locations on x-y plane, respectively. r_h is the magnitude of the difference between $\vec{r}_g$ and $\vec{r}_s$. Due to the cylindrical symmetry, the 3-D source-1-D subsurface data can be transformed to (k_{ri},ω) domain as,

$$D(\vec{k}_g,\vec{k}_s;\omega) = D^{3D1DE}(k_{rh};\omega)(2\pi)^2 \frac{\delta(k_{rg}-k_{rs})\delta(\phi_g-\phi_s)}{k_{rg}}, \tag{7}$$

where $k_{rh} = k_{rg}$. The receivers are required along the r-direction as $D^{3D1DE}(r_h,\omega)$, because

$$D^{3D1DE}(k_{rh};\omega) = 2\pi\int_0^{\infty} D^{3D1DE}(r_h;\omega) J_0(k_{rh}r_h) r_h dr_h. \tag{8}$$

The form of data in $(k_{ri};\omega)$ domain (equation (7)) contains the Dirac delta functions in cylindrical coordinates, which is equivalent to $\delta(k_{xg}-k_{xs})\delta(k_{yg}-k_{ys})$ in Cartesian coordinates. Similar to the 2-D case, b_1 back to depth domain is,

$$b_1(\vec{k}_g,\vec{k}_s,z) = b_1^{3D1DE}(k_{rg},z)(2\pi)^2 \frac{\delta(k_{rg}-k_{rs})\delta(\phi_g-\phi_s)}{k_{rg}}, \tag{9}$$

which is a 3-D un-collapsed Stolt migration. Substitute this term into the full 3-D ISS internal multiple attenuation algorithm in equation (1) with arranging the integral variable from $dk_x dk_y$ to $k_r dk_r d\phi$. The lateral integrals $\iiint\int k_{r1} dk_{r1} d\phi_1$ $k_{r2} dk_{r2} d\phi_2$ can be evaluated due to the Dirac delta functions, as above. The reduced form of the 3-D algorithm is

$$b_3^{3D1DE}(k_{rh};\omega) = \int_{-\infty}^{+\infty} dz_1 b_1^{3D1DE}(k_{rh},z_1) e^{i2qz_1} \int_{-\infty}^{z_1-\varepsilon} dz_2 b_1^{3D1DE}(k_{rh},z_2) e^{-i2qz_2} \times \int_{z_2+\varepsilon}^{+\infty} dz_3 b_1^{3D1DE}(k_{rh},z_3) e^{i2qz_3}, \quad (10)$$

where $k_{rh} = k_{rg} = k_{rs}$ (evaluated by Dirac delta functions), vertical wavenumber $q = sgn(\omega)\sqrt{(\omega/c_0)^2 - k_{rh}^2}$ and $\varepsilon_g = \varepsilon_s$ (receivers and sources are located at the same depth). Equation (10) has the same form as the reduced 2-D internal multiple attenuator (equation (5)) for 1-D subsurface in wavenumber-frequency domain.

$b_3^{3D1DE}(k_{rh};\omega)$ needs to be transformed back to the space domain by an inverse Hankel transform (derived from two dimension Fourier transform due to the independence of the azimuth angle), instead of an inverse Fourier transform. The internal multiple prediction $D_3^{3D1DE}(r_h;\omega)$ can be obtained by using,

$$D_3^{3D1DE}(r_h;\omega) = \frac{1}{2\pi}\int_0^{\infty} J_0(k_{rh}\cdot r_h)\frac{b_3^{3D1DE}(k_{rh};\omega)}{-2iq_s} k_{rh} dk_{rh}. \quad (11)$$

We can rewrite the integral above using Bessel functions of the third kind (Hankel function) H_0^+ as,

$$D_3^{3D1DE}(r_h;\omega) = \frac{1}{4\pi}\int_{-\infty}^{+\infty} H_0^+(k_{rh}\cdot r_h)\frac{b_3^{3D1DE}(k_{rh};\omega)}{-2iq_s} k_{rh} dk_{rh}, \quad (12)$$

where $q = sgn(\omega)\sqrt{(\omega/c_0)^2 - k_{rh}^2}$. Considering the high computational costs in this transform, we can use the approximate asymptotic Hankel function to improve the efficiency. Then the asymptotic Hankel transform is,

$$D_3^{3D1DE}(r_h;\omega) = \frac{1}{2\pi}\int_{-\infty}^{+\infty} \sqrt{\frac{k_{rh}}{i2\pi r_h}}\frac{b_3^{3D1DE}(k_{rh};\omega)}{-2iq_s} e^{ik_{rh}r_h} dk_{rh}. \quad (13)$$

In a specified acquisition geometry that sources and receivers are on the same streamer in 3-D survey, we can make r along any angle in x-y plane, including $r = x$. The equation (10) combining with equation (11) or (13) form the ISS internal multiple attenuator assuming a 3-D point source for 1-D subsurface.

NUMERICAL RESULTS

The synthetic 3-D source data are generated based on a 1-D acoustic layered model in Figure 1 using a broad bandwidth. Since the data set is generated in (k_{rh},q) domain by reflectivity method, we assume that the data is transformed from space-time domain to wavenumber-frequency domain by space Fourier-Bessel transform (Hankel transform) and time Fourier transform. The dataset is one pre-stack shot record (see Figure 2 (a)) without free-surface multiple or ghost, which satisfies the data requirements of both the ISS internal multiple attenuation algorithm assuming a 2-D line source (equation (5),(6)) and a 3-D point source (equation (10), (11) or (13)).

The comparisons between the original data, the 2-D line source prediction and the 3-D point source predictions are shown in four shot gather plots (see Figure 2). The original 3-D source data from a 1-D earth is shown in Figure 2 (a), which contains two primaries and one internal multiple events. Figure 2 (c) presents the internal multiple prediction assuming a 2-D line source, in which the tail spread (a non-spherical wave) is due to the impulse signature in a 2-D Green's function. Both Figure 2 (b) and (d) provides the predictions assuming a 3-D point source. The difference is that the result in (d) employs an asymptotic Bessel function (equation (13)) in order to transform the prediction back to space domain, instead of doing a Hankel transform (equation (11)) in the prediction shown in (b). The reason is because the efficiency of a 3-D point source prediction is the same as a 2-D line source prediction when an asymptotic Bessel function is used.

All the predictions here produce an accurate time of the internal multiple, but different wavelet shape (Figure 2 (c)) or amplitude (Figure 2 (b) (c) (d)) from the original internal multiple. In a further step, we explore the effectiveness of different predictions by comparing results in near-offset (Figure 3 (a) (b), trace 2) and far-offset (Figure 3 (c) (d), trace 60).

Figure 3 (a) and (c) demonstrate that the 2-D line source prediction (blue line) can generate a deviated wavelet and a much larger amplitude than original internal multiple (red line). In this case, direct subtracting the prediction from the data can produce a larger multiple event in the de-multipled result, which is harmful to the subsequent processing. Meanwhile, the 3-D source predictions (**black** line, green line) always will be an attenuator as expected, for both near- and far- offset (smaller amplitude compared to original internal multiple (red line)).

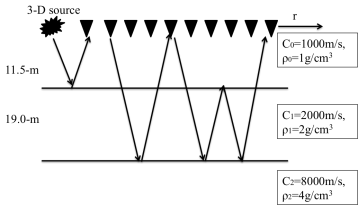

Figure 1: Acoustic model used to generate synthetic 3-D point source data.

Figure 3 (b) and (d) presents the difference between the original data (red line) and the 3-D source predictions on near- and far-offset traces, respectively. The wiggle plots (corresponding to the time slot in red box in Figure 3 (a) and (c)) are shown in a larger scale. The results demonstrate that the predictions assuming a 3-D source are always attenuators, which is the characteristic of the ISS internal multiple attenuation algorithm. For a near-offset trace (see Figure 3 (b)), the prediction using an asymptotic Bessel (green line), which is a far-field approximation, is not as effective as the prediction retaining Hankel

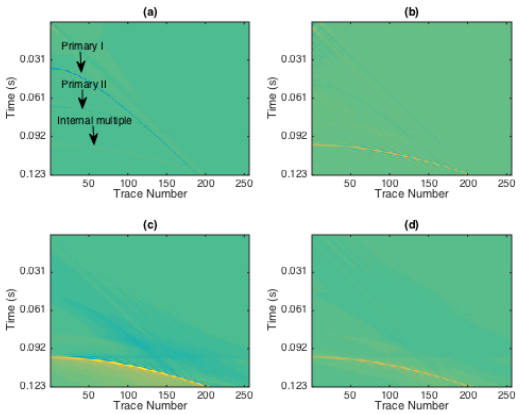

Figure 2: (a) One shot gather of a 3-D source-1-D earth data; (b) ISS internal multiple prediction assuming a 3-D point source; (c) ISS internal multiple prediction assuming a 2-D line source; (d) ISS internal multiple prediction assuming a 3-D point source using an asymptotic Bessel function.

transform in it (**black** line). Nevertheless, for the far-offset trace (see Figure 3 (d)) the amplitudes of these two predictions tend to be the same. Please notice that when the asymptotic Bessel function is applied to a 3-D point source attenuator for 1-D subsurface, the computational cost of it can be reduced to the same as the cost of a 1.5-D line source attenuator, which can finish its prediction in the order of seconds for this small size experimental data.

CONCLUSION

In this paper, a reduced and modified 3-D source ISS internal multiple attenuator has been proposed for a 1-D subsurface, which enhances the effectiveness of predicting the shape and amplitude of the internal multiples. Numerical tests and analysis illustrate that with the data generated by a 3-D point source it is important to incorporate that source dimension in the ISS internal multiple attenuation algorithm. That incorporation will always reduce the internal multiple. Using an internal multiple predictor that assumes a 2-D line source on data from a 3-D point source can make the multiple larger amplitude. Therefore, it is essential to incorporate a 3-D point source in internal multiple algorithms when the subsurface is 1-D, 2-D or 3-D. Ignoring the 3-D source inclusion on real data can result in an effective and useful algorithm making the multiple problem worse. That was an interesting and surprising result for the important role that a 3-D source accommodation is for internal multiple prediction effectiveness.

ACKNOWLEDGMENTS

We are grateful to all the M-OSRP sponsors for their long-term support and encouragements.

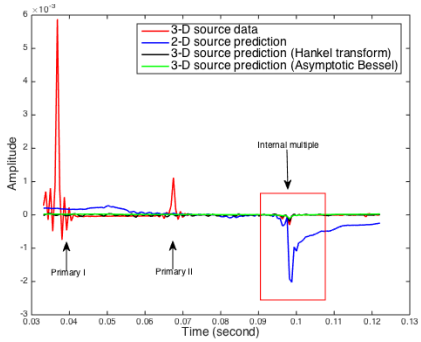

(a) Wiggle comparison of trace 2

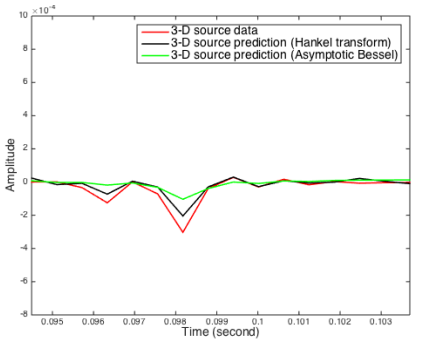

(b) Plot the slot in the red box in (a) without the 2-D source prediction in a larger scale

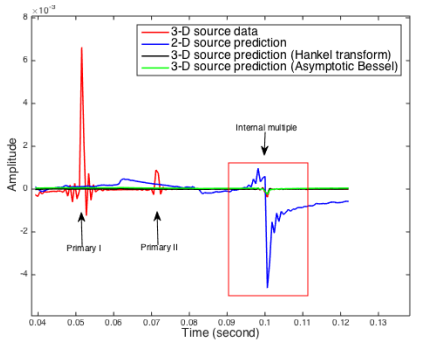

(c) Wiggle comparison of trace 60

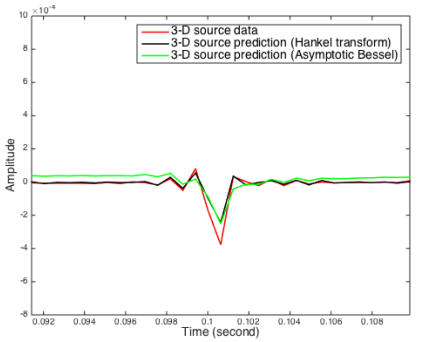

(d) Plot the slot in the red box in (c) without the 2-D source prediction in a larger scale

Figure 3: Wiggle comparison of trace 2 (a) (b) and trace 60 (c) (d); Red line: original 3-D source-1-D earth data; Blue line: ISS internal multiple prediction assuming a 2-D line source; **Black** line: ISS internal multiple prediction assuming a 3-D point source; Green line: ISS internal multiple prediction assuming a 3-D point source using an asymptotic Bessel function.

REFERENCES

Araújo, F. V., A. Weglein, P. M. Carvalho, and R. Stolt, 1994, Inverse scattering series for multiple attenuation: An example with surface and internal multiples: 64th Annual International Meeting, SEG, Expanded Abstracts, 1039–1041.

Carvalho, P. M., 1992, Free-surface multiple reflection elimination method based on nonlinear inversion of seismic data: PhD thesis, Universidade Federal da Bahia.

Duquet, B., A. Chavanne, P. Poupion, M. Rowlands, B. Santos-Luis, and J. M. Ugolini, 2013, Seismic processing and imaging in central north sea area - recents advances and remaining challenges: 75th EAGE conference.

Ferreira, A., 2011, Internal multiple removal in offshore offshore brazil seismic data using the inverse scattering series: Master Thesis, University of Houston.

Fu, Q., Y. Luo, P. G. Kelamis, G. Huo, G.and Sindi, S.-Y. Hsu, and A. B. Weglein, 2010, The inverse scattering series approach towards the elimination of land internal multiples: 80th Annual International Meeting, SEG, Expanded Abstracts, 3456–3461.

Fu, Q., and A. B. Weglein, 2014, Internal multiple attenuation on encana data: 84th Annual International Meeting, SEG, Expanded Abstracts, 4118–4123.

Liang, H., C. Ma, and A. B. Weglein, 2013, General theory for accommodating primaries and multiples in internal multiple algorithm: Analysis and numerical tests: 83th Annual International Meeting, SEG, Expanded Abstracts, 4178–4183.

Luo, Y., P. G. Kelamis, Q. Fu, G. Huo, G. Sindi, S.-Y. Hsu, and A. B. Weglein, 2011, Elimination of land internal multiple based on the inverse scattering series: The Leading Edge, **30**, 884–889.

Ma, C., and A. B. Weglein, 2014, Including higher-order inverse scattering series terms to address a serious shortcoming/problem of the nternal-multiple attenuator: Exemplifying the problem and its resolution: 84th Annual International Meeting, SEG, Expanded Abstracts, 4124–4129.

Matson, K., and A. B. Weglein, 1996, Removal of elastic interface multiples from land and ocean bottom data using inverse scattering: 66th Annual International Meeting, SEG, Expanded Abstracts., 1526–1529.

Terenghi, P., S.-Y. Hsu, A. B. Weglein, and X. Li, 2011, Exemplifying the specific properties of the inverse scattering series internal-multiple attenuation method that reside behind its capability for complex onshore and marine multiples: The Leading Edge, **30**, 876–882.

Weglein, A. B., F. V. Araújo, P. M. Carvalho, R. H. Stolt, K. H. Matson, R. T. Coates, D. Corrigan, D. J. Foster, S. A. Shaw, and H. Zhang, 2003, Inverse scattering series and seismic exploration: Inverse Problems, R27–R83.

Weglein, A. B., F. A. Gasparotto, P. M. Carvalho, and R. H. Stolt, 1997, An inverse-scattering series method for attenuating multiples in seismic reflection data: Geophysics, **62**, 1975–1989.

Zou, Y., and A. B. Weglein, 2014, An internal-multiple elimination algorithm for all reflectors for 1d algorithm, part 1: Strengths and limitations: Journal of seismic exploration, **23**, 393–404.

Incorporating a 3-D point source in the inverse scattering series internal multiple attenuation algorithm for a 2-D subsurface

Xinglu Lin, and Arthur B. Weglein

Abstract

In this report, the inverse-scattering-series (ISS) internal-multiple-attenuation algorithm (Araújo et al., 1994; Weglein et al., 1997, 2003) for a 3-D point source and a 3-D subsurface is modified/reduced for the data coming from a 2-D subsurface in this report. The modified 3-D ISS internal-multiple-attenuation algorithm for a 2-D subsurface presents the same data requirement and computational cost as a 2-D ISS internal multiple attenuation algorithm demands (assuming a 2-D line source and a 2-D subsurface). Unlike the 2-D source-2-D earth algorithm, the modified/reduced algorithm preserves the effectiveness of predicting the amplitude and the shape of internal multiples for a 3-D point source data coming from 2-D subsurface.

1 Introduction

The ISS algorithm provides multidimensional procedures (Carvalho, 1992; Araújo et al., 1994; Weglein et al., 1997, 2003), which has its unique strengths in that it does not require subsurface information and is even independent of the earth model-type. Among these multidimensional methods, the ISS internal-multiple-attenuation algorithm (Araújo et al., 1994; Weglein et al., 1997) can predict the accurate time and approximate amplitude of internal multiples (that are generated by the reflectors below the free-surface). The data requirement of this method depends on how many dimensions are assumed to be spatially variable in the subsurface. For a 3-D subsurface (assuming 3-D point sources and 3-D point receivers), the algorithm needs the sources everywhere on the measurement surface and each source needs the receivers everywhere on the measurement surface. This need for a complete areal data set and hence high computational capability are challenges. Therefore, people choose the 2-D algorithm (which assumes a 2-D line source) to process the 3-D data coming from an approximately 2-D subsurface with inadequate data in the crossline direction.

This report assumes that earth properties vary only in two dimensions (2-D earth/subsurface) but the sources, receivers and wave propagation are in 3-dimensions. These assumptions are named as 2.5-D problems in history (Deregowski and Brown, 1983; Bleistein, 1986). The 2.5-D problems have been presented and discussed by various authors in different contexts, including forward modeling (Deregowski and Brown, 1983; Liner, 1991; Williamson and Pratt, 1995; Miksat et al., 2008), migration (Esmersoy and Oristaglio, 1988) and inversion (Clayton and Stolt, 1981; Stolt and Benson, 1986; Bleistein, 1987). In contast to the above mentioned projects, this paper focuses on a 2.5-D ISS internal multiple attenuation algorithm which can be reduced from a complete 3-D algorithm assuming 3-D sources and receivers.

The complete 3-D ISS internal-multiple-attenuation algorithm was developed by Araújo et al. (1994); Weglein et al. (1997). For a 2-D subsurface, the 3-D ISS internal multiple attenuation algorithm can be reduced in both data requirements and computational cost. It preserves the property of the three-dimensional sources and receivers. This incorporation avoids the serious degradation of

applying a 2-D ISS internal multiple attenuation algorithm, which assumes a 2-D line sources and receivers, on 3-D source data.

2 3-D and 2-D ISS internal-multiple algorithm

The inverse-scattering method for internal-multiple prediction provides a comprehensive theory without requiring any subsurface information. The ISS internal multiple attenuator was originally proposed by Araújo et al. (1994) and Weglein et al. (1997). The preparation of the 3-D ISS internal multiple prediction starts from data $D(x_g, y_g, \epsilon_g, x_s, y_s, \epsilon_s, t)$, where (x_g, y_g, ϵ_g) and (x_s, y_s, ϵ_s) are the receiver- and source-location, respectively. For the fixed depth of sources and receivers (omit ϵ_s, ϵ_g), the b_1 term is defined by the data in wavenumber-frequency domain as $b_1(\vec{k}_g, \vec{k}_s, q_g + q_s) = -2iq_s D(\vec{k}_g, \vec{k}_s; \omega)$, where the vertical wavenumber is $q_i = sgn(\omega)\sqrt{(\omega/c_0)^2 - k_{x_i}^2 - k_{y_i}^2}$, $i \in \{g, s\}$ and $\vec{k_g} = (k_{x_g}, k_{y_g})$, $\vec{k_s} = (k_{x_s}, k_{y_s})$. The b_1 term can be Fourier transformed to the depth domain as ,

$$b_1(\vec{k}_g, \vec{k}_s, z) = \int (-2iq_s) D(\vec{k}_g, \vec{k}_s; \omega) e^{-i(q_g+q_s)z} dk_z, \tag{1}$$

where $k_z = q_g + q_s$ and $q_i = sgn(\omega)\sqrt{(\omega/c_0)^2 - k_{x_i}^2 - k_{y_i}^2}$. $b_1(\vec{k}_g, \vec{k}_s, z)$ corresponds to an uncollapsed Stolt migration. The ISS internal multiple attenuation algorithm in 3-D is

$$\begin{aligned}
& b_3^{3D}(k_{x_g}, k_{y_g}, k_{x_s}, k_{y_s}; \omega) \\
= & \frac{1}{(2\pi)^4} \iint_{-\infty}^{\infty} dk_{x_1} dk_{x_2} \iint_{-\infty}^{\infty} dk_{y_1} dk_{y_2} e^{-iq_1(\epsilon_g - \epsilon_s)} e^{iq_2(\epsilon_g - \epsilon_s)} \\
& \times \int_{-\infty}^{+\infty} dz_1 b_1(k_{x_g}, k_{y_g}, k_{x_1}, k_{y_1}, z_1) e^{i(q_g+q_1)z_1} \\
& \times \int_{-\infty}^{z_1-\epsilon} dz_2 b_1(k_{x_1}, k_{y_1}, k_{x_2}, k_{y_2}, z_2) e^{-i(q_1+q_2)z_2} \\
& \times \int_{z_2+\epsilon}^{+\infty} dz_3 b_1(k_{x_2}, k_{y_2}, k_{x_s}, k_{y_s}, z_2) e^{i(q_2+q_s)z_3},
\end{aligned} \tag{2}$$

where $q_i = sgn(\omega)\sqrt{(\omega/c_0)^2 - k_{x_i}^2 - k_{y_i}^2}$, $i \in \{g, 1, 2, s\}$, and $b_3^{3D}(k_{x_g}, k_{y_g}, k_{x_s}, k_{y_s}; \omega)$ is a 3-D internal-multiple-attenuator in wavenumber-frequency domain. The 3-D algorithm in equation (2) assumes that the acquisition applies 3-D sources and 3-D receivers for a 3-D subsurface. $D(k_{x_g}, k_{y_g}, k_{x_1}, k_{y_1}; \omega)$ indicates that the algorithm needs the sources everywhere on the measurement surface and each source needs the receivers everywhere on the measurement surface. Inverse Fourier transforming $b_3^{3D}(k_{x_g}, k_{y_g}, k_{x_s}, k_{y_s}; \omega)/(-2iq_s)$ can produce the 3-D space-time attenuator, which predicts the internal multiple accurately in time and approximately in amplitude. In addition, $(b_1+b_3)/(-2iq_s)$ can generate the result after multiple removal when it is returned to the space-time domain.

Similarly, a set of 2-D data $D(x_g, x_s, t)$ can be transformed into wavenumber-frequency domain as $D(k_g, k_s; \omega)$, which defines the 2-D $b_1(k_g, k_s, q_g + q_s) = -2iq_s D(k_g, k_s; \omega)$. The uncollapsed Stolt migration can be obtained as,

$$b_1(k_g, k_s, z) = \int (-2iq_s) D(k_g, k_s; \omega) e^{-i(q_g+q_s)z} dk_z, \tag{3}$$

where $k_z = q_g + q_s$ and $q_i = sgn(\omega)\sqrt{(\omega/c_0)^2 - k_i^2}$. The 2-D ISS internal-multiple-attenuation algorithm is

$$\begin{aligned} & b_3^{2D}(k_g, k_s; \omega) \\ = & \frac{1}{(2\pi)^2} \iint dk_1 dk_2 e^{-iq_1(\epsilon_g - \epsilon_s)} e^{iq_2(\epsilon_g - \epsilon_s)} \\ & \times \int_{-\infty}^{+\infty} dz_1 b_1(k_g, k_1, z_1) e^{i(q_g + q_1)z_1} \\ & \times \int_{-\infty}^{z_1 - \epsilon} dz_2 b_1(k_1, k_2, z_2) e^{-i(q_1 + q_2)z_2} \\ & \times \int_{z_2 + \epsilon}^{+\infty} dz_3 b_1(k_2, k_s, z_2) e^{i(q_2 + q_s)z_3}, \end{aligned} \tag{4}$$

where the vertical wavenumber is $q_i = sgn(\omega)\sqrt{(\omega/c_0)^2 - k_i^2}$, $i \in \{g, 1, 2, s\}$, $b_1(k_g, k_s, z)$ is an un-collapsed Stolt migration of 2-D data (transform $b_1(k_g, k_s, q_g + q_s)$ back to depth domain) , and $b_3^{2D}(k_g, k_s; \omega)$ is a 2-D internal-multiple attenuator in wavenumber-frequency domain. The 2-D attenuator in space-time domain can be obtained by inverse Fourier transforming $b_3^{2D}(k_g, k_s; \omega)/(-2iq_s)$. The original 2-D ISS internal-multiple attenuation algorithm in equation (4) (assuming 2-D line sources and 2-D line receivers) requires a collection of shot records on a line.

The following sections will discuss the reduced 3-D algorithm for the data from a 2-D subsurface. For convenience, the superscript $2DE$ represents the 2-D earth assumption for different sources (for example, 3-D point source 2-D earth: $3D2DE$).

3 Reduce the source-side data requirement by applying cross-line symmetry

Data can be rearranged from $D(x_g, y_g; x_s, y_s, t)$ to $D(x_g, x_s, y_h, y_m, t)$, where $y_h = y_g - y_s$ (offset along y-direction) and $y_m = y_g + y_s$ (double the midpoint location along y-direction). Assuming the earth property is invariant along the y direction, then the dependence of data can be reduced from $D(x_g, x_s, y_h, y_m, t)$ to $D^{3D2DE}(x_g, x_s, y_h, t)$, which is independent of y_m. The Fourier transform over the 3-D data for a 2-D subsurface, which is needed for the algorithm, can be shown as,

$$\begin{aligned} & D(k_{x_g}, k_{y_g}, k_{x_s}, k_{y_s}; \omega) \\ = & \iint dx_g dx_s \iint dy_g dy_s e^{i(k_{x_g} x_g + k_{y_g} y_g)} e^{-i(k_{x_s} x_s + k_{y_s} y_s)} \int dt e^{i\omega t} D^{3D2DE}(x_g, x_s, y_h, t) \\ = & \frac{1}{2} \int e^{ik_{y_h} y_h} D^{3D2DE}(k_{x_g}, k_{x_s}, y_h; \omega) dy_h \int e^{ik_{y_m} y_m} dy_m \\ = & D^{3D2DE}(k_{x_g}, k_{x_s}, k_{y_h}; \omega)(2\pi)\delta(k_{y_g} - k_{y_s}), \end{aligned} \tag{5}$$

where $k_{y_h} = \frac{k_{yg} + k_{y_s}}{2}$ and $k_m = \frac{k_{yg} - k_{y_s}}{2}$. The data is independent of y_m and can come out of the integral. Consequently, the Fourier transform integral over y_m can produce a Dirac delta function in k_{y_m}. b_1 is defined as $b_1(k_{x_g}, k_{x_s}, k_{y_h}, k_{y_m}, q_g + q_s) = -2iq_s D(k_{x_g}, k_{x_s}, k_{y_h}, k_{y_m}; \omega)$. The un-collapsed Stolt migration b_1 can be expressed as,

$$\begin{aligned} b_1(k_{x_g}, k_{y_g}, k_{x_s}, k_{y_s}; q_g + q_s) &= -2iq_s D(k_{x_g}, k_{y_g}, k_{x_s}, k_{y_s}; \omega) \\ &= -2iq_s D^{3D2DE}(k_{x_g}, k_{x_s}, k_{y_h}; \omega)(2\pi)\delta(k_{y_g} - k_{y_s}) \\ &= b_1^{3D2DE}(k_{x_g}, k_{x_s}, k_{y_h}; q_g + q_s)(2\pi)\delta(k_{y_g} - k_{y_s}), \end{aligned} \tag{6}$$

where $q_i = sgn(\omega)\sqrt{(\omega/c_0)^2 - k_{x_i}^2 - k_{y_i}^2}$. The symmetry factor in equation 6 is independent of $k_z = q_g + q_s$. In the following step, b_1 needs to be transformed back to depth domain:

$$b_1^{3D2DE}(k_{x_g}, k_{x_s}, k_{y_g}, k_{y_s}, z) = b_1^{3D2DE}(k_{x_g}, k_{x_s}, k_{y_h}, z)(2\pi)\delta(k_{y_g} - k_{y_s}), \tag{7}$$

which is an un-collapsed Stolt migration. When the structure from 2-D earth symmetry in equation (7) is applied into current 3-D ISS internal multiple attenuation algorithm in equation (2), the algorithm becomes,

$$\begin{aligned}
& b_3^{3D2DE}(k_{x_g}, k_{x_s}, k_{y_g}; \omega)\delta(k_{y_g} - k_{y_s}) \\
= & \frac{1}{(2\pi)^2} \iint_{-\infty}^{\infty} dk_{x_1} dk_{y_1} \iint_{-\infty}^{\infty} dk_{x_2} dk_{y_2} \\
& \times \int_{-\infty}^{+\infty} dz_1 b_1^{3D2DE}(k_{x_g}, k_{x_1}, k_{y_g}, z_1) e^{i(q_g+q_1)z_1} \delta(k_{y_g} - k_{y_1}) \\
& \times \int_{-\infty}^{z_1-\epsilon} dz_2 b_1^{3D2DE}(k_{x_1}, k_{x_2}, k_{y_1}, z_2) e^{-i(q_1+q_2)z_2} \delta(k_{y_1} - k_{y_2}) \\
& \times \int_{z_2+\epsilon}^{+\infty} dz_3 b_1^{3D2DE}(k_{x_2}, k_{x_s}, k_{y_2}, z_3) e^{i(q_2+q_s)z_3} \delta(k_{y_2} - k_{y_s}).
\end{aligned} \tag{8}$$

The lateral integrals $\iint dk_{y_1} dk_{y_2}$ can be evaluated due to the Dirac delta functions and then the algorithm can be reduced to,

$$\begin{aligned}
& b_3^{3D2DE}(k_{x_g}, k_{x_s}, k_{y_h}; \omega) \\
= & \frac{1}{(2\pi)^2} \int_{-\infty}^{\infty} dk_{x_1} \int_{-\infty}^{\infty} dk_{x_2} \int_{-\infty}^{+\infty} dz_1 b_1^{3D2DE}(k_{x_g}, k_{x_1}, k_{y_h}, z_1) e^{i(q_g+q_1)z_1} \\
& \times \int_{-\infty}^{z_1-\epsilon} dz_2 b_1^{3D2DE}(k_{x_1}, k_{x_2}, k_{y_h}, z_2) e^{-i(q_1+q_2)z_2} \\
& \times \int_{z_2+\epsilon}^{+\infty} dz_3 b_1^{3D2DE}(k_{x_2}, k_{x_s}, k_{y_h}, z_3) e^{i(q_2+q_s)z_3},
\end{aligned} \tag{9}$$

where $k_{y_h} = k_{y_g} = k_{y_s}$ (evaluated by integrating over k_{y_g} on both sides), the vertical wavenumber $q_i = sgn(\omega)\sqrt{(\omega/c_0)^2 - k_{x_i}^2 - k_{y_h}^2}$ and $\epsilon_g = \epsilon_s$ (receivers and sources are located at the same depth).

In contrast to the complete 3-D ISS internal multiple attenuator, which needs an areal coverage of receivers for each shot gather and also areal coverage of source locations, the reduced algorithm for a 2-D subsurface requires an areal coverage of receivers for each pre-stack shot gather and also multiple sources along the inline direction (x-direction here).

3.1 Test by further reducing the 3-D source 2-D earth ISS internal-multiple-attenuation algorithm for a 1-D earth

This section will test the validity of reduced 3-D source 2-D earth ISS internal-multiple-attenuation algorithm (equation (9)) by algebraically reducing it for a 1-D earth.

The algorithm starts from preparing data in the $(k_{x_g}, k_{x_s}, k_{y_h}; \omega)$ domain. The algorithm in equation (9) requires the data,

$$D^{3D2DE}(k_{x_g}, k_{x_s}, k_{y_h}; \omega) = \iint dx_g dx_s e^{i(k_{x_g} x_g - k_{x_s} x_s)} \int dy_h e^{ik_{y_h} y_h} D^{3D2DE}(x_g, x_s, y_h; \omega), \tag{10}$$

which has been shown in equation (5). When we assume that the earth varies only in the z-direction, the dependence of data turns to be $D(\sqrt{x_h^2 + y_h^2}; \omega)$. Fourier transform the 1-D earth data and change the variables from x_g and x_s to $x_h = x_g - x_s$ and $x_m = x_g + x_s$,

$$\begin{aligned} D^{3D2DE}(k_{x_g}, k_{x_s}, k_{y_h}; \omega) &= \iint dx_g dx_s e^{i(k_{x_g} x_g - k_{x_s} x_s)} \int dy_h e^{ik_{y_h} y_h} D^{3D1DE}(\sqrt{x_h^2 + y_h^2}; \omega) \\ &= \frac{1}{2} \int dx_h e^{ik_{x_h} x_h} \int dy_h e^{ik_{y_h} y_h} D^{3D1DE}(\sqrt{x_h^2 + y_h^2}; \omega) \int dx_m e^{ik_{x_m} x_m} \\ &= \frac{1}{2} \int dx_h e^{ik_{x_h} x_h} \int dy_h e^{ik_{y_h} y_h} D^{3D1DE}(\sqrt{x_h^2 + y_h^2}; \omega) 2\pi\delta(k_{x_m}), \end{aligned} \tag{11}$$

where $k_{x_h} = \frac{k_{x_g} + k_{x_s}}{2}$ and $k_{x_m} = \frac{k_{x_g} - k_{x_s}}{2}$. Since the data is independent of x_m, the integral over x_m will produce a Dirac delta function. Here we introduce the polar coordinates as (r_h, θ_h) for (x_h, y_h) and (k_{r_h}, ϕ_h) for (k_{x_h}, k_{y_h}), so we can write $r_h = \sqrt{x_h^2 + y_h^2}$ and $k_{r_h} = \sqrt{k_{x_h}^2 + k_{y_h}^2}$. Rearrange the formula in polar coordinates,

$$D^{3D2DE}(k_{x_g}, k_{x_s}, k_{y_h}; \omega) = \frac{1}{2} \int_0^\infty r_h dr_h \int_0^{2\pi} d\theta e^{ik_{r_h} r_h cos\theta} D^{3D1DE}(r_h; \omega) 2\pi\delta(k_{x_m}), \tag{12}$$

where $\theta = \theta_h - \phi_h$. Because the data depends only on r_h and ω, the integral over angular variable θ creates a Bessel function of the first kind $J_0(k_{r_h} r_h)$, which makes a Hankel transform

$$\begin{aligned} D^{3D2DE}(k_{x_g}, k_{x_s}, k_{y_h}; \omega) &= \frac{2\pi\delta(k_{x_m})}{2} \int_0^\infty J_0(k_{r_h} r_h) D^{3D1DE}(r_h; \omega) r_h dr_h \\ &= 2\pi\delta(k_{x_g} - k_{x_s}) D^{3D1DE}(k_{r_h}; \omega). \end{aligned} \tag{13}$$

The uncollapsed Stolt migration can be expressed as $b_1^{3D2DE}(k_{x_g}, k_{x_s}, k_{y_h}; z) = 2\pi\delta(k_{x_g} - k_{x_s}) b_1^{3D1DE}(k_{r_h}, z)$. After substituting this expression into equation (9), the 3-D source 2-D earth ISS internal-multiple-attenuation algorithm can be further simplified for a 1-D subsurface as,

$$\begin{aligned} & b_3^{3D1DE}(k_{r_h}; \omega) \\ &= \int_{-\infty}^{+\infty} dz_1 b_1^{3D1DE}(k_{r_h}, z_1) e^{i2qz_1} \\ &\quad \times \int_{-\infty}^{z_1 - \epsilon} dz_2 b_1^{3D1DE}(k_{r_h}, z_2) e^{-i2qz_2} \int_{z_2 + \epsilon}^{+\infty} dz_3 b_1^{3D1DE}(k_{r_h}, z_3) e^{i2qz_3}, \end{aligned} \tag{14}$$

where $q = sgn(\omega)\sqrt{\frac{\omega^2}{c_0^2} - k_{r_h}^2}$ and $k_{r_g} = k_{r_s} = k_{r_h}$ since $k_{x_g} = k_{x_s} = k_{x_h}$ and $k_{y_g} = k_{y_s} = k_{y_h}$. The reduced algorithm for a 1-D subsurface agrees with the result we obtained in Lin and Weglein (2014). The 3-D source 1-D subsurface ISS internal multiple attenuation algorithm has been tested in the referenced report, which proves the validity of the 3-D source-2-D subsurface algorithm in equation (9) in a special case of a 1-D subsurface.

4 Reduce the receiver-side data requirement using the stationary-phase approximation

People choose the 2-D algorithm (which assumes a 2-D line source) to process 3-D data because of missing crossline data and data processing efficiency. The 2-D recording acquisition (multiple shot gathers along the inline direction) does not provide enough information to predict the internal multiple in a 3-D algorithm. Even though we assume the earth varies only in (x, z), the areal coverage of receivers for each source and all the sources on one inline direction are required by the reduced form (equation (9)). That is because the algorithm is initially derived and calculated in the $(k_{y_g}, k_{y_s}; \omega)$ domain. The reduced algorithm in section 3 shows $k_{y_g} = k_{y_s} = k_{y_h}$. To obtain each k_{y_h} (or k_{y_g}, k_{y_s}), the Fourier transform needs all receivers on the measurement surface. If the acquisitions are restricted to the central plane ($y_h = 0$ in this report) assuming a 3-D point source, the asymptotic method will be applied to evaluate the summation of the wavenumber spectra only from the contribution of $k_{y_h} = 0$. The physics behind this approximation can be interpreted as no out-of-plane wave arrivals in the 2.5-D data.

4.1 Asymptotic 3-D ISS internal-multiple-attenuation algorithm for a 2-D subsurface

The uncollapsed Stolt migration $b_1^{3D2DE}(k_{x_g}, k_{x_s}, k_{y_h}, z)$ is related to the data,

$$b_1^{3D2DE}(k_{x_g}, k_{x_s}, k_{y_h}, z) = \frac{1}{2\pi} \int (-2iq_s) D(k_{x_g}, k_{x_s}, k_{y_h}; \omega) e^{-i(q_g+q_s)z} dk_z, \tag{15}$$

where $k_z = q_g + q_s$ and $q_i = sgn(\omega)\sqrt{(\omega/c_0)^2 - k_{x_i}^2 - k_{y_h}^2}$. The acquisition along $y_h = 0$ can provide only $D(k_{x_g}, k_{x_s}, y_h = 0; \omega)$. Reverse the Fourier transform shown in equation (15) as,

$$D(k_{x_g}, k_{x_s}, k_{y_h}; \omega) = \frac{1}{-2iq_s} \int b_1^{3D2DE}(k_{x_g}, k_{x_s}, k_{y_h}, z) e^{i(q_g+q_s)z} dz. \tag{16}$$

To fix the y-offset at $y_h = 0$, the k_{y_h} needs to be inverse Fourier transformed back to the spatial domain as,

$$D(k_{x_g}, k_{x_s}, y_h; \omega) = \frac{1}{2\pi} \int \int \frac{1}{-2iq_s} b_1^{3D2DE}(k_{x_g}, k_{x_s}, k_{y_h}, z) e^{i(q_g+q_s)z} e^{-ik_{y_h} y_h} dz dk_{y_h}. \tag{17}$$

The integration does not have a closed form solution, however, it involves all wavenumber along the y-direction. Using the stationary phase approximation with respect to k_{y_h}, the integral/summation over all the k_{y_h} spectrum can be replaced by the single contribution at $\hat{k}_{y_h} = 0$ for $y_h = 0$ (shown in Appendix A), where the $\hat{k}_{y_h}$ represents the stationary point. Set $y_h = 0$ in equation (17) and approximate the integral $\int dk_{y_h}$, and then we obtain

$$D(k_{x_g}, k_{x_s}, y_h = 0; \omega) \approx \int \frac{e^{-i\frac{\pi}{4}}}{-2i\hat{q}_s} \sqrt{\frac{1}{2\pi z} \frac{\hat{q}_g \hat{q}_s}{\hat{q}_g + \hat{q}_s}} b_1^{3D2DE}(k_{x_g}, k_{x_s}, k_{y_h} = 0, z) e^{i(\hat{q}_g+\hat{q}_s)z} dz, \tag{18}$$

where $\hat{q}_i = sgn(\omega)\sqrt{(\omega/c_0)^2 - k_{x_i}^2}$. A hat sign represents a variable that can be evaluated at a stationary point. Rearrange the formula to calculate the uncollapsed Stolt migration at $k_{y_h} = 0$ as,

$$b_1^{3D2DE}(k_{x_g}, k_{x_s}, k_{y_h} = 0, z) \approx \sqrt{i2\pi z} \frac{1}{2\pi} \int (-2i\hat{q}_s) \sqrt{\frac{1}{\hat{q}_g} + \frac{1}{\hat{q}_s}} D(k_{x_g}, k_{x_s}, y_h = 0; \omega) e^{-i(\hat{q}_g+\hat{q}_s)z} d\hat{k}_z, \tag{19}$$

where $\hat{k}_z = \hat{q}_g + \hat{q}_s$ and $\hat{q}_i = sgn(\omega)\sqrt{(\omega/c_0)^2 - k_{x_i}^2}$. Recall the 3-D source 2-D subsurface ISS internal-multiple-attenuation algorithm which is reduced by crossline (y-direction) symmetry in equation (9). If the wavenumber k_{y_h} is set to be zero, the equation turns to be,

$$\begin{aligned}
& b_3^{3D2DE}(k_{x_g}, k_{x_s}, k_{y_h} = 0; \omega) \\
= & \frac{1}{(2\pi)^2} \int_{-\infty}^{\infty} dk_{x_1} \int_{-\infty}^{\infty} dk_{x_2} \\
& \times \int_{-\infty}^{+\infty} dz_1 b_1^{3D2DE}(k_{x_g}, k_{x_1}, k_{y_h} = 0, z_1) e^{i(\hat{q}_g + \hat{q}_1) z_1} \\
& \times \int_{-\infty}^{z_1 - \epsilon} dz_2 b_1^{3D2DE}(k_{x_1}, k_{x_2}, k_{y_h} = 0, z_2) e^{-i(\hat{q}_1 + \hat{q}_2) z_2} \\
& \times \int_{z_2 + \epsilon}^{+\infty} dz_3 b_1^{3D2DE}(k_{x_2}, k_{x_s}, k_{y_h} = 0, z_3) e^{i(\hat{q}_2 + \hat{q}_s) z_3},
\end{aligned} \tag{20}$$

where $b_1^{3D2DE}(k_{x_g}, k_{x_s}, k_{y_h} = 0, z)$ can be calculated by equation (19). The internal-multiple prediction result can be expressed by $b_3^{3D2DE}(k_{x_g}, k_{x_s}, k_{y_h}; \omega)$ as,

$$D_3^{3D2DE}(.., y_h, t) = \frac{1}{(2\pi)^2} \iint \frac{b_3^{3D2DE}(.., k_{y_h}; \omega)}{-2iq_s} e^{-ik_{y_h} y_h} e^{-i\omega t} dk_{y_h} d\omega, \tag{21}$$

where $q_i = sgn(\omega)\sqrt{(\omega/c_0)^2 - k_{x_i}^2 - k_{y_h}^2}$, D_3 is the internal-multiple prediction in the $(k_{x_g}, k_{x_s}, y_h, t)$ domain, and k_{x_g}, k_{x_s} are omitted for convenience. Applying the same stationary phase approximation strategy with respect to k_{y_h} (Appendix B),

$$D_3^{3D2DE}(k_{x_g}, k_{x_s}, y_h = 0, t) \approx \frac{1}{2\pi} \int \sqrt{\frac{-i\omega}{2\pi t c_0^2}} \frac{b_3^{3D2DE}(k_{x_g}, k_{x_s}, \hat{k}_{y_h} = 0, \omega)}{-2i\hat{q}_s} e^{-i\omega t} d\omega, \tag{22}$$

where $q_i = sgn(\omega)\sqrt{(\omega/c_0)^2 - k_{x_i}^2}$. The complete procedure of the ISS internal-multiple-attenuation algorithm finishes at the prediction D^{3D2DE} in the (x_g, x_s, y_h, t) domain, which can be approximated by equation (22).

For a 2-D subsurface, the ISS internal-multiple attenuator assuming a 3-D point source can be reduced, and it only requires multiple shot gathers on the inline direction (x-direction) where sources and receivers are located at the $y_h = 0$ plane. That input data requirement is the same as the 2-D line source ISS internal-multiple attenuator (equation (4)). The corrections have to be added to preserve the 3-D point source assumption, as shown in equation (19), (20) and (22).

The next section will discuss how $\sqrt{-i\omega}$ works as an asymptotic filter for a homogeneous acoustic medium, which is also a conventional filter to transform 2-D data to 3-D data.

4.2 Conventional asymptotic filters

The $y_h = 0$ to $k_{y_h} = 0$ conversion filters (also understood as point-source to line-source conversion filters) have been presented by various authors in different contexts (Deregowski and Brown, 1983; Bleistein, 1986; Williamson and Pratt, 1995; Miksat et al., 2008). The simplest case is the difference between 2-D and 3-D Green's functions in a homogeneous acoustic medium. The frequency-domain

solution (Fourier transformed Green's function) to the acoustic wave equation assuming a 3-D point source can be expressed as (Aki and Richards, 2002)

$$G^{3D}(r;\omega) = \frac{1}{4\pi r} e^{\frac{i\omega r}{c_0}}, \tag{23}$$

where ω is the angular frequency, $r = \sqrt{x_h^2 + y_h^2 + z_h^2}$ and c_0 is the acoustic wave speed. The 2-D frequency-domain Green's function solution for an acoustic homogeneous full space is given by Abramowitz and Stegun (1965):

$$G^{2D}(r';\omega) = \frac{i}{4} H_0^{(1)}(\frac{\omega r'}{c_0}), \tag{24}$$

where $H_0^{(1)}$ is the Hankel function of the first kind and zeroth order and r' is the distance between source and receiver in 2-D ($r' = \sqrt{x_h^2 + z_h^2}$). Using the large argument approximation of the Hankel function (Morse and Feshbach, 1953), one obtains the asymptotic 2-D acoustic Green's function

$$G^{2D}(r';\omega) \approx \sqrt{\frac{c_0}{8\pi|\omega|r'}} e^{i(\frac{\omega r'}{c_0} + \frac{\pi}{4})}. \tag{25}$$

If we let $y_h = 0$ in equation (23), r reduces to $r' = \sqrt{x_h^2 + z_h^2}$. A simple derivation of the filter function is based on forming the ratio of the acoustic 3-D and the asymptotic 2-D Green's function as,

$$G^{2D}(r';\omega) = G^{3D}(r';\omega)\sqrt{\frac{i2\pi\sigma}{|\omega|}}, \tag{26}$$

where $\sigma = c_0 r'$ for an acoustic homogeneous medium. For a general heterogeneous medium, σ is given as the line integral of the velocity with respect to the arc length s of a ray trajectory (Miksat et al., 2008), $\sigma = \int c(s)ds$, where s is the arc length defined in a ray tracing method.

4.3 Comparisons

The correction filter in equation (19) can be compared to the conventional filter that transfers 3-D source data to 2-D line source data, which is in equation(26). The difference is that formula (19) corrects the source dimension in the image domain, instead of the temporal frequency domain ($\sqrt{r} \sim \sqrt{z}, \sqrt{\frac{1}{|\omega|/c_0}} \sim \sqrt{|\frac{1}{q_g} + \frac{1}{q_s}|}$). In this step, the correction filter $\sqrt{z}$ modifies the geometric spreading in wave propagation from $\sim \frac{1}{r}$ (3-D) to $\sim \frac{1}{\sqrt{r}}$ (2-D) in the depth domain. Also, $\sqrt{i|\frac{1}{q_g} + \frac{1}{q_s}|}$ adds a frequency scale and a $\frac{\pi}{4}$ phase shift on the 3-D data.

The filter we obtained in equation (22) is identical with the conversion filter from $k_{y_h} = 0$ (2-D) to $y_h = 0$ (one 3-D plane) for an acoustic homogeneous medium in equation (26).

For a 2-D subsurface, the 3-D ISS internal-multiple attenuator can be reduced and performed as shown in equation (19), (20) and (22). The successive steps can be interpreted as three procedures. Firstly, the 3-D point source data can be migrated and corrected to a 2-D line source uncollapsed migration result ((19)). The second step applies the $b_1(k_{y_h} = 0;\omega)$ to a reduced 3-D ISS internal multiple attenuator, where the wavenumber k_{y_h} has been set to be zero. In fact, the attenuator is degraded to a 2-D line source ISS internal-multiple attenuator when $k_{y_h} = 0$, because no wave

propagation out of the $y_h = 0$ plane provides a cylindrical wave front as in 2-D propagation. Finally, equation (22) produces the prediction result in the spatial-time domain by inverse Fourier transforming the corrected $b_3(k_{y_h}; \omega)/(-2i\hat{q}_s)$. The correction turns to be a filter that transfers the prediction back to a 3-D source data.

5 Conclusions and future work

In this paper, we reduced the 3-D ISS internal-multiple-attenuation algorithm, which assumes a 3-D point source, for a 2-D subsurface. The earth property is assumed to be changing only in 2-dimensions (e.g. xz-plane). We provided two kinds of reductions from the complete 3-D source algorithm. The first reduction only uses the spatial symmetry along the cross-line direction (defined as the y-direction here). In this step, the reduced algorithm requires an areal coverage of receivers for each pre-stack shot gather and also multiple sources along the inline direction (x-direction here). In contrast to a complete 3-D algorithm, the need for sources decreases from being on a full area to being on one line. The second reduction generates an asymptotic 3-D ISS internal-multiple-attenuation algorithm by applying stationary phase approximations. In this part, the data collection is constrained to the $y_h = 0$ plane and the prediction algorithm assumes a far-field record. The demand of data can be further reduced to be multiple pre-stack shot gathers on one single line. The reduced ISS internal multiple attenuator kernel has the same form/structure as a 2-D line source ISS attenuator. However, the corrections on the input data and output prediction can preserve the effectiveness of predicting the amplitude and the shape of internal multiples for a 3-D point source data coming from 2-D subsurface.

The numerical tests of the reduced 3-D ISS internal multiple attenuation algorithm for a 2-D subsurface will be shown to the sponsors during the annual meeting.

6 Acknowledgements

We are grateful to all M-OSRP sponsors for their encouragement and support. All members in the M-OSRP group are thanked for their valuable discussions and shared information.

Appendix A

Stationary-phase approximation to solve $D(.., y_h = 0; \omega)$

Equation (17) cannot be solved as a closed form,

$$D(k_{x_g}, k_{x_s}, y_h; \omega) = \frac{1}{2\pi} \int \int \frac{1}{-2iq_s} b_1^{3D2DE}(k_{x_g}, k_{x_s}, k_{y_h}, z) e^{i(q_g+q_s)z} e^{-ik_{y_h} y_h} dz dk_{y_h}, \quad \text{(A-1)}$$

where $q_i = sgn(\omega)\sqrt{(\omega/c_0)^2 - k_{x_i} - k_{y_h}}$. If we set a fixed plane at $y_h = 0$, the formula can be expressed as,

$$D(k_{x_g}, k_{x_s}, y_h = 0; \omega) = \frac{1}{2\pi} \int \int \frac{1}{-2iq_s} b_1^{3D2DE}(k_{x_g}, k_{x_s}, k_{y_h}, z) e^{i(q_g+q_s)z} dz dk_{y_h} \quad \text{(A-2)}$$

The integral with respect to dk_{y_h} can be approximated by a stationary phase assumption, which assumes a far-field recording and a smooth b_1^{3D2DE} with respect to k_{y_h}. In a far-field recording, the wave can be considered as propagating as a ray. The oscillating phase can be expressed as,

$$f(k_{y_h}) = (q_g + q_s)z = sgn(\omega)\left(\sqrt{\frac{\omega}{c_0}^2 - k_{x_g}^2 - k_{y_h}^2} + \sqrt{\frac{\omega}{c_0}^2 - k_{x_s}^2 - k_{y_h}^2}\right) z. \quad \text{(A-3)}$$

The saddle point can be solved by finding the root of the equation,

$$f'(k_{y_h}) = sgn(\omega)\left(\frac{-k_{y_h}}{\sqrt{\frac{\omega}{c_0}^2 - k_{x_g}^2 - k_{y_h}^2}} + \frac{-k_{y_h}}{\sqrt{\frac{\omega}{c_0}^2 - k_{x_s}^2 - k_{y_h}^2}}\right) z = 0. \quad \text{(A-4)}$$

Following the equation, the exponential can be stationary at $k_{y_h} = 0$. The second derivative of equation (22) at $\hat{k}_{y_h} = 0$ can be solved,

$$\begin{aligned} f''(\hat{k}_{y_h} = 0) = sgn(\omega)\Bigg(&\frac{-1}{\sqrt{\frac{\omega}{c_0}^2 - k_{x_g}^2 - k_{y_h}^2}} + \frac{-1}{\sqrt{\frac{\omega}{c_0}^2 - k_{x_s}^2 - k_{y_h}^2}} \\ &+ \frac{-k_{y_h}^2}{(\frac{\omega}{c_0}^2 - k_{x_g}^2 - k_{y_h}^2)^{3/2}} + \frac{-k_{y_h}^2}{(\frac{\omega}{c_0}^2 - k_{x_s}^2 - k_{y_h}^2)^{3/2}}\Bigg) z|_{\hat{k}_{y_h}=0} \\ = sgn(\omega)&\left(\frac{-1}{\sqrt{\frac{\omega}{c_0}^2 - k_{x_g}^2}} + \frac{-1}{\sqrt{\frac{\omega}{c_0}^2 - k_{x_s}^2}}\right) z. \end{aligned} \quad \text{(A-5)}$$

If $z > 0$ and $\omega > 0$ are assumed in equation (24), then $f''(k_{y_h} = 0) < 0$, which defines the factor $e^{-i\frac{\pi}{4}}$. The integral formula in (21) can be approximated as,

$$D(k_{x_g}, k_{x_s}, y_h = 0; \omega) \approx \int \frac{e^{-i\frac{\pi}{4}}}{-2i\hat{q}_s} \sqrt{\frac{1}{2\pi z} \frac{\hat{q}_g \hat{q}_s}{\hat{q}_g + \hat{q}_s}} b_1^{3D2DE}(k_{x_g}, k_{x_s}, k_{y_h} = 0, z) e^{i(\hat{q}_g+\hat{q}_s)z} dz, \quad \text{(A-6)}$$

where $\hat{q}_i = sgn(\omega)\sqrt{(\omega/c_0)^2 - k_{x_i}^2}$. Similarly, if $z > 0$ and $\omega < 0$, the $f''(k_{y_h} = 0)$ switches the sign and opening the absolute value can provide the same formula as shown in equation (A-6).

Inverse Fourier transforming to obtain b_1^{3D2DE} gives,

$$b_1^{3D2DE}(k_{x_g}, k_{x_s}, k_{y_h} = 0, z) \approx \sqrt{i2\pi z}\frac{1}{2\pi}\int(-2i\hat{q}_s)\sqrt{\frac{1}{\hat{q}_g}+\frac{1}{\hat{q}_s}}D(k_{x_g}, k_{x_s}, y_h = 0; \omega)e^{-i(\hat{q}_g+\hat{q}_s)z}d\hat{k}_z, \tag{A-7}$$

where $\hat{k}_z = \hat{q}_g + \hat{q}_s$, $\hat{q}_g = sgn(\omega)\sqrt{(\omega/c_0)^2 - k_{x_g}^2}$ and $\hat{q}_s = sgn(\omega)\sqrt{(\omega/c_0)^2 - k_{x_s}^2}$

Appendix B

Stationary phase approximation to solve $D_3(.., y_h = 0; \omega)$

In a general 3-D prediction, the internal multiple attenuator in $D_3(.., y_h = 0; \omega)$ can be obtained as,

$$D_3^{3D2DE}(.., y_h, t) = \frac{1}{(2\pi)^2} \iint \frac{b_3^{3D2DE}(.., k_{y_h}; \omega)}{-2iq_s} e^{-ik_{y_h} y_h} e^{-i\omega t} dk_{y_h} d\omega, \tag{B-1}$$

where the omitted variables are k_{x_g} and k_{x_s} and $q_i = \sqrt{(\omega/c_0)^2 - k_{x_i} - k_{y_h}}$. If we set the fixed plane at $y_h = 0$, the formula can be expressed as,

$$D_3^{3D2DE}(.., y_h = 0, t) = \frac{1}{(2\pi)^2} \iint \frac{b_3^{3D2DE}(.., k_{y_h}; \omega)}{-2iq_s} e^{-i\omega t} dk_{y_h} d\omega, \tag{B-2}$$

The variable ω can be changed to $k_z = q_g + q_s$ as shown in Stolt and Benson (1986) (chapter 3, section 5), which provides the Jacobian term,

$$d\omega = \frac{c_0^2}{\omega} \frac{q_g q_s}{q_g + q_s} dk_z \tag{B-3}$$

Formula (29) turns out to be,

$$D_3^{3D2DE}(.., y_h = 0, t) = \frac{1}{(2\pi)^2} \iint \frac{b_3^{3D2DE}(.., k_{y_h}; \omega)}{-2iq_s} e^{-i\omega(.., k_{y_h}, k_z)t} \frac{c_0^2}{\omega} \frac{q_g q_s}{q_g + q_s} dk_{y_h} dk_z, \tag{B-4}$$

where for positive frequency (negative frequency can produce the same result at the last step)

$$k_z = \sqrt{\frac{\omega}{c_0^2}^2 - k_{x_g}^2 - k_{y_h}^2} + \sqrt{\frac{\omega}{c_0^2}^2 - k_{x_s}^2 - k_{y_h}^2}. \tag{B-5}$$

The integral with respect to dk_{y_h} can be approximated by a stationary phase assumption, which assumes a far-field recording and a smooth integral kernel with respect to k_{y_h}. The saddle point can be solved by finding the root of the equation,

$$\begin{aligned} f'(k_{y_h}) &= -\omega'(k_{y_h}) \\ &= -\frac{c_0^2}{\omega} k_{y_h} = 0. \end{aligned} \tag{B-6}$$

In equation (39), the exponential can be stationary at $k_{y_h} = 0$. The second derivative of of equation (22) at $\hat{k}_{y_h} = 0$ can be solved,

$$f''(\hat{k}_{y_h} = 0) = -\frac{c_0^2}{\omega}. \tag{B-7}$$

Then $f''(k_{y_h} = 0) < 0$ for $\omega > 0$, which defines the factor $e^{-i\frac{\pi}{4}}$. The integral formula in (28) can be approximated as,

$$D_3^{3D2DE}(k_{x_g}, k_{x_s}, y_h = 0, t) \approx \frac{1}{2\pi} \int \sqrt{\frac{-i|\omega|}{2\pi t c_0^2}} \frac{b_3^{3D2DE}(k_{x_g}, k_{x_s}, \hat{k}_{y_h} = 0, \hat{\omega})}{-2i\hat{q}_s} e^{-i\hat{\omega}t} \frac{c_0^2}{\omega} \frac{\hat{q}_g \hat{q}_s}{\hat{q}_g + \hat{q}_s} d\hat{k}_z, \tag{B-8}$$

where $\hat{q}_i = sgn(\omega)\sqrt{(\omega/c_0)^2 - k_{x_i}^2}$. Change the integral variable back to $d\omega$,

$$D_3^{3D2DE}(k_{x_g}, k_{x_s}, y_h = 0, t) \approx \frac{1}{2\pi} \int \sqrt{\frac{-i\omega}{2\pi t c_0^2}} \frac{b_3^{3D2DE}(k_{x_g}, k_{x_s}, \hat{k}_{y_h} = 0, \omega)}{-2i\hat{q}_s} e^{-i\omega t} d\omega, \quad \text{(B-9)}$$

where $\hat{q}_i = sgn(\omega)\sqrt{(\omega/c_0)^2 - k_{x_i}^2}$.

If $\omega < 0$, the second derivative $f''(k_{y_h} = 0) = -\frac{c_0^2}{\omega}$ turns out to be a positive number, which provides the factor $e^{i\frac{\pi}{4}}$. The switched sign on i gives,

$$D_3^{3D2DE}(k_{x_g}, k_{x_s}, y_h = 0, t) \approx \frac{1}{2\pi} \int \sqrt{\frac{i|\omega|}{2\pi t c_0^2}} \frac{b_3^{3D2DE}(k_{x_g}, k_{x_s}, \hat{k}_{y_h} = 0, \omega)}{-2i\hat{q}_s} e^{-i\omega t} d\omega, \quad \text{(B-10)}$$

Since $|\omega| = -\omega$, the formula remains,

$$D_3^{3D2DE}(k_{x_g}, k_{x_s}, y_h = 0, t) \approx \frac{1}{2\pi} \int \sqrt{\frac{-i\omega}{2\pi t c_0^2}} \frac{b_3^{3D2DE}(k_{x_g}, k_{x_s}, \hat{k}_{y_h} = 0, \omega)}{-2i\hat{q}_s} e^{-i\omega t} d\omega, \quad \text{(B-11)}$$

where $\hat{q}_i = sgn(\omega)\sqrt{(\omega/c_0)^2 - k_{x_i}^2}$.

References

Abramowitz, M. and I. Stegun. "Handbook of mathematical functions: With formulas, graphs, and mathematical tables." *Dover Publications* (1965).

Aki, K. and P. G. Richards. "Quantitative seismology." *University Science Books* (2002).

Araújo, F. V., A.B. Weglein, P. M. Carvalho, and R.H. Stolt. "Inverse scattering series for multiple attenuation: An example with surface and internal multiples." *64th Annual International Meeting, SEG, Expanded Abstracts* (1994): 1039–1041.

Bleistein, N. "Two-and-one-half dimensional in-plane wave propagation." *Geophysical Prospecting* 34 (1986): 686–703.

Bleistein, N. "Two-and-one-half dimensional Born inversion with an arbitrary reference." *Geophysics* 52 (1987): 26–36.

Carvalho, P. M. *Free-surface multiple reflection elimination method based on nonlinear inversion of seismic data*. PhD thesis, Universidade Federal da Bahia, 1992.

Clayton, R. W. and R. H. Stolt. "A Born-WKBJ inversion method for acoustic reflection data." *Geophysics* 46 (1981): 1559–1567.

Deregowski, S. M. and S. M. Brown. "A theory of acoustic diffractors applied to 2-D models." *Geophysical Prospecting* 31 (1983): 293–333.

Esmersoy, C. and M. Oristaglio. "Reverse-time wave-field extrapolation, imaging and inversion." *Geophysics* 72 (1988): J53–J64.

Lin, X. and A. B. Weglein. "A short note: Inverse scattering series internal multiple attenuation algorithm for a 3-D source and 1-D subsurface." *Mission-Oriented Seismic Research Program Annual Report* (2014).

Liner, C. L. "Theory of a 2.5-D acoustic wave equation for constant density media." *Geophysics* 56 (1991): 2114–2117.

Miksat, J., T. M. Muller, and F.Wenzel. "Simulating three-dimensional seismograms in 2.5-dimensional structures by combining two-dimensional finite difference modelling and ray tracing." *Geophysical Journal International* 174 (2008): 309–315.

Morse, P. M. and H. Feshbach. *Methods of theoretical physics*. McGraw-Hill Book Co., 1953.

Stolt, Robert H. and Alvin K. Benson. *Seismic Migration: Theory and Practice*. Ed. Klaus Helbig and Sven Treitel. Volume 5 of Seismic Exploration. Geophysical Press, 1986.

Weglein, A. B., F. V. Araújo, P. M. Carvalho, R. H. Stolt, K. H. Matson, R. T. Coates, D. Corrigan, D. J. Foster, S. A. Shaw, and H. Zhang. "Inverse Scattering Series and Seismic Exploration." *Inverse Problems* (2003): R27–R83.

Weglein, A. B., F. A. Gasparotto, P. M. Carvalho, and R. H. Stolt. "An Inverse-Scattering Series Method for Attenuating Multiples in Seismic Reflection Data." *Geophysics* 62 (November-December 1997): 1975–1989.

Williamson, P.R. and R. G. Pratt. "A critical review of acoustic wave modeling procedures in 2.5 dimensions." *Geophysics* 60 (1995): 591–595.

A new Inverse Scattering Series (ISS) internal-multiple-attenuation algorithm that predicts the accurate time and approximate amplitude of the first-order internal multiples and addresses spurious events: Analysis and Tests in 2D

Chao Ma and Arthur B. Weglein

Abstract

The ISS internal-multiple-attenuation algorithm assumes that the free-surface-multiple events have been removed from the input of this algorithm, and that the input consists of only primary events and internal-multiple events. This algorithm selects three events by a "longer-shorter-longer" relationship in the vertical-traveltime domain, and the *primaries* selected in that procedure predict the accurate time and approximate amplitude of all first-order internal multiples, without requiring any subsurface information (Weglein et al., 2003). Because the primaries are always present in the input data, the unique strength of this algorithm (i.e., of predicting all first-order internal multiples without any subsurface information) is always present. However, when internal multiples themselves are selected in that procedure, spurious events (events that do not exist in the data) can also be generated. For the presence of such spurious events, Weglein et al. (2011), Liang et al. (2013), and Ma and Weglein (2014a) show that the spurious events are fully anticipated by the ISS and that specific higher-order terms from ISS will precisely address that spurious-event issue. The inclusion of higher-order terms provides a new ISS internal-multiple-attenuation algorithm that does not generate the spurious events and that, at the same time, retains the strength of the current algorithm.

Last year's annual report (Ma and Weglein, 2014b) documents the work of applying the aforementioned new algorithm to address the spurious-event issue in a 1D case. In this report, we discribe our progress (since last year) on addressing spurious events. We present test results in a 2D case and exemplifying the relevant and practical benefits provided by this new internal-multiple algorithm.

1 The current ISS internal-multiple-attenuation algorithm

In a 2D case, the current ISS internal-multiple-attenuation algorithm (Araujo et al., 1994; Weglein et al., 1997) starts with the input data, $D(k_g, k_s, \omega)$, which are the Fourier transform of the deghosted prestack data, and with the wavelet deconvolved and direct wave and free-surface multiples removed. The second term, $D_3(k_g, k_s, \omega)$, is the attenuator of the first-order internal multiples. In a 2D earth, $D_3(k_g, k_s, \omega)$ is obtained from $b_3(k_g, k_s, \omega) = -2iq_sD_3(k_g, k_s, \omega)$, where $b_3(k_g, k_s, \omega)$

is (Weglein et al., 2003)

$$b_3(k_g,k_s,q_s+q_s) = \frac{1}{(2\pi)^2}\int_{-\infty}^{\infty}dk_1\int_{-\infty}^{\infty}dk_2 e^{-iq_1(z_g-z_s)}e^{iq_2(z_g-z_s)} \times \int_{-\infty}^{\infty}dz_1 b_1(k_g,k_1,z_1)e^{i(q_g+q_1)z_1} \times \int_{-\infty}^{z_1-\epsilon}dz_2 b_1(k_1,k_2,z_2)e^{-i(q_1+q_2)z_2} \times \int_{z_2+\epsilon}^{\infty}dz_3 b_1(k_2,k_s,z_3)e^{i(q_2+q_s)z_3}, \quad (1)$$

where k_s and k_g are the horizontal wavenumbers for the source and receiver coordinates, respectively; q_g and q_s are the vertical source and receiver wavenumbers defined by $q_i = sgn(\omega)\sqrt{\frac{\omega^2}{c_0^2}-k_i^2}$ for $i \in \{g,s\}$ (ω is the temporal freqency); z_s and z_g are source and receiver depths; and z_j ($i \in \{1,2,3\}$) represents pseudo-depth[1] by using a reference velocity migration. The quantity $b_1(k_g,k_s,z)$ corresponds to an uncollapsed migration (Stolt and Weglein, 1985; Weglein et al., 1997) of effective plane-wave incident data.

The data, with their first-order internal multiple attenuated, are

$$D(k_g,k_s,\omega)+D_3(k_g,k_s,\omega). \quad (2)$$

2 The origin of spurious-event predictions

The ISS internal-multiple-attenuation algorithm (i.e., equation 1) selects three events by a "longer-shorter-longer" relationship in the *vertical-travel-time* domain (or, equivalently, a "deeper-shallower-deeper" relationship in the pseudo-depth domain (Nita and Weglein, 2007)), and the *primaries* selected in that procedure predict the accurate time and approximate amplitude of all first-order internal multiples, without requiring any subsurface information (Weglein et al., 2003). However, the input data contain both *primaries* and *internal multiples*. When internal multiples themselves are selected in that procedure, a spurious event can be generated (Weglein et al., 2011).

Ma et al. (2011) and Liang et al. (2013) provide examples to explain that two types of spurious-event predictions can be generated — a primary-internal multiple-primary or "PIP" type (see Figure 1) and a primary-primary-internal multiple, or "PPI"type[2] — under circumstances in which three or more reflectors are involved in the data being processed. Their work also demonstrates that the spurious-event issue is more significant as a consequence of there being numerous internal-multiple generators in many offshore and most onshore plays. Thus, addressing such spurious events is essential and indispensable.

[1]Pseudo-depth refers to the location of an image derived using the background reference velocity. Since the reference velocity is constant (water), pseudo-depth is essentially vertical-travel time (Weglein et al., 2003).

[2] "P" and "I" represent Primary and Internal multiple, respectively. "PIP" means a type of spurious event that is generated by selecting "Primary-Internal multiple-Primary" in this algorithm; "PPI" means a type of spurious event that is generated by selecting "Primary-Primary-Internal multiple" in this algorithm.

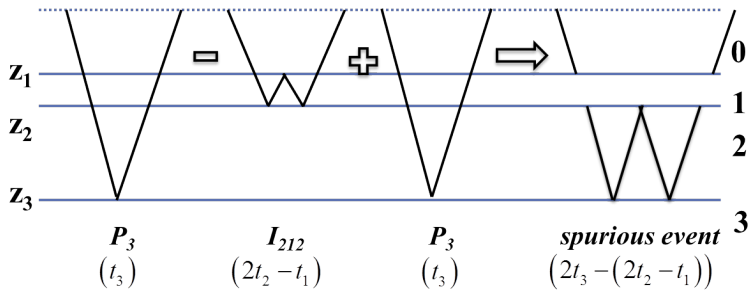

Figure 1: In a three-reflector example, a "Primary-Internal multiple-Primary (PIP) combination predicts a spurious event. The subscripts in P_3 and I_{212} represent the locations of the reflections.

3 A new ISS internal-multiple-attenuation algorithm that predicts the accurate time and approximate amplitude of the first-order internal multiple and addresses spurious events

The spurious-event issue is fully anticipated by the Inverse Scattering Series (ISS), and there are higher-order ISS terms that precisely address that issue. Also, the inclusion of higher-order terms provides a new ISS internal-multiple-attenuation algorithm that does not generate spurious events and retains the strength of the current algorithm.

As an example, in a 2D case, we provide two terms that address the aforementioned two types of spurious events, as follows:

$$\begin{aligned} b_5(k_g,k_s,q_s+q_s)^{PIP} =& \frac{1}{(2\pi)^2}\int_{-\infty}^{\infty}dk_1\int_{-\infty}^{\infty}dk_2 e^{-iq_1(z_g-z_s)}e^{iq_2(z_g-z_s)} \\ &\times\int_{-\infty}^{\infty}dz_1 b_1(k_g,k_1,z_1)e^{i(q_g+q_1)z_1} \\ &\times\int_{-\infty}^{z_1-\epsilon}dz_2 b_3(k_1,k_2,z_2)e^{-i(q_1+q_2)z_2} \\ &\times\int_{z_2+\epsilon}^{\infty}dz_3 b_1(k_2,k_s,z_3)e^{i(q_2+q_s)z_3}, \end{aligned} \tag{3}$$

and

$$\begin{aligned} b_5(k_g,k_s,q_s+q_s)^{PPI} =& \frac{2}{(2\pi)^2}\int_{-\infty}^{\infty}dk_1\int_{-\infty}^{\infty}dk_2 e^{-iq_1(z_g-z_s)}e^{iq_2(z_g-z_s)} \\ &\times\int_{-\infty}^{\infty}dz_1 b_1(k_g,k_1,z_1)e^{i(q_g+q_1)z_1} \\ &\times\int_{-\infty}^{z_1-\epsilon}dz_2 b_1(k_1,k_2,z_2)e^{-i(q_1+q_2)z_2} \\ &\times\int_{z_2+\epsilon}^{\infty}dz_3 b_3(k_2,k_s,z_3)e^{i(q_2+q_s)z_3}. \end{aligned} \tag{4}$$

On the left-hand side of equation 3 and equation 4, the subscript 5 indicates that these two terms are derived from the fifth-order term of the Inverse Scattering Series, and the subscripts PIP and PPI indicate the two higher-order terms that address the PIP and PPI types of spurious events,

respectively. On the right-hand side of equation 4, the number "2" in the numerator of the coefficient is because the PPI type of spurious event could be produced by the attenuator (i.e., equation 1) using an internal multiple subevent in either of the outer integrals (these two cases are equivalent) (Liang et al., 2013).

After all the terms in the series that address the spurious events have been identified, a new ISS internal-multiple-attenuation algorithm is provided by including all those terms. The new algorithm boils down the following,

$$D(x_g, x_s; t) + D_3^{New}(x_g, x_s; t), \tag{5}$$

where $b_3^{New}(k_g, k_s, \omega) = -2iq_s D_3^{New}(k_g, k_s, \omega)$. $b_3^{New}(k_g, k_s, \omega)$ is obtained by

$$\begin{aligned} b_3^{New}(k_g, k_s, q_s + q_s) =& \frac{1}{(2\pi)^2} \int_{-\infty}^{\infty} dk_1 \int_{-\infty}^{\infty} dk_2 e^{-iq_1(z_g - z_s)} e^{iq_2(z_g - z_s)} \\ &\times \int_{-\infty}^{\infty} dz_1 b_1^{New}(k_g, k_1, z_1) e^{i(q_g + q_1)z_1} \\ &\times \int_{-\infty}^{z_1 - \epsilon} dz_2 b_1^{New}(k_1, k_2, z_2) e^{-i(q_1 + q_2)z_2} \\ &\times \int_{z_2 + \epsilon}^{\infty} dz_3 b_1^{New}(k_2, k_s, z_3) e^{i(q_2 + q_s)z_3}, \end{aligned} \tag{6}$$

where $b_1^{New}(k_g, k_s, q_s + q_s)$ is calculated using $[D(k_g, k_s, \omega) + D_3(k_g, k_s, \omega)]$ (see Figure 3). For the purpose of comparison, we provide the current algorithm in Figure 2 and the new algorithm in Figure 3.

The new algorithm addresses the spurious events by reducing the internal multiples and making $[D(k_g, k_s, \omega) + D_3(k_g, k_s, \omega)]$ the new input.

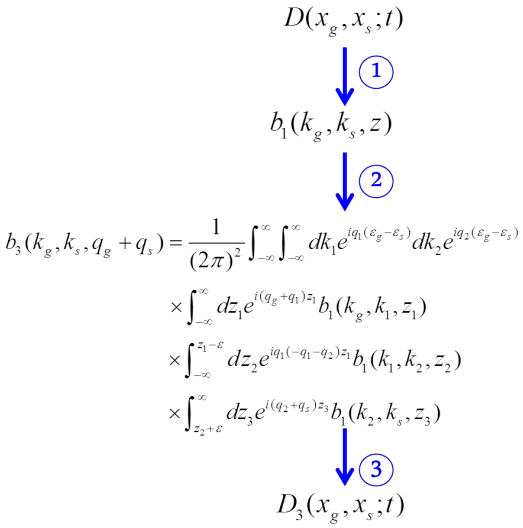

Figure 2: In a 2D case, the workflow of the current ISS internal-multiple-attenuation algorithm. Step 1 is the uncollapsed-Stolt migration, step 2 is the prediction from the attenuator of the first-order internal multiples, and step 3 transforms the prediction back into space-time domain.

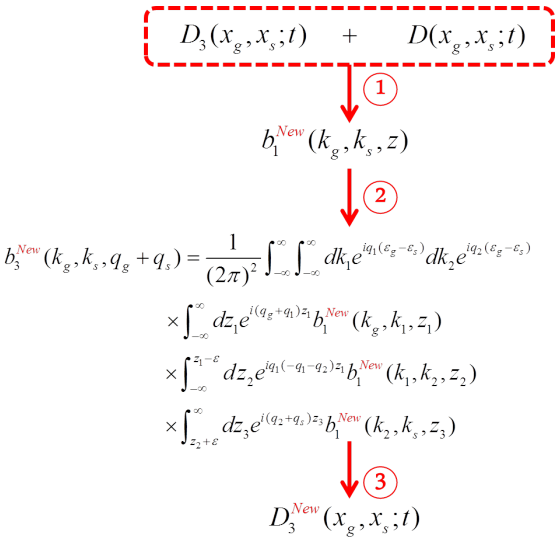

Figure 3: In a 2D case, the workflow of the new ISS internal-multiple-attenuation algorithm, which addresses the issue of spurious events. The steps are the same as in Figure 2, but here a new input is used. $D_3(x_g, x_s; t)$ in the input data are obtained from the current algorithm shown in Figure 2.

4 Numerical tests in 2D

4.1 The current release of the ISS internal-multiple-attenuation code

The current release of the ISS internal-multiple-attenuation code (corresponding to Figure 2 with angle-constraints applied[3]) is in the `The MOSRP_SU` package[4], with an updated `EXAMPLES` directory on *M-OSRP* website *(http://www.mosrp.uh.edu/research/projects/coding)*.

The programs in that package that perform the ISS internal-multiple-attenuation are `su3stoltmig` and `su3issima`[5].

- `su3stoltmig` performs the uncollapsed-Stolt migration using the input data (i.e., step 1 in Figure 2);
- `su3issima` performs the ISS internal-multiple prediction using the output from `su3stoltmig` as input and then transforms the prediction result back to the space-time domain (i.e., step 2 and step 3 in Figure 2).

The updated `EXAMPLES` directory in the current release contains a new demo script that uses `su3stoltmig` and `su3issima` to perform a 2D ISS internal-multiple prediction with a 2D synthetic data set (Terenghi and Weglein, 2011).

[3]See Terenghi and Weglein (2011) for more details on angle constraints.

[4]`MOSRP_SU` package is a software package that is based on and fully consistent with CWP/SU, composed of a variety of programs developed at *M-OSRP*.

[5]The number 3 in `su3stoltmig` and `su3issima` means that these two programs process data generated from a multi dimensional earth. There are two other programs (`su1stoltmig` and `su1issima`) in the package that process data generated from a 1D earth.

4.2 Numerical tests to address the spurious-event issue in 2D

From Figure 2 and Figure 3 we note that, the new algorithm (Figure 3) is similar to the current algorithm (Figure 2) but that it has a different input. Hence, in testing the new algorithm and examining the impact of addressing the spurious-event issue in multi dimensions, we benefit from the current programs by using a different input[6,7].

We will use the same data set provided in the updated `EXAMPLES` directory to verify the correctness of the new algorithm and to study the significance of addressing the spurious-event issue.

The data consist of 251 shots $\times$ 251 receivers, with both shot and receiver-intervals of 25 m; each trace has 500 samples with a total duration of 4s. The internal multiples will be strong because of the large impedance contrast between layers (see Figure 4).

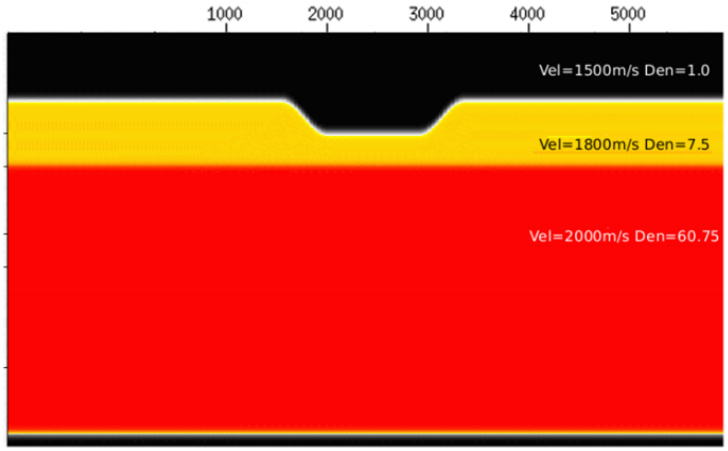

Figure 4: Synthetic velocity and density model used to generate the test data in this section (courtesy of WesternGeco). The average dip of the walls of the trench featured in the center of the model is approximately 20 degree (Figure adapted from Terenghi and Weglein (2011).

Figure 5 and Figure 6 show one shot comparison and one trace comparison, respectively, between the test data and the prediction results **without** (Figures 5a and 6a) and **with** (Figures 5b and 6b) addressing the spurious-event issue. In Figure 5, black arrows and red arrows point to the primaries and internal multiples, respectively. The numbers in the subscript indicate the reflector(s) at which the reflection occur[8]. The blue arrows in Figure 5 indicate the places where the prediction result **better** matches the test data because spurious events have been addressed(see black arrows in Figure 6 for details).

Compared with that in Figure 5a, the prediction of higher-order internal multiples[9] in Figure 5b gets reduced (see red arrows in Figure 6 for details) because of the reduced internal multiple in the

[6]The input of the new algorithm requires both $D_1(x_g, x_s; t)$ (the input of the current algorithm) and $D_3(x_g, x_s; t)$ (the output of the current algorithm), therefore, the current algorithm is first carried out to obtain $D_3(x_g, x_s; t)$.

[7]We will also provide two programs (`su3issima_pip` and `su3issima_ppi`) to address "PIP" and "PPI" type spurious events.

[8]For example, P_1 represents the primary where the reflection happens at the first reflector, and I_{212} represents the first-order internal multiple where the three reflections happen at the second reflector, the first-reflector and the second reflector.

[9]e.g., the second-order internal multiple represented by I_{21212} in Figure 5.

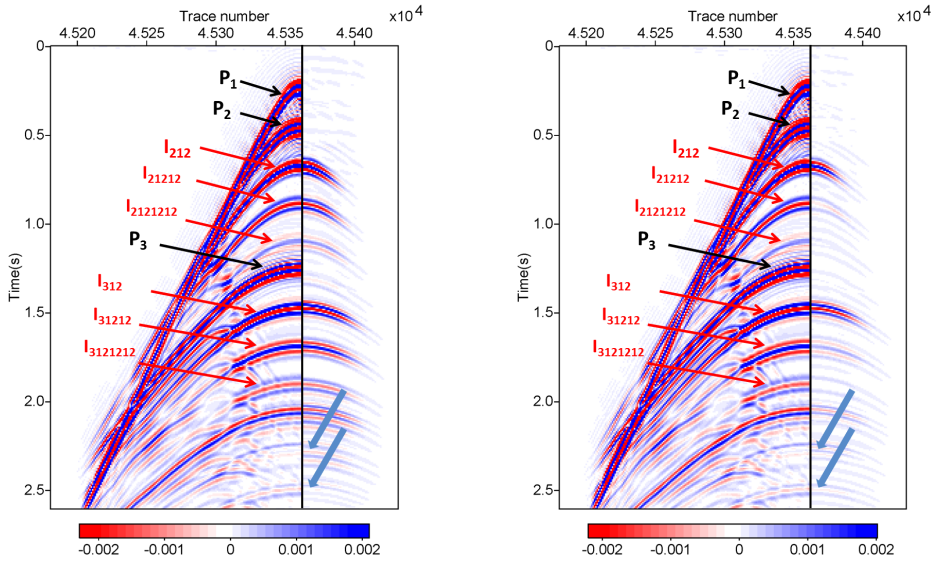

(a) (b)

Figure 5: A shot comparison between the test data (left part) and the ISS internal-multiple prediction (right part) **without** (Figure 5a) and **with** (Figure 5b) addressing the spurious events. Blue arrows point to the places where the predictions results with the addressing the spurious-events issue better match the data.

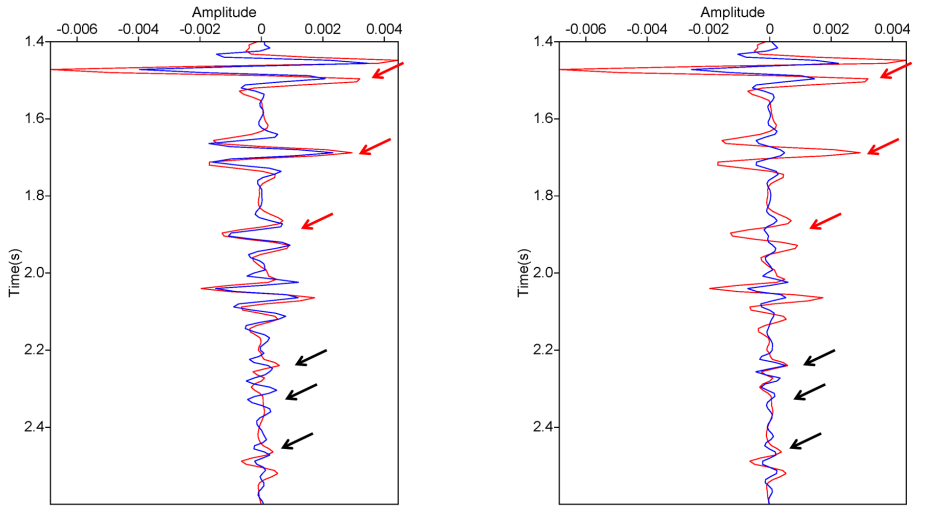

(a) (b)

Figure 6: A trace comparison (from 1.4s to 2.6s) between the test data (red line) and the ISS internal-multiple prediction (blue line) **without** (Figure 6a) and **with** (Figure 6b) addressing the spurious events. Black arrows point to the places where the prediction results with the addressing of the spurious-events issue better match the data.

input data.

It is worth noting that the spurious-event issue in this synthetic test (based on a three-reflector model) is not as significant as the spurious-event issue in many real off-shore and on-shore plays. That is because the spurious-event issue is more significant when there are tens or hundreds of internal-multiple generators, as is the case in the real word (Ma and Weglein, 2014a).

5 Conclusions

We have continued last year's work, and in this report we document our progress on addressing the spurious-event issue of the current ISS internal-multiple-attenuation algorithm. We analyze and test a new ISS internal-multiple-attenuation algorithm, in multi dimensions, that anticipates and removes the spurious events that are generated by the current ISS internal-multiple-attenuation algorithm and at the same time retains the strength of the current algorithm.

The numerical test on a synthetic 2D data set in this report shows the added value of applying the new algorithm to address the presence of spurious events, which can be significant in many real-world applications. This issue will arise when many reflectors generate multiples in complex onshore and offshore plays, and the resulting spurious events can be a serious impediment to interpretation and to effective drilling decisions. The new algorithm in this report addresses that issue.

References

Araujo, F. V., A. B. Weglein, P. M. Carvalho, and R. H. Stolt. "Inverse scattering series for multiple attenuation: An example with surface and internal multiples." *SEG Technical Program Expanded Abstracts* (1994): 1039–1041.

Liang, H., C. Ma, and A. Weglein. "General theory for accommodating primaries and multiples in internal multiple algorithm: Analysis and numerical tests." *SEG Technical Program Expanded Abstracts* (2013): 4178–4183.

Ma, C., H. Liang, and A. Weglein. "Modifying the leading order ISS attenuator of first-order internal multiples to accommodate primaries and internal multiples: fundamental concept and theory, development, and examples exemplified when three reflectors generate the data." *Mission-Oriented Seismic Research Program (M-OSRP) 2011 Annual Report* (2011): 133–147.

Ma, Chao and A. Weglein. "Including higher-order Inverse Scattering Series terms to address a serious shortcoming/problem of the internal-multiple attenuator: Exemplifying the problem and its resolution." *SEG Technical Program Expanded Abstracts* (2014): 4124–4129.

Ma, Chao and A. B. Weglein. "Inverse S ca tterin g Series (ISS) leading-order internal-multiple-attenuation algorithm and higher-order mo dification to accommo date primaries and internal multiples as input: 1-D n ormal incid ent test on interfering events, and extension to multi-D." *Mission-Oriented Seismic Research Program (M-OSRP) Annual Report* (2014): 94–103.

Nita, Bogdan G. and Arthur B. Weglein. "Inverse scattering internal multiple attenuation algorithm: An analysis of the pseudo-depth and time-monotonicity requirements." *SEG Technical Program Expanded Abstracts* (2007): 2461–2465.

Stolt, R. H. and A. B. Weglein. "Migration and inversion of seismic data." *Geophysics* 50 (1985): 2458–2472.

Terenghi, P. and A. B. Weglein. "ISS internal multiple attenuation with angle constraints." *Mission-Oriented Seismic Research Program (M-OSRP) Annual Report* (2011): 242–266.

Weglein, A., Shih-Ying Hsu, Paolo Terenghi, Xu Li, and Robert H. Stolt. "Multiple attenuation: Recent advances and the road ahead (2011)." *The Leading Edge* (2011): 864–875.

Weglein, A. B., F. V. Araújo, P. M. Carvalho, R. H. Stolt, K. H. Matson, R. T. Coates, D. Corrigan, D. J. Foster, S. A. Shaw, and H. Zhang. "Inverse Scattering Series and Seismic Exploration." *Inverse Problems* (2003): R27–R83.

Weglein, A. B., F. A. Gasparotto, P. M. Carvalho, and R. H. Stolt. "An Inverse-Scattering Series Method for Attenuating Multiples in Seismic Reflection Data." *Geophysics* 62 (November-December 1997): 1975–1989.

A new Inverse Scattering Series (ISS) internal-multiple-attenuation algorithm that predicts the accurate time and approximate amplitude of the first-order internal multiples and addresses spurious events: Analysis and Tests in 2D

*Chao Ma * and Arthur B. Weglein, M-OSRP/Physics Dept./University of Houston*

SUMMARY

The ISS internal-multiple-attenuation algorithm assumes that the free-surface multiples have been removed from the input of this algorithm, and the input consists of only primaries and internal multiples. The algorithm selects three events by a "longer-shorter-longer" relationship in the *vertical-travel-time* domain and the *primaries* selected in that procedure predict the accurate time and approximate amplitude of all first-order internal multiples without any subsurface information (Weglein et al., 2003). However, the input data contain both *primaries* and *internal multiples*. When internal multiples themselves are selected in that procedure, two different types of events will be produced. The first type is higher-order internal multiples (e.g., second-order internal multiples (Zhang and Shaw, 2010)), and these predicted higher-order internal multiples will *cooperatively assist and benefit* the attenuating of higher-order internal multiples in the data. The second type is spurious events (events that do not exist in the data). For the second type of events, Weglein et al. (2011), Liang et al. (2013) and Ma and Weglein (2014) show that the spurious events are *fully anticipated* by the ISS, and specific higher-order terms from ISS will precisely address that spurious-event issue. The inclusion of higher-order terms provides a new ISS internal-multiple-attenuation algorithm that does not generate the spurious events and, at the same time, retains the strength of the original algorithm. That original contribution (i.e., the aforementioned new algorithm) was for a one dimensional subsurface. In this paper, we extend the previous work on addressing the spurious events to a multi-D case and show more realistic synthetic test results in 2D. Those tests exemplify the relevant and practical benefit provided by this new internal-multiple algorithm.

INTRODUCTION

The inverse scattering series (ISS) communicates that it is possible to achieve all seismic data processing objectives directly and without subsurface information. The current ISS internal-multiple-attenuation algorithm was first developed by Araujo et al. (1994) and Weglein et al. (1997). The unique strength (always present independent of the circumstances and complexity of the geology and the play) of the ISS internal-multiple-attenuation algorithm is that this algorithm is able to predict internal multiples without any subsurface information. Hence, the ISS internal-multiple-attenuation algorithm is often called upon in the cases in which the multiple-removal is a challenging problem and it is difficult to find the subsurface information for other multiple-suppression methods to be effective. The tests on ISS internal-multiple-attenuation algorithm have shown promising results and unique value compared with other multiple-suppression methods (e.g., K.Maston et al. (1999); Fu et al. (2010); Hsu et al. (2010); Ferreira (2011); Terenghi et al. (2011); Luo et al. (2011); Weglein et al. (2011); Kelamis et al. (2013)).

Early analysis of the current ISS internal-multiple-attenuation algorithm focused on selecting primaries in the input to predict internal multiples. However, the input data contain both primaries and internal multiples and all events in the data will be selected. Internal multiples selected in this algorithm can generate spurious events under the circumstances where three or more reflectors are involved in the data being processed as shown by Weglein et al. (2011), Liang et al. (2013) and Ma and Weglein (2014).

The work of Ma and Weglein (2014) also demonstrates that spurious-event issue is serious and significant when there are tens, hundreds (or even thousands) of internal-multiple generators (e.g., Middle East and North Sea), and addressing the spurious events under those circumstances is essential by applying a new ISS algorithm that addresses the spurious-event prediction and retains the strength of the original algorithm simultaneously. In this paper, we extend the analysis of addressing the spurious events to a multi-D case, and also provide a more realistic numerical test in 2D.

THE CURRENT ISS INTERNAL-MULTIPLE-ATTENUATION ALGORITHM

The current ISS internal-multiple-attenuation algorithm starts with the input data, $D(k_g,k_s,\omega)$, in 2D case, which are the Fourier transform of the deghosted prestack data, and with the wavelet deconvolved and direct wave and free-surface multiples removed. The second term, $D_3(k_g,k_s,\omega)$, is the attenuator of the first-order internal multiples. In a 2D earth, $D_3(k_g,k_s,\omega)$ is obtained from $b_3(k_g,k_s,\omega) = -2iq_sD_3(k_g,k_s,\omega)$, where $b_3(k_g,k_s,\omega)$ is (Weglein et al., 2003)

$$\begin{aligned} b_3(k_g,k_s,q_s+q_s) = &\frac{1}{(2\pi)^2}\int_{-\infty}^{\infty}dk_1\int_{-\infty}^{\infty}dk_2 e^{-iq_1(z_g-z_s)}e^{iq_2(z_g-z_s)} \\ &\times\int_{-\infty}^{\infty}dz_1 b_1(k_g,k_1,z_1)e^{i(q_g+q_1)z_1} \\ &\times\int_{-\infty}^{z_1-\varepsilon}dz_2 b_1(k_1,k_2,z_2)e^{-i(q_1+q_2)z_2} \\ &\times\int_{z_2+\varepsilon}^{\infty}dz_3 b_1(k_2,k_s,z_3)e^{i(q_2+q_s)z_3}, \end{aligned} \tag{1}$$

where k_s and k_g are the horizontal wavenumbers for the source and receiver coordinates, respectively; q_g and q_s are the vertical source and receiver wavenumbers defined by $q_i = sgn(\omega)\sqrt{\frac{\omega^2}{c_0^2}-k_i^2}$ for $i\in\{g,s\}$ (ω is the temporal freqency);

z_s and z_g are source and receiver depths; and z_j ($i \in \{1,2,3\}$) represents pseudo-depth by using a reference velocity migration. The quantity $b_1(k_g,k_s,z)$ corresponds to an uncollapsed migration (Weglein et al., 1997) of effective plane-wave incident data.

The data with their first-order internal multiple attenuated are

$$D(k_g,k_s,\omega)+D_3(k_g,k_s,\omega). \tag{2}$$

For a 1-D earth and a normal incident plane wave, equation 1 reduces to

$$b_3(k)=\int_{-\infty}^{\infty}dz_1e^{ikz_1}b_1(z_1)\int_{-\infty}^{z_1-\varepsilon}dz_2e^{-ikz_2}b_1(z_2) \times\int_{z_2+\varepsilon}^{\infty}dz_3e^{ikz_3}b_1(z_3). \tag{3}$$

The deghosted data, $D(t)$, for an incident plane wave, satisfy $D(\omega)=b_1(\frac{2\omega}{c_0})$, $D(\omega)$ is the temporal Fourier transform of $D(t)$, $b_1(z)=\int_{-\infty}^{\infty}e^{ikz}b_1(k)dk$, and $k=\frac{2\omega}{c_0}$ is the vertical wavenumber.

Equation 2 then reduces to

$$D(t)+D_3(t), \tag{4}$$

where $D_3(t)$ is Inverse Fourier transform of $D_3(\omega)$, and $D_3(\omega)=b_3(\frac{2\omega}{c_0})$, where $k=\frac{2\omega}{c_0}$.

Figure 1 illustrates the idea behind using equation 1 or equation 3 to predict the first-order internal multiple by selecting primaries (events that experience only one upward reflection) in the data as subevents, and combining different subevents that satisfy the "longer(A)-shorter(B)-longer(C)"relationship in vertical-travel-time domain (or equivalently, "lower(A)-higher(B)-lower(C)" relationship in pseudo-depth domain (Nita and Weglein, 2007)).

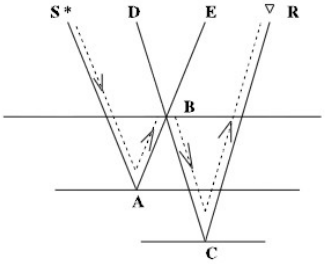

Figure 1: An internal multiple (dashed line) constructed by the lower-higher-lower pattern of three primary subevents (solid line). Figure adapted from Weglein et al. (2003)

THE ORIGIN OF SPURIOUS EVENTS AND ITS RESOLUTION IN 1D

The work of Araujo et al. (1994) and Weglein et al. (1997) focuses on the analysis of the prediction of first-order internal multiples (i.e., equation 1) by using primaries in the data as subevents (see Figure 1). However, data consist of both primaries and internal multiples. Zhang and Shaw (2010) show that higher-order internal multiples will be predicted by b_3 when internal multiples themselves are selected as a subevents in a two-interface case. For example, in Figure 2a, a second-order internal multiples will be predicted when a first-order internal multiple is selected as a subevent.

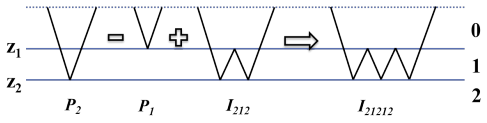

Figure 2a: In a two-reflector example, a "Primary – Primary – Internal multiple" combination predicts a second-order internal multiple.

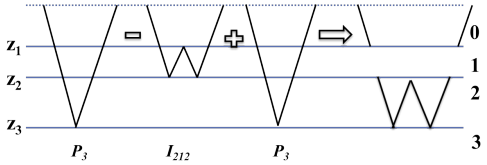

Figure 2b: In a three-reflector example, a "Primary – Internal multiple – Primary" combination predicts a spurious event.

In addition, the situation is considerably more complicated when the data from three or more reflectors are considered. For instance, spurious events can also be generated when an internal multiple is selected as a subevent in a three-reflector example, as shown in Figure 2b. However, these spurious events are also entirely anticipated by the inverse scattering series and there are terms in the series that can exactly address those false event prediction.

After identifying all the terms in the series that address the spurious events, a new ISS internal-multiple-attenuation algorithm is provided by including those terms. The new algorithm boils down as follows,

$$D(t)+D_3^{New}(t), \tag{5}$$

where $D_3^{New}(t)$ is the Inverse Fourier transform of $D_3^{New}(\omega)$, $D_3^{New}(\omega)=b_3^{New}(k=\frac{2\omega}{c_0})$, and $b_3^{New}(k)$ is obtained from

$$b_3^{New}(k)=\int_{-\infty}^{\infty}dz_1e^{ikz_1}(b_1(z_1)+b_3(z_1)) \times\int_{-\infty}^{z_1-\varepsilon}dz_2e^{-ikz_2}(b_1(z_2)+b_3(z_2)) \times\int_{z_2+\varepsilon}^{\infty}dz_3e^{ikz_3}(b_1(z_3)+b_3(z_3)). \tag{6}$$

The new algorithm will address the spurious events by reducing the internal multiples using $(b_1(z)+b_3(z))$ as the new input.

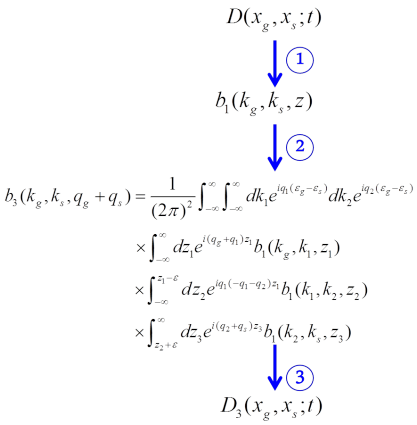

Figure 3a: In a 2D case, the workflow of the current ISS internal-multiple-attenuation algorithm. Step 1 is the uncollapsed Stolt migration, step 2 is the prediction from the attenuator of the first-order internal multiples, step 3 transforms the prediction back to space-time domain.

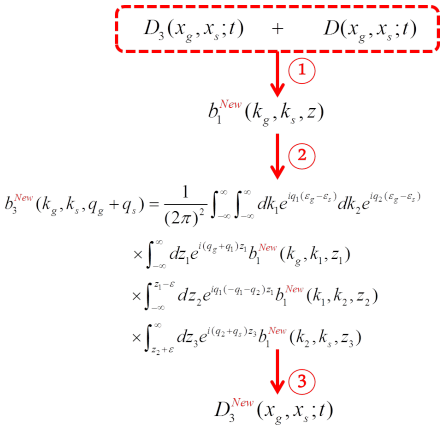

Figure 3b: In a 2D case, the workflow of the new ISS internal-multiple-attenuation algorithm with the addressing of the spurious events. The steps are same as in Figure 3a, but using a new input. $D_3(x_g, x_s; t)$ is the output from the current algorithm in Figure 3a.

A NEW ISS INTERNAL-MULTIPLE-ATTENUATION ALGORITHM THAT PREDICTS THE ACCURATE TIME AND APPROXIMATE AMPLITUDE OF THE FIRST-ORDER INTERNAL MULTIPLE AND ADDRESSES SPURIOUS EVENTS

By understanding the generation of the spurious events and its resolution in 1D case, we provide a new multi-D ISS internal-multiple-attenuation algorithm (Figure 3b) that addresses the spurious events and preserves the strength of the current algorithm. For the purpose of comparison, we show the current ISS internal multiple attenuation algorithm in Figure 3a.

We test the new algorithm using a synthetic 2D data set. Figure 4 shows a three-reflector model used to generate the 2D synthetic data set by finite-difference method. The data consist of 251 shots $\times$ 251 receivers, with both shot- and receiver-interval 25 m, each trace has 500 samples with a total duration 4s. The internal multiples will be strong because of the big impedance contrast between layers. Figure 5 and 6 show one shot and trace comparison between the test data and the prediction results **with** (Figure 5b and 6b) and **without** (Figure 5a and 6a) addressing the spurious-event prediction. In Figure 5, black and red arrows point to the primaries and internal multiples, respectively. The numbers in the subscript indicate the reflectors where the reflection happens. The blue arrows in Figure 5 indicate the places where the prediction result **with** the addressing of spurious events better matches the test data than that **without** addressing the spurious events (see black arrows in Figure 6 for details). Compared with Figure 5a (or 6a), the prediction of higher-order internal multiples (e.g., I_{21212}) in Figure 5b (or 6b) gets reduced (see red arrows in Figure 6 for details) because of the reduced internal multiple in the input data.

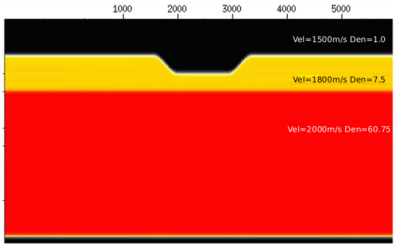

Figure 4: Synthetic velocity and density model used to generate the test data in this section (courtesy of WesternGeco). The average dip of the walls of the trench featuring in the center of the model is approximately 20 degree (Figure adapted from Terenghi and Weglein (2011)).

CONCLUSIONS

In this paper, we analyze, develop and test a new multi-D ISS internal-multiple-attenuation algorithm that anticipates and removes the spurious events that are generated by the current ISS internal-multiple-attenuation algorithm. The numerical test on a synthetic 2D data set in this paper shows the added value of applying the new algorithm to address the spurious events that can be significant many real-world applications. This issue will arise when many reflectors generate the multiples in complex on-shore and off-shore plays, and can be serious impediment to interpretation and making effective drilling decisions. The new algorithm in this paper addresses that issue.

ACKNOWLEDGMENTS

We are grateful to all M-OSRP sponsors for their encouragement and support of this research. WesternGeco is gratefully acknowledged for permission to use their synthetic data.

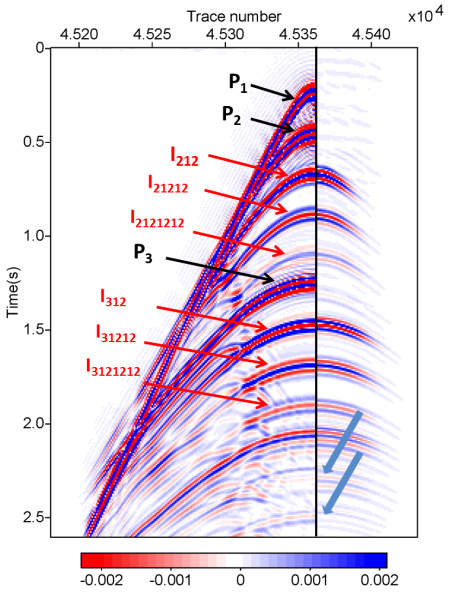

Figure 5a: A shot comparison between the test data (left part) and the ISS internal multiple prediction (right part) **without** addressing the spurious events.

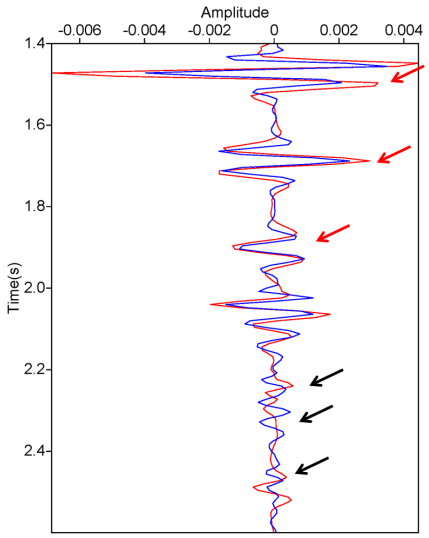

Figure 6a: A trace comparison (from 1.4s to 2.6s) between the test data (red line) and the ISS internal multiple prediction (blue line) **without** addressing the spurious events.

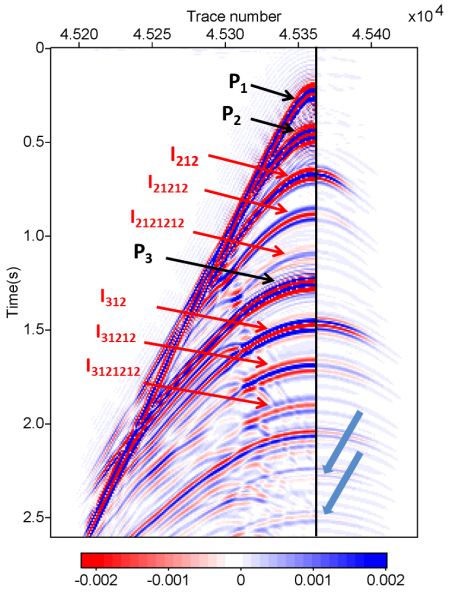

Figure 5b: A shot comparison between the test data (left part) and the ISS internal multiple prediction (right part) **with** addressing the spurious events.

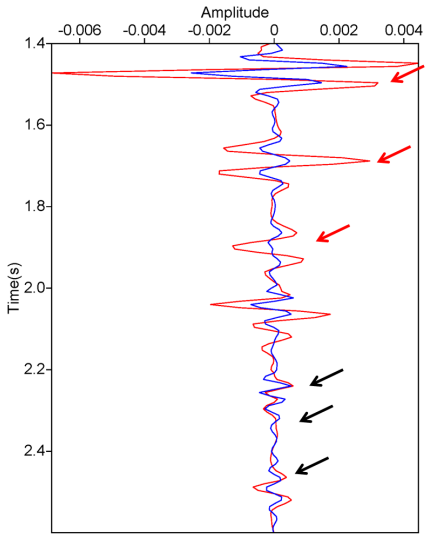

Figure 6b: A trace comparison (from 1.4s to 2.6s) between the test data (red line) and the ISS internal multiple prediction (blue line) **with** addressing the spurious events.

REFERENCES

Araujo, F. V., A. B. Weglein, P. M. Carvalho, and R. H. Stolt, 1994, Inverse scattering series for multiple attenuation: An example with surface and internal multiples: SEG Technical Program Expanded Abstracts, 1039–1041.

Ferreira, A., 2011, Internal multiple removal in offshore brrazil seismic data using the inverse scattering series: PhD thesis, University of Houston.

Fu, Q., Y. Luo, P. G. Kelamis, S. Huo, G. Sindi, S.-Y. Hsu, and A. Weglein, 2010, The inverse scattering series approach towards the elimination of land internal multiples: SEG Technical Program Expanded Abstracts, **29**, 3456–3461.

Hsu, S., P. Terenghi, and A. B. Weglein, 2010, The properties of the inverse scattering series internal multiple attenuation algorithm: Analysis and evaluation on synthetic data with lateral variations, choosing reference velocity and examining its sensitivity to near surface properties: Mission-Oriented Seismic Research Program (M-OSRP) Annual Report, 1628.

Kelamis, P. G., Y. Luo, and A. Weglein, 2013, Strategies of land internal multiple elimination based on inverse scattering series: Presented at the 6th International Petroleum Technology Conference.

K.Maston, D.Corrigan, A.Weglein, C.Y.Yong, and P.Carvalho, 1999, Inverse scattering internal multiple attenuation: Results from complex synthetic and field data examples: SEG Expaned Abstract.

Liang, H., C. Ma, and A. Weglein, 2013, General theory for accommodating primaries and multiples in internal multiple algorithm: Analysis and numerical tests: SEG Technical Program Expanded Abstracts, 4178–4183.

Luo, Y., P. G.Kelamis, Q. Fu, S. Huo, G. Sindi, S.-Y. Hsu, and A. Weglein, 2011, Elimination of land internal multiples based on the inverse scattering series: The Leading Edge, **30**, 884–889.

Ma, C., and A. Weglein, 2014, Including higher-order inverse scattering series terms to address a serious shortcoming/problem of the internal-multiple attenuator: Exemplifying the problem and its resolution: SEG Technical Program Expanded Abstracts, 4124–4129.

Nita, B. G., and A. B. Weglein, 2007, Inverse scattering internal multiple attenuation algorithm: An analysis of the pseudo-depth and time-monotonicity requirements: SEG Technical Program Expanded Abstracts, 2461–2465.

Terenghi, P., S.-Y. Hsu, A. B.Weglein, and X. Li, 2011, Exemplifying the specific properties of the inverse scattering series internal-multiple attenuation method that reside behind its capability for complex onshore and marine multiples: The Leading Edge.

Terenghi, P., and A. B. Weglein, 2011, Iss internal multiple attenuation with angle constraints: Mission-Oriented Seismic Research Program (M-OSRP) Annual Report, 242–266.

Weglein, A., S.-Y. Hsu, P. Terenghi, X. Li, and R. H. Stolt, 2011, Multiple attenuation: Recent advances and the road ahead (2011): The Leading Edge, 864–875.

Weglein, A. B., F. V. Araújo, P. M. Carvalho, R. H. Stolt, K. H. Matson, R. T. Coates, D. Corrigan, D. J. Foster, S. A. Shaw, and H. Zhang, 2003, Inverse scattering series and seismic exploration: Inverse Problems, R27–R83.

Weglein, A. B., F. A. Gasparotto, P. M. Carvalho, and R. H. Stolt, 1997, An inverse-scattering series method for attenuating multiples in seismic reflection data: Geophysics, **62**, 1975–1989.

Zhang, H., and S. Shaw, 2010, 1-d analytical analysis of higher order internal multiples predicted via the inverse scattering series based algorithm: SEG Expanded Abstracts, **29**, 3493–3498.

An internal-multiple elimination algorithm for all first-order internal multiples for a 1D earth

Yanglei Zou, Arthur B. Weglein

Abstract

The ISS (Inverse-Scattering-Series) internal-multiple attenuation algorithm (Araújo et al. (1994),Weglein et al. (1997) and Weglein et al. (2003)) can predict the correct time and approximate amplitude for all first-order internal multiples without any subsurface information. When combined with an energy minimization adaptive subtraction, the ISS internal multiple attenuation algorithm can effectively remove internal multiples when the primaries and internal multiples are separated, and not overlapping or proximal. One of the issues that the adaptive subtraction is addressing is the difference between the amplitude of the internal multiple and the approximate amplitude predicted by the attenuation algorithm. However, under certain circumstances, both offshore and onshore, internal multiples are often proximal to or interfering with primaries and the criteria of energy minimization adaptive subtraction may fail, since the energy can increase when e.g., a multiple is removed from an interfering primary. Therefore, in these situations, the task of removing internal multiples without damaging primaries becomes more challenging and subtle and currently beyond the collective capability of the petroleum industry. Weglein (2014) proposed a three-pronged strategy for providing an effective response to this pressing and prioritized challenge. One part of the strategy is to develop an internal-multiple elimination algorithm that can predict both the correct amplitude and correct time for all internal multiples. In this paper, we provide an ISS internal-multiple elimination algorithm for all first-order internal multiples generated from all reflectors in a 1D earth and provide an example from an elastic synthetic data that shows the value provided by the new algorithm in comparison with the value provided by the internal multiple attenuation algorithm.

1 Introduction

The ISS (Inverse-Scattering-Series) allows all seismic processing objectives, such as free-surface-multiple removal and internal-multiple removal to be achieved directly in terms of data, without any estimation of the earth's properties. For internal-multiple removal, the ISS internal-multiple attenuation algorithm can predict the correct time and approximate and well-understood amplitude for all first-order internal multiples generated from all reflectors, at once, without any subsurface information. If the internal multiples in the data are isolated, the energy minimization adaptive subtraction can fix the gap between the attenuation algorithm prediction and the internal multiples plus, e.g., all factors that are outside the assumed physics of the subsurface and acquisition. However, in certain situations, events often interfere with each other in both on-shore and off-shore seismic data. In these cases, the criteria of energy minimization adaptive subtraction may fail and completely removing internal multiples becomes more challenging and beyond the current capability of the petroleum industry.

For dealing with this challenging problem, Weglein (2014) proposed a three-pronged strategy including

1. Develop the ISS prerequisites for predicting the reference wave field and to produce deghosted data for both on shore and off shore.

2. Develop internal-multiple elimination algorithms from ISS.

3. Develop a replacement for the energy-minimization criteria for adaptive subtraction.

To achieve the second part of the strategy, that is, to upgrade the ISS internal-multiple attenuation algorithm to elimination algorithm, the strengths and limitations of the ISS internal-multiple attenuation algorithm are noted and reviewed. The ISS internal-multiple attenuation algorithm always attenuates all first-order internal multiples from all reflectors at once, automatically and without any subsurface information. That is a tremendous strength, and is a constant and holds independent of the circumstances and complexity of the geology and the play. However, there are two well-understood limitations of this ISS internal-multiple attenuation algorithm

1. It may generate spurious events due to internal multiples treated as subevents.

2. It is an attenuation algorithm not an elimination algorithm.

The first item is a shortcoming of the leading order term (the attenuation algorithm), when taken in isolation, but is not an issue for the entire ISS internal-multiple removal capability. It is anticipated by the ISS and higher order ISS internal multiple terms exist to precisely remove that issue of spurious events prediction. When taken together with the higher order terms, the ISS internal multiple removal algorithm no longer experiences spurious events prediction. Ma et al. (2012) , H. Liang and Weglein (2012) and Ma and Weglein (2014) provided those higher order terms for spurious events removal.

In a similar way, there are higher order ISS internal multiple terms that provide the elimination of internal multiples when taken together with the leading order attenuation term. There are early discussions in Ramírez (2007) and Wilberth Herrera and Weglein (2012) find higher order terms in ISS that can eliminate all first-order internal multiples generated at the shallowest reflector for 1D normal incidence spike plane wave. The next step, elimination of all first-order internal-multiples generated from all reflectors, is a very challenging problem even in a 1D earth. In a model with several reflectors, there is a set of internal multiples generated by each reflector in the data, and for different sets of internal multiples, the amplitude difference between attenuation algorithm prediction and the amplitude of real internal multiples is different. This elimination algorithm must have the capability to remove all the amplitude differences between attenuation algorithm prediction and the real internal multiples for all generators. While the activity of finding higher order terms in ISS that can completely eliminate all internal multiples is undertaken, we derived an elimination algorithm from an alternative approach, i.e. using reverse engineering method as a guide and a tool to understand the internal multiple elimination machinery in the ISS. This elimination algorithm can predict both correct time and amplitude of all first-order internal-multiples generated from all reflectors in a 1D earth. And it is closely related to ISS and preserves the following advantages of ISS attenuation

1. It only needs data, does not require any subsurface information.

2. It provides the capability to remove all internal multiples without choosing or picking generators.

And this elimination algorithm derived by using reverse engineering method is model type dependent. (The ISS internal-multiple attenuation algorithm is model type independent.)

2 The ISS internal-multiple attenuation algorithm and the attenuation factor for 1D normal incidence

First, we will give a review of the ISS internal-multiple attenuation algorithm before introducing the elimination algorithm. The ISS internal-multiple attenuation algorithm was first given by Araújo (1994) and Weglein et al. (1997). The 1D normal-incidence version of the algorithm is presented as follows:

$$b_3^{IM}(k) = \int_{-\infty}^{\infty} dz e^{ikz} b_1(z) \int_{-\infty}^{z-\varepsilon_2} dz' e^{-ikz'} b_1(z') \int_{z'+\varepsilon_1}^{\infty} dz'' e^{ikz''} b_1(z''), \tag{1}$$

Where $b_1(z)$, which is closely related to the data, is the water-speed migration of the data due to a 1D normal-incidence spike plane wave. In the following example, we will show how to obtain $b_1(z)$ from data and predict internal multiples. The terms ε_1 and ε_2 are two small positive numbers introduced to avoid self interaction. This equation can predict the correct time and an approximate amplitude of all first-order internal multiples.

To demonstrate explicitly the mechanism of the ISS internal-multiple attenuation algorithm and to examine its properties, Weglein et al. (2003) considered the simplest two-layer model that can produce an internal multiple. For this model, the reflection data caused by an impulsive incident wave $\delta(t - \frac{z}{c})$ is:

$$D(t) = R_1\delta(t - t_1) + T_{01}R_2T_{10}\delta(t - t_2) + \cdots,$$

where t_1, t_2 and R_1, R_2 are the two-way travel times and the reflection coefficients from the two reflectors,respectively; and T_{01} and T_{10} are the coefficients of transmission between model layers 0 and 1 and 1 and 0, respectively. Then

$$D(\omega) = R_1e^{i\omega t_1} + T_{01}R_2T_{10}e^{i\omega t_2} + \cdots,$$

where$D(\omega)$ is the temporal Fourier transform of $D(t)$.
Given a 1D medium and a normal incident wave, $k_z = \frac{2\omega}{c_0}$ and $b_1(k_z) = D(\omega)$, and the following is obtained:

$$b_1(k_z) = R_1e^{i\frac{2\omega}{c_0}\frac{c_0t_1}{2}} + T_{01}R_2T_{10}e^{i\frac{2\omega}{c_0}\frac{c_0t_2}{2}} + \cdots.$$

The pseudo-depths z_1 and z_2 in the reference medium are defined as follows:

$$z_1 = \frac{c_0t_1}{2} \quad z_2 = \frac{c_0t_2}{2}.$$

The input data can now be expressed in terms of $k = k_z$, z_1, and z_2:

$$b_1(k) = R_1e^{ikz_1} + T_{01}R_2T_{10}e^{ikz_2} + \cdots.$$

The date are now ready for the internal-multiple attenuation algorithm.
Substituting $b_1(k)$ into the algorithm, we derive the prediction:

$$b_3^{IM}(k) = R_1R_2^2T_{01}^2T_{10}^2e^{2ikz_2}e^{-ikz_1},$$

which in the time domain is:

$$b_3^{IM}(t) = R_1R_2^2T_{01}^2T_{10}^2\delta(t - (2t_2 - t_1)).$$

From the example it is easy to compute the actual first-order internal multiple precisely:

$$-R_1 R_2^2 T_{01} T_{10} \delta(t - (2t_2 - t_1)).$$

Therefore, the time prediction is precise, and the amplitude of the prediction has an extra power of $T_{01}T_{10}$, which is called the attenuation factor, thus defining exactly the difference between attenuation (represented by b_3^{IM}) and elimination.

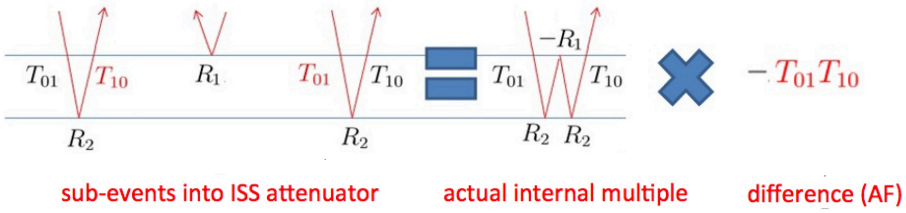

Figure 1: An example of the attenuation factor of a first-order internal multiple generated at the shallowest reflector. Notice that all red terms are extra transmission coefficients

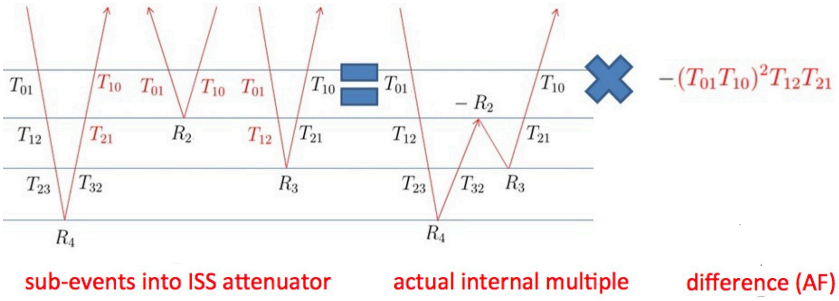

Figure 2: An example of the attenuation factor of a first-order internal multiple generated at the next shallowest reflector. Notice that all red terms are extra transmission coefficients

The procedure for predicting a first-order internal multiple generated at the shallowest reflector is shown in Figure 1. The ISS internal-multiple attenuation algorithm uses three primaries in the data to predict a first-order internal multiple. From the figure we can see that, every sub-event on the left-hand side experiences several phenomena as it makes its way down to the earth then back to the receiver. When compared with the internal multiple on the right-hand side, the events on the left-hand side have extra transmission coefficients, which are shown in red. Multiplying all of those extra transmission coefficients, we get the attenuation factor $T_{01}T_{10}$ for this first-order internal multiple generated at the shallowest reflector. And all first-order internal multiples generated at the shallowest reflector have the same attenuation factor.

Figure 2 shows the procedure for predicting a first-order internal multiple generated at the next shallowest reflector. In this example, the attenuation factor is $(T_{01}T_{10})^2(T_{12}T_{21})$.

To derive a general formula for the amplitude prediction of the algorithm, Ramírez (2007) analyzed a model with n layers and respective velocities C_n, n being an integer. By using the definitions $R_1 = R_1'$, $R_N' = R_N \prod_{i=1}^{N-1} (T_{i-1,i}T_{i,i-1})$, and Einstein's summation, and we apply them to the reflection data from a normal-incident spike wave, we can obtain the following:

$$D(t) = R_n' \delta(t - t_n) + internal\ multiples. \tag{2}$$

The generalized prediction of the attenuation algorithm is obtained by

$$b_3^{IM}(k) = R_i' R_j' R_k' e^{ikz_i} e^{ikz_j} e^{ikz_k}, \tag{3}$$

which in the time domain becomes

$$b_3^{IM}(t) = R_i' R_j' R_k' \delta(t - (t_i + t_k - t_j)) \tag{4}$$

By evaluating equation (3) for different values of i, j, and k, the amplitude prediction of first-order internal multiples is obtained and can be generalized for any number of layers in a 1D model. The generalization of the internal-multiple's amplitude states that the overabundance of transmission coefficients depends on the position of the generating reflector (i.e., where the downward reflection took place). Compared with the real amplitude of internal multiples in the data, we can obtain the attenuation factor.

The attenuation factor, AF_j, in the prediction of internal multiples, is given by the following:

$$AF_j = \begin{cases} T_{0,1}T_{1,0} & (for\ j = 1) \\ \prod_{i=1}^{j-1}(T_{i-1,i}^2 T_{i,i-1}^2) T_{j,j-1} T_{j-1,j} & (for\ 1 < j < J) \end{cases} \tag{5}$$

The attenuation factor AF_j can also be rewritten by using reflection coefficients:

$$AF_j = \begin{cases} 1 - R_1^2 & (for\ j = 1) \\ (1 - R_1^2)^2 (1 - R_2^2)^2 \cdots (1 - R_{j-1}^2)^2 (1 - R_j^2) & (for\ 1 < j < J) \end{cases} \tag{6}$$

The subscript j represents the generating reflector, and J is the total number of interfaces in the model. The interfaces are numbered starting with the shallowest location. The attenuation algorithm b_3^{IM} predicts a first-order internal multiple by using three events within the data. The attenuation factor is directly related to the trajectory of the events, and that trajectory forms the prediction of the internal multiple.

3 The ISS internal-multiple elimination algorithm for 1D normal incidence

The discussion above demonstrates that all first-order internal multiples generated at the same reflector have the same attenuation factor. Also, we derived a generalized formula for the attenuation factor for all reflectors. We can see that the attenuation factor contains all transmission coefficients, from the shallowest reflector down to the reflector generating the multiple. From the examples (shown in Figure 1 and 2), we can also see that the middle event contains all those transmission coefficients. Therefore, our idea is to modify the middle term in the attenuation algorithm to remove the attenuation factor and make the attenuation algorithm an eliminator. That is, we go from

$$b_3^{IM}(k) = \int_{-\infty}^{\infty} dz e^{ikz} b_1(z) \int_{-\infty}^{z-\varepsilon_2} dz' e^{-ikz'} b_1(z') \int_{z'+\varepsilon_1}^{\infty} dz'' e^{ikz''} b_1(z'') \tag{7}$$

to

$$b_E^{IM}(k) = \int_{-\infty}^{\infty} dz e^{ikz} b_1(z) \int_{-\infty}^{z-\varepsilon_2} dz' e^{-ikz'} F[b_1(z')] \int_{z'+\varepsilon_1}^{\infty} dz'' e^{ikz''} b_1(z'') \tag{8}$$

For 1D normal incidence, $b_1(z)$ is expressed as:

$$b_1(z) = R_1\delta(z-z_1) + R_2'\delta(z-z_2) + R_3'\delta(z-z_3) + \cdots + R_n'\delta(z-z_n) + \cdots . \tag{9}$$

To remove all attenuation factors in the prediction, the term $F[b_1(z)]$ should be written as:

$$\begin{aligned} F[b_1(z')] =& \frac{R_1}{AF_{j=1}}\delta(z'-z_1) + \frac{R_2'}{AF_{j=2}}\delta(z'-z_2) + \cdots + \frac{R_n'}{AF_{j=n}}\delta(z'-z_n) + \cdots \\ =& \frac{R_1}{1-R_1^2}\delta(z'-z_1) + \frac{R_2'}{(1-R_1^2)^2(1-R_2^2)}\delta(z'-z_2) + \cdots \\ &+ \frac{R_n'}{(1-R_1^2)^2(1-R_2^2)^2\cdots(1-R_{n-1}^2)^2(1-R_n^2)}\delta(z'-z_n) + \cdots . \end{aligned} \tag{10}$$

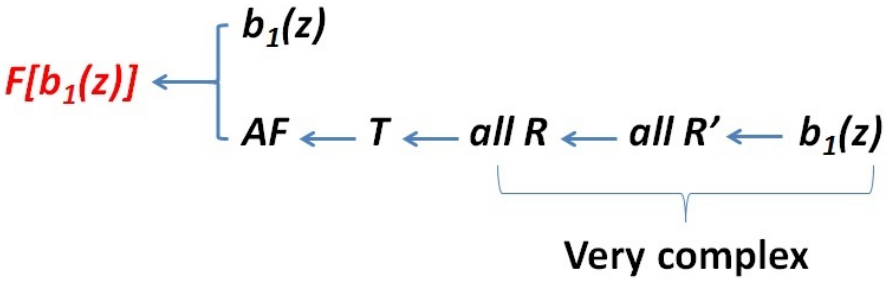

Figure 3: The straight forward strategy

The basic strategy to construct $F[b_1(z)]$ in terms of $b_1(z)$ is to first construct the attenuation factor by $b_1(z)$, and then to construct $F[b_1(z)]$ by using $b_1(z)$ and attenuation factor. The attenuation factor can be written in reflection coefficients, and then we can map the reflection coefficients to R's ($R's$ are the amplitudes of the events in data), finally construct the R's by $b_1(z)$, as shown in figure 3. However, we have tried this approach and found that it is difficult to achieve.

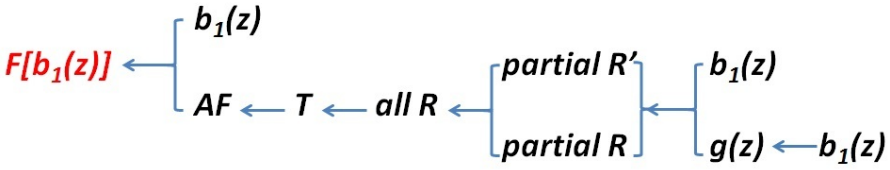

Figure 4: Modified strategy

Next, we propose another way to achieve the goal. By introducing a new function called g(z) in which the amplitude of each event corresponds to a reflection coefficient, we find a way to construct $F[b_1(z)]$ by using $b_1(z)$ and g(z). After that, we find an integral equation about $b_1(z)$ and g(z). If we can solve the latter equation for g(z) and integrate it into the first part, we can achieve our goal (as shown in Figure 4).

By using that modified strategy, the $F[b_1(z)]$ is discovered (See Appendix A for the derivation):

$$F[b_1(z)] = \frac{b_1(z)}{[1-(\int_{z-\varepsilon}^{z+\varepsilon} dz' g(z'))^2][1-\int_{-\infty}^{z-\varepsilon} dz' b_1(z') \int_{z'-\varepsilon}^{z'+\varepsilon} dz'' g(z'')]^2} \tag{11}$$

$$g(z) = \frac{b_1(z)}{1-\int_{-\infty}^{z-\varepsilon} dz' b_1(z') \int_{z'-\varepsilon}^{z'+\varepsilon} dz'' g(z'')} \tag{12}$$

To derive the $F[b_1(z)]$ from $b_1(z)$, g(z) must first be solved in equation (12). Thereafter, g(z) is integrated into equation (11).

4 The ISS internal-multiple elimination algorithm for 1D pre-stack data

4.1 A 2-reflector analytic example for the ISS internal-multiple attenuation algorithm in a 1D pre-stack acoustic medium

Now we will go on to extend the elimination algorithm for a 1D pre-stack data. Before that we need to better understand the mechanism of the attenuation algorithm for a 1D pre-stack data. What does b_1 looks like for a 1D pre-stack data? Is there any analog of the attenuation factors in 1D pre-stack acoustic medium? If yes, what is it?

In order to answer these questions, we will look at an analytic example for a 2-reflector acoustic medium in 1D pre-stack.

The first question is what is b_1 in 1D pre-stack? We know that b_1 is closely related to the measured data D. If we can get the data, we can obtain b_1. Thus, first we need to obtain the data. Let us consider a delta source at (x_s, z_s), wherein the wave generated at (x_g, z_g) by this source is the Green's function:

$$G_0(x_g, z_g, x_s, z_s, \omega) = \frac{1}{2\pi} \int_{-\infty}^{\infty} dk_s' \frac{e^{ik_s'(x_g-x_s)} e^{iq_s'|z_g-z_s|}}{2iq_s'} \tag{13}$$

Let us set $z_s = 0$ and let z_g be positive, so that we can evaluate the absolute value,

$$G_0(x_g, z_g > 0, x_s, z_s = 0, \omega) = \frac{1}{2\pi} \int_{-\infty}^{\infty} dk_s' \frac{e^{-ik_s'x_s}}{2iq_s'} e^{ik_s'x_g + iq_s'z_g}. \tag{14}$$

Then, for simplicity, we will ignore the evanescent part, which means $k_s' < \omega/c$. That does not mean the algorithm can not handle the evanescent part. However, for many cases the evanescent part is small and can be ignored, and the math will be much simpler and easier to understand. Now the Green's function is:

$$G_0(x_g, z_g > 0, x_s, z_s = 0, \omega) = \frac{1}{2\pi} \int_{-\omega/c}^{\omega/c} dk_s' \frac{e^{-ik_s'x_s}}{2iq_s'} e^{ik_s'x_g + iq_s'z_g}. \tag{15}$$

At this point, G_0 can be regarded as a superposition of plane waves $e^{ik'_s x+iq'_s z}$ with weights $\frac{e^{-ik'_s x_s}}{2iq'_s}$.
For a plane wave $e^{ik'_s x+iq'_s z}$ incident in an acoustic medium, the reflected wavefield is: (Note that It can be calculated by using the forward scattering series, as in Nita et al. (2004))

$$D(k'_s, q'_s, x_g, z_g = 0) = R(k'_s, q'_s)e^{ik'_s x_g}e^{2iq'_s z_1}. \tag{16}$$

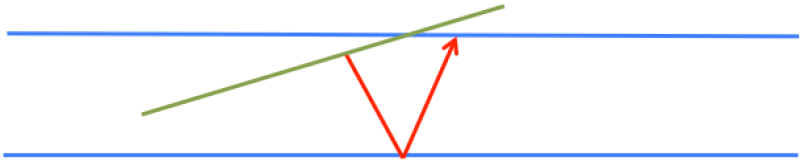

Figure 5: prestack

Then the total wave-field is (we set $z_g = z_s = 0$):

$$D(x_s, z_s = 0, x_g, z_g = 0, \omega) = \frac{1}{2\pi}\int_{-\omega/c}^{\omega/c} dk'_s \frac{e^{-ik'_s x_s}}{2iq'_s} D(k'_s, q'_s, x_g, z_g = 0). \tag{17}$$

Now we get the data at one receiver (x_g,0) from one delta source (x_s,0) and rewrite it as:

$$D(x_s, x_g, \omega) = \frac{1}{2\pi}\int_{-\omega/c}^{\omega/c} dk'_s \frac{e^{-ik'_s x_s}}{2iq'_s} R(k'_s, q'_s)e^{ik'_s x_g}e^{2iq'_s z_1} \tag{18}$$

This is in the frequency-space domain, whereas the attenuation algorithm works in the frequency-wavenumber domain. After Fourier transforming over the source and receivers, we convert the data to the frequency-wavenumber domain[1].

$$D(k_s, k_g, \omega) = \delta(k_s - k_g)\frac{R(k_s, q_s)e^{2iq_s z_1}}{4\pi iq_s}(-\omega/c < k_s < \omega/c) \tag{19}$$

Now we define $b_1(k_s, k_g, \omega)$ as (in the following discussion, we assume that $-\omega/c < k_s < \omega/c$):

$$\begin{aligned} b_1(k_s, k_g, \omega) &= -2iq_s D(k_s, k_g, \omega) \\ &= -\frac{1}{2\pi}\delta(k_s - k_g)R(k_s, q_s)e^{2iq_s z_1}. \end{aligned} \tag{20}$$

[1] See appendix B for derivation

Then, $b_1(k_s, k_g, \omega)$ and the attenuation algorithm prediction $b_3(k_s, k_g, \omega)$ are related by the 2D internal-multiple attenuation algorithm:

$$\begin{aligned} b_3(k_g, k_s, \omega) &= \int_{-\infty}^{\infty}\int_{-\infty}^{\infty} dk_1 dk_2 \int_{-\infty}^{\infty} dz e^{i(q_g+q_1)z} b_1(k_g, k_1, z) \int_{-\infty}^{z} dz' e^{i(-q_1-q_2)z'} b_1(k_1, k_2, z') \\ &\quad \times \int_{z'}^{\infty} dz'' e^{i(q_2+q_s)z''} b_1(k_2, k_s, z'') \end{aligned}$$

Next with the definition of $b_1(k_s, 2q_s)$ and its prediction $b_3(k_s, 2q_s)$ for 1D pre-stack data, we have:

$$b_1(k_s, k_g, \omega) = -\frac{1}{2\pi}\delta(k_s - k_g) b_1(k_s, 2q_s) \tag{21}$$

$$b_3(k_g, k_s, q_g + q_s) = -\frac{1}{(2\pi)^3}\delta(k_g - k_s) b_3(k_s, 2q_s). \tag{22}$$

Then, $b_1(k_s, 2q_s)$ and $b_3(k_s, 2q_s)$ are related by the 1D pre-stack algorithm:

$$b_3(k_s, 2q_s) = \int_{-\infty}^{\infty} dz e^{2iq_s z} b_1(k_s, z) \int_{-\infty}^{z} dz' e^{-2iq_s z'} b_1(k_s, z') \int_{z'}^{\infty} dz'' e^{2iq_s z''} b_1(k_s, z'') \tag{23}$$

Ignoring the subscript s, we have

$$b_3(k, 2q) = \int_{-\infty}^{\infty} dz e^{2iqz} b_1(k, z) \int_{-\infty}^{z} dz' e^{-2iqz'} b_1(k, z') \int_{z'}^{\infty} dz'' e^{2iqz''} b_1(k, z''). \tag{24}$$

In the equation, for the first primary, we have

$$b_1(k, 2q) = R(k, q) e^{2iqz_1}, \tag{25}$$

and $b_1(k, z)$ is the Fourier transform of $b_1(k, 2q)$ from 2q to z.

We can also get the reflection data from the second reflector, and we can obtain a first order internal multiple as shown in Figure 6

Now, b_1 can be written as,

$$\begin{aligned} b_1(k_1, 2q_1) &= R_1(k_1, q_1) e^{2iq_1 z_1} \\ &\quad + T_{01} R_2(k_2, q_2) T_{10} e^{2iq_1 z_1} e^{2iq_2(z_2 - z_1)} \\ &\quad - T_{01} R_2 R_1 R_2 T_{10} e^{2iq_1 z_1} e^{4iq_2(z_2 - z_1)} \end{aligned} \tag{26}$$

Here, q_1 and q_2 are vertical wavenumbers at each layer, and q_2 is a function of q_1. To Fourier transform from q_1 to z, first we need to substitute q_2 with q_1.

Using the relation,

$$q_1^2 + k_1^2 = (\frac{\omega}{c_1})^2 \tag{27}$$

$$q_2^2 + k_2^2 = (\frac{\omega}{c_2})^2 \tag{28}$$

$$k_1 = k_2, \tag{29}$$

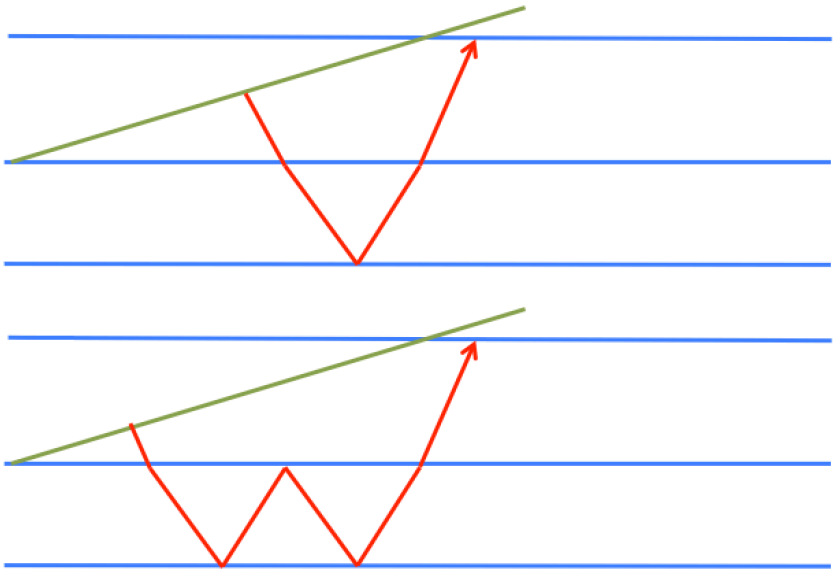

Figure 6: prestack

we can express q_2 in q_1 and k_1:

$$\begin{aligned} q_2 &= \sqrt{(\frac{c_1^2}{c_2^2}-1)k_1^2+\frac{c_1^2}{c_2^2}q_1^2} \\ &= \frac{c_1}{c_2}q_1+[\sqrt{(\frac{c_1^2}{c_2^2}-1)k_1^2+\frac{c_1^2}{c_2^2}q_1^2}-\frac{c_1}{c_2}q_1] \\ &= \frac{c_1}{c_2}q_1+\frac{(\frac{c_1^2}{c_2^2}-1)k_1^2}{\sqrt{(\frac{c_1^2}{c_2^2}-1)k_1^2+\frac{c_1^2}{c_2^2}q_1^2}+\frac{c_1}{c_2}q_1} \\ &= \frac{c_1}{c_2}q_1+S(k_1,q_1) \end{aligned} \tag{30}$$

Now we substitute q_2 with q_1:

$$\begin{aligned} b_1(k_1,2q_1) &= R_1(k_1,q_1)e^{2iq_1z_1} \\ &\quad +R_2'(k_1,q_1)e^{2i(z_2-z_1)S(k_1,q_1)}e^{2iq_1(z_1+\frac{c_1}{c_2}(z_2-z_1))} \\ &\quad -R_{212}'(k_1,q_1)e^{4i(z_2-z_1)S(k_1,q_1)}e^{2iq_1(z_1+\frac{2c_1}{c_2}(z_2-z_1))} \\ &= R_1(k_1,q_1)e^{2iq_1z_1} \\ &\quad +R_2'(k_1,q_1)e^{2i(z_2-z_1)S(k_1,q_1)}e^{2iq_1z_2'} \\ &\quad -R_{212}'(k_1,q_1)e^{4i(z_2-z_1)S(k_1,q_1)}e^{2iq_1(2z_2'-z_1)} \end{aligned} \tag{31}$$

The predicted internal multiple should be:

$$b_3(k_1,2q_1) = R_2'(k_1,q_1)R_1(k_1,q_1)R_2'(k_1,q_1)e^{4i(z_2-z_1)S(k_1,q_1)}e^{2iq_1(2z_2'-z_1)} \tag{32}$$

Comparing the predicted amplitude of the internal multiple with the actual amplitude of the internal multiple, we have:

$$\begin{aligned} R'_{212}(k_1,q_1) &= T_{01}R_2R_1R_2T_{10} \\ &= \frac{R'_2(k_2,q_2)R_1(k_1,q_1)R'_2(k_2,q_2)}{T_{01}(k_1,q_1)T_{10}(k_1,q_1)} \end{aligned} \tag{33}$$

We can see that they differed by a factor $T_{01}(k_1,q_1)T_{10}(k_1,q_1)$. That is the attenuation factor for the 1D pre-stack acoustic medium.

4.2 The ISS internal-multiple elimination algorithm for 1D pre-stack data

Now we have the attenuation factor for the 1D pre-stack acoustic medium and it lights the way to extending the 1D normal-incidence algorithm to 1D pre-stack data. Below shows the 1D pre-stack acoustic algorithm. In the 1D pre-stack elimination algorithm, due to the angle-dependent reflection coefficients, we can no longer just integrate the data in the k-z domain to get the reflection coefficients-we need to go to the k-q domain in which each pair k-q corresponds to a reflection coefficient. The differences between the 1D pre-stack algorithm and the 1D normal incidence algorithm are that the 1D pre-stack algorithm has one more variable k, and it uses the reflection coefficients in the k-q domain instead of the direct integral in the k-z domain.

$$b_E^{IM}(k,2q) = \int_{-\infty}^{\infty} dz e^{2iqz} b_1(k,z) \int_{-\infty}^{z-\varepsilon_1} dz' e^{-2iqz'} F[b_1(k,z')] \int_{z'+\varepsilon_2}^{\infty} dz'' e^{2iqz''} b_1(k,z'') \tag{34}$$

$$\begin{aligned} F[b_1(k,z)] &= \frac{1}{2\pi}\int_{-\infty}^{\infty}\int_{-\infty}^{\infty} dz'dq' \\ &\times \frac{e^{-iq'z}e^{iq'z'}b_1(k,z')}{[1-\int_{-\infty}^{z'-\varepsilon} dz'' b_1(k,z'')e^{iq'z''}\int_{z''-\varepsilon}^{z''+\varepsilon} dz''' g^*(k,z''')e^{-iq'z'''}]^2[1-|\int_{z'-\varepsilon}^{z'+\varepsilon} dz'' g(k,z'')e^{iq'z''}|^2]} \end{aligned} \tag{35}$$

$$g(k,z) = \frac{1}{2\pi}\int_{-\infty}^{\infty}\int_{-\infty}^{\infty} dz'dq' \frac{e^{-iq'z}e^{iq'z'}b_1(k,z')}{1-\int_{-\infty}^{z'-\varepsilon} dz'' b_1(k,z'')e^{iq'z''}\int_{z''-\varepsilon}^{z''+\varepsilon} dz''' g^*(k,z''')e^{-iq'z'''}} \tag{36}$$

5 A numerical test for synthetic elastic PP data

We test the 1D pre-stack internal multiple elimination algorithm for an four-reflector elastic model shown in figure 7. Figure 8 shows the PP data generated from this model by reflectivity method. Figure 9 and figure 10 show a section (2.8s-3.1s) of the data and attenuation and elimination prediction results.

The left picture in figure 9 shows a section in the input data. In this section ,there are 3 major events interfering with each other: a converted P primary, an internal multiple generated from the

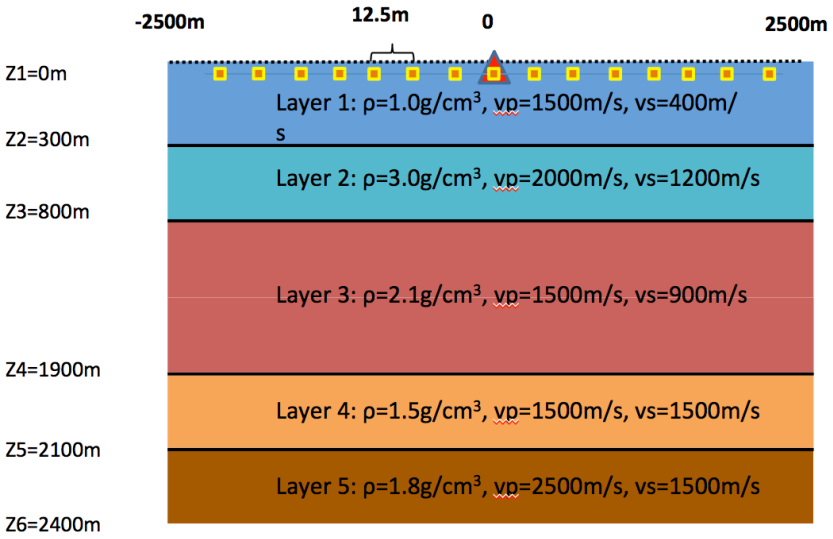

Figure 7: model

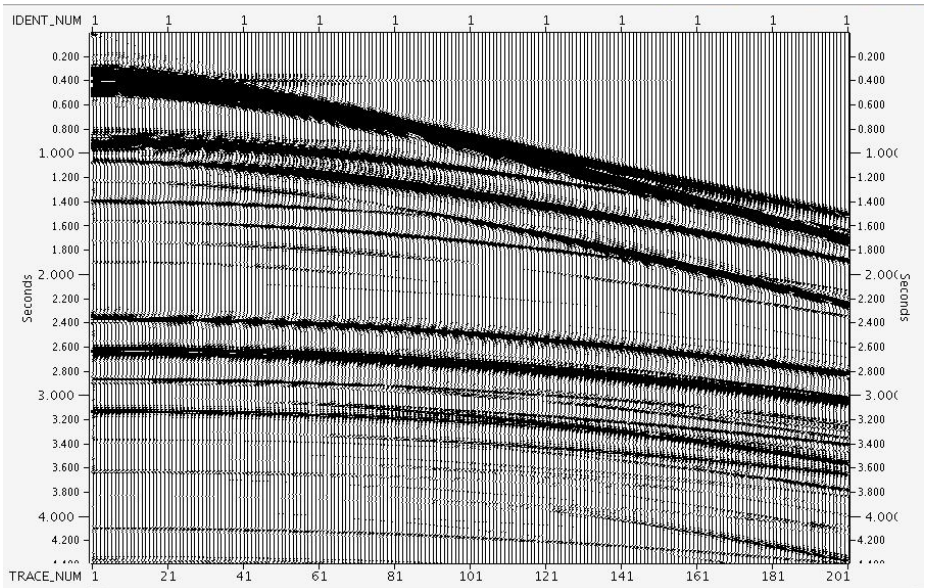

Figure 8: PP data

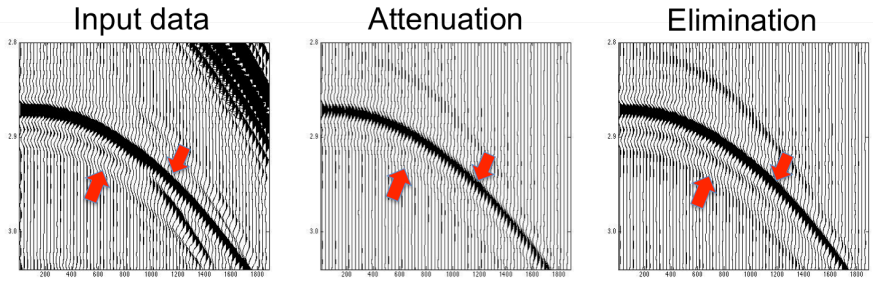

Figure 9: A section of the input data and prediction. Left: input data. Middle: attenuation algorithm prediction. Right:elimination algorithm prediction.

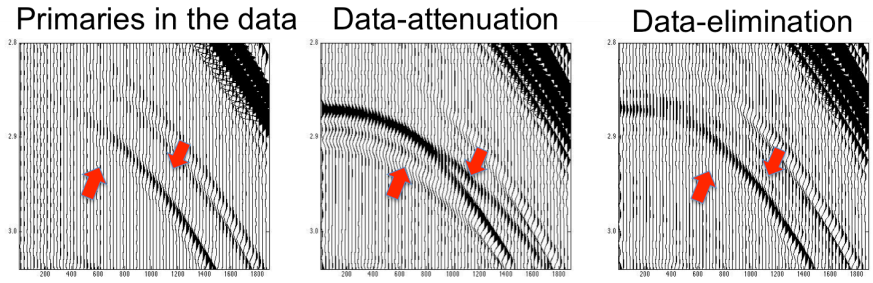

Figure 10: Left: primaries in the input data. Middle: data after internal multiples being attenuated. Right:data after internal multiples being eliminated.

first reflector and another internal multiple generated from the third reflector. The middle picture in figure 9 shows the attenuation algorithm predicted internal multiples, it clearly shows the predicted internal multiples have correct time and approximate amplitude. The right picture in figure 9 shows the elimination algorithm prediction, the time is correct and the amplitude is more accurate. The left picture in figure 10 shows the primaries in the data. (Because it is a synthetic test, we can generate only the primaries and use them as a benchmark.) The middle picture in figure 10 shows the result by subtracting the attenuation algorithm prediction from the data. The internal multiples has been reduced, but there still remains residues. The right picture in figure 10 shows the result by subtracting the elimination algorithm prediction from the data. We can see that the multiples has been (almost) completed eliminated and the primary is recovered. (Note that there is still some small residues in the near offset due to the inaccuracy of numerical Hankel transform.)

6 A limitation of this elimination algorithm and an algorithm to address the limitation

There is a limitation of this elimination algorithm, that is, the primaries in the reflection data that enters the algorithm provides that elimination capability, automatically without requiring the primaries to be identified or in any way separated. The other events in the reflection data, that is, the internal multiples, may alter the amplitude and need assist to completely eliminate the internal multiples. That is a limitation of this elimination algorithm. To deal with this limitation, we can first use ISS

internal multiple attenuation algorithm prediction (b_3) to attenuate the internal multiples in the data (b_1) and then put the subtracted result, i.e., $b_1 + b_3$, which contains primaries and attenuated internal multiples, into the ISS internal multiple elimination algorithm and predict internal multiples with more accurate amplitude. (Note that in the numerical test, this limitation has very small affect on the prediction, thus we do not need to consider addressing this limitation in this test. However, for certain situation, we need to consider this limitation.)

7 Conclusion

The new ISS internal multiple elimination algorithm is a part of the three-pronged strategy which is especially relevant and provide value when primaries and internal multiples are proximal to and/or interfere with each other in both on-shore and off-shore data. We derived this elimination algorithm from a reverse engineering approach and use it as a guide to find the internal multiple elimination terms in the ISS. In this paper, we discussed the 1D pre-stack ISS internal multiple elimination algorithm for all first-order internal multiples from all reflectors and tested this algorithm with an elastic synthetic PP data. The encouraging result shows that this ISS internal multiple elimination algorithm can predict more accurate amplitude of the internal multiples than the attenuation algorithm.

This reverse engineering approach launched by understanding the properties of the ISS attenuation algorithm, and in 1D, reverse engineering a solution, was based on the input being primaries. The primaries in the reflection data that enters the algorithm provide that elimination capability, automatically without our requiring the primaries to be identified or in any way separated. The other events in the reflection data, that is, the internal multiples, will not be helpful in this elimination scheme. This can be a limitation and can sometimes have significant affect on the prediction. We also provide an algorithm to address this limitation in the last section.

8 ACKNOWLEDGMENTS

We are grateful to all M-OSRP sponsors for encouragement and support in this research. We would like to thank Schlumberger Limited for the test data. We would like to thank all our coworkers for their help in reviewing this paper and valuable discussions.

Appendix A: Derivation of the algorithm for the elimination of all first-order internal multiples from all reflectors in a 1D medium

The algorithm is given by:

$$F[b_1(z)] = \frac{b_1(z)}{[1-(\int_{z-\varepsilon}^{z+\varepsilon} dz' g(z'))^2][1-\int_{-\infty}^{z-\varepsilon} dz' b_1(z') \int_{z'-\varepsilon}^{z'+\varepsilon} dz'' g(z'')]^2}$$

$$g(z) = \frac{b_1(z)}{1-\int_{-\infty}^{z-\varepsilon} dz' b_1(z') \int_{z'-\varepsilon}^{z'+\varepsilon} dz'' g(z'')}$$

with

$$\begin{aligned} b_1(z) =& R_1\delta(z-z_1) + R_2'\delta(z-z_2) + R_3'\delta(z-z_3) + \cdots + R_n'\delta(z-z_n) + \cdots \\ g(z) =& R_1\delta(z-z_1) + R_2\delta(z-z_2) + R_3\delta(z-z_3) + \cdots + R_n\delta(z-z_n) + \cdots \end{aligned}$$

($\int_{z-\varepsilon}^{z+\varepsilon} dz'' g(z'')$ is a function of z)

First Let us calculate $\int_{z-\varepsilon}^{z+\varepsilon} dz'' g(z'')$ for the given g(z):

$$\begin{aligned} \int_{z-\varepsilon}^{z+\varepsilon} dz'' g(z'') =& \int_{z-\varepsilon}^{z+\varepsilon} dz''[R_1\delta(z''-z_1) + R_2\delta(z''-z_2) + \cdots + R_n\delta(z''-z_n) + \cdots] \\ =& \int_{-\infty}^{\infty} dz''[R_1\delta(z''-z_1) + R_2\delta(z''-z_2) + \cdots + R_n\delta(z''-z_n) + \cdots] \\ & \times H(z''-(z-\varepsilon))H((z+\varepsilon)-z'') \\ =& R_1 H(z_1-(z-\varepsilon))H((z+\varepsilon)-z_1) + R_2 H(z_2-(z-\varepsilon))H((z+\varepsilon)-z_2) \\ & + \cdots + R_n H(z_n-(z-\varepsilon))H((z+\varepsilon)-z_n) + \cdots \\ =& R_1 H((z_1+\varepsilon)-z)H(z-(z_1-\varepsilon)) + R_2 H((z_2+\varepsilon)-z)H(z-(z_2-\varepsilon)) \\ & + \cdots + R_n H((z_n+\varepsilon)-z)H(z-(z_n-\varepsilon)) + \cdots \end{aligned}$$

$$\begin{aligned} & (\int_{z-\varepsilon}^{z+\varepsilon} dz'' g(z''))^2 \\ =& R_1^2 H((z_1+\varepsilon)-z)H(z-(z_1-\varepsilon)) + R_2^2 H((z_2+\varepsilon)-z)H(z-(z_2-\varepsilon)) \\ & + \cdots + R_n^2 H((z_n+\varepsilon)-z)H(z-(z_n-\varepsilon)) + \cdots \end{aligned}$$

$$\begin{aligned} & b_1(z') \int_{z'-\varepsilon}^{z'+\varepsilon} dz'' g(z'') \\ =& R_1^2\delta(z'-z_1) + R_2R_2'\delta(z'-z_2) + R_3R_3'\delta(z'-z_3) + \cdots + R_nR_n'\delta(z'-z_n) + \cdots \end{aligned}$$

$$
\begin{aligned}
&\int_{-\infty}^{z-\varepsilon} dz' b_1(z') \int_{z'-\varepsilon}^{z'+\varepsilon} dz'' g(z'') \\
=&\int_{-\infty}^{z-\varepsilon} dz' [R_1^2 \delta(z'-z_1) + R_2 R_2' \delta(z'-z_2) + \cdots + R_n R_n' \delta(z'-z_n) + \cdots] \\
=&\int_{-\infty}^{\infty} dz' H((z-\varepsilon)-z') [R_1^2 \delta(z'-z_1) + R_2 R_2' \delta(z'-z_2) + \cdots + R_n R_n' \delta(z'-z_n) + \cdots] \\
=&R_1^2 H((z-\varepsilon)-z_1) + R_2 R_2' H((z-\varepsilon)-z_2) + \cdots + R_n R_n' H((z-\varepsilon)-z_n) + \cdots \\
=&R_1^2 H(z-(z_1+\varepsilon)) + R_2 R_2' H(z-(z_2+\varepsilon)) + \cdots + R_n R_n' H(z-(z_n+\varepsilon)) + \cdots
\end{aligned}
$$

Now we can prove the first part of the equation:

$$
\begin{aligned}
&F[b_1(z)] \\
=&\frac{b_1(z)}{[1-(\int_{z-\varepsilon}^{z+\varepsilon} dz' g(z'))^2][1-\int_{-\infty}^{z-\varepsilon} dz' b_1(z') \int_{z'-\varepsilon}^{z'+\varepsilon} dz'' g(z'')]^2} \\
=&\frac{b_1(z)}{[1-R_1^2 H((z_1+\varepsilon)-z) H(z-(z_1-\varepsilon)) - \cdots][1-R_1^2 H(z-(z_1+\varepsilon)) - R_2 R_2' H(z-(z_2+\varepsilon)) - \cdots]^2} \\
=&\frac{R_1}{1-R_1^2}\delta(z-z_1) + \frac{R_2'}{(1-R_1^2)^2(1-R_2^2)}\delta(z-z_2) + \cdots \\
&+ \frac{R_n'}{(1-R_1^2)^2(1-R_2^2)^2\cdots(1-R_{n-1}^2)^2(1-R_n^2)}\delta(z-z_n) + \cdots \\
=&\frac{R_1}{AF_{j=1}}\delta(z-z_1) + \frac{R_2'}{AF_{j=2}}\delta(z-z_2) + \cdots + \frac{R_n'}{AF_{j=n}}\delta(z-z_n) + \cdots
\end{aligned}
$$

For the second part of the equation, we have:

$$
g(z) = \frac{b_1(z)}{1-\int_{-\infty}^{z-\varepsilon} dz' b_1(z') \int_{z'-\varepsilon}^{z'+\varepsilon} dz'' g(z'')}
$$

$$
\begin{aligned}
&b_1(z') \int_{z'-\varepsilon}^{z'+\varepsilon} dz'' g(z'') \\
=&R_1^2 \delta(z'-z_1) + R_2 R_2' \delta(z'-z_2) + R_3 R_3' \delta(z'-z_3) + \cdots + R_n R_n' \delta(z'-z_n) + \cdots
\end{aligned}
$$

$$
\begin{aligned}
&\int_{-\infty}^{z-\varepsilon} dz' b_1(z') \int_{z'-\varepsilon}^{z'+\varepsilon} dz'' g(z'') \\
=&\int_{-\infty}^{z-\varepsilon} dz' [R_1^2 \delta(z'-z_1) + R_2 R_2' \delta(z'-z_2) + \cdots + R_n R_n' \delta(z'-z_n) + \cdots] \\
=&\int_{-\infty}^{\infty} dz' H((z-\varepsilon)-z') [R_1^2 \delta(z'-z_1) + R_2 R_2' \delta(z'-z_2) + \cdots + R_n R_n' \delta(z'-z_n) + \cdots] \\
=&R_1^2 H((z-\varepsilon)-z_1) + R_2 R_2' H((z-\varepsilon)-z_2) + \cdots + R_n R_n' H((z-\varepsilon)-z_n) + \cdots \\
=&R_1^2 H(z-(z_1+\varepsilon)) + R_2 R_2' H(z-(z_2+\varepsilon)) + \cdots + R_n R_n' H(z-(z_n+\varepsilon)) + \cdots
\end{aligned}
$$

$$
\begin{aligned}
&\frac{b_1(z)}{1-\int_{-\infty}^{z-\varepsilon} dz' b_1(z') \int_{z'-\varepsilon}^{z'+\varepsilon} dz'' g(z'')} \\
=&R_1\delta(z-z_1)+\frac{R_2'}{1-R_1R_1}\delta(z-z_2)+\frac{R_3'}{1-R_1R_1-R_2'R_2}\delta(z-z_3)+\cdots \\
&+\frac{R_n'}{1-R_1R_1-R_2'R_2-\cdots-R_{n-1}'R_{n-1}}\delta(z-z_n) \\
=&R_1\delta(z-z_1)+R_2\delta(z-z_2)+R_3\delta(z-z_3)+\cdots+R_n\delta(z-z_n)+\cdots \\
=&g(z)
\end{aligned}
$$

Thus the second equation is proved.

In the derivation we used:$R_i = \frac{R_i'}{1-R_1R_1-R_2'R_2-\cdots-R_{i-1}'R_{i-1}}$ It can be proved:

$$
\begin{aligned}
R_i =&\frac{R_i'}{(1-R_1^2)(1-R_2^2)\cdots(1-R_{i-2}^2)(1-R_{i-1}^2)} \\
=&\frac{R_i'}{(1-R_1^2)(1-R_2^2)\cdots(1-R_{i-2}^2)-(1-R_1^2)(1-R_2^2)\cdots(1-R_{i-2}^2)R_{i-1}^2} \\
=&\frac{R_i'}{(1-R_1^2)(1-R_2^2)\cdots(1-R_{i-2}^2)-(1-R_1^2)(1-R_2^2)\cdots(1-R_{i-2}^2)R_{i-1}R_{i-1}} \\
=&\frac{R_i'}{(1-R_1^2)(1-R_2^2)\cdots(1-R_{i-2}^2)-R_{i-1}'R_{i-1}} \\
=&\frac{R_i'}{1-R_1R_1-R_2'R_2-\cdots-R_{i-1}'R_{i-1}}
\end{aligned}
$$

Appendix B: Fourier transform of the data from the frequency-space domain to the frequency-wavenumber domain

$$
D(x_s,x_g,\omega)=\frac{1}{2\pi}\int_{-\omega/c}^{\omega/c}dk_s'\frac{e^{-ik_s'x_s}}{2iq_s'}R(k_s',q_s')e^{ik_s'x_g}e^{2iq_s'z_1} \tag{B-1}
$$

$$
\begin{aligned}
D(k_s,x_g,\omega) &= \frac{1}{2\pi}\int_{-\infty}^{\infty}dx_s e^{ik_sx_s}\int_{-\omega/c}^{\omega/c}dk_s'\frac{e^{-ik_s'x_s}}{2iq_s'}R(k_s',q_s')e^{ik_s'x_g}e^{2iq_s'z_1} &\text{(B-2)}\\
&= \frac{1}{2\pi}\int_{-\omega/c}^{\omega/c}\int_{-\infty}^{\infty}dx_s e^{i(k_s-k_s')x_s}dk_s'\frac{R(k_s',q_s')e^{ik_s'x_g}e^{2iq_s'z_1}}{2iq_s'} &\text{(B-3)}\\
&= \frac{1}{2\pi}\int_{-\omega/c}^{\omega/c}dk_s'\delta(k_s-k_s')\frac{R(k_s',q_s')e^{ik_s'x_g}e^{2iq_s'z_1}}{2iq_s'} &\text{(B-4)}\\
&= \frac{R(k_s,q_s)e^{ik_sx_g}e^{2iq_sz_1}}{4\pi iq_s}(-\omega/c<k_s<\omega/c) &\text{(B-5)}
\end{aligned}
$$

$$D(k_s, k_g, \omega) = \int_{-\infty}^{\infty} dx_g e^{-ik_g x_g} \frac{R(k_s, q_s) e^{ik_s x_g} e^{2iq_s z_1}}{4\pi i q_s} (-\omega/c < k_s < \omega/c) \quad \text{(B-6)}$$

$$= \delta(k_s - k_g) \frac{R(k_s, q_s) e^{2iq_s z_1}}{4\pi i q_s} (-\omega/c < k_s < \omega/c) \quad \text{(B-7)}$$

(B-8)

References

Araújo, F. V. *Linear and non-linear methods derived from scattering theory: backscattered tomography and internal multiple attenuation*. PhD thesis, Universidade Federal da Bahia, 1994.

Araújo, F. V., A. B. Weglein, P. M. Carvalho, and R. H. Stolt. "Inverse scattering series for multiple attenuation: An example with surface and internal multiples." *SEG Technical Program Expanded Abstracts* (1994): 1039–1041.

H. Liang, C. Ma and A. B. Weglein. "A further general modification of the leading order ISS attenuator of first-order internal multiples to accommodate primaries and internal multiples when an arbitrary number of reflectors generate the data: theory, development, and examples." *Mission Oriented Seismic Research Program Annual Report* (2012): 148–165.

Ma, C., H. Liang, and A. B. Weglein. "Modifying the leading order ISS attenuator of first-order internal multiples to accommodate primaries and internal multiples: fundamental concept andtheory, development, and examples exemplified when three reflectors generatethe data." *Mission Oriented Seismic Research Program Annual Report* (2012): 133–147.

Ma, C. and A. B. Weglein. "Including higher-order Inverse Scattering Series (ISS) terms to address a serious shortcoming/problem of the ISS internal-multiple attenuator: exemplifying the problem and its resolution." *SEG Technical Program Expanded Abstracts* (2014).

Nita, B. G., K. H. Matson, and A. B. Weglein. "Forward scattering series and seismic events: Far field approximations, critical and postcritical events." *SIAM Journal of Applied Mathematics* 64 (2004): 2167–2185.

Ramírez, A. C. *1.-Inverse scattering subseries for removal of internal multiples and depth imaging primaries; 2.-Green's theorem as the foundation of interferometry and guiding new practical methods and applications*. PhD thesis, University of Houston, 2007.

Weglein, A. B., F. V. Araújo, P. M. Carvalho, R. H. Stolt, K. H. Matson, R. T. Coates, D. Corrigan, D. J. Foster, S. A. Shaw, and H. Zhang. "Inverse Scattering Series and seismic exploration." *Inverse Problems* (2003): R27–R83.

Weglein, A. B., F. A. Gasparotto, P. M. Carvalho, and R. H. Stolt. "An Inverse-Scattering Series method for attenuating multiples in seismic reflection data." *Geophysics* 62 (November-December 1997): 1975–1989.

Weglein, Arthur B. "Multiple attenuation: The status and a strategy that identifies and addresses current challenges." *SEG Technical Program Expanded Abstracts* (2014).

Wilberth Herrera, Hong Liang Paolo Terenghi,Chao Ma and Arthur B. Weglein. "Progressing amplitude issues for testing 1D analytic data in leading order internal multiple algorithms." *Mission Oriented Seismic Research Program Annual Report* (2012): 167–188.

An internal-multiple *elimination* algorithm for all first-order internal multiples for a 1D earth

Yanglei Zou, Arthur B. Weglein, M-OSRP/Physics Dept./University of Houston

SUMMARY

The ISS (Inverse-Scattering-Series) internal-multiple attenuation algorithm (Araújo et al. (1994),Weglein et al. (1997) and Weglein et al. (2003)) can predict the correct time and approximate amplitude for all first-order internal multiples without any subsurface information. When combined with an energy minimization adaptive subtraction, the ISS internal multiple attenuation algorithm can effectively remove internal multiples when the primaries and internal multiples are separated, and not overlapping or proximal. One of issues that the adaptive subtraction is addressing is the difference between the amplitude of the internal multiple and the approximate amplitude of the attenuation algorithm prediction. However, under certain circumstances, both offshore and onshore, internal multiples are often proximal to or interfering with primaries and the criteria of adaptive subtraction may fail, since the energy can increase when e.g., a multiple is removed from an interfering primary. Therefore, in these situations, the task of removing internal multiples without damaging primaries becomes more challenging and subtle and currently beyond the collective capability of the petroleum industry. Weglein (2014) proposed a three-pronged strategy for providing an effective response to this pressing and prioritized challenge. One part of the strategy is to develop an internal-multiple elimination algorithm that can predict both the correct amplitude and correct time for all internal multiples. In this paper, we provide an ISS internal-multiple elimination algorithm for all first-order internal multiples generated from all reflectors in a 1D earth and provide an example from an elastic synthetic data that shows the value provided by the new algorithm in comparison with the value provided by the internal multiple attenuation algorithm.

INTRODUCTION

The ISS (Inverse-Scattering-Series) allows all seismic processing objectives, such as free-surface-multiple removal and internal-multiple removal to be achieved directly in terms of data, without any estimation of the earth's properties. For internal-multiple removal, the ISS internal-multiple attenuation algorithm can predict the correct time and approximate and well-understood amplitude for all first-order internal multiples generated from all reflectors, at once, without any subsurface information. If the events in the data are isolated, the energy minimization adaptive subtraction can fix the gap between the attenuation algorithm prediction and the internal multiples plus, e.g., all factors that are outside the assumed physics of the subsurface and acquisition. However, in certain situations, events often interfere with each other in both on-shore and off-shore seismic data. In these cases, the criteria of energy minimization adaptive subtraction may fail and completely removing internal multiples becomes more challenging and beyond the current capability of the petroleum industry.

For dealing with this challenging problem, Weglein (2014) proposed a three-pronged strategy including

1. Develop the ISS prerequisites for predicting the reference wave field and to produce de-ghosted data.
2. Develop internal-multiple elimination algorithms from ISS.
3. Develop a replacement for the energy-minimization criteria for adaptive subtraction.

To achieve the second part of the strategy, that is, to upgrade the ISS internal-multiple attenuation algorithm to elimination algorithm, the strengths and limitations of the ISS internal-multiple attenuation algorithm are noted and reviewed. The ISS internal-multiple attenuation algorithm always attenuates all first-order internal multiples from all reflectors at once, automatically and without any subsurface information. That is a tremendous strength, and is a constant and holds independent of the circumstances and complexity of the geology and the play. However, there are two well-understood limitations of this ISS internal-multiple attenuation algorithm

1. It may generate spurious events due to internal multiples treated as subevents.
2. It is an attenuation algorithm not an elimination algorithm.

The first item is a shortcoming of the leading order term (the attenuation algorithm), when taken in isolation, but is not an issue for the entire ISS internal-multiple removal capability. It is anticipated by the ISS and higher order ISS internal multiple terms exist to precisely remove that issue of spurious events prediction. When taken together with the higher order terms, the ISS internal multiple removal algorithm no longer experiences spurious events prediction. Ma et al. (2012) , H. Liang and Weglein (2012) and Ma and Weglein (2014) provided those higher order terms for spurious events removal.

In a similar way, there are higher order ISS internal multiple terms that provide the elimination of internal multiples when taken together with the leading order attenuation term. There are early discussions in Ramírez (2007) and Wilberth Herrera and Weglein (2012) find higher order terms in ISS that can eliminate all first-order internal multiples generated at the shallowest reflector for 1D normal incidence spike plane wave. The next step, elimination of all first-order internal-multiples generated from all reflectors, is a very challenging problem even in a 1D earth. In a model with several reflectors, there is a set of internal multiples generated by each reflector in the data, and for different set of internal multiples, the amplitude difference between attenuation algorithm prediction and the real internal multiples is different. This elimination algorithm must have the capability to remove all the amplitude differences between attenuation algorithm prediction and the real internal

multiples for all sets of internal multiples. While the activity of finding higher order terms in ISS that can completely eliminate all internal multiples is undertaken, we derived an elimination algorithm from an alternative approach, i.e. using reverse engineering method as a guide and a way to understand the internal multiple elimination machinery in the ISS. This elimination algorithm can predict both correct time and amplitude of all first-order internal-multiples generated from all reflectors in a 1D earth. And it is closely related to ISS and preserves the following advantages of ISS attenuation

1. It only needs data, does not require any subsurface information.
2. It provides the capability to remove all first-order internal multiples without stripping.

And this elimination algorithm derived by using reverse engineering method is model type dependent. (The ISS internal-multiple attenuation algorithm is model type independent.)

ISS INTERNAL-MULTIPLE ATTENUATION ALGORITHM AND ATTENUATION FACTOR FOR A 1D NORMAL INCIDENCE SPIKE PLANE WAVE

First, we will give an introduction of the ISS internal-multiple attenuation algorithm before we introduce the internal-multiple elimination algorithm. The ISS internal-multiple attenuation algorithm is first given by Araújo et al. (1994) Weglein et al. (1997). The 1D normal incidence version of the algorithm is presented as follows:

$$b_3^{IM}(k) = \int_{-\infty}^{\infty} dz e^{ikz} b_1(z) \int_{-\infty}^{z-\varepsilon_2} dz' e^{-ikz'} b_1(z') \times \int_{z'+\varepsilon_1}^{\infty} dz'' e^{ikz''} b_1(z''). \quad (1)$$

Where $b_1(z)$ is the water speed migration of the data of a 1D normal incidence spike plane wave. ε_1 and ε_2 are two small positive numbers introduced to avoid self interactions. $b_3^{IM}(k)$ is the predicted internal multiples in the vertical wavenumber domain. This equation can predict the correct time and approximate amplitude of all first-order internal multiples.

The procedure of predicting a first-order internal multiple generated at the shallowest reflector is shown in figure 1. The ISS internal-multiple attenuation algorithm automatically uses three primaries in the data to predict a first-order internal multiple. (Note that this algorithm is model type independent and it takes account all possible combinations of primaries that can predict internal multiples.) From this figure we can see, every sub event on the left hand side experiences several phenomena making its way down to the earth then back to the receiver. When compared with the internal multiple on the right hand side, the events on the left hand side have extra transmission coefficients as shown in red. Multiplying all those extra transmission coefficients, we get the AF (attenuation factor) - $T_{01}T_{10}$ for this first-order internal multiple generated at the shallowest reflector. And all first-order internal multiples generated at the shallowest reflector have the same attenuation factor.

Figure 2 shows the procedure of predicting a first-order internal multiple generated at the next shallowest reflector. In this example, the attenuation factor is $(T_{01}T_{10})^2(T_{12}T_{21})$.

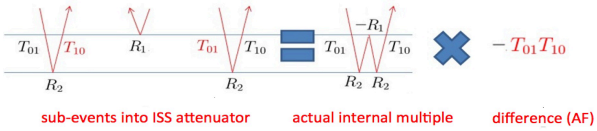

Figure 1: an example of the attenuation factor of a first-order internal multiple generated at the shallowest reflector, notice that all red terms are extra transmission coefficients

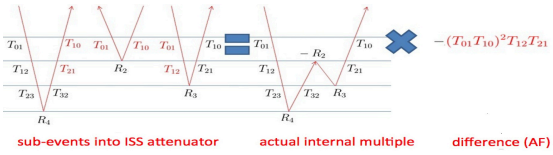

Figure 2: an example of the attenuation factor of a first-order internal multiple generated at the next shallowest reflector, notice that all red terms are extra transmission coefficients

The attenuation factor for predicting a multiple generated by the i^{th} reflector, AF_j, is given by the following:

$$AF_j = \begin{cases} T_{0,1}T_{1,0} & (for\ j=1) \\ \prod_{i=1}^{j-1}(T_{i-1,i}^2 T_{i,i-1}^2) T_{j,j-1}T_{j-1,j} & (for\ 1<j<J) \end{cases} \quad (2)$$

The attenuation factor AF_j can also be performed by using reflection coefficients:

$$AF_j = \begin{cases} 1-R_1^2 & (for\ j=1) \\ (1-R_1^2)^2(1-R_2^2)^2\cdots(1-R_j^2) & (for\ 1<j<J) \end{cases} \quad (3)$$

The subscript j represents the generating reflector, and J is the total number of interfaces in the model. The interfaces are numbered starting with the shallowest location. The attenuation factor is directly related to the trajectory of the events, which forms the prediction of the internal multiple.

ISS INTERNAL-MULTIPLE ELIMINATION ALGORITHM FOR A 1D NORMAL INCIDENCE SPIKE PLANE WAVE

The discussion above demonstrates that all first-order internal multiples generated at the same reflector have the same attenuation factor. We can observe that the attenuation factor contains all transmission coefficients from the shallowest reflector down to the reflector generating the multiple. And from the examples(shown in figure 1 and 2) we can observe that the middle event contains all the information about those transmission coefficients. Following early discussions and work in

Ramírez (2007) and Wilberth Herrera and Weglein (2012), our idea is to modify the middle term in the attenuation algorithm to remove the attenuation factor and make the attenuation algorithm an elimination algorithm. That is from

$$b_3^{IM}(k) = \int_{-\infty}^{\infty} dz e^{ikz} b_1(z) \int_{-\infty}^{z-\varepsilon_2} dz' e^{-ikz'} b_1(z') \times \int_{z'+\varepsilon_1}^{\infty} dz'' e^{ikz''} b_1(z'') \quad (4)$$

to

$$b_E^{IM}(k) = \int_{-\infty}^{\infty} dz e^{ikz} b_1(z) \int_{-\infty}^{z-\varepsilon_2} dz' e^{-ikz'} F[b_1(z')] \times \int_{z'+\varepsilon_1}^{\infty} dz'' e^{ikz''} b_1(z'') \quad (5)$$

where $F[b_1(z)]$ is an intermediate function we need to discover.

By introducing another intermediate function g(z) in which the amplitude of each event corresponds to a reflection coefficient, we discovered a way to construct $F[b_1(z)]$ by using $b_1(z)$ and g(z). After that, we find an integral equation about $b_1(z)$ and g(z). The $F[b_1(z)]$ is first proposed in Zou and Weglein (2013):

$$F[b_1(z) = \frac{b_1(z)}{[1-(\int_{z-\varepsilon}^{z+\varepsilon} dz' g(z'))^2][1-\int_{-\infty}^{z-\varepsilon} dz' b_1(z') \int_{z'-\varepsilon}^{z'+\varepsilon} dz'' g(z'')]^2} \quad (6)$$

$$g(z) = \frac{b_1(z)}{1-\int_{-\infty}^{z-\varepsilon} dz' b_1(z') \int_{z'-\varepsilon}^{z'+\varepsilon} dz'' g(z'')} \quad (7)$$

To derive the $F[b_1(z)]$ from $b_1(z)$, g(z) must first be solved in equation (7). Thereafter, g(z) is integrated into equation (6). Now we will show one way to solve these equations. By iterating $g(z)$ in (7), we can get more accurate approximation. Substitute more accurate approximations of $g(z)$ into $F[b_1(z)]$, we will achieve or obtain higher orders of approximation of the elimination algorithm which can predict correct amplitude of first-order internal multiples generated at deeper reflectors.

ISS INTERNAL-MULTIPLE ELIMINATION ALGORITHM FOR 1D PRESTACK DATA

The 1D prestack data is more complicated than 1D normal incidence data in two aspects: (1) The 1D prestack data has one more variable x (or k in wavenumber domain); (2)The reflection coefficients become angle dependent. Fortunately, following discussions and examples in Zou and Weglein (2014), we discovered that the same elimination algorithm scheme is still valid for 1D pre-stack data. Below shows the 1D prestack internal-multiple elimination algorithm, where $b_1(k,z)$ is the water speed uncollapsed Stolt migration of the data; $b_E^{IM}(k,2q)$ is the elimination algorithm prediction in wavenumber domain; $F[b_1(k,z)]$ and $g(k,z)$ are two intermediate functions and they are related by equation (9) and (10)

$$b_E^{IM}(k,2q) = \int_{-\infty}^{\infty} dz e^{2iqz} b_1(k,z) \int_{-\infty}^{z-\varepsilon_1} dz' e^{-2iqz'} F[b_1(k,z')] \times \int_{z'+\varepsilon_2}^{\infty} dz'' e^{2iqz''} b_1(k,z'') \quad (8)$$

$$F[b_1(k,z)] = \frac{1}{2\pi} \int_{-\infty}^{\infty} \int_{-\infty}^{\infty} dz' dq' \times \frac{e^{-iq'z} e^{iq'z'} b_1(k,z')}{[1-\int_{-\infty}^{z'-\varepsilon} dz'' b_1(k,z'') e^{iq'z''} \int_{z''-\varepsilon}^{z''+\varepsilon} dz''' g^*(k,z''') e^{-iq'z'''}]^2} \times \frac{1}{1-|\int_{z'-\varepsilon}^{z'+\varepsilon} dz'' g(k,z'') e^{iq'z''}|^2} \quad (9)$$

$$g(k,z) = \frac{1}{2\pi} \int_{-\infty}^{\infty} \int_{-\infty}^{\infty} dz' dq' \times \frac{e^{-iq'z} e^{iq'z'} b_1(k,z')}{1-\int_{-\infty}^{z'-\varepsilon} dz'' b_1(k,z'') e^{iq'z''} \int_{z''-\varepsilon}^{z''+\varepsilon} dz''' g^*(k,z''') e^{-iq'z'''}} \quad (10)$$

NUMERICAL TESTS FOR SYNTHETIC ELASTIC PP DATA

We test the 1D pre-stack internal multiple elimination algorithm for an four-reflector elastic model shown in figure 3. Figure 4 shows the PP data generated from this model by reflectivity method. Figure 5 and figure 6 show a section(2.8s-3.1s) of the data and attenuation and elimination prediction results.

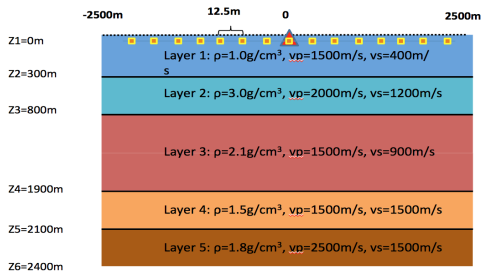

Figure 3: model

The left picture in figure 5 shows a section in the input data. In this section ,there are 3 major events interfering with each other: a converted P primary, an internal multiple generated from the first reflector and another internal multiple generated from the third reflector. The middle picture in figure 5 shows the attenuation algorithm predicted internal multiples,

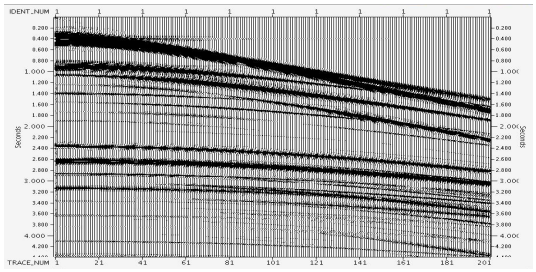

Figure 4: PP data

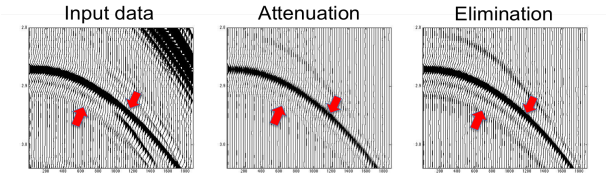

Figure 5: A section of the input data and prediction. Left: input data. Middle: attenuation algorithm prediction. Right:elimination algorithm prediction.

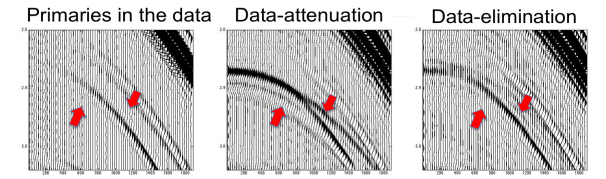

Figure 6: Left: primaries in the input data. Middle: data after internal multiples being attenuated. Right:data after internal multiples being eliminated.

it clearly shows the predicted internal multiples have correct time and approximate amplitude. The right picture in figure 5 shows the elimination algorithm prediction, the time is correct and the amplitude is more accurate. The left picture in figure 6 shows the primaries in the data. (Because it is a synthetic test, we can generate only the primaries and use them as a benchmark.) The middle picture in figure 6 shows the result by subtracting the attenuation algorithm prediction from the data. The internal multiples has been reduced, but there still remains residues. The right picture in figure 6 shows the result by subtracting the elimination algorithm prediction from the data. We can see that the multiples has been (almost) completed eliminated and the primary is recovered. (Note that there is still some small residues in the near offset due to the inaccuracy of numerical Hankel transform.)

A LIMITATION OF THIS ELIMINATION ALGORITHM AND AN ALGORITHM TO ADDRESS THE LIMITATION

There is a limitation of this elimination algorithm, that is, the primaries in the reflection data that enters the algorithm provides that elimination capability, automatically without requiring the primaries to be identified or in any way separated. The other events in the reflection data, that is, the internal multiples, may alter the amplitude and need assist to completely eliminate the internal multiples. That is a limitation of this elimination algorithm. To deal with this limitation, we can first use ISS internal multiple attenuation algorithm prediction (b_3) to attenuate the internal multiples in the data (b_1) and then put the subtracted result, i.e., b_1+b_3, which contains primaries and attenuated internal multiples, into the ISS internal multiple elimination algorithm to predict internal multiples with more accurate amplitude. (Note that in the numerical test, this limitation has very small affect on the prediction, thus we do not need to consider addressing this limitation in this test. However, for certain situation, we need to consider this limitation.)

CONCLUSION

The ISS internal multiple elimination algorithm is a part of the three-pronged strategy which is especially relevant and provide value when primaries and internal multiples are proximal to and/or interfere with each other in both on-shore and offshore data. While the activity of finding higher order terms in ISS that can completely eliminate all internal multiples in multi-D is undertaken, we derive an elimination algorithm from a reverse engineering approach and use it as a guide and a way to understand the internal multiple elimination machinery in the ISS. In this paper, we discussed the 1D pre-stack ISS internal multiple elimination algorithm for all first-order internal multiples from all reflectors and tested this algorithm with an elastic synthetic PP data. The result shows that this ISS internal multiple elimination algorithm can predict more accurate amplitude of the internal multiples than the attenuation algorithm.

This reverse engineering approach launched by understanding the properties of the ISS attenuation algorithm, and in 1D, reverse engineering a solution, was based on the input being primaries. The primaries in the reflection data that enters the algorithm provide that elimination capability, automatically without our requiring the primaries to be identified or in any way separated. The other events in the reflection data, that is, the internal multiples, will not be helpful in this elimination scheme. This can be a limitation and can sometimes have significant affect on the prediction. We also provide an algorithm to address this limitation in the last section.

ACKNOWLEDGMENTS

We are grateful to all M-OSRP sponsors for encouragement and support in this research. We would like to thank Schlumberger Limited for the test data. We would like to thank all our coworkers for their help in reviewing this paper and valuable discussions.

REFERENCES

Araújo, F. V., A. B. Weglein, P. M. Carvalho, and R. H. Stolt, 1994, Inverse scattering series for multiple attenuation: An example with surface and internal multiples: SEG Technical Program Expanded Abstracts, 1039–1041.

H. Liang, C. M., and A. B. Weglein, 2012, A further general modification of the leading order iss attenuator of first-order internal multiples to accommodate primaries and internal multiples when an arbitrary number of reflectors generate the data: theory, development, and examples: Mission Oriented Seismic Research Program Annual Report, 148–165.

Ma, C., H. Liang, and A. B. Weglein, 2012, Modifying the leading order iss attenuator of first-order internal multiples to accommodate primaries and internal multiples: fundamental concept andtheory, development, and examples exemplified when three reflectors generatethe data: Mission Oriented Seismic Research Program Annual Report, 133–147.

Ma, C., and A. B. Weglein, 2014, Including higher-order inverse scattering series (iss) terms to address a serious shortcoming/problem of the iss internal-multiple attenuator: exemplifying the problem and its resolution: SEG Technical Program Expanded Abstracts.

Ramírez, A. C., 2007, 1.-inverse scattering subseries for removal of internal multiples and depth imaging primaries; 2.-green's theorem as the foundation of interferometry and guiding new practical methods and applications: PhD thesis, University of Houston.

Weglein, A. B., 2014, Multiple attenuation: The status and a strategy that identifies and addresses current challenges.

Weglein, A. B., F. V. Araújo, P. M. Carvalho, R. H. Stolt, K. H. Matson, R. T. Coates, D. Corrigan, D. J. Foster, S. A. Shaw, and H. Zhang, 2003, Inverse scattering series and seismic exploration: Inverse Problems, R27–R83.

Weglein, A. B., F. A. Gasparotto, P. M. Carvalho, and R. H. Stolt, 1997, An inverse-scattering series method for attenuating multiples in seismic reflection data: Geophysics, **62**, 1975–1989.

Wilberth Herrera, Chao Ma, H. L. P. T., and A. B. Weglein, 2012, Progressing amplitude issues for testing 1d analytic data in leading order internal multiple algorithms: Mission Oriented Seismic Research Program Annual Report, 167–188.

Zou, Y., and A. B. Weglein, 2013, Internal multiple removal: an amplitude correction equation for internal-multiple attenuator(1d normal incidence): Mission Oriented Seismic Research Program Annual Report, 167–188.

———, 2014, An internal-multiple elimination algorithm for all reflectors for 1d earth part i: strengths and limitations: Journal of seismic exploration.

Direct depth imaging without a velocity model: update and Marmousi model tests

Fang Liu and Arthur B. Weglein, Mission-Oriented Seismic Research Program, University of Houston

SUMMARY

The inverse scattering subseries for direct depth imaging without a velocity model has demonstrated its viability on synthetic and field data. The current direct depth imaging algorithm is: (1) closed form and very fast, and (2) represents only a very small portion of the depth imaging terms/capability within the inverse scattering (ISS) series. In this paper, we demonstrated the effectiveness of the current depth imaging algorithm on the Marmousi data set. Equally important, we witness the promise and potential of direct depth imaging algorithm from the inverse scattering series and its moving closer to belonging in our seismic depth imaging toolbox, taking its place alongside its siblings for free surface and internal multiple removal.

THEORY

In the inverse scattering series (Weglein et al., 2000, 2002), the perturbation α is defined as the difference between the actual and reference velocity: $\frac{1}{c^2}=\frac{1}{c_0^2}(1-\alpha)$, where c is the spatially varying actual velocity, c_0 (in this example just homogeneous water velocity for the entire space) is the reference velocity. In 2D, both α and c are functions of depth z and lateral variable x. The perturbation α is separated into an infinite series in terms of their order of dependence in terms of the data at the measurement surface:

$$\alpha(x,z)=\alpha_1+\alpha_2+\alpha_3+\cdots \tag{1}$$

where the first term α_1 is essentially equivalent to prestack FK migration.

$$\begin{aligned}\alpha_1(k_m,k_z,\theta)&=-4\frac{q_g q_s}{\omega^2/c_0^2}D(k_m,k_z,\omega),\\ \omega&=\frac{c_0k_z}{2}\sqrt{\frac{k_z^2+k_m^2}{k_z^2\cos^2\theta-k_m^2\sin^2\theta}}.\end{aligned} \tag{2}$$

Seismic data, originally a function of time t, x_s (source lateral coordinate) and x_g (receiver lateral coordinate), are sorted into x_m (mid-point) and x_h (offset) domain, and are then Fourier transformed into k_m (the Fourier conjugate of x_m), k_h (the Fourier conjugate of x_h) and ω (temporal frequency) domain to compute the data D in the right-hand-side of equation (2). In the calculation, we choose $k_m=k_g-k_s$, $k_h=k_g+k_s=2\sin\theta\omega/c_0$. And equation (2) can be Fourier transformed from k_m to x, and k_z to z to have α_1 in the spatial (x,z) domain. Note that although α is not a function of the parameter θ, its Born approximation α_1 is. This is the reason why specular reflections are not flat in the angle (or common-image) gather domain, in other words, are imaged at different depth for different angles θ, when employing a constant velocity FK migration.

The second term α_2 can be computed from the first term α_1 as:

$$\alpha_2(x,z)=\alpha_{21}+\alpha_{22}+\alpha_{23}, \tag{3}$$

where its first two terms are:

$$\begin{aligned}\alpha_{21}&=-\frac{\alpha_1^2(x,z)}{2}-\frac{\partial\alpha_1(x,z)}{2\partial z}\int_{-\infty}^{z}\alpha_1(x,z')dz',\\ \alpha_{22}&=\frac{\partial\alpha_1(x,z)}{2\partial x}\int_{-\infty}^{z}dz'\int_{-\infty}^{z'}dz''\frac{\partial\alpha_1(x,z'')}{\partial x}.\end{aligned} \tag{4}$$

And the third term is expressed in the k domain as:

$$\begin{aligned}\widetilde{\alpha}_{23}(k,z)=\frac{1}{8\pi^2}\int_{-\infty}^{\infty}\widetilde{\alpha}_1(\frac{k}{2}-k',z')\int_{-\infty}^{z'}\widetilde{\alpha}_1(\frac{k}{2}+k',z'')\\ \times\widetilde{\xi}_2\left(k,k',\frac{z'+z''}{2}-z,\frac{z'-z''}{2}\right)dz'dz'',\end{aligned} \tag{5}$$

where $\widetilde{\xi}_2(k,k',\varepsilon_0,\varepsilon_1)=\int_{-\infty}^{\infty}e^{i(\varepsilon_0+\varepsilon_1)k_z}(i(k_z^2+k_m^2)/(u_1)e^{i\Delta\psi}-ik_z+\varepsilon_1a_1/2)$, $a_1=k^2-4k'^2$, $u_1=\sqrt{k_z^2+a_1}$, $\Delta\psi=\varepsilon_1(u_1-k_z)$.

So far the second term of α_{21} (the only term in α_2 that does not vanish if the earth has no lateral variation) has been incorporated into the leading-order imaging subseries (LOIS) (Shaw, 2005) and higher-order imaging subseries (HOIS). The other two terms α_{22} and α_{23} will vanish if the earth does not vary laterally, in other words, laterally exclusive (LE) terms.

$$\alpha^{\mathtt{LOIS}}(x,z)=\alpha_1\left(x,z-\frac{1}{2}\int_{-\infty}^{z}\alpha_1(x,z')dz'\right), \tag{6}$$

$$\alpha^{\mathtt{HOIS}}(x,z+\frac{1}{2}\int_{-\infty}^{z}dz'\frac{\alpha_1(x,z')}{\cos^2\theta-\frac{\alpha_1(x,z')}{4}})=\alpha_1(x,z). \tag{7}$$

Both LOIS and HOIS are task-specific subseries for seismic imaging and aim to further migrate primaries in α_1 to their actual location without updating the migration velocity c_0. If the imaging subseries has achieved the actual depth of a reflector, which is independent of the angle θ, the reflector image

should be migrated to the same depth for all angles, or in other words, flattened. This is how can the flatness of events in the angle gather be used as a benchmark for the effectiveness of our algorithm, although the flatness of events does not enter the procedure anywhere.

THE MARMOUSI MODEL AND OUR FINITE-DIFFERENCE MODELING PROCEDURE

The Marmousi model is one of the well know benchmark seismic imaging challenges. The original model is sampled every $1.25(m)$ in both the vertical and the horizontal directions. In the modeling procedure we resample it at $5(m)$ and boost the the wave speed of a low velocity region to water velocity ($1500m/s$) to accomodate the coarser $5(m)$ sampling. In the framework set up in Weglein et al. (2000, 2002), α_1 is the first term in the seismic imaging subseries and is essentially equivalent to a prestack Stolt migration with constant velocity. In this note, α_1 (the first term of inverse scattering series) and the subsequent higher-order imaging subseries are shown. For this model with very big velocity contrast (the highest velocity being $4700m/s$ vs the reference $1500m/s$ water speed) and large lateral variation, the idea of purposeful perturbation (see Weglein (2006) for detail) observed in all previous simpler imaging challenges still holds for the much more complicated Marmousi model.

There are hundreds of reflectors (horizons) in the Marmousi model, to display all of them at the same time will block a significant portion of the data. Therefore in each figure we selected only the major reflectors for display.

The original Marmousi model (see Figure 1) has a small region of very low velocity. Since the wavelength of seismic wave is shorter in the low velocity zone, the extreme low velocity requires very fine sampling in both the x and z directions. Since this low velocity zone is located in the portion of the model with very mild lateral variation, the low velocity contrast by itself (without large lateral variation) was not a major challenge for HOIS. This modification (shown in Figure 2) does not reduce the imaging challenge for our direct depth imaging.

In the finite difference modeling procedure, the interval between two adjacent time step is $0.5ms$, but the sampling interval in the output is $2ms$ to follow the standard choice in seismic data. A typical shot gather is shown in Figure 3. In the modeling procedure, only the P-wave velocity is used.

The wavelet used in the finite-difference procedure is the first derivative of a Gaussian function, lacking zero frequency information. Just as our previous numerical examples in Liu (2006) and real data example in Weglein et al. (2012), low frequency is not an issue. Limited aperture, or lack of data, often seriously compromise a lateral Fourier transform, and evaporize the inherent logic between seismic events that crystalizes in the k-domain, just as shown in internal multiple attenuation examples.

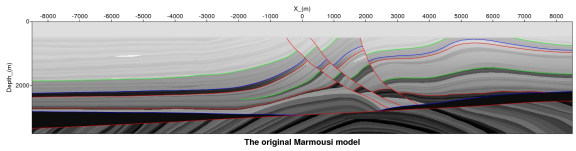

Figure 1: The original Marmousi model. The wave speed of the low velocity region in this model (shown by the bright zone with x-coordinate between $-6000(m)$ and $-5000(m)$) will be boosted to water speed ($1500m/s$). The colored horizons are major reflectors in the model.

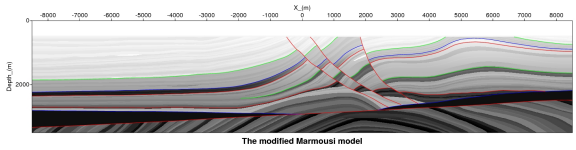

Figure 2: The modified Marmousi model. The modification happened between $x = -6000m$ and $x = -5000m$ where the lateral variation is mild. The low velocity values are boosted to water speed ($1500m/s$). The colored horizons are major reflectors in the model.

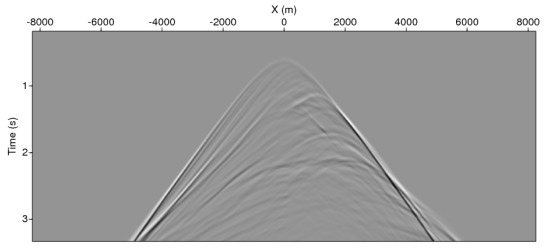

Figure 3: The shot gather with the shot location: $x_s = 0(m)$.

IMAGING RESULTS

The α_1 result for $\theta = 0$ is shown in Figure 4, its corresponding HOIS result is shown in Figure 5. The computational cost from α_1 to $\alpha^{\mathtt{HOIS}}$ is extremely low: 30% of FK migration, but diffractions are not delt with since they are laterally exclusively phenonmena expressed in terms (such as α_{22} and α_{23}).

HOIS results for $\theta = 9^\circ$ (Figure 6) is also shown to demonstrate the fact that: while specular reflections are almost identical for different angle θ, diffractions swings around noticeably for different θ. This is the reason why after summing the HOIS image from all angles (see Figure 8), the specular reflections are boosted and the diffractions are much reduced.

The Marmousi model is the most complicated model we had tested on the inverse scattering based imaging, yet the same dependendable purposefulness of the terms is observed:

1. The common-image gather becomes flat where the correct depth is achieved although the flatness of the common-

image gather does not enter the algorithm. And the bigger the distance from the final image to its actual location, the bigger the curvature of the event in the common-image gather.

2. In the common-image gather the flattening effect is much stronger on specular reflections than on diffractions.

One surprise is that, after summing the imaging results from all angles, the reduction of diffractions is the most effective for the Marmousi experiment compared with all previous models we had tested.

CONCLUSIONS

Testing the current imaging algorithm with partial capture of the direct depth ISS imaging terms demonstrates encouraging results on the Marmousi model data set. HOIS represents only a small fraction of ISS imaging terms. Therefore further ISS terms, for example HOIS+LE (Wang and Weglein, 2010) add further imaging capability that includes terms that only contribute for laterally varying media, and similarly, the laterally exclusive term in α_{23} will be studied and evaluated to incorporate and provide a more effective and capable imaging algorithm. This test is next important milestone on the road for ISS depth imaging toolbox. The promise and potential is to provide an accurate depth image under complex and daunting imaging challenges, where: (1) an adequate velocity cannot be determined and/or (2) the inability to depth image beneath a know and complex velocity model. It will play the same role for depth imaging that inverse scattering free surface and internal multiple removal. They are cut from the same cloth, and will provide differential added value under the same complex and daunting circumstances.

ACKNOWLEDGMENTS

The authors would like to thank all M-OSRP members and sponsors. This work has been partially funded by NSFCMG award DMS-0327778 and DOE Basic Energy Sciences Award DE-FG02-05ER15697. The Marmousi model was downloaded by the first author from the website of the Allied Geophysical Laboratory of University of Houston.

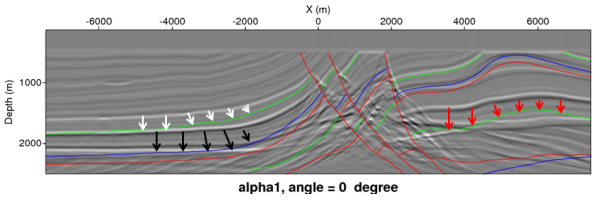

Figure 4: The α_1 imaging result (equivalent with FK migration with $p_h = 0$ or $k_h = 0$). The α_1 result corresponding to equation (2) in this paper and the first and original reference is equation (2.22) of Liu (2006).

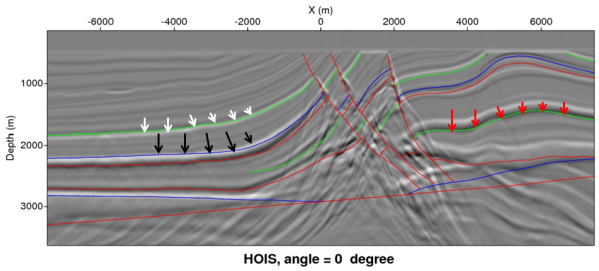

Figure 5: The HOIS imaging result after the calculation of α_1 in Figure 4. The formula to compute this inverse scattering series image is equation (7) of this paper and the first and original reference is equation (2.34) of Liu (2006).

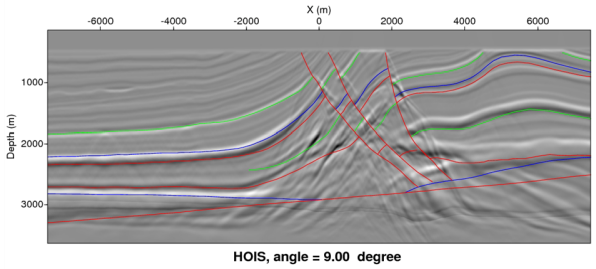

Figure 6: HOIS imaging result for angle $\theta = 9^\circ$.

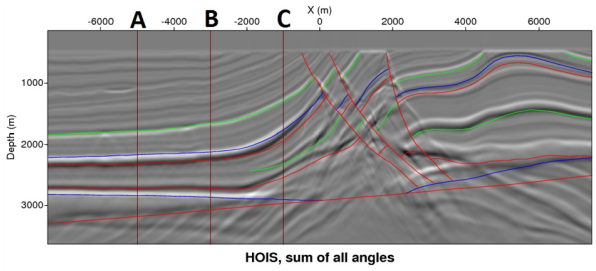

Figure 7: A, B, and C indicate the three locations where the common-image gather analysis in Figure 9 is carried out.

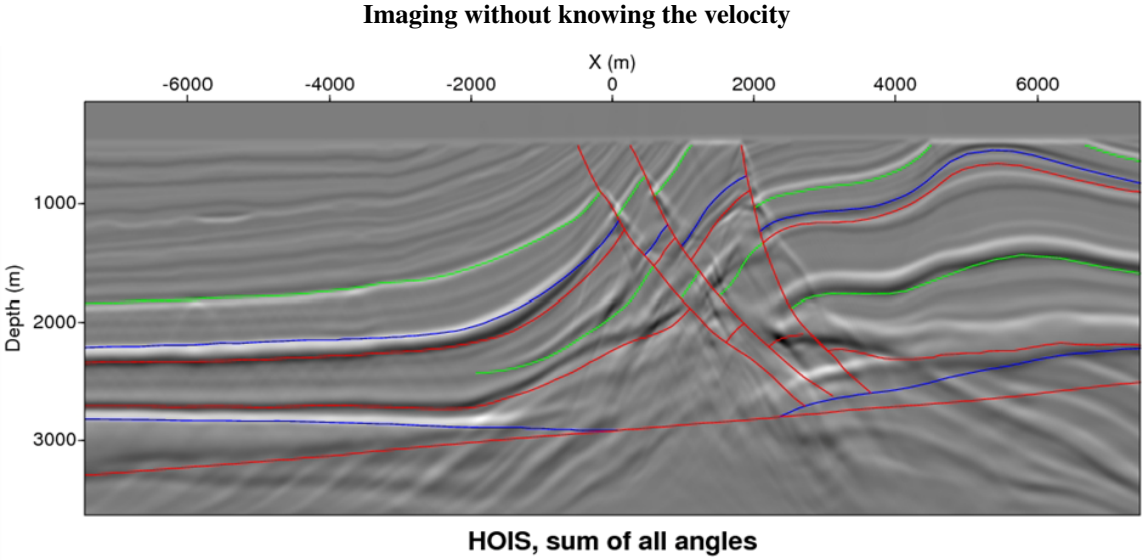

Figure 8: The sum of all HOIS imaging results from all 101 angles between $\theta = 0°$ and $\theta = 9°$.

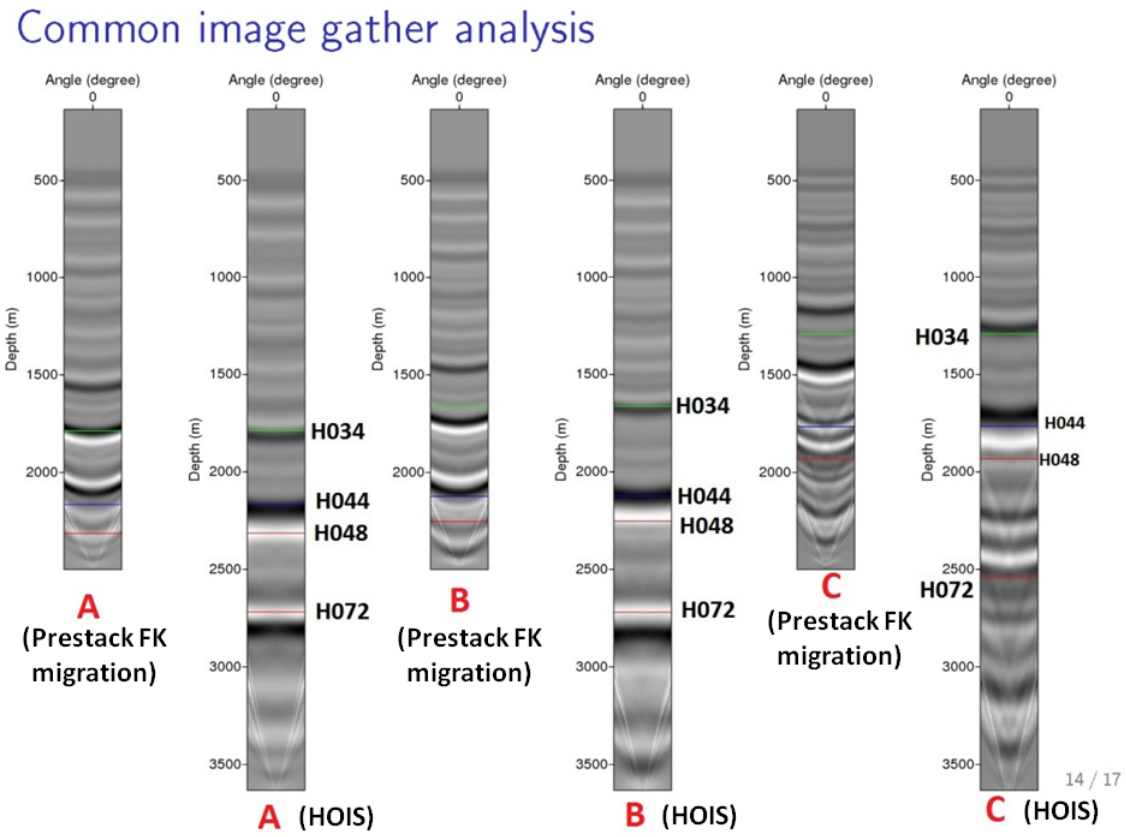

Figure 9: Angle gathers, from left to right: α_1 at location A ($x = -5000(m)$), HOIS at location A; α_1 at location B ($x = -3000(m)$), HOIS at location B; α_1 at location C ($x = -1000(m)$), HOIS at location.

REFERENCES

Liu, F., 2006, Multi-dimensional depth imaging without an adequate velocity model: PhD thesis, University of Houston.

Shaw, S. A., 2005, An inverse scattering series algorithm for depth imaging of reflection data from a layered acoustic medium with an unknown velocity model: PhD thesis, University of Houston.

Wang, Z., and A. B. Weglein, 2010, An investigation of iss imaging algorithms beyond hois, to begin to address exclusively laterally varying imaging challenges: M-OSRP Annual Report, **10**, 105–114.

Weglein, A. B., 2006, Introduction and overview: Mosrp06: M-OSRP Annual Report, **6**, 1–4.

Weglein, A. B., D. J. Foster, K. H. Matson, S. A. Shaw, P. M. Carvalho, and D. Corrigan, 2002, Predicting the correct spatial location of reflectors without knowing or determining the precise medium and wave velocity: initial concept, algorithm and analytic and numerical example: Journal of Seismic Exploration, **10**, 367–382.

Weglein, A. B., F. Liu, X. Li, P. Terenghi, E. Kragh, J. D. Mayhan, Z. Wang, J. Mispel, L. Amundsen, H. Liang, L. Tang, and S. Hsu, 2012, First field data examples of inverse scattering series direct depth imaging without the velocity model, *in* 76th Annual Internat. Mtg., Soc. Expl. Geophys., Expanded Abstracts: Soc. Expl. Geophys., 1–6.

Weglein, A. B., K. H. Matson, D. J. Foster, P. M. Carvalho, D. Corrigan, and S. A. Shaw, 2000, Imaging and inversion at depth without a velocity model: Theory, concepts and initial evaluation, *in* 70th Annual Internat. Mtg., Soc. Expl. Geophys., Expanded Abstracts: Soc. Expl. Geophys., 1016–1019.

A direct inverse solution for AVO/FWI parameter estimation objectives

Arthur B. Weglein, M-OSRP/Department of Physics/University of Houston

Summary

A direct inverse solution is derived from the operator identity relating the change in a medium's properties and the commensurate change in the wavefield. The direct solution is in the form of a series, called the inverse scattering series (ISS). Each term in the series is directly computed in terms of the recorded data, and, without subsurface information. There are isolated task inverse scattering subseries that perform: free surface multiple removal, internal multiple removal, depth imaging, parameter estimation and Q compensation, and each achieves its objective directly and without subsurface information. The general operator identity is combined with the elastic wave equation to form a specific direct solution for changes in elastic properties and density. This paper describes the resulting data requirements and algorithms, a distinct ISS parameter estimation subseries, that provides a fundamental framework and platform for all seismic amplitude analysis and is directly relevant for the objectives of AVO and FWI. A view of a balanced and appropriate role for direct and indirect methods will be presented, as well.

Introduction

Inversion methods can be classified as direct or indirect. An example of a direct solution is given by the solution of the quadratic equation

$$ax^2 + bx + c = 0, \tag{1}$$

as

$$x = \frac{-b \pm \sqrt{b^2 - 4ac}}{2a} \tag{2}$$

whereas an indirect solution could be to find x such that $(ax^2 + bx + c)^2$ is a minimum. Among indicators, identifiers and examples of "indirect" inverse solutions are: (1) model matching, (2) objective/cost functions, (3) search algorithms, (4) iterative linear inversion and (5) methods corresponding to necessary and not sufficient conditions, e.g., CIG flatness.

The Operator Identity

We begin our discussion of direct inverse solutions with the key operator identity mentioned above. Let L_0, G_0, L, and G be the differential operators and Green's functions for the reference and actual media, respectively, that satisfy:

$$L_0 G_0 = \delta \qquad LG = \delta$$

where δ is a Dirac delta function. Define the perturbation operator, V and the scattered wavefield, as follows:

$$V = L_0 - L \qquad \psi_s = G - G_0.$$

The relationship

$$G = G_0 + G_0 V G \tag{3}$$

is an operator identity that follows from

$$L^{-1} = L_0^{-1} + L_0^{-1}(L_0 - L)L^{-1}.$$

For modeling the wavefield, G, for a medium described by L

$$L \to G \qquad L_0, V \to G$$

where the second form has L entering the modeling algorithms in terms of L_0 and V. Modeling using scattering theory requires a complete and detailed knowledge of medium properties.

Direct Forward and Direct Inverse

The operator identity equation 3 can be solved for G as

$$G = (1 - G_0 V)^{-1} G_0 \tag{4}$$

and

$$G = G_0 + G_0 V G_0 + G_0 V G_0 V G_0 + \dots . \tag{5}$$

Equation 5 has the form of a generalized Geometric series

$$G - G_0 = S = ar + ar^2 + \cdots = \frac{ar}{1 - r} \tag{6}$$

where we identify $a = G_0$ and $r = VG_0$ in equation 5, and

$$S = S_1 + S_2 + S_3 + \dots . \tag{7}$$

The portion of S that is linear, quadratic, $\dots$ in r are:

$$S_1 = ar$$
$$S_2 = ar^2$$
$$\vdots$$

and the sum is

$$S = \frac{ar}{1 - r}. \tag{8}$$

Solving equation 8 for r, produces the inverse geometric series,

$$r = \frac{S/a}{1+S/a} = S/a - (S/a)^2 + (S/a)^3 + \dots \\ = r_1 + r_2 + r_3 + \dots$$

and is the simplest prototype inverse series, that is, the inverse of the geometric series. For the seismic inverse problem, we associate S with the measured data

$$S = (G - G_0)_{ms} = \text{Data}$$

and the forward and inverse series follow from treating the forward solution as S in terms of V, and the inverse solution from V in terms of S

$$V = V_1 + V_2 + \dots \tag{9}$$

where V_n is the portion of V, that is nth order in the data. Equation 8 is the forward series; and equation 9 is the inverse series. The identity, equation 3, provides a Geometric forward series rather than a Taylor series. In general, a Taylor series doesn't have an inverse series; however, a Geometric series has an inverse series. All conventional current mainstream inversion, including iterative linear inversion and FWI, are based on a Taylor series concept. Solving a forward problem in an inverse sense is not the same as solving an inverse problem directly.

The r_1, r_2, ... terms in

$$r = S/a - (S/a)^2 + (S/a)^3 + \dots \\ = r_1 + r_2 + r_3 + \dots$$

generalize for the seismic inverse in terms of $V_1, V_2, \dots,$ and G_0, G, $D = (G - G_0)_m$ as follows (see, e.g., Weglein et al., 2003)

$$\begin{aligned} G_0V_1G_0 =& D \\ G_0V_2G_0 =& -G_0V_1G_0V_1G_0 \\ G_0V_3G_0 =& -G_0V_1G_0V_1G_0V_1G_0 \\ & -G_0V_1G_0V_2G_0 - G_0V_2G_0V_1G_0 \\ & \vdots \end{aligned} \tag{10}$$

The operator identity for the 2D heterogeneous elastic wave equation

We exemplify the method for a 2D elastic heterogeneous earth. The starting point for the 3D generalization is found in Stolt and Weglein (2012). The 2D elastic wave equation for a heterogeneous isotropic medium is

$$L\vec{u} = \begin{pmatrix} f_x \\ f_z \end{pmatrix} \qquad \hat{L}\begin{pmatrix} \phi^P \\ \phi^S \end{pmatrix} = \begin{pmatrix} F^P \\ F^S \end{pmatrix}. \tag{11}$$

$\vec{u}$, f_x, f_z are the displacement and force, in displacement coordinates and ϕ_P, ϕ_S and F^P, F^S are the P and S waves and the force components in P and S coordinates. The operators L, L_0 and V are

$$\begin{aligned} L =& \left[\rho\omega^2 \begin{pmatrix} 1 & 0 \\ 0 & 1 \end{pmatrix} + \right. \\ & \left. \begin{pmatrix} \partial_x\gamma\partial_x + \partial_z\mu\partial_z & \partial_x(\gamma - 2\mu)\partial_z + \partial_z\mu\partial_x \\ \partial_z(\gamma - 2\mu)\partial_x + \partial_x\mu\partial_z & \partial_z\gamma\partial_z + \partial_x\mu\partial_x \end{pmatrix}\right] \\ L_0 =& \left[\rho\omega^2 \begin{pmatrix} 1 & 0 \\ 0 & 1 \end{pmatrix} + \right. \\ & \left. \begin{pmatrix} \gamma_0\partial_x^2 + \mu_0\partial_z^2 & (\gamma_0 - \mu_0)\partial_x\partial_z \\ (\gamma_0 - \mu_0)\partial_x\partial_z & \mu_0\partial_x^2 + \gamma_0\partial_z^2 \end{pmatrix}\right] \text{ and} \\ V \equiv& L_0 - L \\ =& \begin{bmatrix} a_\rho\omega^2 + \alpha_0^2\partial_x a_\gamma\partial_x + \beta_0^2\partial_z a_\mu\partial_z \\ \partial_z(\alpha_0^2 a_\gamma - 2\beta_0^2 a_\mu)\partial_x + \beta_0^2\partial_x a_\mu\partial_z \\ \partial_x(\alpha_0^2 a_\gamma - 2\beta_0^2 a_\mu)\partial_z + \beta_0^2\partial_z a_\mu\partial_x \\ a_\rho\omega^2 + \alpha_0^2\partial_z a_\gamma\partial_z + \beta_0^2\partial_x a_\mu\partial_x \end{bmatrix}. \end{aligned}$$

The quantities $a_\rho \equiv \rho/\rho_0 - 1$, $a_\gamma \equiv \gamma/\gamma_0 - 1$, $a_\mu \equiv \mu/\mu_0 - 1$ are defined in terms of γ_0, μ_0, ρ_0, γ, μ, ρ, the bulk modulus, shear modulus and density in the reference and actual media, respectively.

The forward problem is found from the identity equation 5 and the elastic wave equation 11 (in PS coordinates) as

$$\begin{aligned} \hat{G} - \hat{G}_0 =& \hat{G}_0\hat{V}\hat{G} = \hat{G}_0\hat{V}\hat{G}_0 + \hat{G}_0\hat{V}\hat{G}_0\hat{V}\hat{G}_0 + \dots \\ \begin{pmatrix} \hat{D}^{PP} & \hat{D}^{PS} \\ \hat{D}^{SP} & \hat{D}^{SS} \end{pmatrix} =& \begin{pmatrix} \hat{G}_0^P & 0 \\ 0 & \hat{G}_0^S \end{pmatrix}\begin{pmatrix} \hat{V}^{PP} & \hat{V}^{PS} \\ \hat{V}^{SP} & \hat{V}^{SS} \end{pmatrix}\begin{pmatrix} \hat{G}_0^P & 0 \\ 0 & \hat{G}_0^S \end{pmatrix} \\ & + \begin{pmatrix} \hat{G}_0^P & 0 \\ 0 & \hat{G}_0^S \end{pmatrix}\begin{pmatrix} \hat{V}^{PP} & \hat{V}^{PS} \\ \hat{V}^{SP} & \hat{V}^{SS} \end{pmatrix}\begin{pmatrix} \hat{G}_0^P & 0 \\ 0 & \hat{G}_0^S \end{pmatrix} \\ & \times \begin{pmatrix} \hat{V}^{PP} & \hat{V}^{PS} \\ \hat{V}^{SP} & \hat{V}^{SS} \end{pmatrix}\begin{pmatrix} \hat{G}_0^P & 0 \\ 0 & \hat{G}_0^S \end{pmatrix} + \dots \end{aligned} \tag{12}$$

and the inverse solution, equation 10, for the elastic equation 11 is

$$\begin{aligned} & \begin{pmatrix} \hat{D}^{PP} & \hat{D}^{PS} \\ \hat{D}^{SP} & \hat{D}^{SS} \end{pmatrix} = \begin{pmatrix} \hat{G}_0^P & 0 \\ 0 & \hat{G}_0^S \end{pmatrix}\begin{pmatrix} \hat{V}_1^{PP} & \hat{V}_1^{PS} \\ \hat{V}_1^{SP} & \hat{V}_1^{SS} \end{pmatrix}\begin{pmatrix} \hat{G}_0^P & 0 \\ 0 & \hat{G}_0^S \end{pmatrix} \\ & \begin{pmatrix} \hat{G}_0^P & 0 \\ 0 & \hat{G}_0^S \end{pmatrix}\begin{pmatrix} \hat{V}_2^{PP} & \hat{V}_2^{PS} \\ \hat{V}_2^{SP} & \hat{V}_2^{SS} \end{pmatrix}\begin{pmatrix} \hat{G}_0^P & 0 \\ 0 & \hat{G}_0^S \end{pmatrix} \\ =& -\begin{pmatrix} \hat{G}_0^P & 0 \\ 0 & \hat{G}_0^S \end{pmatrix}\begin{pmatrix} \hat{V}_1^{PP} & \hat{V}_1^{PS} \\ \hat{V}_1^{SP} & \hat{V}_1^{SS} \end{pmatrix}\begin{pmatrix} \hat{G}_0^P & 0 \\ 0 & \hat{G}_0^S \end{pmatrix} \\ & \times \begin{pmatrix} \hat{V}_1^{PP} & \hat{V}_1^{PS} \\ \hat{V}_1^{SP} & \hat{V}_1^{SS} \end{pmatrix}\begin{pmatrix} \hat{G}_0^P & 0 \\ 0 & \hat{G}_0^S \end{pmatrix}. \end{aligned} \tag{13}$$

where, for example, $\hat{V}^{PP} = \hat{V}_1^{PP} + \hat{V}_2^{PP} + \hat{V}_3^{PP} + \dots$ and any one of the four matrix elements of V requires

$$\begin{pmatrix} \hat{D}^{PP} & \hat{D}^{PS} \\ \hat{D}^{SP} & \hat{D}^{SS} \end{pmatrix}.$$

A few key points

$\hat{D}^{PP}$ can be determined in terms of

$$\begin{pmatrix} \hat{V}^{PP} & \hat{V}^{PS} \\ \hat{V}^{SP} & \hat{V}^{SS} \end{pmatrix}$$

and $\hat{V}^{PP}$ or $\hat{V}^{PS}$, $\hat{V}^{SP}$, $\hat{V}^{SS}$ require a series in

$$\begin{pmatrix} \hat{D}^{PP} & \hat{D}^{PS} \\ \hat{D}^{SP} & \hat{D}^{SS} \end{pmatrix}.$$

That's what the general relationship $G = G_0 + G_0VG$ requires, that is, a direct non-linear inverse solution is a solution order by order in the data matrix (in 2D)

$$\begin{pmatrix} \hat{D}^{PP} & \hat{D}^{PS} \\ \hat{D}^{SP} & \hat{D}^{SS} \end{pmatrix}.$$

The direct solution is not iterative linear inversion. Iterative linear starts with

$$G_0V_1G_0 = D, \tag{14}$$

solves for V_1, changes the reference medium, finds a new L_0 and G_0 (and require generalized inverses of noisy bandlimited data dependent operators). The next linear step involves V_1',

$$\begin{aligned} G_0'V_1'G_0' &= D' = (G - G_0')_{ms} \\ L_0' &= L_0 - V_1 \\ L_0'G_0' &= \delta \end{aligned}$$

where V_1' is the portion of V linear in the data $(G-G_0')_{ms}$. The direct inverse solution equations 9 and 13 call for a single unchanged reference medium, for computing $V_1, V_2, \ldots$. For a homogeneous reference medium they are obtained by an analytic inverse. The inverse to find V_1 from data, is the same inverse to find $V_2, V_3, \ldots$, from equation 10. There are no numerical inverses, no generalized inverses, no inverses of matrices that contain noisy bandlimited data.

The difference between iterative linear and the direct inverse of equation 13 is much more substantive and serious than merely a different way to solve $G_0V_1G_0 = D$, equation 14, for V_1. If equation 14 is our entire basic theory, you can mistakenly think that $\hat{D}^{PP} = \hat{G}_0^P\hat{V}_1^{PP}\hat{G}_0^P$ is sufficient to update $\hat{D}^{PP} = \hat{G}_0^{P\,\prime}\hat{V}_1^{PP\,\prime}\hat{G}_0^{P\,\prime}$. That step loses contact with and violates the basic operator identity $G = G_0 + G_0VG$ for the elastic wave equation. That's as serious as considering problems involving a right triangle and violating the Pythagorean theorem in your method.

That is, iteratively updating PP data with an elastic model violates the basic relationship between changes in a medium, V and changes in the wavefield, $G - G_0$ for the simplest elastic earth model.

This direct inverse method provides a platform for amplitude analysis, AVO and FWI. It communicates when a "FWI" method should work, in principle. Iteratively inverting multi-component data has the correct data but doesn't corresponds to a direct inverse algorithm. To honor $G = G_0 + G_0VG$, you need both the data and the algorithm that direct inverse prescribes. Not recognizing the message that an operator identity and the elastic wave equation unequivocally communicate is a fundamental and significant contribution to the gap in effectiveness in current AVO and FWI method and application (equation 13). This analysis generalizes to 3D with P, S_h, and S_v data.

There's a role for direct and indirect methods in practical real world application. Indirect methods are to be called upon for recognizing that the world is more complicated than the physics that we assume in our models and methods. For the part of the world that you are capturing in your model (and methods) nothing compares to direct methods for clarity and effectiveness. The listed references provide detail and examples. An optimal indirect method would seek to satisfy a cost function that derives from a property of the direct method. In that way the indirect and direct method would be aligned and cooperative for accommodating the part of the world described by your physical model and the part that is outside.

Conclusions

This paper: (1) describes the direct inverse parameter estimation algorithm (subseries) and its data requirements (2) compares that direct inversion with current FWI approaches; and (3) will provide an application for 4D.

Acknowledgements

The author thanks the M-OSRP sponsors for their encouragement and support. Dr. Jim Mayhan is thanked for his help with preparing this manuscript. The author thanks Dr. Wafik Beydoun for his positive, constructive and much appreciated comments and suggestions.

References

Li, X., 2011, I.- Multi-parameter depth imaging using the inverse scattering series; II.- Multi-component direct non-linear inversion for elastic earth properties using the inverse scattering series: PhD thesis, University of Houston.

Liang, H., 2013, Addressing several key outstanding issues and extending the capability of the inverse scattering subseries for internal multiple attenuation, depth imaging, and parameter estimation: PhD thesis, University of Houston.

Stolt, R. H., and A. B. Weglein, 2012, Seismic imaging and inversion: Application of linear inverse theory: Cambridge University Press.

Weglein, A. B., 2013, A timely and necessary antidote to indirect methods and so-called P-wave FWI: The Leading Edge, **32**, 1192–1204.

———, 2015, Direct Inversion and FWI. Invited keynote address given at the SEG Workshop Full-waveform Inversion: Filling the Gaps, Abu Dhabi, UAE, available at `http://mosrp.uh.edu/events/event-news/arthur-b-weglein-will-present-an-invited-key-note-address-on-direct-inversion-at-the-seg-workshop-on-fwi-30-march-1-april-2015-in-abu-dhabi-uae`.

Weglein, A. B., F. V. Araújo, P. M. Carvalho, R. H. Stolt, K. H. Matson, R. T. Coates, D. Corrigan, D. J. Foster, S. A. Shaw, and H. Zhang, 2003, Inverse scattering series and seismic exploration: Inverse Problems, **19**, R27–R83.

Weglein, A. B., and J. Yang, 2015, A first comparison of the inverse scattering series and iterative linear inverse for parameter estimation: Presented at the 85th Annual Internat. Mtg., SEG, Expanded Abstracts. (Submitted).

Weglein, A. B., H. Zhang, A. C. Ramírez, F. Liu, and J. E. M. Lira, 2009, Clarifying the underlying and fundamental meaning of the approximate linear inversion of seismic data: Geophysics, **74**, WCD1–WCD13.

Zhang, H., 2006, Direct non-linear acoustic and elastic inversion: towards fundamentally new comprehensive and realistic target identification: PhD thesis, University of Houston.

A comparison of the inverse scattering series direct non-linear inversion and the iterative linear inversion for parameter estimation across a single horizontal reflector

Jinlong Yang and Arthur B. Weglein

Abstract

The inverse scattering series (ISS) can achieve all seismic processing objectives directly without requiring any subsurface information. There are isolated task-specific subseries that derived from the ISS, which can perform free-surface multiple removal, internal multiple removal, depth imaging, parameter estimation, and Q compensation. Each isolated subseries assumes that only one task is performed. In this report, we will focus on the parameter estimation subseries and reduce it to a 1D normal incidence wave on a 1D acoustic earth where a single measured pressure wave is the input data. Under that very limited and focused circumstance, we are examining the difference between the iterative linear inverse and the direct inverse represented by the ISS parameter estimation subseries. A direct comparison is realizable in this specific example. The iterative approach shown in this example doesn't incorporate practical issues, e.g., the numerical noise and the different generalized inverses at each step. However, the ISS method performs as it does in practice with an analytic and unchanged inverse at every step. The comparison tests their convergence and the rate of convergence for different velocity contrasts. The rate of convergence of the ISS inversion method is analytically and numerically studied. When the reflection coefficient $R < 0.618$, the ISS inversion subseries monotonically term-by-term improves the estimation of medium properties; when $R > 0.618$, the ISS inversion subseries still converges, but not monotonically. Numerical tests show that when the velocity contrast is small, both inversion methods converge and the ISS inversion method converges faster than the iterative inversion method. When the velocity contrast increases, the iterative inversion method can not be computable and the ISS inversion method always converges. Therefore, for the simplest situation, the iterative linear inversion is not equivalent to the ISS direct non-linear solution. For more complicated circumstances, the difference is much greater, not just on the algorithms, but also on data requirements.

1 Introduction

The objective of seismic inversion is to estimate the medium properties of the subsurface from the recorded wavefield at the surface. Inversion methods can be classified as a direct method or an indirect method. A direct inversion method can solve an inverse problem (as its name suggests) directly depending on the algorithm and its data requirements without searching or model matching. On the other hand, an indirect inversion method solves the inverse problem through indirect ways (Weglein, 2015a): (1) model matching, (2) objective/cost functions, (3) searching algorithms, (4) iterative linear inversion, and (5) methods corresponding to necessary but not sufficient conditions, e.g., common image gather flatness. For example, a quadratic equation $ax^2 + bx + c = 0$ can be solved through a direct method as $x = \frac{-b \pm \sqrt{b^2-4ac}}{2a}$, or it can be solved by an indirect method searching for x such that $(ax^2 + bx + c)^2$ is a minimum.

A direct inverse solution for parameter estimation can be derived from an operator identity that relates the change in a medium's properties and the commensurate change in the wavefield. This

operator identity is a general inversion methodology and can accommodate any model-type, for example, acoustic, elastic, anisotropic, heterogeneous, inelastic. The direct inverse solution is in the form of a series, referred to as the inverse scattering series (Weglein et al., 2003). It can achieve all processing objectives within a single framework without requiring any subsurface information. There are isolated-task inverse scattering subseries derived from the ISS, which can perform free-surface multiple removal, internal multiple removal, depth imaging, parameter estimation, and Q compensation. The direct inverse solution (Weglein et al., 2003, 2009) provides a solid framework and firm math-physics foundation for the data requirements and algorithms to solve the inverse problem. For an elastic heterogeneous medium, Zhang and Weglein (2006) shows that the direct inverse requires multi-component/PS (P-component and S-component) data and prescribes how that data are utilized for a direct parameter estimation solution.

In this paper, we focus on analyzing and examining the ISS inversion subseries for parameter estimation. The distinct issues of: (1) data requirements, (2) model-type, and (3) inversion algorithm for the direct inverse are all important (Weglein, 2015b). For a normal incident wave on a single horizontal reflector in an acoustic medium, we can isolate and focus on the algorithmic difference when mode-type agrees and there is the same data, a single reflector and acoustic P wave. Under that very limited and focused circumstance, a direct comparison is realizable and the iterative approach doesn't incorporate practical issues, e.g., the numerical noise and the different generalized inverses at each step. However, the ISS method performs as it would in practice with an analytic and unchanged inverse at every step. The numerical results show a comparison between the ISS direct non-linear inversion and the iterative inversion (Yang and Weglein, 2015) on a 1D one parameter model with a single horizontal reflector, where the velocity is assumed to be known above the reflector and unknown below the reflector. Their convergence and the rate of convergence will be discussed and studied. In the ISS inversion subseries, each term of the series works towards the final goal. Sometimes when more terms in the series are included, the estimation may be worse locally,but in fact it is purposeful and essential in the contribution towards convergence and the final goal. This property has also been indicated by Carvalho (1992) in the free-surface multiple elimination subseries, e.g., what appears to make a second-order free-surface multiple larger with a first-order free-surface algorithm is actually preparing the second-order multiple to be removed by the higher-order terms. This simple example provides a guide when we move on to the more complicated elastic world.

The report is arranged as follows: First, the ISS direct inversion method is discussed. Second, the direct inversion is presented in the 2D heterogeneous elastic medium. Third, the ISS direct inversion and the iterative linear inversion are examined and compared in a 1D acoustic medium. Finally, we offer a discussion and conclusions.

2 Theory

The direct inverse solution (Weglein et al., 2003; Zhang, 2006) is derived from the operator identity that relates the change in a medium's properties and the commensurate change in the wavefield. Let L_0, G_0, L, and G be the differential operators and Green's functions for the reference and actual media, respectively, that satisfy:

$$L_0 G_0 = \delta \quad \text{and} \quad LG = \delta,$$

where δ is a Dirac δ-function. We define the perturbation operator, V, and the scattered wavefield, ψ_s, as follows:

$$V \equiv L_0 - L \quad \text{and} \quad \psi_s \equiv G - G_0.$$

2.1 The operator identity

The relationship (called the Lippmann-Schwinger or scattering theory equation)

$$G = G_0 + G_0 V G \tag{1}$$

is an operator identity that follows from

$$L^{-1} = L_0^{-1} + L_0^{-1}(L_0 - L)L^{-1}.$$

For forward modeling the wavefield, G, for a medium described by L is given by

$$L \rightarrow G \quad \text{or} \quad L_0, V \rightarrow G$$

where the second form has L entering the modeling algorithms in terms of L_0 and V. Modeling using scattering theory requires a complete and detailed knowledge of medium properties.

2.2 Direct forward series and direct inverse series

The operator identity equation 1 can be solved for G as

$$G = (1 - G_0 V)^{-1} G_0, \tag{2}$$

or

$$G = G_0 + G_0 V G_0 + G_0 V G_0 V G_0 + \dots . \tag{3}$$

Equation 3 has the form of a generalized geometric series

$$G - G_0 = S = ar + ar^2 + \cdots = \frac{ar}{1 - r}, \tag{4}$$

where we identify $a = G_0$ and $r = V G_0$ in equation 3, and

$$S = S_1 + S_2 + S_3 + \dots . \tag{5}$$

The portions of S that are linear, quadratic, $\dots$ in r are:

$$\begin{aligned} S_1 &= ar, \\ S_2 &= ar^2, \\ &\vdots \end{aligned}$$

and the sum is

$$S = \frac{ar}{1 - r}. \tag{6}$$

Solving equation 6 for r, produces the inverse geometric series,

$$\begin{aligned} r &= \frac{S/a}{1+S/a} = S/a - (S/a)^2 + (S/a)^3 + \dots \\ &= r_1 + r_2 + r_3 + \dots . \end{aligned}$$

This is the simplest prototype of an inverse series, i.e., the inverse of the geometric series. For the seismic inverse problem, we associate S with the measured data

$$S = (G - G_0)_{ms} = \text{Data},$$

and the forward and inverse series follow from treating the forward solution as S in terms of V, and the inverse solution as V in terms of S. The inverse series assumes

$$V = V_1 + V_2 + V_3 + \dots , \tag{7}$$

where V_n is the portion of V that is n^{th} order in the data. The identity (equation 1) provides a geometric forward series rather than a Taylor series. In general, a Taylor series doesn't have an inverse series; however, a geometric series has an inverse series. All conventional current mainstream inversion methods, including iterative linear inversion and FWI, are based on a Taylor series concept. Solving a forward problem in an inverse sense is not the same as solving an inverse problem directly.

In terms of the expansion of V in equation 7, and G_0, G, $D = (G - G_0)_{ms}$, the inverse scattering series (Weglein et al., 2003) can be obtained as

$$\begin{aligned} G_0V_1G_0 =& D, && (8)\\ G_0V_2G_0 =& - G_0V_1G_0V_1G_0, && (9)\\ G_0V_3G_0 =& - G_0V_1G_0V_1G_0V_1G_0 \\ & - G_0V_1G_0V_2G_0 - G_0V_2G_0V_1G_0, && (10)\\ & \vdots \end{aligned}$$

The inverse scattering series provides a direct method for obtaining the subsurface information by inverting the series order-by-order to solve for the perturbation operator V, using only the measured data D and a reference Green's function G_0, for any type of medium.

2.3 The operator identity in a 2D heterogeneous elastic medium

The method for a 2D elastic heterogeneous earth is exemplified. The starting point for the 3D generalization is found in Stolt and Weglein (2012). The 2D elastic wave equation for a heterogeneous isotropic medium (Zhang, 2006) is

$$L\vec{u} = \begin{pmatrix} f_x \\ f_z \end{pmatrix} \quad \text{and} \quad \hat{L}\begin{pmatrix} \phi^P \\ \phi^S \end{pmatrix} = \begin{pmatrix} F^P \\ F^S \end{pmatrix}, \tag{11}$$

where $\vec{u}$, f_x, and f_z are the displacement and forces in displacement coordinates and ϕ_P, ϕ_S and F^P, F^S are the P and S waves and the force components in P and S coordinates. The operators L,

L_0 and V are

$$L = \left[\rho\omega^2 \begin{pmatrix} 1 & 0 \\ 0 & 1 \end{pmatrix} + \begin{pmatrix} \partial_x\gamma\partial_x + \partial_z\mu\partial_z & \partial_x(\gamma - 2\mu)\partial_z + \partial_z\mu\partial_x \\ \partial_z(\gamma - 2\mu)\partial_x + \partial_x\mu\partial_z & \partial_z\gamma\partial_z + \partial_x\mu\partial_x \end{pmatrix}\right],$$

$$L_0 = \left[\rho\omega^2 \begin{pmatrix} 1 & 0 \\ 0 & 1 \end{pmatrix} + \begin{pmatrix} \gamma_0\partial_x^2 + \mu_0\partial_z^2 & (\gamma_0 - \mu_0)\partial_x\partial_z \\ (\gamma_0 - \mu_0)\partial_x\partial_z & \mu_0\partial_x^2 + \gamma_0\partial_z^2 \end{pmatrix}\right],$$

$$V \equiv L_0 - L = \begin{bmatrix} a_\rho\omega^2 + \alpha_0^2\partial_x a_\gamma\partial_x + \beta_0^2\partial_z a_\mu\partial_z & \partial_x(\alpha_0^2 a_\gamma - 2\beta_0^2 a_\mu)\partial_z + \beta_0^2\partial_z a_\mu\partial_x \\ \partial_z(\alpha_0^2 a_\gamma - 2\beta_0^2 a_\mu)\partial_x + \beta_0^2\partial_x a_\mu\partial_z & a_\rho\omega^2 + \alpha_0^2\partial_z a_\gamma\partial_z + \beta_0^2\partial_x a_\mu\partial_x \end{bmatrix},$$

where the quantities $a_\rho \equiv \rho/\rho_0 - 1$, $a_\gamma \equiv \gamma/\gamma_0 - 1$, $a_\mu \equiv \mu/\mu_0 - 1$ are defined in terms of the bulk modulus, shear modulus and density (γ_0, μ_0, ρ_0, γ, μ, ρ) in the reference and actual media, respectively.

The forward problem is found from the identity equation 3 and the elastic wave equation 11 (in PS coordinates) as

$$\hat{G} - \hat{G}_0 = \hat{G}_0\hat{V}\hat{G}_0 + \hat{G}_0\hat{V}\hat{G}_0\hat{V}\hat{G}_0 + \dots$$

$$\begin{pmatrix} \hat{D}^{PP} & \hat{D}^{PS} \\ \hat{D}^{SP} & \hat{D}^{SS} \end{pmatrix} = \begin{pmatrix} \hat{G}_0^P & 0 \\ 0 & \hat{G}_0^S \end{pmatrix}\begin{pmatrix} \hat{V}^{PP} & \hat{V}^{PS} \\ \hat{V}^{SP} & \hat{V}^{SS} \end{pmatrix}\begin{pmatrix} \hat{G}_0^P & 0 \\ 0 & \hat{G}_0^S \end{pmatrix}$$

$$+ \begin{pmatrix} \hat{G}_0^P & 0 \\ 0 & \hat{G}_0^S \end{pmatrix}\begin{pmatrix} \hat{V}^{PP} & \hat{V}^{PS} \\ \hat{V}^{SP} & \hat{V}^{SS} \end{pmatrix}\begin{pmatrix} \hat{G}_0^P & 0 \\ 0 & \hat{G}_0^S \end{pmatrix}\begin{pmatrix} \hat{V}^{PP} & \hat{V}^{PS} \\ \hat{V}^{SP} & \hat{V}^{SS} \end{pmatrix}\begin{pmatrix} \hat{G}_0^P & 0 \\ 0 & \hat{G}_0^S \end{pmatrix} + \dots \quad (12)$$

and the inverse solution, equations 8-10, for the elastic equation 11 is

$$\begin{pmatrix} \hat{D}^{PP} & \hat{D}^{PS} \\ \hat{D}^{SP} & \hat{D}^{SS} \end{pmatrix} = \begin{pmatrix} \hat{G}_0^P & 0 \\ 0 & \hat{G}_0^S \end{pmatrix}\begin{pmatrix} \hat{V}_1^{PP} & \hat{V}_1^{PS} \\ \hat{V}_1^{SP} & \hat{V}_1^{SS} \end{pmatrix}\begin{pmatrix} \hat{G}_0^P & 0 \\ 0 & \hat{G}_0^S \end{pmatrix},$$

$$\begin{pmatrix} \hat{G}_0^P & 0 \\ 0 & \hat{G}_0^S \end{pmatrix}\begin{pmatrix} \hat{V}_2^{PP} & \hat{V}_2^{PS} \\ \hat{V}_2^{SP} & \hat{V}_2^{SS} \end{pmatrix}\begin{pmatrix} \hat{G}_0^P & 0 \\ 0 & \hat{G}_0^S \end{pmatrix}$$

$$= -\begin{pmatrix} \hat{G}_0^P & 0 \\ 0 & \hat{G}_0^S \end{pmatrix}\begin{pmatrix} \hat{V}_1^{PP} & \hat{V}_1^{PS} \\ \hat{V}_1^{SP} & \hat{V}_1^{SS} \end{pmatrix}\begin{pmatrix} \hat{G}_0^P & 0 \\ 0 & \hat{G}_0^S \end{pmatrix}\begin{pmatrix} \hat{V}_1^{PP} & \hat{V}_1^{PS} \\ \hat{V}_1^{SP} & \hat{V}_1^{SS} \end{pmatrix}\begin{pmatrix} \hat{G}_0^P & 0 \\ 0 & \hat{G}_0^S \end{pmatrix}, \quad (13)$$

where $\hat{V}^{PP} = \hat{V}_1^{PP} + \hat{V}_2^{PP} + \hat{V}_3^{PP} + \dots$ and any one of the four matrix elements of V requires the four components of the data

$$\begin{pmatrix} \hat{D}^{PP} & \hat{D}^{PS} \\ \hat{D}^{SP} & \hat{D}^{SS} \end{pmatrix}.$$

In summary, from equation 12, $\hat{D}^{PP}$ can be determined in terms of the four elements of V and $\hat{V}^{PP}$, $\hat{V}^{PS}$, $\hat{V}^{SP}$, or $\hat{V}^{SS}$ require the four components of D. That's what the general relationship $G = G_0 + G_0VG$ requires, i.e., a direct non-linear inverse solution is a solution order-by-order in the four matrix elements of D (in 2D).

2.4 Direct inverse and indirect inverse

The direct solution is not iterative linear inversion. Iterative linear inversion starts with equation 8. We solve for V_1 and change the reference medium iteratively. The new differential operator L_0' and the new reference medium G_0' satisfy

$$L_0' = L_0 - V_1 \quad \text{and} \quad L_0'G_0' = \delta. \quad (14)$$

Through the same equation 8 with different reference background

$$G_0' V_1' G_0' = D' = (G - G_0')_{ms}, \tag{15}$$

where V_1' is the portion of V linear in the data $(G - G_0')_{ms}$. We can continually update L_0' and G_0', and finally solve for the perturbation operator V. The direct inverse solution equations 7 and 13 calls for a single unchanged reference medium, for computing $V_1, V_2, \ldots$. For a homogeneous reference medium they are obtained by an analytic inverse. The inverse to find V_1 from data, is the same inverse to find $V_2, V_3, \ldots$, from equations 8-10. There are no numerical inverses, no generalized inverses, no inverses of matrices that contain noisy bandlimited data.

The difference between iterative linear and the direct inverse of equation 13 is much more substantive and serious than merely a different way to solve $G_0 V_1 G_0 = D$, equation 8, for V_1. If equation 8 is our entire basic theory, you can mistakenly think that $\hat{D}^{PP} = \hat{G}_0^P \hat{V}_1^{PP} \hat{G}_0^P$ is sufficient to update $\hat{D}^{PP} = \hat{G}_0'^P \hat{V}_1'^{PP} \hat{G}_0'^P$. This step loses contact with and violates the basic operator identity $G = G_0 + G_0 V G$ for the elastic wave equation. That's as serious as considering problems involving a right triangle and violating the Pythagorean theorem in your method. That is, iteratively updating PP data with an elastic model violates the basic relationship between changes in a medium, V and changes in the wavefield, $G - G_0$ for the simplest elastic earth model.

This direct inverse method provides a platform for amplitude analysis, AVO and FWI. It communicates when a "FWI" method should work, in principle. Iteratively inverting multi-component data has the correct data but doesn't corresponds to a direct inverse algorithm. To honor $G = G_0 + G_0 V G$, you need both the data and the algorithm that direct inverse prescribes. Not recognizing the message that an operator identity and the elastic wave equation unequivocally communicate is a fundamental and significant contribution to the gap in effectiveness in current AVO and FWI method and application (equation 13). This analysis generalizes to 3D with P, S_h, and S_v data.

There's a role for direct and indirect methods in practical real world applications. Indirect methods are to be called upon for recognizing that the world is more complicated than the physics that we assume in our models and methods. For the part of the world that you are capturing in your model (and methods) nothing compares to direct methods for clarity and effectiveness. An optimal indirect method would seek to satisfy a cost function that derives from a property of the direct method. In that way the indirect and direct method would be aligned and cooperative for accommodating the part of the world described by your physical model and the part that is outside.

2.5 The operator identity in a 1D acoustic medium

Considering a simple 1D case, the model consists of two half-spaces with acoustic velocities c_0 and c_1 and an interface located at $z = a$ as shown in Figure 1. If we put the source and receiver on the surface, the pressure wave $P(t) = R\delta(t - 2a/c_0)$ will be recorded, where the reflection coefficient $R = \frac{c_1 - c_0}{c_1 + c_0}$. Without considering the imaging issue, R is the only input to the ISS and the iterative inversion methods. Choosing an acoustic whole-space with velocity c_0 as the reference medium,

the perturbation V (Weglein et al., 2003) can be expanded as

$$V(z) = \frac{\omega^2}{c_0^2} - \frac{\omega^2}{c^2(z)} = \frac{\omega^2}{c_0^2}(1 - \frac{c_0^2}{c^2(z)}) = k_0^2 \alpha(z), \tag{16}$$

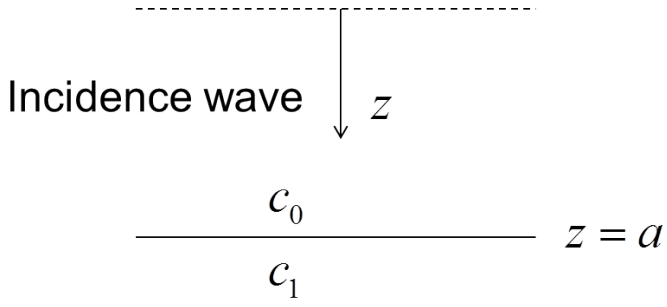

Figure 1: 1D acoustic model with velocities c_0 over c_1

where ω is the angular frequency, $c(z)$ is the local acoustic velocity, $k_0 = \omega/c_0$, and $\alpha(z) \equiv 1 - \frac{c_0^2}{c^2(z)}$. Depending on V, $\alpha(z)$ can be expanded as a series in terms of data, $\alpha(z) = \alpha_1(z) + \alpha_2(z) + \alpha_3(z) + \cdots$. Thus, we have

$$V_1 = k_0^2\alpha_1, \quad V_2 = k_0^2\alpha_2, \quad \cdots . \tag{17}$$

From the inverse scattering series (Equations 8-10), Shaw et al. (2004) isolated the leading order imaging subseries and the direct non-linear inversion subseries.

In this section, we will focus on studying the convergence properties of the ISS inversion subseries. The inversion only terms isolated from the inverse scattering series (Zhang, 2006; Li, 2011) are

$$\alpha(z) = \alpha_1(z) - \frac{1}{2}\alpha_1^2(z) + \frac{3}{16}\alpha_1^3(z) + \cdots . \tag{18}$$

For a 1D normal incidence case, we invert G_0 of the linear equation (8) and obtain,

$$\alpha_1(z) = 4\int_{-\infty}^{z} D(z')dz', \tag{19}$$

where $z' = c_0 t/2$. Inserting data D gives

$$\alpha_1 = 4R, \tag{20}$$

where the reflection coefficient $R = \frac{c_1 - c_0}{c_1 + c_0}$. Substituting α_1 into equation (18), the ISS direct non-linear inversion subseries in terms of R can be written as

$$\alpha = 4R - 8R^2 + 12R^3 + \cdots = 4R\sum_{n=0}^{\infty}(n+1)(-R)^n. \tag{21}$$

After solving for α, the inverted velocity $c(z)$ can be obtained through $c_1 = c_0/\sqrt{1-\alpha}$ (equation 16).

Considering the convergence property of the series for α or the inversion subseries, we can calculate the ratio test,

$$\left|\frac{\alpha_{n+1}}{\alpha_n}\right| = \left|\frac{(n+2)(-R)^{n+1}}{(n+1)(-R)^n}\right| = \left|\frac{n+2}{n+1}R\right|. \tag{22}$$

If $\lim_{n\to\infty}\left|\frac{\alpha_{n+1}}{\alpha_n}\right| < 1$, this subseries converges absolutely. That is

$$|R| < \lim_{n\to\infty}\frac{n+1}{n+2} = 1. \tag{23}$$

Therefore, the ISS direct non-linear inversion subseries converges when the reflection coefficient $|R|$ is less than 1, which is always true. Hence, for this example, the ISS inversion subseries will converge under any velocity contrasts between the two media.

For the iterative linear inversion, we will update the reference velocity $c_0' = c_0/\sqrt{1-\alpha_1}$ by using $\alpha_1 = 4R$. Then, the new linear inversion velocity is calculated by $\alpha_1' = 4R'$, where $R' = \frac{c_1-c_0'}{c_1+c_0'}$. The same procedure will be applied iteratively until we achieve the final inversion result.

3 Numerical examples for the 1D acoustic case

Numerical examples for the 1D acoustic medium case are shown in this section. First, an analytic example for the rate of convergence of the ISS inversion subseries is examined and studied for a 1D normal incidence case. Second, the convergence of the ISS direct inversion and iterative inversion are examined and compared.

3.1 Analytic example

The rate of convergence of the estimated α or the ISS inversion subseries (equation 21) is analytically examined and studied for a 1D normal incidence case. Since α is always convergent when $R < 1$, the summation of this subseries (Zhang, 2006) is

$$\alpha = 4R\sum_{n=0}^{\infty}(n+1)(-R)^n = 4R\frac{1}{(1+R)^2}. \tag{24}$$

If the error between the estimated and the actual α is monotonically decreasing, it means the subseries is a term-by-term added value improvement towards determining the actual medium properties. If this error is increasing before decreasing, it means that the estimation becomes worse before it gets better. In fact, locally worse is purposeful and essential in the contribution towards convergence and the final goal. In other words, the error for the first order and the error for the second order have the relation,

$$|\alpha - \alpha_1 - \alpha_2| > |\alpha - \alpha_1|, \tag{25}$$

i.e.,

$$|4R\frac{3R^2+2R^3}{(1+R)^2}| > |4R\frac{-R^2-2R}{(1+R)^2}|. \tag{26}$$

After simplification, it gives

$$R^2 + R - 1 > 0. \tag{27}$$

We can solve it and obtain the reflection coefficient $R < \frac{-1-\sqrt{5}}{2} = -1.618$ or $R > \frac{-1+\sqrt{5}}{2} = 0.618$. Therefore, when $R > 0.618$, the error increases first. Similarly, if the error for the third order is greater than that for the second order, we get $R > 0.667$. If the error for the fourth order is greater than that for the third order, we obtain $R > 0.721$. In summary, when $R > 0.618$ the error increases and the estimated α gets worse before getting better. The dashed green line in Figure 2 shows that when the reflection coefficient R is equal to 0.618, the error for the first order is equal to the error for the second order. The detail of the numerical tests will be discussed in the next section.

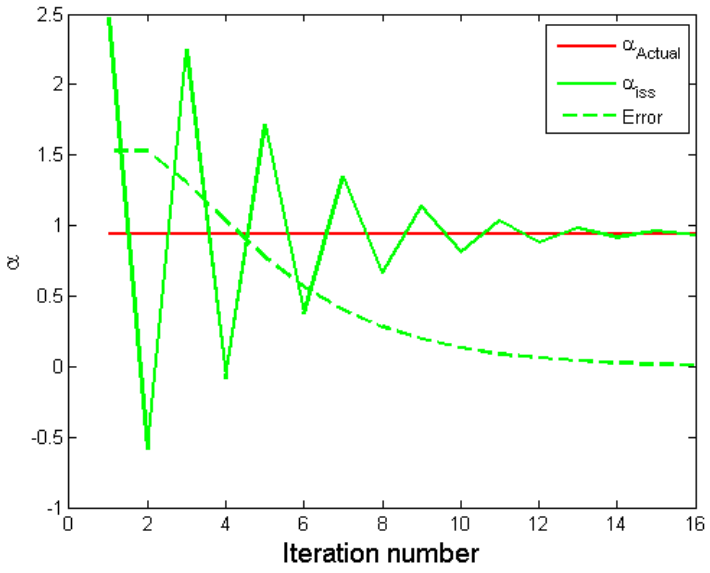

Figure 2: The error (dashed green line) of estimated α at $R = 0.6180$ and $\alpha = 0.9443$.

3.2 Numerical tests

In this section, we will examine the convergence property and the rate of convergence of α by using the ISS inversion subseries (equation 21) and the iterative linear inversion methods for the velocity contrast in the 1D acoustic case. In addition, the inversion results by these two methods are discussed and compared.

In the simple 1D model (Figure 1), only one parameter (velocity) varies and a plane wave propagates into the medium. There is only a single reflector and we assume the velocity is known above the reflector and unknown below the reflector. We will examine and compare the convergence of the perturbation α and the inversion results by using the ISS direct non-linear method and the iterative linear method. In this model, we set the reference velocity $c_0 = 1500m/s$ and the lower half space velocity $c_1 = 2000m/s$.

Figure 3 shows the estimated α by the ISS method (green line) and the iterative inversion method (blue line). The red line represents the actual α that is calculated from our model. The horizontal axis represents the order of the ISS inversion subseries or the iteration numbers. The vertical axis shows the value of α. From the estimated α, it can be seen that at the small velocity contrast, the estimated α by ISS method becomes the actual α after about five orders calculation and the estimated α by the iterative inversion method goes to zero as we expected, because after several iteration, the updated model is close to and approaching to the actual model. Figure 4 represents the velocity estimation. We can see that both methods converge and produce correct velocity after five orders or iterations. From both Figures 3 and 4, we can see that both methods converge very fast at the small velocity contrast and the ISS method converge faster than the iterative inversion method. When the velocity contrast is getting bigger, the iterative inversion method can not be computable in this example, but the ISS inversion method always converges and produces correct results (see green line in Figures 5) after the summation of more orders of α.

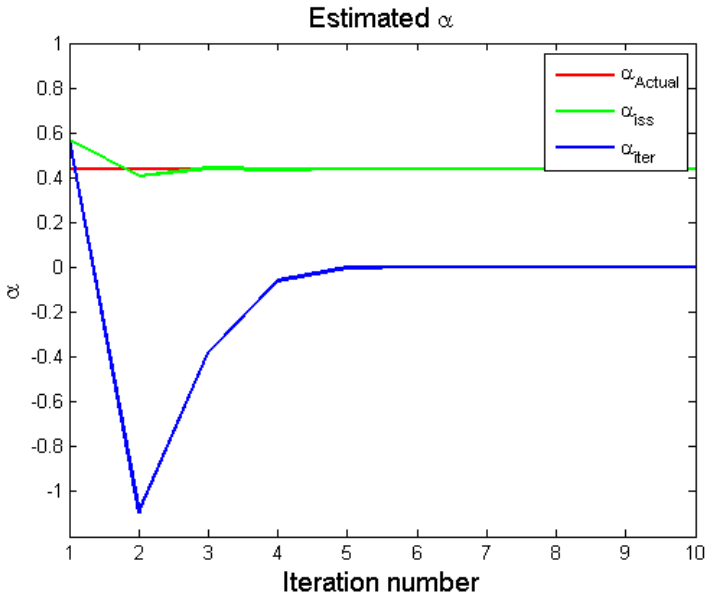

Figure 3: The estimated α at $R = 0.1429$by using the ISS inversion method (green line) and the iterative inversion method (blue line). The red line shows the actual value of $\alpha = 0.4375$. The horizontal axis is the order of the ISS suberies or the iteration numbers, and the vertical axis shows the value of α.

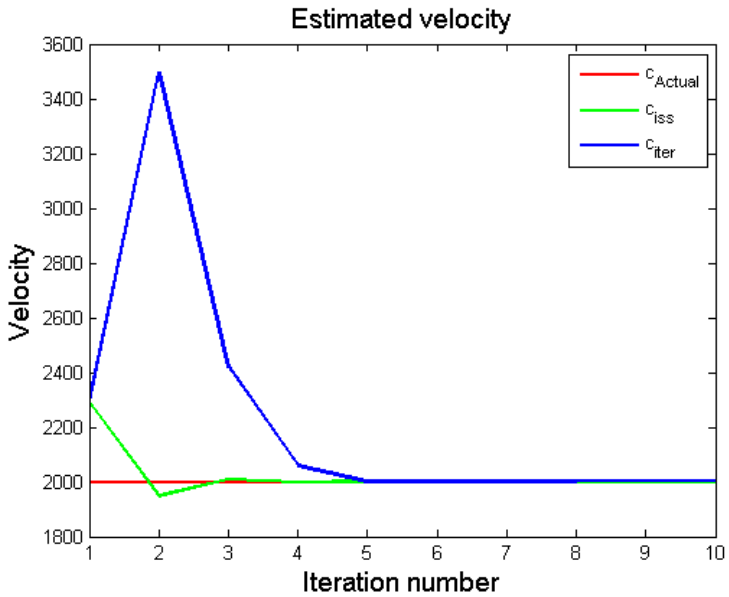

Figure 4: The estimated velocity by using the ISS inversion method (green line) and the iterative inversion method (blue line).

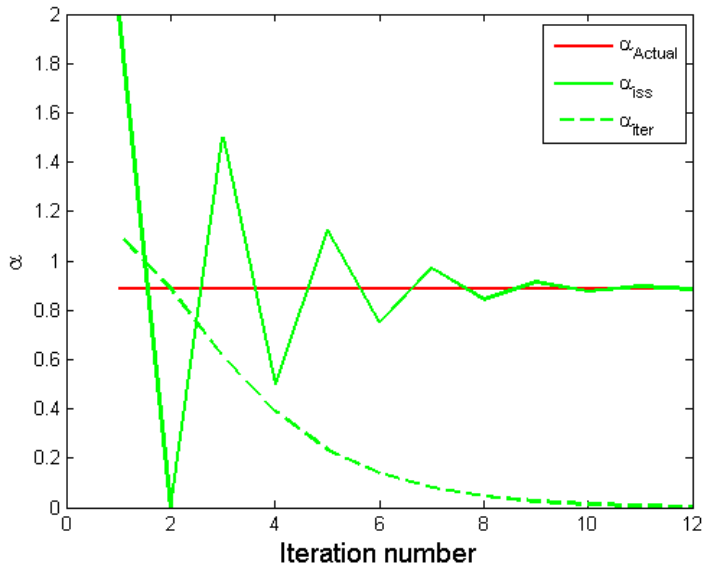

Figure 5: The estimated α at $c_1 = 4500m/s$ and $R = 0.5000$ by using the ISS inversion method.

From the dashed green line in Figures 3 and 5, at the small contrasts, the error between the estimated and the actual α is monotonically decreasing, in other words, the estimation of α is always a term-by-term added value improvement towards determine c_1; when the contrast increasing (Figure 2), the error is not monotonic. The estimation of α can be worse before it gets better. However, when it starts to add value, it is getting better when each further term is added to the series.

As the analytic calculation, when the reflection coefficient R is smaller than 0.618, this inversion subseries gives a monotonically term-by-term added value improvement towards determining c_1. When the reflection coefficient R is equal to 0.618, the error becomes flat as shown in Figure 2. When the reflection coefficient is larger than 0.618, the series still converges, but the estimation of α will become worse before it gets better. From the analytic and numerical examples, we can see that each term in the series works towards the final goal. Sometimes when more terms in the series are included, the estimation looks worse locally, but once it starts to improve the estimation at a specific order, the approximations never become worse again, every single term after that order will produce an improved estimation.

As we know, the reflection coefficient R is almost always less than 0.2 in practice, so that both the ISS method and the iterative method converge, but the ISS method converges faster than the iterative method. Moreover, for more complicated circumstances (e.g., the elastic non-normal incidence case), the difference between the ISS method and the iterative is much greater, not just on the algorithms, but also on data requirements and on how the band-limited noisy nature of the seismic data impact the inverse operators in the iterative method but not in the ISS method.

4 Conclusions

In this report, we discuss a direct inverse method, which is derived from the operator identity that relates the change in a medium's properties and the commensurate change in the wavefield. We

describe the direct inversion algorithm for parameter estimation (ISS subseries) and its data requirements. In a specific 1D acoustic medium, we examine and compare the ISS direct non-linear inversion and the iterative inversion for parameter estimation across a single horizontal reflector, where the velocity is assumed to be known above the reflector and unknown below the reflector. The rate of convergence of the ISS inversion method is analytically and numerically studied. From the analytic example, we show that when the reflection coefficient $R < 0.618$, the ISS inversion subseries is a term-by-term improvement towards determining medium properties; when $R > 0.618$, the inversion subseries still converges, but the estimation will locally be less accurate before it converges. Numerical results show that when the velocity contrast is small, i.e., the reflection coefficient is small, both inversion methods converge and the ISS inversion method converges faster than the iterative inversion method. When velocity contrast increases, the reflection coefficient gets larger, the iterative inversion method can not be computable and the ISS inversion method always converges. Hence, for the simplest situation, the iterative linear inversion is not equivalent to the direct nonlinear solution provided by the inverse scattering series. For more complicated circumstances (e.g., the elastic non-normal incidence case), the difference is much greater, not just on the algorithms, but also on data requirements and on how the band-limited noisy nature of the seismic data impact the inverse operators in iterative linear inversion but not in the ISS direct inversion.

5 ACKNOWLEDGMENTS

The first author is grateful to all M-OSRP sponsors for their support and encourage of this research. Special thanks go to my advisor, Dr. Arthur B. Weglein, for his teaching and guidance.

References

Carvalho, P. M. *Free-surface multiple reflection elimination method based on nonlinear inversion of seismic data*. PhD thesis, Universidade Federal da Bahia, 1992.

Li, X. *I.-Multi-component direct non-linear inversion for elastic earth properties using the inverse scattering series; II.-Multi-parameter depth imaging using the inverse scattering series*. PhD thesis, University of Houston, 2011.

Shaw, S. A., A. B. Weglein, D. J. Foster, K. H. Matson, and R. G. Keys. "Isolation of a leading order depth imaging series and analysis of its convergence properties." *Journal of Seismic Exploration* 2 (November 2004): 157–195.

Stolt, R. H. and A. B. Weglein. *Seismic Imaging and Inversion: Application of linear Inverse Theory*. Cambridge University Press, 2012.

Weglein, A. B. "A direct inverse solution for AVO/FWI parameter estimation objectives." *Submitted to 85rd International Annual Meeting, SEG, Expanded Abstracts* (2015).

Weglein, A. B. "Direct Inversion and FWI." Available at http://mosrp.uh.edu/events/event-news/arthur-b-weglein-will-present-an-invited-key-note-address-on-direct-inversion-at-the-seg-workshop-on-fwi-30-march-1-april-2015-in-abu-dhabi-uae. *Invited keynote address given at the SEG Workshop Full-waveform Inversion: Fillings the Gaps, Abu Dhabi, UAE* (2015).

Weglein, A. B., F. V. Araújo, P. M. Carvalho, R. H. Stolt, K. H. Matson, R. T. Coates, D. Corrigan, D. J. Foster, S. A. Shaw, and H. Zhang. "Inverse scattering series and seismic exploration." *Inverse Problems* 19 (2003): R27–R83.

Weglein, A. B., H. Zhang, A. C. Ramírez, F. Liu, and J. E. M. Lira. "Clarifying the underlying and fundamental meaning of the approximate linear inversion of seismic data." *Geophysics* 74 (2009): WCD1–WCD13.

Yang, J. and A. B. Weglein. "A first comparison of the inverse scattering series non-linear inversion and the iterative linear inversion for parameter estimation." *Submitted to 85rd International Annual Meeting, SEG, Expanded Abstracts* (2015).

Zhang, H. *Direct nonlinear acoustic and elastic inversion: towards fundamentally new comprehensive and realistic target identification*. PhD thesis, University of Houston, 2006.

Zhang, H. and A. B. Weglein. "Direct non-linear inversion of multi-parameter 1D elastic media using the inverse scattering series." *76th International Annual Meeting, SEG, Expanded Abstracts* (2006): 284–311.

A first comparison of the inverse scattering series non-linear inversion and the iterative linear inversion for parameter estimation

Jinlong Yang and Arthur B. Weglein, M-OSRP, University of Houston*

SUMMARY

The inverse scattering series (ISS) direct non-linear inversion and the iterative linear inversion for parameter estimation are examined and compared. The convergence and the rate of convergence of both the ISS inversion subseries and the iterative inversion method are tested for different velocity contrasts on a simple 1D one parameter acoustic model. The rate of convergence of the ISS inversion method is analytically and numerically studied. When the reflection coefficient $R < 0.618$, the ISS inversion subseries monotonically term-by-term improves the estimation of medium properties; when $R > 0.618$, the ISS inversion subseries still converges, but not monotonically. Numerical tests show that when the velocity contrast is small, both inversion methods converge and the ISS inversion method converges faster than the iterative inversion method. When the velocity contrast increases, the iterative inversion method will not converge when $R > 0.5$, while the ISS inversion method always converges.

INTRODUCTION

The objective of seismic inversion is to estimate the medium properties of the subsurface from the recorded wavefield. Typically this begins with a chosen reference medium and the measured wavefield. Then an operator identity is called upon that relates the difference between the medium and reference properties and the difference between the measured total wavefield and the reference wavefield. This identity can be used to find a direct solution to the forward problem or a direct solution to the inverse problem for any type of medium.

If we seek the parameters of an elastic heterogeneous isotropic subsurface, then the differential operator in the operator identity is the differential operator that occurs in the elastic, heterogeneous isotropic wave equation. The elastic isotropic model is the base acceptable earth model-type for amplitude analysis, for example, AVO and FWI. Taking the operator identity (called the Lippmann-Schwinger or scattering theory equation) and the elastic wave equation, we can obtain a direct inverse solution for the changes in elastic properties and density. The direct inverse solution specifies both the data required and the algorithm to achieve a direct solution. The direct inverse (Zhang and Weglein, 2006; Li, 2014) requires multi-component/PS data and prescribes how that data are utilized for a direct parameter estimation solution. The direct solution (Weglein et al., 2003, 2009) provides a solid framework and firm math-physics foundation for the data requirement and algorithms to solve the problem that you are interested. There are many other issues that contribute to the gap in FWI today, e.g., the need for broadband data. But starting with and employing a framework that provides confidence of the data and methods is a significant, fundamental, and practical contribution towards filling the gap (Weglein, 2015). Only a direct solution can provide that clarity, confidence and effectiveness. The current industry standard FWI, using variants of iterative linear inverse, correspondent to model matching procedures, and iteratively linearly updating P data or multi-component data does not correspond to, and will not produce, a direct solution with its clarity and effectiveness.

The direct solution is in the form of a series, referred to as the inverse scattering series (Weglein et al., 2003). It can achieve all processing objectives within a single framework without requiring any subsurface information. There are isolated-task inverse scattering subseries, which can perform free-surface multiple removal, internal multiple removal, depth imaging, parameter estimation, and Q compensation. In this paper, we focus on analyzing and examining the ISS inversion subseries for parameter estimation. The distinct issues of: (1) data requirements, (2) model-type, and (3) inversion algorithm for the direct inverse are all important. For a normal incident wave on a single horizontal reflector in an acoustic medium, we can isolate and focus on the algorithm difference when mode-type agrees and there is the same data, a single reflector acoustic P wave. This allows us to focus on the algorithm issues.

A comparison between the ISS direct non-linear inversion and the iterative inversion will be tested and shown on a 1D, one parameter, and a single horizontal reflector model, where the velocity is assumed to be known above the reflector and unknown below the reflector. Their convergence and the rate of convergence will be discussed and studied. In the ISS inversion subseries, each term of the series works towards the final goal. Sometimes when more terms in the series are included, the estimation may be worse locally, but in fact it is purposeful and essential in the contribution towards convergence and the final goal. This property has also been indicated by Carvalho (1992) in the free-surface multiple elimination subseries, e.g., what appears to make a second-order free-surface multiple larger with a first-order free-surface algorithm is actually preparing the second-order multiple to be removed by the higher-order terms. This simple example provides a guide when we move on to the more complicated elastic world.

THEORY

Starting from the two basic differential equations (Weglein et al., 2003), which govern wave propagation in actual medium and reference medium

$$LG = \delta \quad \text{and} \quad L_0 G_0 = \delta \tag{1}$$

where L, L_0 and G, G_0 are the differential operators and Green's functions in actual and reference medium, respectively. Defining the perturbation $V = L_0 - L$, the forward modeling series

(Born series) can be derived

$$G = G_0 + G_0VG_0 + G_0VG_0VG_0 + \cdots \quad (2)$$

from the Lippmann-Schwinger equation. Expanding V as a series

$$V = V_1 + V_2 + V_3 + \cdots \quad (3)$$

and substituting it into the equation 2, the inverse scattering series is obtained as

$$\begin{aligned} D &= [G_0V_1G_0]_{ms} && (4)\\ 0 &= [G_0V_2G_0]_{ms} + [G_0V_1G_0V_1G_0]_{ms} && (5)\\ &\vdots \end{aligned}$$

where D is $G - G_0$ on the measurement surface. The inverse scattering series provides a direct method for obtaining the subsurface information by inverting the series order-by-order to solve for the perturbation operator V, using only the measured data D and a reference wave field G_0, for any type of medium.

On the other hand, the iterative linear method for estimating the perturbation operator V starts with equation 4. We solve for V_1 and change the reference medium iteratively. The new differential operator L_0' becomes and the new reference medium G_0' satisfies

$$L_0' = L_0 - V_1 \quad \text{and} \quad L_0'G_0' = \delta. \quad (6)$$

Through the same equation 4 with different reference background

$$G_0'V_1'G_0' = D' = (G - G_0')_{ms}, \quad (7)$$

we can continually update L_0' and G_0', and finally solve the perturbation operator V.

Considering a simple 1D case, the model consists of two half-spaces with acoustic velocities c_0 and c_1 and an interface located at $z = a$ as shown in Figure 1. If we choose an acoustic

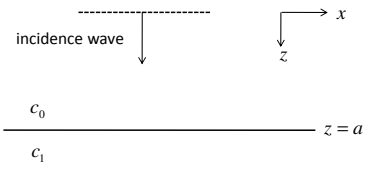

Figure 1: 1D acoustic model with velocities c_0 over c_1

whole-space with velocity c_0 as the reference medium, the perturbation V (Weglein et al., 2003) can be expanded as

$$V(z) = \frac{\omega^2}{c_0^2} - \frac{\omega^2}{c^2(z)} = \frac{\omega^2}{c_0^2}(1 - \frac{c_0^2}{c^2(z)}) = k_0^2\alpha(z), \quad (8)$$

where ω is the angular frequency, $c(z)$ is the local acoustic velocity, and $k_0 = \omega/c_0$. Depending on V, $\alpha(z)$ can be expanded as a series in terms of data, $\alpha(z) = \alpha_1(z) + \alpha_2(z) + \alpha_3(z) + \cdots$. Thus, we have

$$V_1 = k_0^2\alpha_1, \quad V_2 = k_0^2\alpha_2, \quad \cdots. \quad (9)$$

From the inverse scattering series (Equations 4 and 5), Shaw et al. (2004) isolated the leading order imaging subseries and the direct non-linear inversion subseries.

In this paper, we will focus on studying the convergence properties of the ISS inversion subseries. The inversion only terms isolated from the inverse scattering series are

$$\alpha(z) = \alpha_1(z) - \frac{1}{2}\alpha_1^2(z) + \frac{3}{16}\alpha_1^3(z) + \cdots. \quad (10)$$

If the incidence angle is θ, Zhang (2006) showed that α_1 can be expressed as

$$\alpha_1(z) = 4R(\theta)\cos^2\theta H(z-a), \quad (11)$$

where R is the reflection coefficient, and H represents Heaviside function*. For the normal incidence case, we have $R = \frac{c_1-c_0}{c_1+c_0}$. When $z > a$,

$$\alpha_1 = 4R. \quad (12)$$

Substituting α_1 into equation (10), the ISS direct non-linear inversion subseries in terms of R can be written as

$$\alpha = 4R - 8R^2 + 12R^3 + \cdots = 4R\sum_{n=0}^{\infty}(n+1)(-R)^n. \quad (13)$$

After solving α, the inverted velocity $c(z)$ can be obtained through $c_1 = c_0/\sqrt{1-\alpha}$ (equation 8).

Considering the convergence property of the series of α or the inversion subseries, we can calculate the ratio test,

$$\left|\frac{\alpha_{n+1}}{\alpha_n}\right| = \left|\frac{(n+2)(-R)^{n+1}}{(n+1)(-R)^n}\right| = \left|\frac{n+2}{n+1}R\right|. \quad (14)$$

If $\lim_{n\to\infty}\left|\frac{\alpha_{n+1}}{\alpha_n}\right| < 1$, this subseries converges absolutely. That is

$$|R| < \lim_{n\to\infty}\frac{n+1}{n+2} = 1. \quad (15)$$

Therefore, the ISS direct non-linear inversion subseries converges when the reflection coefficient $|R|$ is less than 1, which is always true. Hence, for this example, the ISS inversion subseries will converge under any velocity contrasts between the two media.

For the iterative linear inversion, we will update the reference velocity $c_0' = c_0/\sqrt{1-\alpha_1}$ by using $\alpha_1 = 4R$. Then, the new linear inversion velocity is calculated by $\alpha_1' = 4R'$, where $R' = \frac{c_1-c_0'}{c_1+c_0'}$. The same procedure will be applied iteratively until we achieve the final inversion result.

ANALYTIC EXAMPLE

The rate of convergence of the estimated α or the ISS inversion subseries (equation 13) is analytically examined and studied for a 1D normal incidence case. Since α is always convergent when $R < 1$, the summation of this subseries is

$$\alpha = 4R\sum_{n=0}^{\infty}(n+1)(-R)^n = 4R\frac{1}{(1+R)^2}. \quad (16)$$

*The definition of Heaviside function is: $H(x) = \begin{cases} 0, & x < 0, \\ 1, & x \geq 0. \end{cases}$

If the error between the estimated and the actual α is monotonically decreasing, it means the subseries is a term-by-term added value improvement towards determining the actual medium properties. If this error is increasing before decreasing, it means that the estimation becomes worse before it gets better. In other words, the error for the first order and the error for the second order have the relation,

$$|\alpha - \alpha_1 - \alpha_2| > |\alpha - \alpha_1|, \tag{17}$$

i.e.,

$$|4R\frac{3R^2+2R^3}{(1+R)^2}| > |4R\frac{-R^2-2R}{(1+R)^2}|. \tag{18}$$

After simplification, it gives

$$R^2 + R - 1 > 0. \tag{19}$$

We can solve it and obtain the reflection coefficient $R < \frac{-1-\sqrt{5}}{2} = -1.618$ or $R > \frac{-1+\sqrt{5}}{2} = 0.618$. Therefore, when $R > 0.618$, the error increases first. Similarly, if the error for the third order is greater than that for the second order, we get $R > 0.667$; If the error for the fourth order is greater than that for the third order, we obtain $R > 0.721$. In summary, when $R > 0.618$ the error increases and the estimated α gets worse first. The green dash line in Figure 2 shows that when the reflection coefficient R is equal to 0.618, the error for the first order is equal to the error for the second order. The detail of the numerical tests will be discussed in the next section.

NUMERICAL TESTS

In this section, we will examine the convergence property and the rate of convergence of α by using the ISS inversion subseries (equation 13) and the iterative linear inversion methods to the velocity contrast in the 1D acoustic case. In addition, the inversion results by these two methods is discussed and compared.

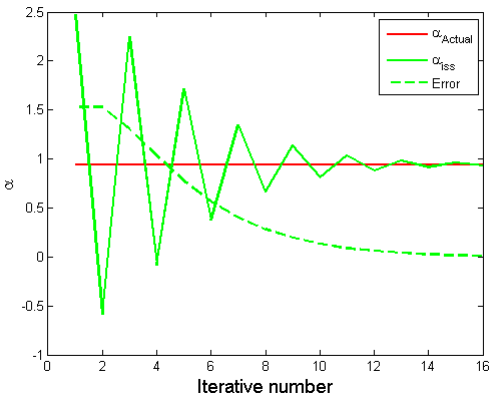

Figure 2: The error (green dash line) of estimated α at $R = 0.618$ and $\alpha = 0.9443$.

In the simple 1D model (Figure 1), only one parameter (velocity) varies and a plane wave propagates into the medium. There is only a single reflector and we assume the velocity is known above the reflector and unknown below the reflector. We will compare the convergence of the perturbation α and the inversion results by using the ISS direct non-linear method and the iterative linear method. With the reference velocity $c_0 = 1500m/s$, four analytic examples with different velocity contrasts for $c_1 = 2000$, 3000, 4500, $9000m/s$ are examined. In Figure 3, the red line represents the actual α that is calculated from our model for each velocity contrast. The horizontal axis represents the orders of the ISS inversion subseries or the iterative numbers. The vertical axis shows the value of α. The green solid line represents the estimated value of α through the ISS inversion method verse the summation of α_n to n^{th} order. The green dash line represents the absolute value of the error between the ISS estimated and the actual value of α. The blue solid line represents the estimated value of α through the iterative inversion method verse the iterative numbers. The blue dash line represents the absolute value of the error between the iterative estimated and the actual value of α.

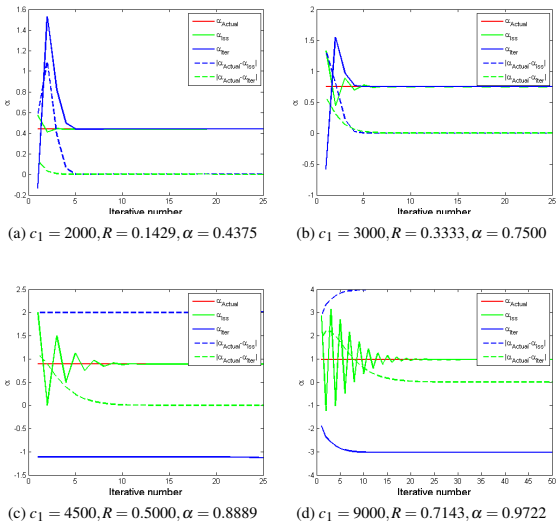

(a) $c_1 = 2000, R = 0.1429, \alpha = 0.4375$ (b) $c_1 = 3000, R = 0.3333, \alpha = 0.7500$

(c) $c_1 = 4500, R = 0.5000, \alpha = 0.8889$ (d) $c_1 = 9000, R = 0.7143, \alpha = 0.9722$

Figure 3: The estimated α: The horizontal axis is the orders of the ISS suberies or the iterative numbers, and the vertical axis shows the value. The red line shows the actual value of α. The green and blue lines show the estimations of α by using the ISS inversion method and the iterative inversion method. The green and blue dash lines are their corresponding absolute difference between the actual value and the estimations.

From the estimated results of α for the different velocity contrasts, we can see that the smaller the contrast, the faster the inversion results will converge as shown in Figure 3. In other words, when the velocity contrast increases, the error of α estimation increases, therefore it takes more terms to deal with the bigger contrast issue as shown in Figure 3d. Another important point is, when the velocity contrast is getting bigger, at some point, the iterative inversion method is not convergent (see the blue solid and dash lines in Figures 3c and 3d). From the analysis, the iterative inversion method can not estimate the

correct inversion result when $R > 0.5$, while the ISS inversion method always produces useful results (see the green solid and dash lines in Figures 3c and 3d). For the simple 1D one reflector example, it shows that the ISS direct non-linear inversion subseries converges for all values of R. Comparing the errors of α (green and blue dash lines in Figures 3a and 3b) by the ISS inversion method and the iterative method, we can see that at small contrast, both methods converge and the ISS inversion method converges faster than the iterative inversion method.

From the green dash line in Figure 3, for a small contrast, the error between the estimated and the actual α is monotonically decreasing, in other words, the estimation of α is always a term-by-term added value improvement towards determine c_1; when the contrast is very large (Figure 3d), the error is increasing before decreasing. It means that the estimation of α becomes worse before it gets better. However, when it starts to add value, it getting better when each further term added to the series. The green dash line in Figure 3 also shows that as more terms are captured and added up, the error always approaches zero, which means the correct estimation is always achieved. Figures 3a, 3b and 3c show that when the reflection coefficient R is smaller than 0.618, this inversion subseries is monotonically term-by-term added value improvement towards determining c_1. When the reflection coefficient R is equal to 0.618, the error for the first order equals the error for the second order as shown in Figure 2. When the reflection coefficient is larger than 0.618 (Figure 3d), the series still converges, but the estimation of α will become worse before it gets better. From the analytic and numerical examples, we can see that each term in the series works towards the final goal. Sometimes when more terms in the series are included, the estimation looks worse locally, but once it starts to improve the estimation at a specific order, the approximations never become worse again, every single term after that order will produce an improved estimation.

The convergence results are also presented for the velocity estimation as shown in Figure 4. At small velocity contrast, both methods are convergent very fast and estimate the correct velocity (Figures 4a and 4b). When the contrast increases, the ISS inversion subseries always converges, but the iterative inversion method does not converge (Figures 4c and 4d).

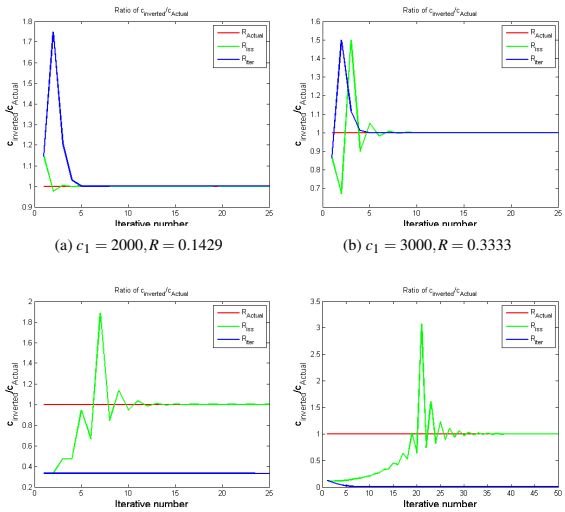

(a) $c_1 = 2000, R = 0.1429$ (b) $c_1 = 3000, R = 0.3333$

(c) $c_1 = 4500, R = 0.5000$ (d) $c_1 = 9000, R = 0.7143$

Figure 4: The ratio of the estimated velocity and the actual velocity: The horizontal axis is the order of the ISS suberies or the iterative numbers, and the vertical axis shows the value. The red line is the actual ratio, which is 1. The green and blue lines show the ratios by using the ISS inversion method and the iterative inversion method.

CONCLUSIONS

The ISS direct non-linear inversion and the iterative inversion are examined and compared in a 1D, one parameter, and a single horizontal reflector case, where the velocity is assumed to be known above the reflector and unknown below the reflector. The rate of convergence of the ISS inversion method is analytically and numerically studied. From the analytic example, we show that when the reflection coefficients $R < 0.618$, the ISS inversion subseries is a term-by-term improvement towards determining medium properties; when $R > 0.618$, the inversion subseries still converges, but the estimation will locally be less accurate before it converges. Numerical results show that when the velocity contrasts are small, i.e., the reflection coefficients are small, both inversion methods converge and the ISS inversion method converges faster than the iterative inversion method. When velocity contrasts increase, the reflection coefficients get larger, the iterative inversion method will not converge when $R > 0.5$, while the ISS inversion method still converges. Hence, for the simplest situation, the iterative linear inversion is not equivalent to the direct non-linear solution provided by the inverse scattering series. For more complicated circumstances (e.g., the elastic non-normal incidence case), the difference is much greater, not just on the algorithms, but also on data requirements and on how the band-limited noisy nature of the seismic data impact the inverse operators in iterative linear inversion but not in the ISS direct inversion.

ACKNOWLEDGMENTS

We are grateful to all M-OSRP sponsors for long-term encouragement and support in this research.

REFERENCES

Carvalho, P. M., 1992, Free-surface multiple reflection elimination method based on nonlinear inversion of seismic data: PhD thesis, Universidade Federal da Bahia.

Li, X., 2014, I. multi-parameter depth imaging using the inverse scattering series; ii. multi-component direct nonlinear inversion for elastic earth properties using the inverse scattering series: PhD thesis, University of Houston.

Shaw, S. A., A. B. Weglein, D. J. Foster, K. H. Matson, and R. G. Keys, 2004, Isolation of a leading order depth imaging series and analysis of its convergence properties: Journal of Seismic Exploration, **2**, 157–195.

Weglein, A. B., 2015, Direct inversion and FWI: Invited keynote address given at the SEG Workshop Full-waveform Inversion: Fillings the Gaps, Abu Dhabi, UAE. (Available at http://mosrp.uh.edu/events/event-news/arthur-b-weglein-will-present-an-invited-key-note-address-on-direct-inversion-at-the-seg-workshop-on-fwi-30-march-1-april-2015-in-abu-dhabi-uae).

Weglein, A. B., F. V. Araújo, P. M. Carvalho, R. H. Stolt, K. H. Matson, R. T. Coates, D. Corrigan, D. J. Foster, S. A. Shaw, and H. Zhang, 2003, Inverse scattering series and seismic exploration: Inverse Problems, **19**, R27–R83.

Weglein, A. B., H. Zhang, A. C. Ramírez, F. Liu, and J. E. M. Lira, 2009, Clarifying the underlying and fundamental meaning of the approximate linear inversion of seismic data: Geophysics, **74**, WCD1–WCD13.

Zhang, H., 2006, Direct nonlinear acoustic and elastic inversion: towards fundamentally new comprehensive and realistic target identification: PhD thesis, University of Houston.

Zhang, H., and A. B. Weglein, 2006, Direct non-linear inversion of multi-parameter 1d elastic media using the inverse scattering series: 76th International Annual Meeting, SEG, Expanded Abstracts, 284–311.